LBL-18635
UC-34

NUCLEAR SCIENCE DIVISION

TWO-WEEK LOAN COPY

This is a Library Circulating Copy which may be borrowed for two weeks.

ANNUAL REPORT

1983–1984

RECEIVED
LAWRENCE
BERKELEY LABORATORY
MAY 22 1985
LIBRARY AND
DOCUMENTS SECTION

May 1985

Lawrence Berkeley Laboratory
University of California

Prepared for the U.S. Department of Energy under Contract DE-AC03-76SF00098

LBL-18635

DISCLAIMER

This document was prepared as an account of work sponsored by the United States Government. While this document is believed to contain correct information, neither the United States Government nor any agency thereof, nor the Regents of the University of California, nor any of their employees, makes any warranty, express or implied, or assumes any legal responsibility for the accuracy, completeness, or usefulness of any information, apparatus, product, or process disclosed, or represents that its use would not infringe privately owned rights. Reference herein to any specific commercial product, process, or service by its trade name, trademark, manufacturer, or otherwise, does not necessarily constitute or imply its endorsement, recommendation, or favoring by the United States Government or any agency thereof, or the Regents of the University of California. The views and opinions of authors expressed herein do not necessarily state or reflect those of the United States Government or any agency thereof or the Regents of the University of California.

LBL 18635

Nuclear Science Division

Annual Report for the Period
October 1, 1983 – September 30, 1984

Division Head
Joseph Cerny

Assistant Division Head
Janis Dairiki

Editor
Jeannette Mahoney

Editorial Committee
R.M. Diamond, J.O. Rasmussen, W.J. Świątecki

Lawrence Berkeley Laboratory
University of California
Berkeley, California, 94720, USA

This work was supported by the Director, Office of Energy Research, Office of High Energy and Nuclear Physics, Division of Nuclear Physics and by the Office of Basic Energy Sciences, Division of Nuclear Sciences, of the U.S. Department of Energy under Contract No. DE-AC03-76SF00098

Acknowledgements

This Annual Report (as well as the two previous Annual Reports) was printed from galleys from a phototypesetter driven by the LBL UNIX Version 7 computer system. Each contribution was stored as a UNIX file. Some contributions were entered and edited by the authors on the VAX computers used in their experiments, then mailed electronically to me. The rest were keyed directly from the NSD office into a UNIX directory from which I retrieved them. UNIX routines enabled me to edit and assemble the files in the order agreed on by the editorial advisory committee; format the text, equations and tables in single- and two-column page layouts, leaving appropriate spaces for the figures; then, using Troff, obtain numbered galleys from the typesetter in exact page layout, eliminating the need for cutting and pasting. I wish to thank all the many people at the computer center who have given me much needed help in using the system, and I particularly wish to express my appreciation of the excellent typesetter simulation code which produces printouts on the Versatec printer with line and page breaks exactly as they will appear from the typesetter, making it possible to proof "galleys" *before* they go through the typesetter. I appreciate the support of the Technical Information Department in general for handling the typeset galleys, supplying and inserting the figures, and arranging for the printing; and in particular for the individual efforts of those who gave help with the typesetter coding and the early transferring of files to UNIX and who provided the excellent editorial assistance that made the final preparations for the printer go so smoothly. Finally, I would like to thank NSD office staff members Paula Rodriquez, the Report Librarian, who has collected, organized and maintains on a Wang word processor all the material which constitute Appendices I–III, which she sent me as computer files, and Paula Conant who keyed in most of the text.

Editor

Cover: View inside the plasma chamber of the electron cyclotron resonance (ECR) ion source showing the copper sleeves of the permanent magnet octupole and the four-fold symmetry of the plasma on the extraction plate.

BBC 847-4935

Introduction

This report presents the activities of the Nuclear Science Division during the period of October 1, 1983 to September 30, 1984. Experimental research for the most part was done using the beams of the three LBL accelerators, the Bevalac, the SuperHILAC and the 88-Inch Cyclotron, often in collaboration with teams from the United States and other countries. Expansion of detector capabilities, improvements in experimental facilities and development of innovative techniques, coupled with the close interaction between experimental and theoretical research groups, have led to greater understanding of processes under investigation and opened exciting new areas of research.

Bevalac experiments using the Plastic Ball/Wall and the Streamer Chamber have provided the first information about the equation of state of nuclear matter at high densities. Streamer Chamber studies of pion and proton spectra from central collisions have yielded new insights into pion formation. Studies of charged pion production, using a spectrometer nearly unique in its ability for 0° and small angle pion spectroscopy, have produced surprising information on the shapes of pion source regions. Analyses of radiochemical survey measurements have demonstrated the general success of the nuclear firestreak model. Beams of unstable nuclei have been used to form ^{19}B and to measure the interaction cross sections of four He isotopes. Results from a prototype detector used to study the problem of delta rays produced by the interaction of fast heavy nuclei with other media have inspired improvements that will enhance the versatility of the HISS facility. Pion studies at TASS have ended, to be replaced initially by electron production studies when the conversion to a di-lepton spectrometer is completed.

The newly begun operation of the electron cyclotron resonance (ECR) source at the 88-Inch Cyclotron has dramatically increased the intensity and stability of heavy ion beams. Studies there and at the SuperHILAC of intermediate energy heavy ion reaction mechanisms are providing a clear picture of the transition from small particle evaporation to fission. The acquisition of 15 of the 21 planned Compton-suppressed Ge detectors for the BGO ball has greatly extended the scope and sensitivity of nuclear structure investigations of high spin states, and Coulomb-excitation data fitted with a University of Rochester code appear likely to resolve some conflicting theoretical predictions on band coupling strengths.

Two new Ra isotopes decaying by ^{14}C emission have been found, as well as several new β-delayed proton emitters, providing material for investigations of these decay mechanisms, in addition to the ongoing study of β-delayed two-proton decay.

At the Bevalac Users' Meeting in May, 1984 workshops were held on computer needs, low energy experiments and the physics of the next 4π detector. An extensive study was conducted in 1983 on the physics to be extracted from a mini collider and the machine parameters and detector requirements for such a collider, and in March, 1984 a workshop to design future high energy heavy ion detectors was attended by over 100 nuclear physicists from around the country and abroad.

The report is divided into 5 sections. Part I describes the research programs and operations, and Parts II and III contain condensations of papers on experiment and theory, respectively, arranged roughly according to program and in order of increasing energy, without any further subdivisions. Improvements and innovations in instrumentation and in experimental or analytical techniques are presented in Part IV. Part V consists of appendices, the first listing publications by author for this period, in which the LBL report number only is given for papers that have not yet appeared in journals; the second contains abstracts of PhD theses awarded during this period; and the third gives the titles and speakers of the NSD Monday seminars, the Bevatron Research Meetings and the theory seminars that were given during the report period. The last appendix is an author index for this report.

Joseph Cerny

PART I: PROGRAMS

Exotic Decay Modes 1

Heavy Element Radiochemistry 2

New Element and Isotope Synthesis 3

Isotopes Project 5

Polarization Phenomena in Nuclear Physics 7

Nuclear Structure Studies at High Angular Momentum 8

Heavy Ion Reactions at Non-Relativistic Energies 10

Damped Nuclear Reactions and Compound Nucleus Studies 12

Relativistic Nuclear Collisions:

- Interactions in Emulsions 14
- Nucleus-Nucleus Collisions 16
- Light Particle Studies 18
- Pion and Correlation Studies 20
- Search for New States of Matter 22
- The Plastic Ball 23
- TASS 24
- Streamer Chamber 26

Nuclear Theory 28

Bevalac Computer Support Group 32

The Berkeley Mini-Collider 33

Workshop on Detectors for Relativistic Nuclear Collisions 38

88-Inch Cyclotron Operations 40

PART II: EXPERIMENT

Beta-delayed Two-proton Decay of ^{22}Al and ^{26}P 45
M.D. Cable, J. Honkanen, E.C. Schloemer, M. Ahmed, J.E. Reiff, Z.Y. Zhou, and Joseph Cerny

Additional Beta-delayed Protons from the $T_z = -3/2$ Nuclei ^{21}Mg, ^{25}Si, ^{29}S, and ^{41}Ti 46
Z.Y. Zhou, E.C. Schloemer, M.D. Cable, M. Ahmed, J.E. Reiff and Joseph Cerny

Angular Correlations in the Beta-delayed Two-Proton Decay of ^{22}Al 48
R. Jahn, R.L. McGrath, D.M. Moltz, J.E. Reiff, X.J. Xu, J. Äystö, and Joseph Cerny

Discovery of Radioactive Decay of ^{222}Ra and ^{224}Ra by ^{14}C Emission 49
P.B. Price, J.D. Stevenson, S.W. Barwick and H.L. Ravn

Radioactive Decay of ^{223}Ra by ^{14}C Emission 51
S. Yashita, K. Gregorich and A. Ghiorso

The Decay of ^{248}Es 52
Wen Xin Li, K.E. Gregorich, R.B. Welch, W. Kot, D. Lee, and G.T. Seaborg

The Decay of ^{250}Fm 54
W.P. Kwan, K.E. Gregorich, Wen Xin Li, D. Lee, R.B. Welch, W. Kot and G.T. Seaborg

Actinide Production in the ^{136}Xe + ^{249}Cf Reaction 54
K.E. Gregorich, R.B. Welch, W. Kot, D. Lee, K.J. Moody and G.T. Seaborg

Potential Energy Surfaces for Xe + Cm Reactions 55
R.B. Welch, K.J. Moody, D. Lee, K.E. Gregorich, W. Kot and G.T. Seaborg

Excitation Functions for Production of Heavy Actinides from Interactions of ^{40}Ca and ^{48}Ca Ions with ^{248}Cm 57
D.C. Hoffman, M.M. Fowler, W.R. Daniels, H.R. von Gunten, D. Lee, K.J. Moody, K. Gregorich, R. Welch, G.T. Seaborg, W. Brüchle, M. Brügger, H. Gäggeler, M. Schädel, K. Sümmerer, G. Wirth, Th. Blaich, G. Herrmann, N. Hildebrand, J.V. Kratz, M. Lerch, and N. Trautmann

First Observation of the Neutron-Rich Isotope ^{19}B 58
J.A. Musser and J.D. Stevenson

Measurements of Interaction Cross Sections and Radii of He Isotopes 59
I. Tanihata, O. Yamakawa, H. Hamagaki, O. Hashimoto, S. Nagamiya, Y. Shida, N. Yoshikawa, K. Sugimoto, T. Kobayashi, D. Greiner, N. Takahashi, and Y. Nojiri

Recent Experimental Results from OASIS 61
P.A. Willmarth, J.M. Nitschke, P.K. Lemmertz and R.B. Firestone

Radioactivity Handbook 63
R.B. Firestone and E. Browne

Analyzing Power Measurements for ^{3}He ($\vec{p}$,p) ^{3}He Elastic Scattering between 20 and 50 MeV 66
J. Birchall, W. t. H. van Oers, J.W. Watson, H.E. Conzett, R.M. Larimer, B. Leemann, E.J. Stephenson, P. von Rossen, and R.E. Brown

Spin-Polarization Effects in the ^{3}H(d,n)^{4}He Fusion Reaction 67
H.E. Conzett and C. Rioux

Polarization Transfer in p-^{16}O Elastic Scattering 68
H.E. Conzett, C. Rioux, F.S. Dietrich and N.L. Back

Deuteron Reactions and Vector Polarization 69
H.E. Conzett

Quadrupole Collectivity and the Shapes of Os-Pt Nuclei 71
C.Y. Wu, D. Cline, A. Backlin, T. Chaki, T. Czosnyka, L. Hasselgren, B. Kotlinski, P. Russo, J.K. Sprinkle, J. Srebrny, I.Y. Lee, P.A. Butler, R.M. Diamond, H. Kluge, R.S. Simon, F.S. Stephens, C. Baktash, G. Dracoulis, J. Leigh, J.O. Newton, W.R. Phillips, and S. Sie

Spin Precession of Unresolved High-Spin States in $^{153\text{-}156}$Dy 73
O. Häusser, D. Ward, H.R. Andrews, P. Taras, B. Haas, M.A. Deleplanque, R.M. Diamond, E.L. Dines, A.O. Macchiavelli, R. McDonald, F.S. Stephens, and C.V. Stager

Mass Dependence of Shell Effects at High Rotational Frequencies 75
A.O. Macchiavelli, H. Muehry, M.A. Deleplanque, R.M. Diamond, F.S. Stephens, E.L. Dines and J.E. Draper

Angular Velocity: A New Dimension in Nuclei 76
R.M. Diamond and F.S. Stephens

Shapes and Alignments at High Spin in Some Rare-Earth Nuclei 77
M.A. Deleplanque, R.M. Diamond, F.S. Stephens, A.O. Macchiavelli, Th. Døssing, J.E. Draper and E.L. Dines

Neutron Transfer Reactions with Very Heavy Ions 78
A.O. Macchiavelli, M.A. Deleplanque, R.M. Diamond, F.S. Stephens, E.L. Dines and J.E. Draper

Evidence for Shape Polarization From the Emission of Complex Fragments by Compound Nuclei 81
G.J. Wozniak, M.L. Padgett, L.G. Sobotka, M.A. McMahan, C. Signarbieux, J.H. Gu, Z.H. Liu, Z.Q. Yao and L.G. Moretto

Sequential Fission Angular Distributions from Mass-Asymmetric Heavy Ion Reactions 82
D.J. Morrissey, G.J. Wozniak, L.G. Sobotka, R.J. McDonald, A.J. Pacheco and L.G. Moretto

Symmetric Splitting of Very Light Systems 84
K. Grotowski, Z. Majka, R. Płaneta, M. Szczodrak, Y. Chan, G. Guarino, L.G. Moretto, D.J. Morrissey, L.G. Sobotka, R.G. Stokstad, I. Tserruya, S. Wald and G.J. Wozniak

Mass Asymmetric Barriers from Excitation Functions for Complex Fragment Emission 86
M.A. McMahan, L.G. Sobotka, L.G. Moretto, M.L. Padgett, G.J. Wozniak and M.G. Mustafa

Complete Mass Distributions in C.M. Decay, and the Role of the Businaro-Gallone Point 88
L.G. Moretto and L.G. Sobotka

Compound Nucleus Decay Along the Mass Asymmetry Coordinate and the Role of the Businaro-Gallone Point 89
L.G. Sobotka, M.A. McMahan, R.J. McDonald, C. Signarbieux, G.J. Wozniak, M.L. Padgett, J.H. Gu, Z.H. Liu, Z.Q. Yao and L.G. Moretto

The Businaro-Gallone Transition as Observed in Complete Charge Distributions from Compound Nucleus Decay 91
L.G. Moretto, G.J. Wozniak and L.G. Sobotka

Use of Reverse Kinematics in the Identification of Large Fragments Evaporated by Compound Nuclei 91
L.G. Sobotka, M.A. McMahan, R.J. McDonald, C. Signarbieux, G.J. Wozniak, M.L. Padgett, J.H. Gu, Z.H. Liu, Z.Q. Yao and L.G. Moretto

Range-Energy Relation for Heavy Ion Inertial Fusion 93
H.R. Bowman, H.H. Heckman, Y.J. Karant, J.O. Rasmussen, A.I. Warwick and Z.Z. Xu

Ho Target Fragmentation Induced by Intermediate Energy ^{12}C and ^{16}O 94
J.H. Kraus, Jr., W. Loveland and G.T. Seaborg

La Target Fragmentation Induced by High Energy La and U Ions 95
Li Wenxin, W. Loveland, K. Aleklett, P.L. McGaughey and G.T. Seaborg

Collective Flow Observed in Relativistic Nuclear Collisions 96
H.A. Gustafsson, H.H. Gutbrod, B. Kolb, H. Löhner, B. Ludewigt, A.M. Poskanzer, T. Renner, H. Riedesel, H.G. Ritter, A. Warwick, and H. Wieman

Observation of Radiative Capture in Relativistic Heavy Ion Collisions 98
R. Anholt, S.A. Andriamonje, E. Morenzoni,, Ch. Stoller, J.M. Molitoris, W.E. Meyerhof, H. Bowman, J.-S. Xu, Z.-Z. Xu, J.O. Rasmussen and D.H.H. Hoffman

Freezeout Density In Relativistic Nuclear Collisions Measured by Proton-Proton Correlations 100
H.A. Gustafsson, H.H. Gutbrod, B. Kolb, H. Löhner, B. Ludewigt, A.M. Poskanzer, T. Renner, H. Riedesel, H.G. Ritter, A. Warwick, and H. Wieman

Measurement of Pions and Light Fragments in 0.8 GeV/nucleon La + La Collisions 101
Y. Miake, H. Hamagaki, X.X. Bai, O. Hashimoto, K. Kimura, T. Kobayashi, G. Shapiro, Y. Shida, I. Tanihata and S. Nagamiya

Production Mechanism of Backward Energetic Protons Studied From Two-Particle Correlations in 800 MeV Proton-Nucleus Collisions 102
Y. Miake, H. Hamagaki, S. Kadota, S. Nagamiya, S. Schnetzer, Y. Shida, H. Steiner and I. Tanihata

Pion Spectra at 0 Degrees in Coincidence with Projectile Fragments in 800 MeV/nucleon $^{139}_{57}$La Induced Reactions 103
O. Hashimoto, J.A. Bistirlich, K.M. Crowe, H. Hamagaki, T.J. Humanic, T. Kobayashi, S. Nagamiya, K. Nakayama, J.O. Rasmussen, Y. Shida, I. Tanihata, O. Yamakawa and N. Yoshikawa

Stopping Power and Collective Flow of Nuclear Matter in the Reaction Ar + Pb at 0.8 GeV/nucleon 105
R.E. Renfordt, D. Bangert, R. Brockmann, J.W. Harris, G. Odyniec, H.G. Pugh, W. Rauch, A. Sandoval, R. Stock, H. Ströbele, D. Schall, and L.S. Schroeder

Uranium Target Fragmentation by Intermediate and High Energy ^{12}C and ^{20}Ne 107
P.L. McGaughey, W. Loveland, D.J. Morrissey, K. Aleklett and G.T. Seaborg

Midrapidity Pion Production in 1.05 GeV/nucleon ^{40}Ca + ^{40}Ca Collisions 108
J.W. Harris, R. Brockmann, K.L. Wolf, E.K. Jackson, J. Miller, H.G. Pugh, P. Renteln, G. Roche, L.S. Schroeder, R.N. Treuhaft, G. Krebs and P. Kirk

Composite Particles and Entropy Production in Relativistic Nuclear Collisions 110
H.-A. Gustafsson, K.G.R. Doss, H.H. Gutbrod, B. Kolb, H. Löhner, B. Ludewigt, A.M. Poskanzer, T. Renner, H. Riedesel, H.G. Ritter, A. Warwick and H. Wieman

^{197}Au Target Fragmentation Induced by 1.8 GeV/nucleon ^{40}Ar 112
Li Wenxin, W. Loveland, K. Aleklett, and G.T. Seaborg

Unusual Behavior of Projectile Fragments Formed in the Bombardment of Copper with Relativistic Ar Ions 113
G. Dersch, R. Beckmann, G. Feige, T. Lund, P. Vater, R. Brandt, E. Ganssauge, K. Aleklett, E.M. Friedlander, P.L. McGaughey, G.T. Seaborg, W. Loveland, J. Herrmann, and N.T. Porile

Charge-changing Reactions of Secondary Fragments Produced in High-Energy Heavy Ion Collisions 115
T.J.M. Symons, M. Baumgartner, H.J. Crawford, J.P. Dufour, J. Girard, D.E. Greiner, P.J. Lindstrom, and D.L. Olson

Two-pion Correlations in Heavy Ion Collisions 117
W.A. Zajc, J.A. Bistirlich, R.R. Bossingham, H.R. Bowman, C.W. Clawson, K.M. Crowe, K.A. Frankel, J.G. Ingersoll, J.M. Kurck, C.J. Martoff, D.L. Murphy, J.O. Rasmussen, J.P. Sullivan, E. Yoo, O. Hashimoto, M. Koike, W.J. McDonald, J.P. Miller and P. Truöl

Pion Production as a Probe of the Nuclear Matter Equation of State 120
J.W. Harris, R. Stock, R. Bock, R. Brockmann, A. Sandoval, H. Ströbele, G. Odyniec, H.G. Pugh, L.S. Schroeder, R.E. Renfordt, D. Schall, D. Bangert, W. Rauch and K.L. Wolf

Strange Particle Production in Central ^{40}Ca + ^{40}Ca Collisions 121
R.E. Renfordt, D. Bangert, R. Brockmann, A. Dacal, J.W. Harris, G. Odyniec, M. Ortiz, H.G. Pugh, W. Rauch, A. Sandoval, L.S. Schroeder, R. Stock, H. Ströbele, and D. Schall

Pion and Proton "Temperatures" in Relativistic Heavy Ion Collisions. 124
R. Brockmann, D. Bangert, J.W. Harris, G. Odyniec, H.G. Pugh, W. Rauch, R.E. Renfordt, A. Sandoval, D. Schall, L.S. Schroeder, R. Stock, H. Ströbele, and K.L. Wolf

Search for Fractionally Charged Nuclei in High-Energy Heavy Ion Collisions 125
S.W. Barwick, J.A. Musser and J.D. Stevenson

Search for Production of Fractional Charges, Rare Long-Lived Particles and Subthreshold Antiprotons in Relativistic Heavy Ion Collisions 127
S. Abachi, J. Carroll, A. Shor, E. Barasch, G. Igo, T. Mulera, P. Fisher, V. Perez-Mendez, S. Trentalange, K. Ganezer and F. Kazeminezhad

Subthreshold K^- Momentum Spectrum for Relativistic Nuclear Collisions 129
E. Barasch, A. Shor, S. Abachi, J. Carroll, P. Fisher, K. Ganezer, G. Igo, T. Mulera, V. Perez-Mendez, and S. Trentalange

Electron Pair Production Study Using the Di-Lepton Spectrometer (DLS) 130
G. Roche, J.B. Carroll, G. Claesson, R.L. Fulton, J.-F. Gilot, T.J. Hallman, D.L. Hendrie, G. Igo, P.N. Kirk, G. Krebs, L. Madansky, H. Matis, D. Miller, J. Miller, T.A. Mulera, V. Perez-Mendez, H.G. Pugh, L.S. Schroeder and S. Trentalange

Direct Electron Production 131
J. Carroll, G. Claesson, J.F. Gilot, T. Hallman, D. Hendrie, G. Igo, P.N. Kirk, G. Krebs, F. Luehring, L. Madansky, H. Matis, J. Miller, D. Miller, T. Mulera, V. Perez-Mendez, H. Pugh, G. Roche, L. Schroeder, A. Shor, S. Trentalange

PART III: THEORY

Calculated Masses and Decay Properties for the Heaviest Elements 135
G.A. Leander, P. Möller, J.R. Nix and W.M. Howard

Nuclear Mass Formula with a Neutron Skin Degree of Freedom and Finite-Range Model for the Surface Energy 137
P. Möller and W.D. Myers

The Surface Energy of Multi-Component Systems 138
W.D. Myers, W.J. Świątecki and C.S. Wang

Surface and Curvature Properties of Neutron-Rich Nuclei 139
K. Kolehmainen, M. Prakash, J. Lattimer and J. Treiner

Finite Range Droplet Model 142
P. Möller, W.D. Myers, W.J. Świątecki and J. Treiner

Bulk Compression Due to Surface Tension in Hartree-Fock Calculations 143
J. Treiner, W.D. Myers, W.J. Świątecki and M.S. Weiss

Theoretical Estimates of the Rates of Radioactive Decay of Radium Isotopes by ^{14}C Emission 144
Y.-J. Shi and W.J. Świątecki

Estimates of Radioactive Decay by the Emission of Nuclei Heavier than Alpha Particles 145
Y.-J. Shi and W.J. Świątecki

A Microscopic Model of Fragment Yields in Nucleus-nucleus Collisions 145
B.G. Harvey

Two-center Shell Model for Deep Inelastic Collisions of Heavy Ions 148
Shi Yi-jin and J. Randrup

Symmetric Splitting of Very Light Systems in the Coalescence and Reseparation Model 149
J. Blocki, K. Grotowski, R. Planeta and W.J. Świątecki

Macroscopic Treatment of Nuclear Dynamics 149
W.J. Świątecki

Dissipative Resistance Against Changes in the Mass Asymmetry Degree of Freedom in Macroscopic Nuclear Dynamics: The Completed Wall-and-Window Formula 150
J. Randrup and W.J. Świątecki

A Simple Treatment of Fermi Jets 150
K. Möhring, W.J. Świątecki and M. Zielińska-Pfabé

One Body-Dynamics and Angular Momentum Dissipation in Damped Nuclear Reactions 151
T. Døssing and J. Randrup

The Role of Rotational Degrees of Freedom in Heavy Ion Collisions 153
L.G. Moretto and G.J. Wozniak

A Feedback Process Controlling Energy Partition and Mass Exchange Between Heavy Ions 154
L.G. Moretto and E.G. Lanza

Pion Interferometry Studies of Relativistic Heavy-Ion Collisions Using the Intranuclear Cascade Model 154
T.J. Humanic

Behavior of Pions Incident on a Slab of Uniform Complex Nuclear Material 157
R.A. Mehrem, H.M.A. Radi and J.O. Rasmussen

Note on the Partitioning of Nuclei 159
L.G. Sobotka and L.G. Moretto

Transverse Momentum Analysis of Collective Motion in Relativistic Nuclear Collisions 161
P. Danielewicz and G. Odyniec

Transport Properties of Excited Nuclear Matter and the Shock-Wave Profile 163
P. Danielewicz

Nuclear Compression Effects on Pion Production in Nuclear Collisions 164
M. Gyulassy, Y. Kitazoe, M. Sano and M. Wakai

Nuclear Stopping Power 166
S. Date, M. Gyulassy and H. Sumiyoshi

Dissipative Phenomena in Quark-Gluon Plasmas 167
P. Danielewicz and M. Gyulassy

Signatures of Quark-Gluon Plasma Production 168
M. Gyulassy

Phase Transitions in a Saturating Chiral Theory of Nuclear Matter 170
Norman K. Glendenning

Supernovae and the Nuclear Equation of State at High Densities 177
E. Baron, J. Cooperstein and S. Kahana

Successful Supernovae, the Anatomy of Shocks, Neutrino Emission and the Adiabatic Index 177
S. Kahana, E. Baron and J. Cooperstein

The Lee-Wick Abnormal Phase Transition 178
Norman K. Glendenning

On the Hydrodynamic Evolution of Quark-Gluon Plasma Produced by Ultrarelativistic Nuclear Collisions 180
N.K. Glendenning and T. Matsui

Relativistic Particle in Periodic Square Potential 185
B. Banerjee, N.K. Glendenning, and V. Soni

Kaons and Quark-Gluon Plasma 186
Norman K. Glendenning and Johann Rafelski

Rapidity Density Fluctuations 190
E.M. Friedlander

Inelasticity Distribution and its Implications for Many-Particle Production Processes 191
G.N. Fowler, E.M. Friedlander, M. Plümer and R.M. Weiner

PART IV: INSTRUMENTATION AND METHODS

The ECR Ion Source for the 88-Inch Cyclotron 195
C.M. Lyneis, L. Brown, D.J. Clark, D. Elo, Y. Jongen, R. Lam, D. Morris and R. Peterson

Prospects for Research with Radioactive Beams at LBL 197
J.M. Nitschke

Computer Simulation of an Electron-Beam-Generated Plasma Ion Source 198
J.M. Nitschke, P.K. Lemmertz and R. Babala

Study of Transfer and Breakup Reactions with the Plastic Box 200
R.G. Stokstad, S.B. Gazes, C.R. Albiston, M. Bantel, Y. Chan, P.J. Countryman, B.G. Harvey, H. Homeyer, M.J. Murphy, I. Tserruya, K. Van Bibber and S. Wald

Charge Measurements of Stopping High-Z Nuclei ($6 \leqslant Z \leqslant 97$) in Nuclear Emulsion 203
M.T. Ghoniem, H.H. Heckman, E.M. Friedlander and Y.J. Karant

Observation of Strong Azimuthal Asymmetry Between Slow and Fast Secondaries in High Energy Nuclear Collisions in the Plastic Ball 204
H.A. Gustafsson, H.H. Gutbrod, B. Kolb, H. Löhner, B. Ludewigt, A.M. Poskanzer, T. Renner, H. Riedesel, H.G. Ritter, T. Siemiarczuk, J. Stepaniak, A. Warwick and H. Wieman

The High Resolution Ball 205
R.M. Diamond, F.S. Stephens, M.A. Deleplanque, M.K. Lee and R.A. Belshe

A Čerenkov Detector for Heavy Ion Velocity Measurements 207
M. Baumgartner, H.J. Crawford, J.P. Dufour, J.D. Girard, D.E. Greiner, P.J. Lindstrom, D.L. Olson and T.J.M. Symons

Prototype Drift Chamber for High Energy Heavy Ions with a Large Dynamic Range 209
T. Kobayashi, F. Bieser, H. Crawford, P. Lindstrom, M. Baumgartner and D. Greiner

Improvements in the Bevalac Computing Facility 209
Charles McParland

First Measurements with a Forward Scintillator Hodoscope at the Streamer Chamber Facility. 210
R. Brockmann, W. Rauch, R. Renfordt, D. Bangert, A. Dacal, J.W. Harris, G. Odyniec, M. Ortiz, H.G. Pugh, A. Sandoval, L.S. Schroeder, R. Stock, H. Ströbele, and D. Schall

Use of a Digitizing Tablet as an On-line Input Device in Analyzing Streamer Chamber Photographs 211
G. Odyniec, D. Bangert, R. Brockmann, J.W. Harris, M. Maier, R.E. Renfordt, H.G. Pugh, W. Rauch, A. Sandoval, R. Stock, H. Ströbele, D. Schall, L.S. Schroeder, and K.L. Wolf

PART V: APPENDICES

Publications Appendix I

Theses Appendix II

Seminars Appendix III

Author Index Appendix IV

Exotic Decay Modes

Studies of nuclei far from the valley of stability can provide tests of the theoretical models which predict the existence, masses, and shapes of exotic nuclei. Additionally, these studies may reveal new modes of radioactive decay as well as develop new spectroscopic data on nuclides with unusual neutron to proton ratios. Exotic nuclei which are expected to define the proton drip line in the light mass region have been produced in low yield reactions at the 88-Inch Cyclotron. Two such nuclei are ^{22}Al and ^{26}P.

Both ^{22}Al and ^{26}P are odd-odd $T_z = -2$ nuclei and both have been produced via the (^{3}He,p4n) reaction at 110 MeV on ^{24}Mg and ^{28}Si targets, respectively. So far, these are the only two isotopes known to exhibit the beta-delayed two-proton mode of radioactivity. Initial studies of the yield of coincident protons at both narrow (~40°) and wide (~120°) relative proton angles have been performed in order to determine the decay mechanism or mechanisms involved.

Further studies have used detectors which were position sensitive as well as energy sensitive. For both isotopes the two protons are emitted sequentially, going through discrete intermediate state(s), rather than being emitted simultaneously. Partial decay schemes for ^{22}Al and ^{26}P have been constructed.

Along with ^{22}Al and ^{26}P, heavier nuclei are expected to exhibit beta-delayed two-proton decay as well. Such nuclei include ^{35}Ca, ^{46}Mn, and ^{50}Co, for which initial searches have been made. As yet, no other beta-delayed two-proton emitters have been detected.

During the course of the above work, it was necessary to re-examine weak groups from beta-delayed single proton emitters. Additional beta-delayed proton groups from several $T_z = -3/2$ nuclei have been observed in the decay of ^{21}Mg, ^{25}Si, ^{29}S and ^{41}Ti. The log *ft* values for beta decay to levels above the isobaric analog state in the beta daughter have been deduced and new energy levels in the daughters have been determined.

Group Leader
Joseph Cerny

M. Ahmed
M.D. Cable
D.M. Moltz
J.E. Reiff*
E.C. Schloemer

X.-J. Xu,
Institute of Modern Physics, Lanzhou, People's Republic of China

Z.Y. Zhou
Nanjing University People's Republic of China

J. Äystö,
University of Jyväskylä Finland

**Graduate Student*

Heavy Element Radiochemistry

Group Leader
G.T. Seaborg

W. Chan*
K. Gregorich*
J. Kobayashi†
W. Kot*
W. Kwan†
D. Lee
R. Welch*
P. Wilmarth*
S. Yashita*

D.C. Hoffman,
Los Alamos National Laboratory

W. Li,
Institute of Modern Physics, Lanzhou, People's Republic of China

W. Loveland,
Oregon State University

**Graduate Students*
†Undergraduates

The group uses all three of the LBL accelerators to produce and characterize new elements and isotopes, to study nuclear reaction mechanisms, and to train students in modern nuclear and radiochemical techniques. Currently, research is focused on:

1. Synthesis and identification of new isotopes and elements in the actinide and transactinide region, along with attempts to synthesize superheavy elements;
2. Study of low-energy heavy ion reaction mechanisms such as massive transfer, complete fusion and deep inelastic scattering; and
3. Characterization of the mechanisms operating in intermediate energy (10–100 MeV/nucleon) and relativistic ($\geqslant$250 MeV/nucleon) heavy ion reactions through studies of the target fragment yields, energies, angular distributions, etc.

Light ($A<25$) heavy ion reactions with heavy actinide targets have been used at the 88-Inch Cyclotron to investigate "transfer" reactions to produce neutron-rich actinides. A comparison of actinide yields for the projectile pairs oxygen-16 and 18 and neon-20 and 22 has been made. The group is trying to understand the mechanism of these reactions by systematically measuring the variation of product yields, energies, angular distributions, etc. with projectile and target mass and energy.

Members of the group have also used the 88-Inch Cyclotron and SC synchrotron at CERN to study intermediate energy heavy ion reaction mechanisms. In particular, they are concerned with studies of the target fragment yields, energies, and angular distributions in light ion-heavy target reactions.

Research at the SuperHILAC has been directed toward the use of deep inelastic transfer and "cold fusion" processes to produce new isotopes or elements and to obtain an understanding of the mechanisms involved. Reactions of Kr and Xe projectiles with heavy actinide targets such as ^{248}Cm and ^{249}Cf have been investigated. Comparisons of above and below target yields are being made.

Research on target fragmentation at the Bevalac has involved single particle inclusive survey measurements of the energy dependence of target fragmentation. An international collaborative radiochemical search for anomalons is also being pursued at the Bevalac.

Together with LLNL, LANL, and ORNL, a proposal for a Large Einsteinium Activation Program (LEAP) was prepared and presented to a DOE review committee. The proposal involves production of some 40 micrograms of ^{254}Es for bombardment with light heavy ions and has three main goals:

1. New search for superheavy elements by bombarding ^{254}Es with ^{48}Ca ions;
2. Production and characterization of new neutron-rich isotopes of the heaviest elements; and
3. Determination of the chemical properties of the elements at the end of the actinide and beginning of the transactinide series.

New Element and Isotope Synthesis

Group Leaders
A. Ghiorso
J.M. Nitschke

P.K. Lemmertz
M.J. Nurmia
R. Babala
F. Theunissen
P.A. Wilmarth*
S. Yashita*

P. Möller,
Lund University, Sweden

**Graduate Student*

The research program of the Heavy Elements Research group is directed toward the synthesis of new nuclides and the determination of the radioactive properties of known nuclides. Graduate students continue to play an important role in this work while simultaneously being trained in the experimental techniques of nuclear physics. Experiments are conducted both at the 88-Inch Cyclotron and at the SuperHILAC; collaborative experiments are sometimes undertaken in other laboratories here and abroad.

The need to identify a number of short-lived spontaneous fission (SF) emitters in the heavy element region requires a fast (milliseconds) and efficient (>10%) on-line mass spectrometer. Last year, using Director's Funds, we showed that the Recoil Ion Mass Separator (RIMA) would satisfy these requirements. Lacking the funds necessary to put RIMA into immediate operation, we are rejuvenating the MG SF system as an interim solution, adding to it an alpha particle capability, and studying better methods of generating aerosols suitable for efficient operation of the helium gas jet system which transports the nuclear recoils from the target chamber to the counting chamber containing the large MG wheel.

Modifications to the magnetic optics of SASSY to compensate for some deficiencies of our focal plane detector produced a system with which we were able to confirm the recent discovery by Rose and Jones of ^{14}C emission from ^{223}Ra. Further modifications will improve the acceptance angle for fusion recoils and make SASSY a very useful instrument for studying nuclides with Z up to 110 or more.

Planning continues for the Large Einsteinium Activation Program (LEAP) following its approval by a national review committee. Interim funds are being requested to allow some preliminary efforts prior to funding in FY87. Studies are being made of the possibility of adding a special high level alpha cave for LEAP experiments at the 88-Inch Cyclotron.

A major research tool of the New Element and Isotope Group is the on-line apparatus for SuperHILAC isotope separation (OASIS). Recoils from heavy-ion-induced nuclear reactions are stopped in a tantalum catcher, which is kept at a temperature just below its melting point inside an ion source. The recoils diffuse out of the catcher, are ionized and then accelerated to an energy of 50 keV. An analyzing magnet selects isobars and focuses them onto various detectors. The beam of isobars can also be guided to a shielded room 4 meters above OASIS where low-background proton-, $\beta^{\pm}$-, γ- and x-ray experiments can be carried out. A fast tape system transports the selected isobar within 200 ms to a detection system that consists of a high purity Ge detector for $\beta^{\pm}$- and x-ray spectroscopy, and an n-type Ge detector for γ- and x-ray measurements. A $\Delta E/E$ telescope placed in front of one of the Ge detectors identifies charged particles. A plastic ΔE detector will be placed in front of the n-type Ge detector to distinguish between γ- and β- radiation, and a new large (>50%) "Gamma-X" detector to detect γ-γ coincidences will be particularly well-suited, because of it large size, to the measurement of high energy γ-rays from the decay of nuclei far from beta stability.

During this report period most of the physics with OASIS was focused on the synthesis and study of new neutron-deficient nuclei in the rare-earth region. Several new beta-delayed proton emitters were discovered and their proton spectra, half-lives and, in some cases, their ground state spins were measured. The isotope separator uniquely determines the mass of a new isotope while Z-identification is achieved by measuring $K_{\alpha,\beta}$-x-rays in coincidence with beta-delayed protons. Information about the spin of the proton precursor is obtained

by measuring gamma radiation from the daughter nucleus in coincidence with protons. In the same experiment the level scheme of the proton-emitting nucleus can be studied through positron-gamma and x-ray-gamma coincidences. One of the Ge detectors also measures positron endpoint energies which are directly related to electron capture Q-values. The most important information, however, is obtained from the proton spectrum itself. It is the result of a two step process – β^+ decay followed by proton emission – and reflects β^+-transition rates to excited states in the intermediate nucleus and the competition between proton and gamma decay of these states. By comparing calculations of this process using a constant β-strength function with the experimental proton spectrum, an experimental β-strength function is obtained which itself can be compared to calculations using, for instance, the gross theory of beta decay or the random phase approximation method.

In collaboration with G.J. Matthews, a calculation of Gamow-Teller strength functions using a realistic finite-range two body interaction will be done on the Cray X-MP at LLNL. Without exception, the new beta-delayed proton emitters were found to have precursors with an odd number of neutrons. This is a manifestation of the fact that for odd-odd nuclei in particular, none of the energy available for $\beta^\pm$ decay is expended in breaking up nucleon pairs and the β^+ strength therefore becomes concentrated at high excitation energies of the intermediate nucleus which have large proton decay widths.

In the future we are planning to expand the OASIS program to study neutron-rich nuclei produced in damped reactions of neutron-rich targets and projectiles. We have developed a high temperature ThO_2 target located inside a surface ionization source and tested it with the $^{232}Th(^{86}Kr;xn,yp)Fr$ reaction. ^{86}Kr is presently the heaviest ion the OASIS beam line can transport; a new beam line with sufficient rigidity for full energy ^{238}U beams is under construction.

Isotopes Project

Group Leaders
J.M. Dairiki
E. Browne
R.B. Firestone

C.M. Lederer
V.S. Shirley

The Isotopes Project compiles and evaluates nuclear structure and decay data and disseminates these data to the scientific community. From 1940–1978 the Project had as its main objective the production of the *Table of Isotopes.* Since the publication of the seventh edition in 1978, the group has coordinated its nuclear data evaluation efforts with those of other data centers via national and international nuclear data networks. The group is currently responsible for the evaluation of mass chains A = 167–194. All evaluated data are entered into the international Evaluated Nuclear Structure Data File (ENSDF) and published in *Nuclear Data Sheets.* In addition to the evaluation effort, the Isotopes Project is responsible for production of the *Radioactivity Handbook.*

Most of the group's effort during the past year was directed toward production of the *Radioactivity Handbook*, scheduled for publication in 1985. The primary purpose of the *Handbook* is to provide applied scientists with a source of recommended decay data that is both detailed enough for use in sophisticated applications and organized clearly so as to be usable in simple routine applications. Nuclear physicists should also find the *Handbook* useful. Recommended decay data are taken from the current version of ENSDF and analyzed to provide adopted values (e.g., radiation energies and intensities) for presentation in the *Handbook.* Additional calculations and evaluation provide recommended data for x-rays, conversion electrons, and continuous radiations (β^-,β^+ and internal Bremsstrahlung).

To facilitate production of the *Radioactivity Handbook*, ENSDF data have been restructured into a database which is accessed via DATATRIEVE, a DEC database management system. Several major computer codes have been developed and put in place. Efforts are now concentrated on the processing of mass-chain data and the production of final publication-quality output generated via UNIX and a phototypesetter.

During the past year evaluations of nuclear structure data for all nuclides with A=192 and A=174 were published in *Nuclear Data Sheets.* Evaluations of A=171 and A=181 have been submitted and accepted for publication. Beginning in 1985, the Isotopes Project will implement an integrated database evaluation system. Many of the codes and procedures developed for production of the *Radioactivity Handbook* will be adapted as tools to increase the efficiency and uniformity of the evaluation process. For example, the code SPINOZA is a valuable physics analysis and checking program; it is especially useful in deriving spin/parity assignments for complicated level schemes. The code GAMUT presents the evaluation network with a uniform, statistical process for deriving alpha-particle and gamma-ray energies and intensities.

A restructured "dynamic" version of ENSDF has been created as a by-product of the *Radioactivity Handbook* effort. To satisfy an expressed goal of the U.S. Nuclear Data Network (to make ENSDF data available to remote users by on-line retrieval) a procedure has been implemented to allow access to this LBL Nuclear Structure Numerical Database. This interactive database, accessible to outside users via DECNET, MILNET and TYMNET, currently contains ENSDF data for mass chains A = 150–266. It also contains files with the adopted alpha-particle, photon and electron data to be presented in the *Radioactivity Handbook*, as well as the 1984 Wapstra mass evaluation and numerous utility programs.

The group has presented a proposal for production of a complementary volume – the *Nuclear Structure Handbook* – to the NAS/NRC Panel on Basic Nuclear Data Compilations which advises DOE. This handbook is intended to

address the needs of the basic nuclear physics community for a compilation of nuclear structure data. Recommended data will be taken from the ENSDF file, and the production mechanisms already developed for the *Radioactivity Handbook* can be used directly for the *Nuclear Structure Handbook.*

Additionally, the Isotopes Project answers specific data requests, maintains recent references (filed by individual isotope) and encourages general use of its extensive library, which contains comprehensive data files and major nuclear physics journals.

Polarization Phenomena in Nuclear Physics

Group Leader
H.E. Conzett

C. Rioux
R.M. Larimer

This group's research uses the polarized beams from the 88-Inch Cyclotron and is concerned with spin-polarization effects in nuclear scattering and reactions. It particularly addresses such fundamental questions as parity violation by the weak interaction component in pp scattering, time-reversal invariance in reactions, and charge symmetry of the nucleon-nucleon interaction. A most important feature of polarization effects is that they often display uniquely the operation of a basic symmetry property of the nuclear interaction, and we continue to pursue fundamentally important experiments of this nature.

Spin-polarization measurements also provide information concerning nuclear structure and reaction mechanisms that is not otherwise available. Thus, studies are made of analyzing powers and polarization transfer in inelastic nucleon scattering and nucleon-transfer reactions in order to deduce the specific spin-dependent nature of the nuclear interactions. For example, the inelastic nucleon scattering results provide detailed information about the spin-dependent components of the effective nucleon-nucleon force in nuclei, which is a subject of considerable current interest. Measurements also are made of polarization-transfer in elastic proton-nucleus scattering, since these results will provide a unique means of establishing the existence of a spin-spin component of this nuclear interaction. Specifically:

a) In collaboration with a group from Lawrence Livermore National Laboratory, we have begun studies of polarization effects in elastic and inelastic proton scattering from light nuclei. Microscopic model calculations, employing effective nucleon-nucleon interactions, are being made for comparison with these results. From these studies, detailed information about the various components (central, spin-orbit, tensor) of the effective nucleon-nucleon force can be obtained.

b) In collaboration with a group from the University of Manitoba, we are studying the spin-dependence in the p-^{3}He interaction from 20 to 50 MeV through measurements in p-^{3}He scattering with our polarized proton beam.

Theoretical studies are also pursued in selected areas of current interest. These include the spin-polarization enhancement of the ^{3}He(d,n)^{4}He fusion reaction cross-section, identical-particle symmetry effects on polarization observables in the pp$\rightarrow\pi$d reaction, and spin-1 reaction amplitude determinations from the spin observables.

In future work this group plans to continue to focus on experiments with polarized particles which examine the operation of the basic symmetries – time-reversal invariance, parity conservation, and charge symmetry – in nuclear scattering and reactions. Also, the study of selected polarization observables to answer specific questions concerning nuclear structure and reactions will be pursued.

Nuclear Structure Studies at High Angular Momentum

Group Leaders
R.M. Diamond
F.S. Stephens

M-A. Deleplanque

J.E. Draper,
E.L. Dines,*
Department of Physics, U.C. Davis

A.O. Macchiavelli,*
Comisión Nacional de Energía Atómica, Buenos Aires, Argentina

P.O. Tjøm,
University of Oslo, Norway

**Graduate Students*

Essentially the whole range of spins possible for most nuclei in the periodic table is accessible using the 88-Inch Cyclotron and SuperHILAC accelerators. Nuclei carry angular momentum principally in two ways: by aligning individual high-j nucleons along a common axis, and by a collective rotation of the nucleus as a whole. Deformed nuclei use both modes and it is the interplay between the single-particle and collective modes that leads to the great diversity of nuclear properties at high spin.

Detailed information about these states and their properties is best obtained through discrete (resolved) γ-ray spectroscopy of their de-exciting transitions. But for the higher spins the population is usually spread over so many states that individual ones cannot be resolved and only average values can be determined. So one of the goals of present-day research is to push discrete spectroscopic studies to higher spin states, reducing the continuum region. To do this requires that the number of cascade pathways observed be reduced to a small enough number so that individual transitions can be identified. One way is to use a combination of sum-energy and multiplicity selection, that is, to define a smaller entry region. Another technique is to set gates on the highest-lying discrete transitions observed and look in coincidence at what precedes them. Either method involves a drastic decrease in the number of cascades selected, so very high efficiency is needed and this means many detectors as close as possible to the target.

Both techniques are being used simultaneously. An array of 21 Ge detectors will be placed at only 5-6 inches from the target. This makes possible higher order coincidence studies than ever done before, such as triple and even quadruple coincidence events. Each of these detectors will have a Compton-suppression shield of bismuth germanate (BGO) scintillator, and the arrangement will permit the most searching look upwards for higher-spin discrete transitions so far attempted. In addition, a small central ball of 40 BGO sectors will provide sum-energy selection almost as good as the much larger NaI crystal balls, though somewhat poorer multiplicity selection (40 sectors vs. 72 or 162).

The planning for this multi-detector array has taken an increasing amount of time and effort during the past 3 years, and during the past year the testing of the first BGO-shielded Ge detectors has taken place. First five, then nine, and, by the end of this report period, fifteen such units have been operated at the 88-Inch Cyclotron. The first experiments concentrated on nuclei just above the N=82 closed shell and the Z=64 sub-shell. This region is where theoretical calculations predict the most likely occurrence of superdeformation at achievable ($\sim 55\hbar$) spins. Also, at somewhat lower spins the nuclei will be either non-collective or only slightly collective so that some of the transitions will have long lifetimes, comparable to the stopping time ($\sim$1 psec) in the lead backing of the target. All of the succeeding transition will then occur after the nucleus has stopped in the lead target backing and thus give sharp, non-Doppler-shifted lines. This setup takes full advantage of the high resolution of the Ge detectors while simultaneously permitting them to be as close to the target (where they subtend a large solid angle) as possible. This is also a good region to observe the predicted termination of bands around spin $40\hbar$ and to study the major changes in nuclear structure that must be involved in such behavior. The study furthest along is of ^{156}Er, but work on ^{158}Er, ^{150}Dy and ^{148}Dy is also currently underway.

The investigation of the continuum γ-ray spectra of the even-even Er nuclei described last year has been extended to the even-even Yb nuclei and to lighter nuclei, ^{84}Sr, ^{108}Pd, ^{118}Te and ^{136}Nd. These studies show that with increasing spin the high-j orbitals from the shell above the valence shell come down to the Fermi surface and are occupied, a condition that results in a large increase in aligned angular momentum at that spin. This phenomenon is a general one throughout the periodic table.

A set of experiments on heavy-ion transfer reactions has also been completed and is in press. This is a study of 1- and 2-neutron transfers in reactions of ^{132}Xe projectiles with three rare earth targets. Simultaneous with the transfer process, there is a very large amount of Coulomb excitation. The experiments were done at an energy $\sim$10% above the Coulomb barrier, and for the 2n process it appears that intermediate states with $\sim$6 MeV of excitation are usually involved. If true, this shows that the enhancement of 2n yields relative to 1n yields at these bombarding energies is not a measure of the pairing correlations in nuclei, as has been generally assumed.

Heavy Ion Reactions at Non-Relativistic Energies

Group Leaders
R.G. Stokstad
B.G. Harvey

C. Albiston*
Y.D. Chan
S. Gazes
H.R. Schmidt
S. Wald

**Graduate Student*

In the energy range from a few MeV/nucleon to 20–30 MeV/nucleon there are rapid changes in the nature of nuclear reactions induced by heavy ions. The complete fusion of projectile and target becomes less probable, while the cross sections for emission of small fragments such as α-particles and Li isotopes with velocities close to that of the beam increase. At the upper end of the range, these cross sections are strikingly similar to those measured in the fragmentation of relativistic heavy ions. The group's goal is to gain a detailed understanding of heavy ion reactions in this transition energy range and, if possible, to arrive at a description of them that will tie together the phenomena that are observed from the lowest to the highest beam energies.

The Plastic Box, a 4π detector for the study of heavy ion reactions, is one of the main devices used by the group. It consists of six $8'' \times 8''$ double plastic paddles arranged as a cube around the target. The use of double walls permits the rejection of signals from neutrons and γ-rays. A slot in a front wall allows one or more E-ΔE telescopes to identify forward-going projectile-like fragments while the plastic walls record the presence (or absence) of additional charged particles. An additional plastic wall behind the telescope detects particles that passed through the slot without hitting a telescope.

The results for ^{20}Ne + ^{197}Au at 11 and 17 MeV/nucleon show that the transfer of at least 14 projectile nucleons can occur in events with no associated charged particles. The most likely number of associated particles is just one. This, combined with the observation that the energy spectra of fragments in coincidence with one charged particle are shifted down in energy by comparison with fragments without an associated particle, is entirely consistent with the production of excited fragments that subsequently decay by α or proton emission.

Particle identification by the walls of the Plastic Box is limited mainly by the large solid angle subtended by each wall and the concomitant large range of angles of incidence. Particle identification has been achieved by introducing a wall consisting of a sandwich of two different scintillators (phoswich) viewed by a photomultiplier on each of its four edges. A position resolution of about 1 cm has been demonstrated, and protons, deuterons and alpha particles are adequately separated. A segmented phoswich has also been developed and used to observe the full breakup cone in the decay of ^{20}Ne*.

The process of incomplete projectile fusion must lead to target-like recoils whose velocities are lower than those coming from complete fusion. The emission of fast forward-going nucleons arising from Fermi jets or pre-equilibrium phenomena could also contribute to the reduction of recoil velocity that has been observed in many systems for projectile energies more than just a few MeV/nucleon above the Coulomb barrier. The time-of-flight spectrometer at the 88-Inch Cyclotron has been used to measure the recoil velocities of fusion-like residues. Our previous studies with an oxygen beam and a variety of heavier targets were extended to include different projectiles, e.g., ^{14}N, ^{19}F and ^{20}Ne. The same gross systematic behavior – that the recoil velocity reduction depends mainly on the relative velocity of the colliding nuclei – was found to hold as well for these different projectiles.

All models predict that the velocity reduction must vanish when projectile and target are identical, but they make differing predictions about just how this limit is approached. Therefore, measurements of more symmetric systems, ^{20}Ne and ^{22}Ne projectiles with targets of ^{24}Mg and ^{26}Mg, have been performed.

The development of the overlap model for transfer and breakup reactions has continued. Its prime assumption – borrowed from the Fireball model for relativistic heavy ion collisions – is that the formation of an ejectile takes place only when the nucleons removed from the projectile overlap in space with the target nucleus. Thus the formation of a small ejectile requires a larger overlap than that for an ejectile close in mass to the projectile. Good agreement is obtained with experimental yields of fragments from ^{4}He to ^{18,19}F in the system ^{20}Ne + ^{197}Au from near the Coulomb barrier to 20 MeV/nucleon.

Work was begun on a microscopic model of nucleus-nucleus collisions at energies above 20 MeV/nucleon. It assumes that ejectiles are formed by the scattering of projectile nucleons by target nucleons. The input to the calculation, which uses the Monte Carlo method, consists only of the free nucleon-nucleon cross sections σ_{nn} ($=\sigma_{pp}$), σ_{np} and the radial distributions of proton and neutron densities in the projectile and target nuclei. These latter are taken from Hartree-Fock-Strutinsky calculations.

The predicted reaction cross sections, σ_R, are in excellent agreement with experimental results, as are the fragment yields from ^{16}O + ^{208}Pb at 20 MeV/nucleon. The observed large yields of neutron-excess fragments from heavy targets at energies up to 44 MeV/nucleon appear to arise from the neutron skin around heavy nuclei combined with the inequality of σ_{np} and σ_{nn} ($\sigma_{np} = 3 \times \sigma_{nn}$). At 2 GeV/nucleon, where $\sigma_{np} \approx \sigma_{nn}$, the enhancement of the neutron-rich fragment yields vanishes, as observed experimentally. Fragments of a given mass are found to be formed in narrow ranges of impact parameter. This provides a natural justification for the assumptions that were made in the geometrical Overlap Model.

During the period under review the group benefited from the contributions of several visiting scientists. K. Grotowski (Crakow, Poland) visited in the Fall of 1983 and R. Kamermans (Utrecht, Netherlands) spent 10 weeks with us in the Fall of 1984. Postdoctoral fellows S. Gazes (MIT) and H.R. Schmidt (Heidelberg) joined the group, while S. Wald returned to the Weizmann Institute. The collaboration with K. Van Bibber's group from Stanford on the Plastic Box experiments continued during this year.

Damped Nuclear Reactions and Compound Nucleus Studies

Group Leader
L.G. Moretto

David Bowman*
Robert Charity
G. Guarino
J.B. Hunter
M.A. McMahan
M. Padgett*
L. G. Sobotka
G.J. Wozniak

J. Gu,
Z. Yao,
Shanghai Institute of Nuclear Research, People's Republic of China

Z.H. Liu,
Institute of Atomic Energy, Beijing, People's Republic of China

C. Signarbieux,
Nuclear Physics Division, CEN, Saclay, France

Alberto Pacheco,
Comisión Nacional de Energía Atómica, Beunos Aires, Argentina

René de Swiniarski
Institut des Sciences Nucléaires, Université de Grenoble, France

**Graduate Students*

Our theoretical and experimental work is directed along two different lines. On the one hand we study deep-inelastic reactions with special attention to the role of angular momentum; on the other we have started working on the compound nucleus emissions of complex particles.

The elucidation of the role of rotational degrees of freedom in the intermediate dinuclear complex has been guided by a statistical model that predicts the distributions and correlations of the spin components in the two fragments. On the experimental side, we have explored the angular momentum transfer and alignment as a function of Q-value and mass asymmetry with a variety of techniques. We have been successful in establishing the rise and fall of angular momentum alignment as a function of Q-value by means of continuum γ-ray angular distributions. We have established the rigid rotation limit by measuring the α-particle angular distributions from one of the two fragments as a function of mass asymmetry. We have successfully tested the asymmetric angular momentum misalignment predicted by the model at large mass asymmetries by measuring in-plane sequential fission angular distributions.

Some recent theoretical work carried out in our group has indicated that the angular momentum transfer should be strongly affected by the magicity of the target and/or projectile. In a search for such effects, we have measured the magnitude and alignment of the spin transferred to the fragments in the deep-inelastic reactions of 7.4 MeV/nucleon ^{208}Pb on ^{208}Pb, ^{197}Au and ^{165}Ho using continuum γ-ray multiplicity and anisotropy techniques. In contrast to the rise and fall of the γ-ray anisotropy with increasing Q-value observed for the Ho + Ho system, the γ-ray anisotropy is smaller and essentially independent of Q-value for these Pb-induced reactions.

Sequential fission angular distributions for the reactions of ^{40}Ar + ^{197}Au and ^{238}U were measured in order to determine the spin misalignment of the primary deep inelastic fragments. The combination of the present data with the data available in literature for different systems has allowed us to extract the dependence of the spin misalignment upon mass asymmetry. This analysis indicates a progressive increase in the rms angular momentum component of the dinuclear axis with increasing mass asymmetry.

Two striking, apparently unrelated, open problems in our understanding of deep-inelastic processes are the lack of drift in mass asymmetry on one hand and the unexpected thermal partition of the energy between fragments even at small Q-values on the other. The former effect can be observed in the reluctance of the Kr-like fragment in reactions such as Kr + Er or Kr + Au to drift toward symmetry, as suggested by the potential energy surface, except at the largest energy losses. The latter effect is the surprising interfragment thermal equilibration, which is observed even at small Q-values and short interaction times. While these two features seem to be unrelated at first glance, we have shown that they can be explained in terms of a dynamical driving force toward larger mass asymmetries because of the attempt of the smaller fragment to contain its temperature gradient (with respect to the heavy fragment) at the expense of its particle number. We have shown that such a feedback could be operative in actual nuclei when the barrier height between the two nuclei as seen by the nucleons being exchanged is close to the Fermi surface.

We have begun a program at the Low Energy Beam Line (LEBL) at the Bevalac with the aim of identifying the reaction mechanisms in collisions between large nuclei at intermediate energies. Preliminary data on the reaction La + La at 60 MeV/nucleon indicate that a possible mechanism for the production of fragments of intermediate mass is the primary excitation of the projectile in a somewhat peripheral interaction followed by evaporation of particles covering the whole mass asymmetry interval.

A statistical approach to the production of fragments in intermediate energy regimes has been explored. The information theory approach of Aichelin and Huefner has been shown to be an approximation to the Euler number partition. The relationship between these theories, percolation theories and liquid vapor equilibrium theories is being investigated.

We have undertaken a major effort to characterize experimentally the compound nucleus emission of large particles. At the 88-Inch Cyclotron we have measured the kinetic energy distributions, angular distributions, charge distributions and excitation functions of the particles emitted in the reaction Ag + ^{3}He with atomic numbers as high as 10. The excitation functions have been fitted with a formula based upon a generalization of the compound nucleus decay theory to the emission of large fragments. From the fit we have obtained empirical values for the height of the conditional saddle points. These empirical barriers allow one to verify in a very direct way the role of finite range forces in nuclei with highly constricted shapes. Simultaneously at the SuperHILAC we have studied a variety of compound nucleus reactions with the inverse kinematics technique, such as Be and C targets + Ge, Nb and La projectiles. With this technique we have been successful in measuring the complete charge distribution from protons to symmetric splitting. The charge distributions of the fragments have shown the transition from a minimum at symmetry below the Businaro-Gallone point to a maximum at symmetry above the Businaro-Gallone point.

Relativistic Nuclear Collisions: Interactions in Emulsions

Group Leader
H.H. Heckman

S. Chatterji
C. Connolly
E. Friedlander
R. Guzman
Y. Karant
H. Yee
C. Zeitlin

M. Ghoniem,
Cairo University
Cairo, Egypt

B. Judek,
National Research Council,
Ottawa, Canada

The Relativistic Heavy Ion Group's experimental program employs nuclear emulsion visual track detectors to carry out studies on the interaction of relativistic nuclei in matter. At the Bevalac, experiments on the interaction properties of relativistic projectile fragments of ~2 GeV/nucleon ^{56}Fe nuclei are in progress, as are studies on the topological characteristics of high-multiplicity ^{238}U-nucleus events and the kinematics of the fission reactions of ^{238}U at relativistic energies. The group initiated and carried out the first phase of Bevalac Exp. #730H on the range-energy, energy loss and effective charge of high-Z nuclei ($E \leq 150$ MeV/nucleon) in matter. The experiment addresses key questions on the energy-loss processes of heavy ion beams pertinent to heavy ion inertial fusion. A paper on this work was given to the 2nd International Workshop on Atomic Physics for Ion Fusion, Rutherford Laboratory, England, September 1984.

An experiment on the interactions of 12 GeV/nucleon ^{4}He nuclei in emulsion has been carried out using the first such ^{4}He beam extracted from the CERN-PS. The first studies are to compare the multiplicity distributions of shower particles and non-relativistic, target-related fragments with those produced in ^{4}He- and proton-nucleus reactions at energies of 2 GeV/nucleon and $6<E<69$ GeV, respectively. The first results were presented at the 7th Heavy Ion Study, Darmstadt, October 1984. Asymmetries in the target fragment and meson distributions yield information on the stopping power of heavy target nuclei. Measurements on the angular distribution of high-multiplicity events will be pursued with regard to possible signals for quark-gluon plasma production.

In connection with the work on the proposal for a mini-collider at LBL and the search for signatures for quark-gluon plasma, a method has been developed for detecting large fluctuations in rapidity density in high-multiplicity nuclear events. This was presented at the LESIP workshop, Bad Honnef September 1984 and at the 7th Heavy Ion Study, Darmstadt, October 1984. Also presented at LESIP were the published results of a study, done in collaboration with the Universities of Marburg and Exeter, of the inelasticity distribution in high energy nuclear collisions interpreting both the scaling violations in multiplicity and the behavior of transverse momenta.

The interaction properties of projectile fragments from 0.9 and 1.8 GeV/nucleon ^{40}Ar collisions in Cu have been investigated by activation methods in collaboration with the radiochemistry groups at LBL, Oregon State University, Purdue University and Marburg University (Bevalac Exp. #660H). Significant evidence has been found at the higher energy for large partial cross sections for the production of ^{24}Na and ^{28}Mg residues which decrease with distance between the detector and target materials.

A major collaborative experiment on particle production and nuclear fragmentation in collisions of ^{16}O beams at 50 and 225 GeV/nucleon, to be carried out at CERN in early 1986, was proposed in May 1984 and approved in September 1984 as SPS Exp. #P198. The experiment will include groups from Berkeley, Cairo, Jammu, Jaipur, Lund (I. Otterlund, spokesman), Ottawa (University and NRC) and Seattle. The impetus for this experiment comes from theoretical estimates that suggest the possibility of a phase transition to a quark-gluon plasma (QGP) at these energies. Such a transition could be favored by large

nuclear stopping power, with signatures being large values of pseudo-rapidity densities and their fluctuations. Use of nuclear emulsion stacks and emulsion chambers will provide the necessary spatial resolution to detect the expected signals even at the highest predicted particle densities. The Interactive Computer Assisted Measuring System (ICAMS), the data acquisition and measurement instrument that is the major development activity of the group, will be an important asset in the measurement and analysis of this experiment.

Relativistic Nuclear Collisions: Nucleus-Nucleus Collisions

Group Leader
P.B. Price

S. Barwick*
R. Claxton
T. Coan*
J. Drach*
J. Musser*
M. Salamon
K. Selby*
M. Solarz
J. Stevenson
G. Tarlé
M. Tincknell

L. Garwin,
University of Cambridge, England

Shi-lun Guo,
Institute of Atomic Energy, Beijing, People's Republic of China

**Graduate Students*

All this group's offices and equipment are located in Birge Hall on the UCB campus, which makes it easy to attract new students but restricts to some extent interaction with Nuclear Science Division staff. Current research falls into the following six principal areas:

1. Relativistic heavy ion research (DOE support)
   a. Production of heavy ion fragments, including exotic neutron-rich nuclides near the dripline
   b. Detailed properties of secondary nuclei with anomalously short interaction lengths ("anomalons")
   c. Search for Lee-Wick matter
   d. High-order effects in electrodynamics of slowing heavy ions
   e. Response of various detectors to heavy ions
   f. Hadron calorimetry for nucleus-nucleus collisions
   g. Search for quark-nucleon complexes;
2. Exotic radioactive decay modes such as ^{14}C emission (DOE support);
3. Search for highly ionizing particles in e^+e^- annihilation (TRISTAN experiment, supported by NSF) and in $\bar{p}p$ annihilation (NSF support);
4. Cosmic-ray astrophysics (NASA and NSF support)
   a. Final engineering design and construction of instruments for a 50 m^2 detector for a two-year space exposure beginning 1986 (being done at LBL)
   b. Construction of an experiment to detect anti-iron nuclei in cosmic rays at a level 3×10^{-7} of iron (in collaboration with Indiana University and the University of Michigan)
   c. Design of a balloon-borne magnetic spectrometer to measure the energy spectrum of antiprotons at $E < 1$ GeV (in consultation with Klaus Halbach, LBL);
5. Search for grand-unification magnetic monopoles (NSF support)
   Use of mica detectors at sensitivity $\lesssim 10^{-19}\ cm^{-2}\ sr^{-1}\ s^{-1}$;
6. Ultrarelativistic nucleus-nucleus collisions (DOE support)
   a. 200 GeV/nucleon ^{16}O collisions at CERN (1986)
   b. 15 GeV/nucleon ^{32}S collisions at Brookhaven (1986).

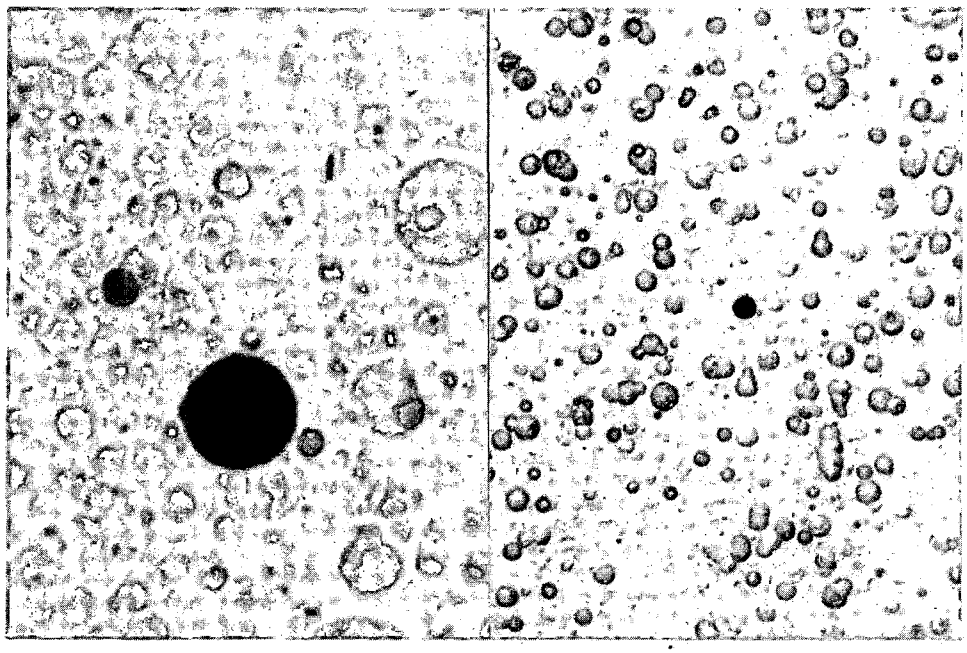

Left Right

Photomicrographs showing head-on views of an etched track of a 30 MeV ^{14}C nucleus emitted in radioactive decay of a ^{223}Ra nucleus. The diameter and depth of a track (dark circular feature) give its charge and energy; lighter background features are due to recoil atoms struck by alpha particles. Branching ratios as low as $\sim 10^{-11}$ for ^{14}C emission relative to alpha emission have been seen (See paper in this Report). To appreciate the extraordinary signal to noise ratio of the technique, note that 2×10^5 alpha particles struck the area on the left and 5×10^6 alpha particles struck the area on the right. XBB 840-8302

Relativistic Nuclear Collisions: Light Particle Studies

Group Leaders
O. Chamberlain
H. Steiner
O. Hashimoto

H. Hamagaki,
T. Kobayashi,
K. Nakayama,
I. Tanihata
INS, University of Tokyo, Japan

S. Nagamiya,
S. Hayashi,
T. Nagae
Department of Physics, University of Tokyo, Japan

K. Kimura
Department of Physics, Kyushu University, Japan

O. Yamakawa
Department of Physics, Nagoya University, Japan

Our group has been studying high energy heavy ion reactions at the Bevalac in a collaboration between the Institute for Nuclear Study (INS), the University of Tokyo, and LBL. The experimental program of the group emphasizes measurements of light particles ($\pi^{\pm}$, K^{+}, p, d) in a wide momentum range with two magnetic spectrometers. One is a compact spectrometer which was built by the group and has been used in experiments 472H and 618H. The other spectrometer is the Heavy Ion Spectrometer System (HISS) which was constructed by the HISS A group. In the past few years, the group has put much of its effort into carrying out experiments E512H and E593H at HISS. In addition, we have started this year a new series of experiments with unstable beams produced through projectile fragmentation processes.

In experiment 472H, two-particle correlations, e.g., p-p and p-d, have been measured in the reactions of protons and Ne on various targets at 400 MeV/nucleon and 800 MeV/nucleon. Two-nucleon momentum distributions inside a nucleus were studied from the pd quasi-scattering data. It was found that the momentum spread of the pn system in the nucleus is smaller than that for deuterons in projectile fragments.

Experiment 512H was one of the first experiments at HISS. We have measured inclusive spectra for p, d and t at a very high p_T region (1.8 GeV/c for protons, 2.5 GeV/c for deuterons and 2.8 GeV/c for tritons) where cross sections are smaller by 8 orders of magnitude than those of the low p_T region. The correlation between particles emitted in opposite directions in the center of mass system was also analyzed.

The data-taking phase of experiment 593H has been completed at HISS. The aim of the experiment is to study the spectra of low momentum pions in coincidence with projectile fragments. Both positive and negative pions are detected by pion arms installed in the HISS magnet. A prominent π^{-} peak at projectile velocity was observed with an 800 MeV/nucleon La beam on C and La targets. The correlation between projectile fragments and negative pions emitted at 0 degrees shows a downshift of the peak momentum with a smaller sum charge of projectile fragments.

In experiment E618H, the inclusive spectra of light particles and pions were measured in 800 MeV/nucleon La + La collisions. New features of the proton and pion spectra have been observed: (1) protons at c.m. 90° showed simple exponential spectra even in a very low p_T region which is in contrast to the spectra for lighter mass collisions. (2) the pion spectrum at c.m. 90° shows a steeper exponential for La + La collisions than for lighter mass collisions. In addition, deuteron spectra at forward angles showed an enhancement at around 2 GeV/c, which may conform to the three-fireball model. We are also preparing another inclusive measurement with much better statistics using a compact 120-element multiplicity counter array now under construction (E733H).

Experiment 690H was successfully carried out as the first of a new series of experiments using unstable beams. Secondary beams were produced at the exit of the Bevatron with the ^{11}B primary beam and were transported about 100 m into the HISS area. Interaction cross sections of $^{3,4,6,8}He$, $^{6,7,8,9}Li$, $^{7,8,10}Be$ and ^{8}B were determined with a transmission method using the HISS magnet. Nuclear radii derived from the cross section were compared with various calculations. A second-generation experiment with unstable beams is also in preparation (E790H), with which magnetic dipole and electric quadrupole moments of $f_{7/2}$ shell nuclei will be measured.

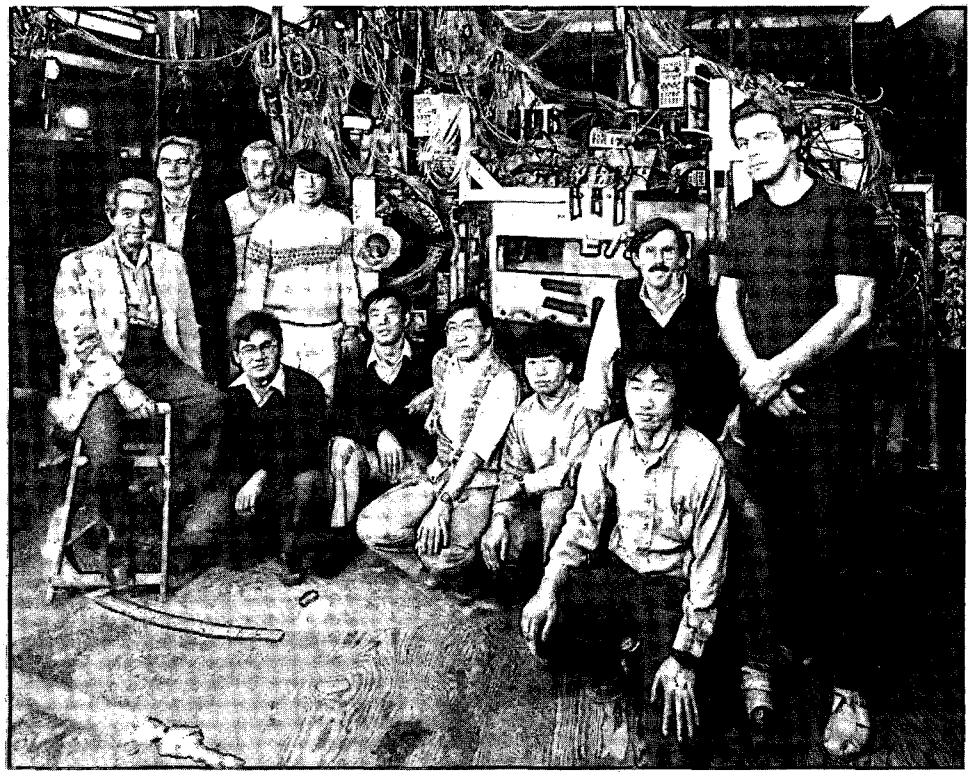

Part of this group and some members of the TASS group are shown in front of the new 120-element counter array and the magnetic spectrometer at BEAM-30.
CBB 8410-8453

Relativistic Nuclear Collisions: Pion and Correlation Studies

Group Leaders
K.M. Crowe
J.O. Rasmussen

J.A. Bistirlich
R.R. Bossingham*
H.R. Bowman
A.D. Chacon*
S. Hubinger*
T.J. Humanic
M. Justice*
J.M. Kurck*
C.A. Meyer*

R. Anholt,
W. Meyerhof,
Stanford University
Stanford, California

Z.-Z. Xu,
Department of Physics
Fudan University,
Shanghai, People's Republic of China

**Graduate Students*

The Berkeley research activities of our group center mainly on the study of charged pions or correlated pairs of particles produced in high-energy heavy-ion collisions at the Bevalac. The technical approach involves a large (~4 meter flight path) dipole-dipole magnetic spectrometer (JANUS) and combinations of fast scintillators and wire chambers interfaced with a CAMAC-VAX 11/750 data acquisition system.

A major part of our research effort involves pion interferometry studies. In the past ten years theorists have predicted that exotic phenomena such as pion condensation and quark-gluon plasmas occur in relativistic heavy-ion collisions. One way to obtain information about these phenomena is to measure the radius, lifetime and coherence of the pion-emitting source produced in the collision. The Hanbury-Brown/Twiss effect, which has been used extensively in astronomy to measure the radii of stars, provides a direct method to measure these pion source parameters. In practice, we measure the momenta ($\vec{p}_1$ and $\vec{p}_2$) of coincident like-charged pions in our spectrometer and, using the two pion yields thus obtained, form the correlation function C ($\vec{p}_1,\vec{p}_2$). This experimental correlation function is then fitted to a model, which assumes a Gaussian space-time distribution for the sources, and the source parameters are extracted. Thus far we have used this technique to measure source parameters for the systems 1.8 GeV/nucleon ^{40}Ar on KCl, 1.8 GeV/nucleon ^{20}Ne + NaF, and 1.7 GeV/nucleon ^{56}Fe on Fe.

In addition to our experimental program in pion interferometry, we are also carrying out theoretical studies based on this method using the intranuclear cascade model (INC). For a given projectile-target system, the INC generates pions of known momentum and known position and time of creation. This information allows a symmetrization to be performed on pions from the same event, which induces the Hanbury-Brown/Twiss effect in the INC. One then uses the same techniques that are applied to experimental two-pion pairs (i.e., form the correlation function and fit it with a Gaussian space-time distribution) to extract INC predictions for the pion source parameters. Reasonably good agreement has thus far been found between INC and measured source parameters.

One part of the work is the determination of the inclusive or tagged cross sections (with an exploration of the angular dependence) for charged pion production in heavy-ion reactions. Our spectrometer is nearly unique for doing 0° and small angle pion spectroscopy at the Bevalac. The existence of both positively and negatively charged pions facilitates determinations of simple Coulomb effects and therefore the charge density evolution in heavy-ion collisions by observation of the π^-/π^+ ratio as a function of pion energy, bombarding energy, and target-projectile charges. In fact, we found that pions produced with low energy in the projectile frame have large π^-/π^+ ratios due to the Coulomb fields of the projectile fragments. Systematic observations of the sharp anomaly were made to compare with various models for production.

Future work that our group intends to pursue will utilize the experimental techniques and apparatus that we have built. The availability of Bevalac beams of the heavier elements (Au, Pb, or U) will allow new pion spectroscopic measurements to search for evidence of highly compressed nuclear matter effects

through the pion interferometry method. We plan to look for such possible exotics as doubly-charged pineuts (2 π^- bound to a cluster of neutrons).

Now that heavy elements can be accelerated at the Bevalac, there are new opportunities in atomic physics. Our earliest Bevalac work involved measuring K x-ray production cross sections. With Stanford collaborators we have measured extensively the x-ray spectra from 190 MeV/nucleon Xe ions and 375 MeV/nucleon U ions. We observed not only target and projectile x-rays but also the radiative electron capture peak. We are relating the results to aid work in heavy ion inertial fusion. We are also collaborators with the Heckman group on stopping-power studies of Au ions at 50 and 150 MeV/nucleon in support of inertial fusion research and development.

Various members of the group are involved in collaborative work centered at other laboratories: muon fusion experiments at SIN; muon and pion experiments at TRIUMF; theoretical nuclear studies are in progress with sabbatical professors in residence from Munich, Madrid, and Rio de Janeiro.

Relativistic Nuclear Collisions: Search for New States of Matter

Group Leaders
V. Perez-Mendez, *LBL*
G. Igo, *UCLA*

T. Mulera,
A. Shor,
LBL

S. Abachi,*
S. Carlson,*
J. Carroll,
S. Trentalange,
UCLA

E. Barasch,*
U.C. Davis

**Graduate Students*

In addition to the staff listed here, which comprises a long standing collaboration led by V. Perez-Mendez and G. Igo, other collaborations have been formed. A current collaboration, formed to study the production of single leptons and lepton pairs in relativistic heavy ion collisions (RHIC), consists of the above listed people plus members of other LBL groups and groups led by L. Madansky at the Johns Hopkins University, D. Miller at Northwestern University and P. Kirk at Louisiana State University.

The group carries on a diverse program of research in relativistic heavy ion physics using projectiles supplied by the Bevalac. The unifying theme of this research program is the search for evidence for the possible formation of a new or "anomalous" states of nuclear matter in RHIC.

Anomalous production of particles below threshold (for nucleon-nucleon collisions at equal energy/nucleon) provides evidence for collective effects that may lead to the production of new states of matter. In the past we have reported the observation of a surprisingly high rate of K^- production in 2.1 GeV/nucleon ^{28}Si + ^{28}Si collisions. We have extended this investigation by measuring the momentum distribution of these subthreshold K^-. This momentum spectrum is approximately exponential in shape with a slope corresponding to a temperature of ~90 MeV. This result indicates that it is unlikely that subthreshold K^- production is due to a ϕ-bremsstrahlung mechanism or is the result of $K\bar{K}$-condensation. Possibilities which are consistent with the observed yield include the existence of 6-quark and 9-quark bags within nuclei or an enhancement in the number of strange sea quarks in nuclei. Further studies are planned which should shed more light on the nature of the production mechanism. In preparation for these studies, a new beam line/spectrometer is now under construction.

During the measurement of the K^- momentum spectrum a simultaneous search for production of fractional charges, rare long-lived particles and subthreshold antiprotons was carried out. No such production was observed and upper limits of from one part in 10^4 to one part in 10^7 were set for exotic particle masses in the region 0.5 to 4 GeV/c^2.

Changes in the effective mass spectra of lepton pairs produced in RHIC, as a function of bombarding energy, may provide the clearest signature of the postulated phase transition to the quark-gluon plasma. We are collaborators in an effort to construct a new major facility at the Bevalac, the dilepton spectrometer, which will be used to study the production of e^+e^- pairs in RHIC. As a prelude to this effort, we have begun an experiment to measure the yield of single direct electrons at the Bevalac. In the first run of this experiment, data were taken for collisions of 2.1 GeV/nucleon p + Be. These data are still under analysis. Running time in the near future will be used to collect data on p + Be collisions at higher bombarding energies and on nucleus + nucleus collisions.

Development of instrumentation remains a major part of our effort. For the experiments described above, we are developing aerogel Čerenkov counters and various types of proportional and drift chambers. In addition, a good deal of long range development of radiation detectors was carried out for its own sake.

Relativistic Nuclear Collisions: The Plastic Ball

Group Leaders
A.M. Poskanzer, *LBL*
H.H. Gutbrod,
H.-G. Ritter, *GSI*

K.G.R. Doss,
T. Renner,
LBL

B. Kolb,
A. Warwick,
H. Wieman,
GSI

H.-A. Gustafsson,
LBL/GSI

K.-H. Kampert,
H. Löhner
University of Münster
West Germany

B. Ludewigt
University of Marburg
West Germany

This group is a 10 year old continuing collaboration between GSI (Gesellschaft für Schwerionenforschung, Darmstadt, West Germany) and LBL. The work of the group now centers on the use of the Plastic Ball to study central collisions of relativistic nuclei with the aim of learning about nuclear matter at high temperature and density.

The Plastic Ball covers 96% of 4π with 815 modules, each consisting of a CaF_2 ΔE detector and a plastic scintillator E detector. The two scintillators are observed by the same photomultiplier tube and the signals are separated electronically by taking advantage of their different decay characteristics. In addition, positive pions are identified by their $\pi^+ \rightarrow \mu^+ \rightarrow e^+$ decay. The small forward angle region is covered by the Plastic Wall placed 6m downstream. The Wall consists of 177 plastic scintillators and identifies particles by their time of flight and energy loss. Data have now been taken for ^{40}Ca on Ca, ^{93}Nb on Nb and ^{197}Au on Au.

Collective flow of nuclear matter has been discovered by observation of the event shapes. Both bounce-off of the spectator matter and side-splash of the participant matter has been seen. The side-splash is taken as direct evidence of the production of high density nuclear matter.

From the proton-proton correlations, the size of the emitting source has been obtained as a function of multiplicity. From this the thermal freeze-out density of an expanding fireball is deduced to be 25% of normal nuclear density. From the ratio of the deuteron yield to the proton yield as a function of multiplicity, values for the chemical freeze-out density and entropy have been deduced.

Many other aspects of the rich harvest of data are being investigated. In the meantime preparations have started for a CERN SPS experiment using 50–200 GeV/nucleon ^{16}O beams. This will be an expanded collaboration involving the University of Münster, Lund University and Oak Ridge National Laboratory.

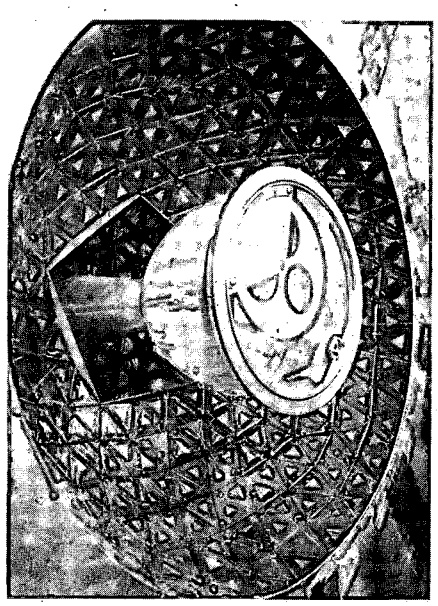

View of the target wheel in half the vacuum chamber at the center of the Plastic Ball. The triangles are the CaF_2 ends of the Plastic Ball modules. CBB 817-6532

Relativistic Nuclear Collisions: TASS

Group Leaders
H.G. Pugh,
L.S. Schroeder, *LBL*
A. Sandoval,
R. Stock, *GSI*

G. Claesson,
H.S. Matis,
J. Miller,
G. Roche,
LBL

J.W. Harris,
GSI

P.N. Kirk,
G. Krebs,
J.-F. Gilot,
Louisiana State University

G. Landaud
University of Clermont-Ferrand, France

The Two-Arm Spectrometer System (TASS) consists of two fully rotatable magnets with accompanying wire chambers and scintillation hodoscopes for particle identification. It was first operated in July 1980 and the first phase of instrumentation and experiments was completed in mid-1983. The present activities on TASS are:

599H This experiment looks at the possible differences of π^- and π^+ inclusive yields primarily in the central region of rapidity but extending also into the projectile fragmentation domain. The chosen system is ^{40}Ca + ^{40}Ca at 1.05 GeV/nucleon, which apart from Coulomb effects, should yield a π^-/π^+ ratio of unity. A ratio different from unity has previously been reported for the ^{40}Ar + KCl system at the same energy. For the experiment, a multiplicity detector system was added to TASS at zero degrees to provide a "streamer-chamber-type" tagging of central and peripheral interactions. Data analysis is nearly completed.

628H This experiment (in association with Michigan State University) involved a search for pionic condensation effects in the 90° c.m. pion inclusive spectrum from La + La collisions at 246 MeV/nucleon. The pion spectrum is observed to fall exponentially, with no hint of a "bump" due to production of the condensate phase in the collisions. In addition, proton spectra at 90° c.m. were measured to study the "nuclear temperatures" achieved at this relatively low Bevalac energy for heavy nuclei. Analysis is complete and the results have been submitted for publication.

670H Following a series of workshops, a collaboration has been formed involving LBL, Johns Hopkins University, Louisiana State University, Northwestern University, UCLA, and the University of Clermont-Ferrand to make a major study of lepton and dilepton production in heavy ion collisions. These particles are believed to be the most reliable probes of the hot conditions produced in the high density phase of the reaction. The problem in their study is the low yield. TASS, in conjunction with Čerenkov detectors added to each arm, has measured the yield of direct electrons in p+Be collisions at 2.1 GeV. Final analysis is proceeding. Direct electron measurements will continue in early 1985 with studies of p+Be at 4.9 GeV and be extended to light ion (Ne+NaF) collisions at 2.1 GeV/nucleon. For the more definitive dilepton measurements, a much larger acceptance system is needed. In the Spring of 1985 we will remove the present TASS magnets and replace them with dipoles having a much larger solid angle (~170 msr per arm). This new system, called the Dilepton Spectrometer (DLS) will be equipped with Čerenkov hodoscopes (for electron/hadron rejection), time-of-flight scintillators and drift chambers. By Fall of 1985 the equipment will be in place for testing. Early measurements (late 1985 through early 1986) of the low-mass dilepton spectrum ($M_{ee} < 800$ MeV) will be conducted for p+Be collisions. At a later stage Ca+Ca collisions at 2.1 GeV/nucleon will be studied.

738H This experiment is an outgrowth of 628H described above. Since TASS is occupied with lepton and dilepton measurements, we have formed a collaboration with the INS/University of Tokyo group to use their single-arm spectrometer at the end of beam line 30. The angular distribution for both π^- and π^+ will be measured in association with the charged particle multiplicity. The experiment will use La+La at 246 MeV/nucleon. Multiplicity selection will allow us to isolate the more central collisions in our search

for collective features in nucleus-nucleus collisions. A 120-element scintillator multiplicity array has been constructed and tested. It provides full azimuthal coverage ($\sim$40 elements in each section) for each of three angular regions spanning $10° < \theta_{lab} < 90°$. Data will be taken in February and March of 1985.

ISR Experiment R 418

Two of us (LSS and HGP) are involved with T.J.M. Symons and C.R. Gruhn, in a large collaboration studying α-α collisions at the CERN ISR. This experiment, one of the last to be carried out on the ISR before its final shutdown, was completed in August 1983, and the data are being analyzed.

Relativistic Nuclear Collisions: Streamer Chamber

Group Leaders
H.G. Pugh,
L.S. Schroeder, *LBL*
A. Sandoval,
R. Stock, *GSI*

J.B. Brannigan,
G. Odyniec,
P. Renteln,
LBL

R. Brockmann,
J.W. Harris,
I.W. Muskovich,
S. Reinsch,
H. Ströbele,
L.M. Tinay,
GSI

D. Bangert,
W. Rauch,
University of Marburg, West Germany

R.E. Renfordt,
D. Schall,
University of Heidelberg, West Germany

K.L. Wolf,
Texas A&M University

A. Dacal,
M. Ortiz,
Instituto de Física, UNAM, Mexico D.F., Mexico

The Streamer Chamber allows the study of charged particle as well as K^0 and Λ production over most of the 4π solid angle in high energy heavy ion collisions. Detailed 4π exclusive data is necessary to study the behavior of nuclear matter under conditions of extreme temperature and density. Up to now projectiles from protons to ^{139}La have been used extensively in our Streamer Chamber experiments. In the near future the Streamer Chamber research will concentrate on heavy beams.

Our group has upgraded the LBL Streamer Chamber to be able to use metallic targets and has reduced the loading effect of the Chamber voltage due to high energy delta rays from heavy projectiles. Instrumentation has been implemented to monitor the chamber performance with, among other things, an UV laser that produces tracks with a well defined ionization. This has enabled us to optimize the Streamer Chamber parameters to obtain the most stable running conditions. All this is necessary to obtain high quality data for the heavy projectiles.

Furthermore, a forward angle 400 element scintillator hodoscope detector was designed and constructed to complement the Streamer Chamber particle identification capabilities in the region of momenta above 1 GeV/c. The signal processing of this detector is done with a Large Scale Digitizer system with 512 ADCs and 384 TDCs which was used previously in a SLAC experiment and modified to meet our needs. A calibration and monitoring system for the hodoscope using a light fiber coupled N_2 laser was constructed.

Besides the work on instrumentation in preparation for experiments with heavy beams, the analysis of previous experiments has continued.

401H In this experiment the excitation function of Ar-induced reactions on KCl from energies between 0.4 and 1.8 GeV/nucleon and the central collisions of Ar on Pb at 800 MeV/nucleon was measured. From the energy dependence of the negative pion production and use of a cascade model, an equation of state of nuclear matter at high density was extracted. A new theoretical approach to interpret the data independently of the intranuclear cascade model is in progress. This experiment has also been analyzed in terms of the total charged-particle final state. This involves the measuring, reconstruction and identification of all charged particles emitted in the interaction as measured in the Streamer Chamber. Work here has concentrated on the 1.8 GeV/nucleon Ar + KCl and 800 MeV/nucleon Ar + KCl and Ar + Pb reactions. Results from a larger statistical sample for the Ar + Pb system, analyzed in terms of the momentum flow tensor, show that for intermediate impact parameters there is a measurable sideward deflection of the emitted particles, while the more central collisions approach a thermal, isotropic distribution.

564H This experiment is a high statistics run of the ^{40}Ca + Ca reaction at 2.1 GeV/nucleon. The main thrust of this experiment is the study of Λ and K^0 production in central collisions of heavy ions at the top Bevalac energy. The production cross sections, transverse momenta and polarization are of great interest. The neutral strange particles are detected by their charged-particle decay (vee). The film of this experiment has been scanned for vees, which have been measured and reconstructed, and the analysis is in progress.

629H This, our active proposal, focuses on the study of interactions of ^{139}La + ^{139}La over the Bevalac energy range. An integral part of this proposal is the detection and identification of the forward emitted particles using a newly developed 400-element scintillator hodoscope. The charge of leading fragments will be used to characterize the impact paramter of the event.

SPS experiment.

Within the LBL/GSI collaboration our group, together with the Plastic Ball group, has an accepted proposal (NA 37) to measure the interactions of ^{16}O with nuclear targets at 50 and 225 GeV/nucleon at the CERN SPS. The necessary injector developments are well in progress; GSI has placed the order for the ion source, and LBL is in the process of commissioning an RFQ for the Bevatron Local Injector similar to the one to be built for the CERN experiment. Furthermore, CERN has started the necessary upgrade of their diagnostics instrumentation. The vertex magnet that will be used for the Streamer Chamber, now operational in the West Hall, will be moved to the North Hall. The Streamer Chamber from the Max Planck Institut in Munich to be used in the experiment is being upgraded. Forward angle calorimeters now employed in the NA 24 will be used for triggering and transverse energy measurement. The experiment will run in 1986 and 1987.

Members of the Streamer Chamber group with a life-size picture of an event as seen in the chamber. CBB 830-9673

Nuclear Theory

Group Leaders
N.K. Glendenning
M. Gyulassy
W.D.Myers
J. Randrup
W.J. Świątecki

P. Danielewicz
T. Døssing
K. Kolehmainen
T. Matsui
M. Redlich

C.S. Wang,
Peking University
Beijing, China

K. Möhring,
Hahn-Meitner Institut
Berlin, West Germany

P. Möller,
Lund University
Sweden

M. Weiss,
Lawrence Livermore
National Laboratory

Y.-J. Shi
Institute of Atomic
Energy, Beijing,
People's Republic
of China

B. Banerjee
Tata Institute
Bombay, India

E. Baron*
SUNY, Stony Brook

C. Dorso
University of
Buenos Aires,
Argentina

The work of the theory group continues to include a broad range of nuclear-, particle-, and astrophysical problems, addressed by a variety of approaches and techniques. We have found it possible to sustain the momentum in the direction of ultra relativistic nuclear physics and the quark-gluon plasma and to strengthen our effort in the astrophysical domain, while actually broadening our support to ongoing experiments at all of LBL's accelerators.

I. Hadronic and Quark Matter at High Energy Density

A major undertaking is the study of matter at very high energy densities. The regime of supernuclear densities is of great interest, impinging as it does on the fields of ultra-relativistic nuclear collisions and astrophysics. At densities below the deconfinement threshold, matter can be discussed in terms of hadrons and their interactions, employing an effective relativistically covariant lagrangian of interacting baryons and mesons and solved in the mean field approximation. A lengthy investigation of neutron star structure and the hyperon content of their cores was completed. The interaction of baryons with scalar mesons was shown to lead for a wide range of couplings to an abnormal phase transition at finite temperature. The abnormal state is characterized by low baryon effective masses and copious baryon-antibaryon pairs. The formulation for a saturating chiral theory was developed, its compatibility with neutron star masses checked, and its finite temperature properties investigated, including the gas-liquid phase transition at low temperature, and full chiral restoration at high. Much interest has focused recently on solitons as representing non-perturberative solutions of QCD for baryons. A number of authors have shown that these solitons resemble nucleons at the 30% level. What we find particularly appealing in the development is that, having a lagrangian that describes the internal structure of the nucleon, one can investigate interesting questions concerning how the internal structure changes when solitons are assembled to form dense matter, and how the properties of matter correspondingly change. To organize the calculation we envision the solitons as arranged in a crystal lattice. As a first step in understanding such problems, the Kronig-Penney model of fermions in periodic square potentials was solved analytically for relativistic particles. Considerable effort has been directed toward the study of the very high energy density domain that is expected to be formed in ultrarelativistic nuclear collisions. Particular interest has focused on the transition from nuclear to quark matter and the evolution of quark matter and its re-hadronization. A quark-gluon plasma (once formed) may disassemble by hydrodynamic expansion or by evaporation or both. The chromoelectric flux tube model provides a phenomenological description of color confinement, and it is shown how it provides a mechanism for the formation and radiation of mesons from the plasma surface. This evaporation process together with the external bag pressure due to the non-perturbative vacuum outside the plasma, impose boundary conditions on the hydro-expansion. For cylindrical geometry with Bjorken longitudinal expansion the resulting disassembly has the following characteristics. The plasma shrinks in the radial direction accompanied by the radiation of mesons from this space-like surface. The interior of the plasma meanwhile retains an almost spatially uniform temperature, which falls due to the longitudinal expansion. A global phase transition resulting from the homogeneity of the plasma defines a time-like surface on which energy-momentum conservation and the second law of thermodynamics require a transition from a supercooled plasma to a superheated hadron gas. This subsequently undergoes a rapid expansion to freezeout. The hadronic and di-lepton spectra

characterizing this unusual disassembly have been calculated.

II. Ultra-Relativistic Nuclear Collisions

The most exciting frontier of nuclear physics today is the study of the quark-gluon degrees of freedom in nuclei. With nuclear collisions induced in a stationary target by beam energies exceeding about 10 GeV/nucleon, estimates indicate that energy densities of at least one, and possibly two, orders of magnitude above the ground state energy density ($\sim$0.15 GeV/fm^3) could be attained. Current QCD lattice calculations predict that above a few GeV/fm^3 nuclear matter dissolves into a quark-gluon plasma. Therefore, it appears that this fundamental transition is accessible to experimental study. The arguments leading to the above conclusions were an important factor in convincing the Nuclear Science Advisory Committee to adopt the construction of a relativistic nuclear collider facility (RNC) as its highest priority project for the future. LBL and the theory group have provided and will continue to provide essential leadership in this forefront area of nuclear physics. We have been active in clarifying the physics potential of several proposals for an RNC at LBL. These include the VENUS, TEVALAC and MINI-COLLIDER options.

We have identified two general energy regimes that warrant special consideration. First, for beam energies less than some 10-100 GeV/nucleon on a stationary target, we have shown that the dominant reaction mechanism is the stopping of baryons in the local center of mass. This leads not only to enormous energy densities but also baryon densities nearly an order of magnitude greater than those at saturation. In this range we expect to be able to observe high baryon density quark-gluon plasmas. Second, for beam energies above 100 GeV/nucleon on a stationary target, we expect that high energy densities are also produced in a low baryon density environment. Thus, these two energy regimes probe complementary regions of the temperature density phase diagram of nuclear matter.

The theoretical effort has concentrated on detailed estimates of the early stages of the collision process, developing the transport theory for the subsequent expansion of the nuclear matter, the theory of the hadronization process, and possible signatures that could be looked for experimentally. For the early stages we have used hydrodynamic models to extrapolate cosmic ray data backward in time in order to relate final rapidity distributions to initial energy densities. We have recently studied nuclear stopping power using new experimental results on $p+A \rightarrow p+X$ and have analyzed the stopping process in terms of the inside-outside cascade scenario. For transport theory we have made extensive analysis of the shear and bulk viscosity coefficients using QCD phenomenology. For the hadronization process a microscopic approach based on string dynamics and a macroscopic approach based on relativistic combustion theory are being considered. Signatures we have studied include dilepton production, strangeness yields, transverse rapidity distributions and large fluctuations of rapidity distributions.

III. Theory of Nuclear Collisions at the Bevalac

The theory group enjoys close contact with the experimental program at the Bevalac which is concerned with nuclear collisions in the range 0.1 to 2.0 GeV/nucleon. In recent years the effort has shifted to exclusive event analysis in the program to map out the nuclear equation of state for densities lower than those where a quark-gluon plasma is expected to be produced. Programs have

been developed to calculate exclusive final states including heavy composite production. We employ a variety of Monte Carlo cascade programs to test dynamical assumptions in simpler models and to test proposed signatures. The theory of global event analysis has been extensively developed and in particular its limitations in finite nuclear conditions have been clarified. New work in this area is the development of very sensitive transverse momentum two-particle correlation methods. With these methods we have analyzed streamer chamber data and have been able to isolate small amounts of collectivity that would be invisible with other methods. The proposals to extract the nuclear matter equation of state from pion excitation functions have also been reanalyzed. With regard to deuteron production, we have developed a general framework for analyzing the data so as to extract space-time information and to check for space-momentum space correlations as signatures of collective flow. This area of research will continue to be a basic part of our overall program.

IV. Low Energy Nuclear Dynamics

The "chaotic regime" macroscopic nuclear dynamics is being applied to a variety of nuclear reactions, including relatively light systems such as ^{6}Li, ^{9}Be and ^{12}C colliding with ^{40}Ca, where theory predicts the formation of superdeformed nuclei (nuclei stretched into cylinder-like shapes by the centrifugal force).

A simple theory of Fermi jets (prompt nucleons emitted in the early stages of a nucleus-nucleus collision) has been used to make a survey of energy and angular distributions of these jets as a function of the masses of the colliding nuclei and of the collision energy.

The recent discovery of the radioactive decay of ^{222,223,224}Ra by the emission of ^{14}C has been interpreted quantitatively in terms of a barrier-penetration phenomenon, analogous to spontaneous fission.

V. Damped Nuclear Reactions

The dynamics of damped nuclear reactions is being studied with a particular view towards the role played by the multiple transfer of nucleons. Current efforts have been devoted to studying the accumulation of angular momentum in the two reacting nuclides and the subsequent disposition of spin through sequential decays. A set of first order differential equations is derived for the evolution of the averages, variances, and covariances of the spin distributions in the two nuclides during the collisions. The stationary solution to the dynamical equations can be interpreted in terms of the six angular momentum bearing modes of the disphere in thermal equilibrium with the remaining intrinsic degrees of freedom. The relaxation times of these modes have been estimated in a model where the angular momenta are generated by nucleon transfers. Relative to the collision time, some of the relaxation times are very short and some are quite long. This implies very specific properties of the distribution of spins in the two nuclei when they separate after the collision. The sequential decay of nuclei resulting from damped reactions is considered with an emphasis of multiplicity distributions and angular correlations. The effect of prior particle evaporation is included. The existence of covariances between the spins of the two reaction products implies that the detection of a decay product from one nucleus may break the reflection symmetry of the angular correlation of decays from the other nucleus; this important effect is presently being probed in a fission-fission experiment. Overall good agreement with a broad range of data is found, but for small energy

losses the calculated spin increases too rapidly, possibly signifying the simultaneous action of an additional dissipative mechanism not carrying angular momentum.

VI. The Macroscopic Approach to Nuclear Properties

A range of programs is underway extending application of macroscopic methods in general, and the Droplet Model in particular. Comparisons with Hartree-Fock calculations have led to the resolution of certain discrepancies that seemed to exist in earlier work, and to the determination of a new direction for subsequent developments. This new direction concerns the possible inclusion of "finiteness" effects in the Droplet Model. Such an approach would not only incorporate the usual "lepdopterous" (thin skin) terms that are traditional, but would also include provision for "holodermous" (all skin) effects. Investigations along these lines have begun with the inclusion of an empirical term in the Droplet Model mass formula that falls off exponentially with nuclear size. Such a term seems to play an important role in the mass formula, and its inclusion has resulted in a number of substantial improvements in the predictive power of the theory. Another, unrelated, application of macroscopic methods is the investigation of the influence on the multipole moments of nuclear charge and mass of possible octupole ground state deformations in some regions of the nuclear chart.

VII. Nuclear Astrophysics

The study of semi-infinite nuclear surfaces is continuing in order to determine the nature of the phase transition that takes place when an increasing neutron excess goes over suddenly to neutron matter. The Thomas-Fermi method is employed with a simple saturating force. The results of these calculations are important for formulating a description of nuclei as they evolve during the collapse of a supernova or for describing nuclei in the surface of neutron stars.

Bevalac Computer Support Group

Group Leader
Charles McParland

Mark Bronson

During the past year, a group was created and placed under the leadership of Charles McParland. This is an expansion of previous Bevalac software efforts and has responsibilities in three major hardware and software areas.

The first area is the support of the existing data acquisition/analysis VAX 11/780s at the Bevalac. We will be responsible for both hardware and software maintenance of these two machines. We will also evaluate and acquire new peripherals and software packages in order to improve the utility of these machines as both acquisition and analysis tools.

The second area is the continued support of present data acquisition programs. These programs include packages that execute on both the central VAXs as well as experimenters' data acquisition machines. The current acquisition program, DATACQ, provides a flexible framework within which an experimenter can specify the particulars of their interactions with CAMAC instrumentation.

The third principal area of effort is the development of new data acquisition systems to meet the increasing needs of the Bevalac experimental program. We will strive to bring the latest developments in both hardware and software to the problems of data acquisition and on-line analysis. In particular, we will push to shorten the time required to apply new technologies (e.g., laser optical disks, inexpensive fast microprocessors) to the problems of experimental data acquisition.

The Berkeley Mini-Collider*

L.S. Schroeder

The primary physics motivation for studying central nucleus-nucleus collisions at c.m. energies of a few GeV/nucleon is illustrated in Fig. 1. Present theoretical estimates and extrapolations of existing high energy data indicate that maximum nuclear compression will occur at these energies and that the heaviest nuclei will "stop" in each other.[1-4] In such a "stopping" regime we expect to:

- probe regions of maximum baryon density up to $\sim 10\times$ that of ordinary nuclei,
- extend the present Bevalac studies of highly excited hadronic matter to higher temperature (T) and density (ρ),
- produce and study the quark-gluon plasma in a baryon-rich environment. The centerpiece of this program will certainly be the search for and study of the baryon-rich quark-gluon plasma. Besides the opportunities associated with a new state of matter, the study of the hadronic to quark-gluon phase transition will test the long range aspects of QCD and our understanding of the confinement-deconfinement process.

A natural first question is: why a collider? Colliders have proven to be a very economical way of covering a large dynamic range. For a program focused on maximum baryon density as well as the potential of producing a baryon-rich quark-gluon plasma, a large dynamic range is needed since there is at present no solid evidence that such phenomena will exhibit a sharp threshold-like behavior. Indeed, just the opposite might be the case and we must be prepared for such an eventuality. A collider is favored from the point of view of detectors

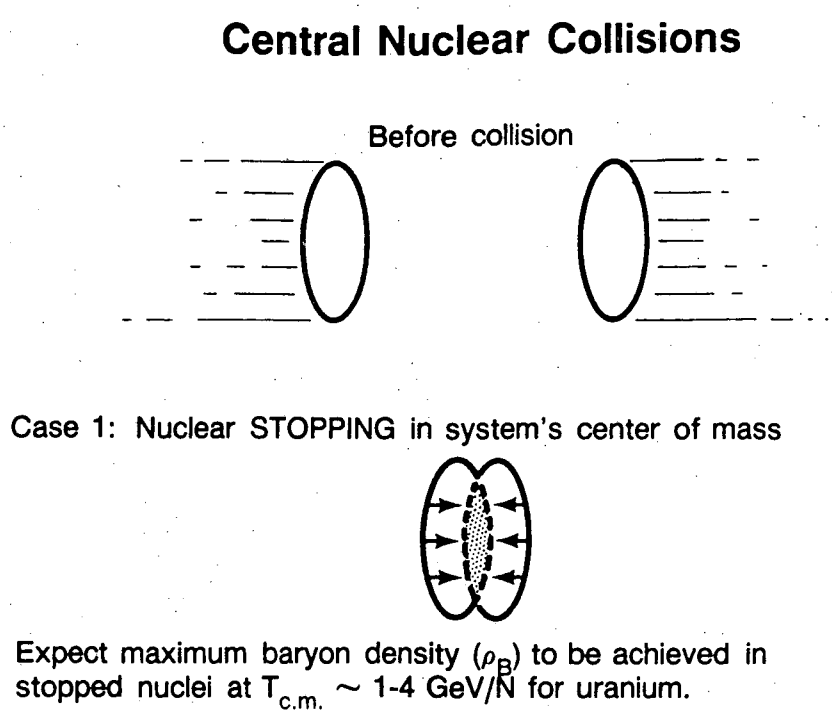

Fig. 1. Characterization of the region of maximum nuclear compression.
XBL 8410-4170

also. Particle multiplicities will be in the hundreds, and possibly even a thousand or so per event, in central uranium-uranium collisions. Spreading these over the full solid angle in the collider mode will reduce some of the demands on detectors. In equivalent fixed target operation, identical numbers of particles will of course be produced. But in this case, they will be tightly focused in the forward direction, putting severe demands on detector granularity, size of individual detector elements and requiring a large dynamic energy range over which particle identification must be made.

At the Mini-Collider, to achieve collisions of the heaviest nuclei at energies well above those available at the Bevalac both on a timely basis and at minimal cost, we want to utilize as much of the existing Bevalac complex as possible. These elements include:

- the SuperHILAC acting as the ion source (protons to uranium),
- the Bevatron as the booster,
- the existing experimental hall as the general site for the colliding rings.

Roughly the following sequence of events will be required to store uranium beams in the Mini-Collider for physics experiments:

- U^{+38} or U^{+40} provided by the SuperHILAC and injected into the Bevatron (no stripping at exit to insure maximum uranium intensity);
- acceleration in the Bevatron to about 400 MeV/nucleon
- single-turn extraction, transfer to collider (stripping to U^{+92} occurs at this stage);
- stochastic accumulation in the collider, allowing the storage of many injector pulses (expect $\sim 10^8 - 10^9$ ions stored in each beam);
- slow acceleration in collider to desired energy (time $\sim$60 seconds to $B_{max} \sim$ 3–4 T) – placing minimum demands on superconducting magnet design;
- continuous stochastic cooling employed to maintain beam quality and reduce the effects of intrabeam scattering.

Detailed lattice calculations remain to be done for the Mini-Collider; however a set of conservatively estimated performance goals is shown in Table I.

Table I. Initial Estimates of Machine Parameters

Particle	Max KE (GeV/N) (C.M. Frame)	Luminosity $\mathscr{L}$($cm^{-2}sec^{-1}$) at 1 GeV/N
uranium	3–4	3×10^{23}
gold	3–4	4×10^{23}
neon	4–5.3	2×10^{25}
proton	9–12	4×10^{26}

Early considerations of a lattice design indicate that the interaction zone will be about one meter long. Since the size of the crossing region directly affects possible detector configurations, future design efforts will be made to squeeze this region down without undue loss of luminosity. Present designs allow for ± 5 meters about the center of the crossing region for detectors. Fig. 2 shows a possible layout for the Mini-Collider in the EPB Hall of the Bevatron. Initially we anticipate two of the interaction regions would be outfitted with detectors. One of them could be located inside Building 64 which has a high-bay area with good crane access. Note that the Mini-Collider as sketched has relatively minimal impact on the rest of the Bevalac area.

Detectors

A major problem confronted in designing detectors suitable for measuring central high energy nucleus-nucleus collisions is the tremendous number of particles appearing in the final state. At current Bevalac energies the GSI/LBL Plastic Ball experiment has already measured $\langle M_{Chg} \rangle \sim 100$–$200$ for central collisions of Au + Au. At these energies the majority of the charged particles are protons or light nuclei, with $\langle M_{\pi} \rangle_{central} < 50$–$60$. However, as we move to Mini-Collider energies the number of pions and other produced particles (e.g., $K^{\pm}$, $\bar{p}$, $\bar{\Lambda}$, . . .) grows significantly. At the mid-range of the Mini-Collider, we can expect several hundred pions to be created in a single central collision event. Thus, consideration of how to handle the enormous particle multiplicities is of prime importance. However, a point in our favor is the fact that the typical energy of these produced particles will be in the range of a few hundred MeV to a few GeV. In this region particle identification techniques are generally straightforward.

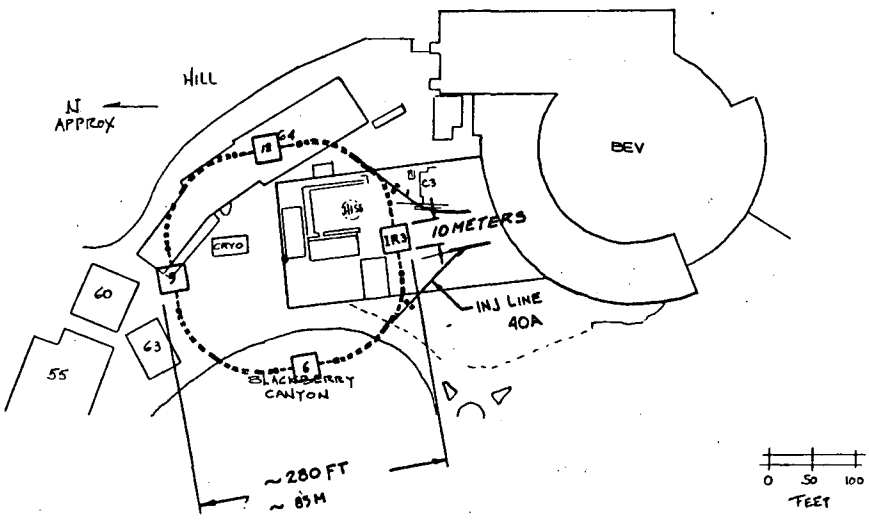

Fig. 2. Possible layout for Mini-Collider in EPB area of the Bevalac. Four crossing regions shown, of which two would initially be instrumented. XBL 849-3691

With a luminosity $\mathscr{L} \sim 10^{24}$ cm^{-2}sec^{-1} for uranium-uranium collisions, and using a total cross section for uranium-uranium of $\sigma_t \sim 10$ barns (10^{-23} cm^2), and further assuming that $\sigma_{central} \sim 0.1\ \sigma_t$ we arrive at the central trigger event rate:

$$N = \sigma_{central}\,\mathscr{L} \sim 1 \text{ central trigger/sec.}$$

For uranium-uranium the event rates will be in the 1–10 Hz range at the Mini-Collider, or about 80–90,000 minimum bias events/day. We are directing our attention to Mini-Collider Detectors (MCD) which are matched to these event rates. Fig. 3 shows an artist's conception of a possible detector consisting of:

- a multiplicity barrel array surrounding the interaction region to provide a particle trigger for central collision events, with the added ability of measuring the pseudorapidity distribution on an event-by-event basis;
- a clam-shell shaped calorimeter to measure both electromagnetic (EM) and hadronic energy flow (suitable end cap calorimeters are also indicated);
- an open region on one side of the MCD into which one could insert a major tracking detector (a magnetic spectrometer or a visual tracking device such as a streamer chamber) which would concentrate on identifying and measuring particle momenta of a limited number of particles very well.

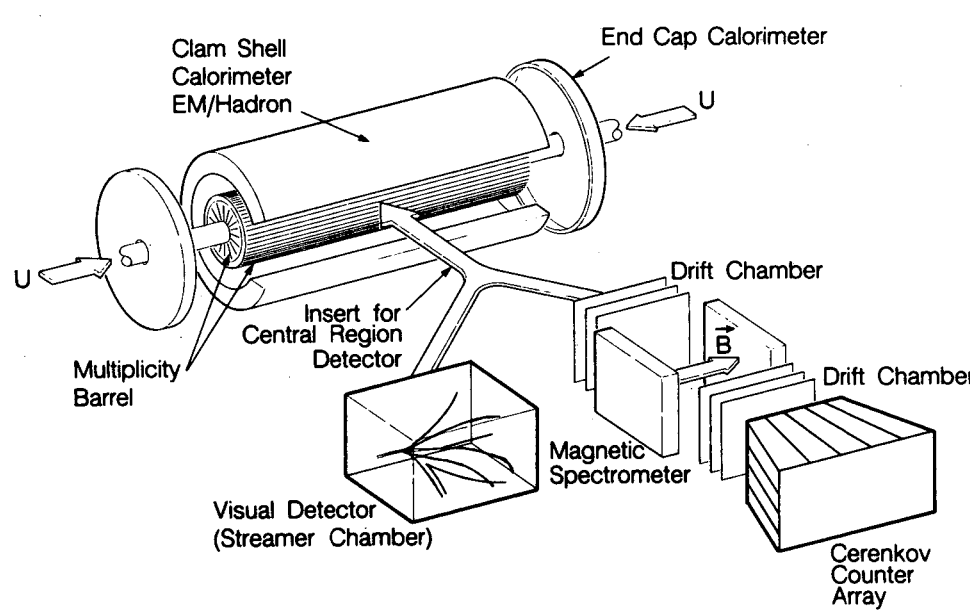

Fig. 3. Concept for a possible Mini-Collider detector (MDC). XBL 846-8451

The general concept is one of providing a major piece of apparatus covering most of the solid angle, with enhanced capability of measuring particles in the mid-rapidity region. Either a magnetic spectrometer with tracking or a streamer chamber can handle large numbers of particles and would be potential candidates for the central region detector. Clearly one would want to tailor the detector to the physics of interest. For example, if one is measuring the charged strange meson ($K^{\pm}$) fraction, the magnetic spectrometer would be favored; if strange baryons were being studied, the characteristic "vee" ($\Lambda^0 \rightarrow p\pi^-$, $\bar{\Lambda}^0 \rightarrow \bar{p}\pi^+$) or "kink" ($\Xi^- \rightarrow \Lambda^0\pi^-$, $\Omega^- \rightarrow K^-\Lambda^0$) patterns would suggest use of the streamer chamber.

Summary

The Mini-Collider offers us the opportunity of exploring exciting physics over the range of a few GeV/nucleon in the c.m. with the heaviest beams. This provides a natural extension of our present Bevalac studies of extreme conditions of temperature and density in hadronic matter with an ultimate goal of producing and studying a baryon-rich quark-gluon plasma in the region of maximum nuclear compression (so-called "stopping" regime).

As presently conceived, the Mini-Collider would consist of twin superconducting accelerating rings to achieve $T_{cm} \sim 1$–4 GeV/nucleon. By using our existing Bevalac complex (SuperHILAC as injector, Bevatron as booster) we would be able to put such a machine together on a relatively short time-scale (probably 2–3 years after funding started) and at minimal cost. To keep costs down, the superconducting magnets would have $B_{max} \sim 3$–4 T, and would use existing superconducting materials and conventional technology (clamping and collaring techniques). Stochastic cooling will be employed to achieve maximum possible luminosity ($\sim 10^{24}$ $cm^{-2}sec^{-1}$ for uranium-uranium) at these energies and long (>24 hours) beam lifetimes.

Detector solutions matched to these luminosities appear quite do-able.

Footnotes and References

*Condensation of an invited talk given at the Conference on the Intersections between Particle and Nuclear Physics, Steamboat Springs, Colorado (May 1984).

1. A. Goldhaber, Nature **275**, 114 (1978).
2. *The Tevalac*, LBL PUB-5081 (December 1982).
3. W. Busza and A. Goldhaber, Phys. Lett. **139B**, 235 (1984).
4. L. P. Csernai and J. I. Kapusta, *Proton Stopping Power of Heavy Nuclei*, to be published in Phys. Rev. **D**, June 1984.

Workshop on Detectors for Relativistic Nuclear Collisions

L. S. Schroeder

A workshop to discuss future high energy heavy ion detector requirements was held March 26–30, 1984 at LBL.[1]

As we move into the mid-80s and beyond, the prospects for higher energy nucleus-nucleus collisions appear quite promising. At Brookhaven, construction of a transfer line between the Tandem Van de Graaff and the AGS will provide light ions ($A \leq 32$) at energies of 15 GeV/nucleon in 1986. At the same time a GSI/LBL collaboration is upgrading the PS injector at CERN, allowing an ^{16}O program at the SPS at energies from 15 to 225 GeV/nucleon beginning in 1986. Finally, the Nuclear Science Advisory Committee of the Department of Energy and the National Science Foundation has recently recommended that the next major nuclear physics facility in the United States should be a relativistic nuclear collider to explore the domain of very high energy densities and hopefully the production of deconfined hadronic matter – the quark-gluon plasma.

Given that new heavy-ion facilities will be available within two years, we felt that it was both timely and necessary to start looking at the detector requirements imposed by these much higher energies well in advance of their coming on-line. The specific goals that we set for this Workshop were:

- Build on the base of information generated at previous meetings held to discuss quark matter – specifically, fixed target detectors discussed at Bielefeld (QM'82) and a SPS workshop held in late 1982; collider detectors discussed at Brookhaven (QM'83).
- Consider detectors for both geometries, i.e., fixed target: spanning the interval 15–225 GeV/nucleon and collider: from 2 + 2 to 100 + 100 GeV/nucleon.
- Identify those critical path items for detectors requiring an R&D effort.

It was clear that the area of high energy nuclear collisions is one where both particle and nuclear physicists can join together in a common endeavor. The meeting provided a natural mixing ground for these two communities. The format for the meeting was as follows:

- Plenary sessions were held in the morning. We tried to provide a blend of theoretical and experimental ideas on the production of the quark-gluon plasma.
- The afternoons were devoted to the individual working groups. Here we identified three areas of detector measurement or technique which were used as the central focus for each group. These were:

  i. *hadrons* - generally, detection of strange particles and antibaryons, Hanbury-Brown/Twiss measurements, i.e., few particle measurements with reduced solid angle coverage;

  ii. *event parameters* - experiments with large ($\sim 4\pi$) solid angle coverage measuring many of the particles in the final state in order to determine, e.g., $\langle M \rangle$, $dn/d\eta$ or dn/dy vs $\langle M \rangle$, fluctuations, etc.;

  iii. *penetrating probes* - experiments measuring photons, leptons, lepton pairs, etc., which are thought to be useful in probing the hot, compressed stage of the collision process.

For each of these categories, there was a separate working group for fixed target and collider geometry. Each working group had conveners who organized and guided the work of the group. The conveners were:

	Hadrons	Event Parameters	Penetrating Probes
Fixed Target	C. Gruhn (LBL) I. Otterlund (LUND)	K. Foley (BNL) A. Poskanzer (LBL)	J. Carroll (UCLA) M. Goldberg (Syracuse)
Collider	W. Carithers (LBL) T.J.M. Symons (LBL) G. Young (ORNL)		T. Ludlam (BNL) L. Madansky (Johns Hopkins)

Reference

1. Proceedings of the Workshop on Detectors for Relativistic Nuclear Collisions, edited by L.S. Schroeder, LBL-18225, UC-37, CONF-8403137 (Aug. 1984).

88-Inch Cyclotron Operations

D.J. Clark
D. Elo
L. Glasgow
R. Lam
R.M. Larimer
C.M. Lyneis
R.G. Stokstad

Operations

The 88-Inch Cyclotron, operated by the Nuclear Science Division, provides a large fraction of the beam time that is used by Division scientists. Variable energy high resolution beams from hydrogen through argon are produced and used for studies of nuclear structure and nuclear reaction mechanisms. The cyclotron is also the Laboratory's major source of medical isotopes and its only source of polarized proton and deuteron beams. Ions as heavy as ^{40}Ar can be accelerated to the Coulomb barrier of 5 MeV/nucleon, while lighter heavy ions can reach 20-30 MeV/nucleon. The new ECR source, which is just coming into operation, will extend the mass range to krypton for Coulomb barrier energies, and will increase the lighter heavy ion energies to 35 MeV/nucleon. The cyclotron thus operates in the important transition region between low and high energies: 10–35 MeV/nucleon.

As a national accelerator laboratory the 88-Inch Cyclotron is used extensively by outside groups from many institutions in the U.S. and abroad. Table I shows the number of users from LBL and elsewhere. Scheduling of experiments for the cyclotron is done in an open meeting on a weekly basis with a lead time of eight days. Outside users who must make travel arrangements in advance are accommodated with advance scheduling. A users' organization has been formed and a Program Advisory Committee instituted. The members of the Users' Executive Committee are Karl Van Bibber (Stanford University), Chairman; Frank S. Dietrich (Lawrence Livermore National Laboratory); and Marie-Agnes Deleplanque (LBL). The Program Advisory Committee consists of C. Konrad Gelbke (Michigan State University), Chairman, Charles Goodman (Indiana University) and Jørgen Randrup (LBL).

The 88-Inch Cyclotron plays a significant educational role. In 1984 seven graduate students from the University of California at Berkeley employed this facility in their research toward the Ph.D. degree. Eight graduate students from other universities participated in research at the cyclotron.

The cyclotron operates 14 1/2 eight hour shifts per week with one additional shift for maintenance at the beginning of the week and one half shift for shutdown for the weekend. The distribution of cyclotron time is shown in Table II. The list of beams available is given in Table III. The particle distribution of ion beams during the past years is shown in Fig. 1.

Improvement Programs

In FY84 the major improvement program was the completion of construction and installation of the new ECR heavy ion source. This is described in a separate article in this annual report.

The new rf anode matching capacitor drive system was installed. This work is part of an improvement project to reduce the power required from the final rf amplifier and increases the tube life. A program is in progress to monitor and log cyclotron operating parameters. Computer programming is being done for this project.

In the experimental area, the new high-resolution γ-ray ball was installed in Cave 5 and experiments were begun. Radiation shielding was improved in several cave areas. The mechanical pump venting system for the experimental areas was completed. An improved filtered vent system for the medical short-lived isotope program was installed.

For the building, the main switching system at the transformer pad has been completed. This provides a separate 12 kV, 200 amp fused disconnect for a 2 MVA transformer. The transformer will be installed early next year to provide additional power for the ECR source and higher energy beams. In the machine shop digital measuring units for milling machines are being installed. They will improve accuracy and decrease effort in machining work.

Table I. Number of users of the Cyclotron during FY84

LBL Staff, U.C. Berkeley		23
Graduate Students		
U.C. Berkeley	7	
Other Universities	8	
		15
Post-doctoral scientists		
LBL	9	
Other laboratories	5	
		14
Outside users and visitors		
Industry	66	
Universities, National Labs.	44	
		110
TOTAL		162

Table II.
Cyclotron operating and maintenance time distribution for the 12 month period 10/1/83 to 9/30/84 covered by this Annual Report

		Hours		%	
Operating Time	Machine Studies	508		8.4	
	Tuning	414		6.8	
	Optics	235		3.9	
	On target	3290		54.5	
	Waiting for experimenter	78		1.3	
	Subtotal	4525		74.9	
Maintenance Time					
	Scheduled maintenance	818		13.5	
	Ion source changes	382		6.3	
	Unscheduled maintenance	132		2.2	
	Other	191		3.1	
	Subtotal	1523		25.1	
	Total		6048		100.0
	Holiday/Shutdown		2736		
	Total Time		8784		

Table III. 88-Inch Cyclotron Beam List 1984

Ion	Energy[a] (MeV)	Ext. Beam Intensity (eμA[b])
p	0.2 – 55	100 – 20
p (polarized)	6 – 50	.7 – .4
d	0.5 – 65	100 – 20
	65 – 70	~0.5
d (polarized)	10 – 65	.7 – .4
$^{3}He^{1+}$ [c]	2 – 47	>20
$^{3}He^{2+}$ [c]	4 – 140	100 – 10
$^{4}He^{2+}$	3 – 130	100 – 10
	130 – 140	~0.5
$^{6}Li^{1+}$ [c]	2 – 23	5
$^{6}Li^{2+}$ [c]	23 – 93	1
$^{6}Li^{3+}$ [c]	93 – 195	0.1
$^{7}Li^{2+}$	20 – 80	1
$^{7}Li^{3+}$	80 – 180	0.1
$^{9}Be^{2+}$	15 – 62	5
$^{9}Be^{3+}$	62 – 140	2
$^{9}Be^{4+}$	140 – 249	.05
$^{10}B^{2+}$ [c]	14 – 56	10
$^{10}B^{3+}$ [c]	56 – 126	50
$^{10}B^{4+}$ [c]	126 – 224	0.3
$^{10}B^{5+}$ [c]	224 – 320	0.001
$^{11}B^{2+}$	12 – 51	10
$^{11}B^{3+}$	51 – 115	50
$^{11}B^{4+}$	115 – 204	0.3
$^{12}C^{2+}$	12 – 47	>20
$^{12}C^{3+}$	47 – 105	30
$^{12}C^{4+}$	105 – 212	5 – .5
$^{12}C^{5+}$	187 – 306	.05 – .001
$^{12}C^{6+}$	292 – 384	10^{5} p/s
$^{13}C^{3+}$ [c]	43 – 97	>20
$^{14}N^{2+}$	10 – 40	20
$^{14}N^{3+}$	40 – 90	15
$^{14}N^{4+}$	90 – 160	15
$^{14}N^{5+}$	160 – 250	2
$^{14}N^{6+}$	250 – 360	10^{6} p/s
$^{14}N^{7+}$	360 – 448	100 p/s
$^{15}N^{4+}$ [c]	84 – 150	15
$^{16}O^{1+}$	9	1
$^{16}O^{2+}$	9 – 35	>5
$^{16}O^{3+}$	35 – 79	20
$^{16}O^{4+}$	79 – 155	30 – .2
$^{16}O^{5+}$	140 – 219	5
$^{16}O^{6+}$	219 – 315	0.3
$^{16}O^{7+}$	315 – 429	10^{7} p/s
$^{16}O^{8+}$	429 – 512	0.2 p/s
$^{18}O^{3+}$ [c]	31 – 70	20
$^{18}O^{4+}$ [c]	70 – 124	>10
$^{18}O^{5+}$ [c]	124 – 194	5
$^{19}F^{3+}$	30 – 66	5
$^{19}F^{4+}$	66 – 118	10
$^{19}F^{5+}$	118 – 184	2
$^{20}Ne^{3+}$	28 – 63	>10
$^{20}Ne^{4+}$	63 – 112	10
$^{20}Ne^{5+}$	112 – 175	5
$^{20}Ne^{6+}$	175 – 252	1
$^{20}Ne^{7+}$	252 – 343	0.01
$^{20}Ne^{8+}$	343 – 448	~50 epA
$^{22}Ne^{5+}$ [c]	102 – 159	~5
$^{22}Ne^{6+}$ [c]	159 – 229	1
$^{24}Mg^{4+}$	50 – 93	2
$^{24}Mg^{5+}$	93 – 146	0.2
$^{25}Mg^{4+}$ [c]	50 – 90	2
$^{26}Mg^{4+}$ [c]	48 – 86	2
$^{26}Mg^{5+}$	86 – 145	.08
$^{28}Si^{5+}$	80 – 125	1
$^{28}Si^{6+}$	125 – 180	0.2
$^{28}Si^{7+}$	180 – 245	0.05
$^{32}S^{6+}$	100 – 158	2
$^{32}S^{7+}$	158 – 238	0.2 – .03
$^{35}Cl^{7+}$	144 – 196	0.5
$^{35}Cl^{8+}$	196 – 256	0.05
$^{37}Cl^{6+}$	95 – 136	0.3
$^{37}Cl^{7+}$	136 – 185	0.08
$^{40}Ar^{2+}$	3.5- 14	0.4
$^{40}Ar^{6+}$	87 – 126	4
$^{40}Ar^{7+}$	126 – 172	2
$^{40}Ar^{8+}$	172 – 224	0.5
$^{40}Ar^{9+}$	224 – 280	10^{5} p/s
$^{40}Ar^{10+}$	280 – 350	10^{3} p/s
$^{40}Ca^{6+}$	87 – 126	1
$^{40}Ca^{7+}$	126 – 172	0.2
$^{56}Fe^{10+}$	180 – 250	1 p/s
$^{63}Cu^{9+}$	142 – 180	5 enA
$^{63}Cu^{10+}$	180 – 222	0.1 enA
$^{63}Cu^{11+}$	222 – 269	$5x10^{3}$ p/s
$^{84}Kr^{2+}$	1.6- 6.6 [d]	.001
$^{84}Kr^{8+}$	82 – 107	.250
$^{84}Kr^{9+}$	107 – 135	.120
$^{84}Kr^{10+}$	135 – 167	.030
$^{84}Kr^{11+}$	167 – 202	.003
$^{197}Au^{13+}$	102 – 120	2 p/s
$^{197}Au^{14+}$	120 – 140	0.1 p/s

a) Heavy ion energy range shows nominal maximum energy for a particular charge state down to energy which can be reached by the next lowest charge state. The maximum energy for several heavy-ion beams has been increased to $E = 160\ Q^2/A$ MeV. Beams can also be run at energies below 1 MeV/nucleon.
b) Electrical microamperes except as noted, $\Delta E/E \sim 0.3\%$. Intensity on target will be less, depending on mode of beam transport.
c) Isotopically-enriched source feed.
d) 15th harmonic.

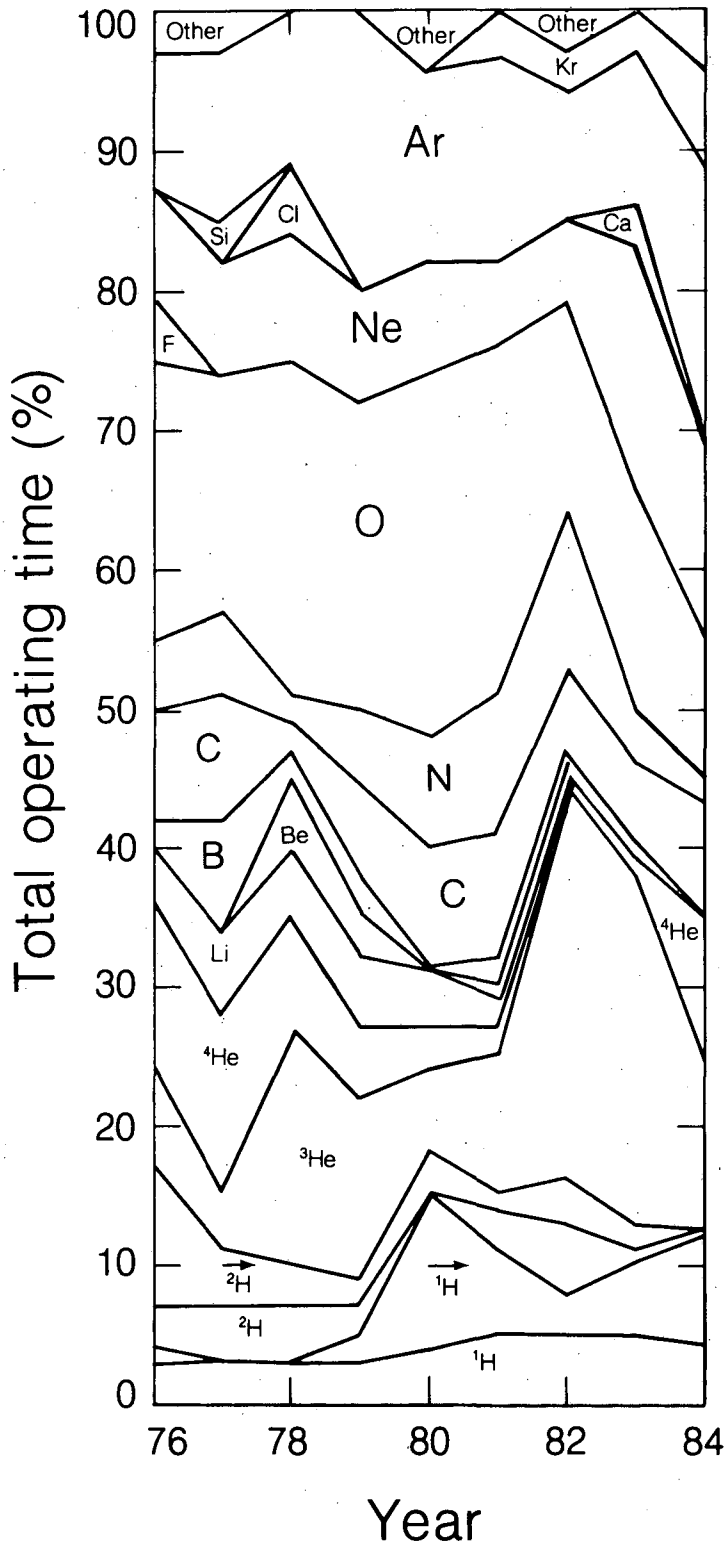

Fig. 1. Distribution of particle type during last 9 years. XBL 8312-6915B

PART II: EXPERIMENTS

Beta-delayed Two-proton Decay of ^{22}Al and ^{26}P*

*M.D. Cable,† J. Honkanen,‡ E.C. Schloemer,§ M. Ahmed,** J.E. Reiff, Z.Y. Zhou,†† and Joseph Cerny*

Following the discovery[1,2] of beta-delayed two-proton emission, we have attempted to establish the mechanism(s) for this decay mode in the decays of both ^{22}Al and ^{26}P. These nuclides were produced at the 88-Inch Cyclotron via the (^{3}He,p4n) reaction at 110 MeV on targets of ^{24}Mg and ^{28}Si, respectively. Proton-proton coincidence experiments have been performed in high geometry configurations at small angles (~0–70°) and at large angles (70–170°). Monte Carlo simulations of the expected proton-proton coincidence data were made for decay by sequential emission, by (transient) ^{2}He emission, or by simultaneous, uncorrelated emission.

The experimental results show that the dominant two-proton emission mechanism is a sequential process for both ^{22}Al and ^{26}P. Figure 1 presents the decay scheme for ^{22}Al most consistent with our overall results. A decay scheme for ^{26}P appears in ref. 2. Some puzzling features of the large-angle two-proton measurements for ^{22}Al have been observed and suggest further investigation.

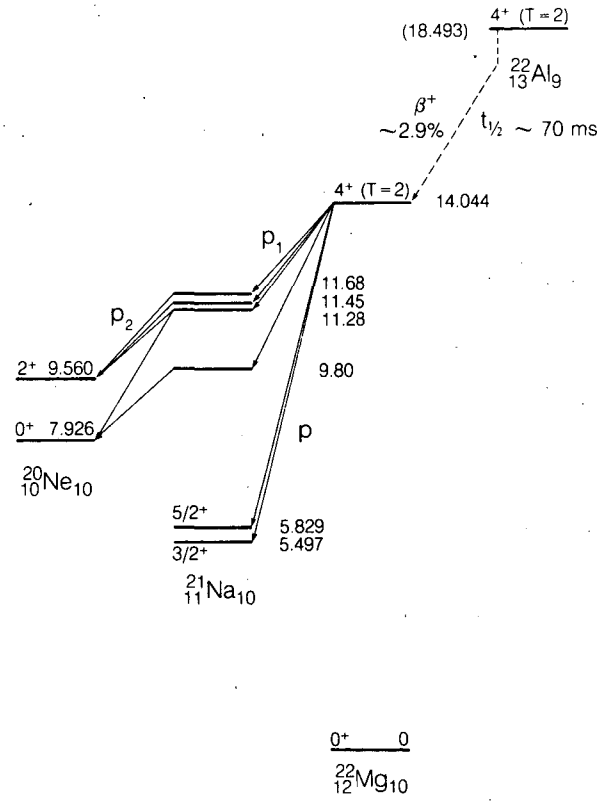

Fig. 1. Proposed new partial decay scheme for ^{22}Al.
XBL 842-9422

Footnotes and References

*Condensed from LBL-17983, Phys. Rev. C, October 1984.

†Present address: Lawrence Livermore National Laboratory.

‡Present address: Department of Physics, University of Jyväskylä, Finland.

§Present address: A.T.&T. Bell Laboratories, Holmdel, NJ.

**Present address: Bell Communications Research Inc., Red Bank, NJ.

††Permanent address: Department of Physics, Nanjing University, Nanjing, China.

1. M.D. Cable, J. Honkanen, R.F. Parry, S.H. Zhou, Z.Y. Zhou and J. Cerny, Phys. Rev. Lett. **50**, 404 (1983).
2. J. Honkanen, M.D. Cable, R.F. Parry, S.H. Zhou, Z.Y. Zhou and J. Cerny, Phys. Lett. **133B**, 146 (1983).

Additional Beta-delayed Protons from the $T_z = -3/2$ Nuclei ^{21}Mg, ^{25}Si, ^{29}S, and ^{41}Ti*

*Z.Y. Zhou,† E.C. Schloemer,‡ M.D. Cable,§ M. Ahmed,** J.E. Reiff and Joseph Cerny*

Beta-delayed proton emission has proven to be a useful tool for understanding nuclei far from stability. Most of the beta decay strength is concentrated at and below the isobaric analog state (IAS) of the parent nucleus (precursor) ground state. Identification of beta strength to states above the IAS is important not only because it provides additional tests of nuclear models of beta decay, but also because proton emission from such beta daughter nuclei frequently constitutes an important component of the background in searches for more exotic nuclei. Therefore we have re-measured the beta-delayed proton spectra of four $T_z = -3/2$ nuclei: ^{21}Mg, ^{25}Si, ^{29}S and ^{41}Ti. Fourteen previously unreported proton groups were observed and beta decay branching ratios were derived for each.

^3He beams from the 88-Inch Cyclotron were used to produce the proton-rich nuclei of interest. A high speed helium jet system transported the activity to a region of low background shielded from the beam and target area. Subsequent beta-delayed proton emission was observed using a high geometry, three-element semiconductor telescope with 38 μm $\Delta E1$, 125 μm $\Delta E2$, and 1000 μm E detector thicknesses. This telescope subtended a solid angle of .38 sr and was sensitive to protons ranging in energy from 4 to 10 MeV.

In all these studies, beam energies and/or measurement conditions were selected to produce the isotope of interest via the (^3He, 2n) reaction with little or no contamination from other beta-delayed particle emitters. ^{21}Mg was produced via the $^{20}Ne(^3He,2n)$ ^{21}Mg reaction at 41.5 MeV while ^{25}Si, ^{29}S and ^{41}Ti were produced from Mg, Si and Ca targets, respectively, at ~32 MeV.

Fig. 1 shows the beta-delayed proton spectrum for ^{41}Ti. This spectrum is also representative of the other three isotopes studied. Due to pile-up effects between events in the strong proton groups and the intense beta-particle background, the weak proton groups of interest lie on a high energy tail from the strong groups. This "background" above these strong groups is assumed to have a shape illustrated by the solid curve in Fig. 1. Principal uncertainties in the extracted intensities of the weak proton groups arise from the uncertainty in this background subtraction as well as the statistical uncertainty in the peak yield. Table I summarizes the states inferred to have been populated in the beta decay of these four isotopes. See ref. 1 for ^{21}Mg studies, ref. 2 for ^{25}Si, ref. 3 for ^{29}S and ref. 4 for ^{41}Ti. Tabulated intensities have been normalized relative to the yield of the most intense proton group of the beta-delayed proton emission from that isotope. From the relative intensities, partial lifetimes and log *ft*s have been derived for each state. Log *f* values have been interpolated from the tables of ref. 5.

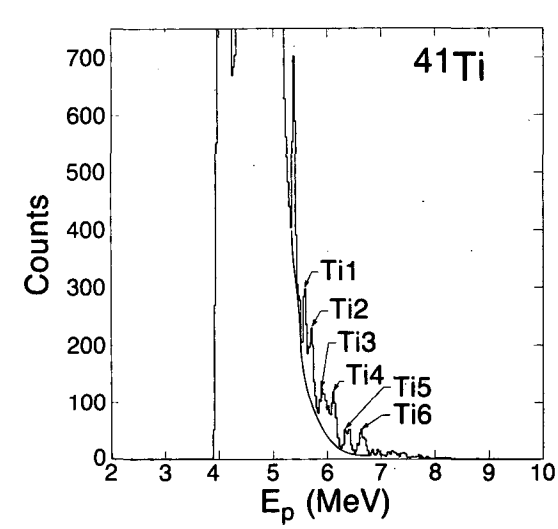

Fig. 1. Beta-delayed proton spectrum from ^{41}Ti. Six new proton groups have been identified. The beta pile-up tail from the peak at 4.7 MeV is represented by the solid curve. XBL 842-10104Y

Footnotes and References

*Condensed from LBL-18853

†Permanent address: Department of Physics, Nanjing University, Nanjing, China.

‡Permanent address: A.T.&T. Laboratories, Holmdel, NJ.

§Permanent address: Lawrence Livermore National Laboratory.

**Permanent address: Bell Communications Research, Inc., Red Bank, NJ

1. R.G. Sextro, R.A. Gough and J. Cerny, Phys. Rev. **C8**, 285 (1973).
2. P.L. Reeder, A.M. Poskanzer, R.A. Esterlund and R. McPherson, Phys. Rev. **147**, 781 (1966).
3. D.J. Vierra, R.A. Gough and J. Cerny, Phys. Rev. **C19**, 177 (1979).
4. R.G. Sextro, R.A. Gough and J. Cerny, Nucl. Phys. **A234**, 130 (1974).
5. N.B. Gove and M.J. Martin, Nuc. Data Tab. **10**, 205 (1971).

Table I. Additional Proton Groups from $T_z = -3/2$ Nuclei

Spectrum Label	Daughter	E_p(keV)	E_x(keV)	Relative[a] Intensity (%)	log *ft*
Mg 1	^{21}Na	6520 ± 30	9280 ± 30	0.12 ± .03	5.41 ± .10
Si 1	^{25}Al	6520 ± 10	9065 ± 10	0.72 ± .04	4.80 ± .03
Si 2		6720 ± 25	9275 ± 25	0.12 ± .02	5.41 ± .09
Si 3		6855 ± 30	9415 ± 30	0.12 ± .02	5.32 ± .07
S 1	^{29}P	6725 ± 50	9715 ± 50	0.10 ± .02	5.64 ± .10
S 2		6860 ± 30	9855 ± 30	0.21 ± .02	5.21 ± .04
S 3		7090 ± 30	10095 ± 30	0.12 ± .01	5.28 ± .05
S 4		7520 ± 30	10535 ± 30	0.18 ± .01	4.78 ± .04
Ti 1	^{41}Sc	5595 ± 15	6825 ± 15	0.26 ± .03	5.53 ± .05
Ti 2		5715 ± 15	6945 ± 15	0.36 ± .03	4.32 ± .05
Ti 3		5950 ± 20	7185 ± 20	0.40 ± .03	5.25 ± .04
Ti 4		6125 ± 20	7365 ± 20	0.29 ± .02	5.39 ± .04
Ti 5		6380 ± 50	7630 ± 50	0.20 ± .03	5.41 ± .09
Ti 6		6650 ± 50	7905 ± 50	0.20 ± .02	5.25 ± .05

a) Intensities quoted are relative to the strongest proton group in the beta-delayed proton spectrum for that nucleus.

Angular Correlations in the Beta-delayed Two-Proton Decay of ^{22}Al*

*R. Jahn,† R.L. McGrath‡ D.M. Moltz, J.E. Reiff, X.J. Xu,§ J. Äystö,** and Joseph Cerny*

^{22}Al and ^{26}P are the only two isotopes known to exhibit beta-delayed two-proton radioactivity.[1,2] The two protons can result from a number of decay mechanisms, which include a final state interaction between the two protons (^{2}He emission), uncoupled simultaneous emission, or sequential emission.[3]

The actual decay mechanism involved in the two proton emission can be deduced from energy and angular correlation measurements between the protons as described in our summary paper[4] on ^{22}Al and ^{26}P. In the case of ^{2}He emission, a strong angular correlation at small angles between the emitted protons is expected. However, a nearly isotropic angular correlation is expected in the non-coupled simultaneous and sequential emission of the two protons.

We have recently performed an experiment which measured the relative angular correlation of the two protons. ^{22}Al was produced via the ^{24}Mg(^{3}He,p4n) reaction using 110 MeV ^{3}He^{2+} beams of 3-7 μA intensities from the 88-Inch Cyclotron. Recoiling product nuclei were transported with a helium jet and collected on a catcher wheel to form thin sources for particle spectroscopy.

Due to the wide angular range covered, two separate detector setups were used. The large angle setup of the telescopes is shown in Fig. 1. Each telescope consisted of 27 μm surface barrier ΔE detectors and 300 μm surface barrier position-sensitive E detectors. This setup measured angles ranging from 70° to 164°. A similar setup was used to measure the angles from 10° to 46°.

The essentially isotropic angular correlation shown in Fig. 2 combined with our prior experimental results on energy correlations at small and large angles confirm that the two proton decay of the 4^{+}, T=2 isobaric analog state in ^{22}Mg to the first excited state in ^{20}Ne is predominantly a sequential process. (For ^{2}He emission, the theoretical proton angular correlation peaks at ~40° and is essentially zero

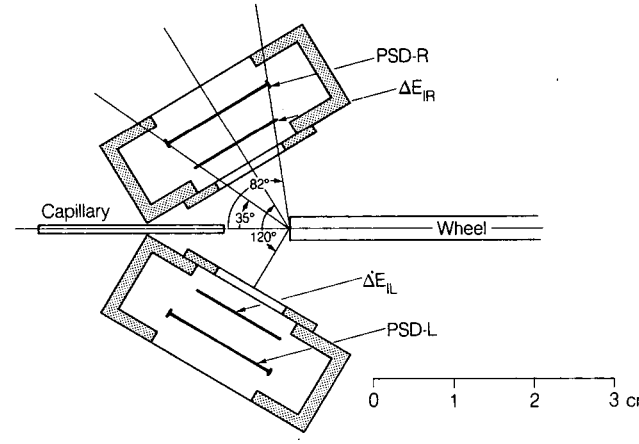

Fig. 1. Schematic diagram of the large angle detector system used to measure the relative proton angles of the two protons in the beta-delayed two-proton decay of ^{22}Al. XBL 8410-8799

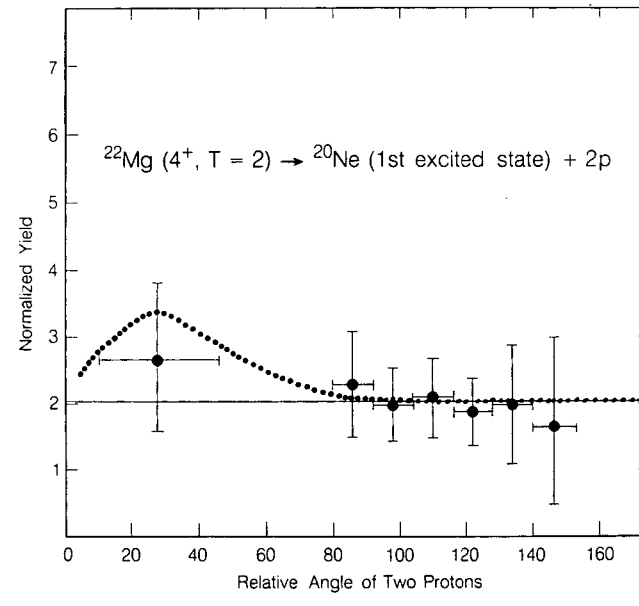

Fig. 2. Normalized angular correlation for the two protons from the beta-delayed two-proton emission of ^{22}Al. XBL 8410-8798

above 55°.) Further studies with substantially improved statistics would be of interest in confirming details of this decay and in searching for weak components from other decay mechanisms.

Footnotes and References

*Condensed from LBL-18864

†Permanent address: Institut für Kernphysik der Universität, Bonn, Federal Republic of Germany.

‡Permanent address: Department of Physics, State University of New York, Stony Brook, NY 11794.

§Permanent address: Institute of Modern Physics, Lanzhou, China.

**Permanent address: Department of Physics, University of Jyväskylä, Jyväskylä, Finland.

1. M.D. Cable, J. Honkanen, R.F. Parry, S.H. Zhou, Z.Y Zhou and J. Cerny, Phys. Rev. Lett. **50**, 404 (1983).
2. J. Honkanen, M.D. Cable, R.F. Parry. S.H. Zhou, Z.Y Zhou and J. Cerny, Phys. Lett. **133B**, 146 (1983).
3. V.I. Gol'danskii, Pis'ma Zh. Eksp. Theor. Fiz. **32**, 572 (1980); JETP Lett. **32**, 554 (1980).
4. M.D. Cable, J. Honkanen, E.C. Schloemer, M. Ahmed, J.E. Reiff, Z.Y. Zhou and J. Cerny, Phys. Rev. **C30**, 1276 (1984).

Discovery of Radioactive Decay of ^{222}Ra and ^{224}Ra by ^{14}C Emission*

P.B. Price,† J.D. Stevenson,‡ S.W. Barwick and H.L. Ravn§

Rose and Jones[1] recently reported the discovery of a new mode of radioactive decay in which a ^{223}Ra nucleus emits a 29.9 MeV ^{14}C nucleus with a branching ratio relative to alpha decay of $(8.5 \pm 2.5) \times 10^{-10}$. Using the ISOLDE on-line isotope separator at CERN to produce sources of ^{221}Fr, ^{221}Ra, ^{222}Ra, ^{223}Ra, and ^{224}Ra, and using polycarbonate track-recording films sensitive to energetic carbon nuclei but not to alpha particles, we have confirmed the Rose and Jones discovery and have discovered two new cases of the rare ^{14}C decay mode – in ^{222}Ra and ^{224}Ra. We have also set a stringent upper limit on the $^{14}C/\alpha$ branching ratio for ^{221}Fr and ^{221}Ra. Table I summarizes our results.

Fig. 1 illustrates the technique of recording ^{14}C tracks during radium isotope production. Figs. 2 and 3 show how the emitted particles are identified as having Z=6 and having exactly the calculated range (and energy) expected from the Q-value for ^{14}C emission.

Searches for modes of decay in which heavier particles such as ^{24}Ne are emitted are in progress.

Footnotes and References

*Condensed from a paper submitted to Phys. Rev. Lett.

†Also at Space Sciences Laboratory.

‡Present address: Physics Department, Michigan State University, East Lansing, MI 48824.

§Address: EP Division, CERN, 1211 Geneve, Switzerland.

1. H.J. Rose and G.A. Jones, Nature **307**, 245 (1984).

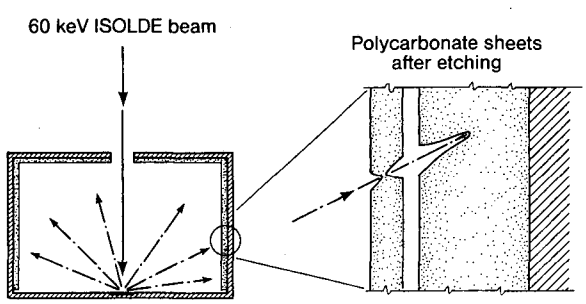

Fig. 1. Radium isotope collector cup, lined with polycarbonate sheets for detection of energetic particles with Z>5 emitted in radioactive decay.

XBL 8410-4284

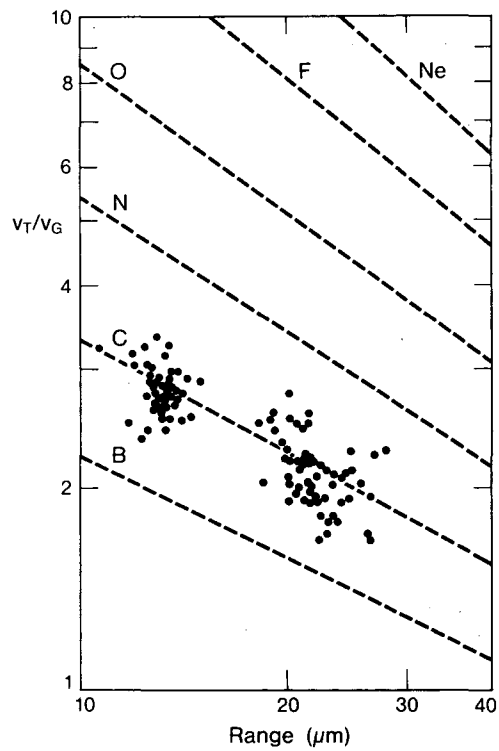

Fig. 2. Comparison of signal of ^{14}C nuclei emitted from ^{223}Ra with calibrations (dashed lines) obtained with heavy ions at Lawrence Berkeley Laboratory SuperHILAC. Ratio of etching rate along track to general etching rate, v_T/v_G, is plotted as a function of residual range. Measurements at two different points along the trajectory are made for each ^{14}C nucleus.
XBL 8410-4286

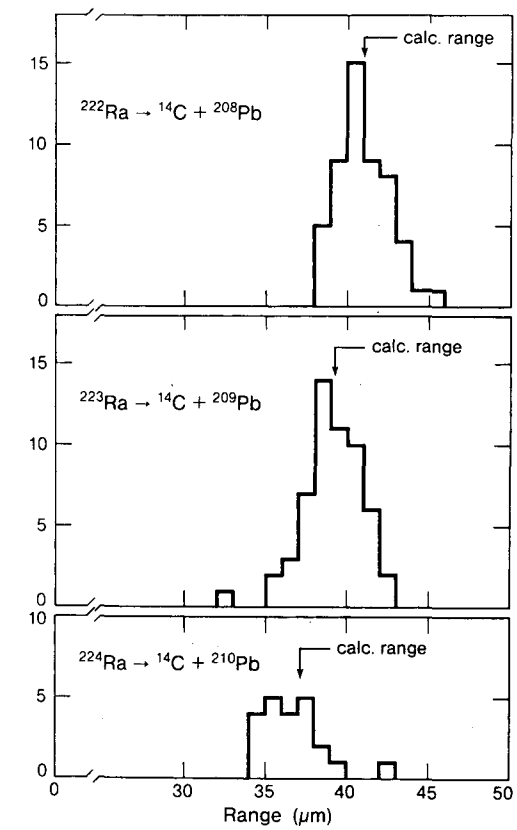

Fig. 3. Measured range distributions for ^{14}C nuclei emitted from ^{222}Ra, ^{223}Ra, and ^{224}Ra, compared with ranges calculated from Q values. XBL 8410-4285

Table I. ^{14}C Decay of Radium Isotopes

Z	A	Q (MeV)	No. of Ra atoms	Obs. decays	Mean range (μm) calc.	Mean range (μm) meas.	Measured B $\equiv\lambda(^{14}C)/\lambda(\alpha)$	Ratio of Gamow factors[a]	Calc. B[b]	Calc. B[c]
87	221	31.26	2.6×10^{12}	0	38.2	—	$<4.4\times10^{-12}$ (90% CL)	8.7×10^{-13}	8.0×10^{-12}	1.4×10^{-14}
88	221	32.39	2.6×10^{12}	0	40.0	—	$<4.4\times10^{-12}$ (90% CL)	6.5×10^{-13}	8.2×10^{-12}	8.0×10^{-13}
88	222	33.05	7.8×10^{11}	52	41.1	41.0 ± 0.2	$(3.7\pm0.5)\times10^{-10}$	7.5×10^{-11}	1.7×10^{-9}	2.5×10^{-12}
88	223	31.87	4.7×10^{11}	56	39.2	39.2 ± 0.2	$(6.1\pm0.8)\times10^{-10}$	$\equiv6.1\times10^{-10}$	6.9×10^{-9}	2.5×10^{-9}
88	224	30.53	2.4×10^{12}	22	37.1	36.5 ± 0.4	$(4.3\pm1.1)\times10^{-11}$	1.4×10^{-11}	6.1×10^{-11}	1.3×10^{-12}

a)for square-well potential and $R = r_0 (A_d^{1/3} + A_x^{1/3})$, $r_0 = 0.98$ fm.

b)Y.-J. Shi and W.J. Świątecki, Phys. Rev. Lett. **54**, 300 (1985)

c)D.N. Poenaru, M. Ivascu, A. Sandulescu, W. Greiner, J. Phys. G **10**, L183 (1984)

Radioactive Decay of ^{223}Ra by ^{14}C Emission

S. Yashita, K.Gregorich and A. Ghiorso

Recently H.J. Rose and G.A. Jones at the University of Oxford reported[1] the very difficult observation of an exotic radioactive decay mode in ^{233}Ra, its spontaneous disintegration by the emission of ^{14}C particles. We felt that it was important to try and confirm their somewhat surprising discovery by an independent method.

Our normally gas-filled magnetic separator, SASSY, was converted for the purpose into a relatively high geometry particle spectrometer operating in vacuum ($\sim 10^{-4}$ torr). Although the usual magnetic configuration was retained it was used in an inverted mode to obtain a larger solid angle (0.022 steradians). The ^{227}Ac source which supplied the ^{223}Ra was placed very close to the quadrupole doublet and mechanically adjusted to the magnetic axis by using its alpha particle emissions. After being focussed by the quadrupole the particles passed through the dipole to impinge upon a silicon detector array placed just outside the dipole magnet. This magnetic system accomplished its purpose in suppressing the intense alpha radiation by a factor greater than 10^4 at the same time that the rare ^{14}C particles were impinging upon the focal plane detector. This allowed us to use the detector system indefinitely since it was not subjected to alpha particle degradation as in the original Oxford experiment.

The ^{227}Ac source was chemically purified and prepared by electrodeposition into a 1 x 10 mm area. The magnetic optics were adjusted and calibrated by the prominent 7.384 MeV ($B\rho$ = 3.928 Kgm) from ^{215}Po, the alpha-decay granddaughter of ^{203}Ra. This tune was checked by using a ^{228}Th source to furnish higher rigidity alpha particles from ^{212}Po (8.785 MeV, $B\rho$ = 4.284 Kgm) and ^{212}Po (10.543 MeV, $B\rho$ = 4.696 Kgm). The spectrometer was then adjusted for the expected energy for ^{14}C particles (29.0 MeV, $B\rho$ = 4.855 Kgm). The 29.0 MeV setting takes into account a calculated 0.9 MeV loss in the source thickness and its carbon cover foil. The energy calibration of the detector array was determined from the various alpha emission lines and by 29 MeV ^{12}C ions delivered in a separate experiment by the SuperHILAC.

During 25 days of exposure we observed a group of 21 events in the 29 MeV range and with a magnetic rigidity of $\sim$4.9 Kgm (Fig. 1). The ^{14}C to α branching ratio in ^{233}Ra was found to be $6 \pm 1 \times 10^{-10}$ assuming a 65% abundance in C^{6+}. Due to the very low alpha counting rate, chiefly due to the small amount of ^{219}Rn that escaped from the source and decayed in the vicinity of the detector, there was no quadruple pileup problem to provide a background. The very small background that was observed was found to be caused by an inadvertent contamination of the source by ^{248}Cm spontaneous fission.

Within our present experimental accuracy the magnetic rigidity, energy and branching ratio support the assignment of ^{14}C emission from ^{223}Ra as proposed by the Oxford experiment.

Reference

1. H.J. Rose and G.A. Jones, Nature **307**, 245 (1984).

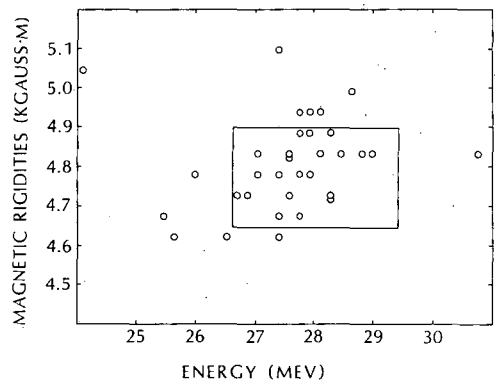

Fig. 1. Plot of magnetic rigidity vs. particle energy indicating the existence of ^{14}C emission. The rectangle represents the limits in E and $B\rho$ for a 3σ variation expected for the source thickness.

XBL 8410-8812

The Decay of ^{248}Es

Wen Xin Li, K.E. Gregorich, R.B. Welch, W. Kot, D. Lee, and G.T. Seaborg

We have studied the electron capture and alpha decays of ^{248}Es. Previous experiments have identified ^{248}Es by means of the 6.87 MeV alpha particles from its 0.25% alpha decay branch,[1,2] but because of a lack of target material or an inappropriate choice of reaction, detailed studies of the decay properties of ^{248}Es were not possible. In the present experiments, a much larger and cleaner source of ^{248}Es was made available. Many gamma rays have been found to accompany the electron capture decay of ^{248}Es. The gamma ray and alpha decay data from the present experiments support the existence of two isomers of ^{248}Es.

The ^{248}Es was produced at the 88-Inch Cyclotron by the ^{249}Cf (p, 2n) ^{248}Es reaction. The target, which was prepared by the molecular plating procedure, consisted of a 330 μg/cm^2 layer of ^{249}Cf as Cf_2O_3 on a 2.75 mg/cm^2 Be backing foil. The target was irradiated with up to 15 μA of 19 MeV protons for 1 hour and the products which recoiled out of the target were stopped in a 1.2 mg/cm^2 gold foil. At the end of irradiation, the gold foil was chemically processed to produce an Es source suitable for simultaneous gamma and alpha counting. The chemical process included elution from a 13M HCl cation exchange column as a group separation of the +3 actinides and an elution with α-hydroxyisobutyrate from a cation exchange column to obtain a pure Es fraction. The Es fraction was ready for counting within 45 minutes from the end of irradiation and was placed in a vacuum chamber next to a Si surface barrier detector. This vacuum chamber was then placed in front of a high purity germanium gamma ray detector. The gamma rays were measured through a 300 mg/cm^2 aluminum vacuum window and through the 55 mg/cm^2 Pt source backing.

In these experiments about 40 gamma-rays which are due to the decay of ^{248}Es were seen. The strongest of these gamma rays has the same energy as the only known gamma ray accompanying the β-decay of 23h ^{248}Bk which feeds the same levels in ^{248}Cf. The apparent half-lives of these gamma rays vary from about 22 minutes to about 45 minutes suggesting the existence of two isomers of ^{248}Es. Table I lists the energies of these gamma-rays, their approximate intensities, and their apparent single component half-lives. The existence of two isomers is further supported by the data arising from the measurement of the ~0.25% alpha decay branch. A plot of a sum of the first thirty minutes of alpha spectra is presented in Fig. 1. In this spectrum, the highest energy alpha group is 6.87 MeV, the previously measured energy for ^{248}Es.[1,2] There is a prominent high energy tail on this peak. When the main part of this peak and the high energy tail are integrated separately and separately fit with decay curves, it is found that the main group has a half-life of 41 minutes and the high energy tail has a half-life of 21 minutes (see Fig. 2). The highest energy part of this tail has an energy which corresponds to the ground state Q value for alpha decay of ^{248}Es when corrected for daughter nucleus recoil. These facts, taken together, lend fairly conclusive evidence to the existence of two isomers of ^{248}Es, one with a half-life of close to 41 minutes and another with a half-life of about 21 minutes.

The existence of two isomers is not surprising because similar behavior is seen in ^{250}Es. In ^{248}Es one expects to see coupling of the 7/2[624] neutron state with the 7/2[633] or 3/2[521] proton state leaving open the possibility for coupling into high spin and low spin states. Further experiments and the analysis of gamma-gamma coincidence data from a similar experiment will be necessary for further understanding of the decay of ^{248}Es.

References

1. A. Chetham-Strode and L.W. Holm, PR **104**, 1314 (56).
2. I. Ahmad *et al.*, NP **A140**, 141 (69).

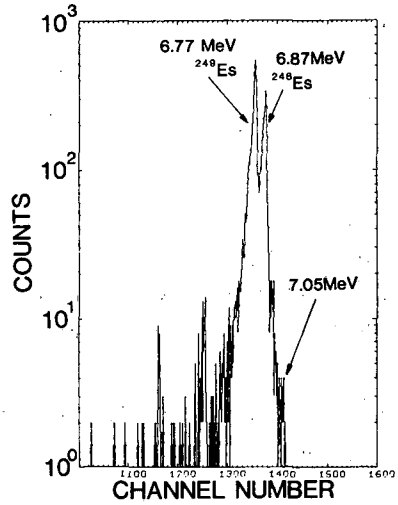

Fig. 1. The sum of the alpha spectra from the first thirty minutes of counting, showing the peaks due to ^{249}Es and ^{248}Es and the high energy shoulder on the ^{248}Es peak. XBL 8410-4162

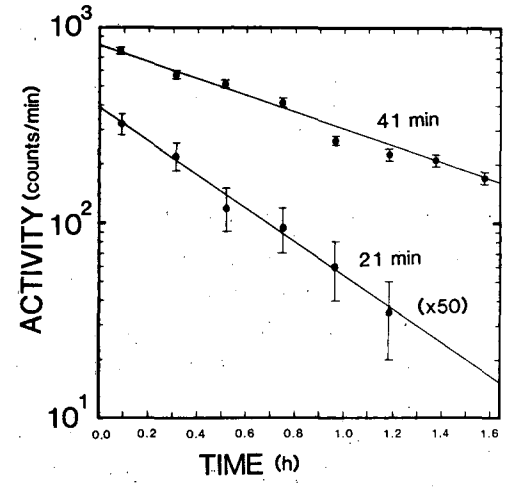

Fig. 2. The decay curves of the 6.87 MeV ^{248}Es alpha peak and the high energy shoulder.

XBL 8410-4160

Table I

Energies, Intensities and Apparent Half-Lives of the ^{248}Es Gamma-rays					
Energy (keV)	Intensity	Apparent Half-Life (min)	Energy (keV)	Intensity	Apparent Half-Life (min)
149.7	M	31.9 ± 0.09	1075.7	M	22. ± 6.
162.9	VW	24. ± 7.	1122.3	S	36.8 ± 1.0
174.3	W	33. ± 4.	1219.0	M	27. ± 9.
200.6	W	29. ± 5.	1236.5	S	41.3 ± 0.6
277.4	W	44. ± 6.	1279.0	W	37. ± 12.
355.7	M	36. ± 3.	1317.9	VS	42.3 ± 0.5
371.2	M	33. ± 10.	1405.0	M	38. ± 16.
414.4	S	33.4 ± 0.4	1495.7	S	41.8 ± 1.3
451.6	VS	31.2 ± 0.4	1522.2	M	45. ± 3.
536.2	W	17. ± 0.8	1537.0	S	40.3 ± 1.9
550.7	VS	37.8 ± 0.3	1671.2	S	42.0 ± 0.7
594.4	W	39. ± 10.	1704.8	S	42.6 ± 0.8
607.2	M	35. ± 2.	1712.9	S	40.2 ± 1.3
617.2	W	47. ± 5.	1837.2	M	40. ± 30.
652.6	S	32.4 ± 0.9	2070.2	S	46. ± 2.
673.7	M	39. ± 3.	2094.5	S	38.8 ± 1.4
723.2	W	36. ± 7.	2114.6	M	45. ± 8.
1002.0	M	24. ± 4.	2144.7	VS	40.7 ± 0.5
1008.0	M	44. ± 22.	2186.4	S	41.5 ± 1.7
1036.2	M	45. ± 5.	2256.6	S	43. ± .2

The Decay of ^{250}Fm

W.P. Kwan, K.E. Gregorich, Wen Xin Li, D. Lee, R.B. Welch, W. Kot and G.T. Seaborg

We have studied the alpha and electron capture decays of ^{250}Fm. Previous experiments have left open the possibility of a large (>10%) electron capture branch in ^{250}Fm,[1] which would present a unique opportunity to study the level structure of ^{250}Es. While no electron capture branch was found in the present experiment, we have remeasured the ^{250}Fm half-life (28.8 ± 0.3 min.) by monitoring the 7.43 MeV alpha decay. and have determined that the electron capture branching ratio is less than 4%.

The ^{250}Fm was produced at the 88-Inch Cyclotron by the ^{249}Cf (^{3}He, 2n) ^{250}Fm reaction. The target, which was prepared by the molecular plating procedure, consisted of a 330 μg/cm^2 layer of ^{249}Cf on a 2.75 mg/cm^2 Be backing foil. The target was irradiated with up to 7 μA of 32 MeV ^{3}He^{+2} ions for 1.5 hours and the products which recoiled out of the target were stopped in a 1.2 mg/cm^2 gold catcher foil. At the end of irradiation, the gold foil was chemically processed to produce a Fm source suitable for simultaneous gamma and alpha counting. The chemical process included elution from a 13M HCl cation exchange column as a group separation of the +3 actinides and elution with α-hydroxyisobutyrate from a cation exchange column to obtain a pure Fm fraction. The Fm source was ready for counting within 45 minutes after the end of irradiation and was placed in a vacuum chamber next to a silicon surface barrier detector. This vacuum chamber was then placed in front of a Ge(Li) gamma ray detector. The gamma rays were measured through a 300 mg/cm^2 aluminum vacuum window and through the 55 mg/cm^2 Pt source backing.

In this experiment, no evidence for the electron capture decay of ^{250}Fm was found. No statistically significant short component in the Es KX-rays was seen above the 5.3 hour component due to ^{251}Fm produced by the ^{249}Cf (^{3}He, n) ^{251}Fm reaction. In addition, no unrecognized gamma rays with about a 30 minute half-life were found, nor were the gamma rays accompanying the electron capture decay of the ^{250}Es daughter seen. The alpha decay of the ^{250}Fm was easily followed by monitoring the 7.43 MeV alpha group. By fitting the decay of this 7.43 MeV alpha group with an error weighted least squares procedure, we have found the half-life of ^{250}Fm to be 28.8 ± 0.3 minutes. By comparing the initial activity of the ^{250}Fm alphas with the minimum 28.8 minute component which would have been detectable in the Es KX-rays and correcting for detection efficiencies and X-ray production rates, we have determined that the upper limit for the electron capture branch in ^{250}Fm is 4%.

Reference

1. S. Amiel *et al.*, Phys. Rev. **106**, 553 (1957).

Actinide Production in the ^{136}Xe + ^{249}Cf Reaction

K.E. Gregorich, R.B. Welch, W. Kot, D. Lee, K.J. Moody and G.T. Seaborg

As part of our ongoing systematic study of the deep-inelastic reaction mechanism in the actinide region, we have been studying actinide production in the ^{136}Xe + ^{249}Cf reaction. The choice of this relatively neutron deficient target in the actinide region allows us to study what effect the position of the target with respect to beta stability has on the deep-inelastic production cross sections for target-like nu-

clides.

A 0.830 mg/cm^2 Cf target (as Cf_2O_3 on a 1.8 mg/cm^2 Be backing) was bombarded at the Super-HILAC with ^{136}Xe ions at energies which corresponded to 1.00, 1.08 and 1.16 times the nominal Coulomb barrier. The target-like products recoiled out of the target and were stopped in a 25 mg/cm^2 gold foil. After irradiation, these gold foils were processed with a variety of chemical techniques to isolate the individual actinide elements. The chemical fractions were counted for gamma, alpha, and spontaneous fission decays. From this radiation counting and the irradiation histories, the production cross sections for isotopes of elements from Np through Md were determined.

The production cross sections for the highest energy bombardments are presented as a contour plot in Fig. 1. The production cross sections for the middle energy are comparable in magnitude to those for the highest energy and shifted very slightly toward the more neutron-rich region. At the lowest bombardment energy, the cross sections are much lower and shifted a bit more toward the neutron-rich region. It can be seen that the largest yields lie along the line of beta stability, but the width of the distribution allows significant yields away from beta stability. Of primary interest are the yields of the neutron-rich, below-target nuclides. These yields suggest that with more neutron-rich targets it is possible to produce new neutron-rich, below-target nuclides in quantities sufficient to allow their identification when fast chemical separations are developed. Another interesting feature is seen in the neutron-deficient, above-target yields. The yields of nuclides with more protons and fewer neutrons than the target nuclide drop off much more rapidly than did the yields for products from analogous transfers in the ^{136}Xe + ^{248}Cm reaction.[1] This may be due to two factors. First, these neutron-deficient, above-target yields may be lowered because they feel the steep rise in energy from the neutron-deficient side of the valley of beta stability. Second, it may be true that fission barriers for the neutron-deficient isotopes of Md and heavier elements are lower than for isotopes closer to beta stability. So these products may have had a lower fission survival rate than the products from analogous transfers from the ^{136}Xe + ^{248}Cm reaction.[1]

Reference

1. K.J. Moody, LBL-16249 (1983).

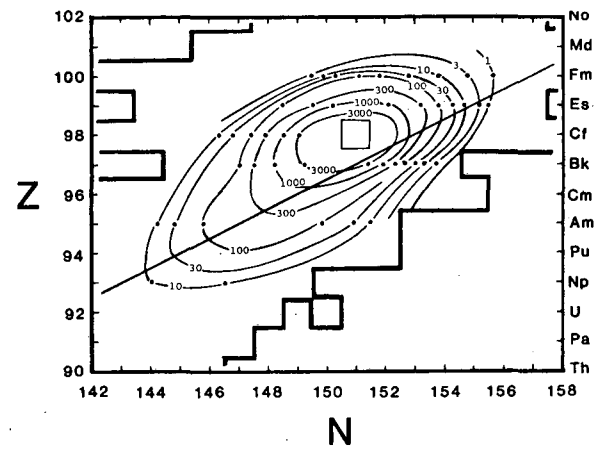

Fig. 1. A contour plot of the production cross sections from ^{136}Xe + ^{249}Cf at 1.16 times the Coulomb barrier. The contours are labeled in μb. The heavy line shows the limit of known nuclides, and the diagonal line shows the position of beta stability.

XBL 8410-4161

Potential Energy Surfaces for Xe + Cm Reactions

R.B. Welch, K.J. Moody, D. Lee, K.E. Gregorich, W. Kot and G.T. Seaborg

Experiments involving the bombardments of ^{248}Cm with ^{129,132}Xe at energies slightly above the Coulomb barrier to determine production cross sections for actinide nuclides have been previously re-

ported.[1] We compare these results with data from a similar bombardment with ^{136}Xe,[2] to study the effect of different neutron numbers as well as non-closed shell neutron numbers on production cross sections in heavy ion bombardments. A useful tool in explaining the differences observed in cross sections due to different projectiles is the potential energy surface.

The potential energy surface shows the difference in total energy between the possible products and the two reactants. The total energy used here is the sum of the ground state shell-corrected, liquid drop masses and the coulomb, centrifugal and a proximity nuclear potential evaluated at the point of closest approach between the reactants. It has been shown that in low energy heavy ion reactions, the potential energy surface adequately describes the evolution of the centroids of the mass distributions. The path of the mass centroid is along the gradient of the surface, starting at the injection point (the target). The interaction time for the reaction, which depends on the initial energy and angular momentum, determines how far the system moves along the path.

The calculated potential energy surface (PES) and mass evolution path for 800 MeV ^{132}Xe on ^{248}Cm with an initial angular momentum of $100\hbar$ is shown in Fig. 1. At the beginning, the net drift of mass involves exchanging neutrons of the target for protons from the projectile. Later, at about $Z_T = 98$, the path turns down along the valley floor and both neutrons and protons flow toward the projectile-like fragment. Because this reaction is at a small energy above the barrier, the interaction time is relatively short and the system does not move far along the path, perhaps stopping upon arrival at the valley floor. The kinks in the surface at N = 148 and Z = 100 are due to an effect in the masses at the closed shell N = 82 and Z = 50 in the projectile-like products. The other PESs have kinks in the appropriate places for their projectile-target combinations. The ^{129}Xe potential surface is similar to the ^{132}Xe surface, except that the injection point is higher up the valley wall, and so the turn in the path occurs at about $Z_T = 99$. For ^{136}Xe, the injection point is within 1 MeV of the minimum in the valley, so the mass centroid does not move far from the injection point.

The PESs generated indicate 1) an increased above-target and decreased below-target nuclide production with the progressively lighter xenon projectiles, and 2) a shift toward a more neutron-deficient peak in the cross sections for a given element with the progressively lighter xenon projectiles. The actual data reflect these trends. Thus, the PES can aid in describing the overall features of a heavy-ion reaction. Also, the apparent projectile-independent cross sections (noted in ref. 1) for the neutron-rich, above-target products ($^{253,254}Cf$, $^{254m,255}Es$ and ^{256}Fm) are probably due to a combination of the increased above-target production and a shift toward the neutron-poor region as one goes from ^{136}Xe to ^{129}Xe, causing the elemental mass distribution curves to move in such a way as not to vary the cross-section for these nuclides by very much.

Footnotes and References

1. R.B. Welch, K.J. Moody, K.E. Gregorich, W. Kot and G.T. Seaborg, NSD Annual Report, pp. 72-73 (1982-1983).
2. K.J. Moody, LBL-16249, Ph.D. Thesis, July 1983.

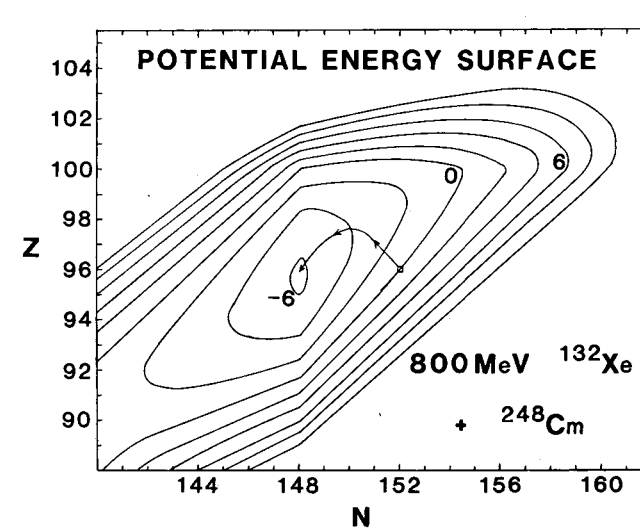

Fig. 1. Potential energy surface for 800 MeV ^{132}Xe + ^{248}Cm. Contours are 2 MeV apart. XBL 8410-4244

Excitation Functions for Production of Heavy Actinides from Interactions of ^{40}Ca and ^{48}Ca Ions with ^{248}Cm

D.C. Hoffman, M.M. Fowler,* W.R. Daniels,* H.R. von Gunten,† D. Lee, K.J. Moody, K. Gregorich, R. Welch, G.T. Seaborg, W. Brüchle,‡ M. Brügger,‡ H. Gäggeler,‡ M. Schädel,‡ K. Sümmerer,‡ G. Wirth,‡ Th. Blaich,§ G. Herrmann,§ N. Hildebrand,§ J.V. Kratz,§ M. Lerch,§, and N. Trautmann§*

Analyses of the data for actinide production from ^{40}Ca and ^{48}Ca reactions with ^{248}Cm have been completed[1] and a paper on production of above-target products has been submitted to Phys. Rev. C. A paper on production of below-target nuclides is in preparation.

From the data, the following conclusions can be drawn.

a. Cross sections are largest for transfers of a few nucleons and decrease rapidly with an increase in the total number of transferred nucleons.

b. A shift of only 2 to 3μ in the mass-yield curves is observed between ^{40}Ca and ^{48}Ca reactions. Thus, the 8-neutron difference between the two projectiles is only partly reflected in the products.

c. The shapes of the isotopic distributions are quite similar and rather symmetric (FWHM $\approx$ 2.5 μ).

d. Reactions with ^{40}Ca are favorable for the production of neutron-deficient isotopes, those with ^{48}Ca for neutron-rich products.

e. "Cold" heavy products are observed in the reactions with ^{40}Ca and ^{48}Ca in the energy range investigated.

f. The cross sections for the reactions with ^{40}Ca are near their maxima at the Coulomb barrier, consistent with calculated positive reaction energies.

g. The excitation functions for ^{48}Ca show maxima about 20 MeV above the Coulomb barrier, but decrease only very slowly with increasing projectile energy.

h. Cross sections for actinide products from transfer of identical combinations of nucleons are very similar for projectiles from ^{18}O to ^{238}U. (See Fig. 1.)

i. The yields of below target elements are much lower for ^{40}Ca than ^{48}Ca reactions.

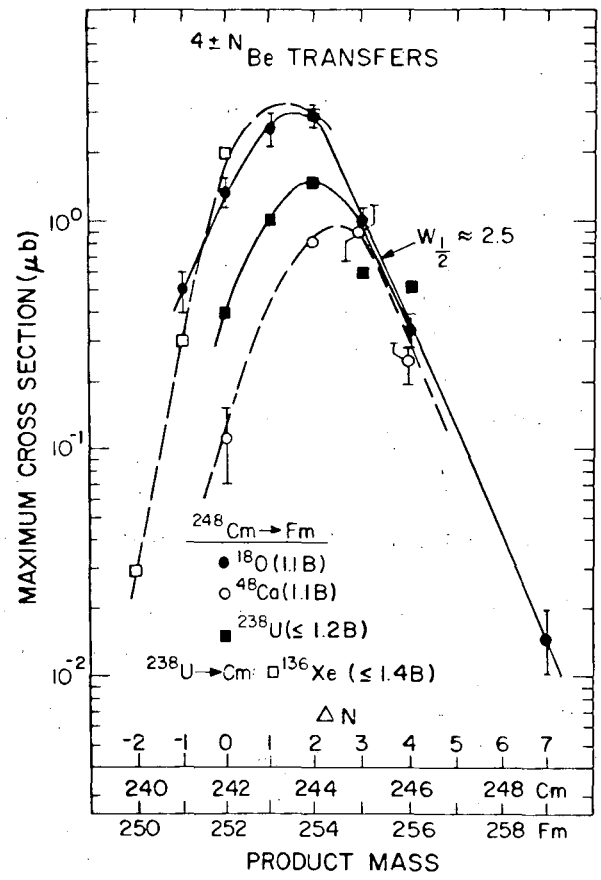

Fig. 1. Cross sections for various mass Be transfers from ^{18}O, ^{48}Ca, and ^{238}U projectiles to ^{248}Cm to produce Fm isotopes and from ^{136}Xe projectiles to ^{238}U to produce Cm isotopes. Values in parentheses give the ratio of projectile energy to Coulomb barrier. (Data from references 2–5.) XBL 8410-4128

Footnotes and References

*Isotope and Nuclear Chemistry Division, Los Alamos National Laboratory, Los Alamos, NM 87545.

†Anorganisch-Chemisches Institut, University of Bern, Bern, Switzerland, and Swiss Institute for Reactor Research, Würenlingen, Switzerland.

‡Gesellschaft für Schwerionenforschung, Darmstadt, Federal Republic of Germany.

§Institut für Kernchemie, Universität Mainz, Mainz, Federal Republic of Germany.

1. 1982-83 LBL Annual Report, LBL-16870, p. 24
2. D. Lee, H. von Gunten, B. Jacak, M. Nurmia, Y-f. Liu, C. Luo, G.T. Seaborg and D.C. Hoffman, Phys. Rev. C **25**, 286 (1982).
3. D. Lee, K.J. Moody, M.J. Nurmia, G.T. Seaborg, H. von Gunten and D.C. Hoffman, Phys. Rev. C **27**, 2656 (1983).
4. M. Schädel, W. Brüchle, H. Gäggeler, J.V. Kratz, K. Sümmerer, G. Wirth, G. Herrmann, R. Stakemann, G. Tittel, N. Trautmann, J.M. Nitschke, E.K. Hulet, R.W. Lougheed, R.L. Hahn and R.L. Ferguson, Phys. Rev. Lett. **48**, 852 (1982).
5. M. Schädel, J.V. Kratz, H. Ahrens, W. Brüchle, G. Franz, H. Gäggeler, I. Warnecke, G. Wirth, G. Herrmann, N. Trautmann and M. Weis, Phys. Rev. Lett. **41**, 469 (1978).

First Observation of the Neutron-Rich Isotope ^{19}B*

J.A. Musser† and J.D. Stevenson‡

The most neutron-rich boron isotope previously observed to be particle-stable is ^{17}B.[1] In the same experiment ^{16}B was shown to be unstable to prompt neutron emission. Current nuclear mass models predict that this even-odd gap structure should continue through ^{18}B and ^{19}B, and that ^{19}B is the most neutron-rich particle-stable boron isotope.

In our experiment we produced projectile fragments by interactions of an intense 670 MeV/nucleon ^{56}Fe beam in a 7.9 g/cm^2 Be target. The charges and masses of the projectile fragments were obtained using the 0° spectrometer facility at the Bevalac in conjunction with a detector telescope[2] (in the focal plane of the spectrometer) consisting of a wire chamber hodoscope, a front scintillator paddle, a set of threshold Čerenkov counters, and a back scintillator paddle. The charges of the projectile fragments were determined by the scintillator and Čerenkov signals. Once a fragment's charge was obtained, its mass could be found from the particle's rigidity, provided by the spectrometer, in combination with the Čerenkov measurement. The back scintillator was used to reject events in which the fragment interacted in the telescope. The charge resolution of the detector was $\sigma_Z = 0.1e$ and the mass resolution $\sigma_A = 0.25$ amu.

Two important features of this detector are its large energy acceptance (~350 MeV/nucleon to ~600 MeV/nucleon) and its ability to determine the mass of a particle without having to bring it to rest. These two properties, not available in detectors previously employed in rare isotope searches, allow the use of very thick targets, which give rise to large production rates.

Fig. 1 is a scatter plot of our data for the heaviest boron isotopes in the Čerenkov plane. Fig. 2 is the resulting mass histogram. The previously observed particle instability of ^{16}B and particle stability of ^{17}B are apparent. Our data indicate for the first time that ^{19}B is particle-stable, whereas ^{18}B is unstable to prompt neutron emission.

With a longer run and minor modifications, it appears possible with our detector system to extend the known limits of particle stability of light, neutron-rich nuclei to the predicted position of the neutron drip line.

Footnotes and References

*Condensed from a paper submitted to Physical Review Letters.

†Present address: Department of Physics, Randall Laboratory, University of Michigan, Ann Arbor, MI 48109.

‡Present address: National Superconducting Cyclotron Laboratory, Michigan State University, East Lansing, MI 48824.

1. J.D. Bowman, A.M. Poskanzer, R.G. Korteling and G.W. Butler, Phys. Rev. **C9**, 836 (1974).
2. J.D. Stevenson and J.A. Musser, Nucl. Instr. & Meth. **213**, 285 (1983).

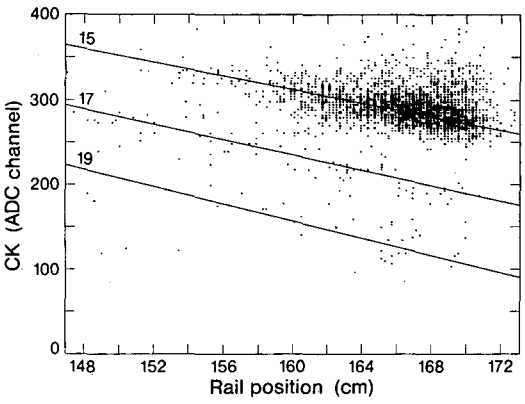

Fig. 1. Data for heaviest boron isotopes. Expected locations of ^{15}B, ^{17}B, and ^{19}B are shown, based on calibrations in ref. 2. XBL 8410-4289

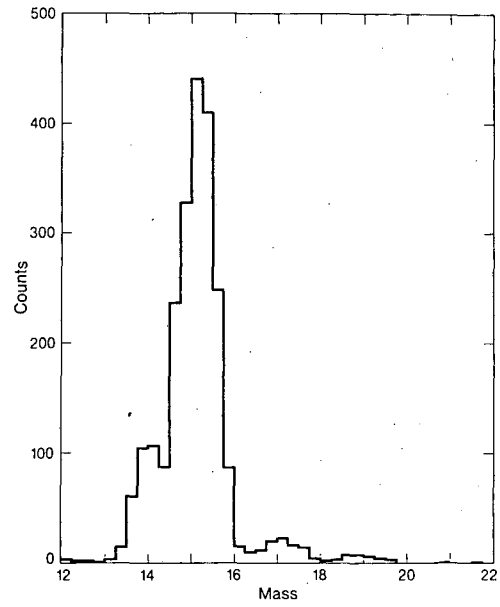

Fig. 2. Histogram of boron isotopes ^{15}B to ^{19}B.

XBL 8410-4290

Measurements of Interaction Cross Sections and Radii of He Isotopes

I. Tanihata, O. Yamakawa,* H. Hamagaki,* O. Hashimoto,* S. Nagamiya, Y. Shida, N. Yoshikawa, K. Sugimoto,† T. Kobayashi, D. Greiner, N. Takahashi,‡ and Y. Nojiri‡*

We have made the first measurements on the interaction cross sections using secondary beams of all known He isotopes. The radii of He isotopes, ^{3}He, ^{4}He, ^{6}He, and ^{8}He, have been deduced from the interaction cross sections.

Secondary beams of He isotopes were produced through the projectile fragmentation of an 800 MeV/nucleon ^{11}B primary beam. Isotopes were rigidity separated and cleaned by the beam line isotope slits system (B-42 at the Bevalac) and then guided to the HISS (heavy ion spectrometer system) experimental area.

The interaction cross section (σ_I), defined as the total cross section for the nucleon (proton and/or neutron) removal from the incident nucleus, was measured by a transmission-type experiment. Incident He isotopes were identified before reaching a reaction target. When the same nuclide was detected beyond the target, the event was counted as non-interacting. The cross section was calculated by the equation

$$\sigma_I = \frac{1}{N_t} \log(R_0/R) \quad , \qquad (1)$$

where R_0 is the ratio of the number of outgoing nu-

clei to the number of incoming nuclei for an empty-target run, and R is the same ratio for a target-in run. With the empty-target run, uncertainties due to the counter inefficiencies and reactions occurring somewhere other than in the target were eliminated. Interaction cross sections were measured for all the He isotopes (^{3}He, ^{4}He, ^{6}He, and ^{8}He) on Be, C, and Al targets. Various thicknesses of the target materials were used to check the effects of multiple Coulomb scattering. No significant dependence on the thickness was observed in the cross sections. The interaction cross sections σ_I thus determined are listed in Table I.

The interaction cross section σ_I between stable nuclei is known to be essentially independent of the beam energy above 200 MeV/nucleon.[1] Also the nucleon-nucleon cross section is at its saturated value at the present beam energy. It is therefore assumed that σ_I reflects a well defined nuclear size. We then operationally define a nuclear radius by the equation

$$\sigma_I = \pi \left(R(p) + R(t)\right)^2 \quad . \qquad (2)$$

It is found that the nuclear radii calculated by this formula using the known data of σ_I between stable isotopes are systematically larger by 0.2 fm than the half-density radii determined by the electron scattering in the whole mass range.[2] This indicates that the presently defined radius corresponds to the sampling of a density point lower than the half density. The justification and the uniformity of this definition will be discussed below along with the target dependence of the radius.

Under the definition of Eq. (2), the difference of the radii between ^{3}He and ^{4}He was calculated as

$$R(^3\mathrm{He}) - R(^4\mathrm{He}) = \sqrt{\sigma_I(^3\mathrm{He},T)/\pi} - \sqrt{\sigma_I(^4\mathrm{He},T)/\pi} \quad , \qquad (3)$$

where T denotes a kind of target nucleus. The differences between the other isotopes were calculated in the same way. The results are shown in Fig. 1. It is seen that the radii of ^{6}He and ^{8}He are much larger than that of ^{4}He. The radii of ^{3}He are also larger than that of ^{4}He, in agreement with the known electron scattering data.[3] It is noted that the differences of the radii obtained from different targets agree with each other in the ± 0.08 fm range, giving support to the uniformity of the present radius definition.

The absolute values of the ^{4}He radius are derived from available ^{4}He + ^{4}He cross section data. The scale of the absolute value thus derived is also shown in Fig. 1.

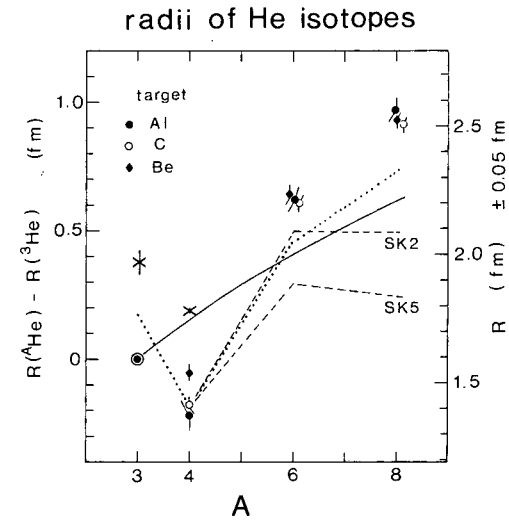

Fig. 1. Radius differences of the He isotopes from ^{4}He are plotted. The absolute value of the radius is also shown on the right-side ordinate scale. A solid curve shows an $A^{1/3}$ dependence of nuclear radii.

XBL 849-4036

Table I. Interaction Cross Sections (σ_I) of He Isotopes

	σ_I in mb			
Target	Beam			
	^{3}He	^{4}He	^{6}He	^{8}He
Be	508 ± 10	489 ± 10	674 ± 13	754 ± 15
C	570 ± 12	518 ± 10	732 ± 15	818 ± 16
		527 ± 26[a)]		
Al	908 ± 18	820 ± 16	1093 ± 22	1205 ± 24
^{4}He		262 ± 19[a)]		

a)data from ref. 3. Present data agree well to values given in ref. 3.

Footnotes and References

*also, Institute for Nuclear Study, University of Tokyo Tanashi, Tokyo 188, Japan.

†Permanent address: Faculty of Science, Osaka University.

‡also, Laboratory for Nuclear Studies, Osaka University, Toyonaka, Osaka 560, Japan.

1. A.S. Goldhaber and H.H. Heckman, Ann. Rev. Nucl. Part. Sci. **28**, 161 (1978).
2. I. Tanihata, Proceedings of the Workshop on Prospects for Research with Radioactive Beams from Heavy Ion Accelerators, April, 1984 Washington, DC, LBL-18187, UC-34A, p. 162.
3. H.R. Collard, L.R.B. Elton, R. Hofstadter, ed. *Nuclear Radii*, H. Schopper, Landolt-Bornstein, New Series, Group 1, Vol. 2, Springer, 1969.

Recent Experimental Results from OASIS

P.A. Willmarth, J.M. Nitschke, P.K. Lemmertz and R.B. Firestone

Our on-going study of the decay properties of very neutron-deficient lanthanides has resulted in the identification of several new isotopes. These new isotopes were produced at the SuperHILAC's on-line isotope separator OASIS and decay studies were carried out in the new spectroscopy laboratory.[1] The isotope of interest is passed through a slit in the focal plane of the mass separator and transported ionoptically to a fast cycling tape which is periodically positioned between an array of detectors. On an event-by-event basis, all possible decay modes are measured and the information written on computer tape for subsequent replay and analysis. Two general classes of decays are of interest: (1) direct or β-delayed particle emission along with any coincident gamma rays, x-rays, or positrons, and (2) gamma rays in coincidence with positrons or x-rays from electron capture and conversion processes.

The preliminary results of our recent work are presented below by mass number and summarized in Table I.

A = 128: The new isotope ^{128}Pr was identified by its beta decay to the known rotational levels in ^{128}Ce. Decay analysis of the gamma lines from the de-excitation of the 2+ and 4+ levels in ^{128}Ce yield a half-life of 3.0 ± 0.1 s. This is considerably shorter than the predicted value of 10 s. A half-life of 4.2 ± 0.2 min. was measured for ^{128}Ce. This is shorter than the previously measured value of 5.5 min.

A = 129: A β-delayed proton activity with a half-life of 5.9 ± 0.6 s at this mass was assigned to ^{129}Nd by Bogdanov *et al.*[2] based on systematics for delayed proton emission. We decided to confirm this result since the high production of this isotope enabled a thorough study of its decay properties. A strong β-delayed proton activity was indeed observed and a more precise half-life of 4.9 ± 0.2 s was measured. Electron capture decay to proton unbound levels in ^{129}Pr give rise to characteristic x-rays in coincidence with protons which confirm the assignment of ^{129}Nd. A strong feeding of the 2+ level of ^{128}Ce was observed via a large peak at 207.3 keV in the gamma spectrum coincident with protons. From these data and comparisons with calculations a spin of 5/2 can be assigned to ^{129}Nd.

A = 130: A weak β-delayed proton activity with a half-life of 2.2 ± 0.5 s was observed at this mass. The x-rays measured in coincidence with the protons identify the new isotope as ^{130}Pm. The measured half-life agrees well with the predicted value of 2 s.

A = 141: We previously reported the observation of weak β-delayed proton activities due to ^{141}Dy and ^{141}Gd.[3] Analysis of gamma spectra from the same experiment yields a half-life of 13.3 ± 1.2 s for ^{141}Gd. Extraction of the half-life for ^{141}Tb of 2.7 ± 1.0 s from x-ray data was also possible. These compare well with the predicted values of 20 and 5 s respectively.

A = 143: In addition to the previously reported isotope ^{143}Dy,[3] a complex gamma ray spectrum in coincidence with positrons was observed. Decay analysis of the major unknown gamma lines yields a half-life of 11.8±.5 s for the new isotope ^{143}Tb. The assignment of all the gamma rays and the determination of the level scheme of ^{143}Gd is still in progress. The half-life is in excellent agreement with the predicted value of 10 s.

A = 144: A short lived proton emitter with a half-life of 0.7±0.1 s was observed. Coincident x-rays identify the new isotope as ^{144}Ho. A second, longer lived proton activity was also observed. The weak activity is either ^{144}Dy or ^{144}Tb^{m} or a mixture of both. The low statistics and similar half-life and energy systematics prevent the assignment of the activity at this time.

The experiments listed above and in ref. 3 are attempts to get detailed structure information about nuclei very far from stability. The construction of the low background spectroscopy laboratory and the continuing work on the theoretical interpretation of β-delayed particle spectra are important tools in this study.

Two new detectors have been added to the array "sandwiching" the tape, see Fig. 1. In front of the coaxial Ge detector located closest to the tape a 1 mm thick plastic scintillator has been added. This should eliminate most of the background in this gamma detector due to beta particles and increase the sensitivity for weak gamma rays. The second detector is a large (52% efficiency) coaxial Ge detector located at 90° to the other detectors. The addition of a second large Ge detector allows gamma-gamma coincidence studies which will be a tremendous aid in constructing the complex level schemes of nuclei far from stability. Its size makes it particularly suitable for the detection of high energy gamma rays that may result from the decay of nuclei with Q_{EC}-values on the order of 10 MeV. Such high Q_{EC}-values are frequently encountered for nuclei near the proton drip line.

References

1. J.M. Nitschke, Nucl. Instr. Meth. **206**, 341 (1983).
2. Bogdanov *et al.*, Nucl. Phys. **A275**, 229 (1977).
3. J.M. Nitschke, *et al.*, Z. Phys. A, **316**, 249 (1984).

Table I.

Reaction	E_{lab} MeV	Isotope	Decay Mode	$T_{1/2}$ s
^{92}Mo(^{40}Ca,3pn)	170	^{128}Pr	β+, EC	3.0±0.1
^{92}Mo(^{40}Ca,2pn)	170	^{129}Nd	βp, β+, EC	4.9±0.2
^{92}Mo(^{40}Ca,pn)	170	^{130}Pm	βp, β+, EC	2.2±0.5
^{92}Mo(^{54}Fe,3p2n)	275	^{141}Tb	β+, EC	2.7±1.0
^{92}Mo(^{54}Fe,4pn)	275	^{141}Gd	βp, β+, EC	13.3±1.2
^{92}Mo(^{56}Fe,3p2n)	275	^{143}Tb	β+, EC	11.8±0.5
^{92}Mo(^{56}Fe,p3n)	257			
^{92}Mo(^{58}Ni,3p3n)	325	^{144}Ho	βp, β+, EC	0.7±0.1
^{92}Mo(^{56}Fe,3p2n)	257			
^{92}Mo(^{58}Ni,4p2n)	325	^{144}Dy	βp?, β+, EC	?
^{92}Mo(^{56}Fe,3pn)	257			
^{92}Mo(^{58}Ni,5pn)	325	^{144}Tb^{m}	βp?, β+, EC	4.5±0.5

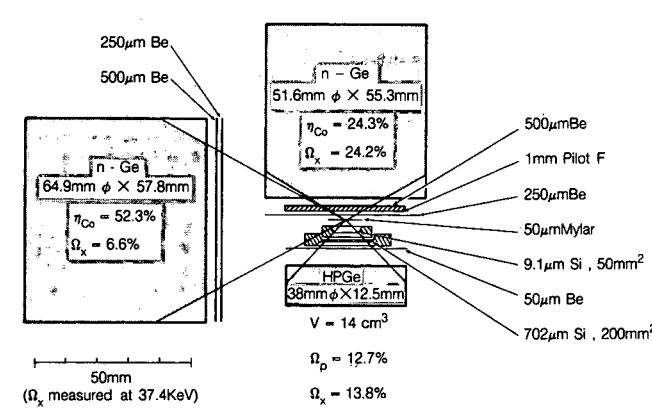

Fig. 1. Current detector arrangement in the OASIS spectroscopy laboratory. The active volume of each detector and its position relative to the other detectors is shown to scale. V = volume, η = standard efficiency, Ω_x = effective, measured solid angle for 37 keV x-rays. XBL 8410-8805

Radioactivity Handbook

R.B. Firestone and E. Browne

The *Radioactivity Handbook* will be published in 1985. This handbook is intended primarily for applied users of nuclear data. It will contain recommended radiation data for all radioactive isotopes. Figs. 1 and 2 are pages from the *Radioactivity Handbook* for A = 221. These have been produced from the LBL Isotopes Project extended ENDSF database.[1,2] The skeleton schemes have been manually updated from the *Table of Isotopes*[3] and the tabular data are prepared using UNIX[4] with a phototypesetter. Some of the features of the *Radioactivity Handbook* are discussed here.

A. *Skeleton Schemes:* Q-values are from the 1984 update to the Wapstra mass tables.[5] Half-life values are from ENSDF except for selected updates[6] and the 1983 GE wall chart[7] with details provided by F. William Walker.[8]

B. *Headers:* Isotope production information is from the *Table of Isotopes.* Half-life units have been standardized.

C. *Photon Tables:* Gamma-ray energies were fit to the level scheme by a least-squares method in order to obtain the best values for all transitions. Gamma-ray intensities were averaged using the method of Tepel[9] for the best branchings from each level and the method of Lederer[10] to remove the covariance. X-ray intensities have been calculated for K, L1, L2, and L3 vacancies produced by internal conversion and electron capture. X-ray energies are calculated from the binding energies of Larkin[11] except for Z = 84–103 which are from Porter and Friedman.[12] The multipolarities in brackets were derived from the level scheme and not measured directly.

D. *Atomic Electron Tables:* Electrons from internal conversion for all atomic subshells and Auger electrons for energies above the M1 binding energy are presented. They are binned in 1-keV intervals, and the most intense bins are shown discretely while the remaining data are grouped.

E. *Continuous Radiation Tables:* The beta spectra for all branches are calculated and binned in standard intervals. Internal bremsstrahlung is also calculated and binned in the same intervals.

F. *Alpha Tables:* The alpha-particle energies are analyzed in the same manner as the gamma rays (described above) to obtain the best energies.

G. *General features:* For all radiations the average energy per decay is provided. The data presented are normally from ENSDF after the aforementioned statistical analyses. Where the ENSDF file is deficient because of missing or incorrect data, additional evaluation is performed. A rounding factor of 25 in the last two significant digits was used, and all data which did not have explicit uncertainties in the ENSDF file were assigned estimated uncertainties.

H. *Text and appendices:* In addition to the information shown in the examples, there will be text and appendices. The inside cover will have a quick-reference definition table to facilitate usage of the book. There will be a full discussion of how to use the book, text describing the various radioactivity processes, and the following appendices,

1) Fundamental constants;

2) Interaction of radiation with matter;

3) Atomic data;

4) Isotope production;

5) Decay equations;

6) Gamma-ray catalog;

7) Alpha-particle catalog.

A = 221

NDS 27, 681 (1979)

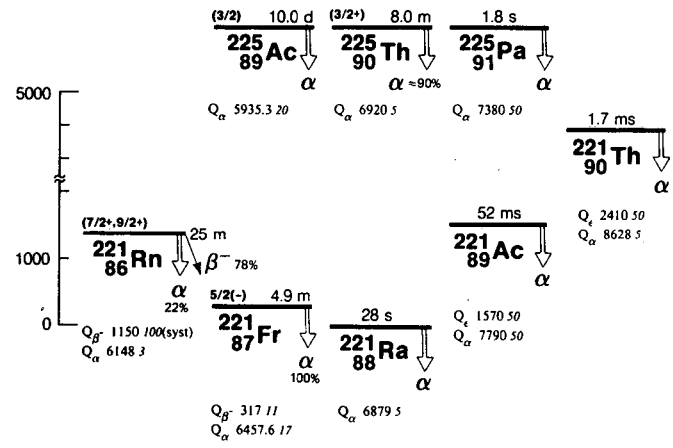

$^{221}_{86}$Rn(25 2 min)

Mode: β-(78 1 %), α(22 1 %)
Δ: 14410 100 keV syst
SpA: 3.4×10^{7} Ci/g
Prod: protons on Th

Alpha Particles (^{221}Rn)

⟨α⟩=1318.1 keV

α(keV)	α(%)
5778 3	1.8
5788 3	2.2
6037 3	18

Photons (^{221}Rn)

⟨γ⟩=120 5 keV

γmode	γ(keV)	γ(%)†
Po Lℓ	9.658	~0.011
Fr Lℓ	10.381	~0.8
Po Lα	11.119	~0.22
Fr Lα	12.017	~14
Po Lη	12.085	~0.0032
Fr Lη	13.255	~0.27
Po Lβ	13.502	~0.21
Fr Lβ	14.775	~16
Po Lγ	15.871	~0.04
Fr Lγ	17.439	~3
γβ-M1(+E2)	36.65 4	>0.008
γβ-M1(+E2)	38.51 3	>0.010
γβ-[E1]	49.20 4	0.071 10
γβ-[E1]	57.77 4	0.023 7
γβ-M1	62.93 4	0.143 17
γβ-M1+17%E2	64.23 4	0.267 20
γβ-E2	69.85 4	0.041 9
γβ-E2	71.71 4	0.119 12
γβ-E2(+<41%M1)	73.60 6	~0.0044
γβ-E1	73.84 4	0.53 3

Photons (^{221}Rn) (continued)

γmode	γ(keV)	γ(%)†
γβ-(M1+~20%E2)	74.90 6	0.17 7
Po Kα2	76.858	~0.32
Po Kα1	79.290	~0.5
Fr Kα2	83.229	8.2 8
Fr Kα1	86.105	13.6 12
γβ-M1	87.39 4	0.21 4
Po Kβ1'	89.639	~0.19
Po Kβ2'	92.673	~0.06
γβ-M1(+E2)	94.87 4	0.12 5
γβ-M1+37%E2	96.17 5	~0.022
Fr Kβ1'	97.272	4.9 5
γβ-M1+3.3%E2	99.58 4	0.16 3
γβ-E1	99.82 6	2.8 6
Fr Kβ2'	100.599	1.56 15
γβ-(M1+~26%E2)	100.88 3	0.29 7
γβ-M1+E2	103.44 4	0.050 13
γβ-M1+22%E2	108.36 3	2.19 13
γβ-[E1]	111.56 3	2.15 12
γβ-	119.87 10	0.29 4
γβ-[E1]	123.76 5	~0.08
γβ-M1+E2	124.81 6	~0.022
γβ-(E1)	126.23 7	0.22 3
γβ-	129.19 4	0.22 3
γβ-	133.70 10	0.54 10 ?
γβ-(E1)	135.01 7	0.65 6
γβ-(M1+~39%E2)	144.67 5	0.55 20
γβ-(E1)	145.15 4	0.69 14
γβ-E1	150.08 3	4.4 3
γβ-[E1]	152.64 4	~0.2 ?
γβ-[E1]	153.93 4	0.83 6
γβ-M1+7.5%E2	157.24 3	0.23 4
γβ-	168.88 13	0.27 3
γβ-	170.91 4	0.47 4
γβ-E1	178.39 3	0.86 6
γβ-[E1]	186.12 5	~0.009
γβ-E1	186.39 4	20.4 12
γβ-E1	187.99 5	~0.2
γβ-M1+37%E2	195.75 3	0.106 23
γβ-	197.79 12	0.74 9
γβ-(E1)	216.86 4	2.3 3
γβ-[E1]	224.64 4	~0.036
γβ-	240.76 4	0.70 7
γβ-	253.29 6	
γβ-[E1]	253.51 4	0.55 9
γα	254.2 3	~2
γβ-	256.24 5	0.33 8

Photons (^{221}Rn) (continued)

γmode	γ(keV)	γ(%)†
γα(M1+E2)	264.68 4	1.14 8
γβ-	273.5 25	0.46 20
γβ-(E1)	279.27 3	1.85 12

† uncert(syst): 9.8% for α, 8.5% for β-

Atomic Electrons (^{221}Rn)

⟨e⟩=56 6 keV

ebin(keV)	⟨e⟩(keV)	e(%)
7	1.23	17.0 13
10 - 14	0.11	1.0 3
15	2.8	~19
16 - 17	0.039	~0.24
18	2.6	~15
19	2.2	~12
20	0.23	<2
21	1.8	<18
22	1.8	<17
23	2.0	~9
24 - 32	1.0	~3
33	1.3	~4
34 - 43	3.0	8 4
44	1.2	2.7 7
45	0.055	0.122 15
46	1.5	3.2 6
48 - 53	1.39	2.8 5
54	1.09	2.03 21
55 - 56	1.22	2.2 5
57	1.27	2.2 4
58 - 84	6.8	9.8 10
85	1.58	1.85 17
86 - 89	0.37	0.43 15
90	4.0	4.4 5
91 - 103	3.0	3.1 8
104	1.12	1.08 11
105 - 154	5.7	4.6 8
155 - 160	0.34	~0.22
161	1.3	<2
163 - 213	2.7	1.6 5
214 - 262	1.5	0.64 20
264 - 279	0.07	0.027 12

Fig. 1. A page for A=221.

XBL 8411-8848

Continuous Radiation (^{221}Rn)

$\langle\beta-\rangle$=236 keV;$\langle$IB$\rangle$=0.23 keV

E_{bin}(keV)		$\langle\ \rangle$(keV)	(%)
0 - 10	β-	0.072	1.43
	IB	0.0113	
10 - 20	β-	0.215	1.44
	IB	0.0108	0.075
20 - 40	β-	0.87	2.89
	IB	0.020	0.070
40 - 100	β-	6.1	8.8
	IB	0.050	0.077
100 - 300	β-	55	28.0
	IB	0.092	0.055
300 - 600	β-	120	27.9
	IB	0.040	0.0101
600 - 1120	β-	54	7.6
	IB	0.0041	0.00062

$^{221}_{87}$Fr(4.9 *2* min)

Mode: α

Δ: 13255 *11* keV

SpA: 1.73×10^{8} Ci/g

Prod: descendant ^{229}Th

Alpha Particles (^{221}Fr)

$\langle\alpha\rangle$=6357 *53* keV

α(keV)	α(%)
5689 *3*	~0.002
5697 *4* ?	~0.0010
5774.4 *7*	0.06 *1*
5783 *4*	0.005 *2*
5813 *3*	~0.004
5925.1 *7*	0.03 *1*
5939.3 *7*	0.17 *3*
5965.9 *7*	0.08 *1*
5979.7 *7*	0.49 *3*
6037 *3*	~0.003
6075.1 *7*	0.15 *3*
6127.0 *7*	15.1 *2*
6243.3 *7*	1.34 *10*
6341.0 *7*	83.4 *8*

Photons (^{221}Fr)

$\langle\gamma\rangle$=27.7 *8* keV

γ_{mode}	γ(keV)	γ(%)†
At L_ℓ	9.897	0.042 *6*
At L_α	11.414	0.79 *10*
At L_η	12.466	0.0167 *17*
At L_β	13.911	0.96 *11*
At L_γ	16.361	0.199 *24*
At $K_{\alpha2}$	78.947	0.85 *11*
At $K_{\alpha1}$	81.517	1.41 *18*
At $K_{\beta1}$'	92.136	0.50 *7*
At $K_{\beta2}$'	95.265	0.155 *20*
γ	97.2 *3*	~0.019
γ M1(+14%E2)	99.51 *13*	0.10 *4*
γ(M1)	118.47 *13*	~0.035
γ(M1+E2)	149.99 *20*	0.07 *3*
γ	171.29 *20*	0.07 *3*
γ E2	217.98 *4*	10.9 *4*
γ	282.54 *15*	~0.009
γ	324.10 *20*	~0.017
γ	359.09 *20*	~0.035
γ	382.05 *15*	~0.035
γ	409.1 *2*	0.13 *4*

† 6.9% uncert(syst)

Atomic Electrons (^{221}Fr)

$\langle e\rangle$=8.44 *19* keV

e_{bin}(keV)	$\langle e\rangle$(keV)	e(%)
4 - 14	0.21	2.2 *4*
17	0.183	1.08 *15*
23 - 67	0.15	0.41 *16*
74 - 118	0.53	0.62 *13*
122	1.83	1.50 *6*
133 - 171	0.16	0.11 *4*
187	0.005	<0.005
200	0.477	0.238 *9*
201	2.16	1.07 *4*
204	1.18	0.581 *22*
214	0.73	0.340 *13*
215	0.350	0.163 *6*
217	0.286	0.132 *5*
218 - 266	0.092	0.041 *7*
268 - 313	0.06	~0.020
320 - 368	0.010	~0.0028
378 - 409	0.017	~0.004

$^{221}_{88}$Ra(28 *2* s)

Mode: α

Δ: 12938 *8* keV

SpA: 1.80×10^{9} Ci/g

Prod: descendant ^{229}U

Alpha Particles (^{221}Ra)

$\langle\alpha\rangle$=9999 *250* keV

α(keV)	α(%)
6160 *25* ?	~0.3
6254 *10*	0.7 *3*
6400 *25* ?	~0.3
6460 *25* ?	~0.4
6578 *5*	3 *1*
6585 *3*	8 *1*
6608 *3*	35 *2*
6669 *3*	21 *2*
6758 *3*	31 *2*

Photons (^{221}Ra)

$\langle\gamma\rangle$=43 *4* keV

γ_{mode}	γ(keV)	γ(%)
γ	90.2 *19*	15 *2*
γ	152.3 *19*	13 *2*
γ	176.1 *19*	2.0 *5*
γ	220 *10*	~0.10
γ	294 *10*	~0.6
γ	321 *10*	~0.7
γ	416 *10*	~0.50

$^{221}_{89}$Ac(52 *2* ms)

Mode: α

Δ: 14500 *50* keV

SpA: 7.4×10^{10} Ci/g

Prod: descendant ^{225}Pa; ^{208}Pb(^{19}F,α2n); ^{205}Tl(^{22}Ne,α2n); ^{208}Pb(^{16}O,p2n); ^{208}Pb(^{18}O,p4n)

Alpha Particles (^{221}Ac)

$\langle\alpha\rangle$=7720 *930* keV

α(keV)	α(%)
7170 *10*	~2
7375 *10*	~10
7440 *15*	20 *5*
7645 *10*	70 *10*

$^{221}_{90}$Th(1.68 *6* ms)

Mode: α

Δ: 16916 *13* keV

SpA: 7.4×10^{10} Ci/g

Prod: ^{208}Pb(^{16}O,3n); ^{208}Pb(^{22}Ne,α5n); ^{208}Pb(^{20}Ne,α3n); ^{209}Bi(^{19}F,α3n)

Alpha Particles (^{221}Th)

$\langle\alpha\rangle$=8330 *310* keV

α(keV)	α(%)
7733 *8*	6 *1*
8146 *5*	56 *3*
8472 *5*	39 *2*

Fig. 2. A page for A=221.

XBL 8411-8849

References

1. *Evaluated Nuclear Structure Data File*, edited and maintained by the National Nuclear Data Center, Brookhaven National Laboratory on behalf of the International Network for Nuclear Structure Data Evaluation.
2. *Implementation of the Evaluated Nuclear Structure Data File into Datatrieve*, a report to the National Academy of Sciences Panel on Basic Nuclear Data Compilations by E. Browne and R.B. Firestone, LBL (1982).
3. *Table of Isotopes*, 7th Edition: C.M. Lederer and V.S. Shirley, editors; John Wiley and Sons, Inc., New York (1978).
4. UNIX is a Trademark of Bell Laboratories.
5. A.H. Wapstra, private communication. To be published in Nucl. Phys. **A** (1984).
6. *Proposed Recommended List of Heavy Element Radionuclide Decay Data*; A. Lorenz, editor; IAEA International Nuclear Data Committee, INDC (NDS)-149/NE (1983).
7. *Chart of the Nuclides*, 13th Edition; prepared by F.W. Walker, D.G. Miller and F. Feiner; Knolls Atomic Power Laboratory (1984).
8. F.W. Walker, private communication (1984).
9. J.W. Tepel in the Summary Report of the IAEA Advisory Group Meeting on Nuclear Structure and Decay Data, IAEA report INDC(NSD)-115/NE, 121 (1980).
10. C.M. Lederer, Nuclear Data Network Memorandum of 13 April, 1982.
11. F.P. Larkins, Atomic Data and Nucl. Data Tables **20**, 338 (1977).
12. F.T. Porter and M.S. Friedman, J. Phys. Chem. Ref. Data **7**, 1267 (1978).

Analyzing Power Measurements for ^{3}He ($\vec{p}$,p) ^{3}He Elastic Scattering between 20 and 50 MeV*

*J. Birchall,† W. t. H. van Oers,† J.W. Watson,‡ H.E. Conzett, R.M. Larimer, B. Leemann, E.J. Stephenson,§ P. von Rossen,†† and R.E. Brown***

The four-nucleon system is of fundamental interest to nuclear physics. It is the lightest system to exhibit the basic nuclear structure property of excited states. Similarly, it is the lightest system to have been studied in terms of the shell model[1] and the cluster (resonating group) model. The cluster model of Tang, Le Mere and Thompson[2] describes the collision of composite nuclei in terms of the individual nucleon-nucleon interactions, employing totally antisymmetric wave functions so that the Pauli principle is immediately satisfied. Sherif[3] has had considerable success in describing p+^{3}He scattering below 20 MeV in terms of an optical model whose real potential includes an ℓ-dependent exchange term. This term is required by the finding of resonating group calculations that antisymmetrization resulted in different potentials for the even and odd ℓ states. Recently, Paez and Landau[4] have constructed a microscopic optical model of p–^{3}He scattering based on antisymmetrized nucleon-nucleon amplitudes.

To assist in the testing and critical development of various modern approaches to the four-nucleon system, a substantial program has been undertaken to obtain high-quality data on the p+^{3}He system in the 20 to 50 MeV range. (Extensive data exist for proton energies below 20 MeV.) In this paper we report analyzing power data $A_y(\Theta)$ for $\vec{p}$+^{3}He scattering at eleven energies between 21.4 and 49.5 MeV, with statistical uncertainties less than 0.03. These data plus differential cross sections and total reaction cross sections are used in a phase shift analysis to determine the spin dependent scattering

amplitudes. The restrictions imposed by invariance under rotations and reflections of the coordinate system as well as time reversal invariance lead to a p+^{3}He scattering matrix which may be written as the sum of six 4x4 matrices with coefficients (amplitudes) a, b, c, d, e, f, which are functions of energy and scattering angle.[5]

$$M(\vec{k}_f,\vec{k}_i) = 1/2[\,(a + b) + (a - b)(\vec{\sigma}_1 \cdot \vec{n})(\vec{\sigma}_2 \cdot \vec{n})$$

$$+ (c + d)(\vec{\sigma}_1 \cdot \vec{m})(\vec{\sigma}_2 \cdot \vec{m}) + (c - d)(\vec{\sigma}_1 \cdot \vec{l})(\vec{\sigma}_2 \cdot \vec{l})$$

$$+ e(\vec{\sigma}_1 + \vec{\sigma}_2) \cdot \vec{n} + f(\vec{\sigma}_1 - \vec{\sigma}_2) \cdot \vec{n}] \quad ,$$

where $\vec{l}$, $\vec{m}$ and $\vec{n}$ are orthogonal unit vectors, and $\vec{\sigma}_1$ and $\vec{\sigma}_2$ are the Pauli spin matrices, acting on the spin space of the proton and the ^{3}He, respectively. Each amplitude is complex, so that measurements of eleven different observables are needed at each incident energy and scattering angle to specify the p+^{3}He system completely (a common phase can be removed from the six amplitudes). Differential cross-section data or differential cross-section plus proton analyzing power data alone do not suffice to determine all of the parameters unambiguously. For example, the spin triplet-singlet (phase shift) mixing parameters appear in the partial-wave expression for the singlet-triplet transition amplitude, $if/\sqrt{2}$. Consequently, the measurement of an observable or a combination of observables that is most sensitive to f is required for best determination of these mixing parameters. The simplest experimental combination that satisfies this criterion is the difference between the proton and ^{3}He analyzing powers, ΔA, since,[5]

$$\Delta A = \frac{2}{\sigma_0} \mathrm{Re}\,(b^*f) \quad ,$$

where σ_0 is the differential cross-section for the scattering of unpolarized protons from ^{3}He. As a result, accurate data for as many observables as possible are essential and logically the next step to the measurement of the proton analyzing powers is the measurement of the $^3\vec{\mathrm{He}}$ analyzing powers.

Footnotes and References

*Condensed from Phys. Rev. C **29**, 2009 (1984).

†University of Manitoba, Winnipeg, Manitoba, Canada R3T 2N2.

‡Kent State University, Kent, OH 44242.

§Indiana University Cyclotron Facility, Bloomington, IN 47405.

††University of Bonn, D-5300 Bonn, West Germany.

**Los Alamos National Laboratory, Los Alamos, NM 87545.

1. P.P. Szydlik, Phys. Rev. **C1**, 146 (1970);

   P.P. Szydlik, J.R. Borowisz and R.F. Wagner, Phys. Rev. **C6**, 1902 (1972).

2. Y.C. Tang, M. Le Mere and D.R. Thompson, Phys. Reports **47C**, 168 (1978).

3. H.S. Sherif, Phys. Rev. **C19**, 1649 (1979).

4. M.J. Paez and R.H. Landau, Bull. Am. Phys. Soc. **27**, 695 (1982);

   R.H. Landau, Proc. 10th Int. Conf. on Few Body Problems in Physics, Karlsruhe 1983, contributed papers volume, p. 194.

5. P. La France, C. Lechanoine, F. Lehar, F. Perrot, L. Vinet and P. Winternitz, Nuovo Cimento **A64**, 179 (1981).

Spin-Polarization Effects in the ^{3}H(d,n)^{4}He Fusion Reaction

*H.E. Conzett and C. Rioux**

A recent investigation has shown that the ^{3}H(d,n)^{4}He fusion reaction rate could be enhanced by a factor of $\frac{3}{2}$ if the fusion plasma consisted of both polarized deuterons and tritons, forming exclusively the channel-spin $S = \frac{3}{2}$, $J = \frac{3}{2}^+$ state.[1] This result follows simply from the statistical weights of

the quartet $S = \frac{3}{2}$ and doublet $S = \frac{1}{2}$ initial states, with the assumption of the single $J = \frac{3}{2}^+$ reaction amplitude.

Since the maximum enhancement of the reaction rate occurs at the peak of the $J = \frac{3}{2}^+$ resonance, corresponding to a deuteron lab energy of 107 keV, it is of obvious interest to know what the enhancement would be at the lower energies that are typical of fusion plasmas. We are able to address this question by extending earlier calculations which gave the values of all of the spin-polarization observables at this $J = \frac{3}{2}^+$ resonance in both the $^3H(d,n)^4He$ and the $^3He(d,p)^4He$ reactions.[2]

We find that enhancement in the reaction rate, defined by σ_p/σ, where σ_p is the cross section with polarized participants and σ is the unpolarized cross section, is directly related to the ratio of the $J = \frac{1}{2}^+$ and $J = \frac{3}{2}^+$ reaction amplitudes. Specifically

$$\sigma_p/\sigma = \frac{3}{2}\,(1 + r^2/2)^{-1} \quad ,$$

$$\text{with} \quad \frac{R(\frac{1}{2})}{R(\frac{3}{2})} \equiv re^{i\delta} \quad , \qquad (1)$$

so $r = |R(\frac{1}{2})| \,/\, |R(\frac{3}{2})|$ is the ratio of the absolute values of the $J = \frac{1}{2}$ and $J = \frac{3}{2}$ reaction amplitudes. Since it is already known that r^2 (107 keV) $\simeq 0.1$, using the known energy dependence of $R(\frac{3}{2},E)$ we estimate that at a deuteron lab energy of 40 keV σ_p/σ (40 keV) $\simeq 1.25$, so that the enhancement factor has been reduced by 50% from its maximum possible value of 1.5. This 40 keV lab energy corresponds to about 12 keV plasma temperature.

Since we also have calculated the spin polarization observables as functions of the parameters r and δ in Eq. (1), we find that the experimental measurement of two of these will suffice to determine r^2. Thus, the fusion rate enhancement can be determined experimentally from such measurements in the presently unexplored energy region below the resonance energy at 107 keV.

Footnote and References

*Present address: Université Laval, Quebec, P.Q., Canada G1K 7P4.

1. R.M. Kulsrud *et al.*, Phys. Rev. Lett. **17**, 1248 (1982).
2. H.E. Conzett, *Few Body Problems in Physics*, ed. B. Zeitnitz (North Holland, Amsterdam, 1984), Vol. II, p. 539.

Polarization Transfer in p-^{16}O Elastic Scattering

H.E. Conzett, C. Rioux, F.S. Dietrich† and N.L. Back†*

It has been emphasized recently that nucleon-nucleus scattering is not as well understood as is generally believed.[1] It was shown that there are many sets of phase shifts, and corresponding optical potentials, which fit the best experimental data that are currently available. These data, which include differential cross sections, analyzing powers, and less accurate reaction cross sections, are not sufficient to specify the scattering amplitudes. To illustrate the ambiguities, Kobos *et al.*[1] found several different phase shift solutions which provided equally good fits to the p-^{16}O scattering data at 27.3 MeV. For each phase-shift set they then calculated the previously unmeasured polarization-transfer coefficient $K_x^{x'}(\theta)$, and they found very substantial differences in this polarization observable for the different phase-shift sets.

The scattering matrix for p-^{16}O scattering, with the spin structure $1/2 + 0 \rightarrow 1/2 + 0$, is

$$M = A + B\sigma_y \quad .$$

The experimental observables are then given in terms of the amplitudes A and B as:

$$\sigma(\theta) = |A|^2 + |B|^2$$

$$\sigma A_y(\theta) = 2 \text{ Re } A^*B \qquad (1)$$

$$\sigma K_x^{x'}(\theta) = |A|^2 - |B|^2$$

Since there are two complex amplitudes, three independent observables are sufficient to specify them to within an overall phase factor, which is not observable. Thus, it is clear that a measurement of the third observable, $K_x^{x'}$ of Eq. (1) should make it possible to determine the amplitudes A and B and, correspondingly, a unique phase-shift solution.

We have made initial measurements from which to determine $K_x^{x'}(\theta)$ in p-^{16}O elastic scattering at 27.3 MeV. Experimentally,

$$K_x^{x'} = P_{x'}/P_x \quad ,$$

where $P_x(P_{x'})$ is the transverse polarization component in the scattering plane for the incident (scattered) protons. Thus, the experiment consists of measuring the transverse polarization component after the scattering of an incident polarized beam. An initial analysis of our results shows that we will be able to clearly discriminate among the phase-shift sets of ref. 1, and we expect to be able to determine the scattering amplitudes A and B from the complete data set of Eq. (1).

Footnotes and Reference

*Present address: Université Laval, Quebec, P.Q. Canada G1K 7P4.

†Lawrence Livermore National Laboratory, Livermore, CA 94550

1. A.M. Kobos, R.S. Mackintosh and J.R. Rook, Nucl. Phys. **A389**, 205 (1982).

Deuteron Reactions and Vector Polarization

H.E. Conzett

In a very recent paper it was shown that in particle or nuclear reactions involving a spin-1 particle, e.g. the deuteron, it is possible to determine all of the reaction amplitudes from measurements of the tensor polarization components alone.[1] Thus, measurements of the deuteron vector polarization are theoretically unnecessary. It may, of course, be simpler in various experiments to measure the vector polarization rather than some of the tensor polarization components, but where that is not the case the theorem states that the tensor polarization measurements provide complete information on the reaction amplitudes.

The proof is straightforward and is illustrated for the simplest reaction spin structure that involves a spin-1 particle, i.e., $0 + 0 \rightarrow 1 + 0$. For such a reaction there are three complex amplitudes, A, B, and C, corresponding to each of the three spin-1 helicity states +1, 0, and −1. Standard expressions for the experimental observables in terms of the amplitudes give:

$$\sigma = |A|^2 + |B|^2 + |C|^2$$

$$\sigma p_{zz} = |A|^2 - 2|B|^2 + |C|^2$$

$$\sigma p_{xz} = \text{Re}[BC^* - AB^*]$$

$$\sigma p_{yz} = \text{Im}[BC^* - AB^*] \qquad (1)$$

$$\sigma(p_{xx} - p_{yy}) = \text{Re}AC^*$$

$$\sigma p_{xy} = \text{Im}AC^* \quad ,$$

where σ is the differential cross section and the p_{ij} are the various tensor polarization components.

From this set of six equations it is then possible to completely determine A, B, and C.

A completely different approach to this question is to examine the general constraints that exist among the spin-1 polarization components, both vector and tensor. If one plots along three orthogonal axes the quantities p_y, p_{yy}, and f_{xz} (p_{xx}, p_{zz}, p_{xz}), where f_{xz} is a known function of the components p_{xx}, p_{zz}, and p_{xz}, and p_y is the vector polarization, the space (p_y, p_{yy}, f_{xz}) is limited to the interior of a cone.[2] The apex of this (Lakin) cone is at $p_{yy} = -2$ and its base is at $p_{yy} = 1$, which are the extreme values available to p_{yy}. A measurement of all the tensor polarization components can then be represented by a point in the (p_{yy}, f_{xz}) plane. However, this does not fix the value of p_y along the axis orthogonal to this plane, except at the singular point $p_{yy} = -2$. Thus, in general, the value of p_y is not determined, so it follows that the reaction amplitudes are not completely determined.

The resolution of this dilemma lies in the fact that parity conservation limits the tensor polarization components to those appropriate to the Lakin cone, so in Eq. (1) $p_{yz} = p_{xy} = 0$. Correspondingly, in the reaction $0 + 0 \rightarrow 1 + 0$ with no parity change, parity conservation restricts the amplitudes to B = 0 and C = A, for which[2]

$$p_{yy} = -2 \quad , \quad p_{xx} = p_{zz} = 1$$

$$p_y = p_{xz} = 0 \quad .$$

Thus, the theorem of ref. 1 is valid when only Lorentz invariance is assumed for the reaction, but when parity conservation is added the theorem no longer applies.

Since the reaction $0 + 0 \rightarrow 1 + 0$ is so completely restricted by parity conservation, it is useful to examine a reaction with the simplest spin structure for which parity conservation does not limit the observables to any subsection of the Lakin cone. This occurs for elastic scattering $1 + 0 \rightarrow 1 + 0$, where time-reversal invariance in addition to parity conservation reduces the 3 x 3 = 9 helicity amplitudes to four independent ones.[2] In terms of these four amplitudes A, B, C, and D,

$$\begin{aligned} \sigma &= |A|^2 + |B|^2 + |C|^2 + 2\,|D|^2 \\ \sigma p_{zz} &= |A|^2 + |B|^2 - 2\,|C|^2 - |D|^2 \\ \sigma p_{yy} &= |A|^2 - 2\,|B|^2 + |C|^2 + 3\,|D|^2 \\ \sigma p_{xz} &= 3\mathrm{Re}\,[A - C]D^* \\ \sigma p_y &= 2\mathrm{Im}\,[A + C]D^* \quad . \end{aligned} \tag{2}$$

Two specific remarks can be made from Eqs. (2). The tensor polarizations alone are clearly not sufficient to determine the four amplitudes, and the vector polarization is distinct from any combination of the tensor components since it is given by the imaginary part of the bilinear combination of amplitudes. In general, four complex amplitudes require seven independent observables for their determination to within an overall phase factor. Thus, even the five observables of Eqs. (2) are insufficient, and measurements of polarization-transfer coefficients are required even in this simple case of spin-1 particle scattering.

References

1. G.R. Goldstein, Proc. 6th Int'l Symposium on High Energy Spin Physics, Marseille, France, Sept. 12–19, 1984.
2. F. Seiler, F.N. Rad, H.E. Conzett and R. Roy, Nucl. Phys. **A296**, 205 (1978).

Quadrupole Collectivity and the Shapes of Os-Pt Nuclei*

C.Y. Wu,† D. Cline,† A. Backlin,† T. Chaki,† T. Czosnyka,† L. Hasselgren,† B. Kotlinski,† P. Russo,† J.K. Sprinkle,† J. Srebrny,† I.Y. Lee, P.A. Butler, R.M. Diamond, H. Kluge, R.S. Simon, F.S. Stephens, C. Baktash,‡ G. Dracoulis,§ J. Leigh,§ J.O. Newton,§ W.R. Phillips,§ and S. Sie§

A prolate to oblate shape transition is known to occur in the osmium-platinum nuclei, but there has been no reliable determination of the softness to the quadrupole shape parameters β and γ. Calculations using the pairing-plus-quadrupole model and the full Bohr collective Hamiltonian[1] reproduce reasonably well the prolate to oblate shape transition in osmium-platinum nuclei and predict potential energy landscapes that are very soft to γ-vibration and moderately stiff to β-vibration.

All the E2 matrix elements involving low-lying states in a nucleus can be determined unambiguously from heavy-ion Coulomb excitation experiments if measurements of the de-excitation γ rays in coincidence with the scattered ions are made for a wide range of Coulomb excitation interaction strength.[2] This is achieved by varying the projectile Z value and scattering angle over wide ranges. The present Coulomb excitation experiments on ^{186,188,190,192}Os and ^{194}Pt have been carried out using 3.3–4.8 MeV/nucleon ^{40}Ca, ^{58}Ni, ^{136}Xe and ^{208}Pb ions from the tandem accelerators in Rochester, Brookhaven National Laboratory, and Canberra and from the SuperHILAC at the Lawrence Berkeley Laboratory. In most experiments a pair of position-sensitive parallel-plate avalanche detectors, covering a wide range of scattering angles, were used to detect both the scattered and the corresponding recoil ions in coincidence with the detection of the de-excitation γ rays in germanium detectors. Fig. 1 shows a typical level scheme resulting from the present work. The E2 matrix elements were determined from an analysis of this Coulomb excitation data using the new semi-classical Coulomb-excitation, coupled-channel, least squares search code, GOSIA,[3] developed at Rochester during the past few years. For each nucleus, 5 to 8 independent sets of random numbers were used as starting values for the fitted E2 matrix elements in the least-squares search to ensure that the final results are model independent and to check the uniqueness of the final solution. The magnitudes and observable signs of between 30 to 38 transitional and diagonal matrix elements were determined with reasonable errors for each nucleus. These include, in most nuclei, static electric quadrupole moments of members of the ground band to spin 10^+, the γ-band to spin 8^+ and the 4^+ head.

By analogy with Bohr's quadrupole shape parameters β,γ, the E2 moments in the principal axis frame can be specified[4] using two parameters Q,δ where $E(2,0)=Q\cos\delta$, $E(2,+2)=E(2,-2)=Q/\sqrt{2}\sin\delta$ and $E(2,-1)=E(2,1)=0$. Zero-coupled products of two or more E2 operators are rotationally invariant and thus their expectation values for any state are the same in both the laboratory and axis frames. The

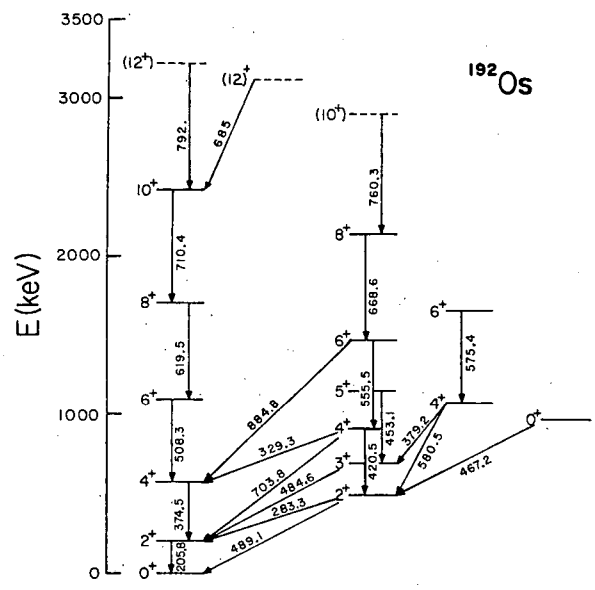

Fig. 1. Level scheme of ^{192}Os derived from the present work. XBL 8410-4211

ground-state expectation values of both the centroids and widths are shown in Fig. 2. The centroid $<Q^2>$ illustrates the gradual reduction in collectivity with increasing mass while the centroid $<\cos 3\delta>$ corresponds to triaxial deformation throughout a prolate to oblate shape transition. Several independent sum rules, using different intermediate spin couplings, occur for determination of the widths. These provide a check of the completeness and convergence of the summations. The results illustrate that reasonable convergence is obtained for the ground states. The appreciable softness in asymmetry, Fig. 2(d), and moderate stiffness in magnitude, Fig. 2(b), of the quadrupole deformation are consistent with the features predicted by Kumar and Baranger using the complete Bohr's Hamiltonian. These data demonstrate that the E2 data for the low-lying levels can be correlated well using only quadrupole collective degrees of freedom. In particular, the collective motion is primarily γ-soft and β-stiff throughout a prolate to oblate transition in these nuclei.

Footnotes and References

*Condensed from a paper submitted to Phys. Rev. Lett.

†Nuclear Structure Research Laboratory, University of Rochester, Rochester, NY 14627.

‡Brookhaven National Laboratory, Upton, NY 11973.

§Australian National University, Canberra, Australia.

1. K. Kumar and M. Baranger, Nucl. Phys. **A122**, 273 (1968).
2. L. Hasselgren and D. Cline, Proc. of the Int. Conf. on Interacting Bose-Fermi Systems in Nuclei. F. Iachello, ed., Plenum Press, New York, p. 59 (1981).
3. T. Czosnyka, D. Cline and C.Y. Wu, Bull. Amer. Phys. Soc. **28**, 745 (1983).
4. D. Cline and C. Flaum, Proc. of the Int. Conf. on Nuclear Structure Studies Using Electron Scattering and Photoreaction, Sendai 1972, ed., K. Shoda and H. Ui, Supplement to Research Report of the Laboratory of Nuclear Science, Tohoku University, Volume **5**, p. 61 (1972).

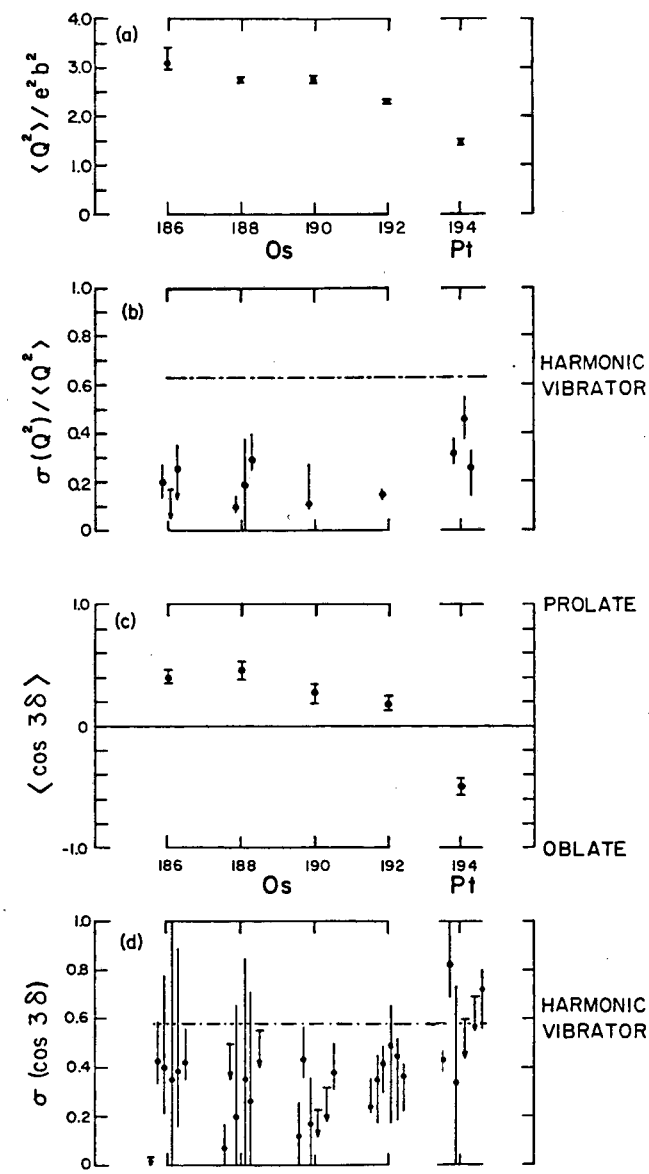

Fig. 2. Centroids (a,c) and vibrational widths (b,d) for the magnitude and asymmetry of quadrupole deformation of the ground state in ^{186,188,190,192}Os and ^{194}Pt. XBL 8410-4213

Spin Precession of Unresolved High-Spin States in $^{153\text{-}156}$Dy*

*O. Häusser,† D. Ward,† H.R. Andrews,† P. Taras,‡ B. Haas,§ M.A. Deleplanque, R.M. Diamond, E.L. Dines, A.O. Macchiavelli, R. McDonald, F.S. Stephens, and C.V. Stager***

Few attempts have been made to deduce electromagnetic properties of the unresolved high-spin states that emit the γ continuum. The most direct evidence for the collective enhancement of transitions in the "E2 bump" has been obtained from Doppler-shift attenuation data.[1] The g factors of the "continuum states" are also of interest since they provide a direct signature[2] of the rotational alignment of quasiparticle spins. Previous experiments[3,4] have utilized the transient magnetic fields experienced by recoil nuclei slowing down in polarized ferromagnetic foils. The spin precession angle ϕ_d accumulated in the unresolved high-spin states is observed as a small, time-integral rotation of the γ ray correlation of the *discrete* transitions. It should be noted that ϕ_d is expected to be nearly constant for the discrete transitions between low-spin states since they are emitted later in the cascade, after the transient field B(t) has ceased to operate.

The γ spectra were observed in coincidence with γ rays absorbed in a large NaI(Tl) sum-energy spectrometer. Selection of sum energy windows allows a variation in the average spin (J_ϕ) at which the measurement probes the g factor. Cuts on the sum energy also help to enhance a particular (HI,xn) evaporation channel. A further bonus offered by the coincidence is the rejection of intense Coulomb excitation background which is associated with very low sum energies. We have used Xe beams from the SuperHILAC and the inverse reactions ^{26}Mg(^{132}Xe,xn) at E = 645 MeV, and ^{24}Mg(^{136}Xe,xn) at E = 610 MeV to investigate g factors of unresolved high-spin states in ^{153,154}Dy and ^{155,156}Dy, respectively. The Xe beams bombarded triple-layered foils consisting of 1 mg/cm^2 thick, isotopically enriched Mg evaporated onto annealed Gd foils of various thicknesses (9, 11 and 12.8 mg/cm^2), and of 15 mg/cm^2 thick Cu evaporated onto the back of the Gd. Intimate contact between the Cu backing and a 0.8 mm thick, liquid N_2 cooled copper plate resulted in target temperature of $\approx$80 K, well below the Curie temperature for Gd (293 K). The polarizing field of 0.115 T, provided by a pair of 2 mm thick SmCo magnets at room temperature, was reversed at 5 min intervals by a mechanical rotation through 180°.

Gamma rays coincident with an event in the sum crystal were observed in pairs of 12.7 cm by 15.2 cm NaI(Tl) detectors at $\theta_\gamma = \pm 65°$, and of Ge(Li) detectors at $\theta_\gamma = \pm 120°$. At the chosen angles the logarithmic slopes of the γ angular correlation, $S = (dW/d\theta_\gamma)/W$, are near the maxima for stretched $\lambda = 2$ transitions between high-spin states. The slopes S for the discrete lines were estimated from angular distributions in ref. 5. For the continuum NaI(Tl) spectra, subsidiary three-point angular distributions (at θ_γ = 90°, 125° 150°) were measured. The raw NaI(Tl) spectra were subjected to an unfolding procedure using measured efficiencies and line shapes for monoenergetic γ rays from radioactive sources. The multiplicity of γ rays above threshold (0.3 MeV) M_γ was derived from the ratio of counts in the unfolded coincidence NaI(Tl) spectra to those in the corresponding singles sum-energy slices.

The yield changes ε associated with reversal of the transient field were obtained in the usual way from intensities of (discrete or continuous) γ rays for two matching [Ge(Li) or NaI(Tl)] detectors and the two directions of B_{ext}. The transient field for Dy recoils (Z = 66) in Gd can be estimated from previous calibration experiments to be $B(v,Z) = (26 \pm 2)Z(v/v_0)\exp(-0.135v/v_0)T$.

The experimental results obtained with a window on the sum energy that was wide enough to include both 4n and 5n channels are presented in Table I. The average precession angles for discrete lines (see Table I) are strongly dominated by the 4n channel because of the larger 4n cross section (62% for ^{154}Dy, 72% for ^{156}Dy) and because more E2 transitions (up to $14^+ \rightarrow 12^+$) are seen clearly above

background. The average initial spins $<I_i>$ of Table I were calculated from the measured γ-multiplicity M_γ after correcting for unobserved ($E_\gamma < 0.3$ MeV) transitions and N_s statistical transitions. They are in good agreement with $<I_i>$ obtained from a standard heavy ion fusion model. The average spin precession, $<I_\phi>$, was calculated with a schematic rotational model in which the complex γ cascade is replaced by E2 decays along a single rotational band. The effective moment of inertia was derived from the high-spin part of the experimentally determined level schemes, and the intrinsic quadrupole moment Q_0 was fitted to the observed precession spectra. (The average g factor obtained for ^{156}Dy is (g) = 0.21 ± 0.03 at $<I_\phi> \approx 23\hbar$. This small value for (g) in ^{156}Dy, when compared to the g factor for the first excited state, $g_{2^+} = 0.39 \pm 0.04$, implies predominant population of neutron-aligned bands on and above the yrast line.

By contrast, the larger g factor found for the N = 88 nucleus ^{154}Dy, (g) = 0.39 ± 0.05 at $<I_\phi> = 26\hbar$, is consistent with aligned spin supplied from both neutron and proton orbitals. There are also indications of a breakdown of the schematic rotational model in ^{154}Dy. Our results are consistent with a decrease in collectivity, and perhaps a shape change from slightly prolate to triaxial, or perhaps even oblate, as the spin increases from $I \approx 20\hbar$ to $I \approx 30\hbar$ in ^{154}Dy.

In ^{156}Dy the collectivity remains large, with evidence for neutron alignment on and above the yrast line.

Footnotes and References

*Condensed from Phys. Lett. **144B**, 341 (1984).

†Atomic Energy of Canada Limited, Chalk River Nuclear Laboratories, Chalk River, Ontario, Canada K0J IJ0.

‡Laboratoire de Physique Nucléaire, Université de Montréal, Montréal, P.Q., Canada H3C 3J7.

§Centre de Recherches Nucléaires, Strasboug, France.

**McMaster University, Ontario, Canada L8S 4K1

1. H. Hübel, U. Smilansky, R.M. Diamond, F.S. Stephens and B. Herskind, Phys. Rev. Lett. **41**, 791 (1978).
2. S. Frauendorf, Phys. Lett. **100B**, 219 (1981).
3. B. Skaali, R. Kalish, J. Eriksen and B. Herskind, Nucl. Phys. **A238**, 159 (1975).
4. N. Rud, D. Ward, H.R. Andrews, O. Hässer, P. Taras, J. Keinonen, M. Neiman, R.M. Diamond and F.S. Stephens, Phys. Lett. **101B**, 35 (1981).
5. H.R. Andrews, D. Ward, R.L. Graham and J.S. Geiger, Nucl. Phys. **A219**, 141 (1974).

Table I. Summary of results

Reaction	E_{Xe} (MeV)	M_γ	N_s	$<I_i>$	$<I_\phi>$ a)	ϕ(0.7 MeV) (mrad)	(ϕ_d) b) (mrad)	(g) c)
^{26}Mg(^{132}Xe,xn)	645	18.4	2.8	30.6	26.5	41 ±3	71 ± 6	0.39 ±0.05
^{154}Dy							72 ± 7	0.40 ±0.05
^{153}Dy							65 ±15	0.36 ±0.09
^{24}Mg(^{136}Xe,xn)	610	14.6	2.8	26.1	22.8	28 ±3	38 ± 5	0.21 ±0.03
^{156}Dy							38 ± 5	0.21 ±0.03
^{155}Dy							42 ±11	0.23 ±0.06

a)Average spin of precession estimated assuming intrinsic quadrupole moments Q_0 of 3 eb for ^{153,154}Dy and 4.5 eb for ^{155,156}Dy.

b)From an average of the $14^+ \rightarrow 12^+, ..., 2^+ \rightarrow 0^+$ transitions in ^{154,156}Dy and the $29/2^+ \rightarrow 25/2^2, ..., 17/2^2 \rightarrow 13/2^+$ transitions in ^{153,155}Dy.

c)Average g factors deduced from (ϕ_d) via $(g) = (\phi_d)/\phi/g)$.

Mass Dependence of Shell Effects at High Rotational Frequencies*

A.O. Macchiavelli,† H. Muehry,‡ M.A. Deleplanque, R.M. Diamond, F.S. Stephens, E.L. Dines§ and J.E. Draper§

In compound nucleus reactions, a few bands up to spin around $45\hbar$ can now be observed with new high-resolution and high-efficiency devices. These are the most intense bands (each of a few percent population). The rest of the population decays through many paths so that, around spin $50\hbar$, continuum (unresolved) γ-rays must be studied. In recent years, methods to extract information from them have been developed. In particular, it was realized[1] that, in quasirotational nuclei, the height of the continuum γ-ray spectrum (once the statistical component is subtracted) is proportional to an effective moment of inertia, $\mathcal{J}^{(2)}_{\rm eff} = dI/d\omega$, which indicates how much spin is generated at each rotational frequency ω. Changes in alignment and deformation at certain frequencies will therefore show up in such spectra[2] as irregularities. Also, these spectra have been corrected[1] for the incomplete feeding at high frequencies in order to extract values of $\mathcal{J}^{(2)}_{\rm eff}$. Early results[1] for ^{166,162}Yb and ^{160}Er suggested that at high frequencies (spins) the aligned high-j orbitals of the first empty shell come down towards the Fermi level. At the "crossing frequency" where they reach it, they become populated, causing a large increase in alignment, which is observed as a large rise in the $\mathcal{J}^{(2)}_{\rm eff}$ spectrum.

This idea has been tested across the periodic table in the nuclei ^{84}Sr, ^{102}Pd, ^{118}Te, ^{136}Nd, which are the main products of compound nuclear reactions at high spins. In general, large deformations around spin 50 don't seem to occur since a strong population of bands with a high collective moment of inertia has not been seen in γ-γ correlation data. Although some changes in deformation cannot be excluded, it is more probable that alignments are the source of increase in $\mathcal{J}^{(2)}_{\rm eff}$ at high frequencies. For each nucleus, the aligned orbitals which contribute can be reasonably well identified by looking at a Nilsson diagram together with a cranking diagram. In ^{84}Sr both $\pi h_{11/2}$ and $\nu h_{11/2}$ could contribute. In ^{102}Pd, $\pi h_{11/2}$ is most likely to align at the observed frequencies. In ^{118}Te $\nu i_{13/2}$ is the best candidate, and in ^{136}Nd, it is the $\pi i_{13/2}$ orbital. These results can be gathered in one figure if the mass dependence of both the moment of inertia and the crossing frequency is removed. Fig. 1 shows $\mathcal{J}^{(2)}_{\rm eff}$ spectra (in these reduced units) for the nuclei studied and for the nuclei ^{160}Er and ^{162}Yb. The calculation of ω_c assumes no deformation and no spread of the Fermi level within a shell, and this explains why ω/ω_c is smaller than 1. Also the fact that the rise in $\mathcal{J}^{(2)}_{\rm eff}$ occurs at very similar values of ω/ω_c in the four nuclei studied may be an accident. However, the results for these nuclei of very different mass, and also the more detailed study of the rare earth region (see next report) are consistent with the alignment picture.

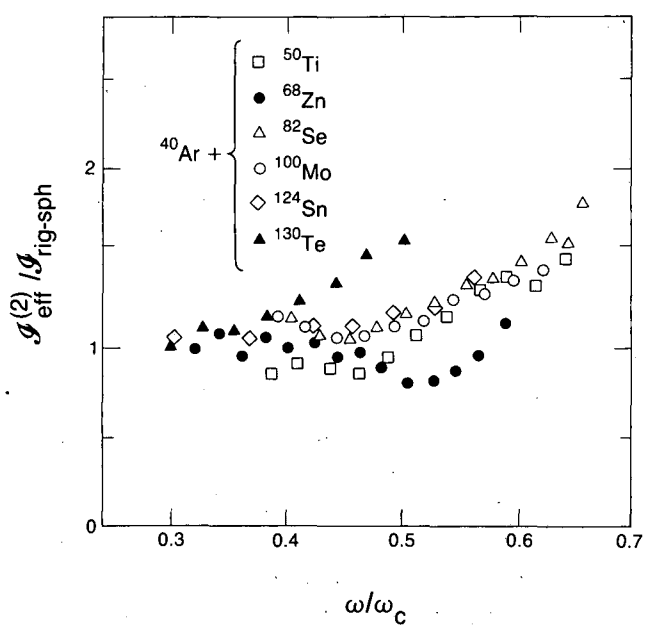

Fig. 1. $\mathcal{J}^{(2)}_{\rm eff}$ spectra, in reduced units (see text), for the systems indicated. XBL 847-10707

Footnotes and References

*Condensed from a paper submitted to Nuclear Physics.

†Permanent address: Comisión Nacional de Energía Atómica, Buenos Aires, Argentina.

‡Physik Institut, Universität Basel, Switzerland.

§Department of Physics, University of California, Davis, CA 95616.

1. M.A. Deleplanque, H.J. Körner, H. Kluge, A.O. Macchiavelli, N. Bendjaballah, R.M. Diamond and F.S. Stephens, Phys. Rev. Lett. **50**, 409 (1983).
2. M.A. Deleplanque, A.O. Macchiavelli, R.M. Diamond, F.S. Stephens, E.L. Dines and J.E. Draper, Phys. Rev. Lett. **51**, 1854 (1983).

Angular Velocity: A New Dimension in Nuclei*

R.M. Diamond and F.S. Stephens

Nuclei can be studied from their ground states ($\sim 0\hbar$) up to angular momenta of order $100\hbar$, where they are literally pulled apart by centrifugal effects. This range of angular momenta can be viewed as resulting from "cranking" the nucleus around a "rotation" axis, where the critical variable is the cranking velocity. The calculated response of nuclei to such an imposed angular velocity corresponds well with recent observations, and includes a rich and varied interplay of collective and single-particle phenomena. Single-particle motion can be calculated in deformed potentials of several types, and, further, these can be cranked about various axes to simulate the rotation. Such calculations, though still approximate, can be an excellent guide. Virtually all the properties now measured can also be calculated, and comparison provides a stimulus both to interpreting the experimental data and to improving the calculations.

The information on high-spin states comes mostly from studies of γ rays; thus there is a strong incentive to develop more powerful γ-ray detector systems. An obvious goal is to measure the energy and angle of every γ ray emitted from a decaying high-spin state (up to 35 transitions in some cases). Two 4π detector systems have been built to accomplish this. These instruments are both shells of NaI about 8 inches in inner radius and 7 inches thick (insuring almost complete absorption of all γ rays). To isolate the individual γ ray, the shell is divided into many elements, 72 for the system built at Oak Ridge[1] and 162 for the one in Heidelberg.[2] These instruments can measure the number of γ rays and the total γ-ray energy emitted, each with about 20% resolution (FWHM). In general, for the decay of high-spin states the number of γ rays is related to the initial spin and the total energy to the initial excitation energy. Thus these instruments can isolate a rather small initial population region. The spectrum of γ rays from this limited region should be much simpler to study than that from the entire reaction. Furthermore, the spin and/or excitation energy (nuclear temperature) of the region can be altered by changes in the gating conditions. Such possibilities are exciting and, already, out of some initial studies,[3] evidence for variations in the γ-ray spectrum with initial temperature has been found.

These "crystal balls" also measure the energy and angle of (nearly) every γ ray. This will surely be interesting to explore, but is not quite as powerful as it might be because the γ-ray energy resolution in NaI is rather poor, 5-6% (FWHM) for a 1-MeV γ ray. In fact, these crystal balls will probably often be used in conjunction with detectors of higher energy resolution, mainly germanium semiconductor detectors, which give about 0.2% resolution at 1 MeV (but cannot be made so large). Such considerations have led to "combination" detector systems; a low-resolution highly efficient shell to give the initial-state selection (as described above) coupled with an array of high-resolution Ge detectors. One such apparatus exists at Daresbury,[4] another is nearly com-

plete at Berkeley, and several others are under construction.

Many questions remain in high-spin physics. Two in the lower-spin region are: where and how are the pairing correlations finally quenched by the rotation; and what is the detailed nuclear shape and how does it vary for different bands (configurations), as a function of spin in a single band, and as a function of nuclear temperature. At higher spins the questions are broader. What are the appropriate quantum numbers to describe the system? This is related to the question of whether there are still large single-particle effects (irregularities) or whether the nucleus has been homogenized at the highest spins and the motion has become fully collective. One is examining in detail here the generation of collective properties out of an underlying single-particle structure. Then there are the interesting questions connected with "superdeformations" and the shape evolution connected with fission. Over a broad range of masses, the angular momentum we can study is limited mainly by fission, so it is clear we can reach situations where the centrifugal force produces major changes. How these are influenced by shell effects or other aspects of the single-particle motion will be fascinating to study. The nucleus provides a chance to study a few-body quantal system over a broad range of a variable, the rotational frequency. The results should enrich our perspectives on such systems.

Footnote and References

*Condensed from Nature **310**, 457 (1984).

1. M. Jaaskelainen *et al.*, Nucl. Instrum. Meth. **204**, 385 (1984).
2. V. Metag, V. Proc. Geiger Memorial Meet. (Springer, Berlin, 1983).
3. I.Y. Lee *et al.*, Proc. Conf. on High Angular Momentum Properties of Nuclei (ed. Johnson, N.R.) 339 (Harwood Academic, New York, 1983).
4. P.J. Twin *et al.*, Nucl. Phys. **A409**, 343c (1983).

Shapes and Alignments at High Spin in Some Rare-Earth Nuclei*

M.A. Deleplanque, R.M. Diamond, F.S. Stephens, A.O. Macchiavelli,† Th. Døssing,‡ J.E. Draper§ and E.L. Dines§

The structure of nuclei at high spins is dominated by an interplay between deformation and alignment effects. Cranking models predict various shapes but at the highest spins, there is a tendency towards large triaxial deformations and sometimes towards very large prolate deformations (superdeformations). Directly involved in the shape changes are aligned orbitals which come down to the Fermi level as the nucleus rotates more rapidly. At a certain frequency, they become populated and cause large alignments.

The mechanism of these changes has been explored by looking at a series of rare earth quasirotational nuclei from Dy to W in the transition region around N = 90 neutrons. The continuum spectra, corrected for incomplete population (feeding) of the high spins, are directly proportional to dynamic effective moments of inertia $\mathcal{J}^{(2)}_{\rm eff}$ which describe how much spin is generated at each rotational frequency. The feeding correction method, whose principle was given in a previous letter[1] is here explored in detail. It is shown that in quasirotational nuclei, it can be applied successfully in realistic cases except when coherent backbends (many paths having a backbend in a narrow spin and frequency range) occur in the feeding region. In general, there will be a rise in the $\mathcal{J}^{(2)}_{\rm eff}$ spectra at frequencies where alignments or increase in deformation occur. We discuss here main-

ly the high frequency part of the spectra.

The heavier nuclei studied (^{170}W, ^{168}Hf, ^{166}Yb, ^{160}Er) have stable deformation and the frequency at which the alignments occur just reflect Fermi level positions, as illustrated in Fig. 1: the $h_{9/2}$, $i_{13/2}$ proton alignments occur at higher frequency for ^{160}Er whose proton Fermi level is lower than for Yb nuclei. The same argument explains ^{168}Hf, ^{170}W spectra. In lighter nuclei, the deformation is in general smaller, which tends to delay alignments towards higher frequencies. This is well illustrated in the series of Yb nuclei (of mass 166, 162, 160, 158) which are rather rigid. In the two lighter nuclei, the rise at high frequency is much less pronounced. The light Er nuclei (mass 158, 156), however, are softer, and the nucleus explores changes in deformation to generate spin. Thus, the $\mathcal{J}^{(2)}_{eff}$ spectra rise at the same frequency in all three Er nuclei. It should be noted that changes towards large deformations also involve high-j orbitals.

This detailed study of the rare-earth region, as well as the survey of a wide mass range (see previous report) offers a consistent picture of the mechanism by which angular momentum is generated at high spins.

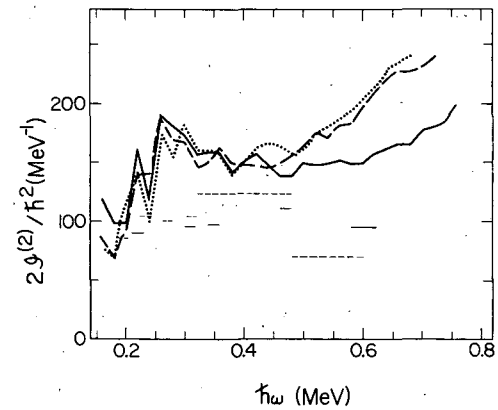

Fig. 1. $\mathcal{J}^{(2)}_{eff}$ as a function of $\hbar\omega$ for the systems ^{124}Sn + ^{40}Ar (thick solid line), ^{126}Te + ^{40}Ar (dotted line), and ^{130}Te + ^{40}Ar (thick dashed line). Also shown are some values of $\mathcal{J}^{(2)}_{eff}$ for ^{124}Sn + ^{40}Ar (thin solid lines) and ^{130}Te + ^{40}Ar (thin dashed lines). XBL 823-233B

Footnotes and References

*Condensed from a paper submitted to Nuclear Physics.

†Permanent address: Comisión Nacional de Energía Atómica, Buenos Aires, Argentina.

‡Present address: The Niels Bohr Institute, University of Copenhagen, DK-2100 Copenhagen Ø, Denmark.

§Department of Physics, University of California, Davis, CA 95616.

1. M.A. Deleplanque *et al.*, Phys. Rev. Lett. **50**, 409 (1983).

Neutron Transfer Reactions with Very Heavy Ions*

A.O. Macchiavelli,† M.A. Deleplanque, R.M. Diamond, F.S. Stephens, E.L. Dines‡ and J.E. Draper‡

We have studied neutron transfer reactions induced by ^{132}Xe on the three rare-earth targets, ^{154}Sm, ^{171}Yb, ^{176}Yb, at a bombarding energy of ~1.1 times the Coulomb barrier energy. There are a number of reasons why such reactions can be an interesting and attractive tool for nuclear physics.

i. They can provide information similar to that obtained with light-ion reactions, but with the unique features associated with very heavy ions, namely, the interplay between single-particle aspects, particle-particle correlations and collective excitations.

ii. They can populate states that cannot be produced with other reactions, for example, high-spin states in nuclei that cannot be reached with conventional (HI,xn) reactions or with Coulomb excitation.

iii. The small amount of mass, angular momen-

tum and energy transferred, i.e. $\Delta M/M$, $\Delta L/L$ and $\Delta E/E << 1$, which together with the large Sommerfeld parameter, $\eta >> 1$, give the possibility of defining a localized classical trajectory for the reaction.

In the last few years several studies have been devoted to transfer reactions with very heavy ions.[1-4] In the present work we have extended particle-γ coincidence methods to very heavy-ion transfer reactions; the Xe beam was provided by the LBL SuperHILAC and the targets were self-supporting metal foils of $\sim$0.5 mg/cm^2. The experimental arrangement consisted of two moderate solid-angle position-sensitive gas avalanche detectors (PSAD) to detect the coincident projectile- and target-like products, while two Ge(Li) counters placed at 180° to the PSADs were used to observe the γ rays emitted in the reaction. A particle-particle-γ coincidence was required as a master gate, and we were able to identify final products and states populated in the one- and two-neutron transfer reactions, as well as in inelastic excitation. Fig. 1 shows Ge(Li) spectra in coincidence with distant- and close-collision events for the ^{154}Sm target.

The yield of γ rays integrated over the angle subtended by the particle detectors can be obtained as a function of spin. From these data we can calculate the total probability of producing an inelastic collision or a simple neutron transfer. Under our bombarding conditions this probability is around 30% of the events triggering the two coincident PSADs. So we have to conclude that we are in a regime where multiparticle transfer and deep-inelastic reactions are important, and this had already been observed in the other (HI, transfer) reactions above the Coulomb barrier. However, although the deep-inelastic products will trigger the PSADs, the γ rays associated with them are likely to form a continuum spectrum due to the low population of individual reaction channels, and so we think the discrete γ-lines we have observed are related to cold or quasi-elastic (effective Q-values <10 MeV) events.

Near or below the Coulomb barrier, the scattering angle of the projectile defines a classical (Coulomb) trajectory and a distance of closest approach $D(\theta)$. The transfer probabilities as a function of $D(\theta)$ are presented in fig. 2 for the different reactions. All the cases show an exponential behavior, i.e.

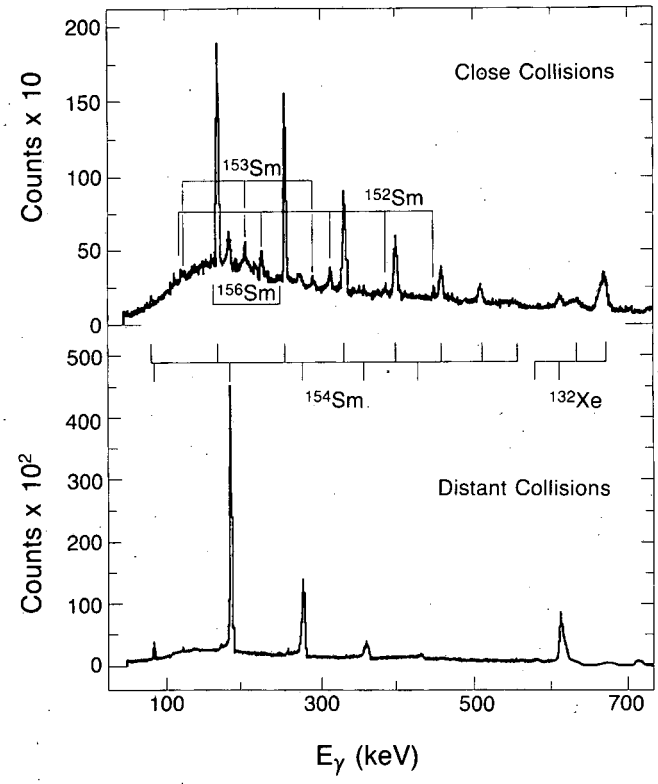

Fig. 1. Gamma-ray spectra seen by Ge(Li) R for the ^{154}Sm runs. Bottom: in coincidence with distant-collision events. Top: in coincidence with close-collision events, the transfer lines are now clearly seen. XBL 843-10127

$$P_{\Delta N}(D(\theta)) \propto \exp(-KD(\theta)) \quad . \qquad (1)$$

For reactions below the Coulomb barrier the transfer of nucleons is usually described by a barrier penetration model, and the parameter K is given by $2\sqrt{2mB}/\hbar$ where B is the average ground-state binding energy of the transferred particle. Above the Coulomb barrier, we can interpret K in (1) as an effective penetration factor $K_{eff} = 2\sqrt{2mB_{eff}}/\hbar$. The values for one-neutron transfer are in reasonable agreement with the values calculated using the appropriate ground-state binding energies. On the other hand, it is expected in either sequential or direct transfer of two neutrons that $K_{2n} = 2K_{1n}$. This fact

is clearly not observed for K_{eff} in this experiment nor in the result of refs. 1 and 2.

The values of the effective binding energies found seem to indicate that intermediate states with higher excitation energies may be important for the transfer of two neutrons at energies above the Coulomb barrier. We can estimate an average excitation energy around 6 ± 2 MeV above the yrast line. We can define an enhancement factor that relates the observed probabilities for 2n transfer to that of an uncorrelated pair. At any distance $D(\theta)$,

$$EF(D) = P_{2n}(D)/P_{1n}^2(D) \quad . \qquad (2)$$

Values of EF ≈ 5–30 are found. An interesting interpretation of this enhancement factor is to relate it to the pairing interaction. One expects pairing to enhance 2n transfers both in a single- (true-pair) and two-step (sequential) process. The authors of ref. 3 have shown that by lowering the bombarding energy below the Coulomb barrier, penetration factors are well reproduced by the average ground-state binding energies. Then a proper discussion of pairing effects is possible. However, as just discussed, above the Coulomb barrier 2n transfer probably proceeds via states of higher excitation energy. Due to the smaller effective barrier the probability for 2n transfer is in this case larger than that expected for a cold transfer. If these intermediate states of low, but finite, excitation energy do occur, their importance cannot be neglected and casts doubt on the interpretation of the "apparent" enhancement factors as arising solely from the pairing interaction. In addition, these kinds of reactions may become a useful tool for nuclear structure studies involving transfer at high spins, and to produce states at high spin in certain nuclei that cannot be made in (HI,xn) reactions.

The authors would like to thank D. Habs for his participation in the early stages of this work, particularly in the design of the PSADs and the scattering chamber. Discussions with T. Dørssing and J. Rasmussen are greatly appreciated.

Footnotes and References

*Condensed from LBL-17647 and Nuclear Physics, to be published.

†Permanent address: Comisión Nacional de Energía Atómica, Buenos Aires, Argentina.

‡Permanent address: Department of Physics, University of California, Davis, CA 95616.

1. H. Siekmann *et al.*, Z. Phys. **307**, 113 (1982).
2. G. Himmele, H. Backe, P.A. Butler, D. Habs, V. Metag, H.J. Specht and J.B. Wilhelmy, Nucl. Phys. **A404**, 401 (1983).
3. W. von Oertzen, B. Gebauer, A. Gamp, H.G. Bohlen, F. Busch and D. Schull, Z. Phys. **A313**, 189 (1983).
4. K.D. Rehm, D.G. Kovar, W. Kutschera, M. Paul, G. Stephans and J.L. Yntema, Phys. Rev. Lett. **51**, 1426 (1983).

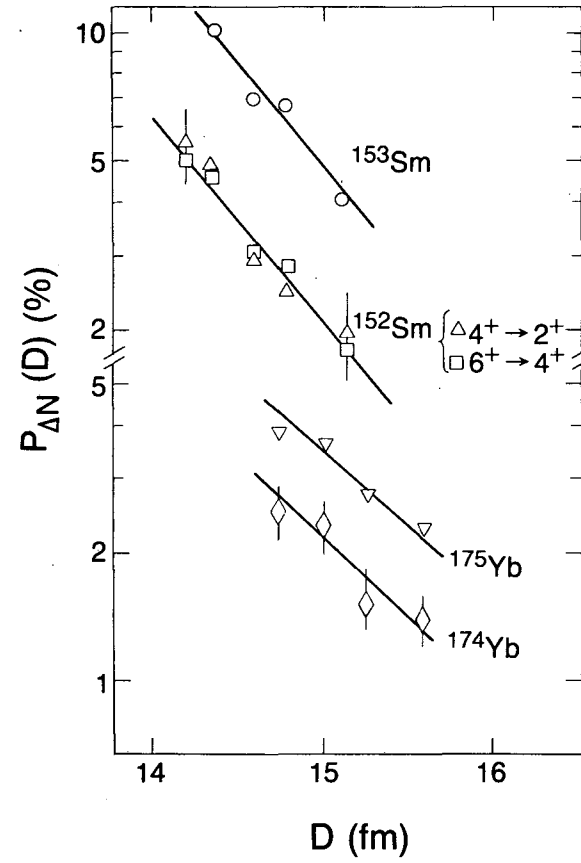

Fig. 2. Probabilities for transferring one and two neutrons as a function of the distance between the two nuclei. Error bars include systematic effects in the determination of the absolute efficiency of the Ge(Li) counter. The effective penetration factors are extracted from the slopes of the lines shown.

XBL 843-10125

Evidence for Shape Polarization From the Emission of Complex Fragments by Compound Nuclei

G.J. Wozniak, M.L. Padgett, L.G. Sobotka, M.A. McMahan, C. Signarbieux,† J.H. Gu,‡ Z.H. Liu,§ Z.Q Yao‡ and L.G. Moretto*

A recent study[1] demonstrated that a rare decay mode of the compound nucleus is the emission of heavy nuclei (He, Li, Be, B, C, N, O and F). An interesting feature in the energy spectra of these decay products was the indication of an evolution from a Maxwellian shape for He and Li ions through a more symmetric shape for B and C to a Gaussian shape for heavier nuclei. Such an evolution has been predicted[2] by Moretto in 1975 and interpreted as resulting from the shape polarization of the heavy fragment induced at scission by the charge of the light fragment.

The degree of shape polarization occurring in the decay of the CN as a function of the exit channel depends not only on the atomic number of the emitted fragment but also on the temperature of the compound nucleus. To determine whether this shape evolution occurs at other bombarding energies and to investigate its temperature dependence, silver targets were bombarded with 40-130 MeV ^{3}He beams. In Fig. 1 c.m. energy spectra for He to Ne decay products observed at different bombarding energies are shown. A striking feature of this figure is the difference in shape observed for the light and heavy decay products He and O, respectively: the He spectra show the typical Maxwellian shape and the O spectra show a Gaussian shape reminiscent of fission. At all bombarding energies, the spectra show an evolution from a Maxwellian to a symmetric shape as the fragment's atomic number increases from He to 0.

This trend in the shape of the energy spectra can be made more quantitative by expressing the degree of symmetry of the spectra in terms of skewness, which is zero for a Gaussian distribution. Extracted values of the skewness are plotted versus the fragment Z value in Fig. 2. The transition from an asymmetric shape (large skewness) at small Z-values to a nearly symmetric shape (small skewness) at large Z-values is dramatically evident.

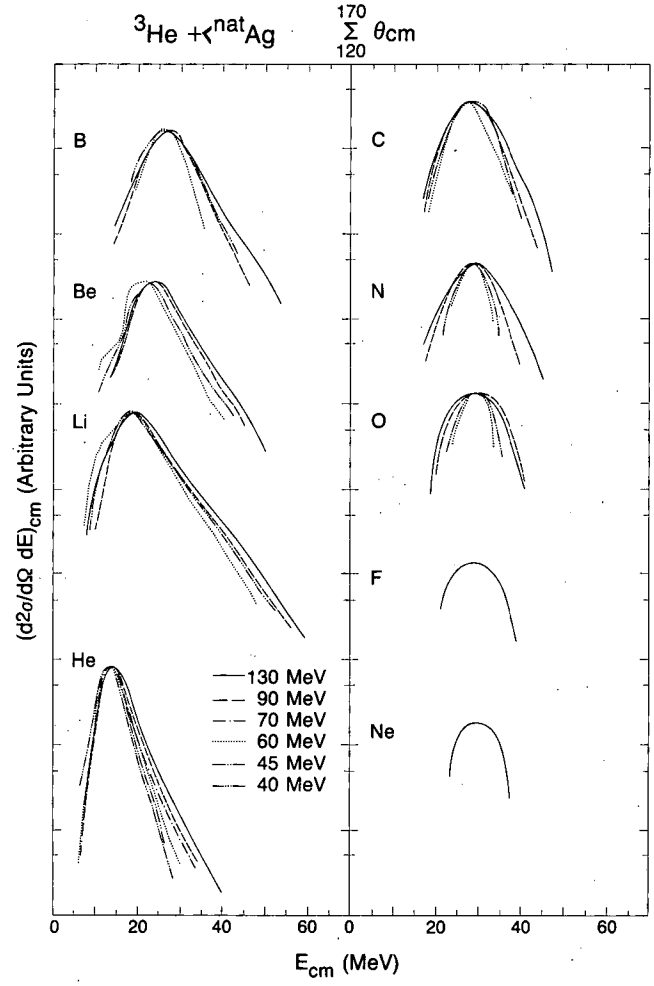

Fig. 1. Center-of-mass energy spectra for He-Ne ions emitted from In compound nuclei formed at different bombarding energies (represented by different curves). For each element all curves have been normalized to the 130 MeV curve to emphasize shape changes. XBL 845-10526

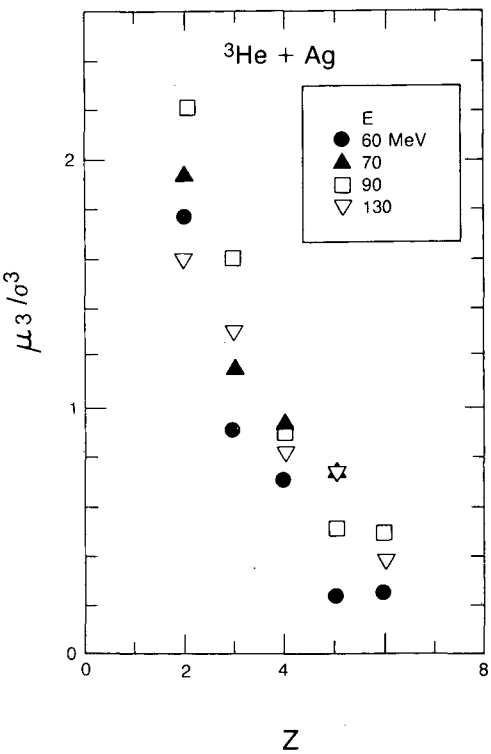

Fig. 2. The skewness (third moment divided by the cube of the width) extracted from the experimental kinetic energy distributions plotted versus the atomic number of the emitted fragment. Data from different bombarding energies are represented by different symbols. XBL 846-10653

The evolution seen in Figs. 1 & 2 can be interpreted as due to the increasing effect of shape polarization on the Coulomb repulsion energy. Because the greatest fraction of the kinetic energy of the particle at infinity originates from Coulomb repulsion and because the distance between the centroids of the two charges is critical in determining the Coulomb energy, different shapes at the time of scission will generate a width in the fragment's kinetic energy distribution. For light charged particles, the shape fluctuation is relatively weak and the basic Maxwellian shape is preserved.[1] For heavier charged particles, the shape polarization is stronger and a Gaussian shape results.

Footnotes and References

*Permanent address: Chemistry Department, Washington University, St. Louis, MO 63130.

†Permanent address: Nuclear Physics Division, CEN Saclay, BP1 91.191 Gif sur Yvette, Cedex, France.

‡Permanent address: Shanghai Institute of Nuclear Research, Shanghai, China.

§Permanent address: Institute of Atomic Energy, Beijing, China.

1. L.G. Sobotka *et al.*, Phys. Rev. Lett. **51**, 2187 (1983).
2. L.G. Moretto, Nucl. Phys. **A247**, 211 (1975).

Sequential Fission Angular Distributions from Mass-Asymmetric Heavy Ion Reactions*

D.J. Morrissey,† G.J. Wozniak, L.G. Sobotka,‡ R.J. McDonald, A.J. Pacheco§ and L.G. Moretto

An important quantity that can be obtained from sequential fission data is the difference between the in-plane variances of the target-like fragment's (TLF) spin distribution. Such a difference is only available from sequential fission angular distributions and is the central reason for the present study. At the same time it is interesting to compare the results of the present study with the previous data for the in-plane sequential fission angular distributions. The data should be placed on the same footing so that meaningful comparisons can be made. For example, in order to study the alignment of the intrinsic spin of the fissioning nucleus as a function of the mass asymmetry of the dinuclear complex, we need a series of reaction systems with the same total mass at the same temperature and total angular momentum. Since such data are not available, comparisons must be made after removing the effects of any quantity that is varying. A survey of the literature shows that extensive data are available in the

range of 100 to 150 MeV energy loss for systems with total masses in the range of 217 to 328 amu. For this limited Q-value range the temperature of the dinuclear system varies slowly as a function of mass asymmetry and can be assumed to be constant. In contrast, the average orbital angular momentum of the system varies substantially with asymmetry and such a variation must be taken into account.

Fitting the fission fragment angular distributions determines the three parameters, q_2, q_3 and q_4. By utilizing the ratio q_3/q_2 one can determine the in-plane anisotropy divided by the square of the aligned spin:

$$q_3/q_2 = (\sigma_y^2 - \sigma_x^2)/2 <I_z>^2 \quad . \qquad (1)$$

The calculation of this ratio for all published data is shown in Fig. 1a as a function of mass asymmetry,

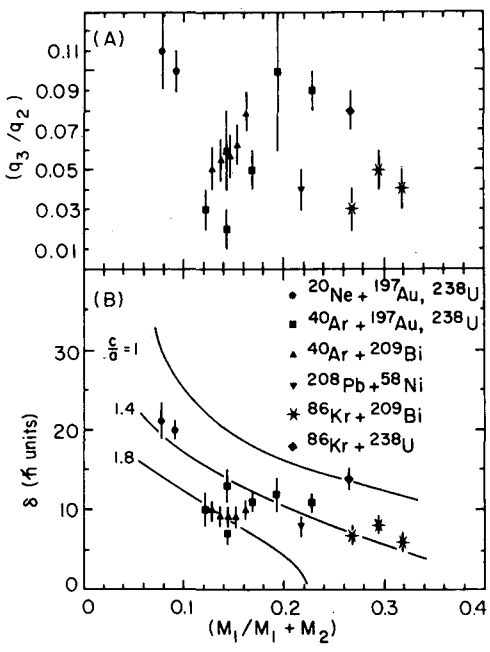

Fig. 1. (A) A measure of the in-plane anisotropy q_3/q_2 is shown as a function of the mass asymmetry of the reaction products. (B) The variation of $<I_z>$ and the total mass of the system has been approximately removed from the in-plane anisotropies shown above as discussed in the text. The curves are statistical equilibrium model calculations for differing ratios (c/a), of the major to minor axes of a spheroidal TLF (See text). XBL 8410-4343

$M_1/(M_1 + M_2)$, of the DIC products. (The data were those for which the energy loss was as near to 150 MeV as possible.) The data in Fig. 1(A) have a large scatter, due to their differing values of $<I_Z>$. In the rigid rotation limit, $<I_Z>$ is given by the ratio of the moment of inertia of the fissioning nucleus, $\mathcal{I}_{TLF}$, to the sum of the moments of inertia multiplied by the average-entrance-channel-orbital-angular momentum, L_{avg}:

$$<I_z>_{RR} = \left(\frac{\mathcal{I}_{TLF}}{\mathcal{I}_{TLF} + \mathcal{I}_{PLF} + \mu R^2}\right) L_{avg} \qquad (2)$$

with $\mathcal{I}_{PLF}$ being the moment of inertia of the nonfissioning nucleus.

We have attempted to remove the variation of $<I_z>$ in the observed values of q_3/q_2 by multiplying this quantity by two times the square of a simple estimate of $<I_z>_{RR}$. For this estimate we have used spherical moments of inertia and have taken L_{avg} to be 2/3 of L_{max}. We have also scaled the values of the moment of inertia of each dinuclear system to that of the $^{40}Ar + ^{238}U$ system. Thus, a new quantity, δ^2, can be defined as:

$$\delta^2 = 2\left(\frac{q_3}{q_2}\right)\left(\frac{278}{A_1 + A_2}\right)^{5/3} \left\{\left(\frac{\mathcal{I}_{TLF}}{\mathcal{I}_{TLF} + \mathcal{I}_{PLF} + \mu R^2}\right) L_{avg}\right\}^2 \qquad (3)$$

which should be approximately equal to the difference between the variances of the spin distribution along the two in-plane coordinates:

$$\delta = (\sigma_y^2 - \sigma_x^2)^{1/2} \quad . \qquad (4)$$

The variation of δ is shown in Fig. 1(B) as a function of mass asymmetry. This simple treatment has gone a long way towards systematizing the data in Fig. 1(A). The striking result of this treatment is that the strong oscillations of q_3/q_2 noted for several entrance channels has been removed. Overall, δ appears to increase when $M_1/(M_1+M_2)$ decreases indicating that σ_y becomes progressively larger than σ_x as the mass split becomes asymmetric. This trend is in qualitative agreement with the statistical equilibrium model.

The predictions of the statistical equilibrium model developed in refs. 1 and 2 can also be quantitatively tested with the systematic data presented in Fig. 1(B). This comparison is quite direct because the model predicts values of σ_x^2 and σ_y^2 as a function of temperature and mass asymmetry of the dinuclear system. The predictions for two touching spheres and a total mass of 278 amu at a temperature of 2.1 MeV are shown in Fig. 1(B). The model calculations for two touching spheres overestimate the misalignment along the symmetry axis throughout the mass asymmetry range. As was shown for the ^{20}Ne + Au and U systems, this discrepancy is probably due to the neglect of either deformation or interfragment separation (neck formation) in the present model.

A first-order estimate of the effect of deformation on the model calculations can be made by allowing the target-like fragment to deform along the line of centers of the dinuclear system. Model calculations of δ for a sphere-spheroid system are also shown in Fig. 1(B), labeled by the ratio of the axes of the spheroid (c/a). As the deformation increases, the tilting mode stiffens, causing σ_y to decrease and thus δ to decrease. The calculations show that an axis ratio of 1.4 to 1.8 is needed to reproduce the dependence of the data on mass asymmetry. Slightly larger deformations of the TLF (c/a = 2) were necessary to reproduce average TKE values in the exit channel of the data from the present study.

Footnotes and References

*Condensed from LBL-18688

†National Superconducting Cyclotron Laboratory, Michigan State University, East Lansing, MI 48824-1321.

‡Permanent address: Department of Chemistry, Washington University, St. Louis, MO 63130.

§Permanent address: Comisión Nacional de Energía Atómica, Buenos Aires, Argentina.

1. L.G. Moretto and R.P. Schmitt, Phys. Rev. **C21**, 204 (1980).
2. R.P. Schmitt and A.J. Pacheco, Nucl. Phys. **A379**, 313 (1982).

Symmetric Splitting of Very Light Systems*

*K. Grotowski,† Z. Majka,† R. Planeta,† M. Szczodrak,† Y. Chan, G. Guarino,‡ L.G. Moretto, D.J. Morrissey,§ L.G. Sobotka,** R.G. Stokstad, I. Tserruya,†† S. Wald and G.J. Wozniak*

Fission reactions that produce fragments close to one half the mass of the composite system are traditionally observed in heavy nuclei. In light systems, symmetric splitting is rarely observed and poorly understood. It would be interesting to verify the existence of the symmetric splitting of compound nuclei with A<100. For systems with A<80, evidence for possible symmetric splitting has been observed in only a few inclusive measurements.[1] Because the above studies were inclusive measurements, the presence of products with about one half the mass of the compound nucleus does not prove the existence of a fission process. In particular, these light compound nuclei were typically formed with sufficient excitation energy to undergo large mass loss due to successive α particle evaporation.

To demonstrate symmetric splitting for highly excited light systems (A~50), it is essential to show in a coincidence experiment that there are two fragments, each having approximately one half the mass of the compound nucleus. It is also important to minimize the production of symmetric fragments via a deep inelastic mechanism by choosing reactions with a large entrance channel mass asymmetry. To this end, the kinetic energy spectra and the in-plane angular correlation of symmetric products were measured for the following reactions: 121 and 186 MeV ^{12}C + ^{40}Ca, 141 MeV ^{9}Be + ^{40}Ca and 153 MeV ^{6}Li + ^{40}Ca. The out-of-plane correlation of symmetric products was also measured for the reaction

186 MeV ^{12}C + ^{40}Ca. The coincidence measurements of the ^{12}C + ^{40}Ca system demonstrated that essentially all of the inclusive yield of symmetric products around 40° results from a binary decay. To characterize the dependence of the symmetric splitting process on the excitation energy of the ^{12}C + ^{40}Ca system, inclusive measurements were made at bombarding energies of 74, 132, 162 and 185 MeV.

The excitation function for the reaction ^{12}C + $^{40}Ca \rightarrow$ symmetric products exhibits a rapid increase with bombarding energy and then flattens out at higher energies (see Fig. 1). Such a dependence is suggestive of a compound nucleus process. Additional evidence that an equilibrated process is responsible for at least a large fraction of these symmetric products comes from the angular distributions. The higher energy ^{12}C + ^{40}Ca data, which are less susceptible to contamination problems, are consistent with the angular distribution expected from the decay of a long lived composite system (1/sin θ_{CM} in the vicinity of 90°).

It is also of interest to compare the TKE of these symmetric products to standard fission systematics. Viola and Sikkeland have measured $<E_k>$ for a number of nuclei between the rare earth and uranium region. The least square analysis of their and other available data[2-4] gives:

$$<E_k> = 0.1071\ Z^2/A^{1/3} + 22.2\ \text{MeV} \quad . \qquad (1)$$

Here Z and A are the atomic and mass numbers of the composite system. According to Viola and Sikkeland this result is consistent with scission shapes corresponding to spheroids whose shapes minimize the total energy of the system.

For a system with Z=0, the total kinetic energy release should also be zero. Thus the Viola systematics, which were determined for large values of $Z^2/A^{1/3}$ and predict a substantial non-zero value for the total kinetic energy release at $Z^2/A^{1/3} = 0$, must fail at small values of $Z^2/A^{1/3} = 0$ like the present case. Nevertheless, it is interesting to see at what value of $Z^2/A^{1/3}$ the Viola systematics begin to deviate from the experimental data. The values of $<E_k>$ measured in this work are plotted in Fig. 2 together with the data of Viola and Sikkeland. In

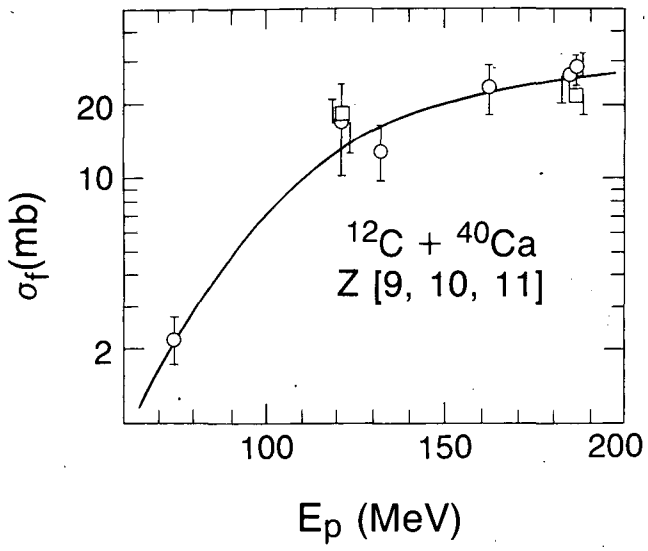

Fig. 1. Measured cross section of symmetric products (Z = 9–11) from the ^{12}C + ^{40}Ca reaction for several bombarding energies. The circles represent inclusive measurements and the squares coincidence measurements. The solid line is drawn through data points in order to guide the eye. XBL 844-10327

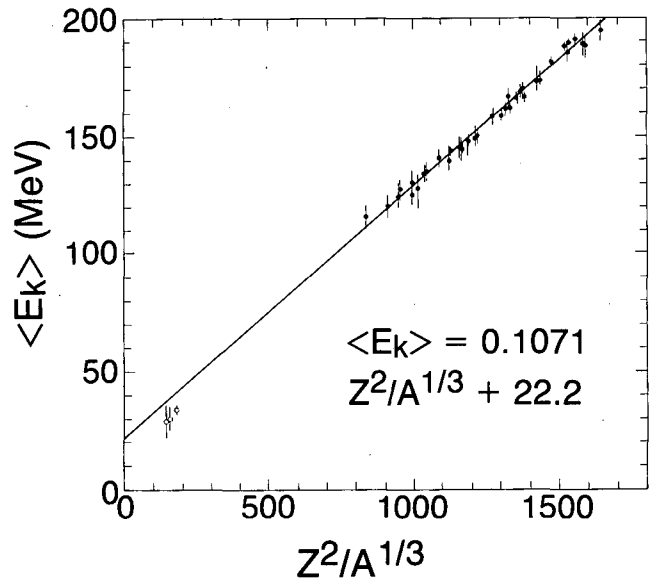

Fig. 2. Total kinetic energy for fission as a function of $Z^2/A^{1/3}$ of the composite system. The data of Viola[4] (solid circles) are in the upper right of the figure and the data from the present work (open circles) are shown in the lower left. The solid line is a fit[4] to the data of Viola (see text). XBL 844-10337

fact the values of $<E_k>$ measured in this work fall 20–30% below the best fit line to the data of Viola and Sikkeland.

Footnotes and References

*Condensed from Phys. Rev. **C30** 1214 (1984).

†Institute of Physics, Jagellonian University, Reymonta 4, Cracow, Poland.

‡Permanent address: Universitá Degli Studi Di Bari, 70100 Bari, Italy.

§Permanent address: National Superconducting Cyclotron Laboratory, Michigan State University, East Lansing, MI 48824-1321.

**Permanent address: Chemistry Department, Washington University, St. Louis, MO 63130.

††Permanent address: Weizmann Institute of Science, Rehovot 76100, Israel.

1. J. Brzychczyk, L. Freindl, K. Grotowski, Z. Majka, S. Micek, R. Planeta, M. Albinska, J. Buschman, H. Klewe-Nebenius, H.J. Gils, H. Rebel and S. Zagromski, Nucl. Phys. **A417**, 174 (1984) and references therein.
2. J.B. Natowitz, M.N. Namboodiri, R. Eggers, P.Gonthier, K. Geoffroy, R. Hanus, C. Towsley and K. Das, Nucl. Phys. **A277**, 477 (1977).
3. V.E. Viola, Jr. and T. Sikkeland, Phys. Rev. **130**, 2044 (1963).
4. V.E. Viola, Jr., Nucl. Data Tables **A1**, 391 (1966).

Mass Asymmetric Barriers from Excitation Functions for Complex Fragment Emission*

M.A. McMahan, L.G. Sobotka,† L.G. Moretto, M.L. Padgett, G.J. Wozniak and M.G. Mustafa‡

Experimentally determined saddle point masses (fission barriers) have played an essential role in establishing key features of nuclear models. On a macroscopic level, barriers extracted from fission excitation functions have been compared with predictions of the rotating liquid drop model. In many cases, it was found that some ad hoc lowering of the liquid drop barrier, $B_f(J)$, was needed to fit the excitation functions.[1] Subsequently, a more realistic liquid drop model, including the effects of finite range and surface diffuseness, was developed.[2,3]

In the present study, ^{3}He + ^{nat}Ag, we are ideally situated to test the finite range model for several reasons. First we are working in the region A~110, where the barriers (~50 MeV) and the finite range corrections (~8 MeV) are largest. Second, with a light ion projectile, such as ^{3}He, only low angular momenta contribute to fusion, and the predicted saddle point barriers are constant over the available range of angular momenta. Third, we have measured the dependence of the barriers on the mass asymmetry coordinate, providing us with an additional degree of freedom to compare with the models. For light systems, in which the saddle point and scission point deformations become nearly degenerate, the properties of the saddle point at a given mass asymmetry can be studied by restricting our observations to products with that exit channel mass asymmetry.

We have measured at the 88-Inch Cyclotron excitation functions for the fragments of $2 \leqslant Z \leqslant 11$ from compound nuclei formed by bombarding ^{nat}Ag with ^{3}He beams ranging from 45–130 MeV. Cross sections were obtained by averaging the data at backward angles (θ_L = 120–160°). The resulting excitation functions are shown in Fig. 1. With increasing bombarding energy, the cross sections rise rapidly and then flatten at higher energies. This is a characteristic signature of compound nucleus emission.

The excitation function data has been fit using a transition-state formalism, analogous to that used for fitting fission excitation functions, with a Fermi gas expression for the level density, and assuming that $\Gamma_z/\Gamma_n \sim \sigma_z/\sigma_R$. A simple angular momentum dependence is included by adding to the barriers rotational energies appropriate to the ground and sad-

dle point deformations.

We have fit the experimental data σ_z/σ_R and extracted the barriers B_z and the ratio a_z/a_n of the level density parameters. The fits are the solid lines in Fig. 1. The agreement between the data and the fits are remarkably good for all Z-values and confirms that these products originate from compound nuclear decay.

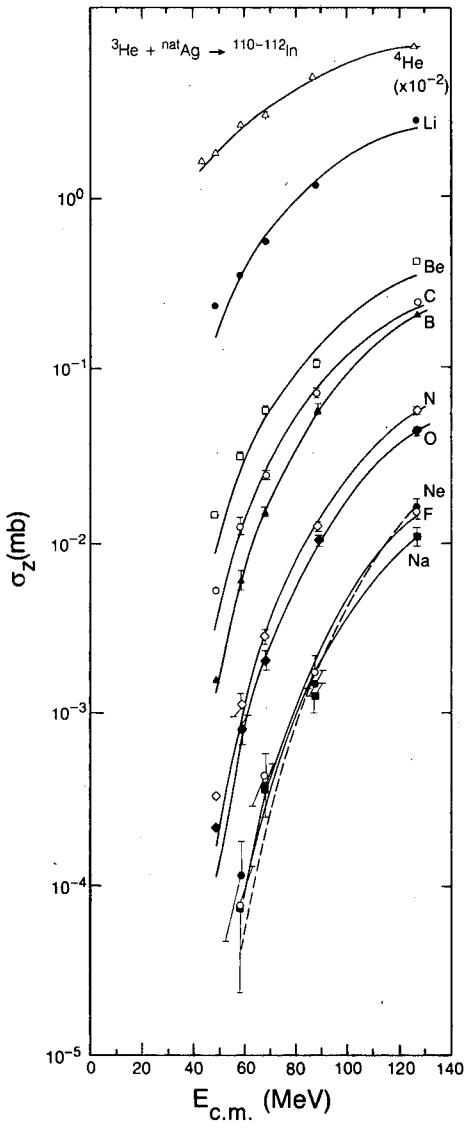

Fig. 1. Dependence of the total integrated cross sections on the center-of-mass energy, $E_{c.m.}$, in the reaction ^{3}He + ^{nat}Ag. The symbols and associated error bars correspond to the experimental cross sections. The curves are fits with the parameters of Fig. 2.

XBL 848-8658

The barriers and values of a_z/a_n extracted from the above fits are shown in Fig. 2 as a function of asymmetry, Z/Z_{CN}. The extracted barriers increase dramatically as the exit channel becomes more asymmetric, in qualitative agreement with the liquid drop model.

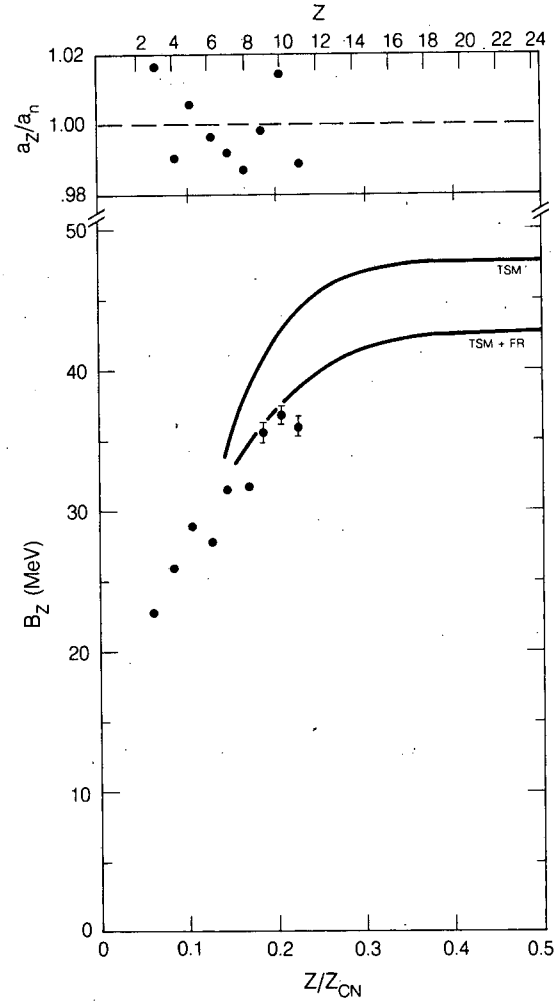

Fig. 2. The emission barriers, B_z, and ratio of level density parameters, a_z/a_n, extracted from fitting of the data as a function of asymmetry. (Z/Z_{CN} = 0.5 corresponds to symmetric splitting.) The points are the extracted parameters, excluding pre-equilibrium emission. The curves (TSM) correspond to barriers with and without finite range, calculated using two spheroids separated by a distance, s = 1.5 fm.

XBL 848-8657

The uncertainties in the extracted barriers due to assumptions made in the fitting procedure are ~2 MeV. This is more than adequate for a comparison with macroscopic fission models. In this mass region, the conditional saddle point configuration can be approximated by a two spheroid model (TSM). The results of the TSM is shown by the upper curve in Fig. 2. The calculation reproduces the trend of the data but overestimates the experimental barriers. An approximate finite range correction has also been calculated for this model. The TSM plus finite range calculation is given by the lower curve in Fig. 2. This simple parametrization reproduces both the magnitudes and the dependence on asymmetry of the barriers.

In conclusion, we have shown that excitation functions for complex fragment emission from compound nuclei can be fit using a transition-state formalism to extract the mass asymmetric emission barriers. The magnitudes of the barriers are smaller than those predicted by the standard TSM but agree with the TSM with finite range and surface diffuseness included. The experimental barriers clearly demonstrate that finite range corrections are important in describing the barriers for complex fragment emission. The measurement of mass asymmetric barriers opens up a sensitive new coordinate for which liquid drop models can be tested and refined. In addition, this type of measurement has the potential of greatly increasing the range of compound nuclei that can be used as tests of the models at low angular momentum. Furthermore, future measurements of both the Z and A of the complex fragment should allow a detailed examination of saddle point shell effects.

Footnotes and References

*Condensed from LBL-18291

†Permanent address: Chemistry Department, Washington University, St. Louis, MO 63130.

‡Lawrence Livermore National Laboratory, Livermore, CA 94550

1. M. Blann and T.T. Komoto, Phys. Rev. **C26**, 472 (1982).
2. H.J. Krappe, J.R. Nix and A.J. Sierk, Phys. Rev. **C20**, 9921 (1971).
3. M.G. Mustafa, P.A. Blaisden and H. Chandra, Phys. Rev. **C25**, 2524 (1982).

Complete Mass Distributions in C.M. Decay, and the Role of the Businaro-Gallone Point*

L.G. Moretto and L.G. Sobotka

Two sets of experiments were performed to measure the angular distributions, energy spectra and yields of fragments intermediate in mass between evaporated particle and fission fragments. In the first set, fragments with charges between 2 and 9 were studied from the reactions 45-130 MeV ^{3}He + Ag. In the second set, complete charge distributions from the reactions 5.9, 7.2 and 8.5 MeV/amu Ge, Nb and La + Be and C were measured. These two sets of experiments indicate that an equilibrium process is responsible for the production of these intermediate mass fragments. The role of the Businaro Gallone point in determining the shape of the mass distributions is then discussed.

Footnote

*Invited paper at the 22nd International Winter Meeting on Nuclear Physics, Bormio, Italy January 1984.

Compound Nucleus Decay Along the Mass Asymmetry Coordinate and the Role of the Businaro-Gallone Point*

*L.G. Sobotka,† M.A. McMahan, R.J. McDonald, C. Signarbieux,‡ G.J. Wozniak, M.L. Padgett, J.H. Gu,§ Z.H. Liu,** Z.Q. Yao§ and L.G. Moretto*

The sharp distinction between evaporation and fission in relatively heavy compound nuclei is a result of a specific topological feature of the liquid drop model potential energy surface V(Z) as a function of mass asymmetry Z. This feature is a deep minimum at symmetry (fission region) flanked at greater asymmetries by the Businaro-Gallone mountains which in turn descend at even larger asymmetries ("evaporation" region). The corresponding mass distribution from compound nucleus decay is approximately proportional to $\exp[-V(Z)/T_Z]$ and shows a peak at symmetry (fission peak) and two wings at the extreme asymmetries (evaporation wings). The qualitative dependence of the potential energy and of the mass yield vs. asymmetry is shown in Fig. 1(a) for a heavy nucleus.

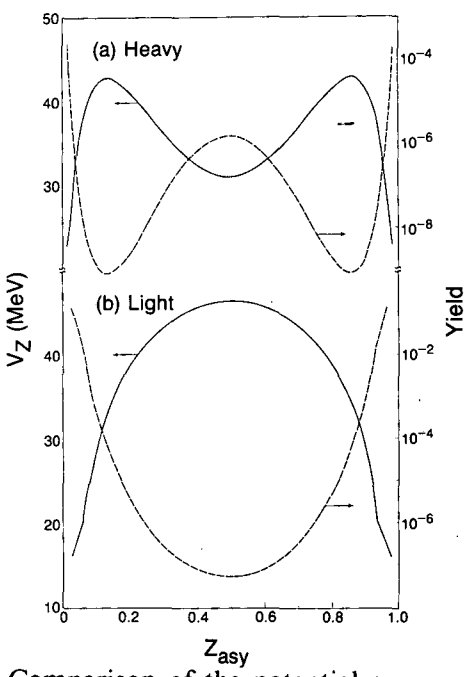

Fig. 1. Comparison of the potential energy surfaces (solid curves) and expected yields (dashed curves) for a heavy a) and a light b) compound nucleus.

XBL 847-10685

With decreasing total mass the potential energy surface undergoes a topological change when the fissility parameter x crosses the so-called Businaro-Gallone point.[1] At this point the second derivative of the potential energy with respect to the mass asymmetry coordinate evaluated at symmetry vanishes.[1-3] Thus, below the Businaro-Gallone point there is no longer a traditional fission saddle point, and the monotonically increasing potential energy towards symmetry implies the disappearance of fission as a process distinct from evaporation. Thus, the mass distribution should show the two evaporation wings extending as far as symmetry where a minimum should be observed. This is illustrated in Fig. 1(b).

Such a transition has never been observed, since it requires the measurement of the entire mass distribution from symmetry to the extreme asymmetry of α,p evaporation for a series of systems straddling the Businaro-Gallone point.

The experimental cross sections for 530-MeV ^{74}Ge, 782-MeV ^{93}Nb and 1157-MeV ^{139}La + ^{9}Be systems are shown in Fig. 2. The cross sections are plotted as a function of charge asymmetry ($Z_{asy} = Z_{detected}/Z_{total}$). The lack of enhancement in yield near the target Z supports the compound nucleus origin of the products rather than a deep-inelastic origin. The yield from the ^{74}Ge + ^{9}Be system, with a fissility parameter of x = 0.31, decreases steadily as one moves towards symmetry. The yields from the ^{93}Nb + ^{9}Be system (x = 0.40) are essentially constant from Z_{asy} = 0.2 to 0.4 while the yields from the ^{139}La + ^{9}Be system (x = 0.50) show the characteristic fission peak at symmetry. These three systems clearly exhibit the qualitative trends expected from the topological changes in the potential energy surface predicted by the liquid drop model[2,3] (see Fig. 1).

A quantitative comparison between these data and a compound nucleus calculation based upon the liquid drop model is also shown in Fig. 2. The absolute yields were calculated from the expression

$$\sigma_Z = \pi \lambda\!\!\!^{-2} \sum_{\ell=0}^{\ell_m} (2\ell + 1) \frac{\Gamma_Z(\ell)}{\Gamma_n + \Gamma_p + \Gamma_\alpha} \quad . \qquad (1)$$

where ℓ_m is the minimum of either ℓ_{max} (the grazing angular momentum) or ℓ_{crit} (the critical angular momentum for fusion[4]). The expression for the decay width for each asymmetry was taken from ref. 5 with the level density parameter a = A/8. The barrier was taken to be

$$U = (U_3 + U_4 - U_{CN}) + U_c + U_{prox} + (U_{rot}^{SP} - U_{rot}^{CN}) \quad . \qquad (2)$$

In this expression U_3, U_4 and U_{CN} are the droplet model masses[6] of the exit channel fragments 3 and 4 and the compound nucleus, respectively. The interfragment Coulomb energy (U_c) was calculated for spheres with a constant separation for each system chosen so that the center-of-mass energies reproduce the data. The nucleus-nucleus interaction is included via the proximity potential (U_{prox}). The ℓ-wave dependence of the barrier height is included in the last two terms of Eq. (2), where the rotation energies of the compound nucleus and that of the dinuclear complex U_{rot}^{SP} (taken as two spheres with the appropriate separation) are taken into account. The mass for a given charge division was calculated (for $Z > 2$) from charge equilibration.

The angular distribution expressions given in ref. 3 were employed to calculate the differential cross section ($d\sigma/d\Omega$). The c.m. angles of the data in Fig. 2 vary as a function of Z. However, the average c.m. angle is approximately 30°, so this angle was chosen for comparison. The agreement in absolute magnitude and in trend between this calculation and the data confirms the compound nuclear origin of these fragments.

In summary, we have shown that fragments with atomic numbers covering the entire range of the mass asymmetry coordinate are produced from the decay of an excited compound nucleus. The observed Z distributions indicate that the topological transition expected at the Businaro-Gallone point does indeed take place in the region of A~100. The exact position of the Businaro-Gallone point and its angular momentum dependence can in principle be established by a systematic study of the Z or A distributions as the fissility parameter x and the rotational parameter y are varied.

Footnotes and References

*Condensed from LBL 17879.

†Chemistry Department, Washington University, St. Louis, MO 63130.

‡Nuclear Physics Division, CEN Saclay, BP1 91.191 gif sur Yvette, Cedex, France.

§Shanghai institute of Nuclear Research, Shanghai, China.

**Institute of Atomic Energy, Beijing, China.

1. U.L. Businaro and S. Gallone, Nuovo Cim. 1, **629**, 1277 (1955).
2. J.R. Nix, Nucl. Phys. **A130**, 241 (1969) and references therein.
3. L.G. Moretto, Nucl. Phys. **A247**, 2111 (1975).
4. R. Bass, Nucl. Phys. **A231**, 45 (1974).
5. W.J. Świątecki, LBL-11403.
6. R.W. Hasse, Ann. of Phys. **68**, 377 (1971).

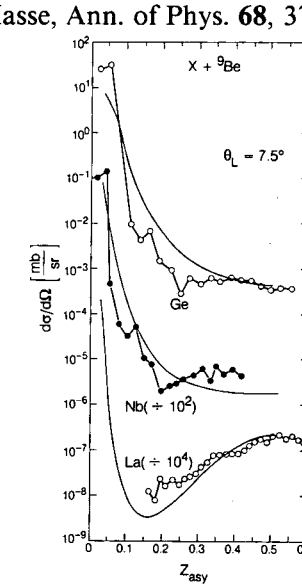

Fig. 2. Center of mass cross sections for products from the ^{74}Ge, ^{93}Nb and ^{139}La + ^{9}Be systems detected at θ = 7.5°. The solid line represents a liquid drop model calculation. XBL 845-9370A

The Businaro-Gallone Transition as Observed in Complete Charge Distributions from Compound Nucleus Decay*

L.G. Moretto, G.J. Wozniak and L.G. Sobotka

The compound nucleus emission of fragments covering the entire mass range has been observed in reactions exploiting both ordinary and reverse kinematics. The compound nucleus mechanisms has been inferred from full momentum transfer, angular independence of the fragment center of mass kinetic energies and excitation functions. The drastic change in the observed charge distributions as one crosses $A \simeq 100$ illustrates the effect of the Businaro-Gallone point.

Footnote

*Invited talk at the International Symposium on Heavy Ion Physics, Mt. Fuji, Japan, August 1984.

Use of Reverse Kinematics in the Identification of Large Fragments Evaporated by Compound Nuclei

L.G. Sobotka, M.A. McMahan, R.J. McDonald, C. Signarbieux,† G.J. Wozniak, M.L. Padgett, J.H. Gu,‡ Z.H. Liu,§ Z.Q. Yao‡ and L.G. Moretto*

Fragments ranging in charge from Z = 2 to Z = $Z_{symmetry}$ have been identified from the compound nucleus decay associated with a variety of heavy ion reactions.

The use of reverse kinematics (projectile heavier than the target) was crucial in performing these measurements. This technique virtually eliminates the problems associated with low cross section measurements due to the presence of light element target contaminants. Likely target contaminants (O, C) are identical or close in mass (and product cross sections) to the targets used (Be, C); therefore, the contamination of the data should be of the order of the ratio of the respective thicknesses. Furthermore, reverse kinematics provides a large center-of-mass (c.m.) velocity which facilitates the verification of full momentum transfer and allows for easy identification of the fragment's atomic number at the higher lab energies.

The experiments were carried out at the SuperHILAC utilizing beams of 550 MeV ^{74}Ge, 782 MeV ^{93}Nb and 1157 MeV ^{139}La, to bombard targets of 0.54 mg/cm^2 ^{12}C and 1.0 mg/cm^2 ^{9}Be. The detection system consisted of four solid state ΔE-E silicon telescopes (40–70 μm, 3–5 mm) situated at 7.5°, 15°, 25° and 35° from the beam with solid angles of approximately 1.0 msr. For the heavier ^{139}La beam these detectors were supplemented by two gas ΔE−solid state E telescopes at −7.5° and −22.5°.

The measured atomic number (Z), laboratory energy and angle permitted us to verify that the recorded events both originated from a system with full momentum transfer and had a c.m. energy independent of angle. This is shown for two representative elements in Fig. 1.

The mean laboratory energies for each Z-value were converted to velocities with two different assumptions for the relationship between the Z and the mass of the detected fragments. The first method assumes that the Z for each mass split is that given by charge equilibration. The second method assumes that the light fragment mass follows the valley of β-stability. These velocities are then decomposed into two components. One component, along the beam direction, is assigned an arbitrary value; the other component is that required to reconstitute the original velocity. (For convenience this second component is shown as the c.m. energy) In this way, for

each laboratory angle we can draw a curve representing the dependence of the c.m. energy upon the c.m. velocity. This procedure is followed for each angle that is smaller than the kinematically allowed maximum angle. The intersection of these lines determines, in a model independent way, both the momentum transfer and the energy in the center of mass. The error bars shown on the lines in Fig. 1 reflect the uncertainty in the mean laboratory energies. The mass uncertainty was investigated by using the two charge-mass relationships mentioned above.

The results from this type of analysis for the $^{93}Nb + ^{12}C$ system are shown in Fig. 2. The upper part of this figure demonstrates that with either mass assumption all of the measured products result from the decay of a system with full momentum transfer. For the other systems studied, the extracted source velocities are also independent of Z within a few percent of the velocity expected for full momentum transfer. The deduced c.m. energies are shown in the lower portion of Fig. 2. These energies are reproduced by a Coulomb calculation for two spheres with a surface separation of 2 fm. This same separation also reproduces the c.m. energies from the ^{74}Ge induced reactions; however a larger separation is required for the ^{139}La data. Both the full momentum transfer and the invariance with angle of the c.m. energies are consistent with compound nucleus decay.

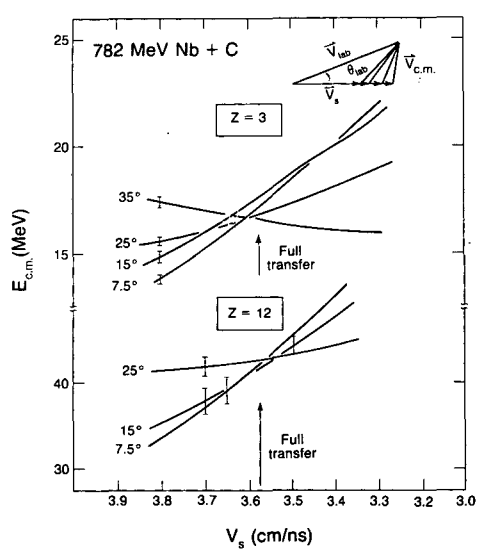

Fig. 1. Method for deducing the source velocity (V_s) and the c.m. energies ($E_{c.m.}$). The line for each angle gives the locus of solutions for both $E_{c.m.}$ and V_s. The velocity corresponding to complete linear momentum transfer is indicated. This figure is drawn assuming that the masses follow the line of β-stability. XBL 8312-7492

Footnotes

*Chemistry Department, Washington University, St. Louis, MO 63130.

†Nuclear Physics Division, CEN Saclay, BP1 91.191 Gif sur Yvette, Cedex, France.

‡Shanghai Institute of Nuclear Research, Shanghai, China.

§Institute of Atomic Energy, Beijing, China.

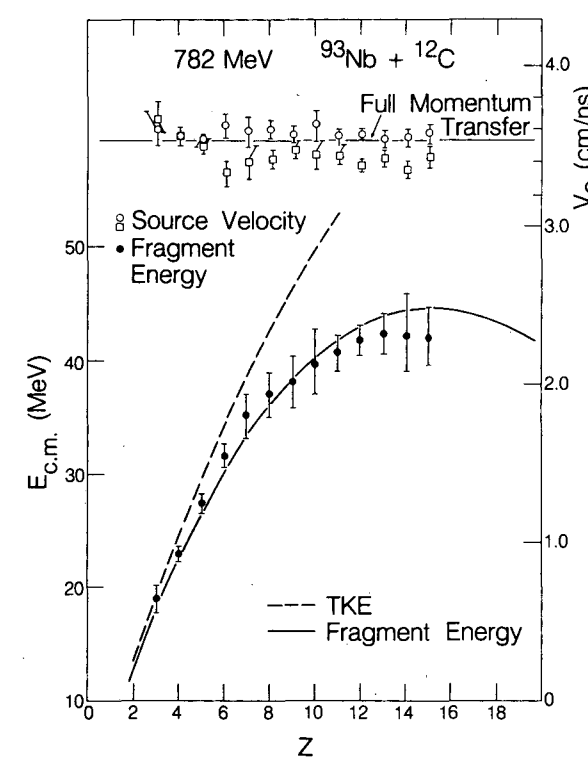

Fig. 2. The deduced c.m. energies and source velocities for the $^{93}Nb + ^{12}C$ system. Source velocities were determined assuming that the product mass followed the line of β-stability (o) or the charge equilibration line (□). The value of the source velocity expected for full momentum transfer is indicated by the horizontal line. The error bars indicate the uncertainty of the intersection point shown in Fig. 1. XBL 846-8959

Range-Energy Relation for Heavy Ion Inertial Fusion

*H.R. Bowman, H.H. Heckman, Y.J. Karant, J.O. Rasmussen, A.I. Warwick and Z.Z. Xu**

Of critical importance to the problem of ion-target coupling for Heavy Ion Fusion (HIF) is the range-energy relation of heavy ions in (cold) matter. A unique feature of heavy ion beams for HIF, $E/A \leqslant 150$ MeV, is the very low charge state at which they will be accelerated. Such beams, upon penetrating the target, will have ionic charge states far from the equilibrium values characteristic of their velocity β and the target material. As a consequence, both the rate of energy loss, dE/dx, and the effective charge Z^* of the incident heavy ions in matter will be initially low, the latter increasing to their equilibrium values as electron stripping takes place. The effects of diminished dE/dx and Z^* will tend to increase the range of the ions in the target.

Bevalac experiment #730H is being carried out to obtain range-energy data pertinent to HIF by measuring the range-energy for Au ions, $E/A \leqslant 150$ MeV, accelerated and incident on CH and Au targets at charge states Z_{accel} = 11, 35 and 61. A crucial aspect of this experiment is the availability of low-charge state, high-rigidity beams of heavy nuclei at the Bevalac.

The first phase of the experiment was performed at Beam-40 in July 1984, using Au^{+61} beams at E = 150 MeV/nucleon and 50 MeV/nucleon to establish the (charge-equilibrated) energy loss rates and ranges of these ions in high- and low-Z target material. The experimental techniques used in these measurements involved:

1. Beam velocities by time-of-flight (TOF), with $\delta t \sim 200$ ps over a 20 m flight path.
2. dE/dx by measurements of ΔE (TOF) vs. foil thickness Δx.
3. Integral ranges by use of visual track detectors and circular wedge-shaped absorbers.
4. Charge spectra of Au beam, $Zi(\beta)$ by use of the Beam-40 0°-magnetic spectrometer.

Figs. 1 and 2 give our direct observations of the range and dE/dx versus energy per amu under equilibrated conditions. The data are preliminary in that, although small, systematic corrections and refined TOF calibration will be implemented as the experiment proceeds. The range data shown in Fig. 1, when fitted to least-squares polynomials (not shown), exhibit dispersions of σ = 1.2% (Au) and 1.9% (CH), dispersions that include all statistical and systematic errors attributable to the velocity and range measurements, TOF calibrations and beam instabilities.

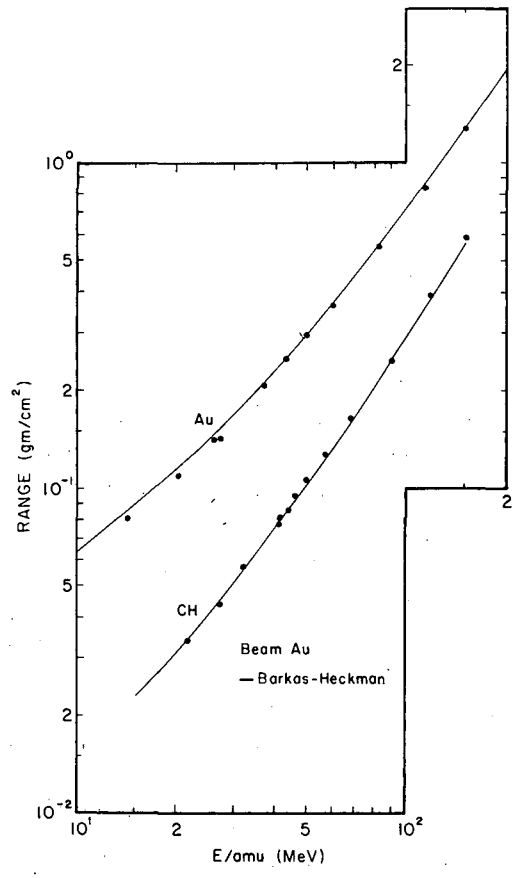

Fig. 1. Range-energy relation for Au ions in CH and Au. Data are preliminary. Curves are based on scaling of the proton range-energy relation and the range-extension of heavy ions due to charge neutralization. XBL 8410-4329

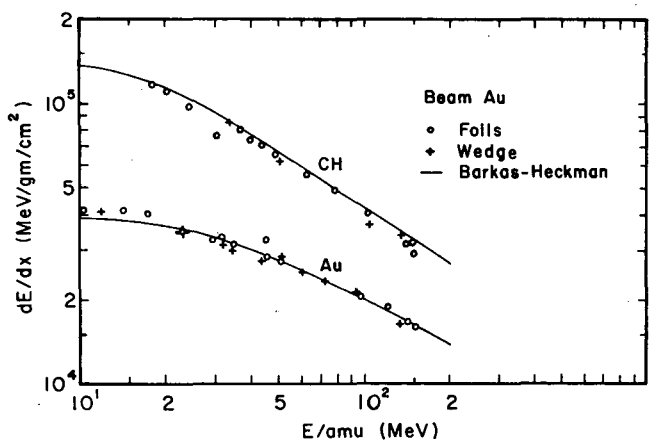

Fig. 2. Measured energy-loss rates of Au ions in CH and Au. Data are preliminary. Curves are described in Fig. 1. XBL 8410-4328

The experimental results are compared with the ranges and dE/dx predicted from calculations using computer code of Benton and Henke,[1] which is based primarily on the proton range-energy relation given by Barkas and Berger[2] and the heavy-ion range data (E/A≤10 MeV) of Heckman *et al.*[3] The values of the ionization potentials for CH and Au used in the calculations were I_{adj} = 63.2 eV and 796.7 eV, respectively.

Footnote and References

*Fudan University, Shanghai, China.

1. E.V. Benton and R.P. Henke, Nucl. Inst. and Methods **67**, 87 (1964).
2. W.H. Barkas and M.J. Berger, NAS-NRL Publ.-1133, 103 (1964).
3. H.H. Heckman *et al.*, Phys. Rev. **117**, 544 (1960).

Ho Target Fragmentation Induced by Intermediate Energy ^{12}C and ^{16}O

J.H. Kraus, Jr., W. Loveland* and G.T. Seaborg*

The study of the fragmentation of rare earth targets, such as Ho, by energetic heavy ions offers certain unique opportunities not found in similar studies with heavier targets. The rare earth nuclei have high fission barriers and as a consequence, unless significant angular momentum is deposited in these nuclei, they will not fission in their de-excitation. This feature offers the experimenter two unique opportunities: (a) to compare the observed fragment yield distributions and kinematic properties to predictions of various theoretical models for energetic heavy ion reactions without the complicating effects of fission. (b) to use what fission is observed in a heavier rare earth such as Ho to help understand the angular momentum transfer in these reactions. In a program begun previously, we have measured the target fragment yield distributions and kinematic properties for the interaction of 17–2100 MeV/nucleon light heavy ions (C, O, Ne) with ^{165}Ho.

In Fig. 1, we show the isobaric yield distributions deduced from measured nuclidic formation cross sections for the interaction of various intermediate energy ^{12}C and ^{16}O ions with ^{165}Ho. Due to

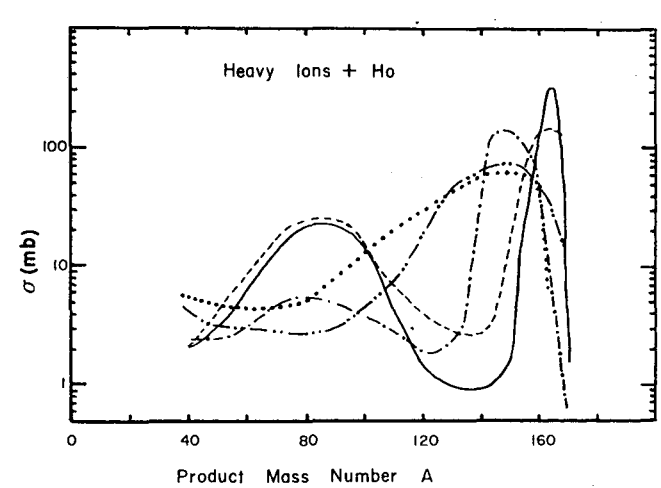

Fig. 1. Measured isobaric yield distributions for the interaction of 208 MeV ^{12}C (solid line), 265 MeV ^{16}O (dashed line), 384 MeV ^{12}C (dot-dash), 965 MeV ^{12}C (dot-dot-dash) and 1536 MeV ^{16}O (dotted line) with ^{165}Ho. XBL 8410-4129

uncertainties in the monitor cross sections used for beam intensity determination for the 384 MeV ^{12}C and 1536 MeV ^{16}O experiments, the absolute cross sections in these experiments are uncertain to approximately ±30%. (We are currently remeasuring these monitor cross sections and hope to lessen these uncertainties.) Nonetheless, it would appear that as the projectile energy is increased beyond 20 MeV/nucleon, the fission cross section (represented by the yield of products with $70 \leq A \leq 100$) decreases and fragmentation (spallation) and incomplete fusion processes increase. Recoil data indicate that for those events leading to fragments with $70 < A < 100$, the average fraction of full momentum transfer is 0.9 ±0.1, 0.9 ±0.1, 0.8 ±0.1, 0.5 ±0.1 and 0.3 ±0.1 for reactions induced by 208 MeV ^{12}C, 265 MeV^{16}O, 384, 965 MeV ^{12}C and 1536 MeV ^{16}O. Comparisons of these data with predictions of the nuclear fire streak and Wilczynski sum-rule models are underway.

Footnote

*Oregon State University, Corvallis, OR 97331

La Target Fragmentation Induced by High Energy La and U Ions

Li Wenxin, W. Loveland,† K. Aleklett,‡ P.L. McGaughey§ and G.T. Seaborg*

In last year's Annual Report,[1] we reported the results of a measurement of the target fragment isobaric yield distribution for the reaction of 245 MeV/nucleon ^{139}La with ^{139}La. The mass distribution showed two features not previously observed in high energy rare earth target fragment mass distributions. These features are (a) the appearance of a large fission fragment-like bump in the yield distribution centered at A~60, whose integrated cross section is ~540 mb, indicating greatly enhanced fission of a target-like species (compared to p-La collisions where $\sigma_f \sim 1$ mb) (b) a low, integrated total residue production cross section of ~3.9 b, possibly indicating the occurrence of a significant number of events that do not lead to the production of target fragments.

As reported in last year's Annual Report, calculations of the expected isobaric yield distribution for this reaction using the nuclear firestreak model showed that neither any significant amount ($\leq$10 mb) of fission was predicted to occur nor any significant amount of "missing" cross section was expected.

As we found in work this year, the intranuclear cascade model has quite different predictions for the primary distributions. The "average" fragment in the primary distribution has A~135 and is more highly excited, E*~590 MeV, with higher angular momentum, J~32$\hbar$ (the comparable firestreak distribution has A~110, E*~370 MeV and J~12$\hbar$). Also there is a broad distribution of J values with the population standard deviation approximately equal to the main value.

The effect of de-excitation by fission or particle emission for this primary distribution involving species with high E* and high J was calculated using the JULIAN/PACE code.[2] The rotating liquid drop fission barriers of Cohen, Plasil and Świątecki[3] were used with the barrier height being taken as 80% of the values given in ref. 3. As before, a_f/a_n=1.02. A fission cross section of 400 mb was predicted along with a total (A>40) residue cross section of ~2.7b, in qualitative, if not quantitative agreement with the data. In this calculation, the increased fission is due primarily to the larger values of J. To gain an appreciation of this effect, one can compare the de-excitation of the A=134 and A=135 members of the primary distribution. Both have similar excitation energies (~630 MeV) but in the case of A=134, J=24$\hbar$ with σ_j=19$\hbar$ while for A=135, J=36$\hbar$, σ_j=35$\hbar$. In the de-excitation of the A=134 primary fragments 1.4% fission while 8.6% of the A=135 fragments are predicted to fission. In the calculation, the relatively

low target residue cross section is a result of the fact that the average number of participants (i.e., struck nucleons) in the target nucleus was 127 while in the projectile it was 136. Thus in the model, there really were few "spectators" to the collision.

As an extension of these studies and as our first attempt to use the ultraheavy high energy beams available from the LBL Bevalac, we measured the target fragment yield distribution from the interaction of 400 MeV/nucleon ^{238}U with ^{139}La. Multiple La targets of thickness ~380 mg/cm^2 were irradiated with a 400 MeV/nucleon ^{238}U beam of intensity ~5 x 10^5 ions/min for 29 hours. Following irradiation the targets were dissolved and 8 chemical fractions were separated. The resulting samples were counted by off-line γ-ray spectroscopy for two months and using techniques described previously, the fragment yield distribution (Fig. 1) was deduced from the measured nuclidic formation cross sections.

The fission cross section, as represented by fragments with $50 \leqslant A \leqslant 80$, appears to be similar to that observed in the La + La reaction with increased yields for near-target and spallation products being observed in the U + La reaction. Comparison of these data with models for target fragmentation should prove interesting.

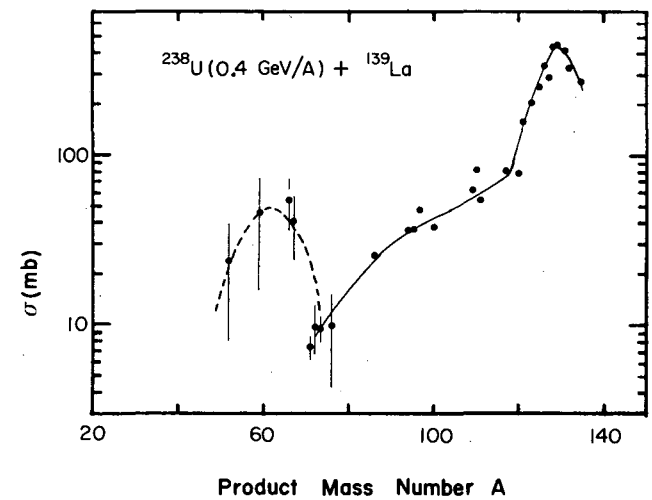

Fig. 1. Fragment isobaric yield distribution for the reaction of 400 MeV/nucleon ^{238}U with ^{139}La.
XBL 8410-4130

Footnotes and References

*Institute of Modern Physics, Lanzhou, People's Republic of China.

†Oregon State University, Corvallis, OR 97331

‡Studsvik Science Research Laboratory, S-611 82 Nyköping, Sweden.

§Los Alamos National Laboratory, Los Alamos, NM 87545.

1. Li Wenxin, *et al.*, LBL-16870, p. 141.
2. A. Gavron, Phys. Rev. **C21**, 230 (1980).
3. S. Cohen, F. Plasil and W.J. Świątecki, Ann. Phys. (N.Y.) **82**, 557 (1974).

Collective Flow Observed in Relativistic Nuclear Collisions

H.A. Gustafsson, H.H. Gutbrod, B. Kolb,* H. Löhner,* B. Ludewigt,* A.M. Poskanzer, T. Renner, H. Riedesel, H.G. Ritter,* A. Warwick,* and H. Wieman**

Data from 4π detectors like the Plastic Ball are ideally suited to study the emission patterns and event shapes of high energy nuclear collisions. The shapes predicted by hydrodynamical and simple intranuclear cascade calculations are quite different. The hydrodynamical model predicts prolate shapes along the beam axis for only grazing collisions. With decreasing impact parameter the flow angle increases, and reaches 90 degrees (with oblate shapes) for zero impact-parameter events.[1,2] Some cascade calculations on the other hand predict zero flow angles at all impact parameters.[3] Approximately 50000 events of 400 MeV/nucleon Nb + Nb and Ca + Ca have been used for an energy flow analysis.[2] The events have been classified according to charged particle multiplicity. The distribution of the flow angle

θ (angle between the major axis of the flow ellipsoid and the beam axis) is shown in Fig. 1 for different multiplicity selections. A striking difference between the Ca and Nb data can be observed. For all but the highest multiplicity bins the distribution of the flow angles for the Ca data is peaked at 0 degrees. For Nb, however, there is a finite deflection angle increasing with increasing multiplicity. The same analysis has been performed with filtered events from a cascade code calculation.[3] For both systems studied the distributions are always peaked at zero degrees. It is not so evident that the Ca + Ca collision differs from its simulation with the cascade model, whereas a new collective phenomenon definitely appears in the larger mass system which is not accounted for by this cascade model. A more detailed study of the contour plots in the reaction plane (p_x/m versus y) reveals two collective flow effects (Fig. 2): The projectile fragments are found slightly displaced from the beam axis (bounce-off), and the intermediate rapidity fragments have a preference for emission angles of 20 to 30 degrees in the center of mass system (side-splash) for the higher multiplicity events of Nb + Nb which is not evident for Ca + Ca.

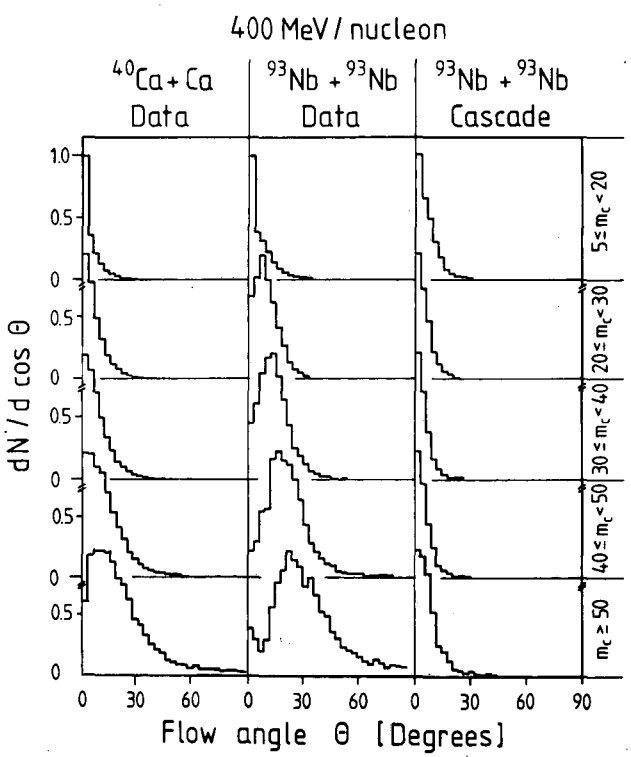

Fig. 1. Frequency distribution of the flow angle θ for two sets of data and a cascade calculation for different multiplicity bins. For the case of Ca the multiplicities are half the indicated values. XBL 841-542

Footnote and References

*Gesellschaft für Schwerionenforschung, Darmstadt, West Germany.

1. H. Stöcker, J. Hofmann, J.A. Maruhn and W. Greiner, Progr. in Part. and Nucl. Phys. **4**, 133 (1980).
2. M. Gyulassy, K.A. Frankel, and H. Stöcker, Phys. Lett. **110B**, 185 (1982).
3. Y. Yariv and Z. Fraenkel, Phys. Rev. **C20**, 2227 (1979).

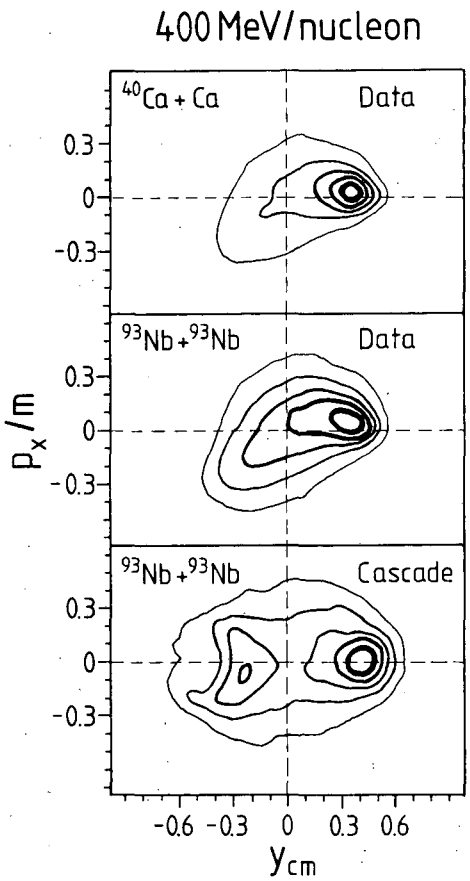

Fig. 2. Contour plots (linear contours) of p_x/m versus cm rapidity for multiplicities between 40 and 49 charged particles. XBL 841-543

Observation of Radiative Capture in Relativistic Heavy Ion Collisions*

*R. Anholt,[†] S.A. Andriamonje,[†‡] E. Morenzoni,[†§], Ch. Stoller,[†] J.D. Molitoris,[†] W.E. Meyerhof,[†] H. Bowman, J.-S. Xu,[††] Z.-Z. Xu,[††] J.O. Rasmussen and D.H.H. Hoffman***

X-ray studies of relativistic heavy ion-atom collisions allow the direct observation of the radiative electron capture photon (REC). The theoretical angular distribution of these photons is approximately $\sin^2\theta_{lab}$, due to the cancellation of electron retardation effects and the Lorentz transformation into the laboratory. Our measured angular distribution agrees. Comparison of measured and calculated cross sections reveals that the number of equilibrium projectile K vacancies present in the solid targets agrees with charge state measurements behind the target.

The charge state of an ion traveling through a solid target is governed by the cross section for loss (ionization) and capture of electrons.[1] Radiative and non-radiative electron capture are possible. For the least well understood non-radiative capture, the electron makes a transition from a target orbital to a projectile orbital, and the difference in electron binding energy is converted to projectile kinetic energy. For radiative capture (REC) of target electrons into the projectile K shell, which is dominant in collisions of heavy projectiles on light target atoms, the electron loses energy, which is converted into electromagnetic energy. The availability of relativistic heavy ions at the Lawrence Berkeley Laboratory Bevalac allows the direct observation of the radiative part of the capture cross section by observing the photon. Since capture into the projectile K shell requires the presence of projectile K vacancies, the number of REC photons seen in sufficiently thick targets is proportional to the number of equilibrium K vacancies, giving a direct measure of this quantity *inside the target.* Comparison is possible in some of the present cases with charge-state measurements behind the target.[2-3]

We measured cross sections for target K-vacancy production, projectile K x-ray production, and REC. The targets used were of equilibrium thickness; also the projectile was stripped to its equilibrium charge state in an upstream Si transmission particle detector.

Fig. 1 shows an x-ray spectrum taken with an intrinsic-Ge x-ray detector in 197 MeV/nucleon Xe + Be collisions. The most prominent feature in this (logarithmic) spectrum is the K REC peak at approximately 125 keV. The REC peak energy E_{peak} in the projectile frame is the sum of the electron kinetic energy, $(\gamma-1)mc^2$, where $\gamma^{-2} = 1 - \beta^2$, $\beta = v/c$, and v is the ion velocity, and the K electron binding energy E_K, which has approximately the value given by the one-electron Dirac equation.[4] In the laboratory, this energy is Doppler shifted according to

$$E_{REC} = E_{peak}\gamma^{-1}(1 - \beta \cos\theta_{lab})^{-1} \qquad (1)$$

where θ_{lab} is the angle between the beam axis and the photon direction. The width is determined mostly by the angular opening $\Delta\theta_{lab}$ of the x-ray detector.

Also seen in Fig. 1 is a shoulder at lower x-ray energies, composed of REC into the projectile L and M shells and a primary bremsstrahlung continuum.[5] Primary bremsstrahlung (or radiative ionization) is the radiative scattering of target electrons from the projectile nucleus. The spectrum has an endpoint in the projectile frame given by the electron kinetic energy $(\gamma - 1)mc^2$, and in the laboratory frame by an equation similar to Eq. (1). Also present in this spectrum are Xe projectile K x-rays and secondary electron bremsstrahlung (SEB). In collisions with $Z_T \gtrsim 50$ target atoms, observation of REC is not possible, because SEB, which increases quadratically with Z_T, dominates over linearly varying REC and primary bremsstrahlung.

Fig. 2 compares our measured and calculated integrated REC cross sections. Where counting statistics are negligible, the absolute uncertainty in the photon cross sections is approximately ±12%. As Z_T increases, the cross sections become increas-

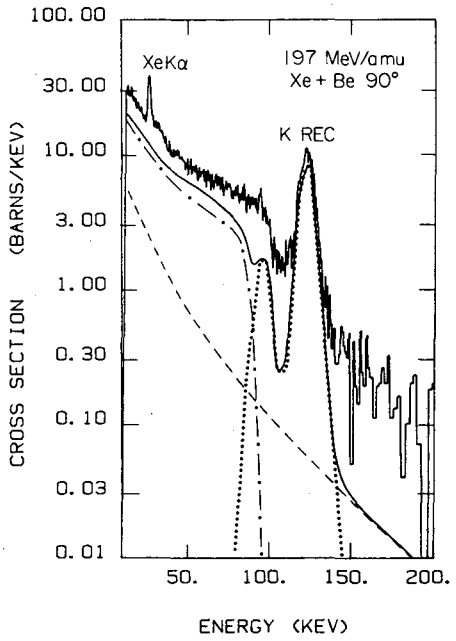

Fig. 1. Spectrum of photons seen at $\theta_{lab} = 90°$ in 197-MeV/nucleon Xe + Be collisions. Calculated[4] contributions from K and L radiative electron capture REC (dotted line), secondary electron bremsstrahlung SEB (dashed line), and primary bremsstrahlung (chain curve) are shown.

XBL 8410-4588

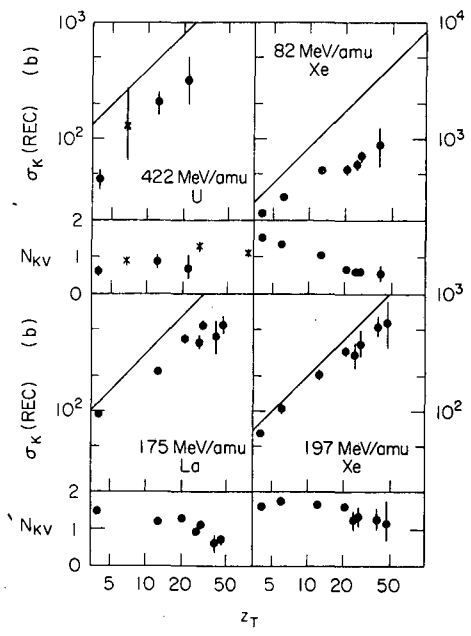

Fig. 2. Measured and calculated K REC cross sections and the deduced average number of projectile K vacancies. Crosses are from magnetic charge-state measurements of Gould *et al.*[2] XBL 8410-4590

ingly uncertain, due to the uncertainty in the background subtraction of SEB. The number of K vacancies can be calculated from

$$N_{Kv} = 2\,\frac{\sigma_{meas}}{\sigma_{calc}} \quad . \tag{2}$$

The projectile charge state is determined by a competition between electron loss and capture.

For the U projectile data one can compare our findings for N_{Kv} within the target with the 437-MeV/nucleon U charge-state determination of Gould *et al.*[2] behind the target. Calling the corresponding K-vacancy number N'_{Kv}, one has

$$N'_{Kv} = 2F_0 + F_1 \quad , \tag{3}$$

where F_0 and F_1 are the charge fractions for zero and one electron, respectively. The values of N'_{Kv} are shown by crosses in Fig. 2.

Gould *et al.*[2] also extracted capture cross sections from the target-thickness dependence of the charge-state fractions. These cross sections should be compared with the capture cross section into all shells of the fully stripped projectile, which when nonradiative capture is negligible (low Z_T) is approximately 30% higher than the theoretical K REC cross section in Fig. 2. Capture cross sections are more difficult to determine in charge state measurements, as reflected by the larger experimental uncertainties in Gould's cross sections than in the photon ones. For 437-MeV/nucleon U + mylar, the charge-state cross sections do not agree well with theory.

Footnotes and References

*Condensed from Phys. Rev. Lett. **53**, 234 (1984).

†Department of Physics, Stanford University, Stanford, CA 94305.

‡Permanent address: Centre d'Etudes Nucléaires, University of Bordeaux, Gradignan, France.

§Permanent address: Laboratory for Medium-Energy Physics, ETH-Zurich, Switzerland.

††Permanent address: Department of Physics, Fudan University, Shanghai, Peoples Republic of China.

**Gesellschaft für Schwerionenforschung, Darmstadt, West Germany.

1. H.D. Betz, Rev. Mod. Phys. **44**, 465 (1975).
2. H. Gould, D. Greiner, P. Lindstrom, T.J.M. Symons, H. Crawford, Phys. Rev. Lett. **52**, 180 (1984).
3. H.D. Betz and L. Grodzins, Phys. Rev. Lett. **25**, 211 (1970).
4. H.A. Bethe and E.E. Salpeter, *Quantum Mechanics of One- and Two-Electron Atoms*, Academic, New York (1957).
5. H.W. Schnopper *et al.*, Phys. Lett. **47A**, 61 (1974).

Freezeout Density In Relativistic Nuclear Collisions Measured by Proton-Proton Correlations*

H.A. Gustafsson, H.H. Gutbrod, B. Kolb, H. Löhner, B. Ludewigt, A.M. Poskanzer, T. Renner, H. Riedesel, H.G. Ritter, A. Warwick, and H. Wieman

Relativistic heavy ion collisions produce a region of hot matter that radiates protons, pions and composite particles. The effective source size of this radiating zone, or fire ball, has been investigated by a number of groups using either proton pair correlations[1] or pion pair correlations[2,3] at small relative momenta. The application of this method in nucleus nucleus collisions is still relatively novel and an effort is being made to explore its potential and understand the significance of the measured radii. It is of particular interest to relate variations in extracted radii to different types of events.

We report here source radii as a function of event proton multiplicity for two different reactions: Ca on Ca and Nb on Nb, both at 400 MeV/nucleon. The proton proton correlations used in this study were measured at the Bevalac with the 4π plastic ball detector.[4] In these measurements the Δp resolution between pairs is limited by the finite angular size of the detector modules. A simple Monte Carlo technique that makes use of this data stream, however, overcomes this problem by adding the angular distortion to the theoretical correlation functions, thus permitting a direct comparison with our measurements. The theoretical correlation function used was taken from Koonin's paper[5] and it includes Coulomb and nuclear final state interactions between the two protons.

Extracted radii are shown in Fig. 1 as a function of participant proton multiplicity, Np, where Np includes protons bound in light clusters but excludes to a large extent protons evaporated from the spectators. For both the Ca + Ca and Nb + Nb systems the radius increases with multiplicity. The curves

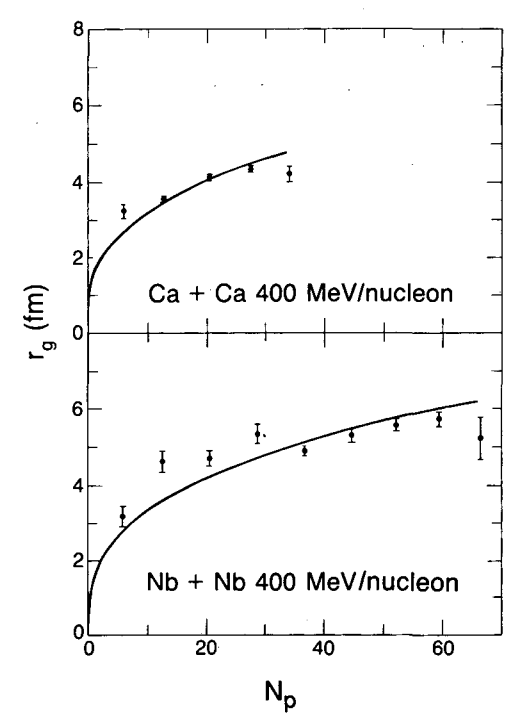

Fig. 1. Extracted gaussian source radii as a function of proton multiplicity (N_p) for the two systems Ca + Ca and Nb + Nb at 400 MeV/nucleon. The curves are fits to the results with the function $r_g = r_0\left(\frac{A}{Z} N_p\right)^{1/3} / \sqrt{5/2}$. XBL 842-10058

show the fit with the following function

$$r_g = r_0\left(\frac{A}{Z} N_p\right)^{1/3} / \sqrt{5/2}$$

where A/Z has been included to reflect the presence of neutrons. Our extracted radii are the radii parameter for a gaussian source distribution, so with the inclusion of $\sqrt{5/2}$ in the above function r_0 becomes the sharp sphere radius parameter of an equivalent rms value. The value of r_0 extracted from the fits is 1.9 fm, essentially the same for both the niobium and calcium systems. Comparing this directly with r_0 = 1.2 fm, the sharp sphere r_0 for normal nuclear matter, yields a participant region density of 1/4 normal nuclear density. This is interpreted as the thermal freezeout density, since the proton-proton correlations measure the radius at which collisions between protons and other fragments cease.

Footnotes and References

*Condensed from H.A. Gustafsson, *et al.*, Phys. Rev. Lett. **53**, 544 (1984).

1. F. Zarbakhsh *et al.*, Phys. Rev. Lett. **46**, 1268 (1981).
2. D. Beavis *et al.*, Phys. Rev. **27C**, 910 (1983).
3. W.A. Zajc *et al.*, Phys. Rev. **29C**, 2173 (1984).
4. A. Baden *et al.*, Nucl. Instr. and Meth. **203**, 189 (1982).
5. S.E. Koonin, Phys. Lett. **70B**, 43 (1977).

Measurement of Pions and Light Fragments in 0.8 GeV/nucleon La + La Collisions

Y. Miake, H. Hamagaki,† X.X. Bai,‡ O. Hashimoto,† K. Kimura,§ T. Kobayashi,† G. Shapiro, Y. Shida,† I. Tanihata† and S. Nagamiya**

Using the upgraded Bevalac, we have measured inclusive spectra of light fragments at θ_{lab} = 15°, 20°, 30°, 40°, 60°, and 80° and negative pions at θ_{lab} = 60°, which corresponds approximately to 90° in the c.m., in 0.8 GeV/nucleon $^{139}_{57}$La + $^{139}_{57}$La collisions.

As shown in Fig. 1, the Lorentz invariant differential cross sections for protons in the La + La collisions show simple exponential spectra at c.m. 90°, $\exp(-E_k/E_0)$, whereas for lighter-mass collisions[1] the spectrum deviates substantially from the exponential in the low-energy region, showing a shoulder-arm shape. Compared to the Ar + KCl data, the value of E_0 is slightly larger for the La + La collisions. It is likely that the simple exponential shape is due to a greater degree of equilibration for the La + La collisions. The explanation of the shoulder-arm shape by a hypothesis of a radially expanding flow[2] does not seem to work for the La + La collisions. However, it should not be excluded that low-energy protons produced through rescatterings with spectators are superposed on the shoulder-arm shape to create a simple exponential shape.

A pion spectrum at c.m. 90° shows a steeper exponential for the La + La collisions than for lighter-mass collisions,[1] and the difference of the spectrum slope between protons and pions is enhanced in the La + La collisions. Such features may be qualitatively understood within the framework of the time-dependent thermal model.[3]

The momentum distribution of deuterons at θ_{lab} = 15° is plotted in Fig. 2 together with the Ar + KCl data, which is multiplied by a factor of 6. Deuteron spectra in La + La at θ_{lab} = 15° show an enhancement at ~2GeV/c and also at ≤0.7GeV/c. Such behavior is not consistent with a single-source model, but can be understood in terms of a three-fireball model. As shown in Fig. 2, the deuteron spectra are fitted reasonably well, and the enhancement at ≤0.7 GeV/c and ~2GeV/c can be interpreted as due to the contribution from the hot target source (y = 0.2, T = 60 MeV) and the hot projectile source (y = 1.02, T = 60 MeV), respectively.

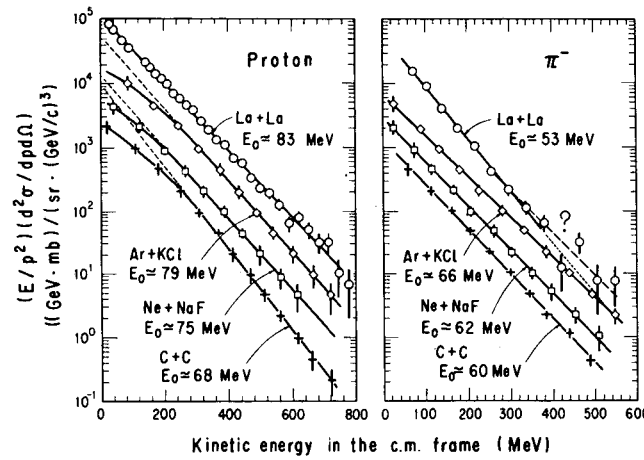

Fig. 1. Proton and π^- energy distribution at $\theta_{cm} = 90°$ in C + C, Ne + NaF, Ar + KCl, and La + La collisions at the beam energy of 0.8 GeV/nucleon. XBL 8410-4280

Footnotes and References

*Department of Physics, University of Tokyo, Tokyo, Japan.

†Institute for Nuclear Study, University of Tokyo, Tokyo, 188, Japan.

‡Institute of Atomic Energy, Beijing, China.

§Department of Physics, Kyushu University, Fukuoka, Japan.

1. S. Nagamiya *et al.*, Phys. Rev. **C24**, 971 (1981).
2. P.J. Siemens and J.O. Rasmussen, Phys. Rev. Lett. **42**, 880 (1979).
3. G.F. Bertsch, Nucl. Phys. **A400**, 221 (1983).

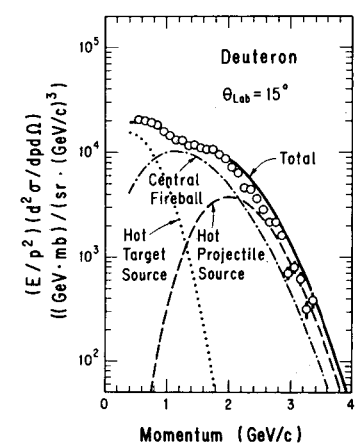

Fig. 2. Inclusive spectra of deuterons at $\theta_{lab} = 15°$ and the fitted spectra by the three-fireball model. XBL 8410-4281

Production Mechanism of Backward Energetic Protons Studied From Two-Particle Correlations in 800 MeV Proton-Nucleus Collisions*

Y. Miake, H. Hamagaki, S. Kadota, S. Nagamiya, S. Schnetzer, Y. Shida, H. Steiner and I. Tanihata

We have measured the distribution of protons and deuterons associated with backward energetic protons (BEP) over a wide kinematical range. The present experiment covers the kinematical region of both p-p and p-d quasi-elastic scatterings (QES) as well as quasi-deuteron breakups. We demonstrated that various reaction mechanisms are kinematically separable. We studied the slope factor of the backward proton spectra, the in-plane to out-of-plane ratio, the angular distribution, and the target mass dependence of those different components. Our data showed that p-p quasi-elastic scatterings give minor contributions to BEP (backward energetic protons). Components of "p-p non-QES" and "p-p OPC (out-

of-plane coincidence)," which turn out to be the main components of the BEP, are considered to be mainly from the proton scattering with a correlated nucleon cluster. It is also supported by the associated nucleon multiplicity <m>=2.4, although the quantitative separation between cluster scattering and multiple scatterings remains for further studies.

The data of p-d quasi-elastic scattering were analyzed with a plane wave impulse approximation (PWIA). It is found that the momentum spread of the pn system ("d") inside the nucleus is smaller than that for deuterons observed in projectile fragments in high-energy heavy-ion collisions. The observed spread (85 ± 15 MeV/c) is also smaller than the width calculated from a purely statistical model. It implies that "d", that is responsible for p-d QES, consists of a pn pair with an anti-parallel momentum coupling between p and n with the coupling stronger than expected from a purely statistical consideration.

From the observed A-dependence of the ratio between p-d QES to p-p QES cross sections, the mean free path of deuterons in the nucleus was estimated to be 1.7 ± 0.3 fm at P_d=1.6 GeV/c. The absolute value and the mass dependence of the p-d QES cross sections are well reproduced by the calculation based on PWIA and the attenuation due to rescattering.

Footnote

*Condensed from LBL-18346.

Pion Spectra at 0 Degrees in Coincidence with Projectile Fragments in 800 MeV/nucleon $^{139}_{57}$La Induced Reactions

O. Hashimoto, J.A. Bistirlich, K.M. Crowe, H. Hamagaki, T.J. Humanic, T. Kobayashi,* S. Nagamiya,† K. Nakayama,* J.O. Rasmussen, Y. Shida,* I. Tanihata,* O. Yamakawa‡ and N. Yoshikawa**

Inclusive pion spectra at 0 degrees produced by 800 MeV/nucleon La ions have been observed using the HISS (Heavy Ion Spectrometer System) at the LBL Bevalac. In addition, correlations between pions and projectile fragments were measured to study collision geometry dependence of the pion spectra.

The experimental setup is illustrated in Fig. 1. It consists of four arms: the A arm for measurement of projectile fragments, the B arm for beam rapidity protons and the C and D arms for the detection of positive and negative pions emitted at forward angles. The HISS dipole is a superconducting magnet with a 2 m diameter and a 1 m gap between pole faces. The TA2 and TA3 time-of-flight walls in the A arm are segmented into 16 and 40 plastic scintillators, respectively. The charge of a projectile fragment is determined from scintillator pulse height. We were able to resolve individual charges up to Z = 18 with the charge resolution decreasing to about ΔZ = 2 at Z = 57. The sum charge of the projectile fragments was obtained by summing all the charges from all the A-arm scintillators.

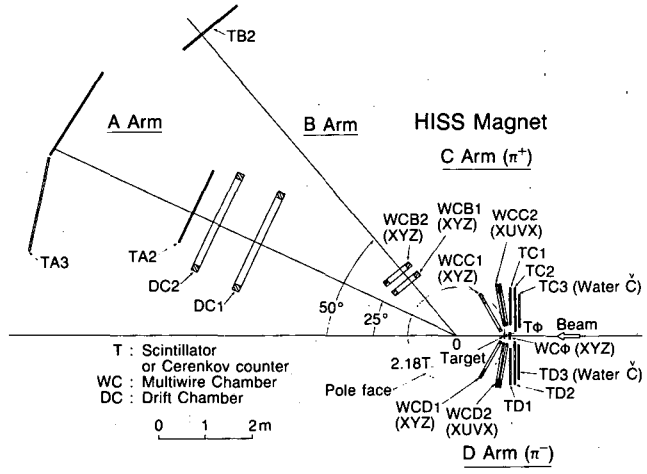

Fig. 1. Experimental setup. XBL 842-10068

The momentum spectrum of negative pions at 0 degrees in a La + C reaction is shown in Fig. 2. A sharp peak has been observed in the spectrum at around the projectile velocity. The FWHM of the peak was ~18 and ~30 MeV/nucleon for La + C and La + La reactions, respectively. On the other hand, the yield of positive pions in this momentum range was very small and did not show a peak as in the case of negative pions. Similar π^- peaks were observed first by Benenson *et al.*[1] and by Sullivan *et al.*[2] with light projectiles such as Ne and Ar. This peak is understood as resulting from a Coulomb interaction between a negative pion and a projectile fragment. The peak observed in the present experiment is far more prominent than in previous studies, since the charge of the projectile is much greater.

A contour plot of the correlations between the sum charge of the projectile fragments and momentum of pions emitted at $0<\theta<2$ for the La+C reaction is shown in Fig. 3. The sum charge spectrum shows a broad peak and has a maximum at around Z_{sum} = 25, although it is not predicted to have the sum charge less than ~40 from a simple consideration of collision geometry. It is also observed that the position of the π^- peak shifts to lower momentum with smaller sum charge. The downshift of the peak, which supposedly corresponds to momentum shift of projectile fragments, is not expected by a clean cut abrasion model.

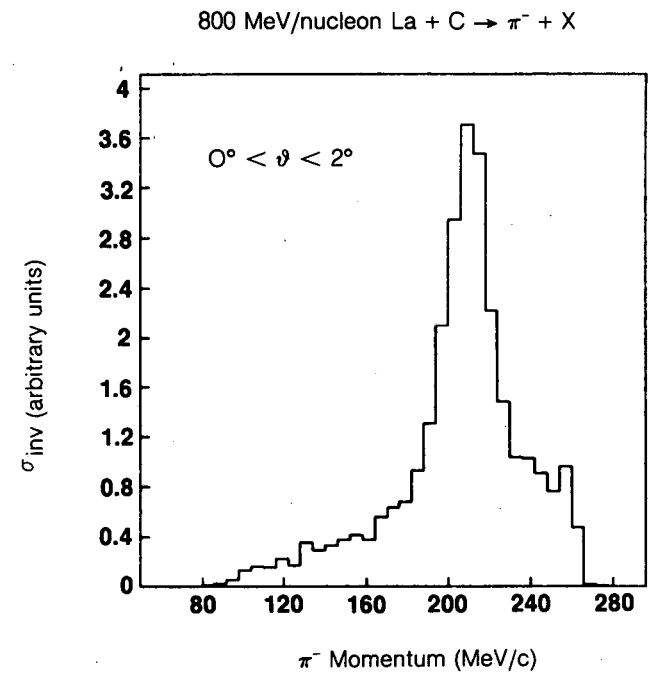

Fig. 2. Spectra of pions emitted at 0 degrees in 800 MeV/nucleon. XBL 8410-4283

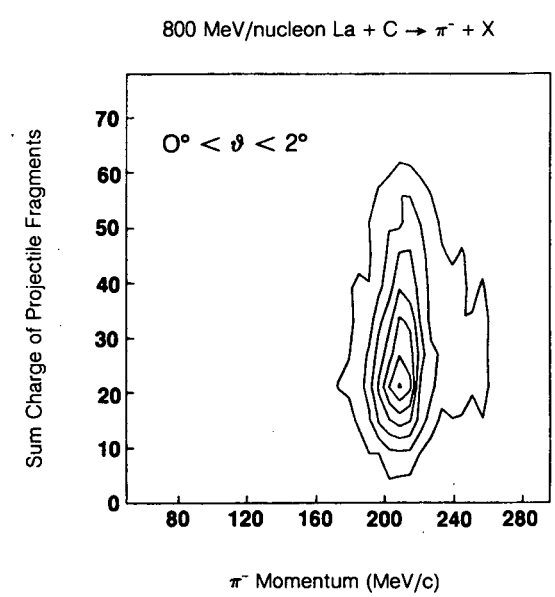

Fig. 3. Contour plot for the correlation between momentum of negative pions emitted at less than 2 degrees and sum charge of projectile fragments in 800 MeV/nucleon La + C collisions.

XBL 8410-4282

Footnotes and References

*Institute for Nuclear Study, University of Tokyo, Tanashi, Tokyo, 188, Japan.

†Department of Physics, University of Tokyo, Tokyo, 113, Japan.

‡Department of Physics, Nagoya University, Nagoya, Japan.

1. W. Benenson *et al.*, Phys. Rev. Lett. **43**, 683 (1979); Errata: **44**, 54 (1980).
2. J.P. Sullivan *et al.*, Phys. Rev. **C25**, 1499 (1982).

Stopping Power and Collective Flow of Nuclear Matter in the Reaction Ar + Pb at 0.8 GeV/nucleon

R.E. Renfordt, D. Bangert,† R. Brockmann,‡ J.W. Harris,‡ G. Odyniec, H.G. Pugh, W. Rauch,† A. Sandoval,‡ R. Stock,‡ H. Ströbele,‡ D. Schall,* and L.S. Schroeder*

Several attempts have been made to identify hydrodynamic sideward flow from inclusive or high multiplicity selected inclusive data[1] with only marginal success. Recently, a sideward deflection of matter was reported[2] for charged-particle exclusive data in the symmetric Nb + Nb system at 400 MeV/nucleon. To search for collective effects and their influence on the flow of nuclear matter in central collisions of non-symmetric target-projectile systems, a charged-particle exclusive experiment was carried out for the reaction ^{48}Ar + Pb at 0.772 GeV/nucleon at the Bevalac Streamer Chamber facility.

The streamer chamber was triggered by requiring that no significant fraction of the projectile nucleus survive the collision. These near-central collisions of Ar + Pb correspond to a trigger cross section of 1.0 barn which in a geometrical picture corresponds to a cutoff in the impact parameter at $b \leq 5.5$ fm. A more refined cut in impact parameter was obtained event-by-event from the multiplicity of participant protons, M_p. The participants were defined as those baryons with momentum per nucleon greater than 270 MeV/c in both the target and projectile c.m. systems. Throughout the subsequent analysis only the energy and momentum carried by the proton in deuterons and tritons were included, thus disregarding not only the unobserved neutrons but also those bound in clusters. The data were compared to the proton distributions of the cascade model of Cugnon *et al.*[3] after subjecting the cascade generated events to a Monte Carlo filtering procedure simulating the experimental biases.

In order to study the momentum flux pattern the normalized flux tensor[4] is used. The choice of this analysis assumes ellipsoidal shapes described by the lengths of two axes of elongation and three angles. Only protons in the forward hemisphere of the c.m. are included. Fig. 1a gives the flow angle distribution $dN/d\cos\theta$ as a function of θ for the multiplicity samples corresponding to impact parameters $b<3$ fm and $3 \leq b \leq 5.5$ fm respectively. The high multiplicity (small impact parameter) events exhibit a fairly flat angular distribution, indicative of a nearly isotropic momentum flow with a slight suppression at forward angles.[1] Events with $3 \leq b \leq 5.5$ fm exhibit a definite sideward deflection of flow angles away from the beam axis. This deflection is predicted by hydrodynamic models.[5] The isotropic distribution of flow angles for small impact parameters is compatible with spherical-shaped distributions. A look at the shape parameters of the ellipsoids producing these flow angles verifies near-spherical shaped events. Thus at our level of statistics we do not find significantly oblate shapes in the Ar + Pb reaction. Indeed, recent hydrodynamical calculations for this reaction[6] also show only slight deviations from spherical flow, at $b \rightarrow 0$. The cascade results presented in Fig. 1b exhibit considerable preference for the forward direction in both samples. This reflects the lack of stopping power in this model.

The finite deflection angles observed for intermediate impact parameters in Fig. 1a make it possible to define a reaction plane by the incident beam direction and the direction of the major axis of the flux ellipsoid for each event. The reaction planes of all events can be aligned and the invariant cross section $d^3\sigma/dp_x dp_z dy$ analyzed as a function of rapidity y and transverse momentum components p_x and p_z in plane and out of plane respectively. This distribution projected onto the reaction plane is displayed in Fig. 2 for the intermediate impact parameter sample. A strong deflection away from the beam axis is observed further supporting the sideward preference of event flow angles observed in Fig. 1a. Furthermore, when the events of Fig. 2 are projected perpendicular

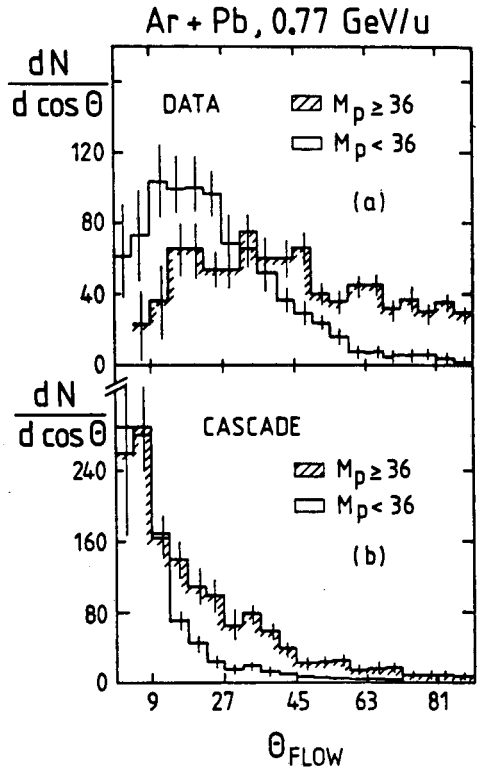

Fig. 1. (a) Distributions of the angle of maximum momentum flow in the c.m. frame for Ar + Pb events with participant proton multiplicities smaller and larger than $<M_p>$. Lines are drawn to guide the eye. (b) Same for the corresponding samples of cascade model generated events. XBL 849-3693

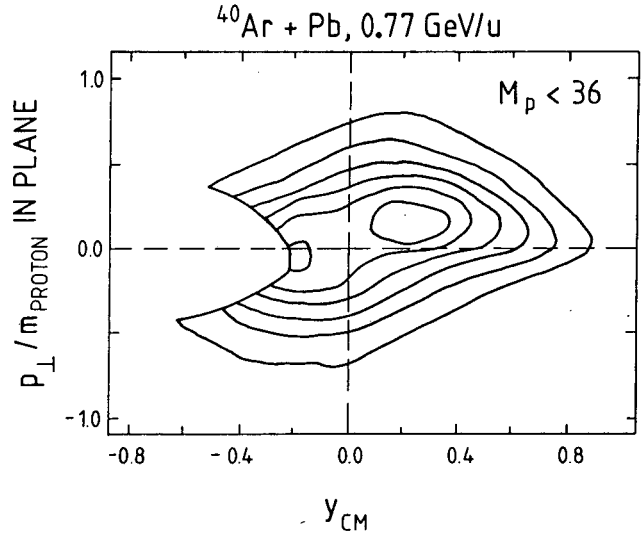

Fig. 2. Projection onto the reaction plane (in-plane transverse momentum p_x vs. rapidity y) of the invariant proton cross section, shown by contour lines, for intermediate impact parameter Ar + Pb events which have been rotated into a common reaction plane orientation. The cut-out at target rapidity reflects the target absorption losses. XBL 849-4046

to the reaction plane, no sideward deflection appears and the results are symmetric with respect to the beam direction, lending further credence to the in-plane off-axis deflection. An analogous plot of the high multiplicity sample is consistent with spherical event shapes.

The sideward deflection has recently been observed for the high multiplicity near-central collisions of Nb + Nb.[2] Such a deflection is observed in the present study of the asymmetric Ar + Pb system for intermediate impact parameters $3 \leq b \leq 5.5$ fm. A qualitative understanding of the difference in the impact parameter ranges can be found by considering the geometries of the two systems. In asymmetric systems such as Ar + Pb collisions at small impact parameters result in the smaller projectile nucleus being completely engulfed by the heavy target nucleus. This is the case for the high multiplicity sample $b<3$ fm for Ar + Pb where complete stopping is observed, the distributions finally become spherical, and no distinct sideward flow can develop. On the other hand, the intermediate impact parameter range for Ar + Pb corresponds to the Ar nucleus just reaching complete overlap with the Pb nucleus. This is analogous to small impact parameter collisions in a symmetric system such as Nb + Nb, thus accounting for the similarity of the observations.

In conclusion, collisions of ^{40}Ar with Pb at 0.772 GeV/nucleon lead to a sideward deflection of the momentum flux at intermediate impact parameters in the vicinity of $b \sim 0.5\ b_{max}$. This deflection is even more pronounced in the reaction Nb + Nb for near-zero impact parameters.[2] Both observations agree qualitatively with the latest predictions of the hydrodynamical model[5,6] providing evidence for the existence of a collective decompression in the flow of nuclear matter and contradicting the intranuclear cascade model prediction which always exhibits transparency. For near-zero impact parameters spherical

momentum flow patterns are observed corresponding to complete stopping. The cascade model which neglects compressional degrees of freedom lacks this stopping power, suggesting the presence of a collective mechanism.

Footnotes and References

*University of Heidelberg, 6900 Heidelberg, West Germany

†University of Marburg, 3550 Marburg, West Germany

‡Gesellschaft für Schwerionenforschung, 6100 Darmstadt, West Germany

1. J. Gosset *et al.*, Phys. Rev. **C16**, 629 (1977); R. Stock *et al.*, Phys. Rev. Lett. **44**, 1243 (1981)
2. H.A. Gustafsson *et al.*, Phys. Rev. Lett. **52**, 1590 (1984)
3. J. Cugnon *et al.*, Nucl. Phys. **A352**, 1505 (1981) and Phys. Rev. **C22**, 2094 (1981)
4. J. Cugnon, J. Knoll, C. Riedel, and Y. Yariv, Phys. Lett. **109B**, 167 (19820
5. H. Stöcker *et al.*, Phys. Rev. Lett. **52**, 1594 (1984)
6. G. Graebner, Thesis, Univ. of Frankfurt 1984 (unpublished) and Phys. Rev. **C22**, 2094 (1981)

Uranium Target Fragmentation by Intermediate and High Energy ^{12}C and ^{20}Ne

P.L. McGaughey, W. Loveland,† D.J. Morrissey,‡ K. Aleklett§ and G.T. Seaborg*

We report herein the final analysis of our measurement of the target fragment production cross sections for nuclides with $24 \leqslant A \leqslant 237$ from the interaction of 1.0, 3.0, 4.8 and 12 GeV ^{12}C and 8.0 and 20.0 GeV ^{20}Ne with ^{238}U.

In Fig. 1, we show the excitation functions for the formation of mostly "independent yield" nuclides that are representative of various classes of U target fragments. The yield of a typical light ($A<60$) fragment, ^{48}Sc, appears to increase strongly with increasing projectile energy up to ~8 GeV (with a modest increase from 8 to 20 GeV) which is consistent with the origin of these fragments being in a high deposition energy process. The yields of n-rich fragments ($80 \leqslant A \leqslant 145$, such as ^{96}Nb and ^{136}Cs) are energy independent from 1-20 GeV consistent with their origin in low energy fission of a uranium-like species. The n-poor fragments ($80 \leqslant A \leqslant 145$, such as ^{88}Zr and ^{122}Sb) have excitation functions consistent with their origin in a deep spallation or high energy fission process. (At a ^{12}C projectile energy of 1.0 GeV, the isobaric yield distributions indicate the n-poor fragments originate primarily from a fission rather than a spallation process.) The excitation functions of the heavy fragments ($160 \leqslant A \leqslant 200$, such

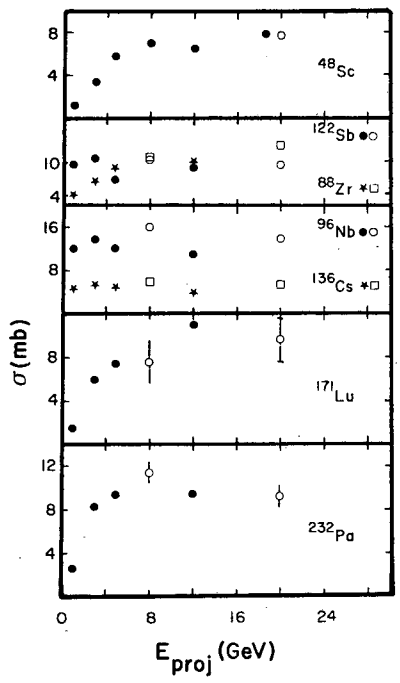

Fig. 1. The measured nuclidic formation cross sections for the interaction of ^{12}C (solid points) and ^{20}Ne (open points) with ^{238}U. The ^{20}Ne data have been scaled by the ratio of the "soft spheres" total reaction cross sections for ^{12}C and ^{20}Ne induced reactions. XBL 8410-4131

as ^{171}Lu) are similar to those of the light fragments while near target fragments such as ^{232}Pa originate in lower deposition energy events.

Fig. 2 shows the isobaric yield distributions deduced from the nuclidic formation cross sections along with predictions of these distributions made using the nuclear firestreak and intranuclear cascade models. Contrary to a previous report, no large yields of fragments with $160 \leqslant A \leqslant 200$ are observed in any reaction. Both the intranuclear cascade model and the nuclear firestreak model satisfactorily predict the observed yields of fragments with A>60 indicating the general pattern of yields of these fragments is governed by the excitation energy deposited in the nucleus during the initial projectile-target interaction and the geometry of the collision.

Footnotes

*Los Alamos National Laboratory, Los Alamos, NM 87545

†Oregon State University, Corvallis, OR 97331

‡Michigan State University, E. Lansing, MI 48824

§Studsvik Science Research Laboratory, S-611 82 Nyköping, Sweden

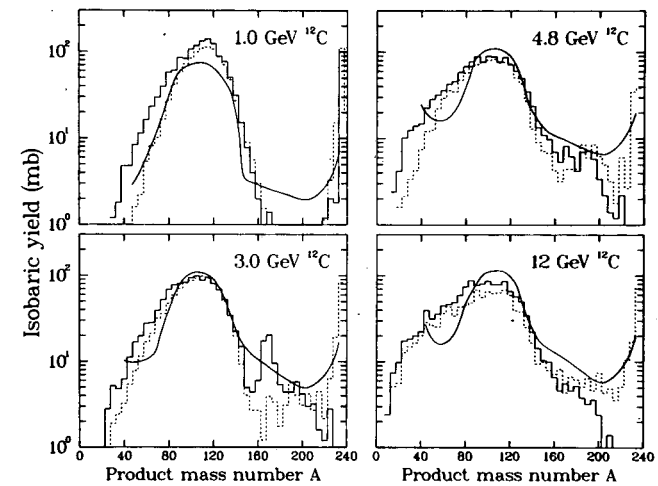

Fig. 2. The measured isobaric yield distributions (solid curves) for ^{12}C induced reactions with ^{238}U are compared to predictions of the intranuclear cascade model (solid histogram) and the nuclear firestreak model (dashed histogram). XBL 844-1339

Midrapidity Pion Production in 1.05 GeV/nucleon ^{40}Ca + ^{40}Ca Collisions

J.W. Harris, R. Brockmann,* K.L. Wolf,* E.K. Jackson, J. Miller, H.G. Pugh, P. Renteln, G. Roche, L.S. Schroeder, R.N. Treuhaft, G. Krebs† and P. Kirk†*

Observations of an enhancement in the π^+ yield at midrapidity (θ_{cm} = 90°) in 800 MeV/nucleon Ne + NaF and 1.05 GeV/nucleon Ar + Ca reactions[1,2] and in the π^-/π^+ ratio at θ_{cm} = 0° in the 400 MeV/nucleon Ne + NaF reaction[3] has been of particular interest. Neither cascade calculations nor predictions based on thermal models have been able to reproduce the midrapidity π^+ peak. This has led to descriptions of the midrapidity pion production in terms of collective hydrodynamic flow, exotic delta or pionic states, Coulomb focusing, and various other interesting mechanisms. Calculations[4-6] incorporating final state π-nucleus electromagnetic effects qualitatively reproduce the π^+ peak at midrapidity and the π^-/π^+ ratio at θ_{cm} = 0° when specific assumptions are made about the space-time dependence of the nuclear distributions during the collision. Recent results[7] from the measurement of low energy π^- and π^+ cross sections at θ_{cm} = 90° in the Ar + KCl reaction at 1.05 GeV/nucleon show a smoothly varying π^-/π^+ ratio in contradiction to the Coulomb explanation for midrapidity pins.

In order to resolve these conflicts and to provide more detailed information on the midrapidity production of pions with which to test the various proposed mechanisms, single-particle inclusive π^+ and π^- cross sections were measured in the Two Arm Spectrometer System (TASS) at the Bevalac for

the isospin-symmetric ^{40}Ca + ^{40}Ca system at 1.05 GeV/nucleon. A complete mapping of the midrapidity region was made for both charges. In addition, an external projectile fragment scintillator array was employed to facilitate off-line selection on the centrality of the collisions. This selection is important to constrain calculations which include final state interactions since they are very sensitive to the numbers of participants and spectators in the collision.

In the experiment both arms of TASS were used simultaneously in singles operation along with the beam fragmentation array as shown in Fig. 1. The forward spectrometer was equipped with three scintillation hodoscopes for position sensitivity and time-of-flight measurement as well as a Čerenkov counter to reject electrons. The rear spectrometer, which used wire chambers, had better resolution and was able to distinguish electrons from pions without using a Čerenkov counter. Spectra were accumulated at θ_{lab} = 10, 20, 25, 30, 45, 65, 90,120 and 150 degrees over the momentum range of 60 to 400 MeV/nucleon for both π^+ and π^-. The invariant cross sections are observed to fall four orders of magnitude in this range of momenta. Detailed acceptance calculations are underway to be able to correct the spectra for energy loss, multiple scattering, and pion decay-in-flight ($\pi \rightarrow \mu + \nu$) in the target, air (helium), and spectrometer elements. Until these corrections have been completed, it would be premature to present the spectra or comment on the existence of a significant midrapidity π^+ and/or π^- peak. On the other hand, it is possible to present the π^-/π^+ ratios since the above-mentioned corrections have identical effects on the π^- and π^+ spectra. Presented in Fig. 2 is the π^-/π^+ ratio as a function of laboratory momentum at a fixed θ_{lab} = 30°. This ratio is exactly one within the statistical errors of the experiment as represented by the error bars on the figure. Also shown is an arrow pointing out the position of the π^+ enhancement as it should appear in this momentum representation. At the other angles of the experiment the π^-/π^+ ratios were also found to be equal to one with approximately the same statisti-

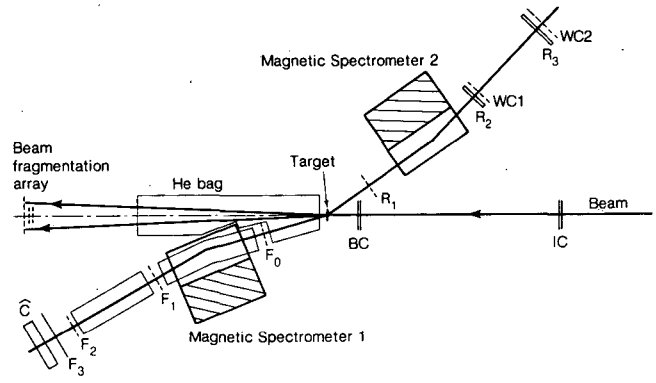

Fig. 1. Schematic diagram of the Two Arm Spectrometer System as equipped for the present experiment. Downstream from the target and subtending the projectile fragmentation cone is the beam fragmentation scintillator array. XBL 8411-4748

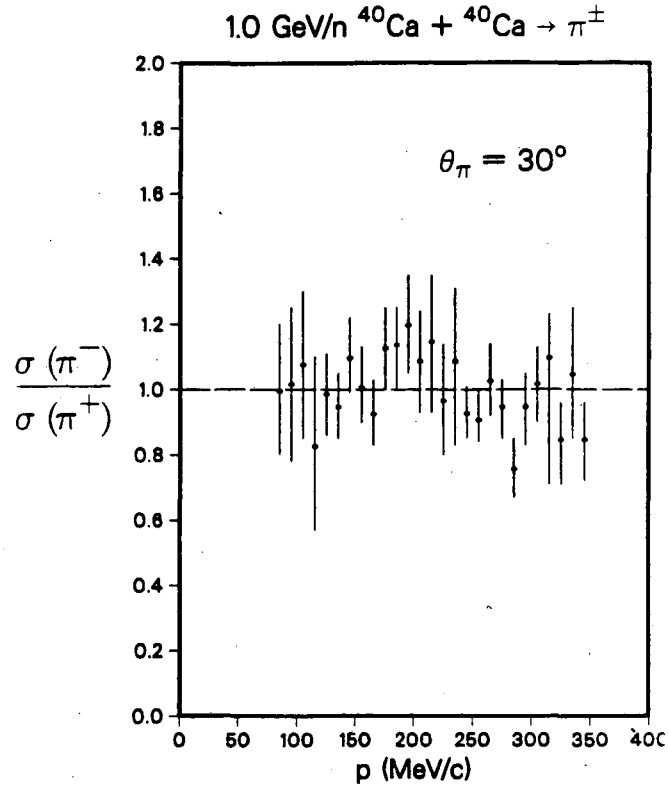

Fig. 2. Ratio of π^- to π^+ cross sections as a function of pion laboratory momentum at θ_{lab} = 30° for the 1.05 GeV/nucleon ^{40}Ca + ^{40}Ca reaction. The arrow indicates the position where the midrapidity π^+ enhancement was observed for 1.05 GeV/nucleon Ar + Ca. XCG 841-13002

cal errors, which at present is < 20%. These errors will decrease as only half of the data has been analyzed at this time. Clearly, there are no gross Coulomb effects observed in these spectra; otherwise, non-unit π^-/π^+ ratios would be present. Furthermore, when off-line multiplicity selection was made on the projectile fragmentation array it was found that there are very few pions at midrapidity associated with particles of charge $Z \geqslant 1$ in the projectile fragmentation cone. Thus, a pion at midrapidity is a good signature for a central collision with very little or no charge remaining in the projectile fragmentation cone.

Footnotes and References

*Gesellschaft für Schwerionenforschung, Darmstadt, West Germany.

†Louisiana State University, Baton Rouge, LA.

1. J. Chiba *et al.*, Phys. Rev. **C20**, 1332 (1979) and K. Nakai *et al.*, Phys. Rev. **C20**, 2210 (1979).
2. K.L. Wolf *et al.*, Phys. Rev. Lett. **42**, 1448 (1979).
3. W. Benenson *et al.*, Phys. Rev. Lett. **43**, 683 (1979).
4. K.G. Libbrecht and S.E. Koonin, Phys. Rev. Lett. **43**, 1581 (1979).
5. M. Gyulassy and S.K. Kaufmann, Nucl. Phys. **A362**, 503 (1981).
6. J. Cugnon and S.E. Koonin, Nucl. Phys. **A355**, 477 (1981).
7. J.O. Rasmussen, LBL Report LBL-14174 (1982).

Composite Particles and Entropy Production in Relativistic Nuclear Collisions

H.-A. Gustafsson, K.G.R. Doss, H.H. Gutbrod,* B. Kolb,* H. Löhner,† B. Ludewigt,‡ A.M. Poskanzer, T. Renner, H. Riedesel,§ H.G. Ritter,* A. Warwick and H. Wieman**

One of the major goals in studying relativistic nuclear collisions is to study the behavior of nuclear matter at densities different from the ground state density. The production of composite particles is suggested[1-3] to be a suitable observable to determine the size of the participant volume at freeze-out. There are also calculations[4-6] showing that the observed ratio of deuterons to protons can be related to the produced entropy in the system. Calculations[7,8] have shown that the produced entropy in nuclear collisions stays constant during the expansion phase, which means that the production of composite particles then give information not only about the freeze-out but also about the initial stage of the collision, where the matter is compressed and hot. Up to now all information about composite particle production, except for ref. 9, is based on single particle inclusive data which average over all impact parameters. Most of the models, however, calculate the different quantities for infinite nuclear matter, which means that it is of great importance to know how the observables vary with impact parameter to be able to make a reasonable comparison with calculated quantities.

Fig. 1 shows the yield ratio d_{like}/p_{like} as a function of participant baryon charge multiplicity (N_p) for Ca + Ca and Nb + Nb at different bombarding energies. The definition of d_{like} and p_{like} was taken from ref. 7. The functional form of the observed ratios can be understood in terms of the coalescence model.[1,10] We have here used an improved version of the model[3] which relates the radii of the deuteron and the participant zone to the coordinate space and the temperature of the interacting region to the momentum space. In this model the radius r_p and the temperature T of the interacting region as well as the deuteron radius r_d are related to d_{like} and p_{like} through

$$d_{like}/p_{like} = 6\big((A-Z)/Z\big)\left(1 + 2(r_p/r_d)^2\right)^{-3/2} \times N_p\left(1 + 2mTr_d^2/3\right)^{-3/2}$$

The radius r_p, assuming a spherical source, is parameterized as $r_p = r_0(A/Z\,N_p)^{1/3}$. In the fits to the

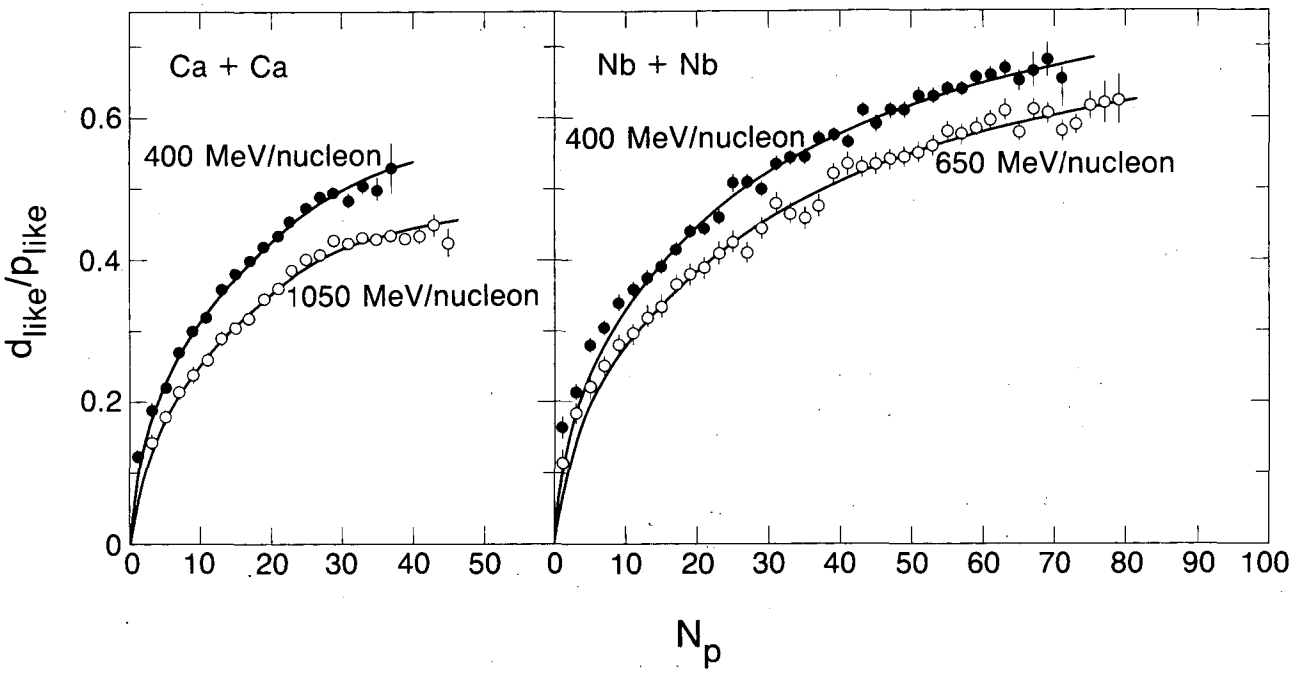

Fig. 1. d_{like}/p_{like} as a function of proton multiplicity (N_p) for Ca + Ca at 400 and 1050 MeV/nucleon and Nb + Nb at 400 and 650 MeV/nucleon. The solid curves are from fits to the coalescence model. XBL 849-10774

observed ratios, r_0 and r_d were free parameters. The temperature T was taken to be the mean temperature obtained from Boltzmann fits[11] to the proton spectra at 90 degrees in the cm system. The result of the fits are presented as solid curves in Fig. 1. The extracted radii from the fits are the rms value for a Gaussian density distribution. To convert these to equivalent sharp sphere radii the extracted values have to be multiplied by $\sqrt{5/3}$. From these radii the density of the participant zone can be determined. Fig. 2 shows the extracted densities as a function of bombarding energy.

Footnotes and References

*Gesellschaft für Schwerionenforschung, Darmstadt, West Germany.

†Universität Münster, Münster, West Germany.

‡Universität Marburg, Marburg, West Germany.

§Present address: Springer-Verlag, Berlin, West Germany.

1. H. Sato and K. Yazaki, Phys. Lett. **98B**, 153 (1981).
2. A.Z. Mekjian, Phys. Rev. **C17**, 1051 (1978).
3. M. Gyulassy and E. Remler, to be published.
4. P.J. Siemens and J.I. Kapusta, Phys. Rev. Lett. **43**, 1486 (1979).

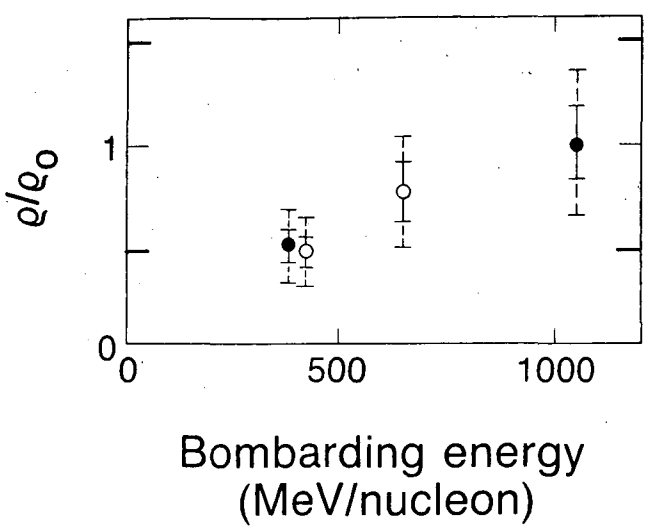

Fig. 2. Freeze out density as a function of bombarding energy for the two system Ca + Ca (filled circles) and Nb + Nb (open circles.) XBL 8410-4566

5. J.I. Kapusta, Phys. Rev. **C29**, 1735 (1984).
6. H. Stöcker *et al.*, Nucl. Phys. **A400**, 63c (1983) and
   B.V. Jacak, H. Stöcker and G.D. Westfall, Phys. Rev. **C29**, 1744 (1984).
7. G. Bertsch and J. Cugnon, Phys. Rev. **C24**, 2514 (1981).
8. J.I. Kapusta, Phys. Rev. **C24**, 2545 (1981).
9. H.H. Gutbrod, H. Löhner, A.M. Poskanzer, T. Renner, H. Riedesel, H.G. Ritter, A. Warwick, F. Weik and H. Wieman, Phys. Lett. **127B**, 317 (1983).
10. H.H. Gutbrod, A. Sandoval, P.J. Johansen, A.M. Poskanzer, J. Gosset, W.G. Meyer, G.D. Westfall and R. Stock, Phys. Rev. Lett. **37**, 667 (1976).
11. H.-A. Gustafsson, H.H. Gutbrod, B. Kolb, H. Löhner, B. Ludewigt, A.M. Poskanzer, T. Renner, H. Riedesel, H.G. Ritter, A. Warwick and H. Wieman, Phys. Lett. **142B**, 141 (1984).

^{197}Au Target Fragmentation Induced by 1.8 GeV/nucleon ^{40}Ar

Li Wenxin, W. Loveland,† K. Aleklett‡, and G.T. Seaborg*

In RHI collisions, it has been found[1] that the "high energy physics" hypotheses of limiting fragmentation and factorization can be applied to describe target and projectile fragmentation. Using a scaling variable of total projectile kinetic energy, one can say that the fragment production cross sections become independent of beam energy above 5 GeV while the target fragment kinematic properties become energy independent at beam energies of 25 GeV and above. Apart from a scaling factor of the ratio of the total reaction cross sections, the shape of the fragment mass yield distributions is, in general, the same for projectiles of the same total kinetic energy.

We have attempted to extend the experimental range of validity of the concepts of limiting fragmentation and factorization for heavy target systems by measuring the fragment production cross sections and kinematic properties for the interaction of 72 GeV ^{40}Ar with ^{197}Au. A range-weighted measure of the target fragment angular distribution is the F/B ratio, the ratio of fragments recoiling forward from a target (F) to those fragments recoiling backwards (B). In Fig. 1, we show the dependence of F/B for selected fragments from ^{197}Au target fragmentation upon the total projectile kinetic energy. (The data shown in Fig. 1 are for the interaction of 4.8[2] and 25 GeV ^{12}C,[3] 7.6 GeV ^{20}Ne,[2] 72 GeV ^{40}Ar, 28 and 300 GeV p[4] with ^{197}Au.) As shown in Fig. 1, the target fragment kinematic property, F/B, does appear to become energy invariant at an energy of ~25 GeV and above this energy, the F/B ratios are the same for proton or RHI-induced reactions. Thus it would appear that the hypotheses of limiting fragmentation and total projectile kinetic energy scaling are well established for heavy target systems.

The failure of the hypothesis of factorization is shown in Fig. 2 where the fragment isobaric yield distributions for the interaction of 28 GeV protons[5] and 72 GeV ^{40}Ar with ^{197}Au are presented. (The 28 GeV p induced reaction is expected to produce the same isobaric yield distribution as the 72 GeV p + ^{197}Au reaction.) While the shapes of the yield distribution are similar for products with $A > 120$, they are really different for the lighter mass products. It is thought that these lighter mass products are the result of high deposition energy events. With a massive high energy projectile such as 72 GeV ^{40}Ar, the production of fragments with $40 \leqslant A \leqslant 90$ by this high deposition energy process apparently becomes possible, and the deviations from factorization become large.

Footnotes and References

*Institute of Modern Physics, Lanzhou, People's Republic of China

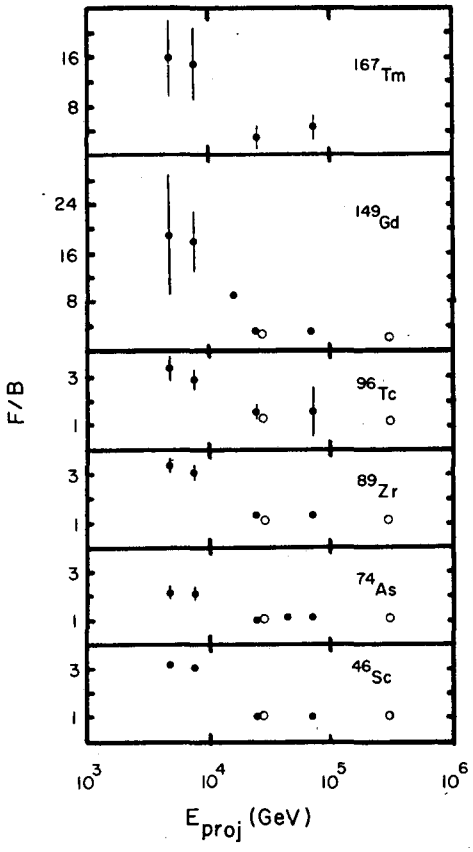

Fig. 1. Variation of F/B of selected fragments vs. projectile kinetic energy for the interaction of heavy ions and protons with ^{197}Au. XBL 8410-4132

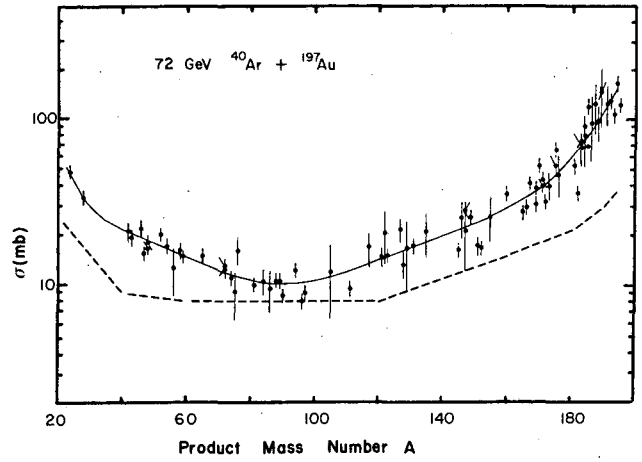

Fig. 2. Fragment isobaric yield distribution for the interaction of 72 GeV ^{40}Ar with ^{197}Au.
XBL 8410-4133

†Oregon State University, Corvallis, OR 97331
‡Studsvik Science Research Laboratory, S-611 82, Nyköping, Sweden

1. See, for example, E.M. Friedlander and H.H. Heckman, LBL-13864, April 1982.
2. S.B. Kaufman, E.P. Steinberg, B.D. Wilkins and D.J. Henderson, Phys. Rev. **C22**, 1897 (1980).
3. Li Wenxin, private communication, 1983.
4. S.B. Kaufman, E.P. Steinberg and M.W. Weisfield, Phys. Rev. **C18**, 1349 (1978).
5. S.B. Kaufman, M.W. Weisfield, E.P.Steinberg, B.D. Wilkins and D. Henderson, Phys. Rev. **C14**, 1121 (1976).

Unusual Behavior of Projectile Fragments Formed in the Bombardment of Copper with Relativistic Ar Ions

G. Dersch, R. Beckmann,* G. Feige,* T. Lund,* P. Vater,* R. Brandt,* E. Ganssauge,* K. Aleklett,† E.M. Friedlander, P.L. McGaughey,‡ G.T. Seaborg, W. Loveland,§ J. Herrmann,** and N.T. Porile***

The interaction properties of projectile fragments from the fragmentation of 0.9 GeV/nucleon and 1.8 GeV/nucleon ^{40}Ar with Cu have been studied using radioactivation techniques. In this experiment, two identical copper blocks, 1 cm thick and 8 cm in diameter, are irradiated by relativistic projectiles in different configurations. In configuration "0", the blocks are touching while in configuration "10" or "20", the blocks are separated by 10 or 20 cm of air, respectively. It is assumed that when the relativistic projectiles interact with the first block of each pair, projectile fragments are created which interact with other nuclei in the first and second blocks. What is measured is the ratio of some target fragment activity, such as ^{24}Na or ^{28}Mg, produced in the second block relative to the first block, R.

Fig. 1 shows the values of R that were measured for different target fragments produced in the interaction of 0.9 and 1.8 GeV/nucleon ^{40}Ar with Cu (two runs at each energy). For each fragment, two values of R are shown; R_0 (open circles) corresponding to the touching configuration and R_{20} (solid squares) corresponding to a 20 cm separation between the blocks. If we examine the bottom panel of Fig. 1 (0.9 GeV/nucleon ^{40}Ar + Cu), we see two different types of behavior. For fragments with $A>40$, the R values decrease significantly as the blocks are moved apart. For the fragments with $7 \leqslant A \leqslant 28$, the R values are generally independent of block separation. This behavior can be explained in terms of conventional concepts about target fragmentation. The fragments with $\Delta A = A_{tgt} - A_{frag} = 10-20$ are produced by the interaction of the primary beam with Cu and *and* by the interaction of secondary projectile fragments with Cu. Fragments with $\Delta A = 10-20$ are thought to arise from low deposition energy, peripheral collisions. Most of the secondary projectile fragments responsible for the large value of R_0 for these fragments are surmised to be light particles (π, n, p, α) with broad angular distributions. As the blocks are moved apart, many of these secondary particles "miss" the second block and the ratio R_{20} becomes smaller than R_0. The fragments with $7 \leqslant A \leqslant 28$ are produced only in higher deposition energy, more central collisions. It is reasoned that the projectile fragment secondaries producing these target fragments are of high energy and their angular distribution is strongly directed along the beam axis. Thus as the blocks are moved apart, no effect on R is seen.

When the projectile energy is increased to 1.8 GeV/nucleon (top panel of Fig. 1), then R values for all fragments decrease with distance between the blocks. In fact, Fig. 2 shows the variation of R with distance between the blocks for the production of ^{24}Na and ^{28}Mg. What has happened as the projectile energy was increased from 0.9 to 1.8 GeV/nucleon? Among the possible explanations are:

(a) The threshold for producing an unusual type of projectile fragment has been exceeded. These unusual projectile fragments would have a lifetime $\sim 10^{-9}$ sec (to account for the decrease of R with distance) and a large cross section for interaction with matter (the R values are higher at 1.8 GeV/nucleon although the total reaction cross section stays the same).

(b) As the ^{40}Ar energy was increased from 0.9 to 1.8 GeV/nucleon, the number of high energy secondary fragments capable of causing the Cu→Na,Mg reaction has increased and their angular distribution has broadened sufficiently to account for the decrease in R with distance.

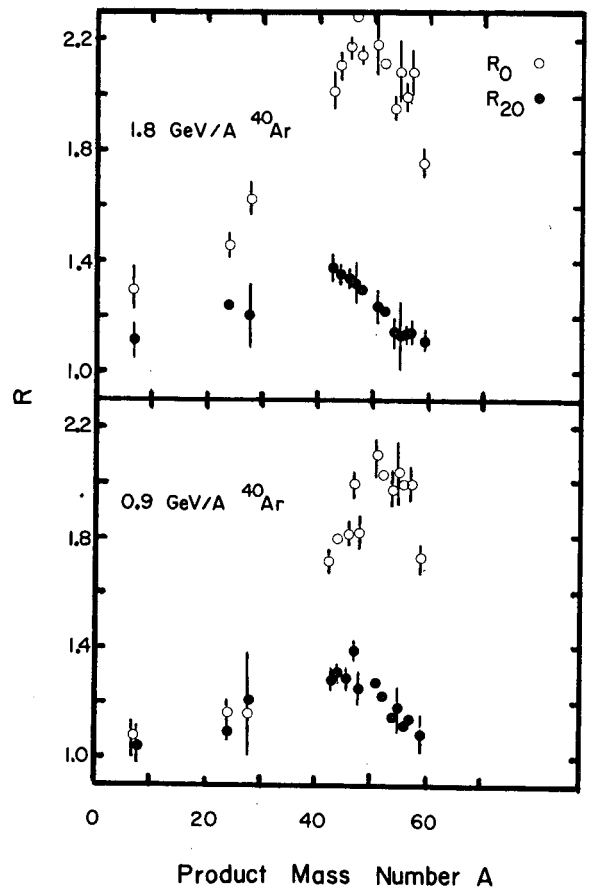

Fig. 1. Target fragment mass number dependence of R. XBL 8410-4134

Explanation (b) was checked experimentally by placing a large annular Cu ring around the second Cu block to check how many fragments with an energy sufficient to cause the Cu→Na,Mg reaction might have "missed" the second block as the dis-

tance between the blocks was increased. It was found that very few fragments capable of causing the Cu→Na,Mg reaction interacted with the annular ring, casting doubt on explanation (b).

A search for a possible explanation for the unusual properties of the observed fragments is underway.

Footnotes and References

*Philipps Universität, D-3550 Marburg, Federal Republic of Germany.

†Studsvik Science Research Laboratory, S-611 82 Nyköping, Sweden

‡Los Alamos National Laboratory, Los Alamos, NM 97545

§Oregon State University, Corvallis, OR 97331

**Purdue University, W. Lafayette, IN 47907

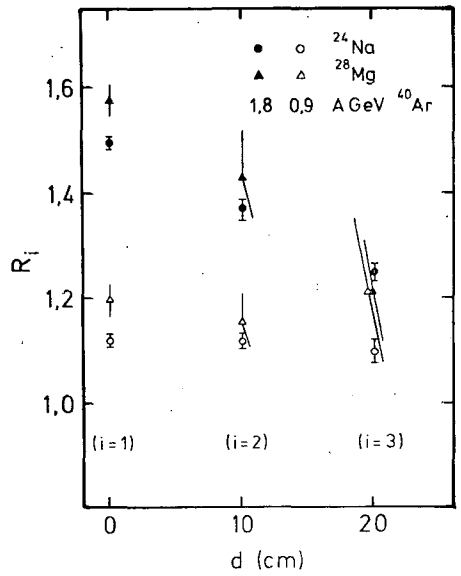

Fig. 2. Variation of R with disk separation d.

XBL 8410-4135

Charge-changing Reactions of Secondary Fragments Produced in High-Energy Heavy Ion Collisions*

T.J.M. Symons, M. Baumgartner, H.J. Crawford,† J.P. Dufour,‡ J. Girard,§ D.E. Greiner, P.J. Lindstrom, and D.L. Olson

One of the most exciting recent developments in experimental nuclear physics has been the report that a substantial fraction of secondary fragments produced in high-energy heavy ion collisions have reaction cross sections that are very much larger than normal. Although there has been controversy over the size of this effect, results have been presented by several groups using nuclear emulsions and CR-39 plastic track detectors.

We have begun a program to measure charge changing cross sections of projectile fragments using a quite different technique that is capable of much higher data acquisition rates. The primary beam impinges on a stack of 50 Lucite strips having an average thickness of 3.17 mm, emitting Čerenkov light as it passes through them. Since at a given velocity the intensity of the light is proportional to Z^2, where Z is the charge of the particle, a fragmentation reaction in a particular strip will be registered as a drop in the light output from that and subsequent strips. We use total internal reflection to transport the light to photomultipler tubes so that there is no wrapping between the strips. Since the energy threshold of the device is ~1.1 GeV/nucleon, low energy target fragments will not contribute to the signal, a distinct advantage over similar schemes using energy loss to measure the fragment charge. The resolution of the individual strips is typically 0.58 charge units, full width at half maximum, allowing reactions to be well localized even for single unit charge changes.

In addition to the Č detectors, scintillators and Si(Li) detectors were used to measure precisely the position and charge of the incoming beam particle. We have taken data using two beams, ^{56}Fe and ^{40}Ar, at 1.88 and 1.82 GeV/nucleon respectively, and two trigger modes, a free trigger to measure the reaction

rate of the incoming beam and an inelastic trigger in which a reaction was required to occur in one of the first 14 Č detectors. A total of 909,000 ^{56}Fe interactions and 460,000 ^{40}Ar interactions have been analyzed so far.

The secondary charge spectrum produced by the ^{56}Fe beam is illustrated in Fig. 1. Individual charges are clearly resolved and broadening of the peaks due to multiple fragmentation can be seen for the lower charges.

Next we consider the variation of reaction rate with distance from the primary interaction point. For brevity, we follow here the procedure adopted by Friedlander *et al.* of accumulating different charges into a single data set. However, rather than using a parametric scaling law, we have scaled the individual charges by their values at distances greater than 3 cm on the assumption that the anomalous effect will be small in these cases. The results are shown in Fig. 2 where we have included charges 13–24 from ^{56}Fe and 11–16 from ^{40}Ar. For reference, we also show the estimates of the mean free path of ^{56}Fe as a function of depth in the stack. No corrections have been made to any points on this plot. However, we have increased the errors on the first point to 2% and the next ten ^{56}Fe points to 1% to take into account our uncertainty concerning the shape of the efficiency curve. The fits for assuming a constant mean free path, the null hypothesis, are good, with χ^2 values of 22.4 and 16.5 for ^{56}Fe and ^{40}Ar with 18 degrees of freedom in each case. Also shown on the graph are the results of two experiments that have been performed using these beam nuclei. The solid curve is the prediction assuming a 6% admixture of fragments with a mean free path of 2.5 cm as originally proposed by Friedlander *et al.* and supported by their repeat experiment.[1,2] It must be emphasized, however, that these two experiments cover a very different range of charge (3–26 for Friedlander *et al.*, 13–24 in our case). The dashed curve represents the 4.8%, 0.75 cm hypothesis suggested by Tinknell and Price,[3] on the basis of ^{40}Ar fragmentation with a range of secondary charges similar to ours. Statistically, these two hypotheses have negligible probabilities. However, we emphasize more strongly the good agreement that we have with the null hypothesis.

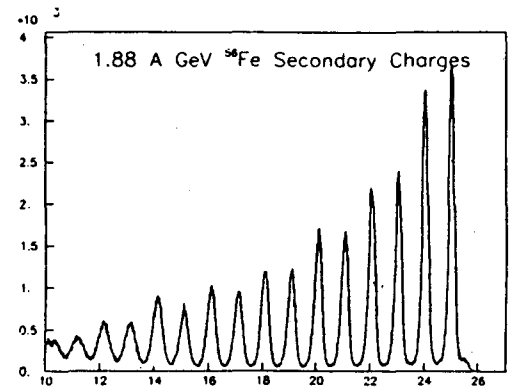

Fig. 1. Spectrum of secondary charges resulting from ^{56}Fe fragmentation at 1.88 GeV/nucleon in Lucite.

XBL 8311-4648

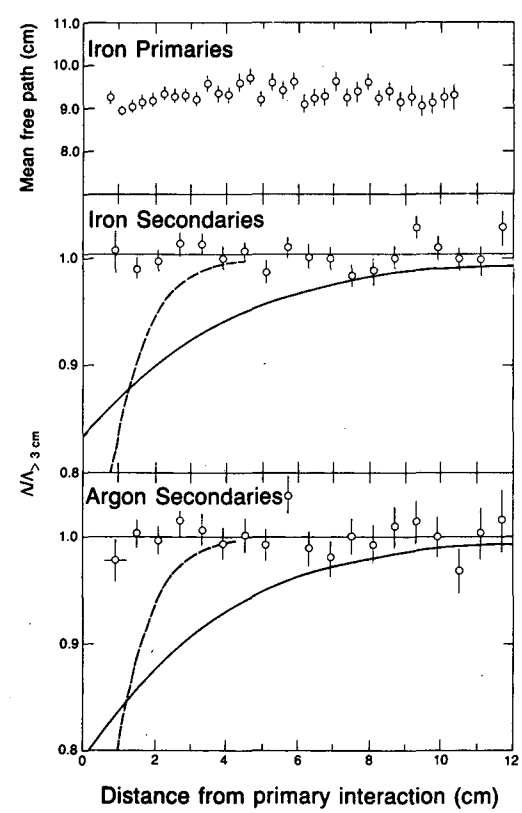

Fig. 2. Ratios of estimated to average mean free paths as a function of distance from the primary interaction point for ^{40}Ar and ^{56}Fe beams.

XBL 8311-3438

In conclusion, we find no evidence for the existence of a short mean free path component in Fe or Ar secondaries with Z = 13–24 and Z = 11–16 respectively. It is, of course, possible that the effect is limited to cases that we have not tested, namely Z<11, distances less than 6 mm, reactions with heavy target nuclei, or reactions in which the charge does not change. Nevertheless, lack of any positive evidence at the levels predicted by the visual detector experiments is surprising. The analysis of this experiment is by no means complete and we shall continue to search for evidence for contributions of an anomalous component in our data. We are also planning further experiments which will increase our sensitivity for lower charges and at shorter distances.

Footnotes and References

*Condensed from LBL 16990

†Space Sciences Laboratory, University of California, Berkeley, CA 94720.

‡Present address: CENBG: Le Haut Vigneau, 33170 Gradignan, France.

§Present address: CEA SACLAY, 91191 Gif-sur-Yvette-Cedex, France.

1. E.M. Friedlander *et al.*, Phys. Rev. Lett. **45**, 1084 (1980); Phys. Rev. **C27**, 1489 (1983).
2. Y. Karant *et al.*, Proceedings of 6th High Energy Heavy Ion Summer Study, Berkeley, 1983.
3. M. Tinknell and P.B. Price, Phys. Rev. Lett., in press.

Two-pion Correlations in Heavy Ion Collisions*

*W.A. Zajc, J.A. Bistirlich, R.R. Bossingham, H.R. Bowman, C.W. Clawson, K.M. Crowe, K.A. Frankel, J.G. Ingersoll, J.M. Kurck, C.J. Martoff, D.L. Murphy, J.O. Rasmussen, J.P. Sullivan, E. Yoo, O. Hashimoto,† M. Koike,† W.J. McDonald,‡ J.P. Miller§ and P. Truöl***

An application of intensity interferometry to relativistic heavy ion collisions (RHIC) is reported. The correlation between two like-charged pions is used to study the reactions Ar + KCl $\rightarrow 2\pi^{\pm}$ + X and Ne + NaF $\rightarrow 2\pi^{-}$ + X, both at an incident beam energy of 1.8 GeV/nucleon. There appears to be a substantial coherent component of the pion source, although measurement is complicated by the presence of final state interactions. The effect of the mutual Coulomb repulsion of the two pions, and of the pion-nuclear Coulomb interactions, on the two-pion correlation function is analyzed.

Intensity interferometry uses the correlations between like particles induced by Fermi or Bose statistics to determine the space and time dimensions of the particle source. The method is quite general, first finding application to the measurement of stellar diameters in the pioneering work of Hanbury-Brown and Twiss.[1] Goldhaber, Goldhaber, Lee, and Pais[2] (GGLP) were the first to extend these methods to particle physics. By modifying the Fermi statistical model to include symmetrization between like particles, GGLP were able to explain the observed differences in opening angles between like-charged pairs and oppositely-charged pairs of pions created in $p\bar{p}$ annihilation. Since then, many authors have used similar approaches to measure the size of hadronic interaction regions. Recently, these methods have been extended to RHIC by the University of California Riverside group.[3]

A particularly convenient approach to intensity interferometry in particle physics proceeds through the introduction of the two-particle correlation function C_2, first introduced by Kopylov and Podgoretskii.[4] An heuristic discussion is presented here for the sake of completeness. For further details, with particular emphasis on RHIC, the reader is referred to the work of Gyulassy *et al.*,[5] and Yano and Koonin.[6]

Beams of 1.8 GeV/nucleon ^{40}Ar and ^{20}Ne from the Bevalac were directed onto KCl and NaF targets, respectively, which in each case provided a nearly symmetric target-projectile system. Targets of 0.5 to 1.0 g cm^{-2}, which provide an interaction probability

on the order of 1%, gave a good compromise between high event rates and multiple scattering of the pions in the target material. Intensities were typically 10^8–10^9 beam particles per pulse, where one pulse is slightly less than a second in duration. At these intensities, between 0.1 and 1 good event per pulse was obtained. (The Bevalac duty cycle is one pulse every six seconds at a magnetic field corresponding to 1.8 GeV/nucleon.)

Pions emerging at 45 ± 8 deg. from the beam direction were accepted into a simple magnetic spectrometer system. A 9 kG central field was provided by an H-type magnet with a 56 cm x 168 cm pole tip and a 21.5 cm gap. The ongoing trajectories of the pions were defined by two small (30.2 cm x 14.2 cm) multiwire proportional counters, MWPC1 and MWPC2. After being bent in the field, the pions pass through two large (200 cm x 25 cm) MWPCs, thereby defining their outgoing trajectories, and hence the bend angle. Each of the four MWPCs consisted of three planes of sense wires with 2 mm wire spacing, with 1.4 cm spacing between the sense planes.

A two-pion trigger is created using the scintillation counters S1 and S2, various combinations of the A and B counters, and a fast signal F0 from the MWPCs. The geometric overlap of a given A counter with a B counter defines 17 allowed combinations $(AB)_k$. Two-pion events are therefore defined by the requirement

$$\text{event} = S1 \cdot S2 \cdot F0 \cdot (AB)_m \cdot (AB)_n \quad ,$$

with $m \neq n$. Time-of-flight (TOF) signals were measured between S2 and the various AB combinations. The pulse height analog-to-digital converter (ADC) for each A and B counter was also recorded.

Monte Carlo calculations have verified that large Gamow corrections persist in the two-pion relative momentum spectra as measured by our spectrometer, precisely because the good momentum resolution of this device enables us to resolve the region of suppression. The net effect of the two-pion Coulomb interaction is to modify the correlation function

$$C_2(q,q_0) \rightarrow G(me^2/hq_{inv})C_2(q,q_0) \quad .$$

It is important that the Gamow correction be applied to the background events, rather than attempting to correct for its influence after the generation of C_2. These results are presented under the heading "Gamow corrected" in Fig. 1. In each case the radius now acquires a nonzero value, and λ increases to the range 0.6-0.7.

Fig. 2 displays the 68% and 95% confidence limits for R and τ allowed by each data set. It is clear that our maximum sensitivity is to some overall measure of the space-time extent (such as $R^2 + \tau^2$). This is simply the spatial consequence of our acceptance in momentum space (where most pions have $q \simeq q_0$). Another consequence of the R-τ correlation is that specifying one of the parameters allows the other to be determined with significantly greater accuracy.

The λ values in our work often lie significantly below unity, as do those of the Riverside group for their 1.2 GeV/nucleon data. Many authors have cited deviations of this parameter from unity as evidence for coherence in the pion source, since for a maximally coherent source one has λ=0. Furthermore, the assumption of a completely chaotic source leading to independent emission of pions is at best an approximation, since the relevant pion wavelengths are not substantially smaller than the inferred source dimensions. Nonetheless, to date, experimental complications prohibit any quantitative conclusions concerning the fraction of coherent emitters implied by a given value of λ. Other effects known to affect the value of λ, such as the averaging over unobserved reaction variables, further obscure the interpretation of deviations of this variable from unity in a given experiment, since a very complete set of measurements indeed would be required to determine which of these many contributions is the dominant one.

We have shown that a high statistics intensity interferometry measurement of pion source parameters in RHIC provides valuable information for dynamical models of these collisions. The effect of the two-pion relative Coulomb interaction has been

analyzed and found to be important, while correction for the pion-nuclear Coulomb interaction produced little change in the extracted radius and lifetime. These final state interactions, and the iterative nature of the background generation, prevent any definite statement quantifying the coherent contribution to the pion source. The results presented here are consistent with previous measurements, and should provide a basis for future experiments using larger acceptance spectrometers to apply these techniques to heavier nuclear systems.

Footnotes and References

*Condensed from Phys. Rev. **C29**, 2173 (1984)

†Institute for Nuclear Study, University of Tokyo, Tanashi, Tokyo 188, Japan.

‡University of Alberta, Edmonton, Alberta, Canada T6G 2J1.

§Boston University, Boston, MA 02215.

**University of Zurich, 8001 Zurich, Switzerland.

1. R. Hanbury-Brown and R.Q. Twiss, Philos. Mag. **45**, 663 (1954).
2. G. Goldhaber, S. Goldhaber, W. Lee and A. Pais, Phys. Rev. **120**, 300 (1960).
3. D. Beavis, S.Y. Fung, W. Gorn, A. Huie, D. Keane, J.J. Lu, R.T. Poe, B.C. Shen and F. Van Dalen, Phys. Rev. **C27**, 910 (1983).
4. G.I. Kopylov and M.I. Podgoretskii, Yad. Fiz. **19**, 434 (1974) [Sov. J. Nucl. Phys. **19**, 215 (1974)], and references contained therein.
5. M. Gyulassy, S.K. Kaufmann and L.W. Wilson, Phys. Rev. C **20**, 2267 (1979).
6. F.B. Yano and S.E. Koonin, Phys. Lett. **78B**, 556 (1978).

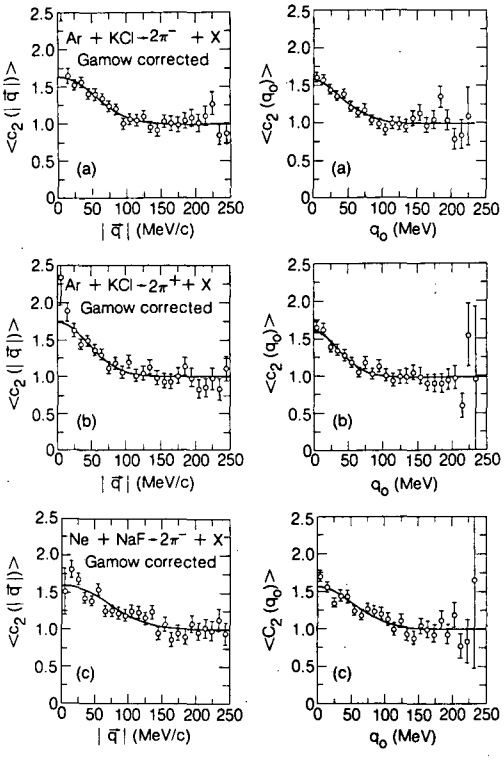

Fig. 1. Projected correlation functions after Gamow correction for the systems (a) Ar+KCl → $2\pi^-$+X, (b) Ar+KCl → $2\pi^+$+X, and (c) Ne +NaF → $2\pi^-$+X.

XBL 8311-7321

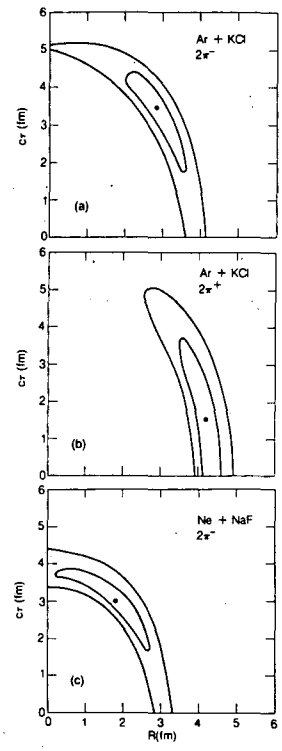

Fig. 2. Contours for the 68% and 95% confidence levels arising from fits to Eq. (10) in the text. (a) Ar + KCl → $2\pi^-$, (b) Ar + KCl → $2\pi^+$ + X, and (c) Ne + NaF → $2\pi^-$ + X.

XBL 8311-7318

Pion Production as a Probe of the Nuclear Matter Equation of State*

*J.W. Harris,† R. Stock,† R. Bock,† R. Brockmann,† A. Sandoval,† H. Ströbele,† G. Odyniec, H.G. Pugh, L.S. Schroeder, R.E. Renfordt,‡ D. Schall,‡ D. Bangert,§ W. Rauch§ and K.L. Wolf***

Equilibrium rate calculations can be used to show that thermal and chemical equilibrium should be reached during the high density stage of central nucleus-nucleus collisions and that freeze-out of the $\pi + \Delta$ chemical abundance occurs near the end of this stage, thus establishing the final pion multiplicity as a probe of the high density stage. For a mixture of π, N, and Δ gases an estimate of the extent to which chemical equilibrium is reached during the high density stage, where $\rho \sim 3\ \rho_0$ in a collision at 1 GeV/nucleon, yields an equilibration time $\tau \simeq 6 \times 10^{-24}$s. The time necessary to reach thermal equilibrium is approximately a factor of two shorter. Using a dynamical model such as the intranuclear cascade, we find the duration $t_{\rho max}$ of the high density stage to be sufficient for attaining thermal and chemical equilibrium since[1,2] $t_{\rho max} \simeq 2\tau$ for Ar + KCl and $t_{\rho max} \simeq 3.5\tau$ for La + La. However, during the expansion phase the N, π, and Δ chemical equilibration time at $\rho = 0.7\ \rho_0$ is $3 \times 10^{-23}\text{s} < \tau < 2 \times 10^{-22}\text{s}$ assuming isoergic (lower) or isentropic (upper) expansion. This time is too long for chemical equilibrium to be maintained through expansion since the time necessary for expansion[2] from ρ to $\rho/2$ is $\sim 10^{-23}$s. Therefore, the $\pi + \Delta$ yield will not freeze out at $\rho \sim \rho_0/2$ to ρ_0 as previously assumed in fireball and hydrodynamic model studies but rather at high densities near the onset of expansion. On the other hand thermal equilibrium, which determines the pion temperatures and source sizes, will be maintained to later times due to the large $\pi N \leftrightarrow$ cross section.

Displayed in Fig. 1 is the experimental pion multiplicity per participant after Δ decay ($\Delta \rightarrow \pi N$) extrapolated to zero impact parameter collisions of Ar + KCl as a function of beam c.m. energy. The experiment was performed at the Bevalac using the Streamer Chamber at 7 incident laboratory energies from 566 to 1808 MeV/nucleon. The techniques employed in the analysis have been described previously.[3] Predictions of the intranuclear cascade models of Cugnon[4] and Yariv-Fraenkel[5] are also shown. These models incorporate binary, quasi-free interactions of hadrons in a nucleus-nucleus collision geometry. Another approach which is strongly suggested by the above rate calculations is the use of a chemical model to predict the $\pi + \Delta$ abundance[6] along with the Rankine-Hugoniot relations for shock compression. This nuclear matter approach which has opposite mean free path assumptions from the cascade, similarly overpredicts the $\pi + \Delta$ to participant ratios. The failure of these models to predict the observed ratios can be attributed to compressional degrees of freedom which are not incorporated in the models. The available c.m. energy can be partitioned into thermal (pion-producing) and compressional energy fractions. An estimate of the compres-

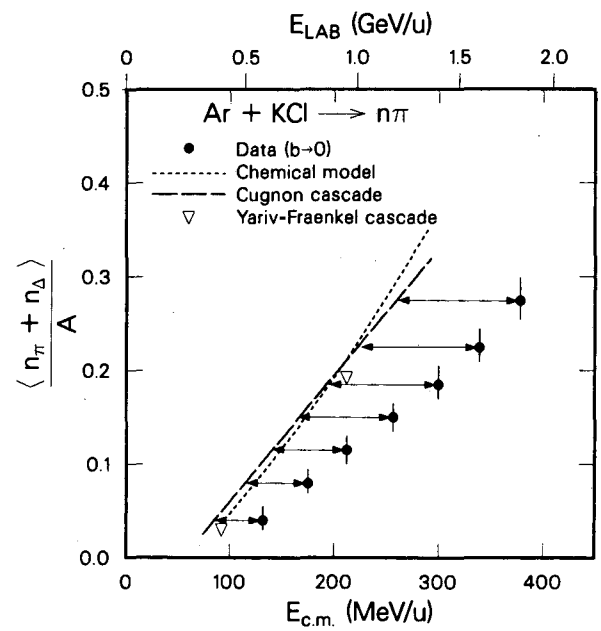

Fig. 1. The $\pi + \Delta$ yield per participant nucleon as a function of c.m. energy (lower axis) and laboratory energy (upper axis) for Ar + KCl. XCG 8312-4933

sional energy can be made from the energy offset, represented by the arrows in Fig. 1, between the energy available in the experiment and the energy at which a given model predicts the observed pion multiplicity. The resulting compressional energies as a function of the densities predicted by the models are shown independently in Fig. 2. Both approaches yield strikingly similar results which suggest a stiff nuclear matter equation of state with the same overall structure as those recently obtained from field theory.[7]

Footnotes and References

*Condensed from LBL-17404

†Gesellschaft für Schwerionenforschung, Darmstadt, West Germany.

‡University of Heidelberg.

§University of Marburg.

**Texas A&M University.

1. R. Stock *et al.*, Phys. Rev. Lett. **49**, 1236 (1982).
2. J.W. Harris and R. Stock, Proceedings of the Seventh Oaxtepec Symposium on Nuclear Physics, Oaxtepec, Mexico (1984) UNAM Press and LBL-17054.
3. A. Sandoval *et al.*, Phys. Rev. Lett. **45**, 874 (1980) and

   R. Stock *et al.*, Physica Scripta **T5**, 130 (1983).
4. J. Cugnon *et al.*, Nucl. Phys. **A352**, 505 (1981) and Nucl. Phys. **A379**, 553 (1982).
5. Y. Yariv, private communication.
6. Chemical model results provided by G.D. Westfall.
7. J. Boguta and H. Stöcker, Phys. Lett. **120B**, 289 (1983).

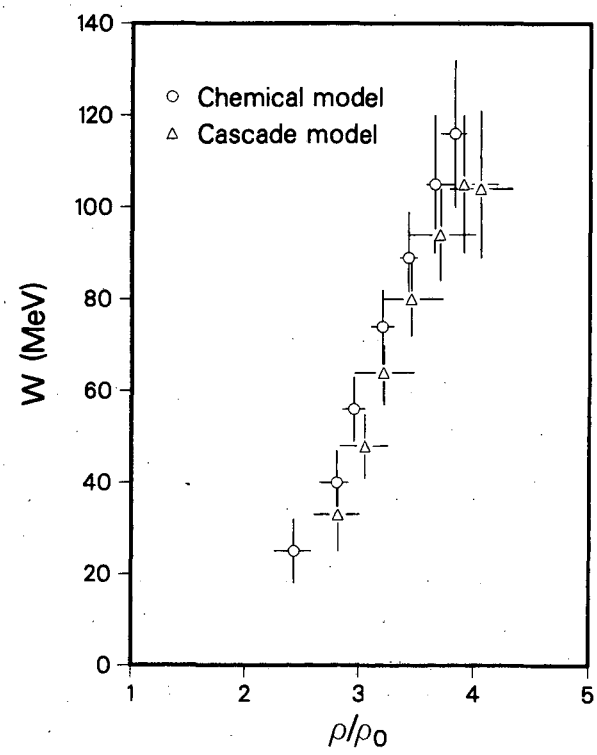

Fig. 2. The compressional energy, minus 10 MeV binding energy, plotted as a function of density in units of normal nuclear density ρ_0 derived from the data using the cascade and chemical models, respectively. XCG 8312-4936

Strange Particle Production in Central ^{40}Ca + ^{40}Ca Collisions

R.E. Renfordt, D. Bangert,† R. Brockmann,‡ A. Dacal,§ J.W. Harris, G. Odyniec, M. Ortiz,§ H.G. Pugh, W. Rauch,† A. Sandoval,‡ L.S. Schroeder, R. Stock,‡ H. Ströbele,‡ and D. Schall**

As a continuation and expansion of a previous experiment (1.8 GeV/nucleon Ar + KCl)[1] strange particle production was studied in central ^{40}Ca + ^{40}Ca collisions at 2.07 GeV/nucleon incident energy using the Streamer chamber facility. Λ^0s and K^0s were identified by their charged-particle decay. A 0.26 cm thick metallic target was used. The central trigger corresponded to 10% of the reaction cross section (σ = 2.5 b) and was associated with impact parameters b < 2.8 fm in a geometrical model.

To assure good accuracy for kinematical fits, the primary vertex of each interaction was reconstructed in space using 4 positively-charged particles and all negatively-charged pions. Only target interactions with a certain minimum χ^2 for the intersection were accepted for further analysis. The decay vertex was reconstructed using the 2 charged decay particles with a similar cut in χ^2.

For the kinematical fits the following hypotheses were tested:

$$\Lambda^0 \rightarrow p + \pi^-, \quad K^0 \rightarrow \pi^+ + \pi^-,$$

$$\bar{\Lambda}^0 \rightarrow \pi^+ + \bar{p}, \quad \gamma \rightarrow e^+ + e^- \quad .$$

For further analysis, 3c fits were used whenever possible, but 1c fits were also accepted.

Several other cuts were then applied to the data in order to avoid contamination caused mostly by gamma conversion into $e^+ e^-$ pairs. Due to finite measurement accuracy and distribution over phase space, these pairs could not always be distinguished by their kinematic fits from the Λ^0s and K^0s.

The invariant masses of Λ^0s and K^0s were required to be within 40 MeV of their theoretical values. The decay length of Λ^0s and K^0s had to be below 60 cm in the particle's rest frame. The invariant mass under the assumption of a gamma decay had to be above 40 MeV. This excluded most efficiently any gamma contamination causing only ~3% loss in the Λ^0 sample. A cut in confidence level has been applied at 0.0001.

It was found that interactions in the upstream trigger scintillator also produced Λ^0s (mainly due to interactions with carbon). The average π^- multiplicity of these events was found to be ~2. In order to completely exclude those, as well as interactions with the plastic material around the target, only events with a π^- multiplicity greater than 3 were allowed for the Λ^0 analysis.

After the above cuts were applied, the final sample consisted of 109 Λ^0s and 15 K^-s. The mean values for $p_\parallel$ and $p_\perp$ were determined. The results are listed in Table I together with the results of a Monte Carlo simulation.

Table I
Mean $p_\parallel$ and mean $p_\perp$ for Λ^0 and K^0 with results of Monte Carlo simulations (see text).

	$\langle p_\parallel \rangle$(RMS) (MeV/c)	$\langle p_\perp \rangle$ (RMS) (MeV/c)
Λ^0 data	423 ±31 (319)	574 ±26 (270)
simulation 1	334 ±24 (252)	560 ±28 (296)
simulation 2	440 ±31 (334)	564 ±25 (269)
K^0 data	232 ±72 (280)	492 ±59 (228)
simulation 1	357 ±64 (248)	564 ±79 (305)

In simulation 1 a thermal source at a temperature T_0 = 130 MeV moving with the velocity of the n-n center of mass was assumed for Λ^0 and K^0:

$$d\sigma/dE = p \cdot E \cdot \exp(-E/T_0)$$

A filter was incorporated into the simulation resembling the experimental biases as closely as possible, including finite fiducial volume, inefficiencies around the target and all the cuts applied to the data mentioned above. As can be seen from the table, this simulation reproduces the $\langle p_\perp \rangle$ very well for both Λ^0s and K^0s, but leads to a somewhat too small $\langle p_\parallel \rangle$ for the Λ^0, while for the K^0 the $\langle p_\parallel \rangle$ turns out to be too large.

In simulation 2, two thermal sources with the same temperature were assumed to move with a velocity ± 15% of the n-n center-of-mass velocity. While $\langle p_\perp \rangle$ remains unchanged, $\langle p_\parallel \rangle$ increases to the value observed for the Λ^0s. Nevertheless, we conclude that the phase space distribution of the Λ^0s and K^0s is surprisingly close to a thermal distribution with a temperature of 130 MeV. The data published previously[1] are compatible with this result.

The measured invariant masses are 1115 MeV (σ=5.1 MeV) and 494 MeV (σ=10.9 MeV) for the accepted Λ^0s and K^0s, respectively. The mean weight for these Λ^0s due to finite fiducial volume and the branching ratio of 0.64 for $\Lambda^0 \rightarrow p + \pi^-$ is 5.9.

In order to investigate the energy balance of the system, we analyzed the π^- multiplicity and the energy distributions of the Λ^0 and K^0 events and compared them to "average" events without Λ^0s or K^0s. The π^- distributions have been fitted to a

Boltzmann distribution. Since the angular distribution of the π^- is not completely isotropic, a separate fit has been performed for π^- emitted around 90 degrees in the CM system. The results are listed in Table II, along with results of the analysis of a subsample of the data containing events without Λ^0s or K^0s.

At the present state of the analysis only a lower bound for the Λ^0 production cross section can be given: $\sigma_{\Lambda^0} > 8$ mb. The K^0 cross section is in the same range.

Footnotes and References:

*Institut für Hochenergiephysik, Universität Heidelberg, D-6900 Heidelberg, West Germany

†Fachbereich Physik, Universität Marburg, D-3550 Marburg, West Germany

‡Gesellschaft für Schwerionenforschung (GSI), D-6100 Darmstadt, West Germany

§Instituto de Física, UNAM, Mexico D.F., Mexico

1 J.W. Harris *et al.*, Phys. Rev. Lett. **47**, 229 (1981)

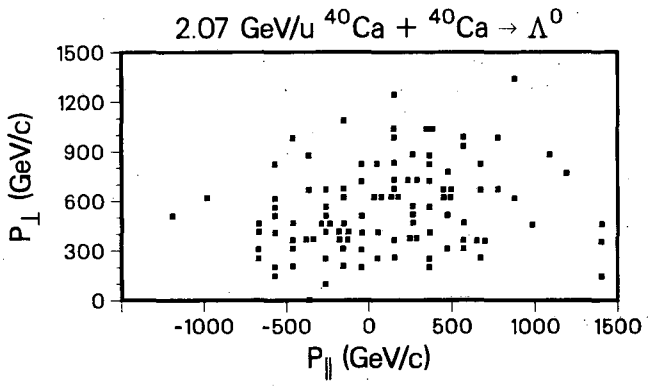

Fig. 1. $p_\parallel$ vs $p_\perp$ in the center of mass for Λ^0s.
XBL 8410-13346

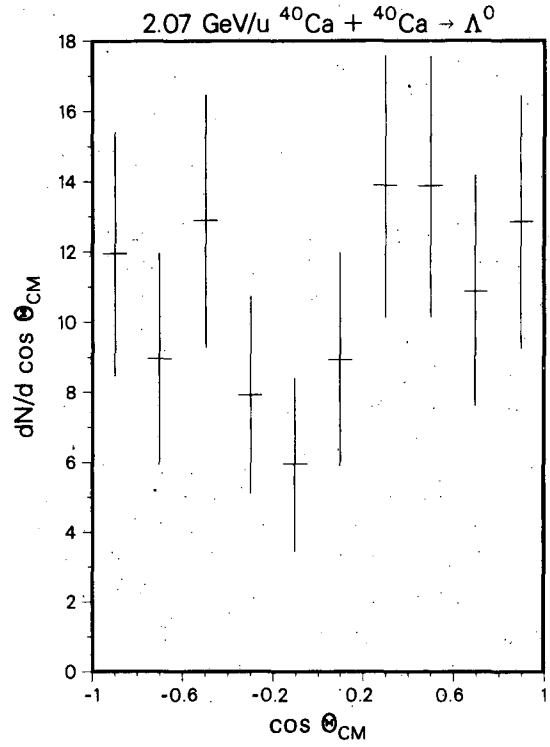

Fig. 2. (a) Distribution of cos θ_{CM} of Λ^0s.
XBL 8410-13347

Table II

Pion temperatures and mean π^- multiplicities of "average" events compared to Λ^0 and K^0 events. For calculation of $<\pi^->$ only multiplicities above 3 have been used, due to the cut applied for the Λ^0s. The apparent lower temperature for the K^0 events is mainly due to the lower statistics, which tend to reduce the mean value for the asymmetric energy and multiplicity distributions.

	T_{all} (MeV)	$T_{90°\pm40}$ (MeV)	$<\pi^->$
"average" events	79 ±1	76 ±1.2	6.5 ±0.1
Λ^0 events	79 ±2	77 ±3	6.8 ±0.2
K^0 events	65 ±6	62 ±8	6.6 ±0.7

Pion and Proton "Temperatures" in Relativistic Heavy Ion Collisions.

R. Brockmann, D. Bangert,† J.W. Harris, G. Odyniec, H.G. Pugh, W. Rauch,† R.E. Renfordt,‡ A. Sandoval,* D. Schall,‡ L.S. Schroeder, R. Stock,* H. Ströbele,* and K.L. Wolf§*

An understanding of pion production in relativistic heavy ion collisions is needed for several reasons. Firstly, pion production has been suggested as a probe of compressional energy in the high density phase of near head-on collisions.[1] Secondly, a comparison between pion and proton energy spectra has been suggested as a method of identifying the presence of collective flow effects in the expanding nuclear system.[2] Previous experimental studies of the pion spectra have been for inclusive measurements only.[3] Attempts have been made to fit the results using a variety of hypotheses, including collective flow[2] and different freeze-out times for the pions and protons.[4] The most successful method has been the intranuclear cascade model,[5] based upon Δ-dominance in the production mechanism.

In the present Streamer Chamber experiment[6] we have used a central collision trigger to provide a well defined collision geometry as close to an idealized "fireball" as possible, and to eliminate complications such as spectator matter effects.

The pion and proton energy spectra at 90° in the NN-cm system are found to be close to Boltzmann-like temperature distributions, but with very different temperatures. For Ar + KCl at 1.8 GeV/nucleon, e.g., we find a proton temperature of T=120 MeV and a pion temperature of T=69 MeV, using a one temperature component fit.

In order to understand the vastly different proton and pion temperatures, it is necessary to consider a thermal system of nucleons and Δs. As far as Δ formation and decay govern the pion production process, most of the observed pions result from a resonance decay. This two body decay introduces a distinctly non-thermal aspect into the pion spectra. Thus, although the Δ fraction of the expanding system may well be in thermal equilibrium with the nucleons, the finally established pion spectra have the two-body decay kinematics superimposed on the thermal distribution of the parent Δ states. The resultant pion and proton spectra are quite similar to Boltzmann distributions, but at effective temperatures which are not equal to the temperature of the emitting system of Δs (and nucleons).

This parent-daughter mechanism provides a simple relationship between proton and pion temperature on the one hand and Δ temperature and mass on the other. Fig. 1 shows the proton and pion "temperatures" (a) as a function of the Δ temperature for a Δ mass m=1232 MeV and (b) as a function of the Δ mass for a fixed Δ temperature T=135 MeV. One sees that the proton temperature reflects mainly the Δ temperature while the pion temperature is sensitive to the Δ mass.[7]

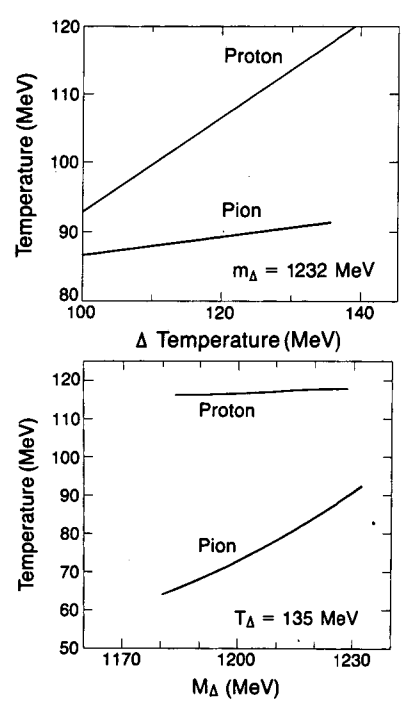

Fig. 1. (a) Dependence of pion and proton temperatures T_π and T_p on Δ temperatures T_Δ for m_Δ = 1232 MeV; (b) Dependence of T_π and T_p on m_Δ for T_Δ = 135 MeV XBL 844-10396A

It is interesting to study next to what extent our conclusions might be modified by the presence of collective flow. We investigated in detail the simplified situation in which a system of thermalized pions and protons with temperature T expands radially with a constant flow velocity.[2] As demonstrated in Fig. 2, pion and proton energy spectra cannot be fitted with the same flow velocity and temperature simultaneously, ruling out the possibility that a simple radial flow superimposed on thermalized pions and protons can explain the difference in the apparent temperature of pions and protons. It remains an open question to what extent more complicated collective flow patterns can be introduced to fit both the proton and pion energy spectra.

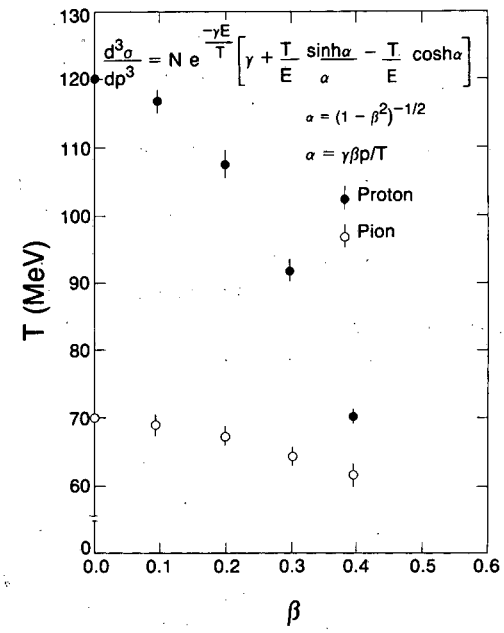

Fig. 2. Dependence of the temperature T of a Boltzmann-like energy spectrum on superimposed collective flow with velocity β. Proton spectrum with T = 120 MeV and pion spectrum with T = 70 MeV. XBL 8410-10901

Footnotes and References

*Gesellschaft für Schwerionenforschung (GSI), D-6100 Darmstadt, West Germany

†Fachbereich Physik, Universität Marburg, D-3550 Marburg, West Germany

‡Institut für Hochenergiephysik, Universität Heidelberg, D-6900 Heidelberg, West Germany

§Cyclotron Laboratory, Texas A&M University, College Station, Texas 77843

1. R. Stock *et al.*, Phys. Rev. Lett. **49**, 1236 (1982)
2. P. Siemens and J. Rasmussen, Phys. Rev. Lett. **42**, 880 (1979); H. Stoecker, A.A. Ogloblin and W. Greiner, Z. Phys. **A303**, 259 (1981)
3. S. Nagamiya *et al.*, Phys. Rev. **C24**, 971 (1981)
4. S. Nagamiya, Phys. Rev. Lett. **49**, 1383 (1982)
5. J. Cugnon, D. Kniet and J. Vandermeulen, Nucl. Phys. **A379**, 553 (1982)
6. A. Sandoval *et al.*, Nucl. Phys. **A400**, 365c (1983)
7. R. Brockmann *et al.*, LBL-17755

Search for Fractionally Charged Nuclei in High-Energy Heavy Ion Collisions*

S.W. Barwick, J.A. Musser† and J.D. Stevenson‡

Projectile fragments of 1.8 GeV/nucleon ^{40}Ar were used to search for fractionally charged nuclei. We present results of the first large statistics electronic counter telescope experiment. Price *et al.*[1] measured the charges of 1027 projectile fragments of 1.8 GeV/nucleon ^{40}Ar using CR-39 plastic track detectors. They found no fragments with residual charge, ΔZ_r = Z - nearest integer, with $|\Delta Z_r| > 0.25e$. Lindgren *et al.*[2] used an indirect detecting technique to place limits on the frequency of production of fractionally charged particles from 1.9 GeV/nucleon Fe + Pb collisions ranging from 1×10^{-4} to 5×10^{-7} per collision (depending on the assumptions made about collection efficiency).

The detector design and trigger logic were dictated by the main objective of the experiment, a search for "anomalons." The detector, shown in Fig. 1a, is a fifteen element telescope. It consisted of a

beam-defining trigger scintillator followed by fourteen Čerenkov detectors in thicknesses of 3.5 mm, 6.25 mm and 1.27 cm. Each element was connected by a lucite light guide to a 3″ diameter (RCA 4900) photomultiplier tube. The detectors were mounted radially about the beam axis (see Fig. 1b). This configuration allowed the detectors to be placed in contact to form a solid segmented stack 8.4 cm long so that fractionally charged nuclei with lifetimes as short as 10^{-10} sec could be observed.

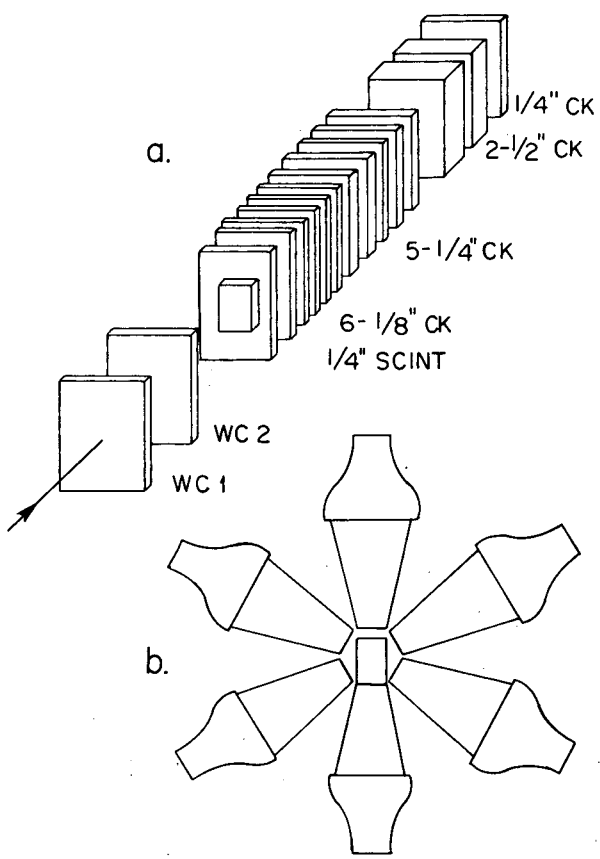

Fig. 1a. A schematic exploded view of the detector consisting of a pair of wire chambers WC1 and WC2, followed by a 15 element detector telescope consisting of a 6.25 mm (1/4″) beam defining scintillator followed by, in order, 6-3.5 mm (1/8″) Čerenkov counters, 5-6.25 mm (1/4″) Čerenkov counters, 2-1.25 cm (1/2″) Čerenkov counters, followed by 1-6.25 mm (1/4″) Čerenkov counter. Fig. 1b. Shows how the detectors were actually mounted to form a solid segmented stack. XBL 841-6578

The charge resolution of the individual detectors for the ^{40}Ar primary beam ranged from σ_z = 0.15e in the 1.27 cm thick detectors to σ_z = 0.25e in the 3.5 mm thick elements. The charge resolution for secondaries degrades from the beam values with decreasing $Z_{leading}$. For $Z_{leading} \leq 13$ the charge resolution was inadequate for the search for fractional charges.

The basic criterion for accepting the event was that the secondary be produced in one of the first two Čerenkov detectors and then survive intact through the rest of the detector stack. Events with two or more interactions were eliminated by requiring the third and last Čerenkov signals to agree to within 0.7e. This cut reliably eliminates events with second interactions in which the charge changes by more than one charge unit. In order to remove ΔZ = 1 interactions, the signals from the Čerenkov detectors 3 to 14 were tested for constancy of charge signal and a chi-squared cut was applied. A total of 1.75 x 10^5 secondary projectile fragments were analyzed. The usable number of events fell to 2.2 x 10^4 after the removal of each secondary that failed to satisfy the chi-squared cut, had $Z_{leading} \leq 13$, did not pass the consistency requirement or had its first interaction downstream of the second Čerenkov counter.

A charge histogram of the data is shown in Fig. 2. The charge resolution ranges from σ_z = 0.098 at Z = 14 to σ = 0.070 at Z = 17. A histogram with an expanded scale, to make single counts visible, is shown in Fig. 3. No counts are present with residual charge greater than 1/3e for events with Z >= 14. Events with apparent residual charge greater than 1/3e first occur on the low side of the Z = 14 peak. Our limits on +1/3e residual charge nuclei differ from limits placed on nuclei of residual charge -1/3e due to the exclusion of the Z = 14 peak from the -1/3e result. The limits on fractional charged projectile fragments are F < 1.72 x 10^{-4} (90% CL) for +1/3e residual charge and F < 2.83 x 10^{-4} (90% CL), where F is the ratio of fractional charge to integer charge projectile fragments. This experiment, although statistics are limited, is clearly quite close to being limited by detector resolution. Rather modest improvements in

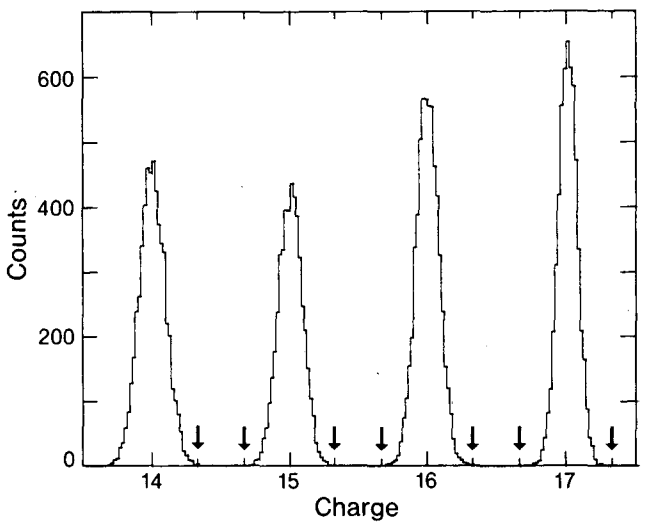

Fig. 2. A charge histogram of the data for charges Z = 14–17. The arrows indicate the peak location for fractionally charged nuclei, with residual charge of ± 1/3e. XBL 8410-4288

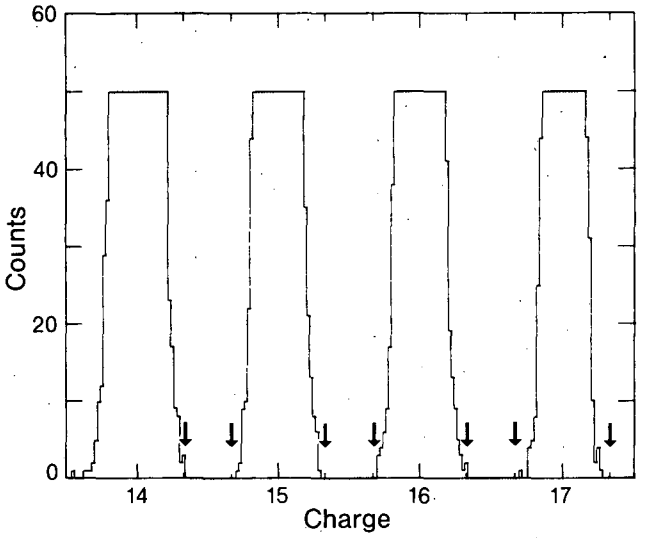

Fig. 3. Same histogram as Fig. 2 but with an expanded vertical scale to allow single counts to be visible. No events greater than Z = 14 have residual charge greater than ± 1/3e. XBL 8410-4287

charge resolution, to σ_z = 0.06e, would reduce the resolution limit to the F < 10^{-6} level. Such an improvement appears to be possible, simply by increasing the total detector thickness to 12 cm.

Footnotes and References

*Condensed from a paper published in Phys. Rev. D Rapid Communications **30**, 691 (1984).

†Present address: Department of Physics, Randall Laboratory, University of Michigan, Ann Arbor, MI 48109.

‡Present address: National Superconducting Cyclotron Laboratory, Michigan State University, East Lansing, MI 48824.

1. P.B. Price *et al.*, Phys. Rev. Lett. **50**, 566 (1983).
2. M.A. Lindgren *et al.*, Phys. Rev. Lett. **51**, 1621 (1983).

Search for Production of Fractional Charges, Rare Long-Lived Particles and Subthreshold Antiprotons in Relativistic Heavy Ion Collisions

S. Abachi,† J. Carroll,† A. Shor,‡ E. Barasch,§ G. Igo,† T. Mulera, P. Fisher, V. Perez-Mendez, S. Trentalange,† K. Ganezer† and F. Kazeminezhad†

Recently Shaw and Slansky[1,2] have proposed a theory in which SU(3) color is spontaneously broken to SO(3) glow. This symmetry breaking allows quark-quark composites with masses on the order of 1 GeV to be created. In particular, they emphasize the possibility of such diquark production via a color screening effect in Relativistic Nuclear Collisions (RNC).

We have previously reported the subthreshold production of K^- in RNC with yields about 20 times larger than explicable by such trivial mechanisms as Fermi momentum of the nucleons.[3,4] A study of antiproton production, whose production threshold is much higher than that for kaons, might shed some light on subthreshold production mechanisms in RNC.

In parallel with our measurement of the momentum spectrum for subthreshold $K^{(mi}$ production[4] we have carried out a search for the production of fractional charges, rare long-lived particles and subthreshold antiprotons in $^{28}Si + ^{28}Si$ collisions at 2.1 GeV/nucleon. Negative secondaries produced at 0° were selected for six values of secondary rigidities and transported along a magnetic beam line. Three bends, each followed by a detector station instrumented with scintillators and Čerenkov counters, allowed multiple measurement of particle velocities which when combined with the rigidity selection yielded the particle mass.

We did not observe production of any fractionally charged or rare long-lived particles nor did we observe any convincing evidence of antiproton production. Some rather stringent upper limits for these processes were obtained and are summarized in Table I. Table I shows the upper limits on $d^2\sigma/d\Omega dR$ where the rigidity $R = P/Z$. The acceptance of the beam line/spectrometer, due to energy degradation and multiple scattering, is a function of mass and charge. The tabulated results, except for those for $\bar{p}$ only, where the mass is known, are averaged over ranges in mass where the upper limits did not vary by more than a factor of three due to acceptance variations. In Fig. 1 these results are translated into upper limits on the total yields of fractional charges in terms of the number produced per collision. These results are obtained from an integration assuming an exponential form for the invariant differential cross section, with a slope of 100 MeV, and isotropy of production in the center of mass. These results have been corrected for acceptance variations as a function of charge and mass.

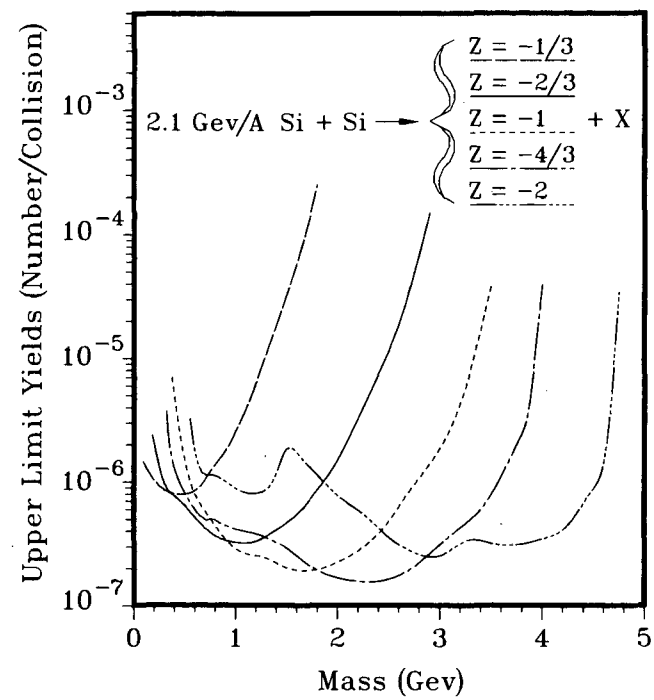

Fig. 1. Upper limits for the yields of fractional charges in terms of the number per nucleus-nucleus collision as a function of particle mass. These results are dependent on a model which assumes an exponential energy spectrum with a slope parameter of 100 MeV and that the particles of interest are produced isotropically in the center of mass.

XBL 8410-4065

Footnotes and References

*Condensed from LBL-17066 (1984) and Physical Review Letters to be published.

†UCLA, Los Angeles, CA 90024.

‡LBL and UCLA, Los Angeles, CA 90024.

§UC Davis, Davis, CA 95616.

1. R. Slansky, T. Goldman and G.L. Shaw, Phys. Rev. Lett. **47**, 887 (1981).
2. G.L. Shaw and R. Slansky, Phys. Rev. Lett. **50**, 1967 (1983).
3. A. Shor *et al.*, Phys. Rev. Lett. **48**, 159 (1982).
4. E. Barasch *et al.*, LBL-17065 (1984) and Phys. Rev. Lett. to be published. A condensed version is included in this report.

Table I. Upper Limits
90% Confidence Level

Rigidity (GeV/c)/Z	Mass Ranges for Different Charges (GeV)						$d^2\sigma/d\Omega dR$ $\left(\frac{\mu \text{ barn}}{\text{sr (GeV/c)/Z}}\right)$
	Z = −1/3	Z = −2/3	Z = −1	Z = −4/3	Z = −2	All Objects	$\bar{P}$ Only
0.732	0.09 →0.50	0.18 →0.55	0.37 →0.80	0.36 →0.82	0.55 →1.05	6.0	1230.0
0.902	0.10 →0.52	0.20 →0.82	0.45 →1.15	0.40 →1.20	0.64 →1.40	4.3	10.8
0.980	*	0.80 →1.10	0.49 →1.20	0.44 →1.30	0.70 →1.50	2.5	4.1
1.420	0.16 →0.80	0.32 →1.25	0.71 →1.55	0.64 →1.65	0.96 →2.20	3.8	5.5
1.950	0.21 →1.20	0.42 →2.10	0.97 →2.60	0.84 →2.70	1.28 →3.10	0.9	0.9
2.370	0.26 →1.70	0.52 →2.60	1.18 →3.20	1.04 →3.50	1.54 →4.20	1.0	1.0

*Old data from 1981 run. These data were not sensitive to charge -1/3 and low mass objects with charge -2/3.

Subthreshold K^- Momentum Spectrum for Relativistic Nuclear Collisions*

E. Barasch,† A. Shor,‡ S. Abachi,§ J. Carroll,§ P. Fisher, K. Ganezer,§ G. Igo,§ T. Mulera, V. Perez-Mendez, and S. Trentalange§

We recently measured the momentum distribution of subthreshold K^- particles produced in the reaction $^{28}Si + ^{28}Si$ at 2.1 GeV/nucleon, using a secondary beam line as a magnetic spectrometer.[1] Particle identification was achieved using multiple measurements of TOF and dE/dx and by using two sets of threshold Čerenkov counters. New results of this measurement are shown in Fig. 1 where we plot the K^- invariant production cross section as a function of the kaon kinetic energy in the Si-Si center of mass frame. This analysis has shown the data to be consistent with an exponential distribution in energy with a slope parameter of 91 ± 7 MeV.

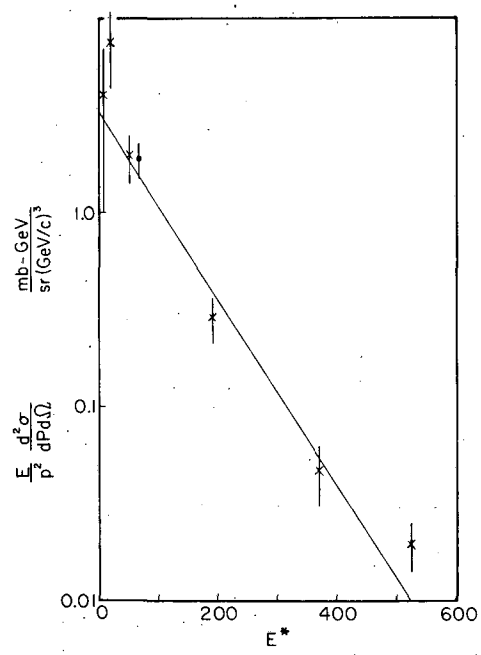

Fig. 1. Energy distribution in the c.m. system of the K^- produced in Si–Si collisions. The straight line represents an exponential with a slope parameter of 91 MeV. XBL 848-3471

Footnotes and References

*Condensed from LBL-17065 (1984) and Physics Letters to be published.

†University of California at Davis, Davis, CA 90024
‡LBL and University of California at Los Angeles (UCLA), Los Angeles, CA 90024
§University of California at Los Angeles (UCLA), Los Angeles, CA 90024

1. A. Shor *et al.*, LBL-16175 and 1983 NSD Annual Report (LBL-16870)

Electron Pair Production Study Using the Di-Lepton Spectrometer (DLS)

G. Roche, J.B. Carroll, G. Claesson, R.L. Fulton, J.-F. Gilot,† T.J. Hallman,‡ D.L. Hendrie, G. Igo,* P.N. Kirk,† G. Krebs, L. Madansky,‡ H. Matis, D. Miller,§ J. Miller, T.A. Mulera, V. Perez-Mendez, H.G. Pugh, L.S. Schroeder and S. Trentalange**

The DLS collaboration is proposing to study the production of low mass electron pairs (up to the ρ mass) in p-nucleus collisions up to 5 GeV and in nucleus-nucleus collisions up to 2 GeV/nucleon. The design of the experimental setup is being done to accommodate multiplicities comparable with those from ^{40}Ca + ^{40}Ca at 2.1 GeV/nucleon. This would be the second step in the study of direct electron production at Bevalac energies, which started with single electron measurements still in progress (see another article in the present Annual Report).

Experimental di-electron production resulting from 13-GeV/c proton bombardment of beryllium targets at KEK,[1] for example, shows low-mass pair production at a level of about 10^{-4} of the pion production rate, and an order of magnitude greater than predicted from the Drell-Yan process. Cross sections for formation of these low mass pairs, using the 16-GeV/c π^- p reaction at SLAC[2] and the 17-GeV/c π^- p reaction at Brookhaven,[3] are comparable with the KEK yields. At higher energies, in p-p collisions at the ISR for example,[4] low-mass low-p_T di-muons and di-electrons are produced at a rate an order of magnitude greater than expected from the hard Drell-Yan quark-antiquark annihilation process or the decay of heavy flavors, e.g., J/Ψ, Υ. Using the lower energy of 800 MeV at LAMPF[5] a single electron experiment found no direct production at the level of 3 x 10^{-6} per pion.

Low-mass lepton pair models are definitively at the quark-gluon level. Possible sources are discussed in ref. 2. The production and semileptonic decay of charmed particle pairs would result in charmed particle cross section values much higher (10 to 100) than the estimated ones at 16 GeV/c. The Drell-Yan mechanism describes di-lepton production in terms of the annihilation of valence quarks in the initial state particles in an impulse approximation approach. As such, it is expected and found to be valid at high di-lepton mass, but not in the region of the low mass continuum. A somewhat more successful class of models is based on the annihilation of $q\bar{q}$ pairs created during the hadron collision or through the formation of a quark-gluon plasma. The mass distribution resulting from these soft parton models agreed fairly well with the data, but the corresponding x and p_T^2 spectra were not very well reproduced. D. Blockus *et al.*[2] have made calculations assuming that the Dalitz-like mechanism $q\bar{q}\rightarrow\gamma\ell\bar{\ell}$ is the dominant source of low-mass di-lepton pairs. This assumption describes quite well the principle features of their 16-GeV/c πp di-lepton data. However, M.R. Adams *et al.*[3] show that the Dalitz-like mechanism cannot be the only process and conclude that gluon and virtual photon radiation from internal quark charges plays a dominant role, together with annihilation of quark-anti-quark pairs. Other models that have been proposed include internal conversion of virtual photons generated by the bremsstrahlung of virtual charged particles produced in the interaction and pion-pion and quark-pion interactions.

The DLS experimental setup consists of a segmented target (about 5 segments) and two symmetric arms, each including a large acceptance dipole magnet, a scintillator hodoscope which provides the first level trigger, segmented gas Čerenkov counters for electron identification and second level trigger, and drift chambers for tracking. Several lead glass blocks located behind the scintillator hodoscope will be used to check the hadron rejection power of the Čerenkov counters. Fig. 1 shows the layout of one arm. It is quite compact. Each arm can move independently from approximately 35° to 70°, which is well suited to 90° cm angles for electrons at beam energies of 4.9 GeV (31.7° lab), 2.1 GeV/nucleon (43.4° lab) and down to 1 GeV/nucleon (53.9° lab).

We are planning to make the front-Čerenkov counter in 2 segments, mostly for technical reasons,

and the rear counter in 8 segments in order to have a probability of 2 charged particles (1 electron and 1 hadron) in the same segment less than about 20% (in Ca + Ca measurements). We are planning to use CO_2 in both counters (or perhaps Freon 114 in the front), the lengths being about 25″ in the front and 35″ in the rear, which would give a $\pi^{\pm}$ to electron rejection factor of the order of 10^5 and an electron efficiency of 90%, according to our present single electron experiment. The front drift chambers will be of the uniform cathode potential type, with 6 sense wire planes. The rear drift chambers will probably be of the field shaping type. A total of approximately 1000 sense wires will be used on each arm. The hodoscopes will have about 16 segments each, with 2 phototubes per segment.

The large aperture dipole magnets have a pole width of 44″ and a useful gap of 15″, which gives an angular acceptance of about 170 msr when the exit of the pole is located at 62″ from the target, as shown in the layout. We assume that a mass resolution of 5% at the ρ peak is good enough. This value can be achieved with a typical central field of 3 kG and a pole length of 20″ (effective field length of 26″).

At the time of writing of this article, we are envisioning the first test runs of the system by the fall of 1985.

Footnotes and References

*University of California at Los Angeles.

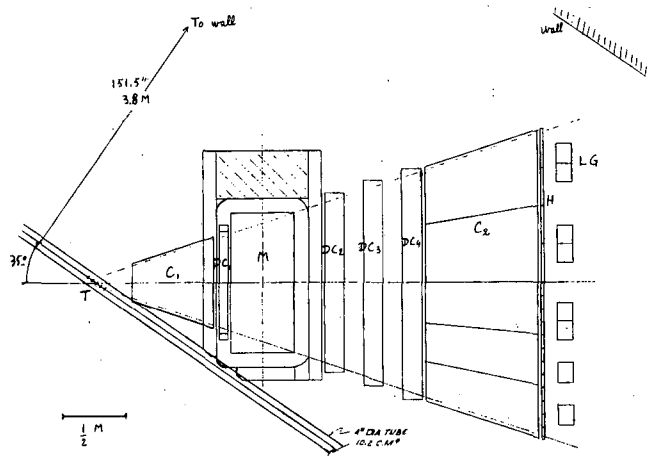

Fig. 1. Layout of one arm of the DLS.

XBL 8410-8806

†Louisiana State University.

‡The Johns Hopkins University.

§Northwestern University.

1. A. Maki *et al.*, Phys. Lett. **106B**, 423 (1981); S. Mikamo *et al.*, Phys. Lett. **106B**, 428 (1981).
2. D. Blockus *et al.*, Nucl. Phys. **B201**, 205 (1982).
3. M.R. Adams *et al.*, Phys. Rev. **D27**, 1977 (1983).
4. M. Barone *et al.*, Nucl. Phys. **B132**, 29 (1978).
5. A.Browman *et al.*, Phys. Rev. Lett. **37**, 246 (1976).

Direct Electron Production

J. Carroll, G. Claesson, J.F. Gilot,† T. Hallman,‡ D. Hendrie, G. Igo,* P.N. Kirk,† G. Krebs, F. Luehring, L. Madansky,‡ H. Matis, J. Miller, D. Miller,§ T. Mulera, V. Perez-Mendez, H. Pugh, G. Roche, L. Schroeder, A. Shor, S. Trentalange**

Several measurements of direct single lepton production in hadron collisions have been made over the past 10 years (See, for example, ref. 1). These data suggest that the electron to pion ratio at low transverse momentum remains surprisingly constant over an enormous range of bombarding energies; its value being approximately 1–5 $\times$ 10^{-4} in the energy interval 10–300 GeV. For example, Maki et al.[1] have recently determined the single electron to pion ratio for p+Be at 12 GeV and obtained results greater than the 10^{-4} level. Proton experiments at Columbia (580 MeV)[2] and LAMPF (800 MeV),[3] however, find no evidence for direct lepton production and place the upper limit on the electron to negative pion ratio at 3–5 $\times$ 10^{-6}. Protons delivered by the Bevalac, then, are especially suited

to explore the lower half of this gap in the data which spans 1 to 12 GeV.

We have recently completed a measurement of the excess electron to pion ratio in the p+Be system at a proton kinetic energy of 2.1 GeV. This experiment was performed on the Two-Arm Spectrometer System (TASS). A schematic diagram of the apparatus is given in Fig. 1.

The two arms of the spectrometer were fitted with identical sets of detectors. Each arm consisted of a dipole magnet, 3 scintillation counters, 3 scintillation hodoscopes, 2 threshold gas Čerenkov counters and a lead glass shower counter. The Čerenkov detectors were filled with carbon dioxide gas at atmospheric pressure; their average electron detection efficiency was found to be about 93%, while the pion rejection power of each pair of Čerenkov counters was measured to be about 5 x 10^{-5}.

The target chamber was designed to reduce the target-out subtraction and sources of systematic errors inherent in previous measurements. Protons were focused onto single beryllium targets which ranged in thickness from 0.020″ to 0.505″. Particles produced in the target then passed through the first scintillation counter which was a thin (0.010″) foil mounted inside the target vacuum box in order to minimize the amount of material between the target and the first detector. Background subtraction in this experiment was found to be negligible.

For a given angle and transverse momentum, one expects the electron to pion ratio to be a linear function of target thickness since the electrons arise from the decay of neutral pions in the target or the conversion of their product gamma rays. We write:

$$R = R_0 + b + ct \quad ,$$

where R is the electron to pion ratio, t is target thickness, c is proportional to the fraction of electrons due to Bethe-Heitler conversion in the target, b is proportional to the combined production from Dalitz decay and Bethe-Heitler conversion in the first detector, and R_0 is the residual production which is the object of our measurement.

The data are usually presented as a graph of R versus target thickness, from which R_0 may be found by extrapolating the data to a negative target thickness, t= −b/c. Since this distance is the ratio of two electron spectra – each produced by kinematically similar mechanisms – it is fairly insensitive to the shape of the parent pion spectrum. Monte Carlo calculations of this extrapolation length using very different pion spectra as input corroborate this fact.

To date, approximately half of the total data sample has been analyzed. As an example, a summary of the analyzed data for the right spectrometer arm is given in Fig. 2 for both positrons and electrons. These points must still be corrected for pion multiple scattering, absorption, and energy loss, as well as electron collision losses, multiple scattering and bremsstrahlung. These quantities must be found through a Monte Carlo simulation of each process. Fortunately, the corrections are both small and accurately computed. The sum of these effects is about −4% for the thickest target, but less than −1% for the thinnest targets. These corrections change the slope of the data, and hence, the extrapolation value. In addition, an overall normalization factor must be calculated to take into account the Čerenkov efficiency and losses due to pion absorption and decay in the spectrometer.

It would be reckless of us, naturally, to speculate on the magnitude of the residual ratio without further careful investigation of these corrections and an analysis of certain diagnostic runs performed at the same time as the above experiment. A definite statement of the error on these measurements can be made, however. For the entire data sample the error on the electron to negative pion ratio should be about 5 x 10^{-5}, while for the positron to positive pion ratio the error will be about 5 x 10^{-6}. Data analysis will be completed within 1 or 2 months.

Two further (preliminary) data sets were taken on the systems p+Be (4.9 GeV) and Ne+NaF (2.1 GeV/nucleon) to investigate the feasibility of extending the single lepton measurements to higher energies and heavier systems. In each case we studied the capability of the counters, as well as key elements of the data analysis, such as track reconstruction and

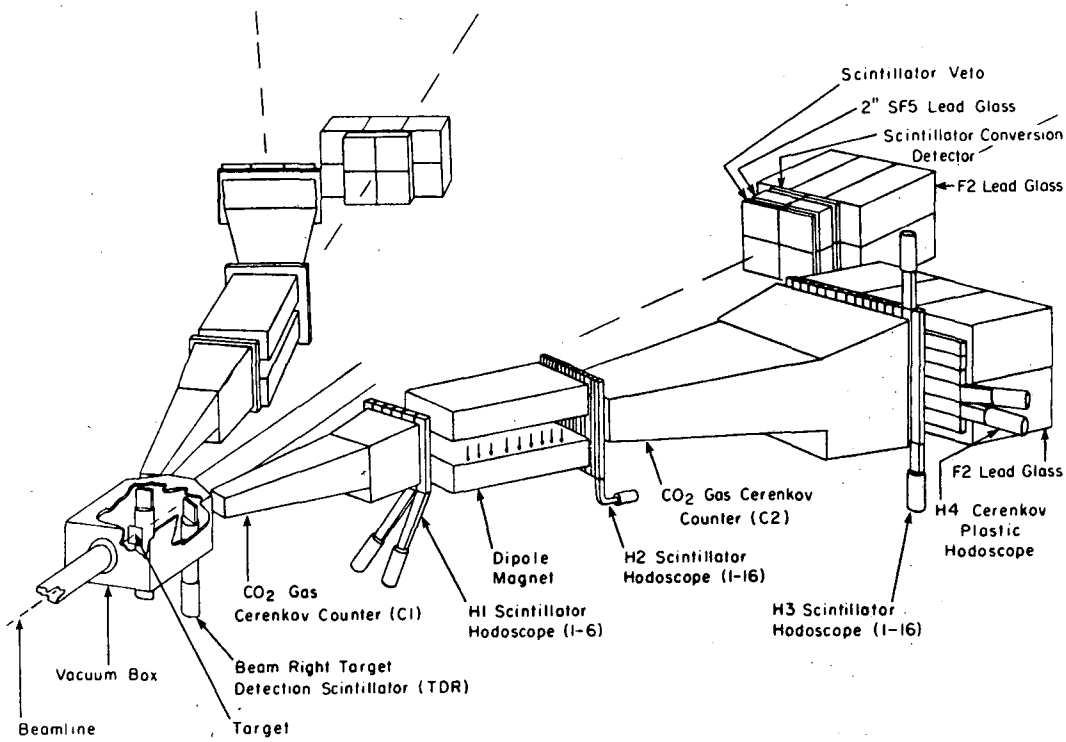

Fig. 1. Schematic diagram of the TASS system. XBL 8411-4753

electron/pion discrimination. These runs demonstrated the ability to handle the higher event multiplicity without modifying the present apparatus. Running time for both of these experiments has been approved and data acquisition will be completed during this fiscal year.

Footnotes and References:

*University of California, Los Angeles
†Louisiana State University
‡Johns Hopkins University
§Northwestern University

1. A. Maki *et al.*, Phys. Lett. **106B**, 423 (1981)
2. E. Dwyer, Ph.D. Thesis, Columbia University, unpublished
3. A. Browman *et al.*, Phys. Rev. Lett. **37**, 246 (1976)

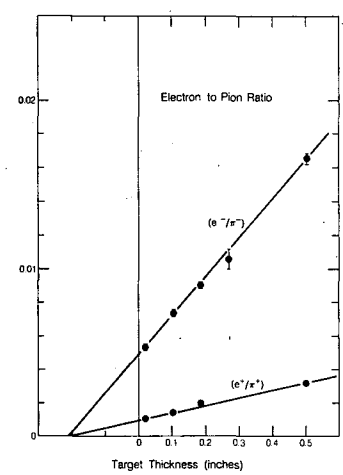

Fig. 2. Average electron to pion ratios vs. target thickness for the system p+Be at 2.1 GeV. Data for both charges are given. Errors on the positive data are roughly the size of the points. XBL 8411-4754

PART III: THEORY

Calculated Masses and Decay Properties for the Heaviest Elements*

*G.A. Leander,† P. Möller,‡ J.R. Nix§ and W.M. Howard***

Apart from the interest in probing the proton drip line and in studying very neutron-rich nuclei, there is great interest in investigating the region of very high Z values. We shall here focus our study on nuclei in this region, in particular on nuclei with Z between 100 and 122. The region from Z=100 and beyond is a fascinating one, with many nuclear properties changing rapidly with proton and neutron number, for instance the fission half-life, the mass-asymmetry in fission and the fission kinetic energies.[1] The most recent new elements identified in this region are nuclei with Z=109[2] and Z=108.[3] Additional nuclei at the tip of the peninsula of known elements, in particular very neutron-rich nuclei, may become accessible to study in the future through the LEAP[4] (Large Einsteinium Accelerator Program).

In our study here we have calculated nuclear ground state masses by use of the model presented in ref. 5, with the parameter set from ref. 8, but extended the calculations to additional nuclei up to Z=122. A table where we list calculated ground-state masses, Q_α, Q_β and Q_{EC} will be published elsewhere. However, since there were some masses missing in the calculation of ref. 5 for Z=108 and Z=109 that are now of interest in connection with the recent discoveries[2,3] of these elements we give the results for these missing elements here. Thus for $^{264}108$ and $^{265}108$ our new calculation gives the mass excesses 120.90 and 121.95 MeV respectively. For the isotopes $^{264\text{-}268}109$ the results are 128.26, 127.77, 128.52, 128.19 and 129.05 MeV respectively.

From the calculated ground-state masses we have determined the corresponding α-decay energies Q_α and α half-lives T_α. In Fig. 1 we show α half-lives for nuclei in the range Z=100 to Z=110, calculated according to the systematics of α-decay as given by Viola and Seaborg.[6] The half-lives vary fairly smoothly as functions of proton and neutron number except for cusps around N=152 and N=162. The

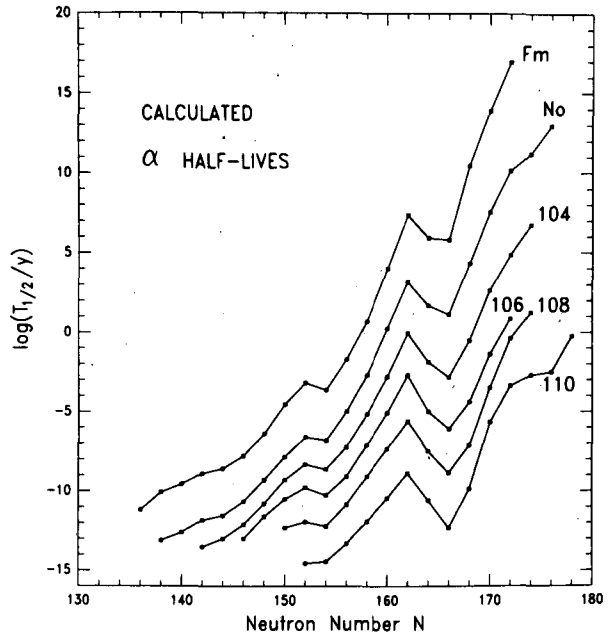

Fig. 1. Calculated α-decay half-lives. XBL 848-3495

cusps at N=152 are connected with a gap in the deformed single-particle level spectrum at this neutron number. The other discontinuity at N=162 is also connected to a gap in the deformed level spectrum and, in addition, to a change to smaller deformations as the N=184 shell is approached. The gap in the level spectrum is clearly manifested in the calculated shell correction as a very pronounced minimum at N=162.

We have also calculated fission half-lives for even-even nuclei in this region. Because the folded-Yukawa single-particle code[5] does not allow the study of axially asymmetric γ-distortions, which lower the first peak in the fission barrier by more than 2 MeV in some cases, we have calculated the fission barriers by use of the modified oscillator (Nilsson) model. The calculation has been carried out as described in ref. 7 but for additional nuclei. The fission half-lives have then been calculated by use of the model described in ref. 8. The results are shown in Fig. 2.

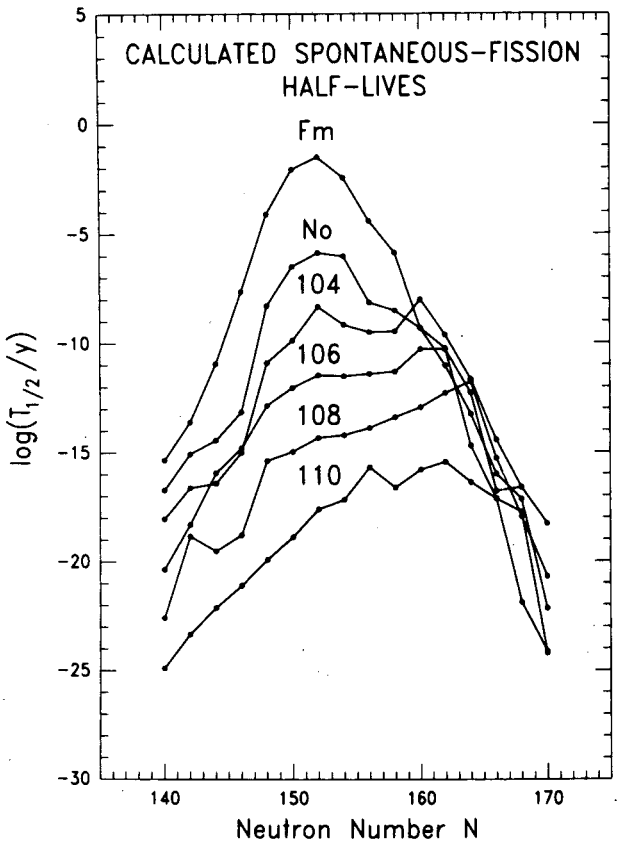

Fig. 2. Calculated fission half-lives. XBL 848-3494

More details about the calculations and a somewhat more extensive discussion of the agreement between the calculated and experimental results are found in ref. 9. The most interesting observation made in ref. 9 is perhaps that in the experiments there may occur a break in the trend of rapidly decreasing fission half-lives with increasing Z values at the element $^{260}106$, whose half-life has been determined to be of the order of a few milliseconds. However, in the calculations the fission half-lives decrease systematically by about two orders of magnitude for each increase by two in the proton number for Z=104 and beyond for N-values between 148 and 160. To investigate this interesting potential disagreement between experiment and theory further, one needs both experimental fission half-lives for additional even-even nuclei in this region and further theoretical calculations.

For elements in the "super-heavy" region the present calculation yields rather different results compared to the previous extensive calculation with the folded-Yukawa single particle model.[10] For instance, the calculated α half-life for the element $^{298}114$ is 1.2 minutes. The nucleus $^{294}110$ is no longer β stable. Instead, the nucleus $^{290}110$ is probably the most long-lived element in the super-heavy region with a half-life of 167 days according to the present calculation. The differences with respect to the earlier calculation are caused not so much by the new macroscopic model but arise mostly because of the different choice of single particle parameters.

Footnotes and References

*Condensed from LBL-18307.

†UNISOR, Oak Ridge Associated Universities under Contract USDOE DE-AC05-76OR00033.

‡Partially supported by the Swedish National Research Council.

§Los Alamos National Laboratory, Los Alamos, NM 87545.

**Lawrence Livermore National Laboratory, Livermore, CA 94550.

1. E.K. Hulet, UCRL-88414.
2. G. Münzenberg, *et al.*, Z. Phys. **A315**, 145 (1983).
3. G. Münzenberg, *et al.*, Z. Phys. **A317**, 235 (1984).
4. A. Ghiorso, *et al.*, LEAP Proposal, Berkeley Preprint PUB-5118.
5. P. Möller and J.R. Nix, At. Data and Nucl. Data Tables **26**, 165 (1981).
6. V.E. Viola, Jr. and G.T. Seaborg, J. Inorg. Nucl. Chem. **29**, 741 (1966).
7. W.M. Howard and P. Möller, At. Data and Nucl. Data Tables **25**, 219 (1980).
8. J. Randrup *et al.*, Phys. Rev. **C13**, 226 (1976).
9. G.A. Leander *et al.*, Proc. 7th Int. Conf. on Nuclear Masses and Fundamental Constants (AMCO-7), 3–7 September 1984, Darmstadt-Seeheim.
10. E.O. Fiset and J.R. Nix, Nucl. Phys. **A193**, 647 (1972).

Nuclear Mass Formula with a Neutron Skin Degree of Freedom and Finite-Range Model for the Surface Energy*

P. Möller† and W.D. Myers

We studied the possibility of extending the model used by Möller and Nix in 1980 to calculate nuclear masses and fission barriers for nuclei throughout the periodic system, to include provision for the existence of a neutron skin.

The calculation[1] in 1980 yielded an r.m.s. deviation in the ground-state mass of 0.835 MeV and r.m.s. in the fission barrier height of 1.331 MeV. This calculation used the approach where the energy, calculated as a function of shape, is a sum of a macroscopic term and a microscopic term. The macroscopic term varies smoothly with particle number and deformation and changes by about 200 MeV during the fission of a heavy system. The microscopic term, which arises due to the non-uniform distribution of single-particle levels, is a rapidly fluctuating term, where the magnitude of the fluctuations are typically a few MeV but may reach values of about 12 MeV at doubly closed shells.

The values above, of the r.m.s. deviations, imply that the model of ref. 1 was very successful in describing the ground state masses and fission barriers. In particular it was able to give correctly, for the first time, the fission barriers of medium heavy nuclei with A = 100 and A = 160. Also, in a survey of various mass models in ref. 2 the above model was the only one that yielded a smaller r.m.s. deviation, for a set of new masses determined in recent experiments, than was obtained in the original adjustment.

We have studied the possibility of generalizing this model to describe compressibility effects and the effect of a neutron skin. These effects have been extensively studied earlier by Myers and Świątecki[3] in the framework of the macroscopic "Droplet Model". Arguments similar to those used to derive the "Droplet Model" may be used to generalize the model studied in ref. 1 to include neutron skin and compressibility effects. No new parameters are introduced. The previously determined surface symmetry energy term is simply written in a slightly different form.

By adding the neutron skin thickness degree of freedom from the Droplet Model we have been able to extend the results of ref. 1 to include a substantially improved prediction of the isotopic trends in charge radii. The excellent fit to masses and fission barriers is retained and no additional parameters are introduced. In addition, a number of important and unresolved issues are raised by this work. For example, we find no indication of curvature or compressibility effects even though there is substantial evidence in the literature that such effects should be present. At the moment we view the approach outlined here as an improvement over ref. 1 but phenomenological in nature because important physical effects have been suppressed to improve the fit to data.

Footnotes and References

*Condensed from LBL-17533

†Permanent address: Department of Mathematical Physics, Lund University, P.O. Box 72S, S-22007, Lund, Sweden.

1. P. Möller and J.R. Nix, Nucl. Phys. **A361**, 117 (1981).
2. P. Haustein, private communication (1982).
3. W.D. Myers and W.J. Świątecki, Ann. of Phys. **55**, 395 (1969).

The Surface Energy of Multi-Component Systems*

W.D. Myers, W.J. Świątecki and C.S. Wang†

We define two surface energies, one associated with a reference energy involving the energy per particle in the bulk, the other associated with the chemical potentials of neutrons and protons under bulk conditions (in infinite nuclear matter). We derived a formula relating the difference between the two surface energy coefficients to the neutron excess and the neutron skin thickness. We have also extended the analysis to the interfacial surface energy between two phases (e.g., a liquid and a vapor). The general formulae needed in a numerical evaluation of the surface energy of a semi-infinite system were derived and then applied to a Thomas-Fermi treatment of a system of nucleons interacting by a velocity-dependent Yukawa interaction (the Seyler-Blanchard interaction).

The *surface-energy* coefficient γ (i.e., the surface energy per unit area of a flat surface) may be defined as the limit:

$$\gamma = \lim_{S/V \to 0} \frac{E - E_{ref}}{S} \quad , \tag{1}$$

where E is the actual energy of the system, E_{ref} is a reference energy taken to represent the volume contribution, and the limit is taken for a large system for which the ratio S/V tends to zero.

The first definition of γ, which we will refer to as the e-definition, γ_e, is based on subtracting from E in Eq. (1) the energy that the total number of particles, A, would have under bulk conditions. Thus, if we denote by e the energy per particle in the bulk, the reference energy is

$$E_e = eA \quad . \tag{2}$$

In the second definition, γ_μ, one introduces, in place of the energy per particle in the bulk, the chemical potentials μ_n, μ_p of the neutrons and protons and the pressure p associated with the bulk conditions. (These quantities tend to definite limits as the system becomes infinitely large.) The reference energy is now taken as

$$E_\mu = \mu_n N + \mu_p Z - pV \quad , \tag{3}$$

where V is the volume of the system defined by A/ρ. The physical meaning of E_μ may be appreciated by recalling the thermodynamic relation

$$dE = \mu_n dN + \mu_p dZ - pdV \quad ,$$

which gives the energy increase dE (in the special case of a system at zero temperature) associated with adding dN particles of one kind, dZ of another and increasing the volume by dV.

In similar studies of the surface-energy problem, von Groote[1] adjusted the parameters of the Seyler-Blanchard[2] interaction to give a good fit to nuclear masses and sizes. He also continued the investigation of neutron rich systems to cover the case we are interested in here, where neutrons become unbound and the nuclei are immersed in a neutron gas. We have repeated von Groote's calculations for a flat semi-infinite surface and we have not only calculated γ_e as a function of the neutron excess, as he did, but we also calculated γ_μ for comparison with the work of other authors[3].

In Fig. 1 the surface energy coefficients γ_e and γ_μ are plotted as the upper and lower solid lines. They are plotted against δ^2 instead of δ (the asymptotic relative neutron excess) because the Droplet Model predicts a δ^2 dependence for small δ values, and the two thin straight lines show the Droplet Model[4] predictions. Here, a maximum in the quantity γ_e was to be expected since the initial behavior is an increase proportional to δ^2, but the value of γ_e is expected eventually to decrease for larger δ because the distinction between the matter inside the surface and the matter outside is then disappearing.

Another aspect of the subtleties of the surface-energy problem is illustrated by the dashed and dot-dashed curves. They test, for the present Thomas-Fermi system with Seyler-Blanchard interactions,

two approximations to the surface energy coefficient γ that have appeared in the literature.

Footnotes and References

*Condensed from LBL-16947

†Permanent address: Department of Technical Physics, Peking University Beijing 100871, People's Republic of China.

1. H. von Groote, Proc. 3rd Int. Conf. on Nuclei far from Stability. R. Klapisch ed., CERN 76-13, 595 (1976).
2. R.G. Seyler and C.H. Blanchard, Phys. Rev. **124**, 227 (1961);

   R.G. Seyler and C.H. Blanchard, Phys. Rev. **131**, 355 (1963).
3. D.G. Ravenhall, C.D. Bennett and C.J. Pethick, Phys. Rev. Lett. **28**, 978 (1972).
4. W.D. Myers and W.J. Świątecki, Ann. Phys. (N.Y.) **55**, 395 (1969).

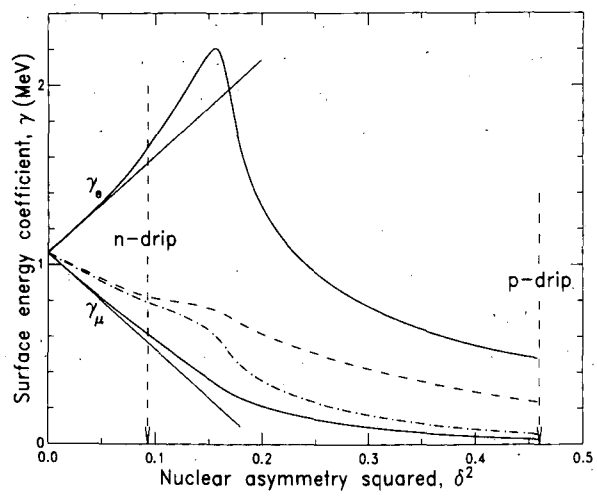

Fig. 1. The surface energy coefficients γ_e and γ_μ are plotted against δ^2, the square of the asymptotic relative neutron excess. The thin straight lines are the Droplet Model prediction for the behavior of these quantities for small values of δ. The dashed and dot dashed lines represent two schemes that were previously proposed for estimating the dependence of γ_e on δ. XBL 841-551

Surface and Curvature Properties of Neutron-Rich Nuclei*

K. Kolehmainen, M. Prakash,† J. Lattimer‡ and J. Treiner§

Surface and curvature properties of nuclei are important in the descriptions of many phenomena in nuclear physics, such as liquid-gas phase transitions in heavy ion collisions and fission barrier heights and saddle point configurations. In astrophysics, surface and curvature properties are important in determining equilibrium sizes of nuclei, electron capture rates, level densities and the phase transition between nuclei and bubbles, all of which may be important in supernovae and neutron stars. We present a simple but accurate method of calculating surface and curvature properties and use our results to calculate fission barrier properties and the nuclei-bubbles phase transition.

A sufficiently large nucleus, where the surface diffuseness is much smaller than the radius, can be approximated by a semi-infinite slab of nuclear matter separated from a vacuum by a plane interface. If Z/A is less than about 0.34, neutrons are no longer bound in nuclei, and hence the vacuum is replaced by a dilute neutron gas. We describe the energy density in both regions by a Skyrme-type effective interaction, with the kinetic energy density given by the extended Thomas-Fermi approximation. We consider only the zero temperature case, and we neglect the Coulomb energy.

For a given value of Z/A, the bulk neutron and proton densities far on either side of the interface are determined by equating the pressure and neutron

and proton chemical potentials in both regions.[1] The neutron and proton density profiles are each assumed to have the form of a constant (the density in the dilute "drip" region) plus a Fermi function raised to a power P_i:

$$\rho_i(z) = \rho_{id} + (\rho_{io} - \rho_{id})/(1 + e^{(z-z_i)/a_i})^{P_i}$$

where i denotes neutrons or protons, ρ_{io} is the density in the nuclear region, and ρ_{id} is the density in the drip region. The total energy is minimized subject to the constraint that the total numbers of both protons and neutrons are fixed, thereby determining the powers P_n and P_p, the diffuseness parameters a_n and a_p, and the difference $z_n - z_p$.

For the slab geometry, the curvature energy is zero, so the surface energy is given by the difference of the total energy and the volume energy. There are two possible reasonable definitions of the volume energy.[2,3] In the first, the volume energy is taken as the energy of a density distribution with $\rho_i = \rho_{io}$ to the left of a position R and $\rho_i = \rho_{id}$ to the right of R, where R is chosen so that this reference distribution has the same total neutron and proton numbers N and Z as the actual density distribution. The resulting surface energy per unit area is denoted by σ_s. The second definition is to take the volume energy as $E_{vol} = \mu_n N + \mu_p Z - PV$, where P is the pressure and the μ_i's are the chemical potentials. The resulting surface thermodynamic potential per unit area is denoted by ω_S. The surface energy per unit area (σ_s or ω_s) is then given by

$$\int_{-\infty}^{\infty} (\varepsilon - \varepsilon_{vol})\, dz$$

where ε is the total Skyrme energy density and ε_{vol} is the appropriate volume energy density. The two surface energies per unit area σ_S and ω_S are shown in Fig. 1 as functions of the square of the bulk asymmetry, $\delta_0 = (\rho_{no} - \rho_{po})/\rho_0 \cong 1 - 2Z/A$. They have very different behavior, but the total energy is of course the same in both cases. Our results agree very well with the results of both Hartree-Fock and more exact variational calculations (where the form of the density profile is not constrained).

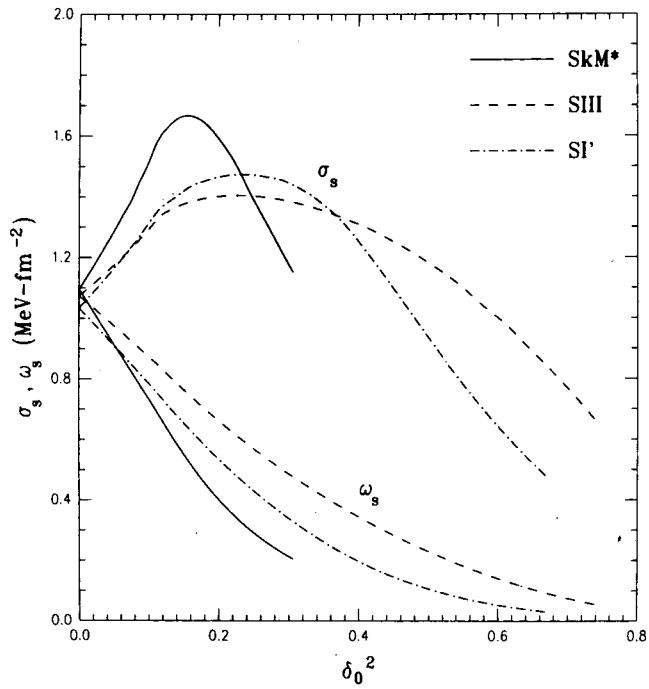

Fig. 1. The surface energy per unit area σ_S and the surface thermodynamic potential per unit area ω_S, as functions of $\delta_0^2 = [(\rho_{no} - \rho_{po})/\rho_0]^2 \cong (1 - 2\,Z/A)^2$.

XBL 848-3607

The total energy of a large nucleus can be written as an expansion in the curvature 1/R about the point 1/R = 0.[4] After subtracting the volume term, the lowest order term is the surface energy of a slab, and the curvature energy per unit length (σ_s or ω_s, depending on which E_{vol} is used) is given by the next term

$$\int_{-\infty}^{\infty} (\varepsilon - \varepsilon_{vol})(z - R)dz$$

plus an additional contribution which always can be set to zero by writing the total Skyrme energy functional in an appropriate manner. Therefore, the curvature energy of a large nucleus can be found in terms of the slab density distributions. The curvature energy per unit length and the curvature thermodynamic potential per unit length are shown in Fig. 2 for several Skyrme-type interactions.

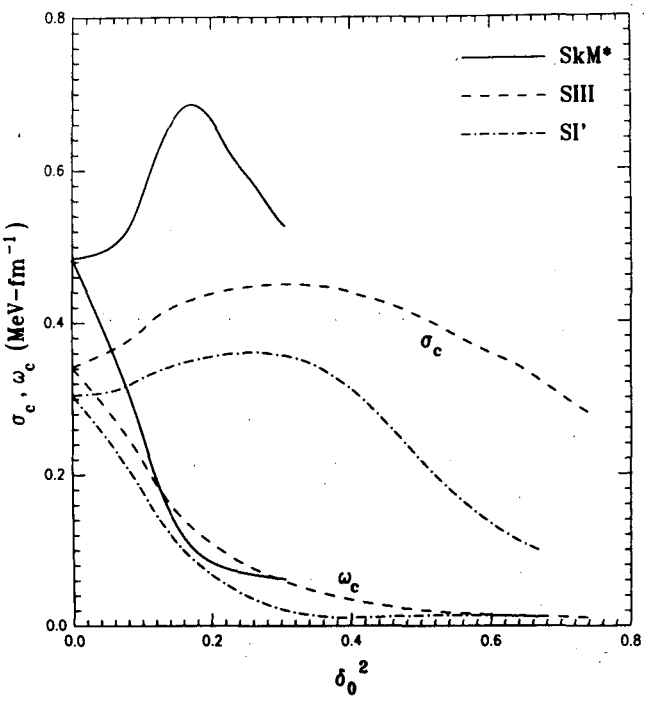

Fig. 2. The curvature energy per unit length σ_C and the curvature thermodynamic potential per unit length ω_C, as functions of δ_0^2. XBL 848-3608

We have calculated the liquid drop model fission barrier height and saddle point elongation and effective moment of inertia for the nucleus ^{240}Pu. We find that with curvature effects included, forces which fit neutron matter calculations well, i.e. SI' and SKM*, give fission properties in close agreement with the empirical values.[5]

At densities slightly less than nuclear saturation density, ρ_0, matter consists of more or less spherical nuclei surrounded by a dilute neutron gas. As the density is raised, the nuclei "turn inside out," leaving spherical regions of dilute neutrons surrounded by the more dense nuclear region. This nuclei-bubbles phase transition occurs at $\rho = \rho_0/2$ when curvature effects are neglected. We have found that with the inclusion of curvature, the transition density is lowered considerably, and the results are quite sensitive to the choice of effective interaction.

In conclusion, we find that our results agree well with the results of more accurate calculations, and our simplified method allows comparisons of many effective interactions over a wide range of asymmetries. The asymmetry dependence of surface and curvature properties are very sensitive to the choice of interaction, and those interactions which fit neutron matter calculations well are found to fit fission properties best. Hence, these forces are probably the best ones to use in describing astrophysical problems, where nuclei are very neutron-rich.

Footnotes and References

*Condensed from LBL-18513, in preparation.

†Department of Physics, State University of New York, Stony Brook, NY 11794.

‡Department of Earth and Space Sciences, State University of New York, Stony Brook, NY 11794.

§Permanent address: Institut de Physique Nucléaire, BP No. 1, 91406 Orsay Cedex, France.

1. J.M. Lattimer and D.G. Ravenhall, Astrophys. J. **223**, 314 (1978).
2. W.D. Myers, W.J. Świątecki and C.S. Wang, LBL-16947.
3. D.Q. Lamb, J.M. Lattimer, C.J. Pethick and D.G. Ravenhall, Phys. Rev. Lett. **41**, 1623 (1978);

   J.M. Lattimer, C.J. Pethick, D.G. Ravenhall and D.Q. Lamb, Nucl. Phys. **A**, in press (1984).
4. W.D. Myers and W.J. Świątecki, Ann. of Physics **55**, 395 (1969);

   C.D. Bennett and D.G. Ravenhall, Phys. Rev. **C10**, 2058 (1974);

   B. Grammaticos, Z. Physik **A312**, 99 (1983).
5. S. Cohen, F. Plasil and W.J. Świątecki, Ann. of Phys. **82**, 557 (1974).

Finite Range Droplet Model*

P. Möller,† W.D. Myers, W.J. Świątecki and J. Treiner‡

The work described here was undertaken in order to combine the features of two different approaches to improving the LDM.[1,2] In ref. 1 (and in earlier work cited there) a Droplet Model (DM) was developed that introduced the possibility of nuclear compression (or dilatation) and the possibility of a neutron skin for nuclei with a substantial neutron excess. The introduction of these degrees of freedom allowed the LDM expansion of the binding energy in terms $A^{-1/3}$ and I^2 (where I = (N-Z)/A) to be carried to one higher order in a consistent way. The folding model approach of ref. 2 had other virtues. Thus, the use of a finite range force for calculating the surface energy automatically generates various corrections necessary for bringing the calculated fission barriers into better agreement with the measured values.

In addition to the revised surface and Coulomb energy expressions with their corresponding dependences on shape we added a new term,

$$-C\,A\,e^{-\gamma A^{1/3}\bar{\varepsilon}}\ , \qquad (1)$$

with two new adjustable parameters C and γ. (The Droplet Model dilation degree of freedom is denoted by $\bar{\varepsilon}$.)

This type of exponential term, non-analytic in the Droplet Model expansion parameter $A^{-1/3}$, appears in folding-type expressions for the interaction energy. It becomes important quantitatively for nuclear configurations in which portions of the surface approach each other to within the range of the folding function. A well-known example is the proximity potential representing the interaction energy of two nuclei about to come into contact. For a single nucleus this type of term becomes important when the nucleus is small enough so that one side of the nucleus can feel the effect of the surface on the other side (i.e., the absence of nuclear matter beyond a certain distance). The usual Yukawa or Yukawa-exponential folding integrals have in them this type of term, but we found that adding an independent contribution of the type of Eq. (1) had striking advantages.

The r.m.s. deviation that we obtained was 0.676 MeV for the masses and 1.135 MeV for the fission barriers. There is no systematic long-range structure in the mass deviations (either along or across the valley of beta-stability) as far as we can tell. The key to these substantially improved results seems to be the empirical, exponential term of Eq. (1). We had originally hoped that all finite range effects would be automatically represented by the folding model surface energy expression, but this was not the case. Fig. 1 serves to illustrate this point. The quantity plotted here versus $A^{-1/3}$ is $(\Delta\rho/\rho_0)_{bulk}$, which is the fractional deviation of the central density of a nucleus from the nuclear matter value. The solid line in the figure is the old DM prediction. The dashed line illustrates the effect produced by including the term from Eq. (1). The behavior of this expression corresponds very closely to that found in earlier Thomas-Fermi calculations. (See Fig. 30 of ref. 3.) It also corresponds quite closely to the behavior we have noted recently in studies of

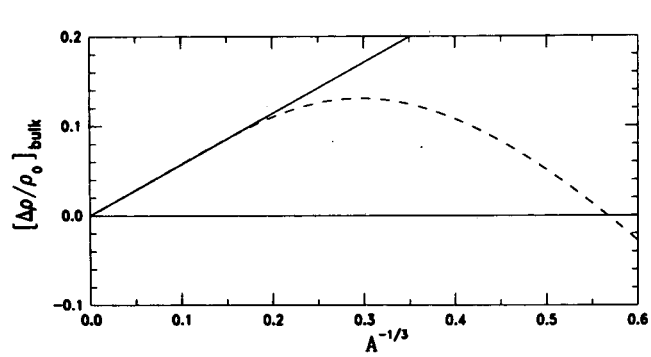

Fig. 1. Fractional deviation of the central density versus $A^{-1/3}$ predicted by the model for hypothetical uncharged nuclei with N = Z. XBL 848-3599

Hartree-Fock calculations. This is all the more remarkable when we recall that the coefficients of this new phenomenological term were determined solely from a least squares fit to masses and fission barriers. No considerations regarding density distributions governed their determination.

The development described in the present paper, based on including an adjustable exponential term, demonstrates the practical utility of such a term and its relation to the problem of surface-tension squeezing of light nuclei. It seems to us that the limit of a useful Droplet Model power expansion in $A^{-1/3}$ is probably reached around A^0, and that future efforts should concentrate on a better understanding of the "exponential," non-analytic term. This term focuses attention on a specific feature of a light system, for which the range of the interaction begins to be comparable with its size. This is the opposite extreme from the limit underlying the standard (leptodermous) treatment of saturating systems. Such non-analytic terms might be described as dealing with "desaturating" effects, which begin to dominate for small (holodermous) systems. A general discussion of such terms and their incorporation in mass formulae is an outstanding problem for the future.

Footnotes and References

*Condensed from LBL-18230

† Permanent Address: Department of Mathematical Physics, Box 725, S-22007 LUND, SWEDEN.

‡Permanent Address: IPN BP n° 1, 97406 ORSAY Cedex, FRANCE.

1. W.D. Myers, *Droplet Model of Atomic Nuclei*, IFI/Plenum Data Co., New York, N.Y. (1977).
2. P. Möller and J.R. Nix, Nucl. Phys. **A361**, 117-146 (1981).
3. W.D. Myers and W.J. Świątecki, Ann. Phys. (N.Y.) **55**, 395-505 (1969).
4. J. Treiner, W.D. Myers, W.J. Świątecki and M. Weiss, manuscript in preparation.

Bulk Compression Due to Surface Tension in Hartree-Fock Calculations*

J. Treiner,† W.D. Myers, W.J. Świątecki and M.S. Weiss‡

A number of recent studies have been devoted to the comparison between the Droplet Model of atomic nuclei and Hartree-Fock calculations.[1,2] Some of these studies raised questions about the validity of the Droplet Model approach for treating the neutron skin in neutron-rich nuclei and, in particular, about an elementary prediction of the Droplet Model concerning the squeezing of nuclei by the surface tension. While the Hartree-Fock calculations were not sufficiently comprehensive to be able to settle these questions, certain features of the numerical results raised concerns over whether or not the Droplet Model was correctly formulated. The relation of the Droplet Model to Thomas-Fermi (rather than Hartree-Fock) calculations had been thoroughly investigated in the original Droplet Model paper[3] and perfect agreement had been found as regards the neutron skin as well as the surface tension squeezing in the appropriate limit of sufficiently large nuclei, in which the Droplet Model should formally be valid. However, two questions still remained. First, does the change from a Thomas-Fermi to a Hartree-Fock treatment, in addition to bringing in the expected oscillations in nuclear properties associated with shell effects, also modify in some unsuspected way the *shell-averaged* behavior, thus invalidating the Droplet Model predictions of average nuclear properties? Second, even if the Droplet Model predictions were found to be formally valid for sufficiently large nuclei, are they *quantitatively* useful for actual nuclei throughout the periodic table?

We found that the prediction of the Droplet Model is, roughly speaking, consistent with the trend of the Hartree-Fock calculations for $A^{-1/3} < 0.15$.

(One cannot be very quantitative about this in view of the large fluctuations in the calculated points as well as the possible ambiguities associated with the extraction of bulk values from the Hartree-Fock densities.) For lighter nuclei, one can discern, despite the large fluctuations, a tendency for the average of relative bulk compression, $\Delta\rho/\rho_0$, to decrease, contrary to the Droplet Model prediction. We had already noted such a trend in the Thomas-Fermi calculations in ref. 3. However, apart from shell fluctuations, there does not appear to be evidence for a fundamental disagreement between Hartree-Fock trends and Droplet Model predictions. The rather different conclusion implied by ref. 1 may be attributed to the three technical points. First, the number of nuclei considered in ref. 1 was not large enough, and the nuclei themselves were not heavy enough, to establish a trend in the Hartree-Fock calculations that could be compared with the Droplet Model. Only some 20 nuclei were analyzed in ref. 1 (and these included Coulomb and asymmetry effects) and only one symmetric case, namely ^{164}Pb, was calculated without Coulomb energy. Second, the extraction of bulk densities from the Hartree-Fock calculations was made by equating Ford-Wills moments of the densities with *approximate* expressions for the Ford-Wills moments of Fermi functions. This approximation may be shown to *underestimate* the bulk densities. Third, the use of Fermi distributions (with zero skewness) is somewhat restrictive. For example, if one fits the square of a Fermi distribution with a Fermi distribution one underestimates the central density of the original function. A generalization of the Droplet Model is suggested, which should make it more accurate for light nuclei.

Footnotes and References

*Condensed from LBL-18477.

†Permanent address: IPN n° 1, 97406 ORSAY Cedex, France.

‡Lawrence Livermore National Laboratory, Livermore, CA 94550.

1. J.M. Pearson, Nucl. Phys. **A376**, 501 (1982).
2. F. Tondeur, J. Phys. **G6**, L71 (1980).
3. W.D. Myers and W.J. Świątecki, Ann. of Phys. **55**, 395 (1969).

Theoretical Estimates of the Rates of Radioactive Decay of Radium Isotopes by ^{14}C Emission*

Y.-J. Shi and W.J. Świątecki

The recently discovered[1] radioactive decay of ^{222,223,224}Ra by the emission of ^{14}C and, in particular, the branching ratios of these decays to alpha emission, can be accounted for with reasonable accuracy by a barrier penetrability calculation, *provided* a realistic potential-energy barrier is used. We took a Coulomb barrier modified by the canonical nuclear proximity attraction from refs. 2 and 3 and obtained branching ratios within a factor of 10 of the observed values without the adjustment of any parameters. (This implies an accuracy in the penetrability integrals of about 3%.)

Footnote and References

*Condensed from LBL-18366 and Phys. Rev. Lett. **54**, 300 (1985)

1. H.J. Rose and G.A. Jones, Nature **307**, 245 (1984);

   P.B. Price *et al.*, submitted to Phys. Rev. Lett. (1984).
2. J. Blocki *et al.*, Ann. Phys. **105**, 427 (1977).
3. J. Blocki and W.J. Świątecki, Ann. Phys. **132**, 53 (1981).

Estimates of Radioactive Decay by the Emission of Nuclei Heavier than Alpha Particles*

Y.-J. Shi and W.J. Świątecki

The barrier penetrability calculations, developed to account for the recently discovered radioactive decay of Ra isotopes by ^{14}C emission (see elsewhere in this report), have been applied to a systematic search for other exotic decays. The potential energy barrier consists of a sum of electrostatic and proximity potentials, supplemented by a power law interpolation from the contact configuration to the configuration of the parent nucleus. Fig. 1 shows two examples, for alpha and ^{14}C emission from ^{222}Ra. Some three dozen candidate decays are listed, with nominal branching ratios of the exotic to alpha decays greater than 10^{-12}. Some of these decays might be detected experimentally in the near future.

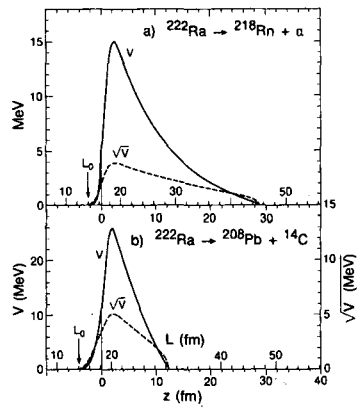

Fig. 1. The deformation-energy barrier V(L) for the emission of an α particle, (a), or a ^{14}C nucleus, (b), from ^{222}Ra. The dashed curves are the integrands in the penetrability integral. The total extension of the configuration is L and the distance between the near surfaces of the fragments is z. Most of the barrier corresponds to separated fragments (the region to the right of the vertical line at z=0). XBL 848-8842

Footnote

*Condensed from LBL-18349, to appear in Nucl. Phys.

A Microscopic Model of Fragment Yields in Nucleus-nucleus Collisions*

B.G. Harvey

Several experiments have shown that the yields of neutron-excess projectile-like fragments (PLF) coming from nucleus-nucleus collisions at energies around 15-40 MeV/nucleon are substantially enhanced when the target nucleus is heavy.[1,2,3] A comparison of the PLF yields for ^{16}O + ^{208}Pb at 20 MeV/nucleon + 2 GeV/nucleon[1] shows that the enhancement of neutron-rich PLFs disappears at the higher energies.

These results suggest that there might be a connection between the PLF yields and the nucleon-nucleon cross sections $\sigma_{nn}(=\sigma_{pp})$ and σ_{np}. At low energies, $\sigma_{np} = 3\sigma_{nn}$. Therefore protons in the projectile have a greater probability of scattering in the target than do projectile neutrons, when the target is neutron-rich. A neutron-rich ejectile is thus formed. At 2 GeV/nucleon, though, $\sigma_{nn} \approx \sigma_{np}$ so that the N/Z ratio of the target is no longer important. Moreover, it is now well established[4] that the fall-off of the reaction cross section σ_R with increasing energy beyond 20 MeV/nucleon is due to the decrease in σ_{nn} and σ_{np} and the onset of nuclear transparency.

The calculations of PLF yields were made by the Monte Carlo method. The projectile follows an

orbit in the Coulomb plus nuclear potential down to some distance ($R_1 + R_2$) corresponding to the top of the barrier. The projectile nucleons then follow straight paths through the target nucleus. The coordinates of each nucleon in the projectile are chosen at random in such a way as to reflect a Fermi density distribution and to preserve the projectile centers of mass and charge. Each nucleon passes through the Fermi density distribution (different for neutrons and protons) of the target, and the probability that it will scatter is calculated by numerical integration along the path. The nucleons that scatter are assumed to be removed from the projectile, whose residue is the PLF (ejectile). The calculation is repeated 1000-2000 times at each of 21 different impact parameters.

Since Pauli blocking inhibits the scatterings in the full-density central region of the target nucleus at low beam energies, the effective values of σ_{nn} and σ_{np} are reduced in such a way as to produce a nucleon mean free path of 5 fm for nucleons of 20 MeV. The cross sections are allowed to increase with radius as 1/(target proton or neutron density) until they reach the free nucleon values in the surface region. At 2 GeV/nucleon, the free nucleon cross sections are used throughout the target volume. The calculation yields values of σ_R for $^{12}C + {}^{12}C$ that are in excellent agreement with experiment and with the calculations of ref. 4. For heavier systems such as $^{16}O + {}^{208}Pb$ and $^{40}Ar + {}^{197}Au$, few measurements of σ_R have been made, but the calculated values are in good agreement with the empirical formula of Kox *et al.*[5] As might be expected, σ_R is determined entirely by the values of σ_{nn} and σ_{np} in the target nucleus surface region.

A comparison of PLF cross section ratios for $^{16}O + {}^{208}Pb$ at 20 MeV/nucleon and 2 GeV/nucleon immediately showed that the observed enhancement of the neutron-rich PLFs at the lower energy could not be obtained just from the N/Z ratio of ^{208}Pb. The inclusion of a neutron "skin," though, made a substantial improvement. Table I shows a comparison of the experimental and calculated ratios σ(20 MeV/nucleon)/σ(2 GeV/nucleon). In the calculation, the neutron and proton radii and diffusivities were taken from the Hartree-Fock-Strutinsky calculations of Tondeur *et al.*[6] These values produce density ratios of neutrons to protons that exceed 10 in the ^{208}Pb surface.

The individual PLF cross sections (rather than ratios) can be calculated by taking account of the separation energies of the projectile into the PLF and the scattered residue, using the prescription of Friedman.[7] The results thus obtained are in good agreement with the 20 MeV/nucleon experiment, as shown in Table I. The calculation, though, consistently overestimates the yields of neutron-excess PLFs at 2 GeV/nucleon.

Footnote and References

*Condensed from LBL-17762, May 1984, with revisions.

1. G.K. Gelbke *et al.*, Phys. Rep. **42** No. 5, 312 (1978).
2. Ch. Egelhaaf, Thesis, Hahn-Meitner Institut, Berlin (1982).
3. M. Lefort, private communication.
4. R.M. DeVries and J.C. Peng, Phys. Rev. Lett. **43**, 1373 (1979) and Phys. Rev. 322, 1055 (1980);

   N.J. DiGiacomo, J.C. Peng and R.M. DeVries, Phys. Rev. Lett. **45**, 527 (1980) and Phys. Lett. **101B**, 383 (1981);

   J.C. Peng, R.M. DeVries and N.J. DiGiacomo, Phys. Lett. **98B**, 244 (1982).
5. S. Kox *et al.*, Nucl. Phys. **A420**, 162 (1984).
6. F. Tondeur, J.P. Arcoragi and J.M. Pearson, Contribution to the International Workshop on Semiclassical Methods in Nuclear Physics, Institut Laue-Langevin, Grenoble, 1984.
7. W.A. Friedman, Phys. Rev. C **27**, 569 (1983).

Table I.
Comparison of Experimental and Calculated Cross Sections
for $^{16}O + ^{208}Pb$ at 20 MeV/nucleon and 2 GeV/nucleon

Ejectile	σ(20 MeV/nucleon) (mb) exp	σ(20 MeV/nucleon) (mb) calc	σ(2 GeV/nucleon) (mb) exp	σ(2 GeV/nucleon) (mb) calc	σ(20 MeV/nucleon) / σ(2 GeV/nucleon) exp	σ(20 MeV/nucleon) / σ(2 GeV/nucleon) calc
^{6}Li	54^{+19}_{-16}	25.7	56 ± 13	39.2	$1.0^{+.4}_{-.3}$	0.66
^{7}Li	93^{+33}_{-19}	47.0	39.7 ± 4.3	42.1	$2.3^{+.9}_{-.6}$	1.12
^{8}Li	16^{+6}_{-8}	18.0	–	6.89	–	2.61
^{9}Li	$5^{+1.8}_{-2.3}$	6.9	–	0.78	–	5.00
^{7}Be	$15^{+7.5}_{-3}$	19.4	43.3 ± 6.4	43.2	$0.35^{+.3}_{-.1}$	0.45
^{8}Be	–	198	–	294.8	–	0.67
^{9}Be	54^{+27}_{-8}	56.2	15.3 ± 2.1	42.6	$3.5^{+1.8}_{-.7}$	1.32
^{10}Be	39^{+20}_{-10}	23.7	6.8 ± 1.1	14.5	$5.7^{+3.2}_{-1.8}$	1.63
^{9}B	–	24.7	–	46.5	–	0.53
^{10}B	50^{+18}_{-18}	38.9	35 ± 11	49.2	$1.4^{+.8}_{-.8}$	0.79
^{11}B	114^{+40}_{-17}	53.7	52.9 ± 5.9	42.9	$2.2^{+.8}_{-.4}$	1.25
^{12}B	23^{+8}_{-12}	14.6	3.98 ± 0.75	8.74	$5.8^{+2.4}_{-3.3}$	1.67
^{13}B	–	9.9	0.70 ± 0.44	4.65	–	2.13
^{10}C	–	5.0	7.2 ± 1.4	13.9	–	0.36
^{11}C	28^{+4}_{-14}	26.0	36.9 ± 5.7	48.2	$0.76^{+.2}_{-.4}$	0.54
^{12}C	198^{+30}_{-30}	189.2	126 ± 25	234.1	$1.6^{+.4}_{-.3}$	0.81
^{13}C	127^{+19}_{-32}	61.5	45.4 ± 8.3	52.8	$2.8^{+.7}_{-.9}$	1.16
^{14}C	$43^{+6.5}_{-22}$	52.0	12.3 ± 2.2	33.4	$3.5^{+.8}_{-1.8}$	1.56
^{13}N	$27^{+5.4}_{-14}$	26.5	17.0 ± 3.2	46.7	$1.6^{+.5}_{-.9}$	0.57
^{14}N	140^{+42}_{-42}	83.6	71 ± 22	95.8	$2.0^{+.8}_{-.8}$	0.87
^{15}N	211^{+53}_{-53}	249.6	(202 ± 2)[a]	203.3	–	1.23

a) The ^{15}N yield at 2 GeV/nucleon contains a large photonuclear component.

Two-center Shell Model for Deep Inelastic Collisions of Heavy Ions*

Shi Yi-jin† *and J. Randrup*

Deep Inelastic Collisions of Heavy Ions (DIC) provide some of the most interesting problems in nuclear physics. Most of the work in this field describes DIC as a kind of equilibrating process[1] and some statistical assumptions are introduced. But the validity of the statistical assumptions are still open to question.[2] Therefore, a pure quantum-mechanical treatment of DIC without any statistical assumptions is needed for comparison and for deeper understanding as well. TDHF,[3] of course, is a candidate to think of first. But since the requirement of self consistency requires the use of too much computer time, there are no complete calculations of this type so far. It is possible to drop the demand for self-consistency and introduce a shell-model instead.[4] Since the shell-model is well understood, its introduction will not give rise to unacceptable ambiguity.

Our treatment follows this line. In order to investigate the single-particle exchange mechanism more clearly, a second quantization representation has been introduced which is based on the usual shell model. That is, two sets of shell-model wave functions $|\alpha)$, $\alpha = 1, \ldots, K_A$; $|\beta)$, $\beta = 1, 2, \ldots, K_B$, are taken as an adiabatic basis.

Because of nonorthagonality of the basis, we have used the dual basis introduced by Moshinsky and Seligman in their second quantization procedure.[5] That is, we have

$$|k> = \sum_{k'} |k') M^{-1}_{k'k} \qquad k = \alpha,\beta$$

where M^{-1} is the inverse of the overlap matrix $M \equiv \{ (k'|k) \}$. Correspondingly, the creation operators are defined as

$$a_k^\dagger \; |0) = |k)$$

$$b_k^\dagger \; |0) = |k>$$

and

$$a_k^\dagger, b_{k'} = \delta_{kk'} \quad .$$

Since the operator for the total number of particles is

$$\hat{N} = \sum_k a_k^\dagger b_k = \sum_\alpha a_\alpha^\dagger b_\alpha + \sum_\beta a_\beta^\dagger b_\beta \quad ,$$

we can define the operator for the number of particle in the projectile-like nucleus B as

$$\hat{N}_B = \sum_\beta a_\beta^\dagger b_\beta \quad .$$

Then the transferred number of particles along a trajectory $\vec{R}(t)$ is

$$N_{\vec{R}}(t) = <\Phi \; |\hat{N}_B \; |\Phi(T)) - <I \; |\hat{N}_B \; |I)$$

where $|I)$ is the initial state consisting of $|\alpha)$, $|\beta)$ and $|\Phi(t))$ is a state coming from $|I)$, that is,

$$|\Phi(t)) = e^{-\frac{i}{\hbar}\int Ht} \; |I)$$

where H is the total Hamiltonian of the system under consideration.

Footnotes and References

*Work in progress.

†Permanent address: Institute of Atomic Energy, P.O. Box 275 (18), Beijing, China.

1. For example, S. Ayik, B. Schürmann and W. Nörenberg, Z. Phys. **A277**, 299 (1974).
2. M. Berlarger *et al.*, Z. Phys. **A291**, 133 (1979), for example.
3. K.T.R. Davies *et al.*, Phys. Rev. Lett. **41**, 632 (1978), for example.
4. D. Glas and U. Mosel, Nucl. Phys. **A264**, 268 (1976),

   G. Bertsch and R. Schaeffer, Nucl. Phys. **A277**, 509 (1977),

   M. Baldo *et al.*, Nucl. Phys. **A391**, 249 (1982).
5. M. Moshinsky and T.H. Seligman, Ann. Phys. **66**, 311 (1971).

Symmetric Splitting of Very Light Systems in the Coalescence and Reseparation Model*

J. Blocki, K. Grotowski, R. Planeta and W.J. Świątecki

This is a theoretical study stimulated by recent experiments at the 88-Inch Cyclotron on the binary decay of the light composite systems ^{46}V, ^{49}Cr and ^{52}Fe produced in collisions of ^{6}Li, ^{9}Be and ^{12}C with ^{40}Ca. The dynamics of the collision is followed using the "chaotic regime" idealization (Liquid-Drop potential energy, wall-and-window dissipation and Werner-Wheeler inertia). The parametrization of the nuclear shapes is that of ref. 1. and angular momentum is included. According to the model calculations, the decay of these systems is predicted to be the result of the fission of a rotating "super-deformed" configuration. The calculations suggest an angular momentum window for this type of reaction between about $30\hbar$ and $43\hbar$. The relevant saddle-point configurations are close to scission and there is relatively little damping before fission.

We found that the total kinetic energy of the fission fragments contains a considerable contribution from the centrifugal force (30–50%). The orbital motion of the fragments carries about 90% of the total angular momentum, leaving only 10% for the spins of the fragments. This is the result of the scission configuration being considerably more elongated than tangent spheres (for which the angular momentum split would be 5/7 orbital and 2/7 spins).

The theoretical calculations suggest that exotic, super-deformed configurations of the V, C, Fe nuclei had actually been produced in the experiments in question; more incisive evidence for these unusual shapes would be desirable.

Footnote and Reference

*To be submitted to Nuclear Physics.

1. J. Blocki and W.J. Świątecki, LBL-12811

Macroscopic Treatment of Nuclear Dynamics*

W.J. Świątecki

A qualitative classification of nucleus-nucleus reactions into four types is described, a consequence of the existence of (up to) three "milestone configurations" that a fusing nuclear system may be faced with (the touching configuration, the conditional saddle point at fixed asymmetry and the unconditional saddle point). These considerations lead to phenomenological formulae for fusion and compound-nucleus cross sections that may be compared with experiments by the use of "rectilinear cross section plots" where all theoretical predictions are segments of straight lines.[1] A dynamical model of nucleus-nucleus collisions (or fission) is described which incorporates the recently formulated mass-asymmetry friction in the wall- and window-formula.

Recent work on a simple treatment of promptly emitted nucleons (Fermi jets) in nucleus-nucleus collisions is described,[2] leading to closed algebraic formulae for some of the properties of the jetted particles.

The role of the Pauli exclusion principle in mean-field (one-body) dissipation theories is discussed and it is shown how, because of Liouville's theorem, nucleons automatically make room for each other in phase space and no additional Pauli blocking factors are necessary. Also in connection with the one-body dissipation dynamics, a discussion is given of the question of the conservation of linear and angular momentum.

Footnote and References

*Condensed from LBL-17837, a talk presented at the International Conference on the Theoretical Approaches to Heavy Ion Reaction Mechanisms, Paris, France, May 14-18, 1984; to be published in Nucl. Phys.

1. S. Bjørnholm and W.J. Świątecki, Nucl. Phys. **A391**, 471 (1982).

2. K. Möhring, W.J. Świątecki and M. Zielińska-Pfabé, in preparation.

Dissipative Resistance Against Changes in the Mass Asymmetry Degree of Freedom in Macroscopic Nuclear Dynamics: The Completed Wall-and-Window Formula

J. Randrup and W.J. Świątecki

This research, described in last year's annual report,[1] has been completed. It is written up as LBL-17273 and has appeared in Nuclear Physics A.

Reference

1. NSD Annual Report 1982-1983, LBL-16870

A Simple Treatment of Fermi Jets*

K. Möhring, W.J. Świątecki and M. Zielińska-Pfabé

The simple, partly analytic treatment of Fermi jets described in last year's annual report[1] has been used to make a comprehensive survey of various properties of the jetted neutrons and protons. Estimates are given of the total cross sections, as well as of energy spectra and angular distributions for nucleons that are predicted to be jetted in reactions between colliding nuclei with different masses and different collision energies. Fig. 1 shows a sample of the results.

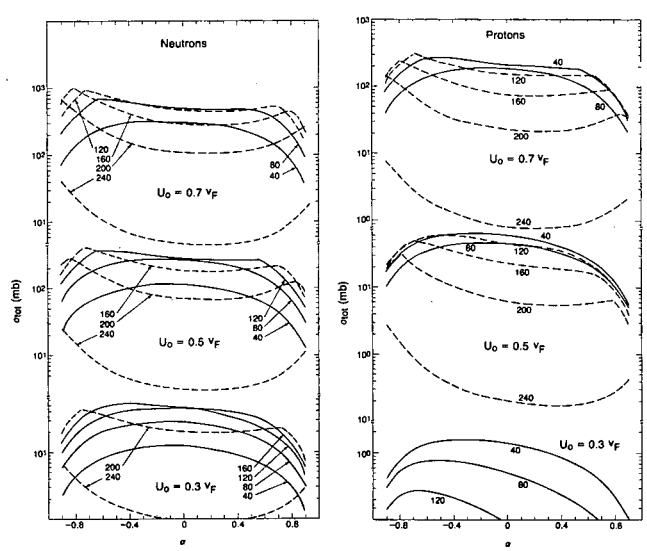

Fig. 1. The cross-section for jetting through one of the nuclei is shown as a function of the mass asymmetry α, defined as $(A_1-A_2)/(A_1+A_2)$, for different total mass numbers A_1+A_2. The collision velocity at contact, U_0, is indicated in units of the Fermi velocity v_F. XBL 845-10550A

Footnote and Reference

*Condensed from LBL-17919 and submitted for publication in Nucl. Phys.

1. NSD Annual Report 1982-1983, LBL-16870

One-Body Dynamics and Angular Momentum Dissipation in Damped Nuclear Reactions

T. Døssing and J. Randrup

Theories of damped nuclear reactions are often expressed in terms of degrees of freedom which are familiar from simpler nuclear reactions, such as surface vibrations and nuclear transfer. However, the clean characteristics of such elementary nuclear excitations are largely washed out due to the complexity of a damped reaction where high excitations and large distortions occur. The experimental study of damped nuclear reactions is therefore, with few exceptions, limited to observables subject to overall conservation after the reaction: the mass and charge numbers, the momentum and energy, and the angular momentum. (Parity is also conserved, but is of little use.)

If the induced elementary nuclear excitations carry significant amounts of a particular observable, the distribution of this observable in the reaction complex may reach the asymptotic (long-time) limit, for which the distribution in this observable is statistical. For the angular momentum observables it is clear from experiment that the mean spin vectors do not generally reach their equilibrium values. But the statistical limit has been advocated for describing the high spin variances.

As reported last year, equations for mean spin vectors and variances derived on the basis of nuclear exchange transport with standard form factors describe correctly the proper long-time limit for statistical equilibrium.[1] The relaxation times for approach to equilibrium are, however, quite different for the different spin modes. The relaxation times for the two wriggling modes are very short while that for the tilting mode is quite long, typically 2 to 5 times larger than the reaction times. Indeed, if recoil is neglected, as in the present treatment, nuclear transfer does not directly excite the tilting mode, which then only is indirectly excited from the wriggling modes by the orbital rotation. As a result, the spin variances in the nuclei will be small along the line connecting their centers.

After the reaction the angle θ_0 from the beam axis to the major in-plane principal direction of the spin variances will be approximately equal to half the scattering angle in the center of mass system, i.e.

$$\theta_0 \approx \frac{\theta_{CM}}{2} \tag{1}$$

This direction is approximately perpendicular to the line connecting the centers of the nuclei at their closest approach.

In contrast to this result, the statistical spin covariances in the plane perpendicular to the orbital angular momentum vector are isotropic. The transformation of the spin distribution to the external coordinate system introduces a small anisotropy in the spin variance perpendicular to the reaction normal, and the major in-plane principal direction of the spin variances has a direction given by

$$\theta_0 \approx \frac{\theta_{CM}}{2} + \frac{\pi}{4} + \frac{\langle S_y^A + S_y^B \rangle}{4J} \cot \theta_{CM} \tag{2}$$

where $\langle S_y^A + S_y^B \rangle$ denote the sum of mean spin vectors in the two nuclei.

Sequential fission of a heavy nucleus after the reaction gives information about the location of the major in-plane principal direction. Fission fragments are emitted preferentially perpendicular to the spin vector so, for a distribution of spin vectors, the fission angular distribution within the reaction plane will have a maximum along the minor in-plane direction and a minimum along the major in-plane direction.

Fig. 1 shows experimental[2] and calculated in-plane angular correlations for three different kinetic energy losses for two reactions. The calculated values are based upon spin distributions as obtained with nucleon exchange transport and sequential fission in competition with neutron evaporation in all

decay steps has been included. Clearly, the location of the extrema are well in accordance with our results, and thereby with the approximate relation (1) and in disagreement with the statistical result (2) which would correspond to shifting the extrema by approximately 45°. The amplitude of the calculated variation is too small relative to the data by a factor of two. However, it should be kept in mind here that two other data sets for similar reactions with Bi or Pb disagree with the data shown on Fig. 1: one displays in-plane anisotropies of approximately the same magnitude as calculated; and the other shows almost no in-plane variation.

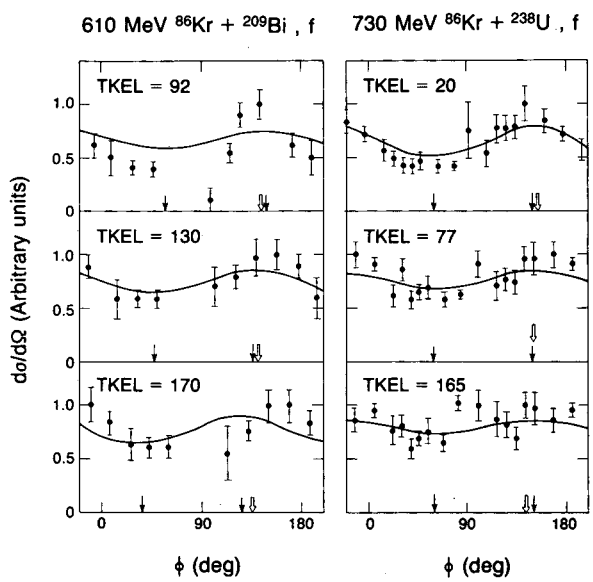

Fig. 1. Angular correlation in the reaction plane for fission of the heavy nucleus produced in the reactions 610 MeV ^{86}Kr + ^{209}Bi and 730 MeV ^{86}Kr + ^{238}U. ϕ = 90° corresponds to the beam axis. The open arrow for each TKEL shows the target recoil direction in the lab-frame and the solid arrows point to the directions of principal axes of the in-plane components of the spin variance tensor. The data points are taken from ref. 2, and they cover an interval of 40 MeV wide in TKEL for each data set. Some of the error bars in the left hand part of the figure correspond to the size of the dots in the figure in ref. 2, and should thus actually be somewhat smaller. XBL 841-94

From the combined comparison with many data sets on γ-ray multiplicities and angular correlations of sequential fission we conclude that the spin variances are well described by nuclear exchange transport with standard form factors, whereas the mean spin vector is increasing too rapidly for small total kinetic energy losses.

To evaluate the significance of this disagreement with data, we have studied the sensitivity of the result to certain less well-founded prescriptions for the dynamics of the interaction zone between the two nuclides. Fig. 2 shows our result for the spin magnitude in the reaction 610 MeV Kr + Sm, both with our standard implementation of the model (the thick solid curves) and including some modifications. The data points are extracted from the γ-multiplicity data of ref. 3 using the following relations between spin magnitude moments and γ-multiplicity moments: $\langle S\rangle = 2(\langle M_\gamma\rangle - 3)$ (open circles), $\langle S\rangle = 1.6 \langle M_\gamma\rangle$ (solid circles), $\sigma_S = 2\sigma_{M\gamma}$ (open triangles), $\sigma_S = 1.6\ \sigma_S = 1.6\ \sigma_{M\gamma}$ (solid triangles). The TKEL of the data points has been corrected for neutron evaporation, which decreases the kinetic energy of the krypton-like nucleus prior to its measurement. The thin solid curves are obtained by lowering the density of nucleons in the interaction region from the full to half the density inside nuclei. This reduces the dissipative efficiency of the nucleons, both with respect to spin and energy loss; therefore the resulting effect in Fig. 2 is only moderate. The other types of modification considered concern the wall dissipation associated with the neck motion. This dissipation effectively damps the radial motion. In the standard implementation of the model this wall dissipation is reduced for long thin necks due to the expected symmetry-induced memory correlating successive nucleon reflections from the walls in that case. The dash-dotted curves in Fig. 2 are obtained with the extreme prescription of entirely removing the reduction in the wall damping and including in the neck dissipation also a proximity part. In this case the radial friction increases significantly relative to the tangential friction, and the mean spin for given TKEL decreases by about 50%. On the other hand, the mass dispersion, which

is in good agreement with data with the standard implementation, is then also reduced, by about 30%.

Thus, the disagreement for small TKEL can be reduced by more refined treatment of the neck dynamics but only at the cost of affecting the behavior of other observables as well. We therefore attach some significance to this discrepancy. The cause of this failure is not clear to us at this stage but the problem might be helped by an improved treatment of the nucleon transfer process and future studies may be focused in this direction.

Footnotes and References

1. T. Døssing and J. Randrup, Nucl. Phys. **A433**, 215;280 (1985).
2. P. Dyer *et al.*, Nucl. Phys. **A322**, 205 (1979);
   R.J. Puigh *et al.*, Phys. Lett. **86B**, 24 (1979);
   R. Vandenbosch, private communication (1983).
3. P.R. Christensen *et al.*, Nucl. Phys. **A390**, 336 (1982).

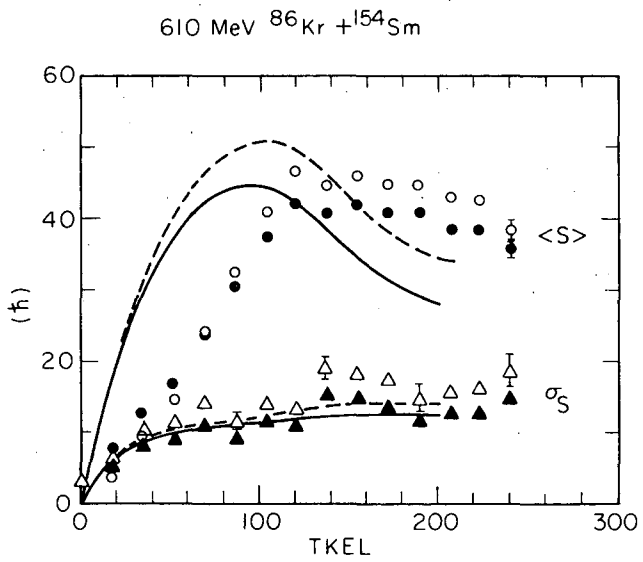

Fig. 2. Average spin magnitude <S> and dispersion σ_S as functions of TKEL for the reaction 610 MeV ^{86}Kr + ^{154}Sm. Dashed and dot-dashed curves show results obtained with a neck wall dissipation rate determined by the motion of the effective neck radius (instead of the geometric neck radius); the dashed curves are obtained including the standard reduction factor of the neck wall dissipation for elongated neck shapes, whereas this reduction is removed for the results denoted by the dot-dashed curves. XBL 841-7502

The Role of Rotational Degrees of Freedom in Heavy Ion Collisions*

L.G. Moretto and G.J. Wozniak

Angular momentum plays a very pervasive role in deep inelastic collisions. Angular momentum defines the range of existence of this very process and its boundaries as well, with complete fusion on one side and direct reactions on the other. The angular distribution of the ensuing products is controlled by angular momentum in more than one way. On one hand the interaction time is angular momentum dependent, and so is the angular velocity. On the other, the orbital angular momentum that is dissipated, as well as the dissipated kinetic energy both depend on the angular momentum. Furthermore, the different exit channel asymmetries are fed by different ℓ waves. All this contributes to making the angular distributions dependent on just about any variable in the Hamiltonian. The relaxation of angular momentum leads to the secular equilibrium of the system which can rotate like a rigid body. However, the presence of angular momentum bearing degrees of freedom allows for fluctuations that can

misalign the aligned component of the fragment angular momentum. The excitation of these modes can be studied through the angular distribution of particles and gamma rays emitted by the fragments.

The present understanding of the role of angular momentum has crystallized in a variety of theories ranging from conditional equilibrium statistical theories, to assorted transport theories and including Time Dependent Hartree Fock. At this stage it may be premature to say if any given theory satisfies all the details brought to light by experiment.

Footnote

*Condensed from Annual Review of Nuclear and Particle Science **34**, 189 (1984).

A Feedback Process Controlling Energy Partition and Mass Exchange Between Heavy Ions*

L.G. Moretto and E.G. Lanza†

The thermal energy partition between fragments and the lack of mass drift under the action of a driving force are explained in terms of a temperature-dependent particle exchange. A feedback mechanism driven by the relative motion minimizes the temperature gradient between the fragments at the expense of the light fragment mass.

Footnotes

*Invited paper at the international meeting on "Theoretical Approaches to Heavy Ion Reaction Mechanisms," Paris May 1984.

†Max-Planck Institut für Kernphysik, Heidelberg, Germany.

Pion Interferometry Studies of Relativistic Heavy-Ion Collisions Using the Intranuclear Cascade Model

T.J. Humanic

Intranuclear cascade (INC) models have been widely used to understand various features of relativistic heavy-ion collisions. For example, they have had some success in predicting proton, pion, and kaon inclusive cross sections for laboratory bombarding energies in the range 0.4-2.1 GeV/nucleon, and for a variety of projectile-target combinations.[1,2] Because they are classical models, and the positions and momenta of all particles taking part in the cascade are known as a function of time, they also lend themselves well to understanding the geometric aspects of the collision, such as the size of the interaction region and the duration of particle production. In fact, this is just the kind of information obtained from pion interferometry measurements, where the radius, lifetime, and coherence of the pion source are extracted. Although some theoretical work has been carried out to study the geometry of the pion source with an INC model,[2] no study has yet been made which is directed towards understanding existing pion interferometry measurements. Additional incentives come from recent measurements which have become available for the systems ^{20}Ne + NaF and ^{40}Ar + KCl.[3-5] Thus, the goal of the present work

is to extract radius, lifetime, and coherence parameters from an INC model which can be directly compared with the results of these recent measurements.

The procedure for obtaining these INC model predictions consists of three steps:

(a) run the INC code for the system of interest to produce a set of "final" pions (pions which survive to the end of the calculation), recording their momenta and the space-time location where they were created;

(b) symmetrize the N-pion outgoing wave function assuming the outgoing wave function of each pion is a plane wave, where N is the like-pion multiplicity; and

(c) form the two-pion correlation function from these symmetrized pions, and fit a Gaussian space-time pion distribution to the correlation function to extract R, τ, and λ, the radius, lifetime, and coherence parameters for the distribution.

Cugnon's CASCADE code[2] was used to make the INC model calculations. In this model, the Δ-isobars, which are the mechanisms for producing and absorbing pions, are given a Lorentzian mass distribution and an exponential lifetime distribution. Therefore, pions are produced and reabsorbed throughout the time of the collision. At the end of the calculation, the momentum vector of each final pion is tagged with the position and time at which its "parent" Δ-isobar decayed and then is stored for later use.

The next step is to symmetrize the N-pion outgoing wave function, where N is the number of like-charged pions in the final state. If we assume that the outgoing wave functions for the individual pions can be represented by plane waves, $\Phi_i(\bar{x})$, of the form

$$\Phi_i(\bar{x}) = \exp\left(i\,(\bar{k}_i \cdot \bar{r} - \omega_i t)\right) \quad , \qquad i = 1,\ldots,N \quad , \tag{1}$$

then the symmetrized N-pion wave function, $\Psi_N(\bar{x}_1,\ldots,\bar{x}_N)$, will be

$$\Psi_N(\bar{x}_1,\ldots,\bar{x}_N) = C_N \sum_{j=1}^{N!} P_j \Phi_1(\bar{x}_1)\ldots\Phi_N(\bar{x}_N) \quad , \tag{2}$$

where P_j is the permutation operator, C_N is a normalization constant, and $\bar{k}_i$ and ω_i are the momentum and energy of the ith pion, respectively. In order to apply Eq. 1 and Eq. 2 to the list of pions produced by CASCADE in the first step, the N-pion probability, P_N, is formed,

$$P_N(\bar{x}_1,\ldots,\bar{x}_N) = |\Psi_N(\bar{x}_1,\ldots,\bar{x}_N)|^2 \quad , \tag{3}$$

and groups of N pions are weighted by P_N.

The final step in the procedure is to form the two-pion correlation function from the symmetrized pions and to extract the R, τ, and λ predictions.

It is important to note that the computer codes used to form the correlation function and to carry out the Gaussian fitting are identical to the ones used by Zajc *et al.*[3] and similar to those of Beavis *et al.*[5] in analyzing their two-pion correlation data. This should minimize programming biases and allow the CASCADE predictions for R, τ, and λ to be more comparable with the experimental results.

A typical correlation function generated from CASCADE with its Gaussian fit (projected onto the q-axis) is shown in Fig. 1 for the system 1.5 GeV/nucleon $^{40}Ar + {}^{40}Ar$. This case was run with a 4π geometry (as is the case of the streamer chamber in ref. 5), impact parameter, b, of 2 fm, minimum center-of-mass momentum, k_{min}, of 50 MeV/c ($k_{min} \leq k_1, k_2$), and about 270,000 two pion pairs. Error bars reflect statistical uncertainties only. Note the prominent Bose-Einstein enhancement at small q, which is a consequence of the pion wave function symmetrization carried out with Eq. 2. For this example, the extracted pion source parameters are R = 3.6 ± 0.1 fm, τ = 3.2 ± 0.5 fm/c, and λ = 0.94 ± 0.05.

Comparisons between the CASCADE predictions of the present work and recent pion interferometry measurements are presented in Fig. 2. The measurements of Zajc *et al.*[3] were performed with a narrow acceptance magnetic spectrometer which was set to accept pions centered about 90° in the center-of-mass with respect to the beam direction, whereas the measurements of Beavis *et al.*[4,5] were performed with a streamer chamber having an

almost 4π solid angle acceptance. These acceptances were simulated, to some extent, for the CASCADE predictions. Generally speaking, the CASCADE predictions are seen to agree rather well with the experimental results.

In summary, a method has been presented by which an INC model may be used to obtain pion source parameter predictions which can be directly compared with pion interferometry experiments. This method has been applied with Cugnon's INC model to extract predictions for recent pion interferometry measurements, and generally good agreement is found.

References

1. Y. Kitazoe *et al.*, Phys. Rev. C **29**, 828 (1984).
2. J. Cugnon and S.E. Koonin, Nucl. Phys. **A355**, 477 (1981).
3. W.A. Zajc *et al.*, Phys. Rev. C **29**, 2173 (1984).
4. D. Beavis, *et al.*, Phys. Rev. C **27**, 910 (1983).
5. D. Beavis, *et al.*, Phys. Rev. C **28**, 2561 (1983).

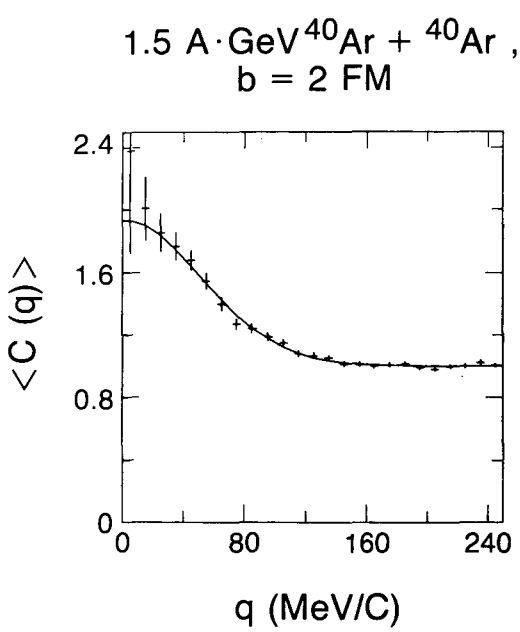

Fig. 1. Projected two-pion correlation function from CASCADE for the reaction 1.5 GeV/nucleon ^{40}Ar + ^{40}Ar, b = 2 fm, k_{min} = 50 MeV. XBL 849-10799

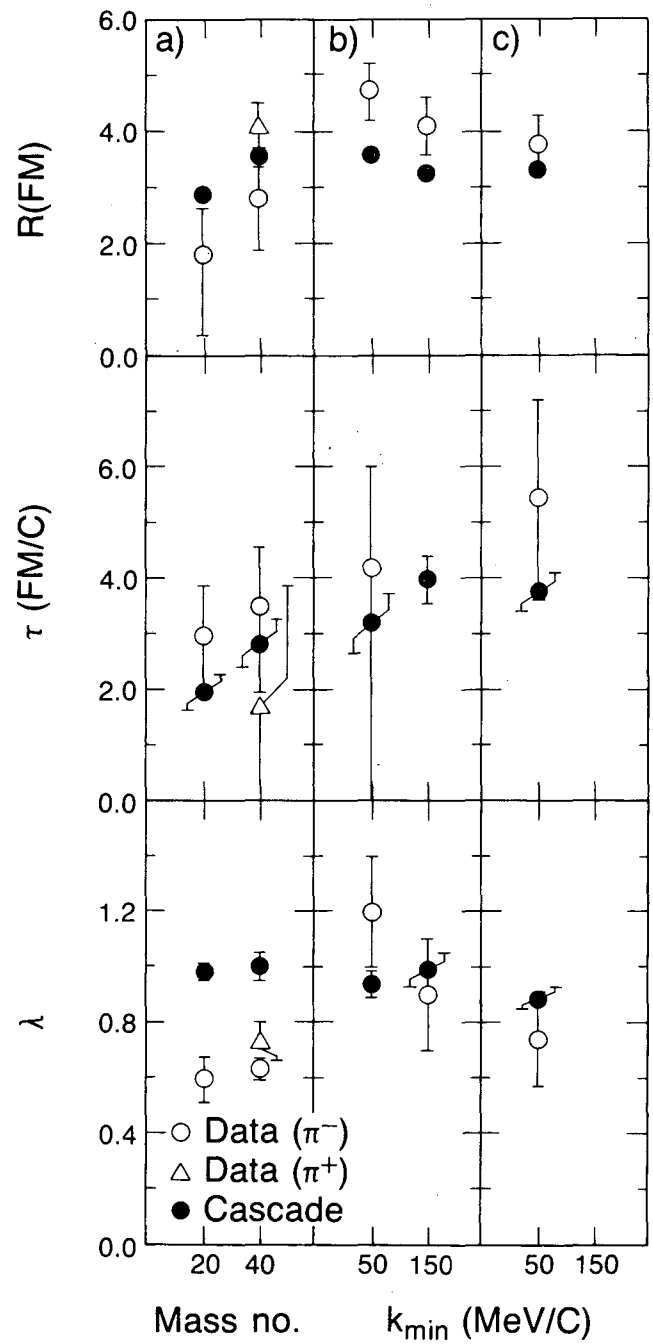

Fig. 2. Comparison between pion source parameters from CASCADE predictions and pion interferometry measurements: a) 1.8 GeV/nucleon ^{40}Ar + KCl and ^{20}Ne + NaF (ref. 3), b) 1.5 GeV/nucleon ^{40}Ar + KCl (ref. 4,5), and c) 1.2 GeV/nucleon ^{40}Ar + KCl (ref. 5). XBL 8410-10909

Behavior of Pions Incident on a Slab of Uniform Complex Nuclear Material*

R.A. Mehrem,† H.M.A. Radi† and J.O. Rasmussen

We have need for a simple model for pion production in nuclei, so as to facilitate heavy ion pion Monte Carlo studies. A model is presented for the scattering of obliquely incident relativistic pions from a region of uniform nuclear matter. A simple analytic method that incorporates a second-order optical potential in the Klein-Gordon equation is constructed. This method gives only one physically acceptable solution for which the real and imaginary parts of the wave number, k, inside nuclear matter are positive for all possible values of incident pion wave numbers, k_0. Reflectivity of pions indicates that the nuclear surface has higher transmission around $T_\pi \simeq 35$ MeV than at other energies, since the index of refraction of nuclear matter is near to unity there. The pion mean free path as a function of pion energy is plotted and discussed.

Considerable attention has recently been focused on the use of reflection and absorption of pions in relativistic heavy ion collisions involving pion production.[1] Also, information about the π-nucleus optical potential has recently become available.[2-4] The remarkable success achieved by this potential is that it has been able to reproduce the recent experimental cross sections[5-9] for the low energy region ($T_\pi \geqslant 50$ MeV). For the energy region ($T_\pi = 50$ MeV), the cross section is reproduced by properly taking into account the quasielastic scattering process.[2]

The optical potential operator used for this analysis is taken from the work of Stricker *et al.*[2,3] and of Carr *et al.*[4,10] It was developed with parameters to fit the shifts and widths of the energy levels in pionic atoms, as well as fitting pion-nucleus scattering data.

The Klein-Gordon equation for pions has two solutions for (pc),[2] and hence we have four possible solutions for p. However, these solutions will depend on the optical potential parameters b_0, b_1, c_0, c_1, B_0, B_1, C_0, C_1, and λ; these parameters are complex.

Only one solution is physically meaningful. In the lower part of Fig. 1, k_1 and k_2 are plotted as a function of the incident π^0 wave number k_0 for the ^{207}Pb nucleus. The mean free path for absorption is shown in the upper part of Fig. 1 [$\lambda^{tot} = 1/(2k_2)$]. It is interesting that we get a mean free path curve similar to Hecking's.[11] His Fig. 1 (full curve, set 1) is similar to our Fig. 1 (upper part) except that it is a factor of order of 1.6 higher than our curve. Hecking arbitrarily replaced k^2 (the local wave number) in Eq. (4) by k_0^2 (the wave number at infinity). By solving his Eq. (4) exactly and by using the parameters in his table, we can see that this replacement is to avoid getting a negative mean free path for energies $\geqslant 25$ MeV. Our selection of the physically meaningful Klein-Gordon solution avoids this arbitrary step.

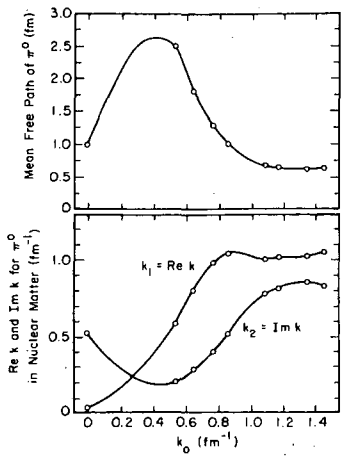

Fig. 1. The lower part represents the real and imaginary part of the π^0 wave number inside the ^{207}Pb nucleus, k_1 and k_2, respectively, versus the incident π^0 wave number k_0 (all are in fm^{-1}). The upper part represents the mean free path of π^0 (in fm) vs the incident π^0 wave number k_0 (in fm^{-1}) for the same nucleus. The circles are points obtained by using set C of ref. 10. The solid curve is a computer cubic fit.

XBL 8310-12029

The problem Hecking had with negative mean free paths or growing solutions arises at low energies with the Schrödinger equation and the velocity-dependent optical potential because the sign of the local k^2 is negative and the velocity-dependent imaginary term becomes a source, not a sink. In our treatment this spurious behavior does not occur because the physical meaningful solution of the Klein-Gordon equation is selected.

The next step is to consider the oblique incidence of a plane wave k_0 (representing the incident pion) on a sharp nuclear boundary.

The reflectivity $|R|^2$ is plotted as a function of k_0 in Fig. 2. It shows a minimum at $k_0 \approx 0.55$ fm^{-1} ($\approx$35 MeV) for all angles <90°. On the other hand, more than 50% of the pions will be transmitted for almost all energies at angles of incidence $\theta_0 \leq 60°$. Snell's law of refraction and reflection is applicable where the nuclear surface diffuseness is smaller than the pion wavelength, and this condition is satisfied for pions below the Δ resonance, where the Kisslinger potential is applicable.

The model presented in this paper has been used by us in Monte Carlo studies of reflection of relativistic pions from spectator fragments in heavy ion collisions.

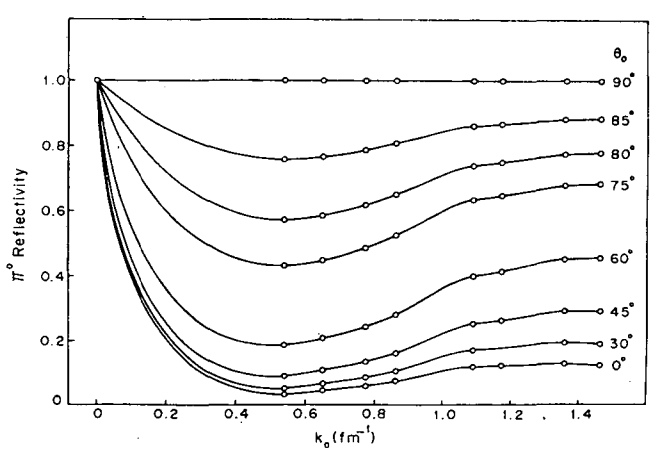

Fig. 2. π_0 reflectivity from the nuclear surface is displayed as a function of the incident wave number k_0 (in fm^{-1}) with curves for different incident angles ranging from 0° to 90°. XBL 8310-12032

*Condensed from Phys. Rev. 330, 1 (1984).

†Physics Department, Kuwait University, Kuwait.

1. H.M.A. Radi, J.O. Rasmussen, K.A. Frankel, J.P. Sullivan and H.C. Song, Phys. Rev. C **27**, 606 (1983).
2. K. Stricker, H. McManus and J.A. Carr, Phys. Rev. C **19**, 929 (1979).
3. K. Stricker, J.A. Carr and H. McManus, Phys. Rev. C **22**, 2043 (1980).
4. J.A. Carr, H. McManus and K. Stricker, Phys. Rev. C **25**, 952 (1982).
5. B.M. Preedom, S.H. Dam, C.W. Darden III, R.D. Edge, D.J. Malbrough, T. Marks, R.L. Burman, M. Hamm, M.A. Moinester, R. P Redwine, M.A. Yates, F.E. Bertrand, T.P. Clearly, E.E. Gross, N.W. Hill, C.A. Ludeman, M. Blecher, K. Gotow, D. Jenkins and F. Milder, Phys. Rev. C **23**, 1134 (1981).
6. K. Nakai, T. Kobayashi, T. Numao, T.A.Shibata, J. Chiba and K. Masutani, Phys. Rev. Lett. **44**, 1446 (1980).
7. M. Blecher, K. Gotow, D. Jenkins, F. Milder, F.E. Bertrand, T.P. Clearly, E.E. Gross, C.A. Ludemann, M.A. Moinester, R.L. Burman, M. Hamm, R.P. Redwine, M. Yates-Williams, S. Dam, C.W. Darden III, R.D. Edge, D.J. Malbrough, T. Maks and B.M. Preedom, Phys. Rev. C **20**, 1884 (1979).
8. S.A. Dytman, J.F. Amann, P.D. Barnes, J.N. Craig, K.G.R. Doss, R.A. Eisenstein, J.D. Sherman, W.R. Wharton, G.R. Burleson, S.L. Verbeck, R.J. Peterson and H.A. Thiessen, Phys. Rev. C **19**, 971 (1979).
9. C. Olmer, D.F. Geesaman, B. Zeidman, S. Chakravarti, T.-S.H. Lee, R.L. Boudrie, R.H. Siemssen, J.F. Amann, C.L. Morris, H.A. Thiessen, G.R. Burleson, M.J. Devereux, R.E. Segel and L.W. Swenson, Phys. Rev. C **21**, 254 (1980).
10. J.A. Carr, Ph.D. thesis, Michigan State University, 1982 (unpublished).
11. P. Hecking, Phys. Lett. **103B**, 401 (1981).

Note on the Partitioning of Nuclei*

L.G. Sobotka and L.G. Moretto

The inclusive charge and mass distributions of high energy proton and heavy ion bombardments are frequently interpreted in terms of a liquid-gas phase transition.[1,2] However, Aichelin and Huefner[3] have recently shown that the charge distributions for high energy p + Kr, Ag, Xe and U can be reproduced by a calculation which is portrayed to produce the least biased distribution. We show that the approach of Aichelin and Huefner is an approximation to the Euler number partition and that such an approximation breaks down for large fragment size. Furthermore, we show that the most reasonable application of these types of theories differs substantially from the previously published work.[3] Although this theory is not inconsistent with the data its applicability to the nuclear case is made uncertain by the lack of appropriate geometrical constraints.

We wish to calculate the part size distribution when an integer is decomposed.

The number of times a part of size a occurs when the integer N is fractured in each of the P(N) ways is

$$P_a(N) = P(N - a) + P(N - 2a) + P(N - 3a) + \cdots P(0) \quad , \qquad (1)$$

where P(X) is the number of unrestricted partitions of the integer X. Aichelin and Huefner calculate the equivalent probability P(a) as follows. They define the probability P(m,a) of producing a fragment of size a with a multiplicity m as,

$$\sum_{m=0} P(m,a) = 1 \quad \text{for each } a$$

$$\text{and} \sum_{m=0} \sum_{a}^{N} ma\, P(m,a) = N \quad , \qquad (2)$$

where N is the size of the object being fragmented. The information contained in P is

$$I = \sum_{m=0} \sum_{a}^{N} P(m,a) \ln P(m,a) \quad . \qquad (3)$$

Introducing the constraints 3, 4 one obtains the maximum

$$\frac{\partial}{\partial P(m,a)} \sum_{m} \sum_{a}^{N} [P(m,a) \ln P(m,a) - K(a)P(m,a) + DmaP(m,a)] = 0 \quad . \qquad (4)$$

From which

$$P_a(N) \simeq \left(\exp 1.28a/\sqrt{N} - 1\right)^{-1} \quad . \qquad (5)$$

Conditions 2, 3, 4 make this problem a saddle point method approximation to the Euler number partition. Therefore the part size distribution from Eq. (1) should be identical to that obtained with the method reproduced above. Fig. 1 shows the part size distributions for two values of N for both Eqs. (1) and (5). We can immediately notice that the two calculations are nearly identical for small fragments. However, the calculations diverge as the part size increases.

The comparison between the calculation and data presented in ref. 3 is obtained by identifying N with Z_0, the total charge minus a certain number of charges presumably directly knocked out by the projectile. However since these theories do not involve any potentials and all "fractures" are equally likely, the only consistent application of these theories is to identify N with the total number of nucleons. Unfortunately Eq. (5) shows that the partition theory does not scale trivially from Z to A. In other words the calculation is not invariant with respect to the transformation A = Zf(Z) where f(Z) is a slowly varying function of Z. Therefore the calculation yields dramatically different results if one uses Z rather than A. The point is illustrated in Fig. 2. The solid line is an "inappropriate" calculation of the charge distribution obtained by calculating the number of

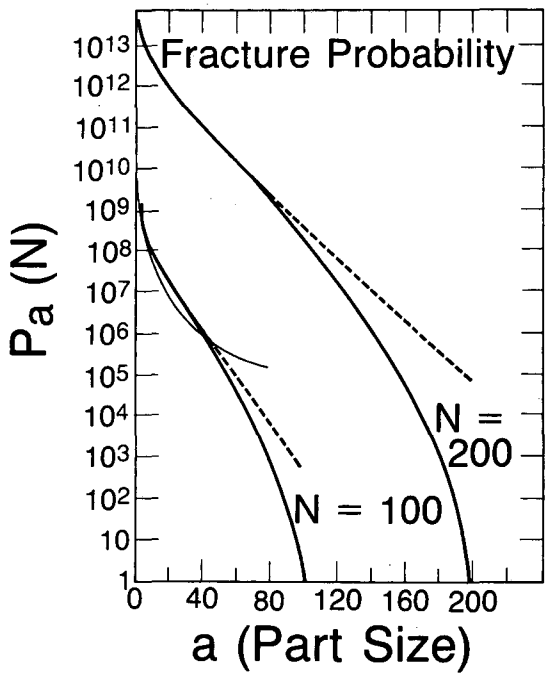

Fig. 1. Part size distributions. The solid lines are the calculation using partition theory (Eq. 1) while the dashed line uses the expression of Aichelin and Huefner (Eq. 5). This second calculation (Eq. 5) is normalized to the number theory calculation at a=1. The thin curve is a distribution given by $a^{-2.64}$ which fits both p + Kr and p + Xe data of ref. 1.

XBL 843-10292

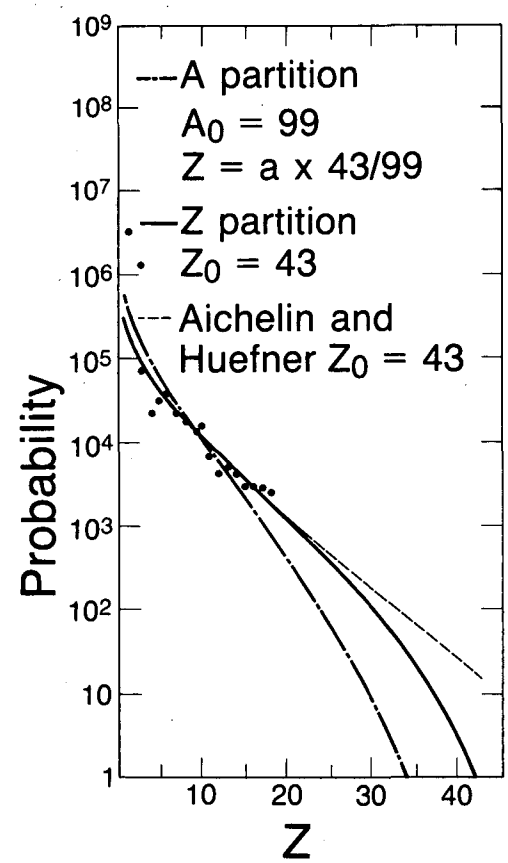

Fig. 2. The charge distributions calculated in various ways (see text). XBL 843-10293

partitions of Z_0 = 43 charges. If we calculate the number of partitions of A_0 = 99 and transform the mass distribution into a charge distribution by assuming an average charge per part of $Z = a \times Z_0/A_0$ we obtain the dot-dashed curve. This curve, which, we believe, is the only approach consistent with the spirit of the theory, has a steeper slope than a calculation where the charges are partitioned and the neutral particles ignored (solid line).

The experimental charge distributions[4] are compared to calculations in Fig. 2. The data are more or less reproduced by number partitions in either of the versions, but cannot distinguish between them. In conclusion we find the connection between number partition and fragmentation somewhat tenuous and we wonder whether the fair comparison between data and theory may not be fortuitous.

Footnote and References

*Condensed from LBL 17699.

1. J E. Finn *et al.*, Phys. Rev. Lett. **49**, 1321 (1982).
2. A.D. Panagiotou *et al.*, Phys. Rev. Lett. **52**, 496 (1984) and references therein.
3. J. Aichelin and J. Huefner, Phys. Lett. **136B**, 15 (1984).
4. G.D. Westfall *et al.*, Phys. Rev. **C17**, 1368 (1978).

Transverse Momentum Analysis of Collective Motion in Relativistic Nuclear Collisions

P. Danielewicz and G. Odyniec

Novel transverse-momentum technique is used to isolate collective motion in the Ar+KCl reaction at 1.8 GeV/nucleon. Previous analysis of this reaction,[1] employing the standard sphericity tensor, revealed no significant effect. In the present analysis, collective effects are observed. They are substantially stronger than in the Cugnon cascade model, and weaker than in the hydrodynamic model. The semi-exclusive data of the near-symmetric Ar+KCl (1.8 GeV/nucleon) reaction come from central-trigger measurements in the streamer chamber at the Bevalac. Details of the experiment have been reported previously.[1]

To estimate the reaction plane in the collisions we construct a vector from transverse momenta $\vec{p}_\nu^{\perp}$ of detected particles:

$$\vec{Q} = \sum_{\nu=1}^{M} \omega_\nu \vec{p}_\nu^{\perp} \qquad (1)$$

where ν is a particle index and ω_ν is a weight. We put $\omega_\nu = 0$ for pions; for the baryons $\omega_\nu = 1$ for $y_\nu > y_{cms}+\delta$, $\omega_\nu = -1$ for $y_\nu < y_{cms}-\delta$, and $\omega_\nu = 0$ otherwise. The quantity $\delta = 0.3$ is inserted to remove particles from midrapidity that would contribute unwanted fluctuations.

To determine the accuracy of the procedure we divided randomly each event into two, and compared the reaction planes extracted from the two sub events. The azimuthal correlation between the constructed vectors $\vec{Q}_I$ and $\vec{Q}_{II}$ is shown in Fig. 1a. The fact that the distribution is not flat testifies to the determination of the reaction plane. To verify that this result is not due to inefficiencies in the streamer chamber acceptance, we performed a similar test using Monte Carlo events generated by mixing particles from events within the same multiplicity range. The resulting distribution is shown in Fig. 1b. It is completely flat. By simple arguments one can deduce that the distribution of the observed $\vec{Q}$ with

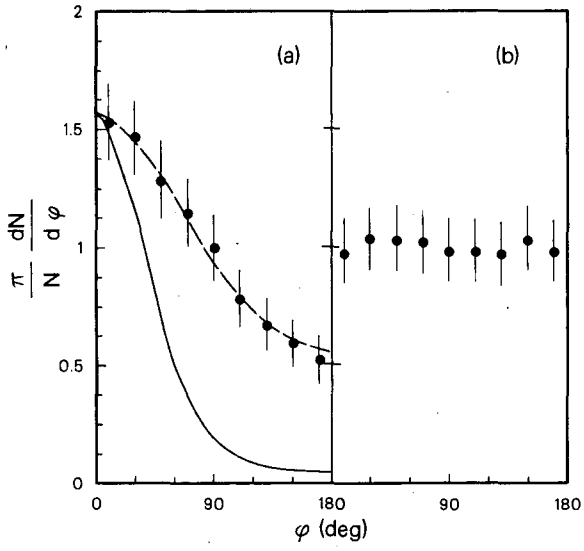

Fig. 1. Azimuthal angle distribution of vectors $\vec{Q}_I$ and $\vec{Q}_{II}$ from subevents with respect to each other: (a) for data, (b) for Monte Carlo events. Dashed line is for the simulation with two Gaussian sources. Solid line represents azimuthal angle distribution of vector $\vec{Q}$ from the sources with respect to the reaction plane (this is normalized to the height with the sampling distribution). XCG 8410-13380

respect to the reaction plane should be narrower than that of Fig. 1a by a factor of 2.

The magnitude of $\vec{Q}$ can be used to determine average transverse momenta and transfer in the reaction plane. Thus, to the extent that correlations, other than that stemming from existence of the reaction plane, are weak,

$$\overline{Q^2 - \sum p^{\perp 2}} = \sum_{\mu\neq\nu} \overline{(\omega_\mu \vec{p}_\mu^{\perp})(\omega_\nu \vec{p}_\nu^{\perp})}$$

$$= \sum_{\mu\neq\nu} \left(\overline{\omega_\mu p_\mu^x}\right)\left(\overline{\omega_\nu p_\nu^x}\right) \quad , \qquad (2)$$

where the averages at the r.h.s. are in the coordinate system associated with the reaction plane, and x

denotes a vector component in the reaction plane. With a fragment mass a_ν, and the total mass $A = \sum a$, we estimate average momenta per nucleon in the reaction plane from

$$\overline{\omega p^x/a} \approx \left(\overline{(Q^2 - \sum p^{\perp 2})} \,/\, \overline{(A^2 - \sum a^2)}\right)^{1/2}$$

$$= 95 \pm 5 \text{ MeV/c}, \qquad (3)$$

and the average transverse-momentum transfer in the reaction plane, $\overline{Q^x}$, with

$$\overline{Q^x} \approx \overline{A} \cdot \overline{\omega p^x/a} = 2.17 \pm 0.11 \text{ GeV/c}. \qquad (4)$$

For total transverse momentum in the forward region, $y > y_{cms} + \delta$, in terms of nuclear charges, $\overline{P_f^x}$, we estimate

$$\overline{P_f^x} \approx \overline{Z_f} \cdot \overline{\omega p^x/a} = 1.04 \pm 0.05 \text{ GeV/c}. \qquad (5)$$

Utilizing (3), we attempted to simulate the data with two Gaussian sources associated with the reaction plane in the transverse-momentum space. Carrying with the sources the procedure as with data for Fig. 1a, we get the dashed line in Fig. 1a. The solid line in Fig. 1a indicates the azimuthal angle distribution of $\vec{Q}$ from the sources with respect to the reaction plane.

Subsequently, we establish the average transverse momentum per nucleon in the reaction plane as a function of rapidity $\overline{p^x/a}(y)$. We also determine the average differential transverse momentum deposition (per unit rapidity) in the reaction plane, $\overline{dP^x/dy}$, in terms of nuclear charges. This variable, integrated over a rapidity interval, yields the total transverse momentum deposited in nuclear charges in an interval. To avoid finite-multiplicity distortions, the reaction plane has to be estimated for each particle separately from the remaining particles in an event

$$p_\nu^{x'} = \vec{p}_\nu^{\perp} \cdot \vec{Q}_\nu / Q_\nu \;, \qquad \vec{Q}_\nu = \sum_{\mu \neq \nu} \omega_\mu \vec{p}_\mu^{\perp} \;. \qquad (6)$$

The prime on x stresses that the momenta are not projected on the true reaction plane, but on the estimated one. The average momenta evaluated with (6), $\overline{p^{x'}/a}(y)$, and deposition $\overline{dP^{x'}/dy}$ in the estimated plane are shown in Fig. 2a and c, respectively. Fig. 2b and d, with the same results for Monte Carlo events, illustrate absence of the distortion from statistical fluctuations. As the particle momenta are not being projected onto the true reaction plane, the average momenta get reduced: $\overline{p^{x'}}(y) = \overline{p^x}(y) \cdot \overline{\cos\phi}$, where ϕ is the azimuthal angle deviation of the estimated plane from the true one. Normalizing momenta with the total observed momentum (4), l.h.s. scales in Fig. 2a and c, we find $\overline{Q^{x'}}/\overline{Q^x} = \overline{\cos\phi} = 0.64 \pm 0.06$, which is in agreement with the simulated distribution of $\vec{Q}$ in Fig. 1a.

With the result (5) and Fig. 2c, we estimate total transverse momentum transfer between hemispheres ($y \gtrless y_{cms}$) in terms of nuclear charges of p, d, t from the reaction, at 2.3 ± 0.2 GeV/c. Assuming a corresponding amount of transfer in neutrons would bring the total transfer in the reaction to $\gtrsim$ 4.9 GeV/c.

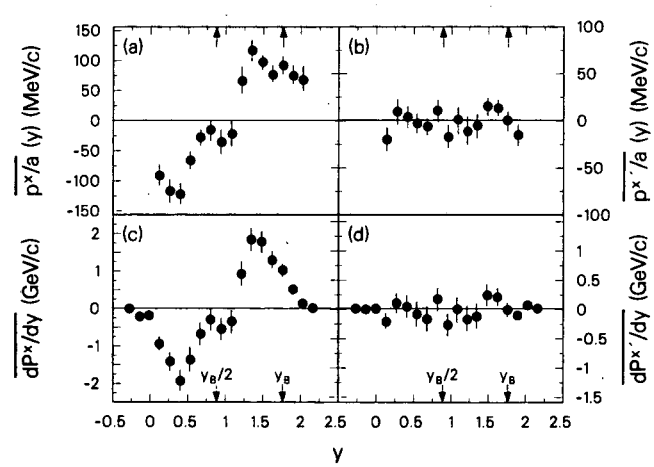

Fig. 2. (a,b) Average momentum per nucleon in the estimated reaction plane $\overline{p^{x'}/a}(y)$, for data and Monte Carlo events, respectively. (c,d) Differential, per unit rapidity, transverse momentum deposition in the estimated reaction plane in terms of nuclear charges $\overline{dP^{x'}/dy}$, for data and Monte Carlo events, respectively. L.h.s. scales in (a) and (c) yield respective estimated average momenta per nucleon $\overline{p^x/a}(y)$, and deposition $\overline{dP^x/dy}$, in the true reaction plane.

XCG 8410-13381

Comparison of the findings with results of the ideal-fluid hydrodynamic calculation,[2] reveals that the hydrodynamic model, scaled appropriately to the bombarding energy, overestimates the average transverse momenta per nucleon of the data (3), by a factor ~3–4. Calculations of the Ar+KCl (1.8 GeV/nucleon) reaction, with the Cugnon[3] intranuclear code, yield average transverse momenta in the reaction plane smaller than these of the data, by a similar factor, $\overline{\omega p^x} \approx 20-30$ MeV/c. The sampling distribution, as in Fig. 1a, is quite flat for the cascade model.

Footnotes and References

*Condensed from LBL-18600, submitted to Physics Letters B.

1. H. Ströbele *et al.*, Phys. Rev. **C27**, 1349 (1983); H. Ströbele, Nucl. Instr. and Meth. **221**, 523 (1984).
2. G. Buchwald *et al.*, Phys. Rev. **C28**, 2349 (1983); H. Stöcker *et al.*, Phys. Rev. **C25**, 1873 (1982).
3. J. Cugnon, Phys. Rev. **C23**, 2094 (1981).

Transport Properties of Excited Nuclear Matter and the Shock-Wave Profile*

P. Danielewicz

Despite the years of development of the hydrodynamic approach to intermediate energy heavy-ion collisions, one finds that a major ingredient of the approach, the magnitude of the transport coefficients, has not been settled. The importance of the coefficients is that they establish the size of the region in which thermal equilibrium can be maintained.

I derive expressions for the shear viscosity η and heat conduction κ coefficients associated with the Uhlenbeck-Uehling equation. The expressions smoothly interpolate between the degenerate Fermi-gas, $\eta \sim T^{-2}$, $\kappa \sim T^{-1}$, and Boltzmann limits, η, $\kappa \sim T^{1/2}$. The coefficients, calculated with the experimental nucleon-nucleon cross sections, and displayed in Fig. 1, exceed by a factor of two or more those used until now in hydrodynamic calculations of nuclear collisions.[1]

Using these results for the coefficients, I solve subsequently the relativistic hydrodynamic equations for the shock wave profile in nuclear collisions. Variation of the widths of the shock wave with the bombarding energy per nucleon is shown in Fig. 2. The widths ($\gtrsim$4 fm in terms of the normal nuclear matter) agree reasonably with those extracted from cascade calculations.[2] The figure indicates that shock phenomena are not possible in nuclear collisions at energies $E_{lab} \lesssim 100$ MeV/nucleon. At higher energies, a fully developed shock wave with the associated creation of high-density equilibrated matter requires rather heavy ($A \gtrsim 100$) nuclei.

Footnote and References

*Condensed from Phys. Lett. **146B**, 168 (1984).

1. L.P. Csernai, B. Lukács and J. Zimanyi, Lett. Nuovo Cimento **27**, 111 (1980); H.H. K. Tang and C.Y. Wong, Phys. Rev. **C21**, 1846 (1980); G. Buchwald, L.P. Csernai, J.A. Maruhn, W. Greiner and H. Stöcker, Phys. Rev. **C24**, 135 (1981).
2. E.C. Halbert, Phys. Rev. **C28**, 295 (1981); J. Cugnon, T. Mizutami and J. Vandermeulen, Nucl. Phys. **A352**, 505 (1981).

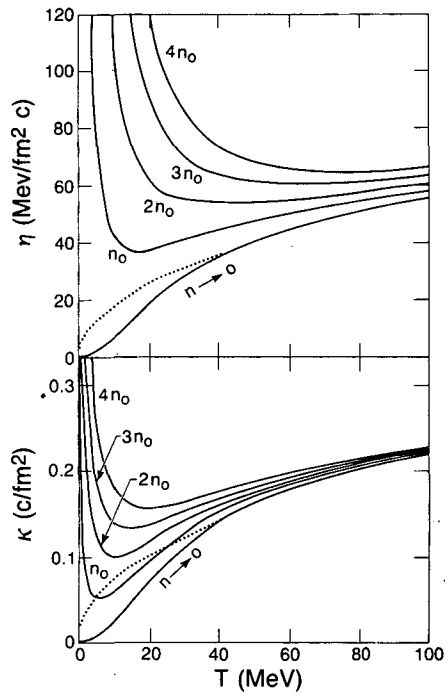

Fig. 1. The temperature and density dependence of the nuclear transport coefficients. The normal nuclear density has been taken as $n_0 = 0.145$ fm^{-3}. Dotted lines denote the Chapman-Enskog results, with the effective isotropic cross section set equal to 30 mb. XBL 842-10062A

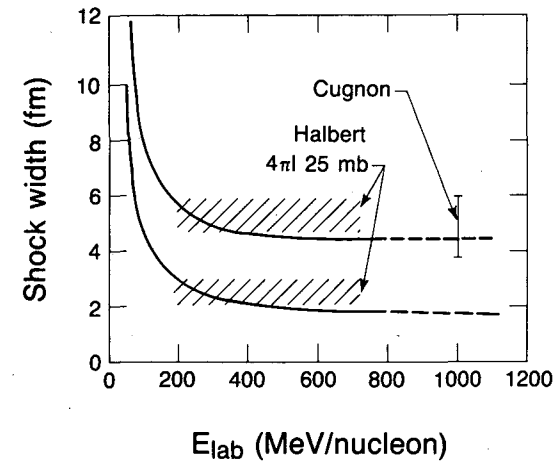

Fig. 2. Bombarding-energy variation of the shock widths defined in terms of the 70% point of asymptotic density rise. The lower curve is the distance over which the density rise occurs in the shock frame. The upper curve is the equivalent distance in normal nuclear matter. Continuation with the dashed lines emphasizes the increasing abundance of π mesons and Δ resonances that are not included in the treatment. The dashed areas and the error bar represent the shock widths extracted from cascade calculations.[2] XBL 844-10402

Nuclear Compression Effects on Pion Production in Nuclear Collisions*

M. Gyulassy, Y. Kitazoe, M. Sano and M. Wakai

The pion multiplicity produced in nuclear collisions between 0.2 and 2 GeV/nucleon is calculated assuming shock formation. We correct the procedure of extracting the nuclear equation of state as proposed by Stock *et al.*. We find that the nuclear equation of state would have to be extremely stiff for this model to reproduce the observed multiplicities.

The observed[2] negative pion multiplicity, $N_\pi^{obs}(E)$, produced in central nuclear collisions increases approximately linearly with incident kinetic energy E. While cascade calculations[2,3] using the Cugnon code also lead to a linear dependence of $N_\pi^{cas}(E)$, on E, the calculated values systematically overestimate the observed multiplicity. Stock *et al.*[2] suggested that this discrepancy could be exploited to extract information about the nuclear matter equation of state at high densities and temperatures. They noted that if thermal and chemical equilibrium is reached in such collisions, then the number of pions depends on the available thermal kinetic energy per nucleon, $K(E_{cm})$. For a given center of mass kinetic energy per nucleon, E_{cm}, $K(E_{cm}) = E_{cm} - U(E_{cm})$, where $U(E_{cm})$ is potential energy per nucleon at the point where the pion abundance freezes out.

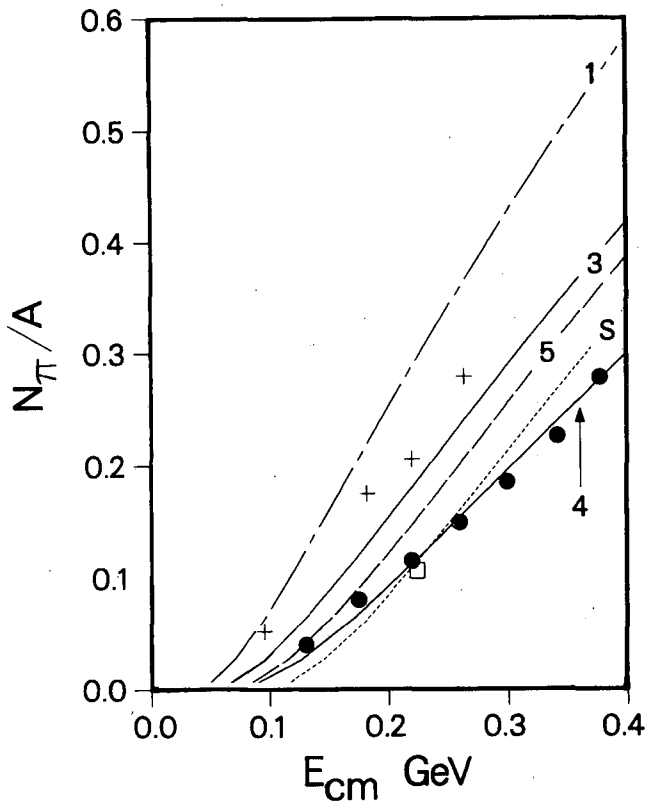

Fig. 1. The pion to baryon ratio as a function of E_{cm}. Curves are described in text. Solid dots are data points extrapolated to zero impact parameter for Ar+Ca, while open square is for La+La. Curve S corresponds to the calculations in ref. 2 where the ground state kinetic energy, $K_N(\rho,0)$, was doubly counted. XBL 8410-4098

That potential energy, on the other hand, clearly depends on the baryon density, $\rho(E_{cm})$, the freeze out point. Since one expects ρ to be an increasing function of energy, the energy dependence of the pion multiplicity should then be sensitive to the form of $U(\rho)$.

To extract $U(\rho)$ from the data they noted further that the cascade calculation explicitly neglects potential energy. Therefore, $N_\pi^{cas}(E)$, is the pion multiplicity under the condition that $K = E_{cm}$. Hence, they proposed to extract $U(E_{cm})$ by equating

$$N_\pi^{cas}\big(E_{cm} - U(E_{cm})\big) = N_\pi^{obs}(E_{cm}) \quad . \qquad (1)$$

Using eq. (1) and the maximum compression $\rho(E_{cm})$ computed via cascade, they found a remarkable similarity between their $U(\rho)$ curve and the energy functional, $W(\rho,T = 0)$, for compressibility $K = 250$ MeV. They were therefore tempted to identify $U(\rho)$ with $W(\rho,0)$. The correct connection is, however, $W(\rho,T) = K(\rho,T) + U(\rho)$, with $K(\rho,T) = \sum_\alpha K_\alpha(\rho,T)$ where K_α is the kinetic energy per baryon for $\alpha = N,\Delta_{33}\ \pi, \ldots$. In the limit T=0, K reduces to

$$K(\rho,0) = K_N(\rho,0) \approx (21\ \text{MeV})(\rho/\rho_0)^{2/3}$$

where $\rho \approx 0.145\ \text{fm}^3$ is the saturation density. Note that the conventional compression energy functional, $W_c(\rho)$, is given by $W_c(\rho) = K_N(\rho,0) + U(\rho)$. The popular quadratic or linear forms of the equation of state refer to W_c rather than to U. Therefore, to compare with nuclear models for $W(\rho,0)$ it is necessary to add the degeneracy kinetic energy to the $U(E_{cm})$ deduced from (1). This procedure leads empirically to a much stiffer equation of state than deduced in ref. 1.

The reliability of that empirical equation of state depends on the assumption made about the freeze out density, $\rho(E^{cm})$ at which the pion to baryon ratio ceases to change. The surprising result obtained from the cascade study of ref. 2 was that the pion abundance froze out very early in the collision. We follow ref. 2 and assume that the Rankine-Hugoniot shock conditions are attained.

However, in ref. 2 the Rankine-Hugoniot equation was not solved consistently because the thermal pressure was assumed to of the ideal gas form $p_T = \rho T$ while the compression pressure, $p_c = \rho^2 \partial W(\rho,0)/\partial\rho$, again included the zero temperature degeneracy pressure.

Because of the importance of this independent determination of the equation of state we recalculated the Rankine-Hugoniot conditions using

$$U(\rho) = -B - K_N(\rho,0)\ \frac{+K}{18\rho_0^2}\ (\rho - \rho_0)^2 \ , \qquad (2)$$

where $B \approx 8$ MeV is the binding energy and K is the compressibility. Note that the zero temperature energy $K_N(\rho,0)$ is removed from the quadratic term in order for nuclear matter to saturate at ρ_0.

The dependence of N_π/A on cm kinetic energy is shown in Fig.(1). For a conventional equation of state with K = 250 MeV, see curve 3, the ratio of pions to baryons is similar to the cascade results. For curve 5 we modified the term proportional to K by replacing $(\rho - \rho_0)^2/\rho_0^2$ by a "linearized" form $(\rho - \rho_0)^2/(\rho\rho_0)$ and used K=800 MeV. This still overestimates the ratio. Curve 4 with the quadratic form for $W(\rho,T)$ and K=800 MeV does reproduce the data. We can recover the results of ref. 2 see the curve labeled S in Fig. (1), by setting K=250 MeV *and* neglecting the K_N in (5). Therefore, we have verified the consistency of the empirical potential obtained via eq. (1) and that obtained by fitting N_π/A using shock dynamics. Our main conclusion is, however, that this empirical equation of state is rather unphysical from the point of view of conventional nuclear physics.

Footnotes and References

*This work is condensed from Institute of Nuclear Study preprint begun while M.G. was visiting INS between March and June 1894.

1. R.Stock *et al.*, Phys. Rev. Lett. **49**, 1236 (1982).
2. J.W.Harris and R. Stock Proc. Seventh Oaxtepec Meeting on Nuclear Physics, Oaxtepec, Mexico Jan.1984; LBL-17054 and LBL- 17404 (1984).

Nuclear Stopping Power*

S. Date, M. Gyulassy and H. Sumiyoshi

The recent data[1] on p + A → p + X at 100 GeV have generated a great deal of interest in nuclear stopping power. The first analysis of that data[1] indicated that a high energy proton can lose over 90% of its initial energy when penetrating the diameter of a heavy nucleus. This is a surprise in light of a decade of previous data indicating that nuclei are rather transparent at high energies. In terms of rapidity shift it appeared that up to 2.5 units of rapidity loss is possible. If the data and interpretations are correct, then they have profound consequences for the energy density that could be generated in nuclear collisions between 10 an 100 GeV/nucleon.

If $\Delta y(z)$ is the rapidity shift suffered by a baryon on traversing a distance z in normal nuclear matter, then we can expect the central core of two nuclei to stop each other in the cm if their energy is less than

$$E_{stop} = m_N \cosh \Delta y(2R) \equiv \gamma_{stop} m_N \quad , \qquad (1)$$

where R is the nuclear radius. In the stopping regime the energy density achieved increases quadratically with γ_{stop} as

$$\varepsilon_{max} \approx \left(1 + \frac{1}{c_S^2}\right) \gamma_{stop}^2 \varepsilon_0 \sim e^{2\Delta Y} \varepsilon_0 \qquad (2)$$

with $\varepsilon_0 \approx m_N \rho_0$ and c_S being the speed of sound.

The new data therefore indicate that $\frac{\varepsilon_{max}}{\varepsilon_0} \sim 100$ could possibly be reached at a collider kinetic energy of only 5 + 5 GeV/nucleon.

Because of the importance of this conclusion we reanalyzed the data using the multichain model[2] which allows (1) treatment of diffuse nuclear geometry, (2) differential energy loss, and (3) secondary (π, K, ...) production. Exact geometry is essential for extracting the true dynamical effect. Point (2) allows us to calculate $\Delta y(z)$ rather than just Δy for inner and outer half of the nucleus as in (1). Point (3) provides a check on the overall consistency of the approach. In addition this model can be readily analyzed as to the space time development of the stopping process. Thus, we are able to compute the distance scales over which the energy is deposited in a manner consistent with longitudinal growth phenomena.

The basic equations we solve[2] involve the fractional momentum distribution of particles of type i, Glauber probabilities of n interactions, the probability that after n scattering the baryon cluster has fractional momentum x, and the fragmentation function for particle i taken from pp data. The sought-after dynamical information is P(x), the probability that in each scattering the fractional energy loss is 1−x. We parameterized $P(x) = \alpha x^{\alpha-1}$ and used the pA → p data[1] to determine that $\alpha = 3 \pm 1$. Thus, all the data of ref. 1 is reduced to one number α. We have verified that not only the proton but also the $\pi^{\pm}$ data can be accounted for with this α.

A simple calculation then shows that

$$\Delta y(z) = \frac{1}{\alpha}\left(\frac{z}{\lambda}\right) + \frac{\alpha - 1}{\alpha}\left(1 - e^{-z/\lambda}\right) \qquad (3)$$

with $\lambda = (\sigma_{in}\rho_0)^{-1} \sim 2$ fm being the mean free path. Eq. (6) is the main result. For $z \sim 12$ fm, $\Delta y \sim 2.7$ which is consistent with the extrapolations of ref. (1). We thus conclude that a much more detailed analysis of the Busza data[1] leads to essentially the same conclusion as the simple extrapolation of ref. 1. However, our result 3 is more general.

We showed that the baryon stopping distance in the center of mass system was

$$L_{cm} = \frac{\Lambda_p}{2\gamma_{cm}} \log \frac{E^{cm}}{m_N} \qquad (4)$$

where $\Lambda_p = \lambda/\log(1 + 1/\alpha) \approx 8$ fm.

The condition that $L_{cm} \leqslant R/\gamma_{cm}$ leads then to the maximum energy where nuclei stop each other to be

$$E_{cm}^{max} = m_N e^{2R/\Lambda_p} \approx 6 \pm 2\text{GeV/nucleon} \quad . \qquad (5)$$

We checked whether L_{cm} was consistent with longitudinal growth at E_{cm}^{max}. The essential result was that the hadronization of chain i extends to

$$\ell_i = \frac{E^{cm}}{\sigma(1 + \alpha)}\left(\frac{\alpha}{1 + \alpha}\right)^i + i\lambda \qquad (6)$$

For $\alpha = 3$ and $\sigma \approx 1$ GeV/fm, we found that $z_i \lesssim L_{cm}$ for $E_{cm} \lesssim e_{cm}^{max}$. Hence, the stopping energy (5) is consistent with longitudinal growth.

Footnotes and References

*Condensed from Institute of Nuclear Study preprint (1984); work done while MG was Visiting Professor at INS March through June 1984.

1. W. Busza and A.S. Goldhaber, Phys. Lett. **139B**, 235 (1984).
2. L.P. Csernai and J.I. Kapusta, Phys. Rev. **29D**, 2664 (1984).

Dissipative Phenomena in Quark-Gluon Plasmas*

P. Danielewicz and M. Gyulassy

One of the most important questions concerning very high energy nuclear collisions is whether the transport coefficients of the produced plasma are small enough to allow local equilibrium to be maintained in the finite nuclear geometries involved. Only in that case is there any hope of extracting the thermodynamic properties of quark-gluon plasmas from experiments with nuclear collisions. We have completed a detailed study of all three transport coefficients.

First, we calculated the heat conductivity coefficient, k, using the relaxation time formalism first applied to this problem in ref. 1. While only the gluon contribution to k was considered in ref. 1, we showed that the quark contribution diverges in the limit of zero baryon chemical potential, μ_B. However, we showed that the correction, ν_B^{α}, to the baryon flux is finite and obtained the new result

$$\nu_B^i = -\frac{N_c N_f}{81}\tau_q T^3 \nabla_i\left(\frac{\mu_B}{T}\right) \quad , \qquad (1)$$

where N_c, N_f are the number of colors and flavors of

the plasma, and τ_q^{-1} is the quark collision frequency in the plasma. Note that ν_B^i vanishes in the symmetric, $\mu_B = 0$, matter limit. We also clarified the difference between the Landau-Lifschitz and Eckart definitions of relativistic fluid dynamics and in connection with heat conduction showed that the only sensible definition is the Landau-Lifschitz one.

Next we derived the general bounds on the shear viscosity coefficient, η,

$$2T^3 \lesssim \eta \lesssim 3T^3(\tau T) \quad . \tag{2}$$

The lower bound follows by noting that the mean free path cannot be smaller than the thermal Compton wavelength or the interparticle spacing. The upper bound arises from demanding the applicability of the Navier-Stokes theory; namely that gradients of field quantities must be small compared to the collision frequencies. The upper bound is only a practical constraint.

We then estimated η directly using QCD phenomenology. We paid careful attention to the running QCD coupling constant and the difference between color electric and color magnetic shielding. Our final result was that $\eta = T/\sigma_\eta$, where

$$\sigma_\eta = \frac{2\pi}{17T^2}\,\alpha_T^2\Big[\, I(x_E,x_E) + 2I(x_E,x_M) + I(x_M,x_M)\Big] \quad , \tag{3}$$

where α_T is the thermal running constant, $x_E = \alpha_T(1 - \sqrt{\alpha})$, is the color electric screening cutoff and $x_M \approx \alpha_T^2$ is the color magnetic screening cutoff. The elementary integral I(x,y) is derived in ref. 2. The numerical results show that Navier-Stokes theory should hold for $T/\Lambda_{QCD} \gtrsim 1$ but that in the interesting domain $1 \lesssim T/\Lambda_{QCD} \lesssim 10$ the dissipative corrections to ideal hydrodynamics are large.

Thirdly, we estimated the bulk viscosity coefficient, ξ, due to the finite relaxation time τ^* involved in the plasma to hadron phase transition. The result is

$$\xi = \tau^* c_\lambda^2(\varepsilon + p_c) \quad , \tag{4}$$

where c_λ is the speed of sound of the matter in the mixed phase and the energy density ε is between the critical values $\varepsilon_H \sim 0.5$ GeV/fm^3 and $\varepsilon_Q \sim 2$ GeV/fm^3 and the critical pressure p_C is the pressure at the transition point. Numerically, ξ was found to on the order of η.

Finally, we applied our results to analyze cosmic ray data. We found that the initial energy densities extracted from final rapidity densities was between the bounds derived in an earlier study.[2] Observable consequences of dissipative phenomena were also considered.

Footnotes and References

*Condensed from Phys. Rev. **D31**, 53 (1985).

1. A. Hosoya and K. Kajantie, University of Helsinki preprint HU-TFT-83-62 (1983).
2. M. Gyulassy and T. Matsui, Phys. Rev. **D29**, 419 (1984).

Signatures of Quark-Gluon Plasma Production*

M. Gyulassy

A critical analysis of a variety of proposed signatures for quark-gluon formation in ultrarelativistic nuclear collisions is given. We emphasize that longitudinal growth rather than the nuclear radius controls the time scales for expansion. Thus, the relevant four volume for observables scales as $R^2\tau_0^2$ rather than R^4. We pointed out the qualitative difference of the evolution of the plasma produced in the stopping regime E ~ 10 GeV/nucleon and the scaling regime E > 1 TeV/nucleon. This difference reflects itself in the thermal profile function

$$\phi(T) = \int d^4x\,\delta\,(T - T(x)) \quad , \tag{1}$$

where T(x) is the local temperature field. This func-

tion enters in the calculation of penetrating probes such as $\mu^+\mu^-$ via

$$\frac{dN}{dM} = \int dT\, \Gamma(T)\phi(T) \qquad (2)$$

where $\Gamma(T)$ is the rate per unit mass as calculated in perturbation theory. For the scaling regime, $T(\tau) = T_0(\tau_0/\tau)^{1/3}$, and

$$\phi(T) = \pi R^2 2Y_{cm}\tau_0^2 \frac{1}{T_0}\left(\frac{T_0}{T}\right)^7 \theta\,(T_f<T<T_0)\,, \quad (3)$$

where Y_{cm} is the cm rapidity of the nuclei. Note the $R^2\tau_0^2$ scaling and the very rapid fall-off with T. These features make the dilepton probe difficult to analyze because the background noise (Drell-Yan) scales as R^4 and most of the thermal history is spent at lower temperatures.

On the other hand, in the stopping domain

$$\phi(T) \approx \pi R^2\left(\frac{R}{\gamma_{cm}} - \gamma_{cm}\tau_0\right)^2 \delta\,(T - T_0) \quad . \quad (4)$$

Thus, ϕ scales closer to R^4 enhancing the signal to noise ratio and also ϕ peaks at the interesting highest temperature point. Therefore, dilepton production in the stopping region should be an effective probe of the plasma temperature.

We also studied the transverse rapidity enhancement proposed in ref. 1. Based on the theory of simple waves, we calculated the transverse flow rapidity as

$$y_\perp = \int_{\varepsilon_f}^{\varepsilon_0} \frac{C_0(\varepsilon)d\varepsilon}{\varepsilon + p(\varepsilon)} \quad , \qquad (5)$$

where $C_0(\varepsilon)$ is the speed of sound at energy density ε and $p(\varepsilon)$ is the pressure. In (5) ε_0 is the initial energy density reached in the plasma and ε_f is the freezeout density beyond which local equilibrium cannot be maintained. Using the relation[2]

$$\varepsilon_0 \propto \left(\frac{dN}{dy}\right)^{1+C_0^2} \quad , \qquad (6)$$

in terms of the final rapidity density, we obtain $<p_\perp> \propto (dN/dy)^{C_0}$, in contradiction with data. This difficulty is removed by the realization that the center of the plasma can freeze out due to longitudinal expansion before the transverse rarefaction wave hits it. This effect can be incorporated by treating ε_0 in (5) as a function of the transverse coordinates. For a fluid element initially at r the energy density as the time that the transverse rarefaction wave hits is

$$\varepsilon_0(r) = \varepsilon_0/(1 + (R - r)/C_0\tau_0) \quad . \qquad (7)$$

Averaging over the transverse coordinate leads then to the formula

$$<p_\perp> \approx p_T\left(\frac{dN}{dy}\right)^{C_0} F(\varepsilon_0/\varepsilon_f,\, R/C_0\tau_0) \quad , \qquad (8)$$

where F is the finite size form factor that reduces significantly the transverse flows predicted. In (8), $p_T \propto 2T_f$ is the average thermal transverse momentum at freezeout.

Finally, we studied the effect of a first order plasma to hadron matter transition on $<p_T>$. In terms of the Bag model equation of state,[2] we obtained the anticipated step-like structure

$$<p_\perp>/p_T \approx \qquad (9)$$

$$\begin{array}{lll} (\varepsilon_0/\varepsilon_f)^{C_0/(1+C_0^2)} & : & \varepsilon_0 < \varepsilon_H \\ (\varepsilon_H/\varepsilon_f)^{C_0/(1+C_0^2)} & : & \varepsilon_H < \varepsilon_0 < \varepsilon_Q \\ \left(\frac{\varepsilon_H}{\varepsilon_f}\right)^{C_0/(1+C_0^2)}\left(\frac{\varepsilon_0 - B}{\varepsilon_Q - B}\right)^{\sqrt{3/4}} & : & \varepsilon_0 < \varepsilon_Q \quad . \end{array}$$

Therefore, $<p_\perp>$ is an interesting observable that can serve as a barometer of the plasma.

Footnote and References

*Condensed from Nucl. Phys. **A418**, 59c (1984).

1. L. Van Hove, Phys. Lett. **118B**, 138 (1982).
2. M. Gyulassy and T. Matsui, Phys. Rev. **D29**, 419 (1984).

Phase Transitions in a Saturating Chiral Theory of Nuclear Matter*

Norman K. Glendenning

The formalism of a relativistically covariant saturating chiral field theory of nuclear matter is developed in the mean field approximation, and some of the properties are studied. The theory possesses the normal saturated state of nuclear matter and is compatible with the data on neutron star masses. The finite temperature properties are examined. A normal gas-liquid phase equilibrium region exists below $T \approx 23$ MeV. At all temperatures but *low* densities an abnormal phase exists which at zero temperature is an isolated point at zero baryon density. At finite temperature the abnormal phase, for which the baryon effective mass is vanishingly small, and in which there is an abundance of pairs, extends to finite density. The normal and abnormal phases are disconnected except at a single point where phase equilibrium occurs. Above a critical temperature the normal branch at low density disappears and the abnormal one is the only existing branch. The abnormal characteristic of small effective mass however is confined to *low* density. Chiral symmetry is restored in this sense as the temperature is increased, but only in matter of low baryon density.

I. Introduction

Chiral symmetry is a good hadron symmetry, ranking only below isotopic spin symmetry in accuracy. For this reason it is highly desirable that any theory of dense matter should possess it. It is equally desirable that such a theory should be capable of describing the bulk properties of nuclear matter, most importantly the binding energy, saturation density, compressibility, and symmetry energy. Until recently a theory satisfying both conditions was not available. The chiral σ-model introduced by Gell-Mann and Levy which embodies the results of current algebra, the partial conservation of the axial current, and low-energy pion phenomenology, has been widely used to discuss pion condensation in nuclear and neutron matter but it does not have a saturated state of nuclear matter. On the other hand, the Walecka model and its extensions by Boguta and Bodmer and by Banerjee, Glendenning, and Gyulassy possesses the desired bulk nuclear properties and describes many single-particle properties of finite nuclei as well, but does not possess chiral symmetry.

In the context of neutron star matter it was realized by Källman[1] that a theory based on the coupling of nucleons and *massless* vector bosons, as suggested by Kirtznits and Linde,[2] leads to an equation of state for dense matter that goes asymptotically to $p = 1/3\varepsilon$. This contrasts with the causality limit $p = \varepsilon$ emphasized by Zel'dovich, for massive vector bosons.

Recently Boguta[3] has made the very important observation that the σ-model can be made to saturate by the same device of introducing a massless vector gauge field. In his work he simplified the problem by neglecting the pions and studied only the normal state of nuclear matter in its ground state. In view of the success in finally reconciling chiral symmetry and low-energy pion physics and the bulk properties of nuclear matter in a single relativistically covariant theory, it is very appealing to develop the formalism in greater generality and to investigate some of the predictions of the theory for matter under extreme conditions of temperature and compression.

II. Lagrangian, Field Equations, Vacuum Masses

The gauge field ω_μ of a massless vector meson is introduced into the σ-model through the covariant derivatives

$$D_\mu = \partial_\mu + ig_\omega \omega_\mu \quad . \tag{1}$$

Thus, using the conventions of Bjorken and Drell, the Lagrangian is,

$$\mathscr{L}_\sigma = \frac{1}{2}\,(D^*_\mu\sigma\, D^\mu\sigma + D^*_\mu\boldsymbol{\pi}\cdot D^\mu\pi)$$

$$+\bar{\Psi}_N\, i\gamma_\mu D^\mu\Psi_N - g\bar{\Psi}_N(\sigma + i\gamma_5\boldsymbol{\tau}\cdot\boldsymbol{\pi})\,\Psi_N$$

$$-V(\sigma,\boldsymbol{\pi}) - \frac{1}{4}\,\omega_{\mu\nu}\,\omega^{\mu\nu} \qquad (2)$$

$$\omega_{\mu\nu} = \partial_\mu\omega_\nu - \partial_\nu\omega_\mu \qquad (3a)$$

$$V(\sigma,\boldsymbol{\pi}) = \frac{1}{4}\,\lambda\,(\sigma^2 + \boldsymbol{\pi}^2 - v^2)^2 - n\sigma \qquad (3b)$$

The last term in Eq. (2) is the Lagrangian for the massless ω meson. The linear term, $n\sigma$, in Eq. (3) is the symmetry breaking term by which the pion acquires a finite mass. In addition to the σ-meson, which contributes a repulsive energy and carries spin and isospin $(1^+,0)$, the theory has the scalar meson $\sigma(0^+,0)$ and the pseudoscalar pion $(0^-,1)$. The nucleon field is denoted by Ψ_N which is an eight component spinor.

The fields should be expanded around the stable point defined by the potential. The potential parameters of the theory can then be defined by the experimental masses and coupling constants.

III. Charged Pion Condensate

In this section the theory will be developed, in the mean field approximation, for a charged pion condensate defined by

$$\pi_\pm = \frac{1}{\sqrt{2}} <\pi_1 \pm i\pi_2> = \frac{r}{\sqrt{2}}\,\sin\theta\, e^{\pm ikx} \quad ,$$

$$(kx = k_0x_0 - k\cdot x)\ ,\ \pi_0 = 0\ ,\ \sigma = r\cos\theta \qquad (4)$$

where the mean fields are parametrized by a chiral radius and angle, r,θ. We will derive the Dirac equation for quasi-particle fields in the presence of this condensate, the dispersion relation for the eigenvalues, and the propagator. Then the self-consistency conditions for the meson field strengths, which are non-linear and coupled through various nucleon currents, will be derived. The energy density and pressure are obtained from the canonical form of the stress-energy tensor, and the conditions for the lowest energy pion mode are derived. Then we will show how to calculate the various ground state expectation values of the nucleon currents that appear in the theory.

The Dirac equation following from Eq. (2) can be manipulated into the form

$$(\not{p} - g_\omega\omega - M + \frac{1}{2}\not{k}\tau_3\cos\theta + \frac{1}{2}\not{k}\gamma_5\tau_2\,\sin\theta)\Psi = 0 \qquad (5)$$

where a new quasi-fermion field is defined by

$$\Psi = e^{\frac{1}{2}\gamma_5\tau_1\theta}\, e^{\frac{1}{2}kx\tau_3}\,\Psi_N \qquad (6)$$

and the nucleon effective mass in the medium is

$$M = gr \quad . \qquad (7)$$

The Dirac equation for the new field, Ψ, is now space-time independent. Clearly, the spinor Ψ describes a combination of neutron and proton which we refer to as a quasi-particle.

The dispersions relation for the eigenvalues can be found by rationalizing the Dirac operator in Eq. (4). The result is

$$0 = D(p_0,\mathbf{p}) \equiv [\,P_\mu P^\mu - \varepsilon_0^2]^2 - (\,P_\mu k^\mu)^2$$

$$+\ M^2\, k_\mu k^\mu \sin^2\theta \qquad (8)$$

with

$$\varepsilon_0^2 = M^2 - \frac{1}{4}\,k_\mu k^\mu \quad P_\mu = p_\mu - g_\omega\,\omega_\mu \quad . \qquad (9)$$

The first term of Eq. (8) corresponds to the Walecka model, or if the meson fields are zero, to the free Dirac equation. This fourth order equation for p_0 is easily solved if $k_0 = 0$ (which we shall see corresponds to symmetric nuclear matter). In this case the two particle and two antiparticle eigenvalues, denoted by $\varepsilon_\pm$ and $\bar{\varepsilon}_\pm$ are

$$\varepsilon_\pm = g_\omega\omega_0 + E_\pm \quad ,\quad \bar{\varepsilon}_\pm = -g_\omega\omega_0 + E_\pm$$

$$E_\pm \equiv P_0 =$$

$$\left\{\mathbf{p}^2 + \varepsilon_0^2 \pm \sqrt{(\mathbf{P}\cdot\mathbf{k})^2 + M^2\,\mathbf{k}\cdot\mathbf{k}\,\sin^2\theta}\right\}^{1/2}, \qquad (10)$$

if $(k_0 \equiv 0)$

$$\varepsilon_0 = M^2 + \frac{1}{4}\,\mathbf{k}\cdot\mathbf{k}$$

Each momentum state, $\varepsilon_\pm$, can be occupied by two

quasiparticles. In the general case, ($k_0 \neq 0$), the eigenvalues do not have simple analytic expressions.

In the mean field approximation the nucleon ground state is constructed as a degenerate Hartree state out of the solutions of the Dirac equation with all meson fields replaced by their mean values. The nucleon currents that appear in the mean field equations are replaced by the expectation values in the ground state so defined. The resulting coupled equations define the self-consistent values of the mean meson fields.

It is convenient to define the four densities

$$\rho_s = <\bar{\Psi}\,\Psi>$$

$$\rho = <\bar{\Psi}\,\gamma_0\,\Psi> = <\Psi^\dagger\Psi>$$

$$\rho_{51} = <\bar{\Psi}\,\gamma_5\tau_1\,\Psi>$$

$$\rho_{52} = <\bar{\Psi}\,\gamma_5\tau_2\,\Psi> \quad . \tag{11}$$

The bracket denotes the expectation value in the ground state. The meson field equations then take the form,

$$\rho_{52} \equiv 0$$

$$[\,k_\mu k^\mu \sin^2\theta - \lambda(r^2 - v^2) + g_\omega^2\omega_0^2]\,r + \eta\cos\theta - g\rho_s = 0$$

$$k_\mu k^\mu\, r\sin\theta\cos\theta - ig\,\rho_{51} - \eta\sin\theta = 0$$

$$g_\omega\omega_0\, r^2 = \rho$$

$$g_\omega\boldsymbol{\omega}\, r^2 = <\bar{\Psi}\,\boldsymbol{\gamma}\,\Psi> = 0 \quad . \tag{12}$$

Notice that the dynamic ω mass in the baryonic medium is

$$M_\omega = g_\omega r \tag{13}$$

The conserved four-currents can be constructed through Noether's theorem and correspond to the invariance of the lagrangian under various infinitesimal transformations. The charge, baryon, and isospin currents are

$$j^\mu = <\bar{\Psi}\,\gamma^\mu\,\frac{1+\tau_3}{2}\,\Psi> + k^\mu r^2\sin^2\theta$$

$$j_B^\mu = <\bar{\Psi}\,\gamma^\mu\,\Psi>$$

$$j_3^\mu = \frac{1}{2}<\bar{\Psi}\,\gamma^\mu\,e^{i\gamma_5\tau_1\theta}\,\tau_3\,\Psi> + k^\mu r^2\sin^2\theta \tag{14}$$

where the currents are now expressed in terms of the quasiparticles. The other two isospin four-currents can be shown to vanish identically. The canonical stress-energy tensor is

$$\mathscr{T}_{\mu\nu} = -g_{\mu\nu}\mathscr{L} + \sum\frac{\partial\mathscr{L}}{\partial(\partial^\mu\phi)} \tag{15}$$

where the sum is over the fields Ψ, ω_μ, σ, $\boldsymbol{\pi}$. Introducing the mean meson fields and the quasiparticle fields this becomes

$$\bar{\mathscr{T}}_{\mu\nu} \equiv <\mathscr{T}_{\mu\nu}> = -g_{\nu\mu}\bar{\mathscr{L}} + <\bar{\Psi}\,\gamma_\mu p_\nu\,\Psi> + k_\mu J_{3\nu} \tag{16}$$

and

$$\bar{\mathscr{L}} \equiv <\mathscr{L}_0> = \frac{1}{2}\,(\,k_\mu k^\mu\sin^2\theta + g_\omega^2\omega_\mu\omega^\mu)\,r^2$$

$$= \frac{1}{4}\,\lambda(\,r^2 - v^2)^{\,2} + \eta r\cos\theta \quad . \tag{17}$$

The energy density is therefore

$$\varepsilon = \bar{\mathscr{T}}_{00} = -\bar{\mathscr{L}} + <\bar{\Psi}\,\gamma_0 p_0\,\Psi> + k_0\,J_3^0 \tag{18}$$

where the last term is recognized as the time-like component of the isospin four-current, which is related to the charge and nucleon density by Eq. (32). It is very useful to recognize this fact because variations of the energy density at fixed charge and nucleon density leave J_3^0 constant. In particular, we wish to find the lowest energy mode in which the pions can condense. This will be given by the conditions

$$\frac{\delta\varepsilon}{\delta k_0} = \frac{\delta\varepsilon}{\delta\mathbf{k}} = 0 \tag{19}$$

where the variation δ means that charge and nucleon density are held fixed. We find that

$$-\frac{\delta\varepsilon}{\delta\mathbf{k}} = \mathbf{J}_3 \tag{20}$$

where the right side is the 3-current of isospin. Therefore the condition that the pions condense in the lowest mode places a condition on their wave

vector **k**, which is to be chosen so that the isospin 3-current vanishes. Likewise the first condition of Eq. (19) places a constraint on k_0. Together they read,

$$J_3^0 = \frac{1}{2} <\bar{\Psi}\, \gamma^0 e^{i\gamma_5\tau_i\theta}\, \tau_3\, \Psi> + k^0$$

$$r^2\sin^2\theta = q - \frac{1}{2}\rho$$

$$\mathbf{J}_3 = \frac{1}{2} <\bar{\Psi}\, \boldsymbol{\gamma}\, e^{i\gamma_5\tau_i\theta}\, \tau_3\, \Psi> + \mathbf{k}\, r^2\sin^2\theta = 0\,. \quad (21)$$

It can be demonstrated that the tensor Eq. (15) is diagonal and its equal space components give the pressure,

$$p = \bar{\mathscr{L}} + \frac{1}{3} <\bar{\Psi}\, \boldsymbol{\gamma}\cdot\mathbf{p}\, \Psi> \quad . \quad (22)$$

IV. Coupling of Baryon Resonances

The theory can be easily extended to incorporate N^* resonances as Dirac fields. Such an extension becomes relevant in the high temperature or density regime because the effective baryon masses may become small. The effective mass, according to Eq. (19), is M = gr and the vacuum mass according to Eq. (8) is $m = gf_\pi$. Accordingly the baryons should be coupled so that their vacuum masses are

$$m_B = g_B f_\pi \quad . \quad (23)$$

where B denotes the spin-isospin multiplet of mass m_B and isospin degeneracy γ_B.

The interaction term in the Lagrangian is replaced as

$$g\bar{\Psi}(\sigma + i\gamma_5\boldsymbol{\tau}\cdot\boldsymbol{\pi}\pi)\Psi \rightarrow \sum_B g_B\bar{B}(\sigma \pm i\gamma_5\boldsymbol{\tau}\cdot\boldsymbol{\pi})B\,. \quad (24)$$

where, in context, B denotes the spinor for baryon of mass m_B. The structure of all the densities computed previously remains unchanged except that they are now summed over the various nucleon masses and their spin degeneracies, with effective mass, M = gr, replaced by

$$M_B = g_B r \quad . \quad (25)$$

V. Properties of Symmetric Matter

Here we compare the properties of normal matter in this theory with the empirical properties. The vacuum masses of nucleon and pion are given their σ-mass is taken as a parameter. The vector meson coupling, g_ω, appears in the combination $g_\omega\omega_0$ in infinite matter and can be eliminated through the field equation. The coupling constant g is related through the vacuum nucleon mass to the pion decay constant f_π through $m = gf_\pi$. The normal Goldhaber-Treeman relation, however, reads $g_A m = gf_\pi$ with $g_A = 1.25$, and $f_\pi = 93$ MeV.

In principle the theory has only one parameter, m_σ. This turns out to be insufficient to reproduce the three properties, saturation density, binding, and compressibility. This is not surprising, of course. So we take f_π as an additional parameter. With m_σ = 642.5 MeV and f_π = 116 MeV the saturation density and binding energy per nucleon in normal symmetric matter have the acceptable values

$$\rho_0 = 0.153\ \text{fm}^{-3} \quad , \quad B/A = 15.95\ \text{MeV}$$

The compressibility, however, is large, K = 650 MeV, as compared to 240 MeV.

VI. Neutron Star Masses

As an additional test of the theory we calculate the mass of a neutron star approximating the matter as pure neutron matter described by this theory. One condition for stability of the star is that $dM/d\rho_c \geqslant 0$ where ρ_c is the central density. The equality yields the maximum mass that can be sustained against gravitational collapse. A second condition is that the adiabatic index of the equation of state $\gamma = d\ln p/d\ln\varepsilon$ should be greater than or equal to 4/3. Values of γ that are less than 4/3 can lead to oscillations that may destroy the star. In Fig. 1 the mass as a function of central density is shown. The central density corresponding to the Oppenheimer-Volkoff limit is $\rho_{O.V.} = 4.6\rho_0$ for which the star mass is 2.4 $M_\odot$. Stars with central densities in the range $\rho_0 < \rho_c \leqslant \rho_{O.V.}$ are gravitationally stable. Almost all of these stars are also stable against oscillations in the core. Stars with central densities $\rho_c < 4.3\ \rho_0$ possess this stability. The maximum star mass of $M_\odot$, which is stable in all respects, exceeds the observed masses of 1.4 $M_\odot$ for the crab and Her-1. Thus the theory is acceptable as far as data on neutron star masses is concerned.

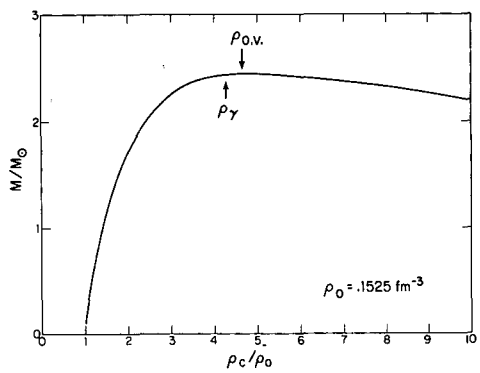

Fig. 1. Neutron star mass in units of solar mass $M_\odot$ as a function of central density ρ_c. XBL 837-1890

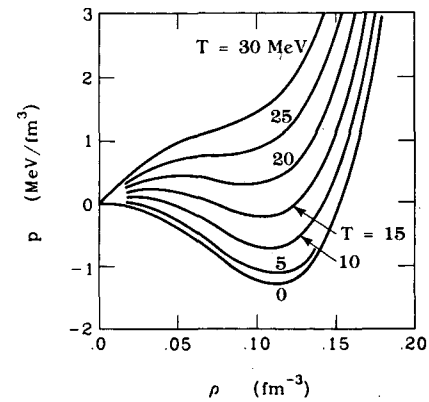

Fig. 2. Pressure as a function of density in the low-temperature regime of the liquid-gas phase coexistence. The T = 0 isotherm passes through p = 0 at the equilibrium density $_0$ = 0.153 fm^{-3} of symmetric nuclear matter in this theory. The binding energy at saturation is 16 MeV/nucleon. XBL 845-10562

VII. Low-Temperature Behavior: Gas-Liquid Transition

For the normal state (θ = 0) of symmetric nuclear matter (k_0 = 0), we show in Fig. 2 the pressure, as function of the net baryon density ρ in the low temperature domain. The saturation density of symmetric nuclear matter corresponds to the density at which p = 0 on the T = 0 isotherm. The pressure exhibits the typical Van de Waals behavior for which the Maxwell construction for phase equilibrium can be made. The critical temperature above which the matter is homogeneous with respect to gas and liquid in the normal state of matter is $T_c \approx 23$ MeV. As we shall see in the next section, at considerably higher temperature new phase transitions are possible.

VIII. Chiral Restoration in Low-Density High-Temperature Matter

The original σ-model of Gell-Mann and Levy, insofar as its nuclear matter properties are concerned, is remarkable for the absence of a normal saturated state, as was emphasized first by Kerman and Miller. It does possess both a pion condensed state and as discussed by Lee and Wick[4] an abnormal state in which the nucleon mass becomes very small, *above* a critical baryon density or temperature.

In contrast the present version of the chiral model, as emphasized by Boguta,[3] has a normal saturated state. The properties connected with abnormal states, as discussed below are also quite different.

In the following calculations, all well established T = 1/2 baryon resonances, strange and nonstrange with masses up to 1.8 GeV are included, the strange ones only in baryon, anti-baryon pairs. Very similar results hold if the resonances are neglected, but the critical temperatures discussed below are increased. For the present exploration, we confine ourselves to the θ = 0 case (no condensed pions).

For vanishing baryon density, the field equation has a solution, which corresponds to very small effective nucleon mass, M = gr. This solution would be precisely M = 0 if chiral symmetry were exact ($n = f_\pi m_\pi^2 = 0$). But this is an isolated solution confined to ρ = 0 at T = 0. For finite temperature, the situation is rather more interesting. The reason, as has been stated elsewhere,[5] is that the scalar field is coupled to the sum of baryon and antibaryon densities, as a consequence of which an instability can set in at finite temperature since the departure of the scalar field from its vacuum value reduces the baryon masses, thus making pair creation more energetically favorable, which further drives the scalar field reducing baryon masses even further. Therefore the new phase appears at an extremely low tem-

perature compared to the vacuum mass of a pair because of the near vanishing of the effective mass. The vector field does not inhibit the instability because it is coupled to the *net* baryon density. The present model possesses such an abnormal phase, corresponding to small baryon effective mass and abundant pairs, but it is confined to the *low*-density regime, again in contrast to the usual σ-model. This is due to the fact that here, the vector field is introduced as a gauge boson that is coupled to the scalar field. It derives its effective mass from this. Analysis of the field equations (12) shows that small values of r are not allowed except for small ρ.

The above assertions are illustrated in Fig. 3. Over some range of temperature and density there are three solutions to the field equations. Two of them correspond to minima in the free energy per nucleon regarded as a function, at fixed temperature and density, of the chiral radius r, or equivalently the effective mass M = gr, and one corresponds to the maximum lying at intermediate effective mass. The *isolated* solution lying at $M = \rho = 0$ at zero temperature develops into a pair of solutions at finite temperature, extending to finite baryon density. On one of the stable branches, the effective mass is near the vacuum value, and we call it the normal branch. On the other, the effective mass is very small, and we refer to it as abnormal. On the normal branch, the effective mass decreases as a function of density to a minimum and thereafter increases monotonically. It is the particular gauge coupling of the vector field as remarked above that gives rise to this behavior. As the temperature is raised the abnormal branch extends to higher and higher density until it intercepts the normal branch. Beyond the critical temperature, T_K, at which this occurs, the normal branch no longer extends continuously from low to high density. It becomes a remnant of its former self. In contrast, the abnormal branch extends continuously from low to high density. However as the density increases, its nature evolves, and it assumes the character of a normal state at high density. Beyond another critical temperature, T_c, it is the only solution and the remnant of the normal state ceases to exist.

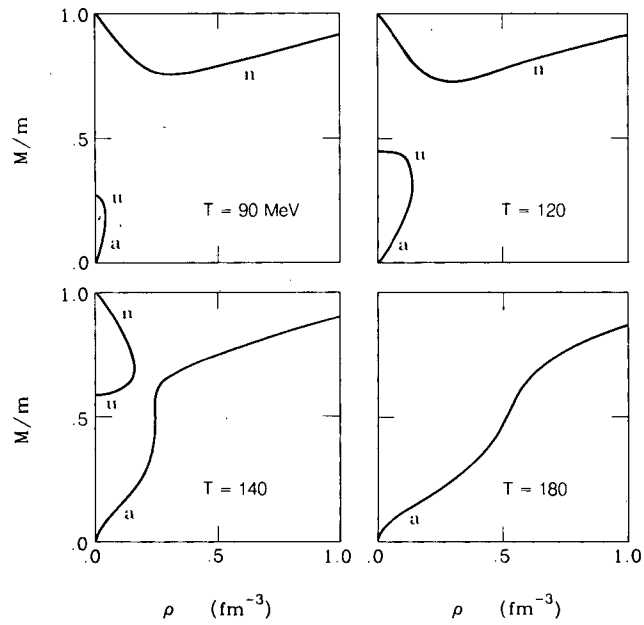

Fig. 3. For four temperatures, the ratio of effective baryon mass to vacuum mass $M/m = r/f_\pi$ shown as a function of total baryon density. (All baryons scale in the same way, c.f. eqs. (23,24). Three solutions exist in the low density regime below a critical density $T_c \approx 163$ MeV, two stable and one unstable. The normal branch with $M \approx m$ is marked by n, the abnormal with $M \approx 0$ is marked by a, and the unstable branch by u. Note at a critical temperature $T_K \approx 135$ MeV the abnormal branch intercepts the normal one, and the latter becomes a remnant that disappears above T_c. XBL 845-10577

Fig. 4 shows the evolution of the solutions as a function of temperature at zero baryon density. To understand this figure, we note that in the absence of baryons to drive the meson fields to finite values, there ought to be a solution with effective nucleon mass equal to its vacuum mass, and this is indeed so for temperatures up to ~160 MeV. This is the normal branch. At remarkably low temperature, the instability with respect to pair production sets in, signaling the appearance of the abnormal phase together with an unstable solution. This one bifurcates with the normal one at $T_c \approx 163$ MeV, which corresponds to the end point of the normal branch at zero baryon density.

The abundance of pairs[5] which besides the low-effective mass is the other remarkable feature of the abnormal phase, is shown in Fig. 5.

The normal phase is one of broken chiral symmetry. What we have found above is that at high temperature, the symmetry is recovered, but only at *low* density, indeed, strictly speaking, at vanishing density. This result is σ-model, and as remarked earlier, is due to the particular gauge coupling of the vector meson to the scalar field.

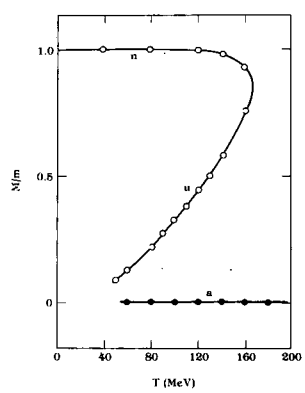

Fig. 4. At zero baryon density $\mu = \rho = 0$, the three solutions are shown as a function of temperature. Above $T_c \approx 163$ MeV, only the abnormal solution exists. XBL 845-10572

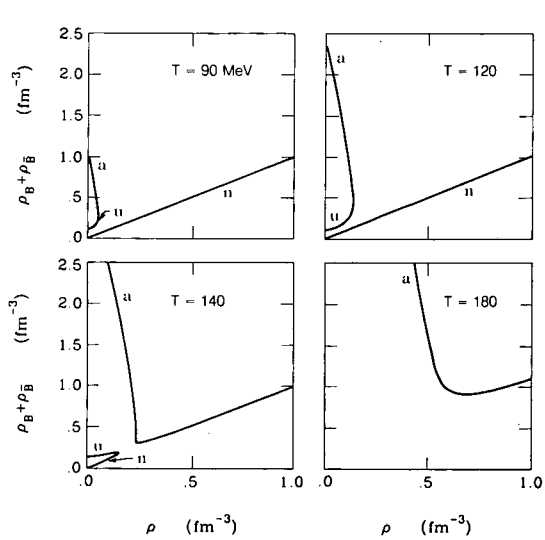

Fig. 5. Total number of baryons and antibaryons as a function of net baryon density. The abnormal branch is characterized by an abundance of baryon-antibaryon pairs. The normal branch has almost no antibaryons. XBL 845-10575

IX. Summary

We have developed the self-consistency equations that govern the normal and pion-condensed states in a chiral theory with an vector meson introduced as a gauge field. As Boguta first observed, such a theory saturates in the normal σ-model. We have shown in addition that the theory is compatible with data on neutron star masses. This finding is non-trivial inasmuch as the ideal neutron gas equation of state which has the same asymptotic behavior, $p = 1/3\ \varepsilon$, as the present theory has too small a limiting mass.

The theory was extended to incorporate N^* resonances as Dirac fields, as is appropriate for studying the high temperature or high density regimes.

We then examined the finite temperature properties. A normal phase transition between liquid and gas occurs below $T \sim 23$ MeV. There exists as well at all temperatures an isolated abnormal phase characterized by *small baryon* effective mass, and at non-zero temperature, *abundant baryon-antibaryon pairs* of low effective mass. Phase equilibrium between this and the normal phase occurs at only a single point, T_K. Above a critical temperature T_c, there is only one phase, which at *low* density corresponds to the chirally restored phase. As a function of density, and above T_c, this phase evolves continuously into a normal phase as the density is increased. In this theory, chiral symmetry is restored at high temperature but only in matter of low baryon density.

Footnotes and References

*Condensed from LBL-17708.

1. C.-G. Kallman, Fundamentals of Cosmic Physics **4**, 167 (1979) (published by Gordon and Breach Science Pub.).
2. D.A. Kirtznits and A.D. Linde, Ann. Phys. **101**, 195 (1976).
3. J. Boguta, Phys. Lett. **120B**, 34 (1983).
4. T.D. Lee and G.C. Wick, Phys. Rev. **D9**, 2291 (1974).

5. N.K. Glendenning, LBL-17653 (1984) to be published in Phys. Lett.; S.I.A. Garpman, N.K. Glendenning and Y. Karant, Nucl. Phys. **A322**, 382 (1979).

Supernovae and the Nuclear Equation of State at High Densities

E. Baron, J. Cooperstein† and S. Kahana‡*

An extensive study of the shock-explosive mechanism for generating Type II Supernovae is presented. The nuclear high density equation of state plays an important role in the propagation and energetics of the shock, which it is hoped will expel the mantle and envelope of a massive star leading to the observed Type II supernovae display, and subsequent nucleosynthesis of heavy elements.

We use the adiabatic index and nuclear compressibility to parametrize the equation of state at high density. Greatly increased shock energy is found with equations of state that are soft, but not unreasonably so. It is pointed out that values of the nuclear compressibility K_0 softer than the oft quoted value of 220 MeV is quite reasonable given that the matter is very neutron rich. A definition of shock energy which can be used throughout the life of the shock is introduced.

Footnotes

*Department of Physics, State University of New York, Stony Brook, NY 11794 and Brookhaven National Laboratory, Upton, NY.

†Department of Physics, State University of New York, Stony Brook, NY 11794 and NORDITA, Copenhagen, Denmark.

‡Brookhaven National Laboratory, Upton, NY.

Successful Supernovae, the Anatomy of Shocks, Neutrino Emission and the Adiabatic Index*

S. Kahana,† E. Baron‡ and J. Cooperstein§

Hydrodynamic calculations of stellar collapse in Type II supernovae are described using a variable adiabatic index and compressibility for the nuclear equation of state at high density. Initial models employing a relatively small mass core with low central entropy are necessary to achieve viable shocks; near success the models are sensitive to both neutrino emission and the high density equation of state. The treatment of neutrino production and transport is sketched and recent results reported.

Footnotes

*Invited talk delivered at The Workshop on Stellar Collapse, Université Paul Sabatier, Toulouse, France, November 7–11, 1983; from *Problems of Collapse and Numerical Relativity*, eds. D. Bancel and M. Signore, Amsterdam: North Holland (1984).

†Brookhaven National Laboratory, Upton, NY.

‡Department of Physics, State University of New York, Stony Brook, NY 11794.

§Department of Physics, State University of New York, Stony Brook, NY 11794 and NORDITA, Copenhagen, Denmark.

The Lee-Wick Abnormal Phase Transition*

Norman K. Glendenning

A decade ago Lee and Wick suggested that matter might exist in an abnormal state in which the nucleon effective mass nearly vanishes. The excitement that was provoked eventually waned as it was realized that the theory employed to describe the abnormal state could not simultaneously describe the properties of ordinary matter, not even its saturation, as Kerman and Miller showed.

In this note we draw attention to the fact that a first order phase transition of a similar character has been found[1] in a relativistic nuclear field theory that is an extension to include baryon resonances of the so called Walecka model,[2] which does describe ordinary matter and single-particle properties of finite nuclei rather well.[3] Because of its success with ordinary matter and its relativistic covariance it has proven interesting to study the predictions of the theory for the properties of matter under extreme conditions of temperature and compression including the high temperature behavior with and without the inclusion of baryon resonances, high compression as in neutron stars, pion condensation, delta isomerism, and hyperon matter.

Although a phase transition was observed in the theory several years ago,[1] it was not at that time associated with the Lee-Wick state, and its phase diagram was not calculated. Below we shall show that the transition from the normal to the abnormal state is expected to occur at moderate energy densities and therefore *below* the quark deconfinement phase transition. If this is so, the transition to the deconfined phase is from the abnormal Lee-Wick phase, and vice versa, rather than from the normal phase, as is customarily believed.

Recall that the relativistic nuclear field theory of ref. 2 involves nucleons that are Yukawa coupled to a scalar (σ) and vector meson (ω_μ). Because the phase transition that we are interested in is one in which the scalar field becomes large and hence baryon masses become small, it is necessary to take account of baryon resonances, even at moderate temperature. Therefore we couple universally all well established baryon resonances of mass up to 1.8 GeV both strange and non-strange and include in addition a thermal gas of pions. If produced in a collision, the evolution of the system will presumably occur on a time scale that is small compared to that of strangeness non-conserving reactions ($\sim 10^{-10}$) sec). Therefore the chemical potentials of the strange baryons are chosen to be zero. The equations describing the mean field approximation to the field theory in the general case of finite temperature and baryon number and including resonances can be found in the appendix to ref. 1.

To understand *why* such a phase could exist in hadronic matter, we reproduce below the equations governing the mean amplitudes of the scalar (σ) and vector (ω_0) fields in a thermal ensemble at temperature T,

$$g_\sigma\sigma = \left(\frac{g_\sigma}{m_\sigma}\right)^2 \frac{2}{\pi^2}\int_0^\infty \frac{m^*}{\sqrt{p^2+m^{*2}}}(n(p,\mu)+n(p,-\mu))p^2dp \quad (1)$$

$$g_\omega\omega_0 = \left(\frac{g_\omega}{m_\omega}\right)^2 \frac{2}{\pi^2}\int_0^\infty (n(p,\mu) - n(p,-\mu))p^2dp \quad (2)$$

where $n(p,\mu)$ and $n(p,-\mu)$ are the Fermi-Dirac distribution functions for nucleons and antinucleons respectively,

$$n(p,\mu) = \left\{1 + \exp(\sqrt{p^2 + m^{*2}} - \mu)/T\right\}^{-1} \quad (3)$$

and $m^* = m - g_\sigma\sigma$ is the nucleon effective mass. The generalization to include resonances is given in ref. 3. Note that (1) is an equation which determines $g_\sigma\sigma$ *self-consistently* in the medium. The scalar field gives rise to an attractive energy because it reduces the nucleon mass by $g_\sigma\sigma$, while the vector field con-

tributes a repulsive energy by shifting each nucleon eigenvalue by $g_\omega \omega_0$, i.e.

$$E_p = g_\omega \omega_0 + \sqrt{p^2 + (m - g_\sigma \sigma)^2} \qquad (4)$$

(Comparing (3) and (4) note that the true chemical potential is $\mu + g_\omega \omega_0$).

Now it is possible to see what drives the phase transition. Notice that the vector repulsion is driven by the *difference* in baryon and antibaryon densities, (2), i.e. by the net baryon density denoted by ρ, while the scalar attraction is driven by the *sum* of the scalar densities (1). Consequently it can become advantageous at sufficiently high temperature or compression, for copious baryon pairs to appear in the medium, which reduces the baryon effective masses through a growth in the scalar field, at no cost in repulsion from the vector field. We can also note that the possibility of such a phase transition is not tied to a particular choice of Lagrangian. The presence of baryons automatically insures that scalar and vector densities $<\bar{B}B>$and$<\bar{B}\gamma_\mu B>$ will exist which can drive meson fields having the corresponding quantum numbers. Thus such a phase may be a very general phenomenon occurring for some range of coupling constants and energy densities in any relativistic field theoretic description of matter which is solved self-consistently. Of course the particular form that the self-consistency condition (1) takes will depend on the couplings and self-interactions, i.e., on the particular Lagrangian. The contribution of this note and ref. 3 is to show that, within such uncertainties, the Lee-Wick phase is compatible with the properties of ordinary nuclear matter.

The phase diagram for the transition is shown in Fig. 1. The solid line marks the trajectory of Maxwell points and the dashed lines mark the boundaries of the coexistence region throughout which both phases are stable. According to these calculations, the transition to the Lee-Wick phase lies below the deconfinement transition, which is expected at $T \approx 200$ MeV when $\rho = 0$.

To assess the experimental accessibility of the abnormal phase we have solved the relativistic Rankine-Hugoniot shock condition to estimate

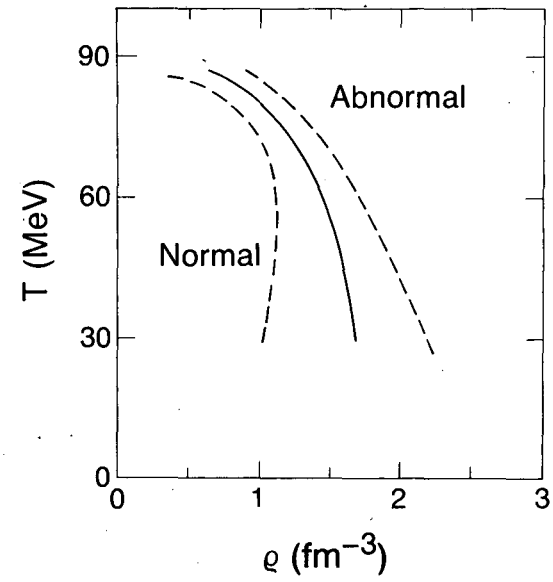

Fig. 1. Phase diagram in the T – ρ plane. The solid line joins the mid-density of the Maxwell constructions. The dashed lines mark the boundaries between which both phases are stable.

XBL 844-10325

the conditions that would be produced in a collision of two normal nuclei. As Fig. 2 shows, above a total center of mass energy per nucleon in the medium of about 2 GeV, matter is produced in the abnormal phase. The temperature, entropy per nucleon and baryon density in the shock zone are shown as a function of the relativistic factor $\gamma_{c.m.}$ which is related to the center of mass energy per nucleon by $E_{c.m.}/A = \gamma_{c.m.}(m-B)$ with B the binding per nucleon in the normal state. Of particular note is the high entropy in the abnormal phase. This corresponds to the abundance of low-mass baryon pairs.

To summarize, the Lee-Wick abnormal phase exists in a relativistic nuclear field theory that simultaneously describes the normal state correctly. Baryon resonances up to masses of 1.8 GeV are universally coupled to the meson fields. We discussed only the mean field solutions. Within that limitation the phase transition is first order, all baryon masses are strongly shifted from their vacuum values, the baryon charge is carried mainly in

resonances rather than nucleons, at finite temperature there is an abundance of low-mass baryon-antibaryon pairs, both strange and non-strange, and the entropy is high. The phase diagram indicates that the abnormal phase exists between the normal and deconfined phases, and the shock condition suggest that it can be produced at moderate center of mass energy per nucleon in the range 2–4 GeV.

Footnote and References

*Condensed from LBL-17653 and Phys. Lett. **144B**, 158 (1984).

1. S.I.A. Garpman, N.K. Glendenning and Y.J. Karant, Nucl. Phys. **A322**, 382 (1979).
2. M.H. Johnson and E. Teller, Phys. Rev. **98**, 783 (1955).

   H.P. Duerr, Phys. Rev. **103**, 469 (1956).

   J.D. Walecka, Ann. Phys. (N.Y.) **83**, 491 (1974).

   S.A. Chin, Ann. Phys. (N.Y.) **108**, 301 (1977).
3. B.D. Serot and J.D. Walecka, Phys. Lett. **87B**, 172 (1980).

   J. Boguta, Phys. Lett. **B106**, 245 (1981); Phys. Lett. **B106**, 250 (1981); Nucl. Phys. **A372**, 368 (1981).

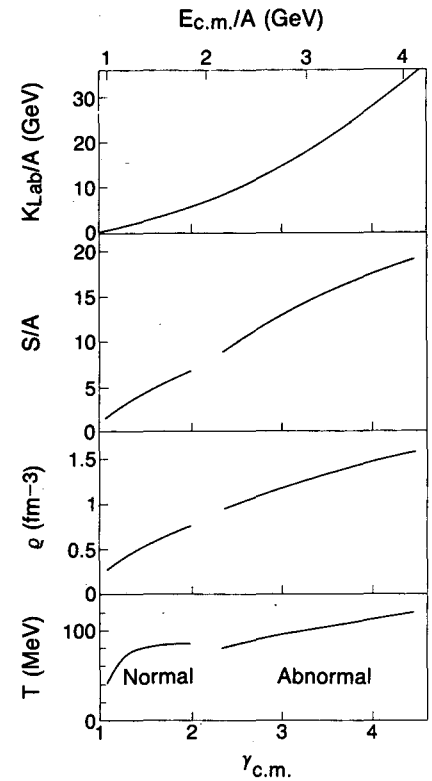

Fig. 2. Temperature, density and entropy per net baryon reached in the shock zone as a function of $\gamma_{c.m.}$ or, on the top scale, the total center of mass energy per net baryon. For convenience, the laboratory kinetic energy per projectile nucleon is plotted for a symmetric collision with fixed target.

XBL 844-10278

On the Hydrodynamic Evolution of Quark-Gluon Plasma Produced by Ultrarelativistic Nuclear Collisions*

N.K. Glendenning and T. Matsui

The hydrodynamic evolution of a quark-gluon plasma produced in the central rapidity region is studied, incorporating the external bag pressure acting on the plasma surface. It is shown that the plasma fluid, which undergoes the scaling longitudinal expansion, generates a non-trivial transverse flow pattern, near the plasma surface, consisting of a rarefaction wave and a compression wave, instead of a simple rarefaction wave in the case of free expansion without a surface boundary condition. We also discuss a possible global phase transition of supercooled plasma in the interior of the cylinder to a superheated dense hadron gas through a time-like surface of discontinuity.

1. At very high energies, $E_{CM} \gtrsim (30 - 50)$ GeV per nucleon, where the nucleus becomes almost transparent with respect to incident nucleons, a hot plasma with small net baryon number is expected to be formed in the central rapidity region just after two nuclei pass through each other. The space-time evolution of the hadronic matter produced in the latter regime was described by Bjorken, using the relativistic hydrodynamics with a Lorentz-boost invariant initial condition on account of the ansatz of the central plateau formation in the rapidity distribution. Bjorken's one-dimensional scaling solution to the subsequent longitudinal hydrodynamic expansion of the central regime was extended recently by Baym *et al.*,[1] to include the transverse flow, assuming cylindrical symmetry for the collision volume. Although these authors considered that the hadronic matter is formed in the deconfined quark-gluon plasma phase, the hadronization stage of the plasma has not yet been described in these studies. The aim of this paper is to put forward the above hydrodynamic picture of ultrarelativistic nuclear collisions, supplemented by two possible mechanisms of the hadronization of the plasma, and to study the dynamical effect of the hadronization on the hydrodynamic evolution of the plasma fluid.

Consider a space-time picture of the transverse plasma evolution, as schematically shown in Fig. 1, where the plasma domain is surrounded by two types of surface; one is a *space-like* surface with a *space-like* unit normal vector n_μ ($n^2 \equiv \mathbf{n}^2 - n_0^2 > 0$) and the other a *time-like* surface with an opposite relation $n^2 < 0$. The space-like surface corresponds to the ordinary surface in three-dimensional coordinate space, which travels with a velocity smaller than the light velocity, while the time-like surface appears when an instantaneous bulk phase transition of the plasma occurs.

A semi-classical microscopic description of the hadronization process at a space-like surface of the quark-gluon plasma was obtained by the present authors by making use of the chromoelectric flux tube model.[2] It was shown that only high momentum quarks ($k_0 >$ GeV) in the thermal distribution can penetrate the surface, accompanied by fission of the

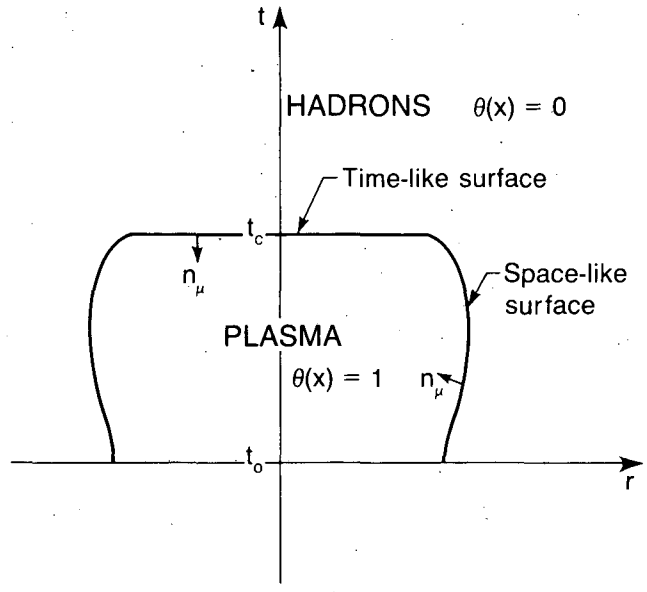

Fig. 1. Schematic space-time picture for the transverse evolution of a quark-gluon plasma produced in the central rapidity region. The plasma domain is surrounded by a space-like surface ($n^2 = \mathbf{n}^2 - n_0^2 > 0$) and a time-like surface ($n^2 < 0$) as well. XBL 841-10023

flux tube (hadronization), and most of the low momentum thermal quarks are reabsorbed by the plasma due to color confinement. We shall use this result to derive a boundary condition at the space-like surface of the plasma fluid. Our problem is then reduced to the problem of gas flow in the cylindrical domain which is covered by an almost impenetrable membrane with the external bag pressure acting on it. It will be shown that the resultant transverse flow, which couples to the scaling longitudinal expansion, consists of an inward moving rarefaction wave and a compression wave generated near the surface. This is in contrast to the result of a free expansion to the vacuum without a surface boundary condition,[1] where a simple rarefaction occurs. We will see that, with reasonable values for the initial plasma temperature, the compression wave dominates the rarefaction wave and, consequently, the plasma *shrinks* rather than expands. This happens due to the longitudinal expansion which causes a uniform rapid decrease of the interior plasma pressure *below* the external bag pressure. If the interior re-

gion of the plasma is sufficiently supercooled an instantaneous global phase transition to a superheated dense hadron gas may take place through a time-like surface, followed by an explosive transverse expansion of the system. We shall estimate the increase of the temperature and pressure of the system by this dynamical phase transition.

2. The basic equations in the following analysis are obtained from the energy-momentum conservation law:

$$\partial_\mu T^{\mu\nu} = 0 \quad . \tag{1}$$

Eq. (1) splits into three equations; for the interior, exterior and boundary between plasma and hadronic regions where, in deriving the last equation, we used $\partial_\mu \theta(x) = n_\mu \delta(x)$ with a surface delta function $\delta(x)$ and a surface normal unit vector n_μ.

In the collision dominated plasma region, the stress-energy tensor may be written in a form of perfect fluid gas in terms of a local pressure p(x), a local energy density $\varepsilon(x)$ and a local four fluid velocity $u^\mu(x)$

$$T^{\mu\nu}_{IN} = (p + \varepsilon)u^\mu u_\nu + pg^{\mu\nu} \tag{2}$$

3. The stress-energy tensor in the region outside of the plasma takes a more complex form. It contains a vacuum term corresponding to quantum fluctuations in the non-perturbative QCD vacuum, which we represent by the phenomenological bag term $Bg^{\mu\nu}$. In addition, there is a hadronic term whose form depends on the state of the hadrons coming out of the plasma. If the hadron gas is sufficiently dense and locally thermalized, the hadronic term is reduced to the hydrodynamic form as in Eq. (2). This approximation has been taken in ref. 9, 10, 8 to obtain a macroscopic description of the space-like surface of the plasma by making use of relativistic combustion theory. However it was found in a microscopic calculation of the hadronization at the space-like plasma surface[2] that the chemical reaction from the deconfined quarks to mesons proceeds very slowly due to color confinement. This implies that mesons would stream out of the plasma rather freely without strongly interacting with each other once they are formed at the plasma surface. In this case the stress-energy tensor outside of the plasma becomes

$$T^{\mu\nu}_{OUT}(x) = Bg^{\mu\nu} + \int dn(k,x)\frac{k^\mu k^\nu}{E} \tag{3}$$

where dn(k,x) is the density of hadrons with four momentum $k^\mu = (E,k)$ at x. Near the plasma surface the meson density is obtained from the radiating meson flux normal to the surface as

$$\frac{d^2n}{dk_n dE} = d^2(\text{MesonFlux})_n \frac{1}{v_n + v_s} \tag{4}$$

where k_n and $v_n = k_n/E$ are the meson momentum and velocity normal to the surface, measured on the rest frame of the plasma fluid element in the vicinity of the surface. Note here that the plasma surface is moving inward with velocity v_s on this frame because the plasma is being eaten away by the meson radiation. Thus the unit four vector normal to the surface is given by $n_\mu = \gamma_s(v_s, \mathbf{n}$ where $\gamma_s = (1 - v_s^2)^{-1/2}$ and $\mathbf{n}$ is the unit three vector normal to the surface.

The meson flux from the plasma was given in ref. 2 as

$$\frac{d^2(\text{MesonFlux})_n}{dK_n dE} =$$

$$\frac{2\gamma}{(2\pi)^3}\int d\mathbf{k}_0\, f(k_0/T_s)v_{no}\frac{1}{k_c^2}\exp\left(\frac{k_0(k_n-k_{no})^2}{2k_{no}k_c^2}\right)$$

$$\theta(k_n<v_{no}E)\cdot\theta(v_{no}E<k_{no})\cdot\theta(k_n<k_{no})\cdot\theta(k_{n>0})\,. \tag{5}$$

Here the integration is over the thermal flux of massless quarks and antiquarks with four momentum $k_0^\mu = (k_0\mathbf{k}_0)$, with $f(k_0/T_s)$, the thermal distribution function with surface plasma temperature T_s. One can readily derive the boundary condition at the space-like plasma surface from

$$p_{pl}(T_s) = B + \int dk_n dE\, \frac{d^2(\text{MesonFlux})_n}{dk_n dE} k_n \quad , \tag{6}$$

$$\varepsilon_{pl}(T_s)v_s = -Bv_s + \int dk_n dE\, \frac{d^2(\text{MesonFlux})_n}{dk_n dE}\, E \,, \tag{7}$$

which are to be solved for the surface temperature T_s and combustion velocity v_s. The leading order term in a power series expansion of $T_s k_0$ can be easily

computed analytically by taking a Boltzman distribution function for $f(k_0/T_s)$. The result is

$$T_s = [0.705 + 0.0655(B^{1/2}/k_c^2) + 0(B/k_c^4)]B^{1/4} \quad (8)$$

$$v_s = 0.50(T_s/k_c)^2 = 0.25(B^{1/2}/k_c^2) + 0(B/k_c^4) \quad (9)$$

Choosing $B^{1/4}$=280 MeV T_s=198 MeV and v_s=0.0075. For comparison note here that the critical temperature T_c of the first order phase transition from quark-gluon plasma to massless pion gas is determined by the Gibbs condition and is $T_c = 0.72B^{1/4} = 202$ MeV. Thus we see that the space-like surface of the plasma is slightly supercooled. Also note here that although our bag constant is much larger than that determined phenomenologically by hadron spectroscopy ($B^{1/4}$ = 140 - 210 MeV), it serves as a good parametrization of the result of a Monte Carlo calculation on the SU(3) lattice (T_c = 190 ± 20 MeV).

4. We now solve the hydrodynamic equations to determine the transverse flow of the plasma fluid, constrained by the surface boundary conditions (Eqs. (8) and (9)) at the transverse edge ($r = R_s$) of the plasma domain. As shown in ref. 1, for a cylindrically symmetric expansion accompanying the scaling longitudinal expansion, the hydrodynamic equations are reduced to a single characteristic equation

$$\frac{\partial}{\partial t}a + \frac{v_r + c_s}{1 + v_r c_s}\frac{\partial}{\partial r}a = \frac{-c_s}{1 + v_r c_s}\left(\frac{v_r}{r} + \frac{1}{t}\right)a \quad (10)$$

where a and v_0 are functions of r and t defined in the extended space interval $-R_s < r < R_s$. The local temperature and fluid velocity are given in terms of a(r,t) by

$$T(r,t) = T_0\,[a(r,t)\,a(-r,t)]^{c_s/t} \quad (11)$$

$$v_r(r,t) = \frac{a(r,t) - a(-r,t)}{a(r,t) + a(-r,t)} \quad . \quad (12)$$

This form automatically incorporates the boundary condition on the central axis of the cylindrical plasma domain, $v_r(r = 0, t) = 0$.

A numerical solution is presented in Fig. 2, where we start with the initial internal temperature T_0 = 210 MeV, which gives the initial energy density ε = 3.1 GeV/fm^{3}3 (note that this energy density be-

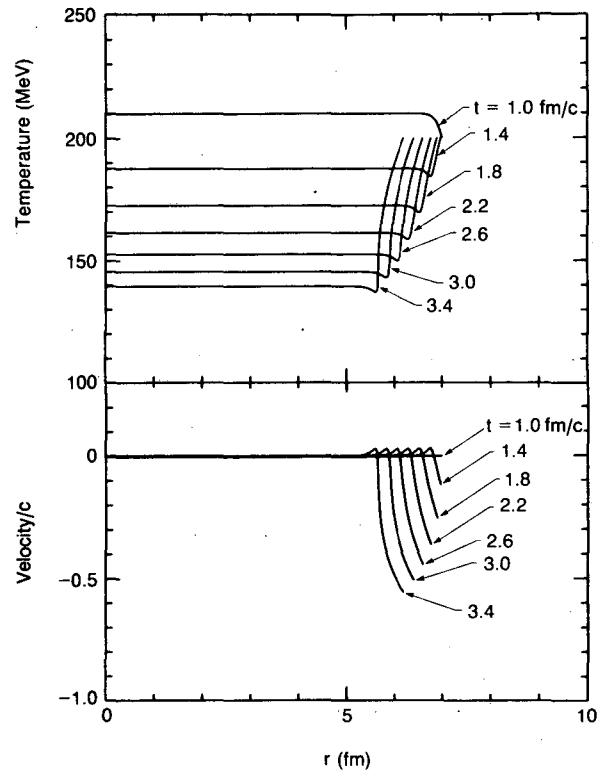

Fig. 2. Temperature and fluid velocity distribution as functions of transverse distance r from the central axis of cylinder. The time which corresponds to each curve is indicated on the curve. Initial conditions at $t = t_0$ = 1 fm/c are set to T_0 = 210 MeV in the interior and v(r) = 0 for $0 \leq r \leq R_0$ = 7 fm. At the surface boundary, the plasma temperature is always maintained at T_s = 200 MeV according to the surface boundary condition (see Eq. (18)).

XBL 842-10040

comes $\varepsilon + B$ = 3.9 GeV/fm^3 when it is measured from the non-perturbative QCD vacuum), and with the initial time t_0 = 1 fm/c and the initial radius of the system $R_s(t = t_0$ = 7 fm, corresponding to central U + U collisions. It is observed that, near the surface, a small rarefaction wave, generated by the initial pressure gradient, travels inward with the velocity of sound and a compression wave follows this. The rarefaction wave converts the heat energy of the fluid into the collective transverse flow energy, while the compression wave heats up the system again to reach the fixed surface temperature T_s. In the meantime, the temperature of the interior region falls off

uniformly due to the longitudinal scaling expansion. This cooling is so rapid that, in the presence of the external bag pressure, significant compression occurs near the surface and, as a result, the system shrinks in the transverse direction. Eventually the compression wave would lead to a formation of a shock discontinuity, signaled by a crossing of characteristic lines, if a global hadronization, as described below, does not take place before.

5. As time elapses, the interior region of the plasma continues to be diluted and, when it is sufficiently supercooled, a dynamical phase transition to a dense hadron gas may occur from the interior. On account of the stability argument on the longitudinal scaling solution and the spatial uniformity in the transverse temperature distribution (see Fig. 2), we consider here an instantaneous uniform phase transition. Since the fluid is at rest in the interior (at z = 0) this happens in the space-time picture through a time-like surface characterized by a time-like four vector normal to this surface, $n_\mu = (1,0,0,0)$. If the temperature is T_Q on the plasma side of this surface and T_H on the hadron gas side, the continuity of energy-momentum through this surface imposes

$$\varepsilon_{pl}(T_Q) = -B + \varepsilon_{had}(T_H) \quad . \tag{14}$$

Also there is another constraint due to the second law of thermodynamics, which requires the increase of entropy density in this phase transition

$$\sigma_{pl} = (T_Q) \leqslant \sigma_{had}(T_H) \quad . \tag{15}$$

To illustrate the consequence of these constraints we use here a massless pion gas approximation, neglecting effects of interactions. In Fig. 3 we illustrate the constraints (14) and (15) between T_Q and T_H. The shaded region is forbidden due to the entropy increase law. We see that the allowed combinations of T_Q and T_H are limited to a very narrow range on the solid curve. Also the increase of pressure due to this bulk phase transition does not depend on the entropy increase:

$$\Delta p = B + p_{had}(T_H) - p_{pl}(T_Q) = \frac{4}{3} B \quad . \tag{16}$$

Thus the bulk phase transition generates high internal pressure which exceeds the external vacuum pressure and, therefore, the system starts to expand in the transverse direction. This stage of evolution of the system can be described by ordinary hydrodynamics without a surface boundary condition. Note that since this transverse expansion starts at t_c ($\gg t_0$), or perhaps later, the effect of the scaling longitudinal expansion is reduced and the internal fluid energy is more efficiently used to generate a transverse flow before the system breaks up into free streaming particles.

Footnotes and References

*Condensed from Phys. Lett. **141B**, 419 (1984).

1. G. Baym, B.L. Friman, J.-P. Blaizot, M. Soyeur and W. Czyz, Nucl. Phys. A (1983) in press.
2. B. Banerjee, N.K. Glendenning and T. Matsui, Phys. Lett. **127B**, 453 (1983).

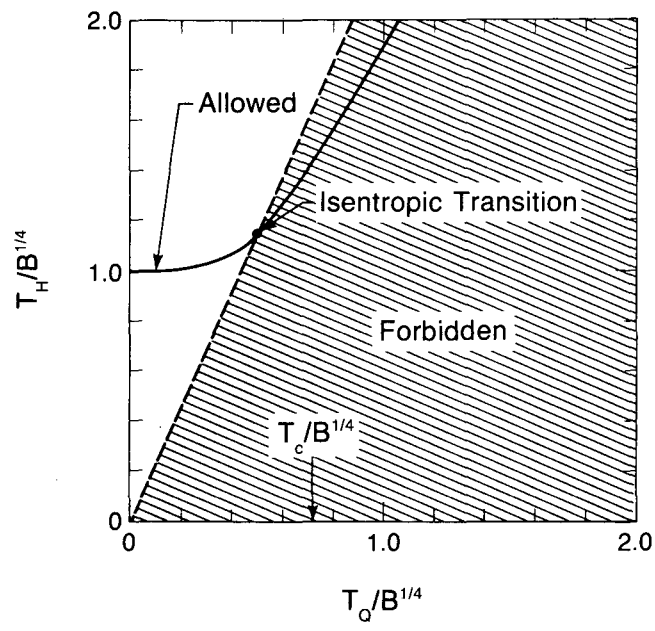

Fig. 3. Temperature of supercooled quark-gluon plasma (T_Q) versus a temperature of superheated hadron gas (T_H) at the global phase transition point. The allowed combinations are indicated by a solid curve. The shaded region is forbidden by the entropy increase law. XBL 841-10024

Relativistic Particle in Periodic Square Potential

B. Banerjee, N.K. Glendenning, and V. Soni

In solid state physics such as in crystals the electrons feel a periodic potential. For a square well potential and non-relativistic particles the problem was solved analytically long ago by Kronig and Penney. Their solution explicitly exhibits a band structure in the spectrum. There are also several physical systems where *relativistic* particles feel a periodic potential. The electrons in neutron stars are relativistic and, if the nucleons of the dense core form a solid lattice, they would experience a periodic potential.

The particular interest that we have in this problem arises from recent interest in soliton models of the nucleon as representing a non-perturbative solution to Q.C.D. in the large N_c limit. We have posed the question whether matter, described as interacting solitons with bound quarks, might exhibit a phase transition in which, as in metals, some of the quarks become liberated from the solitons in which they are normally bound.

In this note we obtain an analytic solution for the Dirac equation, which in one space dimension can be written,

$$(\vec{\alpha}\cdot\vec{p} + \beta(m + U) - E)\,\psi(x) = 0 \ , \ \psi = \binom{u}{v} \quad (1)$$

where

$$\alpha = \sigma_2 = \begin{pmatrix} 0 & -i \\ i & 0 \end{pmatrix}, \ \beta = \sigma_1 = \begin{pmatrix} 0 & 1 \\ 1 & 0 \end{pmatrix} \quad (2)$$

The resulting linear coupled equations for u and v can be rewritten in terms of one of these, say u, which satisfies

$$u'' + uU' = \Big[(m + U)^2 - E^2\Big]u \quad (3)$$

For a periodic square potential U, a discontinuity is produced in the derivative of the solution. For

$$U(x) = \begin{cases} 0 \ , & |x| \leqslant a \\ V \ , & a < |x| \leqslant a + b \end{cases} \quad (4)$$

we have

$$U' = -V\Big[\delta(x + a) - \delta(x - a)\Big] \quad (5)$$

and hence

$$u'' - uV\Big[\delta(x + a) - \delta(x - a)\Big] = \Big[(m + U)^2 - E^2\Big]u \quad (6)$$

Integrate this about a small neighborhood of each discontinuity to find the discontinuity in derivative of the solution,

$$u'(-a + \eta) - u'(-a - \eta) = Vu(-a)$$

$$u'(a + \eta) - u'(a - \eta) = -Vu(-a) \quad (7)$$

Now define,

$$Q^2 = (m + V)^2 \ , \ K^2 = E^2 - m^2 > 0 \quad (8)$$

In each of the three regions the solution has the form,

$$u_1 = Ae^{Qx} + Be^{-Qx} \ , \ -(a + b) \leqslant x < -a$$

$$u_2 = \alpha e^{iKx} + \beta e^{-iKx} \ , \ -a \leqslant x < a \quad (9)$$

$$u_3 = Ce^{Qx} + De^{-Qx} \ , \ a < x \leqslant a + b$$

The Bloch theorem can be used to relate the wave function at points separated by an integer number of cell lengths. Thus

$$\psi(-a - b) = \psi(a + b)\exp(2i(a + b)k)$$

$$\psi'(-a - b) = \psi'(a + b)\exp(2i(a + b)k) \quad (10)$$

which solve to give

$$C/A = e^{-2(a+b)(Q+iK)} \ , \ D/B = e^{2(a+b)(Q+-iK)} \quad (11)$$

The continuity of the function, and the specific discontinuity of the derivative derived above yield in particular

$$u_1(-a - \eta) = u_2(-a + \eta)$$

$$u_1(-a - \eta) + Vu_1(-a + \eta) = u_2'(-a + \eta)$$

$$u_3(a + \eta) = u_2(a - \eta) \quad (12)$$

$$u_3'(a + \eta) + Vu_3(a + \eta) = u_2'(a - \eta)$$

in which the limit $\eta \to 0$ can now be taken.

Taking into account (11), these four equations determine all the constants in the solution provided the determinant of the coefficients of the unknowns vanishes. Thus,

$$0 = \begin{vmatrix} 1 & 1 & 1 & -1 \\ Q + V & -Q - V & -ik & ik \\ e^{-2QB}e^{-2ik(a+b)} & e^{2QB}e^{-2ik(a+b)} & -e^{2iKa} & -e^{-2iKa} \\ (Q + V)e^{-2Qb}e^{-2ik(a+b)} & -(Q - V)e^{2Qb}e^{-2ik(a+b)} & -iKe^{2iKA} & iKe^{-2iKA} \end{vmatrix} \tag{13}$$

After some manipulation this yields our final answer,

$$\frac{Q^2 - K^2 - V^2}{2QK} \sinh 2Qb \sin 2Ka + \cosh 2Qb \cos 2Ka = \cos 2k(a + b) \tag{14}$$

This provides the eigenvalues, E, in terms of the crystal momentum, k. The band structure arises because the left side cannot equal the right except over continuous ranges of energies that are separated by gaps. This is similar to the Kronig-Penney result but differs explicitly in the appearance of V^2 on the left side, and implicitly in the relativistic equations (8). This result embraces the entire range of energies and reduces in the non-relativistic limit to Kronig-Penney.

Kaons and Quark-Gluon Plasma*

Norman K. Glendenning and Johann Rafelski†

1. Introduction

The primary aim of experiments involving colliding nuclei is the discovery of the new state of matter consisting of quarks and gluons.[1] From the point of view of its detection, an important distinction of this quark-gluon plasma from the normal form of hadronic matter made of undissolved hadrons is the appearance of numerous gluons. Gluons carry, aside from spin, only color, the strong interaction charge, and hence their detection in an experiment can only be indirect, as color is confined. However, the numerous gluons are very efficient in generating strange quark pairs in QGP.[2] The reactions depicted in Fig. 1a can saturate the available phase space within $\sim 2 \cdot 10^{-23}$ sec, while quark based reactions, Fig. 1b, need typically 10 times this time. Since QGP is expected to be a high pressure state, its lifetime after formation has been estimated to be less

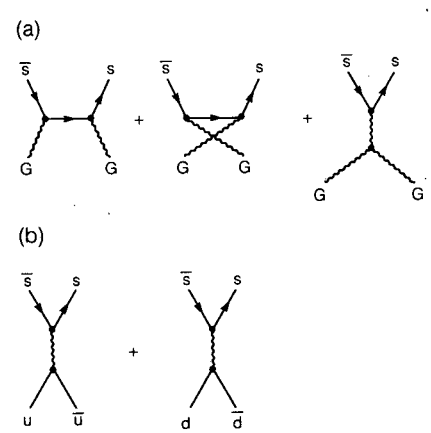

Fig. 1. Strangeness-generating processes in quark-gluon plasma: a) glue-glue b) $q\bar{q}$ driven processes.
XBL 846-8978

than $2 \cdot 10^{-23}$ sec. Consequently, observation of an anomalously large strangeness abundance may be taken as the observation of the gluonic degrees of freedom in the plasma.

The density and total number of strange quarks in the plasma has been proposed as a characteristic plasma signal on several occasions.[3] However, discussion has focused on the observation of rare antibaryons. A much simpler, though less characteristic (as we shall see), experiment would only focus on the observation of kaons. The purpose of this communication is to determine the precise magnitude of the expected effect of QGP formation, defined at CM-energies of ~4 GeV/nucleon, on the Kaon abundance. We will focus here on the abundance of $K^+ = \bar{s}u$ for the following two reasons: 1) the $K^0 = \bar{s}d$ neutral Kaon is not an eigenstate and $K_0 - \bar{K}_0$ oscillates, wiping out the $\bar{s}$-quark signal. 2) Kaons containing an s-quark ($K^- = s\bar{u}$, $K^0 = s\bar{d}$) have a large strangeness-exchange cross section and their population will be representative of the late stages of the HG phase into which the plasma will transform during the evolution of the system.[4]

It is very likely that about half of the $\bar{s}$ quarks from the plasma will be used in making K^+-mesons, the other half contributing to the $K_0 \pm \bar{K}^0$ states, and a smaller, and for this consideration, insignificant number of $\bar{s}$ quarks being contained in the anti-strange baryons; $\overline{sss}$, $\overline{ssq}$, $\overline{sqq}$, or $\bar{s}s$ mesons, as it is self-evident that such states have a much smaller chance of emerging from a baryon-rich plasma than does a $\bar{s}q$-meson. A further positive aspect of baryon rich plasma is the depletion of anti-baryons, which have the capacity, through strangeness-exchange reactions, to deplete the $\bar{s}q$ meson abundance. Though cross sections for such processes, e.g.,

$$\bar{s}q + \overline{qqq} \rightarrow \overline{sqq} + (\bar{q}q)_\pi \qquad (1)$$

are large and they are highly exothermic, they will nevertheless proceed very slowly if antibaryons are rare, as will be the case due to $\bar{q}$-suppression in baryon rich QGP.[3]

From this discussion we are thus led to conclude that the K^+-abundance will be a significant measure of the properties of QGP. However, QGP events are expected in central nuclear collisions, which are defined in terms of high particle multiplicity. This introduces a bias, as a minimum multiplicity trigger will always be a minimum K^+ abundance trigger. Thus only abundance ratios, such as K^+/π^+, K^+/p^+, will be significant. We have selected equal charges here in order to minimize leading particle effects and other non-QGP distortions arising from normal hadronic processes. The ratio K^+/K^- is, as already mentioned, a measure of the properties of the hadronic gas at the freeze out condition.[4]

The ratio K^+/π^+ will however show a much less dramatic rise than would be expected from the K^+-mesons alone. This is because pions, being the "cheapest" carriers of entropy, will be copiously produced in the QGP to HG phase transformation. The plasma state contains a high entropy density in part due to the strong gluon component. An easy way to compute the π^+ abundance is to divide the entropy excess in GQP (excess over entropy of residual baryons) and divide it by the entropy carried by each pion[5] which will be, as we shall see, nearly 4 units (k = 1). The K^+/p^+ ratio will depend on the baryon content of the plasma and the calculations below will serve to determine the conditions under which a baryon-rich plasma will be formed.

In the following sections we discuss in turn the entropy content of the plasma, the K^+/π^+ and K^+/p^+ ratios followed by brief summary and outlook.

2. Kaon to Pion Ratio in Nuclear Collisions

The pion number is obtained by calculating the entropy contained in the plasma ($V\sigma$), subtracting from it the entropy carried away by the baryon number and dividing by the entropy per pion. As can be seen from the results presented in Fig. 2, K^+/π^+ ratio varies little with μ and is ~0.4 at μ = 3T, the case we have discussed qualitatively. Furthermore, the dominant T-dependence, or T^3 factor drops out leaving an almost T-independent K^+/π^+ ratio.

In p-p collisions of comparable energy this ratio is below 0.1.[6] Consequently we suggest the measurement of the K^+/π^+ ratio as function of multiplici-

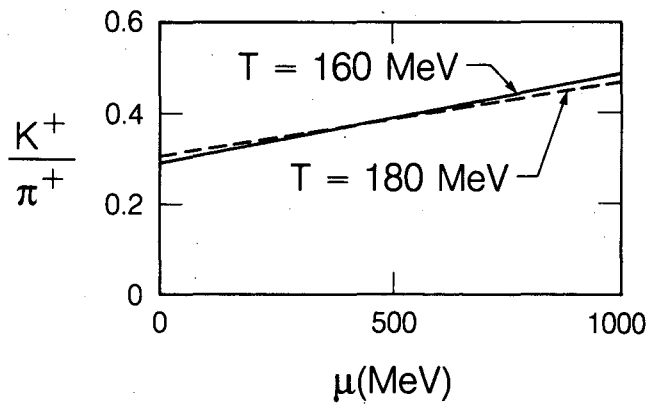

Fig. 2. K^+/π^+ ratio from quark-gluon plasma at T = 160 and 180 MeV, as function of baryochemical potential μ (m_s = 180 MeV, α_c = 0.5, 2Z/A = 1).
XBL 846-2473

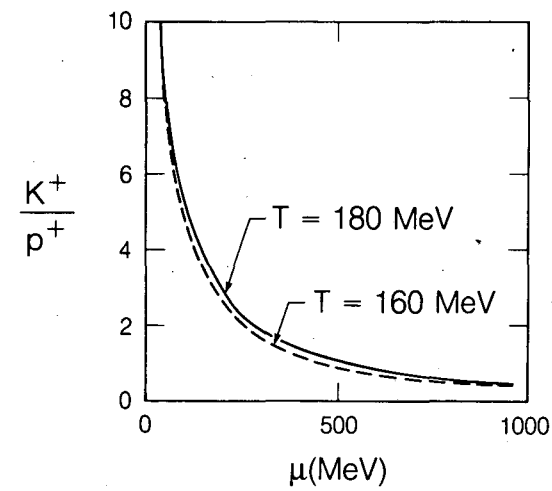

Fig. 3. K^+/p^+ ratio from quark-gluon plasma (same parameters as Fig. 2). XBL 846-8977

ty and expect a rise by a factor three as the multiplicity moves to high values associated with the quark-gluon plasma. It is important to sum the transverse momentum pions and kaons to account for their different expected temperatures—pions are "cooled" by rescattering during the hadronic gas expansion phase while the weakly interacting kaons reflect earlier higher temperatures. However, rapidity should be kept as a variable, indicating where plasma formation has occurred.

3. Kaon to Baryon Ratio in Quark-Gluon Plasma

It is likely that depending on the energy and atomic number, A, of the colliding nuclei, there will be different domains in rapidity space involving: 1) baryon rich plasma; 2) baryon poor plasma; or 3) no plasma at all. Since the abundance of K^+ is independent of baryon number density, on the hypothesis that it reflects the gluon density via s quarks, it seems that the ratio K^+/p^+ will be a useful measure to distinguish the three regions mentioned above. This ratio shown in Fig. 3 as a function of μ is quite sensitive to a variation in μ, when $\mu < 600$ MeV. It is unlikely that $\mu > 600$ MeV is explored in quark-gluon plasma forming nuclear collisions, as this would lead to quite enormous baryon and energy densities at $T \gtrsim 150$ MeV.

Thus we conclude this brief section noting that a measurement of the K^+/p^+ ratio as function of rapidity would provide a qualitative measure to the distribution of the baryon number in plasma. This information is not provided by π^+/p^+ since pions are neither characteristic of the plasma, nor are they *in principle,* as $\bar{s}$ quarks are, insensitive to the values of the baryochemical potential, or said differently, to the baryon density of the plasma.

4. Summary and Outlook

We have discussed here the K^+ mesons emerging as messengers of the quark-gluon plasma in nuclear collisions. We have shown that a mild enhancement of the K^+/π^+ multiplicity ratio may be expected leading to a rise by a factor of three in this ratio as function of multiplicity, if a quark-gluon plasma is formed. Here the hypothesis is that low multiplicity collisions are similar to p-p collisions, while quark-gluon plasma formation is accompanied by *high* particle multiplicity.

It has been argued previously that a quark-

gluon plasma may be created in relativistic nuclear collisions both in baryon rich and baryon poor forms, the latter being expected in the central rapidity region at ultrarelativistic energies, the former in moderate energy very heavy ion nuclear collisions, say U on U at (5 GeV/nucleon)$_{CM}$ also at central rapidity. Since the high absolute abundance of K^+ is independent of baryon density, viz baryochemical potential in the plasma, it is possible by studying simultaneously the K^+ and p^+ abundance to determine the baryon number content of the plasma as a function of e.g., rapidity. To facilitate this study we have computed the relative K^+ to proton abundance as function of baryochemical potential and have shown that in the baryon rich plasma this ratio would be near to unity. We should remember that part of the p^+ abundance may be in the form of strange baryons, since reactions such as

$$qqq + s\bar{q} \rightarrow sqq + (q\bar{q})_\pi$$

are exothermic and cross sections are quite substantial. Consequently strange baryons must be carefully counted. Calculations in the hadronic gas[4] indicate that, depending on the chemical potential, freeze out hyperons could indeed be more numerous than $s\bar{q}$ (K^-) mesons. However interesting, such behavior is characteristic of a hadronic gas, not of quark-gluon plasma which must be studied through observation of antistrange quark content of hadrons.

Here perhaps the most characteristic and promising avenue, though difficult experimentally, seems to be the study of strange and multistrange antibaryons [3]. E.g. in a quark recombination model the $\bar{\Lambda}/\bar{p}$ abundance would follow the $\bar{s}/\bar{q}$ abundance ratio at the phase transition, which at $\mu \sim 500$ MeV, $T \sim 1/3\ \mu$ would make $\bar{\Lambda}$ more abundant than $\bar{p}$, a quite unlikely circumstance in the hadronic gas phase. Similarly significant may be the observation of $\bar{s}\bar{s}$ clustering in anti-cascades which in the hadronic gas phase has a relative probability of 10^{-3} at $\mu \sim 500$ MeV (with reference to single-$\bar{s}$ hadrons),[7] while in quark-gluon plasma it is 10^{-4}.

Footnotes and References

*Condensed from LBL-17938; to be published in Phys. Rev. C.

†Department of Physics, University of Capetown Rondebosch 7700 Capetown, South Africa

1. See, e.g., J. Rafelski and M. Danos, "Perspectives in High Energy Nuclear Collisions," NBS-IR-83-2725.
2. J. Rafelski and B. Muller, Phys. Rev. Lett. **48** (1982) 1066.
3. (a) J. Rafelski, "Extreme States of Nuclear Matter" in Proceedings of Workshop on Future Relativistic Heavy Ion Experiments; Darmstadt, October 1980, GSI Report 81/6, May 1981, p. 282; and Frankfurt preprint UFTP 52/1981. (b) J. Rafelski, Phys. Rep. **88** (1982) 331. (c) J. Rafelski, "Strangeness in Quark-Gluon Plasma," Frankfurt preprint UFTP 86/1982 and: South. Afr. J. Phys. (1983). (d) J. Rafelski, Nucl. Phys. **A418** (1984) 489C.
4. P. Koch, J. Rafelski and W. Greiner, Phys. Lett. **123B** (1983) 151.
5. J. Rafelski, "Strangeness and Phase Changes in Hot Hadronic Matter" in Proceedings of 6th High Energy Heavy Ion Study, LBL 16281, p. 489 (1984).
6. See, e.g., G. Giacomelli and M. Jacob, Phys. Rep. **55** (1979) 1.
7. P. Koch and J. Rafelski, to be published.

Rapidity Density Fluctuations

E.M. Friedlander

We discuss here fluctuations of the rapidity density

$$\rho \equiv dn/dy \tag{1}$$

of secondary particles produced in high-multiplicity events, e.g., of the kind expected for A-A collisions in the mini-collider.

There appears to be a consensus[1,2,3] on a necessary condition for quark-gluon plasma (QGP) formation, namely that this process requires a relatively high energy density:

$$\varepsilon > 1 \div 2 \text{ GeV/fm}^3 \tag{2}$$

which is linearly related to the rapidity density:

$$\varepsilon \sim m_T \rho \tag{3}$$

Thus, high values of ρ may signal favorable (albeit not sufficient!) conditions for transition to a QGP. Such high values of ρ can be realized in two ways (or combinations thereof) viz.:

a. Large overall values of $<\rho>$, i.e., large overall particle multiplicities, because of the finite range of $y \sim \ln s$.

b. Large "local" fluctuations of ρ, in other words fluctuations restricted to narrow intervals of y, possibly correlated with large values of m_T, hence of the transverse momenta. Such spikes in y could be regarded as "hot spots" localized in space-time.

Large ρ-values of type b) have been seen in a few isolated very high energy A-A collisions, observed in cosmic rays (e.g., ref. 4 and references quoted within).

Large fluctuations of ρ could occur also at much lower energies than the cosmic ray events mentioned above (100 TeV and up) where $<\rho>$ is not sufficiently high, even in the central region, to satisfy Eq. (1). Fig. 1 shows the pseudo-rapidity distribution of an event induced by a 300 GeV proton from a FNAL beam on a Ag,Br target in nuclear emulsion. The smooth curve is the average of 34 events from the same beam and of a similar multiplicity ($<n> \sim 36$). The huge spike near $\eta \sim 2.5$ is localized within 0.5 pseudo-rapidity units and clearly lies outside statistical fluctuations. This event is by no means unique. Fluctuations of this kind occur in a few percent of the events with high multiplicity (say, $n > 30$) at all energies from ~ 70 GeV upwards.

The fact that these spikes are so narrow, typically 1/2 units of η, makes it difficult to explain them away as "garden variety" clusters. Indeed, if such a cluster decays isotropically in its own rest frame, the dispersion D_η in η is:

$$D_\eta^{iso} = \sqrt{\frac{\pi^2}{12}} \simeq 0.907 \quad . \tag{4}$$

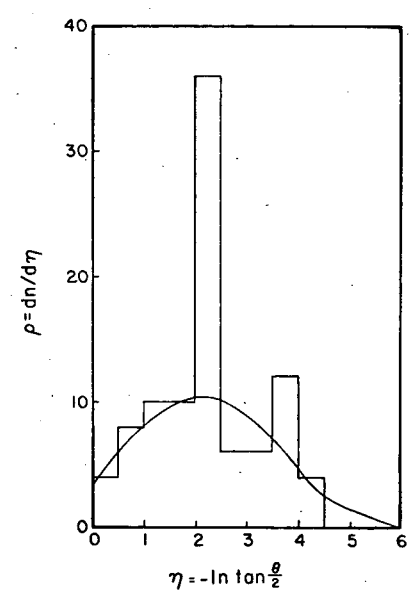

Fig. 1. An example of a large fluctuation in rapidity density; the event was produced by a 300 GeV proton. The smooth line is the average rapidity density of events with the same meson multiplicity produced by the same beam. XBL 8410-4324

A Monte Carlo calculation has shown that if the mean transverse momentum of secondaries from the cluster is raised to $<p_T> \sim 0.6$ GeV/c, while leaving the longitudinal momentum component unchanged, D_η immediately drops to ~ 0.3–0.4 yielding a spike as narrow as the observed ones. Furthermore, the total energy content of the spike is raised to $\gtrsim 110$ GeV, i.e., the cluster carries by itself $\sim 1/3$ of the primary energy. Adding the rest of the secondaries one finds that this raises the inelasticity of the event from ~ 0.5 to $\gtrsim 0.7$. This ties in with the obvious depletion of the forward η-bins and suggests a relatively large energy loss of the incident proton. In order to select such "spikes" in ρ from the background of "normal" statistical fluctuations we consider the average "normal" rapidity density (continuous line on Fig. 1) for the class of events with a given total multiplicity n, such that

$$\int_0^{\eta_{max}} \rho(\eta) d\eta = n \quad . \tag{5}$$

Denote by p_i the probability for a particle to fall in the ith η-bin of width Δ

$$p_i = \frac{1}{n} \int_{(i-1)\Delta}^{i\Delta} \rho(\eta) d\eta \quad , \tag{6}$$

and by k_i the number of particles falling into this bin in a given event. Then, for independent particles the probability of k_i will be

$$Q(k) = \binom{n}{k_i} p_i^{k_i} (1 - p_i)^{n-k_i} \tag{7}$$

It turns out that bins with Q below, say, 10^{-3} or even 10^{-4} turn up with much higher frequency than expected and are connected with $k_i \gg np_i$ rather than with $k_i \ll np_i$.

Comparison with a Monte Carlo calculation has shown that in a sample of ~ 1200 events induced by 200 and 300 GeV proton beams from the FNAL accelerator, large "spikes," reaching $\rho \gtrsim 20$ (i.e., satisfying Eq. 2) appear 3–4 times more frequently than expected from random fluctuations.

References

1. R. Anishetty, R. Koeler and L. McLerran, Phys. Rev. **D22**, 2793 (1980).
2. J.D. Bjorken, Phys. Rev. **D27**, 140 (1983).
3. M. Gyulassy, LBL-15175, October 1982.
4. J. Iwai *et al.*, Nuovo Cimento **69A**, 295 (1982).

Inelasticity Distribution and its Implications for Many-Particle Production Processes*

G.N. Fowler,[†‡] *E.M. Friedlander, M. Plümer*[‡] *and R.M. Weiner*[‡]

Although the leading particle effect has been known in high energy physics for many years, its implications have not been fully realized until comparatively recently.

In statistical and hydrodynamical models, which were invented from the beginning to describe high multiplicity reactions, it is the energy

$$W = K \sqrt{s}$$

effectively used for the production of secondaries, which determines the dynamics; K is the elasticity coefficient. In these approaches the energy carried away by the leading particles, $(1 - K)\sqrt{s}$, is subtracted from the total available energy $\sqrt{s}$ and only the remainder W is taken as the input for theoretical considerations.

It must be noted that the inelasticity K which defines the amount of energy deposited by the leading particles varies from event to event so that one has to introduce a distribution $\chi(K)$

$$\int_0^1 \chi(K,s)dK = 1 \quad .$$

Until very recently, $\chi(K,s)$ was not known either theoretically or experimentally. The only information available was the first moment of χ, namely

$$<K> = \int_0^1 K\,\chi(K,s)\,dK \quad . \qquad (1)$$

Up to and including ISR energies it was found that $<K> \sim 0.5$. The only reference from which experimental information on $\chi(K,s)$ can be extracted is the work by Brick *et al.*[1] describing bubble chamber measurements at $p_{lab} = 147$ GeV. Contrary to what one might have expected starting from a flat x distribution for one leading particle, the inelasticity distribution $\chi(K,s)$ turns out to be a function with a maximum at $K \sim 0.5$. It is interesting to mention that if there are two leading particles which are uncorrelated, as experiments seem to indicate,[2] in a simple model one indeed obtains a $\chi(K,s)$ similar to that in Fig. 1 (cf. ref. 3).

In order to use $\chi(K,s)$ or ref. 1 in theoretical formulations, we fitted the data with a beta distribution

$$\chi(K,s) = K^{a-1}(1-K)^{b-1}/B(a,b) \quad ,$$

$$B(a,b) = \Gamma(a)\Gamma(b)/\Gamma(a+b) \quad , \qquad (2)$$

with $a = b = 2.5$ for $\sqrt{s} = 16.6$ GeV. This gives

$$<K> = a/(a+b) = 0.5 \quad .$$

Evidently, the s dependence if any of $\chi(K,s)$ is contained in the parameters a and b.

That $\chi(K,s)$ is an essential ingredient in all attempts to interpret multiparticle events must have become evident to almost everybody when it was found[4] that the dependence of the distribution $\chi(K,s)$ on s is essential for a satisfactory account of the data on the mean inelasticity and mean multiplicity.

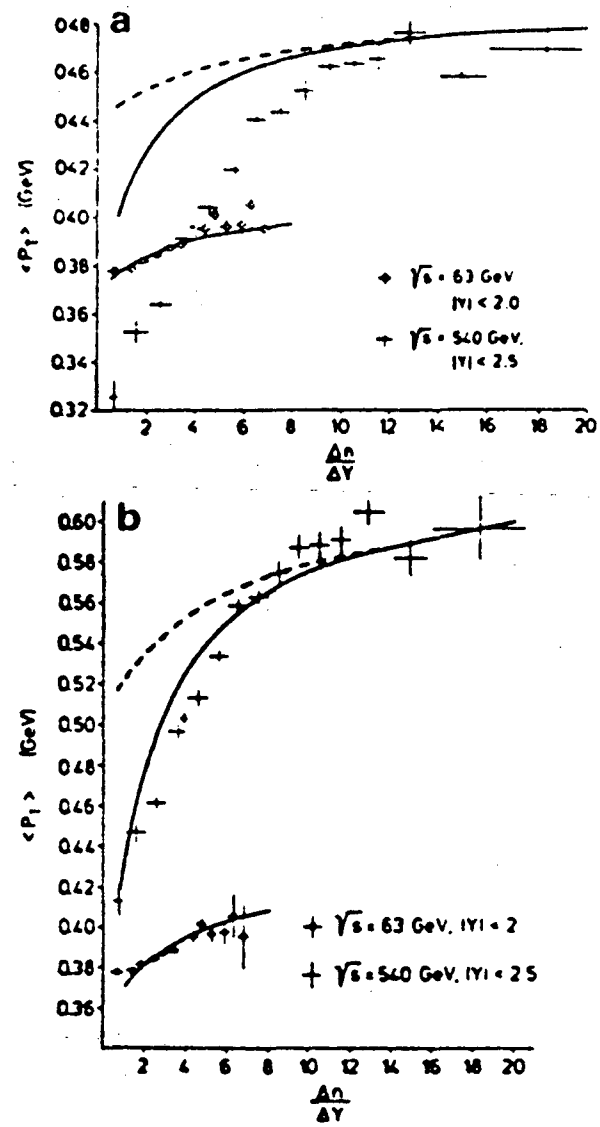

Fig. 1. Mean transverse momentum vs. central rapidity density for pp collisions at the ISR ($\sqrt{s} = 53$ GeV) and $p\bar{p}$ collisions at the CERN SPS collider ($\sqrt{s} = 540$ GeV). Theoretical curves: a) without s-dependence of χ; b) with the s-dependence of χ required to fit the multiplicity data.

XBL 8410-4323

The most important result is that the inelasticity distribution changes with s in such a way that $<K>$ decreases with s. This conclusion emerges from several independent pieces of evidence which are summarized in this paper. These concern the dependence on s of (i) the energy of the produced particles, (ii) the mean multiplicity when the leading particle effect is properly accounted for, and (iii) the dependence of $<p_T>$ on multiplicity n, and (iv) the dependence of $<p_T>$ on s. At the same time a natural explanation for the phenomena above is given.

We first summarize the information gained from ref. 4 from a study of the mean multiplicity $<n(s)>$ and the total mean energy in the secondary particles, $\int \cosh(y) \times (dN/dy)dy$, with $\eta \approx y$, where η is the pseudorapidity and y the rapidity. This is

$$<K^{1/2}>_{\sqrt{s}\,=\,540\ \mathrm{GeV}} / <K^{1/2}>_{\sqrt{s}\,=\,63\ \mathrm{GeV}} = 0.86$$

and

$$<K>_{\sqrt{s}\,=\,540\ \mathrm{GeV}} / <K>_{\sqrt{s}\,=\,63\ \mathrm{GeV}} = 0.6$$

respectively, assuming that the mean multiplicity at fixed K follows the rule observed up to ISR energies $\bar{n} \propto W^{1/2}$. Using the parameterization of $\chi(K,s)$ given earlier one finds with a = 2.5, b = 2.5 at ISR energies and a = 1.5, b = 3.0 at collider energies for the values of the ratios given above 0.66 and 0.78 respectively, compared with unity in both cases if χ were independent of energy. Turning to the multiplicity we have

$$P_n(s) = \int_0^1 dK \chi(K,s)\, P(n \mid K) \quad , \qquad (3)$$

where $P(n \mid K)$ is the conditional probability to observe n particles when the inelasticity is K.

We consider now the dependence of $<p_T>$ on central multiplicity n. We parameterize the W dependence of $\bar{p}_T$ as suggested by the hydrodynamical model namely

$$\bar{p}_T = A\left(K\sqrt{\beta}\right)^{\alpha} \quad , \qquad (4)$$

where A and α are constants. Then

$$<p_{T;n}> = \frac{A\int_0^1 dK\left(K\sqrt{s}\right)^{\alpha} P(n \mid K)\, \chi(K,s)}{\int_0^1 dK P(n \mid K)\, \chi(K,s)} \quad . \qquad (5)$$

The function $P(n \mid K)$ used in Eq. (5) has been found from experimental data as explained earlier using relation (3) with $\chi(K,s)$ given in Eq. (2) with a = b = 2.5 for ISR and a = 1.5, b = 3.0 for collider data.

The first thing to notice about Eq. (5) is that as n becomes large only $K \sim 1$ will contribute and $<p_T;n>$ tends to a constant value $\propto s^{\alpha/2}$. We can use this fact to try to determine from the ratio of the plateau seen in the ISR and collider data with the result that $\alpha \sim 0.08$. With this value the fit to the rest of the collider data is poor as shown in Fig. 1a.

However, using the values a = 1.5, b = 3.0 which bring into agreement multiplicities at the ISR and at the $p\bar{p}$ collider we obtain the good fit shown in Fig. 1b.

Finally the energy dependence of $<p_T>$ may be found by summing Eq. (5) over n which permits an independence comparison when multiplicity distributions covering the whole rapidity range are used. We find

$$<p_T>_{\sqrt{s}\,=\,540\ \mathrm{GeV}} / <p_T>_{\sqrt{s}\,=\,63\ \mathrm{GeV}} = 1.26$$

This agrees with an experimental value of 1.21 as compared to 1.43 if $\chi(K,s)$ were independent of s.

Footnotes and References

*Published in Physics Letters **145B**, 407 (1984).

†Physics Department, University of Exeter, UK.
‡Physics Department, University of Marburg, Federal Republic of Germany.

1. D. Brick *et al.*, Phys. Lett. **103B**, 242 (1981).
2. M. Basile *et al.*, Nuovo Cimento **73A**, 329 (1983).
3. F. Takagi, Z. Phys. **C13**, 301 (1982).
4. E.M. Friedlander and R.M. Weiner, Phys. Rev. **D28**, 2903 (1983).

PART IV: METHODS AND INSTRUMENTATION

The ECR Ion Source for the 88-Inch Cyclotron

C.M. Lyneis, L. Brown, D.J. Clark, D. Elo, Y. Jongen, R. Lam, D. Morris and R. Peterson*

During this second year of a 2 year construction program, the fabrication and installation of the ECR (Electron Cyclotron Resonance) heavy ion source for the cyclotron[1,2,3] (Fig. 1) was essentially completed. As described in last year's report, the ECR source will increase the energies of heavy ion beams from the cyclotron by a factor of 2–3 for masses between neon and argon, and will extend the mass range from argon to krypton for beams at the Coulomb barrier of 5 MeV/nucleon. In addition operational efficiency will be improved because the frequent source changes of the present PIG source will not be necessary.

The LBL ECR ion source began test operation in January 1984. The source has already produced a wide variety of ion beams with sufficient intensities to be used in the cyclotron for both nuclear physics and applied research, Table I.

An important development of the ECR source in 1984 was the replacement of the sextupole magnet with an octupole magnet in the second stage. The advantage of the octupole is that the radial gradient is smaller than that of the sextupole, resulting in less azimuthal electron drift and thus higher electron energies. A prototype octupole structure was built using six $SmCo_5$ magnets plus two spares from the original sextupole. The advantage of this approach was that a rapid and inexpensive test of the octupole could be made. The LBL ECR source is the first to use an octupole. Table II shows that the best performance of the octupole source is significantly superior to that of the sextupole for argon and krypton. Because of the great success of the octupole test, the LBL ECR has been named the OCTIGUN (OCTupole Ion GUN).

The main disadvantage of the octupole is that adding two additional magnets required a substantial reduction in the spacing between the bars, which is useful for radial pumping, insertion of solid feed material, and for the injection of microwave power

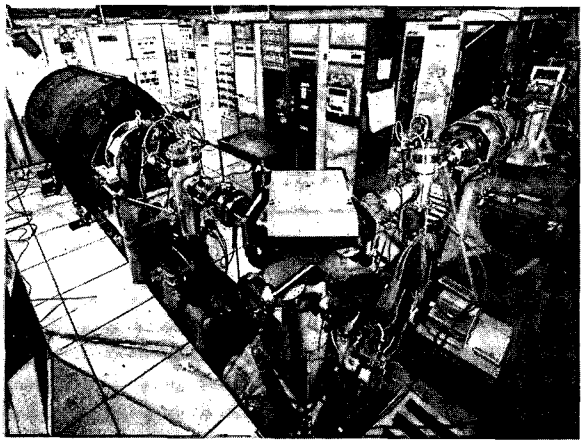

Fig. 1. The ECR source (left), 90° analyzing magnet (center) and horizontal beam line (right) for the 88-Inch Cyclotron. CBB 8410-7535

into the second stage. The RF feed into the main stage was modified so that the RF could be injected on axis to eliminate problems encountered with coupling to the plasma through the narrow gap between the bars. A new octupole structure is being constructed which will use smaller bars of $SmCo_5$ and provide larger spacing between bars.

The source has been extensively tested with argon and oxygen. For all the gases listed, adding a lighter mixing gas to the plasma was found to increase the average charge state. Helium was used as a mixing gas for nitrogen, oxygen, and neon. Similarly, oxygen was used as a mixing gas for argon and krypton. Systematically, the introduction of a lighter mixing gas increases the average charge state while the introduction of a heavier mixing gas decreases it. It seems that introducing a lighter gas into the plasma increases the ion confinement time of the heavier ions.

Metallic ions were produced both by inserting solid feed material directly into the main stage plasma chamber and by directing vapor from a small oven into the same region, Table I. Aluminum,

Table 1.
Ion Currents of the LBL ECR Source

	Gases					Metallic Ions	
	^{14}N	^{16}O	^{20}Ne	^{40}Ar	^{84}Kr	^{27}Al	^{40}Ca
1^+	43.	48					
2^+	47.	75.	24.				
3^+	47.	80.	34.	28.			
4^+	42.	72.	48.	27.			
5^+	21.	79.	*	34.			
6^+	1.5	51.	45.	48.	8.0	36.	
7^+	*	4.3	5.0	59.	*	22.	
8^+		*	3.8	89.	14.	10.	36.
9^+			.06	52.	18.		31.
10^+				*	20.		
11^+				9.2	20.	0.065	11.
12^+				2.5	18.		4.6
13^+				.38	12.		1.2
14^+				.036	10.		0.2
15^+					4.4		
17^+					.48		
18^+					.34		

All currents in eμA at 10 kV extraction voltage.
*Indicates not measured because a mixture of two ions with identical charge to mass ratios were present.

calcium and titanium beams were produced by inserting a solid material radially between the sextupole bars midway between the main stage magnetic coils. For all the metallic ion tests oxygen was used as a support gas. To operate the source on a routine basis with this type of injection it may be necessary to build a feedback loop using the RF power to keep the plasma density constant. To avoid the problems inherent in using direct plasma heating to produce metallic ions, a small resistance heated calcium oven was built. The metal vapor from the oven was directed radially into the plasma chamber at the same point that the rod had been inserted. The currents produced for calcium with this method were slightly lower than those produced by direct insertion, but the operating stability was remarkably improved. The source produced between 18 and 20 eμA of Ca^{9+} over a 12 hour period without any adjustment.

Table II.
Comparison of the Performances of the LBL ECR with the Octupole and the Sextupole

Ion	Octupole (eμA)	Sextupole (eμA)
$^{40}Ar^{8+}$	89.	42.
$^{40}Ar^{9+}$	52.	13.
$^{40}Ar^{11+}$	9.2	1.2
$^{40}Ar^{12+}$	2.5	0.28
$^{40}Ar^{13+}$	0.38	0.013
$^{84}Kr^{8+}$	14.	1.1
$^{84}Kr^{9+}$	19.	1.3
$^{84}Kr^{10+}$	20.	1.4
$^{84}Kr^{11+}$	20.	2.2
$^{84}Kr^{13+}$	12.	2.5
$^{84}Kr^{15+}$	4.4	1.2

The beam transport system to the cyclotron starts with 6 meters of horizontal beam line containing 2 magnetic quadrupole doublets to bring the beam from the 90° analyzing system to the vertical section. A 15° and 75° magnet bend the beam into the 5 meter long vertical transport line, which contains 3 solenoid lenses. Beam diagnostics consist of fixed 4-jaw collimators and movable Faraday cups. The vacuum system uses cryopumps and turbopumps with all metal seals on flanges to provide the necessary vacuum of less than 10^{-7} torr. Beam pipe is constructed largely of magnetic steel with nickel plating, to shield the beam from the stray cyclotron field. An electrostatic mirror bends the beam 90° into the cyclotron midplane for acceleration.

In June 1984 the source and new horizontal beam line were connected to the old vertical axial injection line, and beams of Ar^{8+} and Ar^{11+} were successfully injected and extracted from the cyclotron. During the summer 1984, the new vertical injection line was installed. During October 1984 beams were injected into and extracted from the cyclotron: 340 MeV Ne^{7+}, 175 MeV Ar^{8+}, and 180 MeV N^{5+}. The Ne^{7+} and N^{5+} were used in experiments, and provided stable high intensity beams, without the usual ion source changes required by the present PIG sources.

The N^{5+} beam had 30 μA at the ECR source and 2 μA on the beam stop at full cyclotron energy. The final center region electrodes will be installed in early FY85, to improve transmission for high energy beams. The ECR source will be placed into normal operation during the early part of FY85.

Footnote and References

*On leave from Cyclotron Laboratory, Louvain-la-Neuve, Belgium.

1. D.J. Clark, J.G. Kalnins and C.M. Lyneis, IEEE Trans. Nucl. Sci. **NS-30**, 2719 (1983).
2. D.J. Clark, Y. Jongen and C.M. Lyneis, 10th International Conference on Cyclotrons and their Applications, E. Lansing, MI (1984), p. 133.
3. C.M. Lyneis (in press), 8th Conference on the Applications of Accelerators in Research and Industry, Denton, TX (1984).

Prospects for Research with Radioactive Beams at LBL

J.M. Nitschke

Research with heavy ion (HI) beams has become a major field of physics. Nuclei of all naturally occurring elements and isotopes can be accelerated to energies as high as 2 GeV/nucleon with even higher energies expected in the future. With the advent of relativistic heavy ion accelerators and the development of high intensity on-line isotope separators it has now become possible to explore a new dimension in nuclear physics based on the production and application of radioactive beams (RIB). More than 1400 unstable nuclei with half lives greater than 1 μs are known and could potentially serve as projectiles in RIB experiments. In the past RIBs have been used mostly in astrophysical research and biomedical applications or at low energies ($\sim$50 keV) in conjunction with on-line isotope separators. Now there are several promising possibilities to obtain RIBs of acceptable intensity, and a large variety of scientific questions could be addressed should such beams become routinely available. The highest intensities can be expected from RIB production methods where the radioactive species are stopped and reaccelerated, and methods where the RIB emerges as a secondary beam from a suitable nuclear reaction. For the latter method the "conversion efficiency" for RIBs of nuclei near stability is on the order of 10^{-2} to 10^{-3} for target thicknesses of about 20 g/cm^2 and energies in the 100 to 1000 MeV/nucleon range. At the highest energies the electromagnetic dissociation of the projectile may aid in the production of unstable beams. The kinematic focusing of the projectile fragments makes it possible to analyze and "purify" these beams with monochromators consisting of dispersive magnetic elements and a position dependent absorber (wedge). These high energy RIBs can be used for experiments directly, but can also be injected very efficiently into a general purpose accumulator and storage ring that is equipped with an RF accelerating or decelerating section and capabilities to *cool* the circulating beams.

The cooling can be achieved with either electrons or lasers or by a stochastic method, depending on the mass, charge state, energy and intensity of the beam, and the required time constant. The net result of any of the cooling methods is a vast improvement of the emittance and the associated luminosity of the beam. The RF section would also allow the deceleration of the beam (while it is being cooled!) to energies as low as 5 MeV/nucleon for low energy nuclear physics experiments. These can be performed with thin (10$-$100 ng/cm^2) internal targets or with an extracted, external beam in the conventional way. The addition of a *second* ring would of course greatly improve the operational flexibility of such a facility.

A completely different approach for RIBs at LBL is, to start with the SuperHILAC. A comparison of different RIB production methods[1] shows that the combination of a high intensity, low energy, commercial cyclotron with a target/ion source and

an RFQ booster injecting into the SuperHILAC would deliver RIBs of light elements with intensities in the 10^8 to 10^{11} s^{-1} range, at energies from .1 to 8.5 MeV/nucleon. The same cyclotron could also be used to irradiate a UC_2 target to produce fission fragments. In this way *neutron-rich* isotopes with intensities of 10^8 s^{-1} (after acceleration) for masses near the peak of the fission distribution could be produced. All these beams could of course be "post-accelerated" in the Bevatron. In another method, instead of using the external cyclotron, a heavy ion beam from the SuperHILAC itself could be taken to produce exotic isotopes in a target/ion source. After pre-acceleration in an RFQ these RIBs could be accelerated in the HILAC during machine pulses "stolen" from the primary beam. This method would lend itself particularly well to the production of neutron deficient RIBs via compound nucleus reactions and neutron rich beams via damped reactions. Intensities are limited due to thin targets. RIBs of interest in astrophysics could also be generated by starting with a high intensity, stable primary beam and converting it via a gas target using resonance reactions. RIB intensities in this case are limited by the small effective target thickness and the low conversion factors. An alternative to RIBs is in some cases the use of radioactive targets.

Questions relevant to radioactive beams and targets were discussed at a workshop organized by the SuperHILAC users executive committee on April 26 and 27 in Washington, D.C.[2] The main purpose of the workshop was to bring together a diverse group of scientists who had already done experiments with radioactive beams or were interested in their use in the future. The topics of the talks ranged from general nuclear physics, astrophysics, production of radioactive beams and high energy projectile fragmentation to biomedical applications.

References

1. J.M. Nitschke, Proceedings of the TRIUMF-ISOL Workshop, Mont Gabriel, Québec, June 13–16, 1984, TRIUMF Report TRI-84-1.
2. Proceedings of the Workshop on Prospects for Research with Radioactive Beams from Heavy Ion Accelerators, J.M. Nitschke, ed., Washington, D.C., April 26–27, 1984, LBL 18187, UC-34A, CONF-8404154.

Computer Simulation of an Electron-Beam-Generated Plasma Ion Source*

J.M. Nitschke, P.K. Lemmertz and R. Babala

A novel ion source based on an electron-beam-generated plasma has been developed for the on-line isotope separator OASIS at the SuperHILAC. This source has been studied extensively in on-line and off-line experiments.

The operating principle of the ion source can best be understood by referring to Fig. 1(a) and (b) which shows an idealized version of the actual device. The anode of the source consists of two circular end pieces mechanically and electrically connected by a cylindrical grid. One end wall acts as a thin window that admits the radioactive species from heavy ion nuclear reactions and the other has a central opening for the extraction of the ion beam. The anode grid is surrounded at close distance by a coaxial cathode. The cathode is indirectly heated by electron bombardment and kept at a negative potential V_0 (typically $\sim$100 V) with respect to the anode. The whole ion source is operated at a high potential V_{ex} (typically 10–30 KV) with respect to an extraction electrode located in front of the perforated anode endplate. The function of this electrode is to extract, accelerate and shape the ion beam.

During the start-up phase of the source, electrons are drawn from the cathode and traverse the anode grid as shown in Fig. 2(a). The electrons enter the anode volume where they create a space charge-well of sufficient depth to form a virtual cathode that

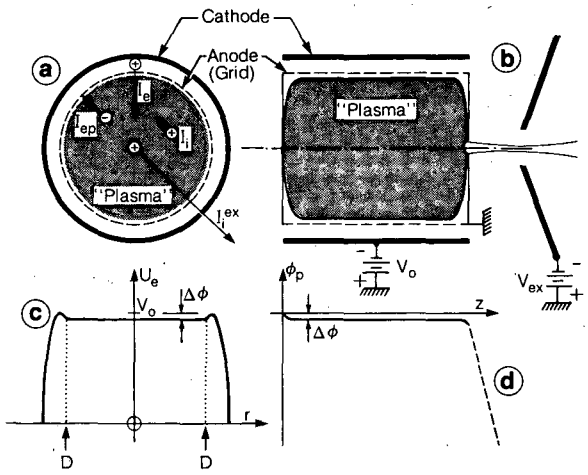

Fig. 1. Schematic representation of the electron-beam-generated plasma (EBGP) ion source. (a) Radial cut. (b) Axial cut: I_e=electron bombardment current, I_{ep}=plasma electron current, I_i=ion current, I_i^{ex}=extracted ion current, V_o=electron bombardment potential, V_{ex}=extraction potential. (c) Radial dependence of the potential V_e and the associated electron kinetic energy eU_e with space charge compensation (full line) and without space charge compensation (dotted line). D indicates the location of the virtual cathode in the absence of space charge compensation. $\Delta\phi$=potential difference between plasma and anode. (d) Axial dependence of the plasma potential ϕ_p. XBL 841-9458

reflects them back toward the anode grid. In the next step ions are formed inside the anode volume by inelastic collisions of the electrons with the rest gas and with the radioactive species that have diffused out of one of the walls of the source. These ions are trapped in the (negative) space charge-well and accumulated until they have completely compensated the electron space charge, at which point they will either be extracted or "free fall" towards the cathode.

If the extracted ion current is equal to the ion formation rate in the anode volume no ions will be lost to the cathode and a high ionization efficiency results. (Ionization efficiencies of 40% for Kr, 50% for Hg, and 60% for Rn have been measured.) Fig. 2(b) shows calculated electron trajectories for the fully space-charge compensated case; the electrons are no longer deflected or slowed down inside the source and in some cases are reflected by the cathode on the side opposite their starting point. These calculations indicate that the charge carrier densities near the axis of the source are about five times higher than those near the anode grid, a condition favorable for the efficient extraction of an ion beam with high current density.

The computer simulations shown in Fig. 2 were carried out with the SLAC Electron Trajectory Program (EGUN) written by W.B. Herrmannsfeldt. It computes trajectories of charged particles in electrostatic and magnetostatic focusing systems including the effects of space-charge ρ and self-magnetic fields. The program solves Poisson's equation by finite difference equations using the appropriate boundary conditions. It starts out by first solving Laplace's equation (ρ=0) followed by electron trajectory calculations (still with ρ=0). Secondly, the space charge distribution is calculated and used as input for the next iteration which solves Poisson's equation ($\rho \neq 0$). Several iterations of trajectory- and space charge-calculations followed by solving Poisson's equation are carried out until the solution has converged sufficiently.

Footnote

*Condensed from LBL-17643, to be published in Nuclear Instruments and Methods.

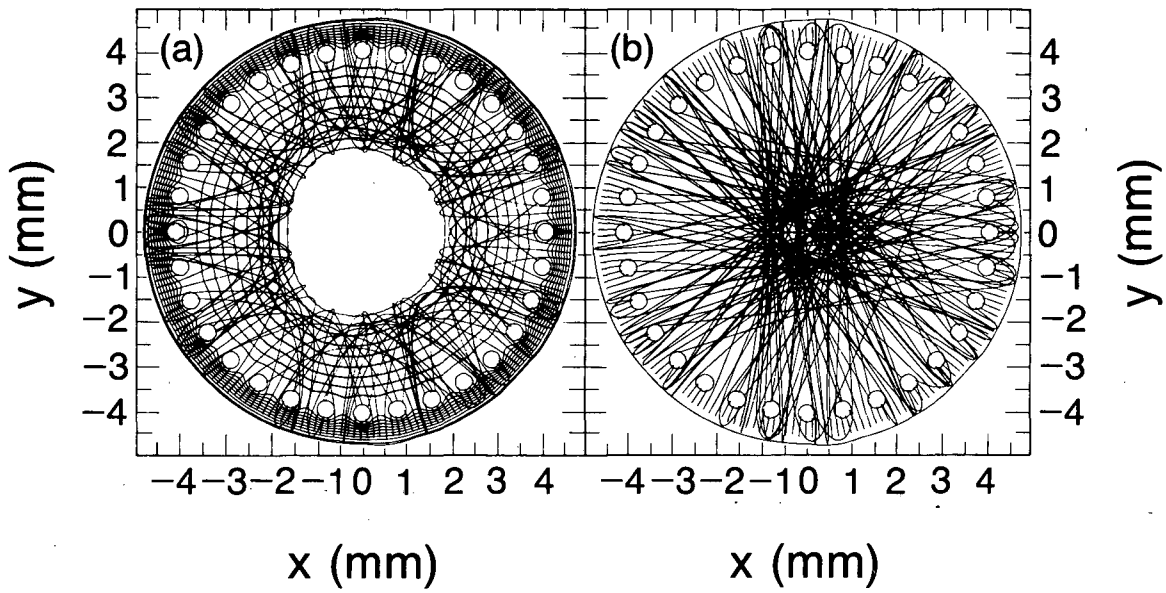

Fig. 2. (a) Computer simulation of the EBGP source *without* space charge compensation. The potential between the cathode and the anode wires is 100 V. Equipotential lines are drawn starting at 5 V (near the cathode) in steps of 10 V up to 85 V. (Two grid wires show a 95 V potential line.) Inside the anode wire "cage" the space charge build up is quantitatively represented by equipotential lines of 85 V (95 V) near the anode wires descending in 10 V steps to 5 V towards the axis of the source. The virtual cathode is located 2.3 mm from the anode. The cathode current density of 10^3 A/m^2 is distributed among 194 rays. 96 rays are intercepted by the anode wire which is equivalent to a transmission of the anode grid of 50%. (b) The same conditions as (a) *with* space charge compensation. (Equipotential lines have been omitted.) XBL 849-10769

Study of Transfer and Breakup Reactions with the Plastic Box*

R.G. Stokstad, S.B. Gazes, C.R. Albiston, M. Bantel, Y. Chan, P.J. Countryman,† B.G. Harvey, H. Homeyer,‡ M.J. Murphy, I. Tserruya, K. Van Bibber† and S. Wald

The plastic box is an array of plastic scintillator paddles, light guides and phototubes arranged around the target in the fashion shown schematically in Fig. 1. The light guides and phototubes are shown only for the top wall (wall 5) of the cube. Each wall consists of two separate scintillator paddles made of NE102A, each 20 cm high, 20 cm wide, and 1 mm thick. The beam and the projectile-like fragments (PLF) emerge through a slot in wall 1. Two movable telescopes, each having three solid-state elements, can cover the angular range from ~5° to ~21°. Additional scintillator paddles (not shown) are located behind the telescopes and downstream close to 0° in order to detect most of the light particles that escape through the slot in wall 1.

The symmetry of the cube and location of the beam axis along a diagonal gives us forward/backward and in-plane/out-of-plane information. A crude form of angular correlation for the light particles is given in Fig. 2. For each PLF, the

count rate in the different walls is indicated. Recall from Fig. 1 that walls 1 and 2 are in the forward direction, 3 and 4 are back of 90° and walls 5 and 6 are up and down, respectively. In all cases, the forward walls are the most likely to observe a charged particle. The lighter corresponding PLFs (Li–C), however, are relatively more likely to be associated with particles in walls 3–6. It does not seem reasonable that these backward-going particles are the result of a projectile breakup reaction. The likely explanation is that they arise from the decay of the excited target-like fragments (TLF) by charged-particle evaporation. If this is indeed the case, these events belong in the category of a transfer reaction. The following consistency check was therefore made. Assuming a complete charge transfer occurred, the excitation energy and the angular momentum of the TLF were estimated for each corresponding PLF. These estimates were then used in a statistical model calculation[1] to calculate the competition among neutron, charged particle, and fission decay. These predictions were found to be consistent with the observations. In addition, the most likely form of charged particle decay was predicted to be proton (rather than alpha-particle) emission. A separate experiment done with improved particle identification was performed to check this prediction and it was verified. Given this consistency, a correction based on the particles detected by the backward walls was therefore applied to all walls in order to include these events in the classification of transfer events.

The dependence of the transfer/breakup relationship on the angle of the PLF is shown in Fig. 3. (The crosshatched area in each panel indicates the size of the evaporation correction described above. Henceforth, all references to transfer or "S=0" events include this correction.) This dependence varies slowly with angle and thus can be extrapolated with confidence. This enables us to use inclusive measurements at other angles to establish the differential cross sections for transfer and breakup over a range of angles wide enough to integrate and obtain total cross sections. Fig. 4 gives the inclusive angular distributions and the transfer component for oxygen, carbon, and lithium ejectiles. The interpolated and extrapolated values of the transfer differential cross sections are given by the dashed lines. The angle-integrated cross sections are presented in Fig. 5. The absolute errors are typically ±20%.

The overlap model[2] of Harvey and Homeyer calculates the yield of PLFs by assuming that the projectile can be factored into two portions, according to the fragmentation model of Friedman,[3] and that there must be a geometrical overlap of the portion to be removed and the target. Since it is possible, with additional assumptions, to calculate the probability that the projectile factors into two portions, one of which is excited above a particle decay threshold, the model is capable of handling the sequential decay problem. Preliminary predictions made with this model are given in Fig. 5. The present model does not specify whether the portion removed from the projectile is captured *completely* by the target. Thus, the prediction corresponds to an upper limit for the experimental S = 0 yields. The calculation reproduces the main trends in the experimental results.

At present, it appears that the charged particles accompanying a PLF are mainly protons and alpha particles rather than heavier ions. In the future it will be possible to identify the light particles and measure their angles with position-sensitive plastic walls that have been developed.[4] Such experiments should enable a reconstruction of the primary yields from the observed sequential decay products.

Footnotes and References

*Condensed from LBL-18240.

†Department of Physics, Stanford University, Stanford, CA 94305.

‡Hahn-Meitner Institute, Berlin, Federal Republic of Germany.

1. M. Blann, private communication.
2. B. Harvey and H. Homeyer, LBL-16882 (1983).
3. W. Friedman, Phys. Rev. **C27**, 569 (1983).
4. M. Bantel, *et al.*, Nucl. Inst. Meth., in press (LBL-17063).

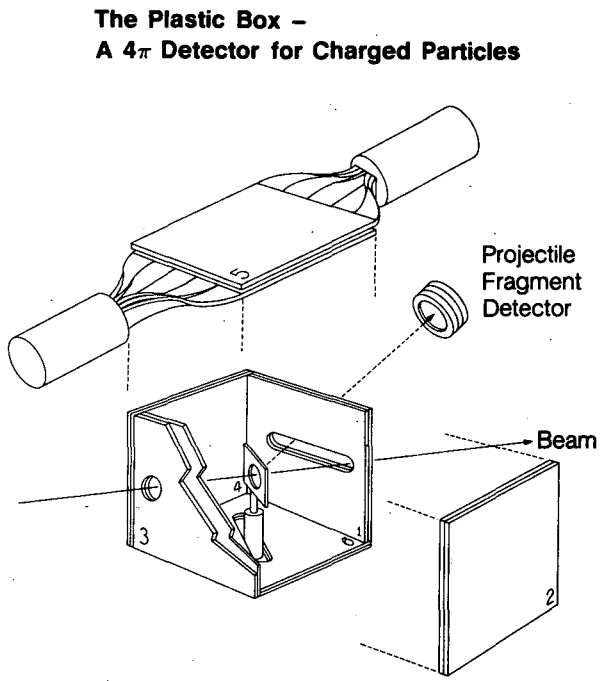

Fig. 1. Schematic diagram of the plastic box.
XBL 842-828

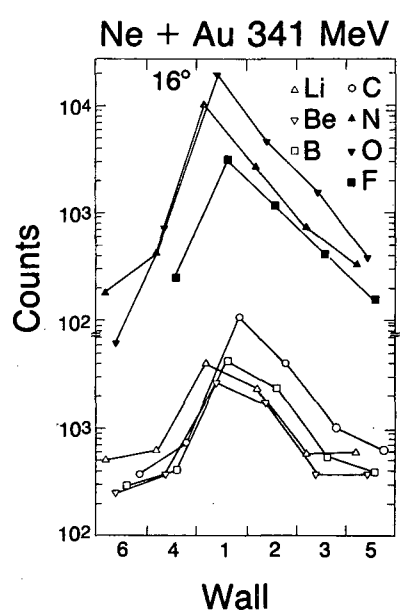

Fig. 2. The relative frequency with which each wall detects a light particle in coincidence with ejectiles from Li to F. XBL 843-10248

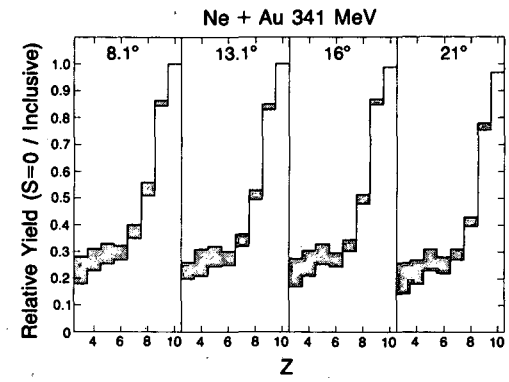

Fig. 3. The fraction of events that represent complete charge transfer for ejectiles at different angles. The shaded area gives the size of the correction for charged-particle evaporation by the target.
XBL 844-10438

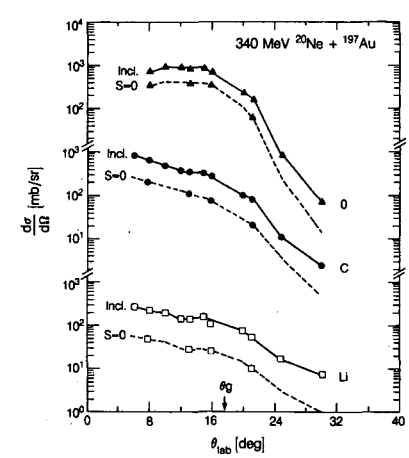

Fig. 4. Differential cross sections for inclusive and transfer reaction products. XBL 846-8827

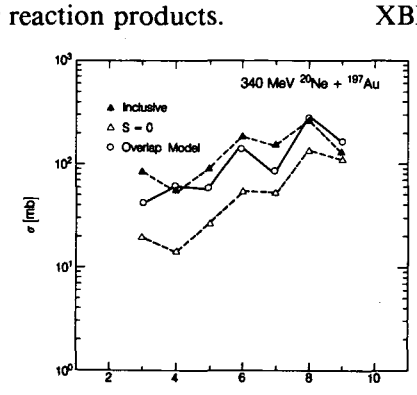

Fig. 5. Angle-integrated cross sections for inclusive and transfer reaction products. The circles are the predictions of the overlap model.[2] XBL 846-8824

Charge Measurements of Stopping High-Z Nuclei ($6 \leqslant Z \leqslant 97$) in Nuclear Emulsion

M.T. Ghoniem, H.H. Heckman, E.M. Friedlander and Y.J. Karant*

A technique of charge measurement of highly charged nuclei that stop in nuclear emulsion has been developed by the conventional method of track-width measurements. The method utilizes the last 1 mm of the ionization track of the stopping ion, where the track widths ω_i are measured by use of a filar micrometer at each 50 μm in the interval of range $50 \leqslant R \leqslant 1000$ μm; the sum $\omega = \Sigma w_i$ constitutes a quantity proportional to the area of the ionization track which we adopt as a measure of charge.

We have carried out such measurements on stopping tracks of C_6, Fe_{26}, La_{57}, and U_{92} in Ilford G · 5 emulsion. The reproducibility of an observer for measuring the quantity ω is typically $d\omega/\omega = \pm 1\%$ for a given track, whereas the intrinsic rms distribution of a sample of stopping tracks of the same charge Z $d\omega/\omega \approx 5\%$.

The method requires the calibration of track areas versus depth in the emulsion pellicle owing to optical and processing gradients in the emulsion. All measurements of ω were therefore extrapolated to zero depth in the emulsion, giving a normalized value of ω_0 for the track area.

Fig. 1 gives the charge-calibration results obtained by M.T.G. (Each observer must be independently calibrated.) The data on atomic number Z versus track area ω_0 are fitted to a least-squares polynomial, shown by the smooth curve. For $d\omega_0/\omega_0 = \pm 0.05$, this method of charge analysis yields charge measurements to accuracies of $\Delta Z = 0.8$, 1.3, and 3.0 at Z = 6, 26, and 92, respectively.

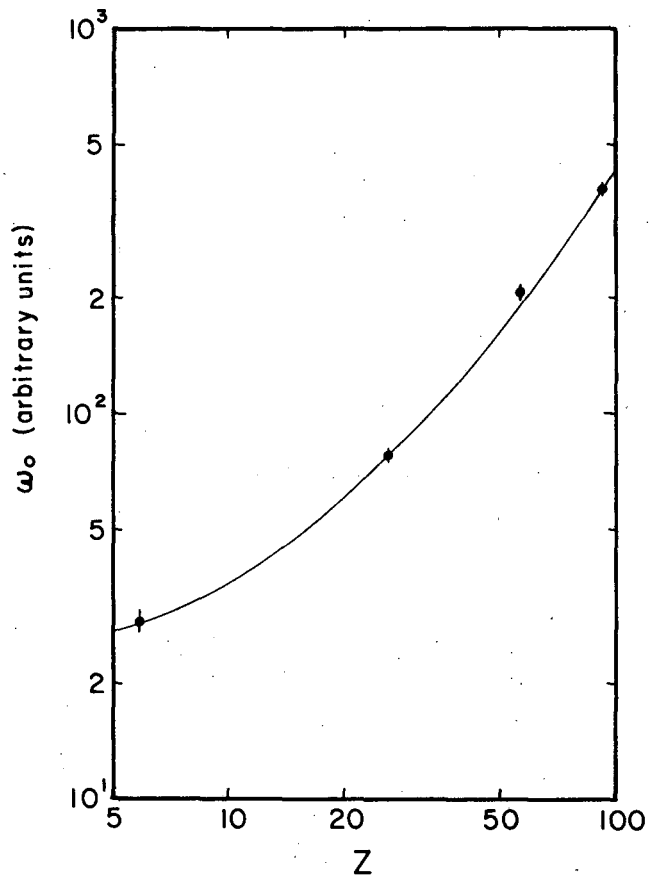

Fig. 1. Track area of stopping nuclei as a function of atomic number. XBL 8410-4315

Footnote

*Cairo University, Faculty of Science, Cairo, Egypt.

Observation of Strong Azimuthal Asymmetry Between Slow and Fast Secondaries in High Energy Nuclear Collisions in the Plastic Ball

H.A. Gustafsson, H.H. Gutbrod, B. Kolb, H. Löhner, B. Ludewigt, A.M. Poskanzer, T. Renner, H. Riedesel, H.G. Ritter, T. Siemiarczuk, J. Stepaniak,* A. Warwick and H. Wieman*

Parallel to the global analysis of the Plastic Ball[1] data (energy flow and minimum spanning tree), a very straightforward analysis for azimuthal asymmetries in the particle flow between slow and fast reaction products has been performed. It is expected that energy and impact parameter dependence of the azimuthal asymmetry is a sensitive tool for reaction mechanism studies.

To study the azimuthal correlation between slow and fast secondaries, the following procedure has been developed: to each particle a vector of unit length is ascribed in the direction of the transverse component of its momentum and the resultant vectors R_s and R_F have been calculated separately for the slow (stopped in the Plastic Ball) and fast (punch through $E_p < 240$ MeV) secondaries. A uniform distribution of the angle α_{FS} between R_S and R_F vectors is expected if there is no azimuthal asymmetry between those groups of particles.

All the distributions, independently of the incident energy, target and projectile masses, exhibit remarkable similarity in the type of asymmetry: there is a significant excess of events with large α_{FS} angles. In order to investigate and exclude spectrometer-related correlations, a Monte Carlo procedure was used to calculate the background. The Monte Carlo events were built from the real recorded particles in a way that only one particle (slow or fast) was taken from each real event, ensuring that any possible two- or many-particle correlations present in real events was destroyed. The numbers of slow (n_S) and fast (n_F) particles in the Monte Carlo event were generated from the two-dimensional n_F vs. n_S experimental distribution, taking thus into account the correlation between F and S particle multiplicities. The Monte Carlo background normalized to the experimental data is shown in Fig. 1 by the dotted line. The number of Monte Carlo events was 5 to 10 times higher than the number of real ones. One can see that the background is almost uniform.

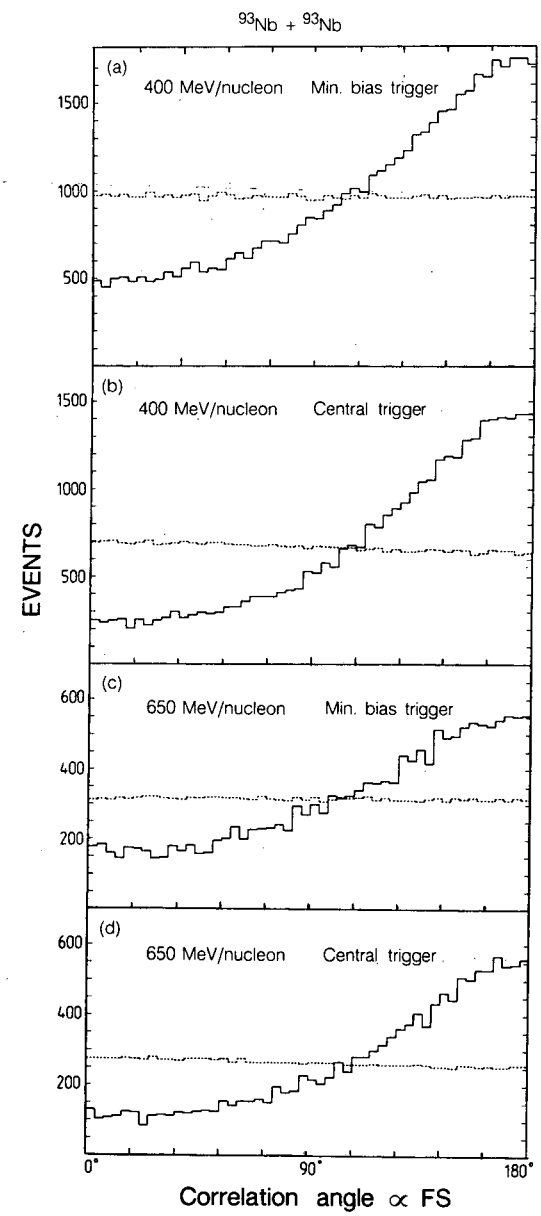

Fig. 1. α_{FS} distribution for Nb + Nb at different energies and for different triggers. XBL 847-8497

The experimental data corrected for any background asymmetry are shown in Fig. 2, where the ratio R = D-B/D+B is plotted against α_{FS}. D and B are the numbers of real and background events in the corresponding α_{FS} bin. The solid lines are drawn by hand to guide the eye. The inspection of Fig. 2 reveals that (i) the asymmetry decreases somewhat with the increase of the incident energy and that (ii) the asymmetry is stronger for the central trigger as compared to the minimum bias one. A comparison with Ca+Ca shows, that for the equal mass target and projectile experiments, the asymmetry gets stronger for larger A. Furthermore, the asymmetry for the Ne+Pb experiment at 0.8 GeV/nucleon (central trigger) is less pronounced than for any other experiments with a central trigger (Ca+Ca, 1 GeV/nucleon, 0.4 GeV/nucleon; Nb+Nb, 0.65 GeV/nucleon, 0.4 GeV/nucleon).

The observed asymmetry corroborates the findings of the energy flow analysis and sets strong constraints on the possible mechanism of nucleus nucleus collisions.

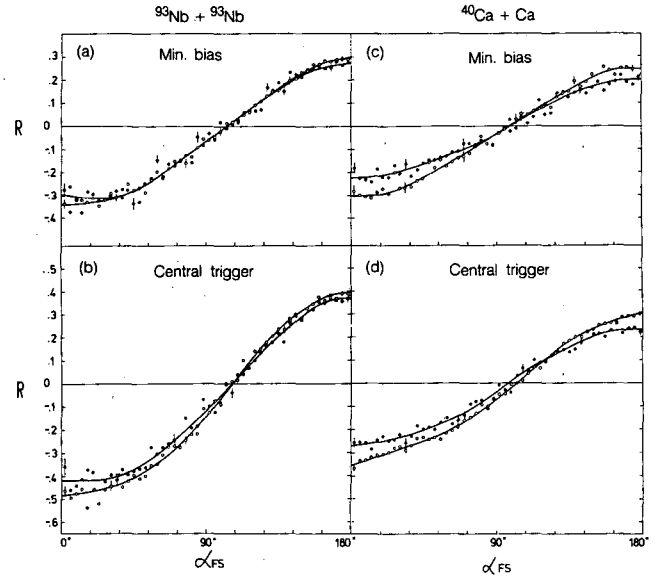

Fig. 2. R distribution as a function of α_{FS} for Nb + Nb at E/A = 400 (open circles) and E/A = 650 MeV (black dots) and Ca+Ca at E/A = 400 MeV (open circles) and E/A = 1050 MeV (black dots).

XBL 847-8496

Footnotes and References

*On leave of absence from the Institute for Nuclear Studies, 00-681 Warsaw, Hoza 69, Poland.

1. A. Baden *et al.*, Nucl. Instr. Meth. **203**, 189 (1982).

The High Resolution Ball

R.M. Diamond, F.S. Stephens, M.A. Deleplanque, M.K. Lee and R.A. Belshe

The High Resolution Ball (HRB) is a composite γ-ray detection system aimed at the most complete possible determination of the γ-rays emitted by a source. A spherical shell of 40 bismuth germanate (BGO) scintillators ~2½ inches thick, called the central ball, measures the energy and angle of nearly every γ ray emitted, but at somewhat low energy resolution (~20%). Small apertures to 21 Compton-suppressed germanium detectors ~5½ inches from the source provide a sampling of the γ rays at very high energy resolution, ~0.2%, and reasonably high efficiency, ~0.5% of 4π each.

The purpose of the central ball is to characterize the nature of the event – in high spin studies to define the initial spin and excitation energy. The Ge array will then provide some detailed information about the event. The Compton suppression by the BGO cylinders improves the full energy peak to total ratio (P/T) from about 17% for these 2″ diameter by 2″ thick Ge detectors to about 50%. For a coin-

cident event in two Ge detectors the rates go as the squares of these numbers – from ~3% to ~25% – and for three-fold coincidences the P/T goes from ~0.5% to ~12%, an enormous improvement. The 21 modules are to provide high rates. They give ~200 times the double coincidence rate of two detectors and over 1000 times the triple coincidence rate of three detectors. We expect Compton-suppressed doubles rates of ~20,000 per second in typical high-spin experiments (6000 per second has been achieved with 15 detectors), and triples rates of ~4000 per second.

Sixteen Compton-suppressed Ge systems are presently (October, 1984) on hand and 15 have been used in experiments. A setup with 12 is shown in Fig. 1.

These units arrive at the rate of one per month, so that the full 21 will be here in February, 1985. The central ball has been designed, and the plans sent to three vendors. Two estimates have come back, and no serious problems have appeared. The central ball consists of two parts, the first of which is 21 cylindrical cones of NaI that serve as: (1) backscatter suppressors for the Ge detectors; (2) active collimators that will anti the γ rays forward scattered into the Ge detectors; and (3) part of the central ball total energy and multiplicity system. The second part of the central ball is the 40 BGO elements for the main γ ray energy and multiplicity determination. We are currently ready to go out for bids on both of these parts.

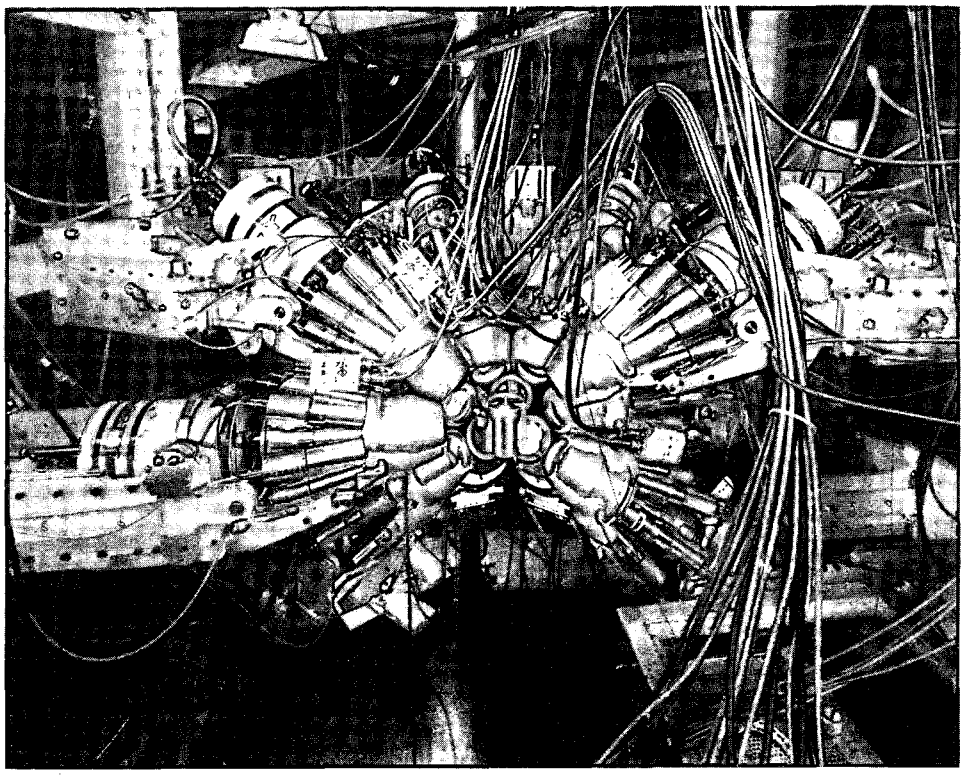

Fig. 1. Photograph of 12 Compton-suppressed Ge modules in place around a small target chamber.
CBB 846-4587

Another element of the full HRB project is a new data acquisition system, of which 8 channels now work using the prototype of a new multiplexer unit. One megaword of external memory has been ordered (the first of four megawords) for fast storage of the double coincidence events. Only the triple and higher-fold events will be written event-by-event on magnetic tape. Finally, color graphics to help visualize the two and three dimensional arrays is planned, but not yet ordered.

Data were first taken with the HRB array when only four Compton-suppressed Ge systems existed (~November 1983), and has continued with additional detector systems added as they arrived; 15 were used recently. We have chosen to study first the region around N = 82 and Z = 64 because: (1) the γ-ray lines from lead-backed targets are not Doppler broadened, due to the long feeding times; (2) the level schemes are complex and thus represent a challenge; and (3) the physics of the region is interesting, involving many shape changes and the (theoretical) promise of superdeformed shapes at rather low spins ($\sim 50\hbar$). Thus far data have been taken for several nuclei and analyses are in progress. Nearest completion is the level scheme for ^{156}Er where a preliminary scheme exists involving ~130 γ rays. A dramatic shape change to noncollective behavior has been seen at spin $30\hbar$. However, it appears that some collective bands extend beyond this spin. These are new features in nuclear structure studies, made possible by the quality of the data. It is clear that the HRB system will set new standards for γ-ray studies.

A Čerenkov Detector for Heavy Ion Velocity Measurements*

M. Baumgartner, H.J. Crawford,† J.P. Dufour,‡ J.D. Girard,§
D.E. Greiner, P.J. Lindstrom, D.L. Olson and T.J.M. Symons

We have developed a highly sensitive velocity measuring detector using total internal reflection Čerenkov counters of a type described by Jelley[1] in 1958. The detector uses the Čerenkov light which is produced at an angle $\theta_c = \cos(1/\beta n)$, when a charged particle with velocity β passes through a medium with an index of refraction n. If the Čerenkov angle is bigger than the angle of total reflection, and the radiator is shaped so that all surfaces are either perpendicular or parallel to the direction of the particle, the produced Čerenkov light is trapped in the radiator. By placing a photomultiplier in optical contact with the radiator some distance away from the particle track only the trapped Čerenkov light is detected. Since real materials are dispersive, $n = n(\lambda)$, the Čerenkov light is produced over a range of angles and the intensity for the trapped light is not a step function but has some width in velocity. Fig. 1 shows a calculation of this response curve of the detector for three different materials: (a) fused silica, (b) lucite, and (c) BK7W optical glass. By choosing

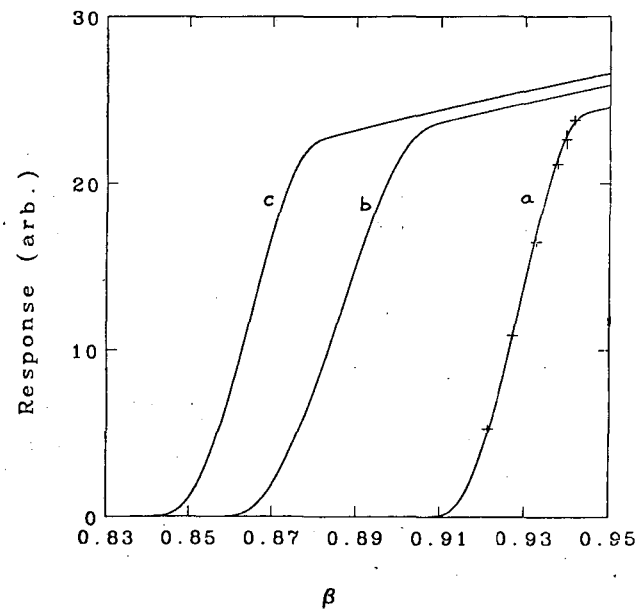

Fig. 1. Response function of detector for (a) fused silica, (b) lucite, (c) BK7W glass radiators.

XBL 8410-4295

different materials and the velocity dependent part of the response curve can be shifted to different absolute velocities.

We have performed detailed tests of this detector. We exposed this device to a ^{56}Fe beam of variable velocities, which was obtained from a 1.9 GeV/nucleon Fe beam by degrading its energy with copper plates of different thicknesses. The crosses on Fig. 1 show the measured result for the response function. For these results we can estimate that the resolution in velocity corresponds to a mass resolution of $\sigma = 0.07$ u for equal rigidity isotopes of iron. One should note that the predicted mass dependence of this signal is proportional to A/Z and so responds only weakly to the mass of the particle.

We tested the mass resolution by fragmenting a 1.6 GeV/nucleon Ar beam at the input to the LBL zero degree spectrometer and detecting the rigidity analyzed fragments after the spectrometer with our detector. With a rigidity acceptance of 0.5% we were able to resolve argon isotopes with $\sigma = 0.1$ u as seen in Fig. 2. Fig. 3 is a scatter plot of all the isotopes observed and combined data from many rigidity settings.

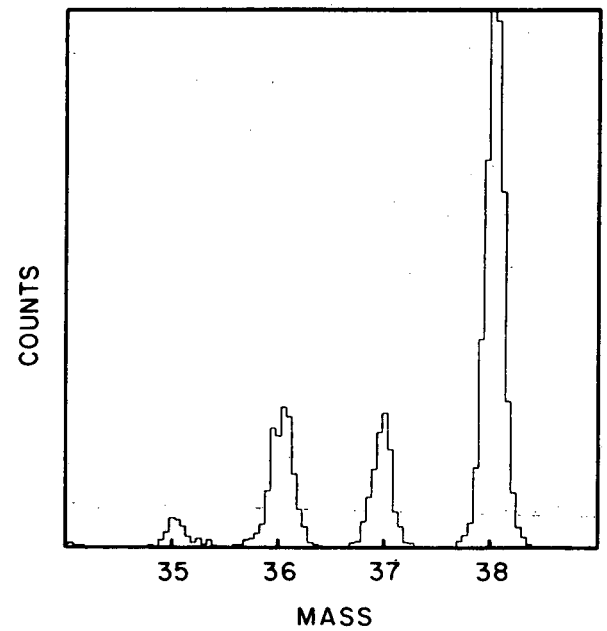

Fig. 2. Mass resolution obtained for argon isotopes. XBL 8410-4297

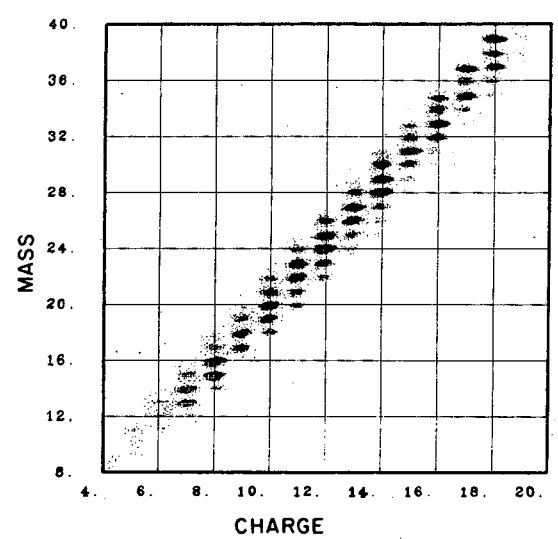

Fig. 3. Charge against mass plot for all observed isotopes produced by fragmentation of a 1.6 GeV argon beam. XBL 8410-4296

Footnotes and References

*Condensed from LBL-18259.

†Space Sciences Laboratory, University of California, Berkeley, CA 94720.

‡Centre d'Etudes Nucléaires de Bordeaux-Gradignan, Le Haut Vigneau, F-33170 Gradignan, France.

§Commissariat a l'Energie Atomique de Saclay, F-911191 Gif-sur-Yvette, Cedex, France.

1. J.W. Jelley, Čerenkov Radiation and its Application (Pergamon Press, London, 1958), p. 138.

Prototype Drift Chamber for High Energy Heavy Ions with a Large Dynamic Range

T. Kobayashi, F. Bieser, H. Crawford, P. Lindstrom, M. Baumgartner and D. Greiner*

We have constructed and tested a small prototype drift chamber designed for high energy heavy ions. When a drift chamber is used as a tracking detector for heavy projectile fragments from high-energy nucleus-nucleus reactions, the major problem comes from the many spurious hits due to delta-rays. Three methods have been developed to solve this problem. The first one is to use a constant fraction discriminator to pick up the timing signal from the core ionization under the large background of delta-rays. The second one is to use pulse height information from the drift chamber to find the cell hit by the heavy ion. The last one is the idea of "distributed planes." Modular planes (12 in our case) are distributed 10 cm apart on a rigid base plate to provide accurate relative positioning of the wires.

The performance of the prototype chamber has been measured as a function of the high voltage bias and of the charge of the heavy ion from protons up to uranium at around 1 GeV/nucleon. By using the pulse height information, it is possible to reject the spurious hits due to delta-rays even for the uranium beam. The chamber can be fully efficient for any beam with less than 250 micron position resolution by adjusting the high voltage and hence the gas gain, but not for all possible particles at the same time. We could not find a single operating condition, where the chamber was fully sensitive to ions between Z = 1 and Z = 92 with sufficient position resolution (say 300 micron). Instead, we found some limited operating conditions with enough position resolution depending on the experiment, e.g., Z = 1 to Z = 26 at −1.5 KV or Z = 5 to 92 at −1.2 KV. The time-distance relation under the second condition is shown in Fig. 1 as an example.

Footnote

*Space Sciences Laboratory, University of California, Berkeley, CA 94720.

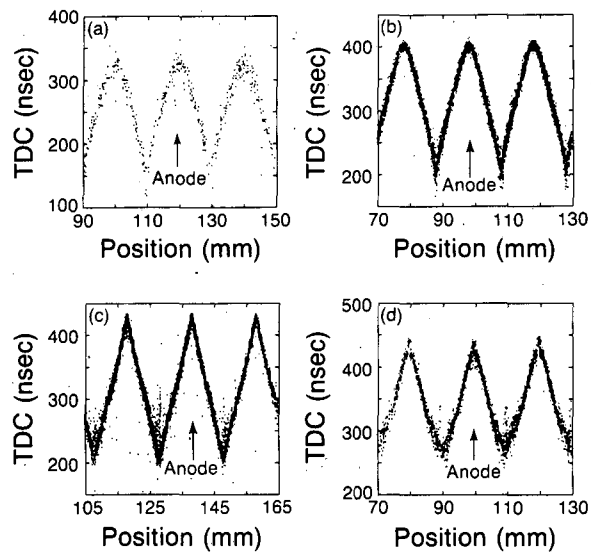

Fig. 1. Time-distance relation at HV = −1.2 KV for four kinds of heavy ions. (a) Boron (Z = 5), (b) Iron (Z = 26), (c) Xenon (Z = 54) and (d) Uranium (Z = 92). XBL 8411-4644

Improvements in the Bevalac Computing Facility

Charles McParland

There have been several improvements in Bevalac computing over the last year. The long-awaited NSD Bevalac VAX (called BEVAX) has been installed in the newly constructed 51L comput-

er area. This facility is designed to allow experimental data acquisition computers using the DATACQ software package to analyze and display experimental data on-line. Following installation, data acquisition and analysis software from both the HISS and GSI VAX were moved to this system. This now makes a consistent data acquisition and programming environment available to almost all experimental areas at the Bevalac. The system currently supports 21 Bevalac experimenters doing both data acquisition and analysis. To date, two experimental efforts at the Low Energy Beam Line (LBL, Michigan State) have used the system for on-line analysis during their experimental runs.

We have anticipated the networking requirements of new experimental computers at the Bevalac by the installation of a facility-wide Ethernet system. The system consists of 500 meters of specially designed coaxial cable installed as a continuous loop throughout Building 51. This cable passes within 40 meters of all current experimental areas. Computers are connected by means of cable "taps" that pierce the cable in several places and make precise contact with its conductors. This network currently connects the HISS, GSI, and BEVAX 11/780 machines as well as the HISS PDP 11/34 and the GSI and Beam 30 11/750s. The success of this installation was instrumental in the decision to connect all buildings of the LBL "central research area" to a common computer network. We anticipate an optical fiber link between the Bevalac and Building 50 networks to be completed by January of 1985.

Other efforts aimed at the improvement of data acquisition and analysis facilities have included the evaluation of the new graphics standard GKS. It is hoped that this standard will see wide use on most laboratory VAXs. Analysis software, especially graphics software, should then be easily transportable between most LBL VAXs to better utilize the variety of graphics display devices within the division. Along with the Physics Division, we are evaluating several currently available GKS software packages. We expect to make a recommendation shortly and will soon have a version installed and running on the BEVAX machine.

First Measurements with a Forward Scintillator Hodoscope at the Streamer Chamber Facility.

R. Brockmann, W. Rauch,† R. Renfordt,‡ D. Bangert,† A. Dacal,§ J.W. Harris, G. Odyniec, M. Ortiz,§ H.G. Pugh, A. Sandoval,* L.S. Schroeder, R. Stock,* H. Ströbele,* and D. Schall‡*

A 384-element scintillator hodoscope has been installed behind the Streamer Chamber to enhance its particle identification capability. The overall design of the hodoscope has been described previously.[1] Data have been taken with this Streamer Chamber-hodoscope hybrid system for the reaction La + La at energies between 0.6 and 1.25 GeV/nucleon.

In order to allow measurements over a large range of nuclear charges (i.e., to extend the dynamic range of the phototubes) a dynode output supplements the standard anode signals in those parts of the hodoscope where heavy fragments are expected. A typical on-line pulse height spectrum is shown in Fig. 1 (a) and (b) for the dynode and anode of a scintillator element located at about 3 degrees to the beam during a run in minimum bias trigger mode. Charges up to Z=10 can easily be resolved in the raw data. The pulse height as a function of the nuclear charge is plotted in Fig. 2. For Z>2 the pulse height has a less than linear dependence on the charge, contrary to what one would expect from an uncorrected Bethe-Bloch formula, where a quadratic dependence is predicted. It should be pointed out, however, that these data are not corrected for nonlinearities caused by the phototubes, which can be fairly large for the type of phototube used (PM 2982, 1 inch diameter).

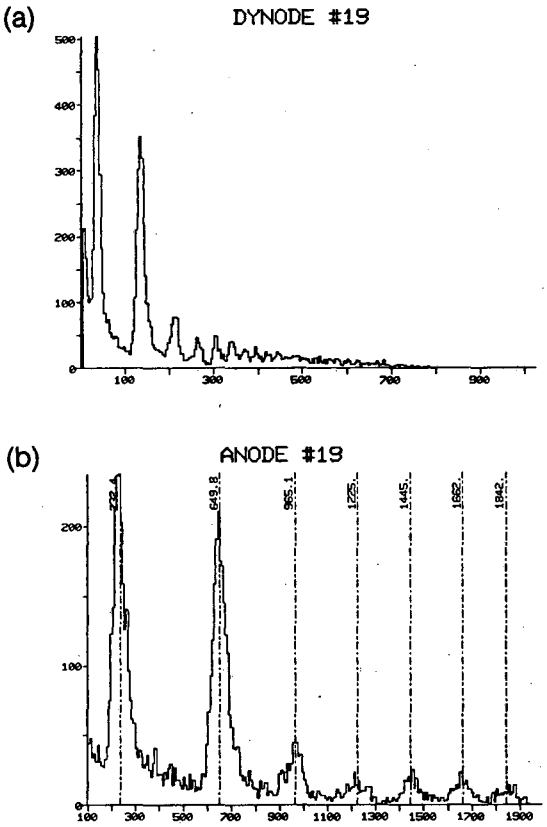

Fig. 1.
(a) Dynode pulse height spectrum XBL 8410-4078
(b) Anode pulse height spectrum XBL 8410-4079

The time of flight resolution between a channel plate start detector in front of the Streamer Chamber and the individual elements of the hodoscope is 350 psec (FWHM).

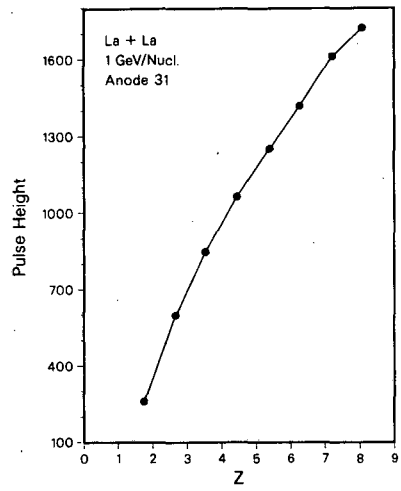

Fig. 2. Dependence of the maximum pulse height on the charge state XBL 8410-13348

Lanthanum beam tracks were measured, reconstructed in space and successfully matched with hits in the corresponding elements of the hodoscope. The measurement and reconstruction of events in the central trigger mode is in progress and the first results are expected soon.

Footnotes and Reference

*Gesellschaft für Schwerionenforschung (GSI), D-6100 Darmstadt, West Germany

†Fachbereich Physik, Universität Marburg, D-3550 Marburg, West Germany

‡Institut für Hochenergiephysik, Universität Heidelberg, D-6900 Heidelberg, West Germany

§Instituto de Física, UNAM, Mexico D.F., Mexico

1. R. Brockmann *et al.* LBL-16870

Use of a Digitizing Tablet as an On-line Input Device in Analyzing Streamer Chamber Photographs

G. Odyniec, D. Bangert, R. Brockmann,† J.W. Harris,‡ M. Maier, R.E. Renfordt,‡ H.G. Pugh, W. Rauch,* A. Sandoval,† R. Stock,† H. Ströbele,† D. Schall,‡ L.S. Schroeder, and K.L. Wolf§*

Until recently, the methods of scanning and measuring streamer chamber photographs at LBL were not significantly different from the methods used in 1966, when the first bubble chamber photographs were analyzed. A modified version of the three-dimensional reconstruction program, TVGP (Three View Geometry Program), is still used in the analysis of the data collected from the photographs today. The present procedure is as follows: The photographs of events are measured on a film-plane

measuring device called II-B, then written to magnetic tapes for transfer to a computer for analysis. The three-dimensional reconstruction program, TVGP, is then run off-line on the CDC 7600 using the data from the magnetic tapes as input.

Several problems have recently arisen, showing the need for revision of this procedure: higher multiplicity events, the planned decommissioning of the CDC 7600, and the reconstruction program's inability to reconstruct certain tracks. Because of the film-plane measuring machine's small low-contrast viewing screen, some tracks are more difficult to see in higher multiplicity events. Specifically, these events have more products than earlier light ion collisions, up to 170 tracks being now visible, compared with the less than a dozen visible tracks of the bubble chamber experiments. A solution to this difficulty has been to sketch the tracks from the scanning table before measuring. However, this method is quite inefficient. The second problem, departure of the CDC 7600, creates a need for a version of the reconstruction program that can run on the VAX 11/780. The last problem, inability of the reconstruction program to reconstruct certain tracks, has in the past been solved either by ignoring the tracks and including efficiency corrections or by remeasuring the events if they are of specific importance.

All of the above problems could be solved by running the reconstruction program on-line on a VAX and using a digitizing tablet to input the track coordinates. This method would allow immediate remeasurement of tracks that fail. The digitizing tablet could be placed on the scanning table directly with little or no modification of the table, eliminating the necessity of pre-sketching the tracks for the film-plane measuring machine, II-B.

During the summer of 1984 such a system was implemented. There were several stages to this project. To get TVGP running on the VAX, an off-line VAX version of TVG was acquired from a group at the University of Michigan. The conversion to on-line running was accomplished by recoding the reconstruction program's input routine. The next step was to run the program which calculates the optical distortion coefficients. While we managed to run the program on our data, a few changes still remain to be made.

The next part of the project involved the input/output problems of hooking up a digital tablet to the computer. We used the auxiliary input port on a VT240 terminal as the input/output port for the digitizing tablet, with a special adapter between 25 pin and 9 pin EIA standard RS232C/RS423 connectors and new software to establish two-way communication between the tablet and the computer. Also we wrote software which allows the scanner to see a picture of what has been measured on the table.

The final step was to piece together the routines so that the program would run on-line and take input from the digitizing tablet. The main problem here was the data management: creation of the output files and their proper contents, informing the operator of the program's progress, and trying to make the program clear and fool-proof.

The prototype system is up and running. This on-line version of TVGP, with its interactive capabilities, is expected to improve scanner efficiency and speed the analysis of the data. Two scanning stations are planned for upgrade in this manner, each with digitizing tablet and terminal, both controlled by a VAX 11/730 front end computer which itself is backed by one of the Bevalac VAX 11/780 computers.

Footnotes

*Fachbereich Physik, Universität Marburg, D-3550 Marburg, West Germany

†Gesellschaft für Schwerionenforschung (GSI), D-6100 Darmstadt, West Germany

‡Institut für Hochenergiephysik, Universität Heidelberg, D-6900 Heidelberg, West Germany

§Cyclotron Laboratory, Texas A&M University, College Station, Texas 77843

PART V: APPENDICES

Appendix I Publications

ABACHI, S. See BARASCH, E. LBL-17065

ABRAMS, P.C. See LINDGREN, M.A. LBL-17897

AHMED, M. See CABLE, M.D. LBL-17720

AHMED, M. See CABLE, M.D. LBL-17983

ALBISTON, C.R. See STOKSTAD, R.G. LBL-18240

ALBISTON, C.R. See WALD, S. LBL-16899

ALEKLETT, K. See KRAUS, R.H. LBL-17303

ALEKLETT, K. See LI, W. LBL-17328

ALEKLETT, K. See LOVELAND, W. LBL-16931

ALEKLETT, K. See MCGAUGHEY, P.L. LBL-18453

ALEKLETT, K., W. Loveland, T.T. Sugihara, D.J. Morrissey, L. Wenxin, W. Kot, G.T. Seaborg LBL-17887
Incomplete and Complete Fusion in Intermediate Energy Heavy Ion Reactions
Presented at the Fifth Nordic Meeting on Nuclear Physics, Jyväskylä, Finland, March 12-16, 1984.

ANDRIAMONJE, S.A. See ANHOLT, R. LBL-18488

ANHOLT, R., S.A. Andriamonje, E. Morenzoni, Ch. Stoller, J.D. Molitoris, W.E. Meyerhof, H. Bowman, J.-S. Xu, Z.-Z. Xu, J.O. Rasmussen, D.H.H. Hoffmann LBL-18488
Observation of Radiative Capture in Relativistic Heavy-Ion-Atom Collisions
Phys. Rev. Lett. **53**, 234 (1984).

AVIGNONE, F.T. See MOLTZ, D.M. LBL-18316

BAI, X.X. See HAMAGAKI, H. LBL-17276

BANERJEE, B. See MATSUI, T. LBL-16819

BANGERT, D. See BROCKMANN, R. LBL-17755

BANGERT, D. See HARRIS, J.W. LBL-17404

BANTEL, M. See STOKSTAD, R.G. LBL-18240

BANTEL, M. See WALD, S. LBL-16899

BANTEL, M., R.G. Stokstad, Y.D. Chan, S. Wald, P.J. Countryman LBL-17063
A Two-Dimensional Position-Sensitive Phoswich Detector
Nuclear Instruments and Methods **226**, 394 (1984).

BARASCH, E., A. Shor, S. Abachi, J. Carroll, P. Fisher, K. Ganezer, G. Igo, T. Mulera, V. Perez-Mendez, S. Trentalange LBL-17065
K^- Momentum Spectrum for Subthreshold Production in Relativistic Nuclear Collisions
Phys. Lett. B

BAUMGARTNER, M. See OLSON, D.L. LBL-18259

BAUMGARTNER, M. See SYMONS, T.J.M. LBL-16990

BENDJABALLAH, N. See SCHUCK, C. LBL-17281

Appendix I Publications

BIRCHALL, J., W.T.H. van Oers, J.W. Watson, H.E. Conzett, R.M. Larimer, B. Leemann, E.J. Stephenson, P. von Rossen, R.E. Brown LBL-17479
Analyzing Power Measurements for $^3He(\vec{p},p)^3He$ Elastic Scattering between 20 and 50 MeV
Phys. Rev. **C29**, 2009 (1984).

BISTIRLICH, J.A. See ZAJC, W.A. LBL-16930

BISTIRLICH, J.A. See ZAJC, W.A. LBL-17171

BLAND, R.W. See LINDGREN, M.A. LBL-17897

BOCK, R. See HARRIS, J.W. LBL-17404

BOSSINGHAM, R.R. See ZAJC, W.A. LBL-16930

BOSSINGHAM, R.R. See ZAJC, W.A. LBL-17171

BOWMAN, H. See ANHOLT, R. LBL-18488

BOWMAN, H.R. See ZAJC, W.A. LBL-16930

BOWMAN, H.R. See ZAJC, W.A. LBL-17171

BREWER, J.H. See CLAWSON, C.W. LBL-16944

BROCKMANN, R. See HARRIS, J.W. LBL-17404

BROCKMANN, R. See RENFORDT, R.E. LBL-16451

BROCKMANN, R., J.W. Harris, A. Sandoval, R. Stock, H. Ströbele, G. Odyniec, H.G. Pugh, L.S. Schroeder, R.E. Renfordt, D. Schall, D. Bangert, W. Rauch, K.L. Wolf LBL-17755
Pion and Proton "Temperatures" in Relativistic Heavy Ion Reactions Phys. Rev. Lett. **53**, 2012 (1984).

BROWN, R.E. See BIRCHALL, J. LBL-17479

CABLE, M.D., J. Honkanen, E.C. Schloemer, M. Ahmed, J.E. Reiff, Z.Y. Zhou, J. Cerny LBL-17720
Study of Beta-Delayed Two-Proton Emission in ^{22}Al and ^{26}P and Search for New Emitters
Presented at the 5th Nordic Meeting on Nuclear Physics, Jyväskylä, Finland, March 12-16, 1984.

CABLE, M.D., J. Honkanen, E.C. Schloemer, M. Ahmed, J.E. Reiff, Z.Y. Zhou, J. Cerny LBL-17983
Beta-Delayed Two-Proton Decays of ^{22}Al and ^{26}P Phys. Rev. **C30**, 1276 (1984).

CARROLL, J. See BARASCH, E. LBL-17065

CARROLL, J. See ROCHE, G. LBL-18064

CERNY, J. See CABLE, M.D. LBL-17720

CERNY, J. See CABLE, M.D. LBL-17983

CHAN, Y. See GROTOWSKI, K. LBL-17560

CHAN, Y. See STOKSTAD, R.G. LBL-18240

CHAN, Y.D. See BANTEL, M. LBL-17063

CHAN, Y.D. See VAN BIBBER, K. LBL-16799

CHAN, Y.D. See WALD, S. LBL-16899

Appendix I Publications

CHANG, C.C. See ROCHE, G. LBL-18064

CLARK, D.J. LBL-17069
Cyclotrons as Mass Spectrometers
Presented at the Tenth International Conference on Cyclotrons and their Applications, Michigan State University, East Lansing, MI April 30 - May 3, 1984.

CLARK, D.J., Y. Jongen, C.M. Lyneis LBL-17068
Progress on the LBL ECR Heavy Ion Source
Presented at the Tenth International Conference on Cyclotrons and their Applications, Michigan State University, East Lansing, MI April 30 - May 3, 1984.

CLAWSON, C.W. See ZAJC, W.A. LBL-16930

CLAWSON, C.W. See ZAJC, W.A. LBL-17171

CLAWSON, C.W., K.M. Crowe, E.E. Haller, S.S. Rosenblum, J.H. Brewer LBL-16944
Effects of Electronically Neutral Impurities on Muonium in Germanium
Proceedings of the Yamada Conference VII, Muon Spin Rotation, Shimoda, 1983 Hyperfine Interactions 17-19, pp. 603 (1984).

COLE, A.J. See RAE, W.D.M. LBL-17266

CONZETT, H.E. LBL-16383
Spin-Polarization Observables at the $J=\frac{3}{2}^{+}$ Resonance in the Reactions $^{3}H(d,n)^{4}He$ and $^{3}He(d,p)^{4}He$
Few Body Problems in Physics, Vol. II, pp. 539, B. Zeitnitz, Editor, Elsevier Science Publishers B.V., 1984.

CONZETT, H.E. See BIRCHALL, J. LBL-17479

CORK, B. See HOANG, T.F. LBL-17706

COUNTRYMAN, P.J. See BANTEL, M. LBL-17063

COUNTRYMAN, P.J. See STOKSTAD, R.G. LBL-18240

COUNTRYMAN, P.J. See VAN BIBBER, K. LBL-16799

COUNTRYMAN, P.J. See WALD, S. LBL-16899

CRAWFORD, H. See GREINER, D.E. LBL-18486

CRAWFORD, H.J. See HOANG, T.F. LBL-17706

CRAWFORD, H.J. See OLSON, D.L. LBL-18259

CRAWFORD, H.J. See SYMONS, T.J.M. LBL-16990

CROWE, K.M. See CLAWSON, C.W. LBL-16944

CROWE, K.M. See ZAJC, W.A. LBL-16930

CROWE, K.M. See ZAJC, W.A. LBL-17171

CSERNAI, L.P., G. Fái, J. Randrup, LBL-16440
Effect of Fluctuations on Global Analysis of Fluid Dynamical Calculations for High-Energy Nuclear Collisions
Phys. Lett. **140B**, 149 (1984).

Appendix I Publications

DANIELEWICZ, P. LBL-17707
Transport Properties of Excited Nuclear Matter and the Shock-wave Profile Phys. Lett. **146B**, 168 (1984).

DANIELEWICZ, P., M. Gyulassy LBL-17278
Dissipative Phenomena in Quark Gluon Plasmas Phys. Rev. **D31**, 53 (1985).

DATE, S. See SUMIYOSHI, H. LBL-16663

DELEPLANQUE, M.A. LBL-17082
Nuclear Moments of Inertia at High Spins Nucl. Phys. **A421**, 339c (1984).

DELEPLANQUE, M.A. See MACCHIAVELLI, A.O. LBL-17647

DIAMOND, R.M. LBL-17575
High-Spin Gamma-Ray Spectroscopy
Presented at the International Symposium on Nuclear Spectroscopy and Nuclear Interactions, Osaka, Japan, March 21-25, 1984.

DIAMOND, R.M. See MACCHIAVELLI, A.O. LBL-17647

DIAMOND, R.M. See SCHUCK, C. LBL-17281

DIAMOND, R.M., F.S. Stephens LBL-14331
Angular Velocity: A New Dimension in Nuclei Nature **310**, 457 (1984).

DINES, E.L. See MACCHIAVELLI, A.O. LBL-17647

DOSS, K.G.R. See GUSTAFSSON, H.-A. LBL-18380

DOSS, K.G.R. See POSKANZER, A.M. LBL-18357

DRAPER, J.E. See MACCHIAVELLI, A.O. LBL-17647

DUFOUR, J.P. See OLSON, D.L. LBL-18259

DUFOUR, J.P. See SYMONS, T.J.M. LBL-16990

DØSSING, T., J. Randrup LBL-16825
Dynamical Evolution of Angular Momentum in Damped Nuclear Reactions. I. Accumulation of Angular Momentum by Nucleon Transfer
Nucl. Phys. **A433**, 215 (1985).

DØSSING, T., J. Randrup LBL-16826
Dynamical Evolution of Angular Momentum in Damped Nuclear Reactions. II. Observation of Angular Momentum Through Sequential Decay
Nucl. Phys. **A433**, 280 (1985).

DØSSING, T. See RANDRUP, J. LBL-17836

ELLIS-AKOVALI, Y. See SCHUCK, C. LBL-17281

ENGELAGE, J. See TREUHAFT, R.N. LBL-14910

FÁI, G. See CSERNAI, L.P. LBL-16440

FISHER, P. See BARASCH, E. LBL-17065

FRANKEL, K.A. See ZAJC, W.A. LBL-16930

Appendix I Publications

FRANKEL, K.A. See ZAJC, W.A. LBL-17171

GAGLIARDI, C.A. See MOLTZ, D.M. LBL-18316

GANEZER, K. See BARASCH, E. LBL-17065

GANEZER, K. See SHOR, A. LBL-17067

GARRETT, J.D. See SCHUCK, C. LBL-17281

GAZES, S. See STOKSTAD, R.G. LBL-18240

GEAGA, J.V. See TREUHAFT, R.N. LBL-14910

GIRARD, J. See SYMONS, T.J.M. LBL-16990

GIRARD, J.G. See OLSON, D.L. LBL-18259

GLENDENNING, N. K. LBL-17708
Phase Transitions in a Saturating Chiral Theory of Nuclear Matter — Annals of Physics

GLENDENNING, N.K. LBL-15976
Neutron Stars are Giant Hypernuclei? — Astrophysical Journal **293**, 309 (1985).

GLENDENNING, N.K. LBL-17653
The Lee-Wick Abnormal Phase Transition is Alive and Well — Phys. Lett. **144B**, 158 (1984).

GLENDENNING, N.K. See MATSUI, T. LBL-16819

GLENDENNING, N.K., J. Rafelski LBL-17938
Kaons and Quark Gluon Plasma — Phys. Rev. C

GLENDENNING, N.K., T. Matsui LBL-17351
On The Hydrodynamic Evolution of Quark-Gluon Plasma Produced by Ultrarelativistic Nuclear Collisions
Phys. Lett. **141B**, 419 (1984).

GREINER, D.E. See OLSON, D.L. LBL-18259

GREINER, D.E. See SYMONS, T.J.M. LBL-16990

GREINER, D.E., H. Crawford, P.J. Lindstrom, J.M. Kidd, D.L. Olson, W. Schimmerling, T.J.M. Symons LBL-18486
Uranium Nuclear Reactions at 900 MeV/Nucleon

GROTOWSKI, K., Z. Majka, R. Planeta, M. Szczodrak, Y. Chan, G. Guarino, L.G. Moretto, D.J. Morrissey, L.G. Sobotka, R.G. Stokstad, I. Tserruya, S. Wald, G.J. Wozniak LBL-17560
Symmetric Splitting of Very Light Systems — Phys. Rev. **C30**, 1214 (1984).

GU, J.H. See SOBOTKA, L.G. LBL-17879

GUARINO, G. See GROTOWSKI, K. LBL-17560

GUSTAFSSON, H.-A. See POSKANZER, A.M. LBL-18357

GUSTAFSSON, H.-A., K.G.R. Doss, H.H. Gutbrod, B. Kolb, B. Ludewigt, A.M. Poskanzer, T. Renner, H. Riedesel, H.G. Ritter, A. Warwick, H. Wieman LBL-18380
The GSI- LBL Plastic Ball/Wall Spectrometer
Presented at the Conference on Instrumentation for Heavy Ion Nuclear Research, Oak Ridge, TN, October 22-24, 1984.

Appendix I Publications

GUSTAFSSON, H.-A., H.H. Gutbrod, B. Kolb, H. Löhner, B. Ludewigt, A.M. Poskanzer, T. Renner, H. Riedesel, H.G. Ritter, A. Warwick, F. Weik, H. Wieman LBL-17399
Collective Flow Observed in Relativistic Nuclear Collisions Phys. Rev. Lett. **52**, 1590 (1984).

GUSTAFSSON, H.-A., H.H. Gutbrod, B. Kolb, H. Löhner, B. Ludewigt, A.M. Poskanzer, T. Renner, H. Riedesel, H.G. Ritter, A. Warwick, F. Weik, H. Wieman LBL-17678
Freezeout Density in Relativistic Nuclear Collisions Measured by Proton-Proton Correlations
Phys. Rev. Lett. **53**, 544 (1984).

GUTBROD, H.H. See GUSTAFSSON, H.-A. LBL-18380

GUTBROD, H.H. See GUSTAFSSON, H.-A. LBL-17399

GUTBROD, H.H. See GUSTAFSSON, H.-A. LBL-17678

GUTBROD, H.H. See POSKANZER, A.M. LBL-18357

GUTBROD, H.H., M. Gyulassy, H.H. Heckman, W.D. Myers, L.S. Schroeder, H.G. Pugh LBL-16281
Proceedings of the 6th High Energy Heavy Ion Study and 2nd Workshop on Anomalons
Lawrence Berkeley Laboratory, University of California, June 28 - July 1, 1983.

GYULASSY, M. LBL-16800
Signatures of New Phenomena in Ultrarelativistic Nuclear Collisions Nucl. Phys. **A418**, 59c (1984).

GYULASSY, M. See DANIELEWICZ, P. LBL-17278

GYULASSY, M. See GUTBROD, H.H. LBL-16281

HAGEBO, E. See KRAUS, R.H. LBL-17303

HAHN, A.A. See LINDGREN, M.A. LBL-17897

HALDORSEN, I.R. See KRAUS, R.H. LBL-17303

HALLER, E.E. See CLAWSON, C.W. LBL-16944

HALLMAN, T. See ROCHE, G. LBL-18064

HAMAGAKI, H. See MIAKE, Y. LBL-18346

HAMAGAKI, H., X.X. Bai, O. Hashimoto, S. Kadota, K. Kimura, Y. Miake, S. Nagamiya, K. Omata, Y. Shida, I. Tanihata, N. Yoshikawa LBL-17276
Measurements of High P_T Light Fragments at C.M. 90 in 800 A MeV C+C Collisions

HARRIS, J.W. See BROCKMANN, R. LBL-17755

HARRIS, J.W. See RENFORDT, R.E. LBL-16451

HARRIS, J.W. See TREUHAFT, R.N. LBL-14910

HARRIS, J.W., R. Stock LBL-17054
From Pion Production to the Nuclear Matter Equation of State
Presented at the Seventh Oaxtepec Meeting on Nuclear Physics, Oaxtepec, Mexico, January 3-6, 1984.

HARRIS, J.W., R. Stock, R. Bock, R. Brockmann, A. Sandoval, H. Ströbele, G. Odyniec, H.G. Pugh, L.S. Schroeder, R.E. Renfordt, D. Schall, D. Bangert, W. Rauch, K.L. Wolf LBL-17404
Pion Production as a Probe of the Nuclear Matter Equation of State

Appendix I Publications

HARVEY, B.G. LBL-17760
A Microscopic Calculation of Fragment Formation in Nucleus-Nucleus Collisions

HARVEY, B.G. See RAE, W.D.M. LBL-17266

HARVEY, B.G. See STOKSTAD, R.G. LBL-18240

HARVEY, B.G. See WALD, S. LBL-16899

HASHIMOTO, O. See HAMAGAKI, H. LBL-17276

HASHIMOTO, O. See ZAJC, W.A. LBL-16930

HASHIMOTO, O. See ZAJC, W.A. LBL-17171

HECKMAN, H.H. See GUTBROD, H.H. LBL-16281

HERSKIND, B. See SCHUCK, C. LBL-17281

HOANG, T.F., B. Cork, H.J. Crawford LBL-17706
Effective Radii from High Energy Nuclear Reactions

HODGES, C.L. See LINDGREN, M.A. LBL-17897

HOFFMANN, D.H.H. See ANHOLT, R. LBL-18488

HOMEYER, H. See STOKSTAD, R.G. LBL-18240

HOMEYER, H. See WALD, S. LBL-16899

HONKANEN, J. See CABLE, M.D. LBL-17720

HONKANEN, J. See CABLE, M.D. LBL-17983

HONKANEN, J.A. See NITSCHKE, J.M. LBL-17345

HOWARD, W.M. See LEANDER, G.A. LBL-18307

IGO, G. See BARASCH, E. LBL-17065

INGERSOLL, J.G. See ZAJC, W.A. LBL-16930

INGERSOLL, J.G. See ZAJC, W.A. LBL-17171

JOHNSON, R.T. See LINDGREN, M.A. LBL-17897

JONGEN, Y. LBL-17086
Electron Cyclotron Resonance (E.C.R.) Ion Sources
Presented at the Tenth International Conference on Cyclotrons and Their Applications, Michigan State University, East Lansing, MI April 30 - May 3, 1984.

JONGEN, Y. See CLARK, D.J. LBL-17068

JOYCE, D.C. See LINDGREN, M.A. LBL-17897

KADOTA, S. See HAMAGAKI, H. LBL-17276

KADOTA, S. See MIAKE, Y. LBL-18346

KIDD, J.M. See GREINER, D.E. LBL-18486

Appendix I Publications

KIMURA, K. See HAMAGAKI, H. LBL-17276

KIRK, P.N. See ROCHE, G. LBL-18064

KIRK, P.N. See TREUHAFT, R.N. LBL-14910

KNOOP, T.D. See LINDGREN, M.A. LBL-17897

KOIKE, M. See ZAJC, W.A. LBL-16930

KOIKE, M. See ZAJC, W.A. LBL-17171

KOLB, B. See GUSTAFSSON, H.-A. LBL-18380

KOLB, B. See GUSTAFSSON, H.-A. LBL-17399

KOLB, B. See GUSTAFSSON, H.-A. LBL-17678

KOLB, B. See POSKANZER, A.M. LBL-18357

KOONTZ, R. See ROCHE, G. LBL-18064

KOONTZ, R. See TREUHAFT, R.N. LBL-14910

KOT, W. See ALEKLETT, K. LBL-17887

KRAUS, R.H., W. Loveland, K. Aleklett, P.L. McGaughey, T.T. Sugihara, G.T. Seaborg, T. Lund, Y. Morita, E. Hagebo, I.R. Haldorsen LBL-17303
Target Fragment Angular Distributions for the Interaction of 86 MeV/A ^{12}C with ^{197}Au
Nucl. Phys. **A432**, 525 (1985).

KREBS, G. See ROCHE, G. LBL-18064

KREBS, G. See TREUHAFT, R.N. LBL-14910

KUDO, H., K.J. Moody, G.T. Seaborg LBL-17202
Mass Distributions in the Reaction of 240 MeV $^{12}0$ with ^{197}Au Phys. Rev. **C30**, 1561 (1984).

KURCK, J.M. See ZAJC, W.A. LBL-16930

KURCK, J.M. See ZAJC, W.A. LBL-17171

LACKNER, K.S. See LINDGREN, M.A. LBL-17897

LARIMER, R.M. See BIRCHALL, J. LBL-17479

LEANDER, G.A., P. Moller, J.R. Nix, W.M. Howard LBL-18307
Calculated Masses and Half-Lives for Nuclei in the Region $100 \leqslant K \leqslant 110$
Presented at the 7th International Conference on Atomic Masses and Fundamental Constants (AMCO-7), Darmstadt-Seeheim, West Germany, September 3-7, 1984; to be published in the proceedings.

LEEMANN, B. See BIRCHALL, J. LBL-17479

LEMMERTZ, P.K. See NITSCHKE, J.M. LBL-17345

LI, W., W. Loveland, K. Aleklett, P.L. McGaughey, G.T. Seaborg LBL-17328
Target Fragment Mass Distribution for the Interaction of 245 MeV/A ^{139}La with ^{139}La

LINDENBERGER, K.H. See SCHUCK, C. LBL-17281

Appendix I Publications

LINDGREN, M.A., D.C. Joyce, P.C. Abrams, R.W. Bland, R.T. Johnson, T.D. Knoop, M.H. Savage, M.H. Scholz, B.A. Young, C.L. Hodges, A.A. Hahn, G.L. Shaw, K.S. Lackner, H.G. Pugh, R. Slansky LBL-17897
Search for Fractional Charges Produced in Heavy-Ion Collisions at 1.9 GeV/ nucleon
Phys. Rev. Lett. **51**, 1621 (1983).

LINDSTROM, P.J. See GREINER, D.E. LBL-18486

LINDSTROM, P.J. See OLSON, D.L. LBL-18259

LINDSTROM, P.J. See SYMONS, T.J.M. LBL-16990

LIU, Z.H. See SOBOTKA, L.G. LBL-17879

LOVELAND, W. See ALEKLETT, K. LBL-17887

LOVELAND, W. See KRAUS, R.H. LBL-17303

LOVELAND, W. See LI, W. LBL-17328

LOVELAND, W. See MCGAUGHEY, P.L. LBL-18453

LOVELAND, W., C.P. Oertel, D.J. Morrissey, P.O. McGaughey, G.T. Seaborg, K. Aleklett LBL-16931
Heavy Target Fragmentation and The Energy Dependence of Nucleus-Nucleus Total Reaction Cross Sections

LÖHNER, H. See GUSTAFSSON, H.-A. LBL-17399

LÖHNER, H. See GUSTAFSSON, H.-A. LBL-17678

LÖHNER, H. See POSKANZER, A.M. LBL-18357

LUDEWIGT, B. See GUSTAFSSON, H.-A. LBL-18380

LUDEWIGT, B. See GUSTAFSSON, H.-A. LBL-17399

LUDEWIGT, B. See GUSTAFSSON, H.-A. LBL-17678

LUDEWIGT, B. See POSKANZER, A.M. LBL-18357

LUDLAM, T.W. See SCHROEDER, L.S. LBL-17961

LUND, T. See KRAUS, R.H. LBL-17303

LYNEIS, C.M. See CLARK, D.J. LBL-17068

MACCHIAVELLI, A.O., M.A. Deleplanque, R.M. Diamond, F.S. Stephens, E.L. Dines, J.E. Draper LBL-17647
Neutron Transfer Reactions with Very Heavy Ions

MADANSKY, L. See ROCHE, G. LBL-18064

MAIER, M. See RENFORDT, R.E. LBL-16451

MAJKA, Z. See GROTOWSKI, K. LBL-17560

MARTOFF, C.J. See ZAJC, W.A. LBL-16930

MARTOFF, C.J. See ZAJC, W.A. LBL-17171

MATSUI, T. See GLENDENNING, N.K. LBL-17351

Appendix I Publications

MATSUI, T., B. Banerjee, N.K. Glendenning LBL-16819
Meson Radiation from Quark-Gluon Plasma
Presented at the Conference on Manifestations of Hadron Substructure in Nuclear Physics, Bloomington, IN, October 19-21, 1983.

MCDONALD, R.J. See SOBOTKA, L.G. LBL-17879

MCDONALD, W.J. See ZAJC, W.A. LBL-16930

MCDONALD, W.J. See ZAJC, W.A. LBL-17171

MCGAUGHEY, P.L. See KRAUS, R.H. LBL-17303

MCGAUGHEY, P.L. See LI, W. LBL-17328

MCGAUGHEY, P.L., W. Loveland, D.J. Morrissey, K. Aleklett, G.T. Seaborg LBL-18453
Uranium Target Fragmentation by Intermediate and High Energy ^{12}C and ^{20}Ne Ions

MCGAUGHEY, P.O. See LOVELAND, W. LBL-16931

MCHARRIS, WM. C., John O. Rasmussen LBL-17375
High-Energy Collisions between Atomic Nuclei Scientific American **250**, 58 (1984).

MCMAHAN, M.A. See SOBOTKA, L.G. LBL-17879

MEHREM, R.A., H.M.A. Radi, J.O. Rasmussen LBL-18494
Behavior of Pions Incident on a Slab of Uniform Complex Nuclear Material Phys. Rev. **C30**, 301 (1984).

MEYERHOF, W.E. See ANHOLT, R. LBL-18488

MIAKE, Y. See HAMAGAKI, H. LBL-17276

MIAKE, Y., H. Hamagaki, S. Kadota, S. Nagamiya, S. Schnetzer, Y. Shida, H. Steiner, I. Tanihata LBL-18346
Production Mechanism of Backward Energetic Protons Studied from Two-Particle Correlations in 800 MeV Proton-Nucleus Collisions

MILLER, J.P. See ZAJC, W.A. LBL-16930

MILLER, J.P. See ZAJC, W.A. LBL-17171

MIYAMURA, O. See SUMIYOSHI, H. LBL-16663

MOHRING, K. LBL-17936
What Can We Learn from Heavy-ion Sub-Barrier Fusion Excitation Functions?
Presented at the International Conference on Fusion Reactions Below the Coulomb Barrier, Cambridge, MA, June 13-15, 1984.

MOLITORIS, J.D. See ANHOLT, R. LBL-18488

MOLLER, P. See LEANDER, G.A. LBL-18307

MOLTZ, D.M., J.D. Sullivan, R.E. Tribble, C.A. Gagliardi, K.S. Toth, F.T. Avignone LBL-18316
Neutron Deficient Mass Surface Between the $1f_{7/2}$ and $1g_{9/2}$ Shells: The Masses of ^{77}Kr and ^{75}Kr
Presented at the 7th International Conference on Atomic Masses and Fundamental Constants (AMCO-7), Darmstadt-Seeheim, West Germany, September 3-7, 1984; and to be published in the Proceedings.

MOODY, K.J. See KUDO, H. LBL-17202

MOODY, K.J. See TANAKA, S. LBL-17201

Appendix I Publications

MORENZONI, E. See ANHOLT, R. LBL-18488

MORETTO, L.G. See GROTOWSKI, K. LBL-17560

MORETTO, L.G. See SOBOTKA, L.G. LBL-17699

MORETTO, L.G. See SOBOTKA, L.G. LBL-17879

MORETTO, L.G., G.J. Wozniak LBL-17426
The Role of Rotational Degrees of Freedom in Heavy Ion Collisions
Annual Review of Nuclear and Particle Science **34**, 189 (1984).

MORITA, Y. See KRAUS, R.H. LBL-17303

MORRISSEY, D.J. See ALEKLETT, K. LBL-17887

MORRISSEY, D.J. See GROTOWSKI, K. LBL-17560

MORRISSEY, D.J. See LOVELAND, W. LBL-16931

MORRISSEY, D.J. See MCGAUGHEY, P.L. LBL-18453

MÖLLER, P., W.D. Myers LBL-17533
Nuclear Mass Formula with A Neutron Skin Degree of Freedom and Finite-Range Model for The Surface Energy Presented at The Winter Workshop on Nuclear Dynamics III, Copper Mountain, CO, March 5-9, 1984.

MÖLLER, P., W.D. Myers, W.J. Świątecki, J. Treiner LBL-18230
Finite Range Droplet Model

MULERA, T. See BARASCH, E. LBL-17065

MULERA, T. See ROCHE, G. LBL-18064

MURPHY, D.L. See ZAJC, W.A. LBL-16930

MURPHY, D.L. See ZAJC, W.A. LBL-17171

MURPHY, M.J. See STOKSTAD, R.G. LBL-18240

MURPHY, M.J. See VAN BIBBER, K. LBL-16799

MURPHY, M.J. See WALD, S. LBL-16899

MYERS, W.D. See GUTBROD, H.H. LBL-16281

MYERS, W.D. See MOLLER, P. LBL-17533

MYERS, W.D. See MOLLER, P. LBL-18230

MYERS, W.D., W.J. Świątecki, C.S. Wang LBL-16947
The Surface Energy of Multi-Component Systems

NAGAMIYA, S. See HAMAGAKI, H. LBL-17276

NAGAMIYA, S. See MIAKE, Y. LBL-18346

NAGAMIYA, S., J. Randrup, T.J.M. Symons LBL-17332
Nuclear Collisions at High Energies Annual Review of Nuclear and Particle Science **34**, 155 (1984).

NEWTON, J.O. See SCHUCK, C. LBL-17281

Appendix I Publications

NITSCHKE, J.M. LBL-17935
Prospects for Research with Radioactive Beam and Targets
Invited paper presented at the TRIUMF-ISOL Workshop, Montreal, Canada, June 13-16, 1984.

NITSCHKE, J.M., Editor LBL-18187
Proceedings of The Workshop on Prospects for Research with Radioactive Beams From Heavy Ion Accelerators, Washington, DC, April 26-27, 1984.

NITSCHKE, J.M., P.A. Wilmarth, P.K. Lemmertz, W.-D. Zeitz, J.A. Honkanen LBL-17345
Beta-Delayed Proton Emission Observed in New Lanthanide Isotopes

NIX, J.R. See LEANDER, G.A. LBL-18307

OCHIAI, T. See SUMIYOSHI, H. LBL-16663

ODYNIEC, G. See BROCKMANN, R. LBL-17755

ODYNIEC, G. See HARRIS, J.W. LBL-17404

OERTEL, C.P. See LOVELAND, W. LBL-16931

OLSON, D.L. See GREINER, D.E. LBL-18486

OLSON, D.L. See SYMONS, T.J.M. LBL-16990

OLSON, D.L., M. Baumgartner, J.P. Dufour, J.G. Girard, D.E. Greiner, P.J. Lindstrom, T.J.M. Symons, H.J. Crawford LBL-18259
A Čerenkov Detector for Heavy Ion Velocity Measurements
Presented at the Conference on Instrumentation for Heavy-ion Nuclear Research, Oak Ridge, TN September 22-24, 1984.

OMATA, K. See HAMAGAKI, H. LBL-17276

PADGETT, M.L. See SOBOTKA, L.G. LBL-17879

PEREZ-MENDEZ, V. See BARASCH, E. LBL-17065

PEREZ-MENDEZ, V. See SHOR, A. LBL-17067

PLANETA, R. See GROTOWSKI, K. LBL-17560

POSKANZER, A.M. See GUSTAFSSON, H.-A. LBL-18380

POSKANZER, A.M. See GUSTAFSSON, H.-A. LBL-17399

POSKANZER, A.M. See GUSTAFSSON, H.-A. LBL-17678

POSKANZER, A.M., K.G.R. Doss, H.-A. Gustafsson, H.H. Gutbrod, B. Kolb, H. Löhner, B. Ludewigt, T. Renner, H. Riedesel, H.G. Ritter, A. Warwick, H. Wieman LBL-18357
Compression and Expansion at the Bevalac
Invited paper presented at the 5th Adriatic International Conference on Nuclear Physics, Hvar, Yugoslavia, September 24-29, 1984.

PUGH, H.G. LBL-18165
A New Collider Scheme at LBL
Invited paper presented at the Fourth International Conference on Ultra-Relativistic Nucleus-Nucleus Collisions, Helsinki, Finland, June 17-21, 1984.

Appendix I Publications

PUGH, H.G. LBL-18166
Equilibration, Compression and Flow at the Bevalac
Invited paper presented at the Fourth International Conference on Ultra-Relativistic Nucleus-Nucleus Collisions, Helsinki, Finland, June 17-21, 1984.

PUGH, H.G. See BROCKMANN, R. LBL-17755

PUGH, H.G. See GUTBROD, H.H. LBL-16281

PUGH, H.G. See HARRIS, J.W. LBL-17404

PUGH, H.G. See LINDGREN, M.A. LBL-17897

PUGH, H.G. See RENFORDT, R.E. LBL-16451

PUGH, H.G. See ROCHE, G. LBL-18064

PUGH, H.G. See TREUHAFT, R.N. LBL-14910

SCHROEDER, L.S., Editor LBL-18225
Proceedings of the Workshop on Detectors for Relativistic Nuclear Collisions,
Lawrence Berkeley Laboratory, University of California, Berkeley, CA, March 26-30, 1984.

RADI, H.M.A. See MEHREM, R.A. LBL-18494

RAE, W.D.M., A.J. Cole, B.G. Harvey, R.G. Stokstad LBL-17266
A High Resolution Study of the Breakup of ^{16}O and ^{20}Ne at 9 MeV/A Phys. Rev. **C30**, 158 (1984).

RAFELSKI, J. See GLENDENNING, N.K. LBL-17938

RANDRUP, J. See CSERNAI, L.P. LBL-16440

RANDRUP, J. See DØSSING, T. LBL-16825

RANDRUP, J. See DØSSING, T. LBL-16826

RANDRUP, J. See NAGAMIYA, S. LBL-17332

RANDRUP, J., T. Døssing LBL-17836
Dynamics of Angular Momentum Accumulation in Damped Nuclear Reactions
Nucl. Phys. **A428**, 255c (1984).

RANDRUP, J., W.J. Świątecki LBL-17273
Dissipative Resistance Against Changes in the Mass Asymmetry Degree of Freedom in Macroscopic Nuclear Dynamics: The Completed Wall-and-Window Formula Nucl. Phys. **A429**, 105 (1984).

RASMUSSEN, J.O. See ANHOLT, R. LBL-18488

RASMUSSEN, J.O. See MEHREM, R.A. LBL-18494

RASMUSSEN, J.O. See ZAJC, W.A. LBL-16930

RASMUSSEN, J.O. See ZAJC, W.A. LBL-17171

RASMUSSEN, JOHN O. See MCHARRIS, WM. C. LBL-17375

RAUCH, W. See BROCKMANN, R. LBL-17755

RAUCH, W. See HARRIS, J.W. LBL-17404

Appendix I Publications

REIFF, J.E. See CABLE, M.D. LBL-17720

REIFF, J.E. See CABLE, M.D. LBL-17983

RENFORDT, R.E. See BROCKMANN, R. LBL-17755

RENFORDT, R.E. See HARRIS, J.W. LBL-17404

RENFORDT, R.E., R. Brockmann, J.W. Harris, M. Maier, F. Riess, A. Sandoval, R. Stock, H. Ströbele, K.L. Wolf, H.G. Pugh, L.S. Schroeder, D. Schall, K. Tittel LBL-16451
Search for Flow in the Reaction Ar + Pb
Presented at the Sixth High Energy Heavy Ion Study and Second Workshop on Anomalons, Lawrence Berkeley Laboratory, Berkeley, CA, June 28 - July 1, 1983.

RENNER, T. See GUSTAFSSON, H.-A. LBL-18380

RENNER, T. See GUSTAFSSON, H.-A. LBL-17399

RENNER, T. See GUSTAFSSON, H.-A. LBL-17678

RENNER, T. See POSKANZER, A.M. LBL-18357

RIEDESEL, H. See GUSTAFSSON, H.-A. LBL-18380

RIEDESEL, H. See GUSTAFSSON, H.-A. LBL-17399

RIEDESEL, H. See GUSTAFSSON, H.-A. LBL-17678

RIEDESEL, H. See POSKANZER, A.M. LBL-18357

RIESS, F. See RENFORDT, R.E. LBL-16451

RITTER, H.G. See GUSTAFSSON, H.-A. LBL-18380

RITTER, H.G. See GUSTAFSSON, H.-A. LBL-17399

RITTER, H.G. See GUSTAFSSON, H.-A. LBL-17678

RITTER, H.G. See POSKANZER, A.M. LBL-18357

ROCHE, G. See TREUHAFT, R.N. LBL-14910

ROCHE, G., J. Carroll, C.C. Chang, T. Hallman, P.N. Kirk, R. Koontz, G. Krebs, L. Madansky, T. Mulera, H.G. Pugh, L.S. Schroeder, J. Vicente LBL-18064
Particle-Gamma Coincidence Measurements in ^{12}C + ^{12}C and ^{12}C + Pb Collisions at 2.1 GeV/Nucleon Incident Energy

ROSENBLUM, S.S. See CLAWSON, C.W. LBL-16944

RUIZ, C.L. See TREUHAFT, R.N. LBL-14910

SANDOVAL, A. See BROCKMANN, R. LBL-17755

SANDOVAL, A. See HARRIS, J.W. LBL-17404

SANDOVAL, A. See RENFORDT, R.E. LBL-16451

SAVAGE, M.H. See LINDGREN, M.A. LBL-17897

SCHALL, D. See BROCKMANN, R. LBL-17755

Appendix I Publications

SCHALL, D. See HARRIS, J.W. LBL-17404

SCHALL, D. See RENFORDT, R.E. LBL-16451

SCHIMMERLING, W. See GREINER, D.E. LBL-18486

SCHLOEMER, E.C. See CABLE, M.D. LBL-17720

SCHLOEMER, E.C. See CABLE, M.D. LBL-17983

SCHNETZER, S. See MIAKE, Y. LBL-18346

SCHOLZ, M.H. See LINDGREN, M.A. LBL-17897

SCHROEDER, L.S. LBL-17990
The Berkeley Mini-Collider
Presented at the Conference on the Intersections between Particle and Nuclear Physics, Steamboat Springs, CO, May 23-30, 1984.

SCHROEDER, L.S. LBL-18310
Detectors for High Energy Nucleus-Nucleus Collisions
Invited paper presented at the Fourth International Conference on Ultra-relativistic Nucleus-Nucleus Collisions, Helsinki, Finland, June 17-21, 1984.

SCHROEDER, L.S. See BROCKMANN, R. LBL-17755

SCHROEDER, L.S. See GUTBROD, H.H. LBL-16281

SCHROEDER, L.S. See HARRIS, J.W. LBL-17404

SCHROEDER, L.S. See RENFORDT, R.E. LBL-16451

SCHROEDER, L.S. See ROCHE, G. LBL-18064

SCHROEDER, L.S. See TREUHAFT, R.N. LBL-14910

SCHROEDER, L.S., T.W. Ludlam LBL-17961
Heavy Ion Physics - Introduction to the Heavy Ion Parallel Sessions at CIPANP
Presented at the Conference on the Intersections between Particle and Nuclear Physics, Steamboat Springs, CO, May 23-30, 1984.

SCHUCK, C., N. Bendjaballah, R.M. Diamond, Y. Ellis-Akovali, K.H. Lindenberger, J.O. Newton, F.S. Stephens, J.D. Garrett, B. Herskind LBL-17281
Evidence for Reduced Neutron Pairing Correlations in ^{165}Yb

SEABORG, G.T. See ALEKLETT, K. LBL-17887

SEABORG, G.T. See KRAUS, R.H. LBL-17303

SEABORG, G.T. See KUDO, H. LBL-17202

SEABORG, G.T. See LI, W. LBL-17328

SEABORG, G.T. See LOVELAND, W. LBL-16931

SEABORG, G.T. See MCGAUGHEY, P.L. LBL-18453

SEABORG, G.T. See TANAKA, S. LBL-17201

Appendix I Publications

SEABORG, GLENN T. LBL-17731
Modern Alchemy The Science Teacher **50**, 29 (1983).

SHAW, G.L. See LINDGREN, M.A. LBL-17897

SHI, Y-J., W.J. Świątecki LBL-18349
Estimates of Radioactive Decay by the Emission of Nuclei Heavier Than Alpha Particles Nucl. Phys.

SHI, Y.-J., W.J. Świątecki LBL-18366
Theoretical Estimates of the Rates of Radioactive Decay of Radium Isotopes by ^{14}C Emission
Phys. Rev. Lett. **54**, 300 (1985).

SHIDA, Y. See HAMAGAKI, H. LBL-17276

SHIDA, Y. See MIAKE, Y. LBL-18346

SHOR, A. LBL-18272
Φ-Meson Production as a Probe of the Quark-Gluon Plasma

SHOR, A. See BARASCH, E. LBL-17065

SHOR, A., K. Ganezer, V. Perez-Mendez LBL-17067
Internal Nuclear Momentum and Coherent Recoil of Clusters as Mechanisms for Subthreshold Anti-Proton Production in P-Nucleus Collisions

SIGNARBIEUX, C. See SOBOTKA, L.G. LBL-17879

SLANSKY, R. See LINDGREN, M.A. LBL-17897

SOBOTKA, L.G. See GROTOWSKI, K. LBL-17560

SOBOTKA, L.G., L.G. Moretto LBL-17699
Note on the Partitioning of Nuclei

SOBOTKA, L.G., M.A. McMahan, R.J. McDonald, C. Signarbieux, G.J. Wozniak, M.L. Padgett, J.H. Gu, Z.H. Liu, Z.Q. Yao, L.G. Moretto LBL-17879
Compound Nucleus Decay Along the Mass Asymmetry Coordinate and the Role of The Businaro-Gallone Point Phys. Rev. Lett. **53**, 2004 (1984).

STEINER, H. See MIAKE, Y. LBL-18346

STEPHENS, F.S. LBL-18042
Spectroscopy of the Highest-Spin States
Presented at the International Symposium on In-Beam Nuclear Spectroscopy, Debrecen, Hungary, May 14-18, 1984.

STEPHENS, F.S. See DIAMOND, R.M. LBL-14331

STEPHENS, F.S. See MACCHIAVELLI, A.O. LBL-17647

STEPHENS, F.S. See SCHUCK, C. LBL-17281

STEPHENSON, E.J. See BIRCHALL, J. LBL-17479

STOCK, R. See BROCKMANN, R. LBL-17755

STOCK, R. See HARRIS, J.W. LBL-17054

STOCK, R. See HARRIS, J.W. LBL-17404

Appendix I Publications

STOCK, R. See RENFORDT, R.E. LBL-16451

STOKSTAD, R.G. LBL-17455
The Momentum Distribution of Projectile Fragments

STOKSTAD, R.G. See BANTEL, M. LBL-17063

STOKSTAD, R.G. See GROTOWSKI, K. LBL-17560

STOKSTAD, R.G. See RAE, W.D.M. LBL-17266

STOKSTAD, R.G. See VAN BIBBER, K. LBL-16799

STOKSTAD, R.G. See WALD, S. LBL-16899

STOKSTAD, R.G., C.R. Albiston, M. Bantel, Y. Chan, P.J. Countryman, S. Gazes, B.G. Harvey, H. Homeyer, M.J. Murphy, I. Tserruya, K. Van Bibber, S. Wald LBL-18240
Study of Transfer and Breakup Reactions with the Plastic Box
Presented at the INS-RIKEN International Symposium on Heavy-Ion Physics, Mt. Fuji, Japan, August 27-31, 1984.

STOLLER, C. See ANHOLT, R. LBL-18488

STRÖBELE, H. See BROCKMANN, R. LBL-17755

STRÖBELE, H. See HARRIS, J.W. LBL-17404

STRÖBELE, H. See RENFORDT, R.E. LBL-16451

SUGIHARA, T.T. See KRAUS, R.H. LBL-17303

SUGIHARA, T.T. See ALEKLETT, K. LBL-17887

SULLIVAN, J.D. See MOLTZ, D.M. LBL-18316

SULLIVAN, J.P. See ZAJC, W.A. LBL-16930

SULLIVAN, J.P. See ZAJC, W.A. LBL-17171

SUMIYOSHI, H., S. Date, N. Suzuki, O. Miyamura, T. Ochiai LBL-16663
Quark-Gluon Plasma Formation in The Central Rapidity Region and Finite Size Effects of Colliding Nuclei

SUZUKI, N. See SUMIYOSHI, H. LBL-16663

ŚWIATECKI, W.J. See MOLLER, P. LBL-18230

ŚWIATECKI, W.J. LBL-17837
Macroscopic Treatment of Nuclear Dynamics
Presented at the International Conference on the Theoretical Approaches to Heavy Ion Reaction Mechanisms, Paris, France, May 14-18, 1984.

ŚWIATECKI, W.J. See MYERS, W.D. LBL-16947

ŚWIATECKI, W.J. See RANDRUP, J. LBL-17273

ŚWIATECKI, W.J. See SHI, Y-J. LBL-18349

ŚWIATECKI, W.J. See SHI, Y.-J. LBL-18366

SYMONS, T.J.M. See GREINER, D.E. LBL-18486

Appendix I Publications

SYMONS, T.J.M. See NAGAMIYA, S. LBL-17332

SYMONS, T.J.M. See OLSON, D.L. LBL-18259

SYMONS, T.J.M., M. Baumgartner, J.P. Dufour, J. Girard, D.E. Greiner, P.J. Lindstrom, D.L. Olson, H.J. Crawford LBL-16990
Charge-Changing Reactions of Secondary Fragments Produced in High-Energy Heavy Ion Collisions
Phys. Rev. Lett. **52**, 982 (1984).

SZCZODRAK, M. See GROTOWSKI, K. LBL-17560

TANAKA, S., K.J. Moody, G.T. Seaborg LBL-17201
Transfer Reaction Cross Sections from the Interactions of ^{20}Ne and ^{22}Ne with ^{232}Th
Phys. Rev. **C30**, 911 (1984).

TANIHATA, I. See HAMAGAKI, H. LBL-17276

TANIHATA, I. See MIAKE, Y. LBL-18346

TITTEL, K. See RENFORDT, R.E. LBL-16451

TOTH, K.S. See MOLTZ, D.M. LBL-18316

TREINER, J. See MÖLLER, P. LBL-18230

TRENTALANGE, S. See BARASCH, E. LBL-17065

TREUHAFT, R.N., J.V. Geaga, R. Koontz, H.G. Pugh, G. Roche, L.S. Schroeder, C.L. Ruiz, J. Engelage, P.N. Kirk, G. Krebs, J.W. Harris LBL-14910
Forward-Backward Particle Correlation Measurements in Proton-Carbon Collisions at 2.1 GeV
Phys. Rev. **C30**, 616 (1984).

TRIBBLE, R.E. See MOLTZ, D.M. LBL-18316

TRUÖL, P. See ZAJC, W.A. LBL-16930

TRUÖL, P. See ZAJC, W.A. LBL-17171

TSERRUYA, I. See GROTOWSKI, K. LBL-17560

TSERRUYA, I. See STOKSTAD, R.G. LBL-18240

TSERRUYA, I. See VAN BIBBER, K. LBL-16799

TSERRUYA, I. See WALD, S. LBL-16899

VAN BIBBER, K. See STOKSTAD, R.G. LBL-18240

VAN BIBBER, K. See WALD, S. LBL-16899

VAN BIBBER, K., P.J. Countryman, M.J. Murphy, Y.D. Chan, R.G. Stokstad, I. Tserruya, S. Wald LBL-16799
The Plastic Box – A 4π Detector for Intermediate Energy Heavy Ion Physics
Presented at the IEEE Nuclear Science Symposium, San Francisco, CA, October 19-21, 1983.

VAN OERS, W.T.H. See BIRCHALL, J. LBL-17479

VICENTE, J. See ROCHE, G. LBL-18064

Appendix I Publications

VON ROSSEN, P. See BIRCHALL, J. LBL-17479

WALD, S. See BANTEL, M. LBL-17063

WALD, S. See GROTOWSKI, K. LBL-17560

WALD, S. See STOKSTAD, R.G. LBL-18240

WALD, S. See VAN BIBBER, K. LBL-16799

WALD, S., C.R. Albiston, M. Bantel, Y.D. Chan, B.G. Harvey, M.J. Murphy, I. Tserruya, R.G. Stokstad, P.J. Countryman, K. Van Bibber, H. Homeyer LBL-16899
Identification of Complete Charge Transfer Reactions for $^{20}Ne+^{197}Au$ with a 4π Detector

WANG, C.S. See MYERS, W.D. LBL-16947

WARWICK, A. See GUSTAFSSON, H.-A. LBL-18380

WARWICK, A. See GUSTAFSSON, H.-A. LBL-17399

WARWICK, A. See GUSTAFSSON, H.-A. LBL-17678

WARWICK, A. See POSKANZER, A.M. LBL-18357

WATSON, J.W. See BIRCHALL, J. LBL-17479

WEIK, F. See GUSTAFSSON, H.-A. LBL-17399

WEIK, F. See GUSTAFSSON, H.-A. LBL-17678

WENXIN, L. See ALEKLETT, K. LBL-17887

WIEMAN, H. See GUSTAFSSON, H.-A. LBL-18380

WIEMAN, H. See GUSTAFSSON, H.-A. LBL-17399

WIEMAN, H. See GUSTAFSSON, H.-A. LBL-17678

WIEMAN, H. See POSKANZER, A.M. LBL-18357

WILMARTH, P.A. See NITSCHKE, J.M. LBL-17345

WOLF, K.L. See BROCKMANN, R. LBL-17755

WOLF, K.L. See HARRIS, J.W. LBL-17404

WOLF, K.L. See RENFORDT, R.E. LBL-16451

WOZNIAK, G.J. See GROTOWSKI, K. LBL-17560

WOZNIAK, G.J. See MORETTO, L.G. LBL-17426

WOZNIAK, G.J. See SOBOTKA, L.G. LBL-17879

XU, J.-S. See ANHOLT, R. LBL-18488

XU, Z.-Z. See ANHOLT, R. LBL-18488

YAO, Z.Q. See SOBOTKA, L.G. LBL-17879

Appendix I Publications

YASHITA, S. LBL-15562
The Identification of New Astatine Isotopes Using the Gas-Filled Magnetic Separator, SASSY
Ph.D. Thesis, February 1984.

YOO, E. See ZAJC, W.A. LBL-16930

YOO, E. See ZAJC, W.A. LBL-17171

YOSHIKAWA, N. See HAMAGAKI, H. LBL-17276

YOUNG, B.A. See LINDGREN, M.A. LBL-17897

ZAJC, W.A., J.A. Bistirlich, R.R. Bossingham, H.R. Bowman, C.W. Clawson, K.M. Crowe, K.A. Frankel, J.G. Ingersoll, J.M. Kurck, C.J. Martoff, D.L. Murphy, J.O. Rasmussen, J.P. Sullivan E. Yoo, O. Hashimoto, M. Koike, W.J. McDonald, J.P. Miller, P. Truöl LBL-16930
Two-Pion Correlations in Heavy Ion Collisions Phys. Rev. **C29**, 2173 (1984).

ZAJC, W.A., J.A. Bistirlich, R.R. Bossingham, H.R. Bowman, C.W. Clawson, K.M. Crowe, K.A. Frankel, J.G. Ingersoll, J.M. Kurck, C.J. Martoff, D.L. Murphy, J.O. Rasmussen, J.P. Sullivan, E. Yoo, O. Hashimoto, M. Koike, W.J. McDonald, J.P. Miller, P. Truöl LBL-17171
Pion Source Parameters in Heavy Ion Collisions

ZEITZ, W.-D. See NITSCHKE, J.M. LBL-17345

ZHOU, Z.Y. See CABLE, M.D. LBL-17983

ZHOU, Z.Y. See CABLE, M.D. LBL-17720

Appendix II Theses

A Search for Nuclei Far from Stability for the Elements Boron through Neon

J.A. Musser

The design and operation of a detector used to study the particle stability of light isotopes are described. This detector is capable of achieving greater sensitivity than any previously employed in the observation of new rare isotopes.

The study of nuclei off the valley of beta stability is primarily motivated by the desire to understand the isospin dependence of nuclear system behavior. In particular, obtaining information about nuclidic masses as a function of isospin determines the variation of the nuclear Hamiltonian with this generalized coordinate. The purpose of this experiment is to define the limits of stability of the nuclear system for extreme values of the isospin.

This thesis contains the results of an experiment performed at the LBL Bevalac, which is capable of accelerating heavy ions to maximum energies of 2 GeV/nucleon. A 600 MeV/nucleon ^{56}Fe beam interacting in a 7 g/cm^2 Be target produced neutron-rich projectile fragments whose masses and charges were analyzed in an electronic detector telescope. A total beam fluence of $\sim 1 \times 10^{11}$ particles was obtained during the course of a 72 hour run. This allowed the first observation of ^{19}B, and of the apparent particle stability of ^{18}B, in agreement with the predictions of current mass models.

The Identification of New Astatine Isotopes Using the Gas-Filled Magnetic Spectrometer, SASSY

S. Yashita

A He-filled on-line mass separator system was built at the SuperHILAC and used to study the fusion products in the reaction ^{56}Fe+^{141}Pr. The new neutron-deficient isotopes ^{194}At and ^{195}At were produced in this bombardment as three- and two-neutron-out products, respectively, and were identified by the α-α time-correlation technique. The measured α energies and half lives are 7.20 ± 0.02 MeV and 180 ± 80 msec for ^{194}At, and 7.12 ± 0.02 MeV and 200 ± 100 msec for ^{195}At.

Appendix II Theses

A Sea Level Search for Grand Unification Magnetic Monopoles

Tony Michael Liss

An experiment to search for super-heavy ($M \gtrsim 10^{16}$ GeV/c^2) Grand Unification magnetic monopoles using a novel detector at sea level is described. The technique involves the use of a single 2.8 m^2 slab of plastic scintillator 7.6 cm thick, which is viewed by 52 photomultiplier tubes. Super-heavy monopoles, which are expected to be moving at velocities near 10^{-3}c, would be separated from the large flux of relativistic cosmic rays by the anomalously wide photomultiplier tube anode signal produced as they traverse the thick slab at very low velocity. The experiment was live for a total of 3852 hours, during which time no monopole candidates were observed. A limit of $F \leqslant 4.1 \times 10^{-13}$ $cm^{-2}sr^{-1}s^{-1}$ (1 event significance) is set on the flux of super-heavy monopoles with velocities $6.1 \times 10^{-4}c \lesssim V \lesssim 2.1 \times 10^{-3}c$, and is compared to other experimental and theoretical limits.

The thesis is organized as follows: Chapter 1 comprises a survey of some experimentally important aspects of the theory of Grand Unification monopoles. In Chapter 2 the stopping power of very low velocity magnetic monopoles is reviewed in some detail. In Chapter 3 the stopping power is applied to the evaluation of the response of plastic scintillators to Grand Unification monopoles. A specific model for the scintillation response is reviewed, and the work done to extend this model to the particular type of scintillator used in this experiment is described. In Chapter 4 the design and assembly of the detector and the data taking and data analysis for the experiment are described in detail.

Appendix III Seminars

Monday Seminars

October 3, 1983	U. Goerlach CERN	Recent Results from AFS Spectrometer in pp and α-α Collisions with the ISR
October 10, 1983	A. Chacon and M. Tincknell LBL	Two Pion Correlations in Relativistic Heavy Ion Collisions and Observation of Anomalous Projectile Fragments in CR39 Plastic Track Detector
October 11, 1983	J. Stachel SUNY Stony Brook/GSI	Nuclear Structure Around A=100 Nuclei
October 17, 1983	C. Stoller Stanford Univ.	Atomic In-the-shell Ionization and the Clock for Nuclear Reactions
October 31, 1983	J. Nitschke LBL	OASIS: The SuperHILAC On-Line Isotope Separator
November 7, 1983	M. Bantel and M. Padgett LBL	A Position Sensitive Phoswich Detector and Compound Nucleus Decay Via Emission of Heavy Nuclei (Z>3)
November 14, 1983	S. Gurvitz Weizmann Institute and TRIUMF	Two Body Scaling in Nuclear Reactions
November 28, 1983	B. Herskind Niels Bohr Inst.	Nuclei in Rapid Rotation with Constant Dynamical Moment of Inertia
December 5, 1983	E.L. Dines and J. Musser LBL	Investigation of Spin-γ-Ray Correlations in the γ-Ray Continuum and Search for Nuclei Far from Stability
December 12, 1983	B. Harvey LBL	The Overlap Model for Heavy Ion Reactions
January 9, 1984	C. Albiston and P. Wilmarth LBL	Incomplete Momentum Transfer in Fusion-like Processes and The OASIS Tape System and Its Use in New Isotope Studies
January 12, 1984	J.A. Cizewski Yale Univ.	Experimental Tests of Supersymmetry in Iridium and Gold Nuclei
January 17, 1984	R. Brandt Philipps Univ.	Radiochemical Search for Anomalons
January 19, 1984	C.N. Yang SUNY Stony Brook	Stony Brook Multiplicity Asymmetry in pp Collisions at 540 GeV
January 19, 1984	J. Birchall Univ. of Manitoba	Breaking of Charge Symmetry in Neutron-Proton Scattering

Appendix III Seminars

January 24, 1984	I. Tanihata INS, Univ. of Tokyo/LBL	Measurements of pd Quasi-Elastic Scattering in 800 MeV pA Collisions and the Momentum Spread of the pn System Inside the Nucleus
January 30, 1984	H. Wieman GSI/LBL	Two-Particle Correlation Measurements with the Plastic Ball Detector
February 6, 1984	G. Smith SIN	Search for Dibaryons – Measurement of Vector Analyzing Power in Elastic Scattering
February 7, 1984	A Sandoval GSI/LBL	Search for the Quark-Gluon Plasma in a Planned Experiment at the CERN SPS
February 9, 1984	D. Nagle LAMPF	Parity Violation in pp Scattering
February 13, 1984	J. Miller and T. Coan LBL	Search for Pionic Instability with Heavy Beams and EXAM, A Search for Extra Galactic Anti-matter
February 21, 1984	E.B. Norman Univ. of Washington and Seattle Univ.	Some Effects of High Temperature and Density on Heavy Element Nucleosynthesis
February 27, 1984	H. Matis LBL	Study of the Nuclear Isovector Monopole Resonance
February 28, 1984	D. Sober Catholic Univ.	Electron Scattering and the M1 Strength in the N=28 Isotones
March 5, 1984	D. Murphy and K. Gregorich LBL	Subthreshold Pion Production by Neon Projectiles and Actinide Production in the $^{136}Xe + ^{249}Cf$ Reaction
March 8, 1984	M. Faessler CERN	Experiments with Nuclei and the CERN SPS and ISR
March 19, 1984	B. Mottelson Neils Bohr/LBL	Elementary Introduction to the Study of Nuclei with Very Large Angular Momentum
March 22, 1984	W. Geist CERN	Jet Production at High Transverse Momentum at the ISR
March 27, 1984	W. Lynch MSU	Formation and Decay of a Localized Region of High Excitation in Heavy Ion Reactions
March 30, 1984	Heinz Gaeggeler GSI	Measurements of Target-like Transfer Products from the Reactions Between ^{40}Ca and ^{48}Ca with ^{248}Cm
April 2, 1984	H.G. Ritter GSI, LBL	Collective Flow Effects in High Energy Nuclear Collisions

Appendix III Seminars

April 4, 1984	J. Harris LBL	Probing Hot, Dense Nuclear Matter for the Nuclear Equation of State
April 9, 1984	R. Anholt Stanford Univ.	X-Ray Studies of Relativistic Heavy Ion-Atom Collisions
April 12, 1984	N. Arata CBPF, Rio de Janeiro	Recent Results of the Brazil-Japan Collaboration
April 16, 1984	A. Macchiavelli and Wing Kot LBL	Moments of Inertia at High Rotational Frequencies; and Chemical Procedures Used in the Determination of Actinide Production Cross-section in Heavy Ion Reactions
April 23, 1984	N. Glendenning LBL	The Lee-Wick Phase Transition Is Alive and Well
April 30, 1984	B. Mottelson Neils Bohr/LBL	Continuation of An Elementary Introduction to the Study of Nuclei with very Large Angular Momentum
May 7, 1984	R. Welch and J. Reiff LBL	Actinide Production from ^{129,132}Xe and ^{248}Cm and The Search for New Beta-delayed Two-proton Emitters
May 14, 1984	B.L. Berman LLNL	Channeling Radiation
May 21, 1984	H. Bingham UC Berkeley/LBL	Deep Inelastic Neutrino Scattering in Nuclei
May 23, 1984	S. Abachi UCLA/LBL	Search for Fractional Charges and Subthreshold Antiproton Production in RNC
July 2, 1984	K. Hildenbrand GSI	Deep Inelastic Collisions of Mo on Mo at Energies Between 12 and 18 MeV/u
July 5, 1984	B. Svetitsky Cornell Univ.	What Lattice Calculations Tell Us About Hot Quark Soup
July 9, 1984	S.A. Chin UCLA	Guided Random Walks for Solving Hamiltonian Lattice Gauge Theory
July 12, 1984	F.R. Klinkhamer UC Santa Barbara	Large-N QCD with a Twist
July 16, 1984	A. Shor LBL/UCLA	Phi-meson Production as a Probe of the Quark-Gluon Plasma: A Suggestion and Call for Discussion
July 23, 1984	R. Babinet Saclay	Diogene, a 4π Detector to Study Central Heavy Ion Collisions at Saturne II
July 30, 1984	H. Satz Bielefeld	Quark Matter 1984 - A Summary

Appendix III Seminars

August 13, 1984	P-O. Larsson Göteborg, Sweden	Direct Proton Emission in ^{58}Ni Induced Fusion Reactions
August 20, 1984	G. Goldhaber Brookhaven	Relation of the Interacting Boson Approximation to the Variable Moment of the Inertia Model at the Magic Limit: Two Opposing Views
August 21, 1984	S. Ogaza Cracow & Australian National Univ.	Fusion-Fission Studies Down Under
August 23, 1984	J. Roberts Rice Univ.	Proton-Nucleus and π-Nucleus Interactions at High Transverse Energy
August 27, 1984	R. Jahn Univ. of Bonn	Systematics of n-n and n-p States with High Spin: A Study of the α-He2 and α-d Reaction of f-p Shell Nuclei
September 12, 1984	J. Polonyi Univ. of Illinois	Latest Developments in Lattice QCD
September 17, 1984	P. Ring Univ. Munich/LBL	Theory of Shape Changes and Phase Transitions in Rapidly Rotating Nuclei
September 20, 1984	S. Gales Orsay/MSU	Exotic Nuclear Decay of Natural Radioactive Nuclei by Emission of Heavy Clusters
September 26, 1984	C. de Tar Univ. of Utah	Modes of Excitation of the Quark-Gluon Plasma

Appendix III Seminars

Bevalac Research Meetings

October 25, 1983	R. Stock GSI	Pion Production and Nuclear Compressional Energy
November 17, 1983	A. Kusumegi KEK	Heavy Liquid Calorimeters and Heavy Ions at KEK
December 6, 1983	D. Hendrie LBL	A Dilepton Spectrometer Based on the Lampshade Magnet
December 13, 1983	U. Heinz Vanderbilt Univ.	Quark-Gluon Plasma Transport Theory
December 21, 1983	C. Gruhn LBL	Relativistic Light Ion Collisions at CERN
February 7, 1984	G. Claesson LBL	The Lund-India Search for Anomalons in Nuclear Emulsion
March 6, 1984	Discussion Group	Discussion of BNL Meeting: Progress Reports from Minicollider Working Groups
March 20, 1984	A. Shor LBL/UCLA	Subthreshold K^- Production in Relativistic Nuclear Collisions
April 17, 1984	J. Boguta LBL	Chiral Symmetry at the Mini-Collider
May 15, 1984	H. Pugh LBL	A Micro-TPC at the Mini-collider or a Mini-TPC at the Micro-Collider? Some Ideas on the Design of an Experiment to Look for Multistrange Baryons
May 29, 1984	R. Madey Kent State Univ.	Neutron Emission from Relativistic Nucleus-Nucleus Collisions
June 5, 1984	J. Rafelski Capetown Univ.	Signatures of Strangeness from the Quark Plasma
July 25, 1984	S. Nagamiya Univ. of Tokyo	Light Particle Production at Large Angles in La-La Collisions at 800 MeV/nucleon
August 14, 1984	H. Stocker Michigan State Univ.	Microscopic Theory of Pion Production and Sidewards Flow in Heavy Ion Collisions
September 27, 1984	J. Moss LANL	Pionic Enhancement of the Nuclear Sea Quark Distribution

Appendix III Seminars

Theory Seminars

November 2, 1983	Karen Kolehmainen LBL	π Condensation at T > 0
November 3, 1983	Paul Bonche Orsay	Hot Nuclei up to Boiling
November 22-28, 1983	Bo Anderson Lund	String Dynamics, Lectures I-IV
December 2, 1983	K. Kolehmainen LBL	Surface & Curvature Energies of Neutron Rich Nuclei
December 6, 1984	P. Moller Lund W.D. Myers LBL	Mass Formulae and Macroscopic Models, Part 1
December 21, 1984	Mike Nitschke LBL	Physics with Radioactive Heavy-Ion Beams
January 27, 1984	Larry McLerran Seattle	Coherent Photon Bremsstrahlung in FermilabUltra-Relativistic Heavy Ion Collisions
January 24-25, 1984	V. Ruuskanen Finland	Finite Size Effects in the Hydrodynamics of High Energy Nucleus-Nucleus Collisions
February 10, 14 & 17, 1984	B. Mottelson Neils Bohr/LBL	Chaos and Nuclear Physics - A Pedestrian Introduction in 3 Parts: I – III
February 24, 1984	D. Hartman UCSC G. Mathews LLL R. Mayle UCB	Supernova discussion group (Theory group members)
March 22, 1984	J. I. Kapusta Univ. of Minnesota	Phase Transition Signals
May 2, 1984	Larry Willets Univ. of Washington	Projecting and Boosting the Relativistic Bag
May 4, 1984	O. Maxwell TRIUMF	The Bag Model

Appendix III Seminars

May 8, 1984	Henning Esbensen Neils Bohr Inst.	Surface Response of Fermi Liquids
May 10, 1984	R. Schaeffer Saclay	Neutron Stars with Dense Cores
June 5, 1984	J. Rafelski Capetown Univ.	Signatures of Strangeness from the Quark Plasma
June 13, 1984	Oren Maxwell TRIUMF	Quantum Fluctuations in the Bag and Nucleon Observations
June 27, 1984	B. Svetitsky Cornell Univ.	Monte-Carlo Methods in Quantum Mechanics
July 5, 1984	B. Svetitsky Cornell Univ.	What Lattice Calculations Tell Us About Hot Quark Soup
July 9, 1984	Sui Ah Chin UCLA	Guided Random Walks for Solving Hamiltonian Lattice Gauge Theory
July 11, 1984	U. Mosel Univ. of Giessen	Lattice Model for Nuclear Fragmentation
July 12, 1984	F. Klinkhamer ITP, Santa Barbara	Large-N QCD with a Twist
July 14, 1984	F. R. Klinkhamer ITP, Santa Barbara	A Saddle-Point Solution in the Weinberg-Salam Theory
July 17, 1984	Berndt Muller Frankfurt	Meson Radiation from the Quark-Gluon Plasma
July 18, 1984	R. Pisarski ITP, Santa Barbara	The Chiral Phase Transition in QCD
July 19, 1984	H. Satz Bielefeld	Lepton-Pair Production as a Signal for Collective Behavior in High-Energy Nuclear Collisions
July 20, 1984	Qi Xi-Jun NRI, Shanghai	Nucleon-Nucleon Interaction in Quark Model with Relativistic Treatment
July 23, 1984	Berndt Muller Frankfurt	Fission of Bags
July 24, 1984	Berndt Muller Frankfurt	Pionic Bremsstrahlung
July 26, 1984	H. Satz Bielefeld	Thermodynamics of Gluon Matter

Appendix III Seminars

July 30, 1984	C. Y. Wong ORNL	Estimates of Energy Density Achieved in High Energy Nuclear Collisions
July 30, 1984	H. Satz Bielefeld	Quark Matter 1984 - A Summary
July 31, 1984	W. Busza MIT	Nuclear Stopping Power
August 2, 1984	H. Satz Bielefeld	Thermodynamics of the Quark-Gluon Plasma
August 7, 1984	Steve Moszkowski UCLA	Microscopic Theory of the Interacting Boson Model
August 9, 1984	L. Csernai Univ. of Minnesota	Comparison of Models for Nuclear Stopping Power
August 14, 1984	H. Stocker Michigan State Univ.	Microscopic Theory of Pion Production and Sidewards Flow in Heavy-Ion Collisions
August 21, 1984	P. Quentin ORSAY	Temperature Dependence of the Fission Barrier
August 24, 1984	N. Takigawa MSU	Effects of Internal Degrees of Freedom on the Heavy-Ion Fusion Cross Section
September 13, 1984	Janos Polonyi Univ. of Illinois	Magnetic Screening in QCD
September 14, 1984	C. F. Liu Kentucky Univ.	Time Dependence of Skyrme Solitons
September 27, 1984	R. Vinh Mau Orsay	Hedgehog-Hedgehog Interaction
September 28, 1984	J. R. Nix LASL	One-Body Dissipation for Fission and Heavy-Ion Reactions

Appendix IV Author Index

Abachi, S. 127, 129
Ahmed, M. 45, 46
Albiston, C.R. 200
Aleklett, K. 95, 107, 112, 113
Andrews, H.R. 73
Andriamonje, S.A. 98
Anholt, R. 98
Äystö, J. 48

Babala, R. 198
Back, N.L. 68
Backlin, A. 71
Bai, X.X. 101
Baktash, C. 71
Banerjee, B. 185
Bangert, D. 105, 120, 121, 124, 210, 211
Bantel, M. 200
Barasch, E. 127, 129
Baron, E. 177
Barwick, S.W. 49, 125
Baumgartner, M. 115, 207, 209
Beckmann, R. 113
Belshe, R.A. 205
Bieser, F. 209
Birchall, J. 66
Bistirlich, J.A. 103, 117
Blaich, Th. 57
Blocki, J. 149
Bock, R. 120
Bossingham, R.R. 117
Bowman, H.R. 93, 98, 117
Brandt, R. 113
Brockmann, R. 105, 108, 120, 121, 124, 210, 211
Brown, L. 195
Brown, R.E. 66
Browne, E. 63
Brüchle, W. 57
Brügger, M. 57
Butler, P.A. 71

Cable, M.D. 45, 46
Carroll, J.B. 127, 129, 130, 131
Cerny, J. 45, 46, 48
Chaki, T. 71
Chan, Y. 84, 200
Claesson, G. 130, 131
Clark, D.J. 195
Clawson, C.W. 117
Cline, D. 71
Conzett, H.E. 66, 67, 68, 69
Cooperstein, J. 177
Countryman, P.J. 200
Crawford, H.J. 115, 207, 209
Crowe, K.M. 103, 117
Czosnyka, T. 71

Dacal, A. 121, 210
Danielewicz, P. 161, 163, 167
Daniels, W.R. 57
Date, S. 166
Deleplanque, M.A. 73, 75, 77, 78, 205
Dersch, G. 113
Diamond, R.M. 71, 73, 75, 76, 77, 78, 205
Dietrich, F.S. 68
Dines, E.L. 73, 75, 77, 78
Doss, K.G.R. 110
Døssing, Th. 77, 151
Dracoulis, G. 71
Draper, J.E. 75, 77, 78
Dufour, J.P. 115, 207

Elo, D. 195

Feige, G. 113
Firestone, R.B. 61, 63
Fisher, P. 127, 129
Fowler, G.N. 191
Fowler, M.M. 57
Frankel, K.A. 117
Friedlander, E.M. 113, 190, 191, 203
Fulton, R.L. 130

Gäggeler, H. 57
Ganezer, K. 127, 129
Ganssauge, E. 113
Gazes, S.B. 200
Ghiorso, A. 51
Ghoniem, M.T. 203
Gilot, J.-F. 130, 131
Girard, J.D. 115, 207
Glendenning, N.K. 170, 178, 180, 185, 186
Gregorich, K.E. 51, 52, 54, 55, 57
Greiner, D.E. 59, 115, 207, 209
Grotowski, K. 84, 149
Gu, J.H. 81, 89, 91
Guarino, G. 84
von Gunten, H.R. 57
Gustafsson, H.-A. 96, 100, 110, 204

Appendix IV Author Index

Gutbrod, H.H. 96, 100, 110, 204
Gyulassy, M. 164, 166, 167, 168

Haas, B. 73
Hallman, T.J. 130, 131
Hamagaki, H. 59, 101, 102, 103
Harris, J.W. 105, 108, 120, 121, 124, 210, 211
Häusser, O. 73
Harvey, B.G. 145, 200
Hashimoto, O. 59, 101, 103, 117
Hasselgren, L. 71
Heckman, H.H. 93, 203
Hendrie, D.L. 130, 131
Herrmann, G. 57
Herrmann, J. 113
Hildebrand, N. 57
Hoffman, D.C. 57
Hoffman, D.H.H. 98
Homeyer, H. 200
Honkanen, J. 45
Howard, W.M. 135
Humanic, T.J. 103, 154

Igo, G. 127, 129, 130, 131
Ingersoll, J.G. 117

Jackson, E.K. 108
Jahn, R. 48
Jongen, Y. 195

Kadota, S. 102
Kahana, S. 177
Karant, Y.J. 93, 203
Kazeminezhad, F. 127
Kimura, K. 101
Kirk, P.N. 108, 130, 131
Kitazoe, Y. 164
Kluge, H. 71
Kobayashi, T. 59, 101, 103, 209
Koike, M. 117
Kolb, B. 96, 100, 110, 204
Kolehmainen, K. 139
Kot, W. 52, 54, 55
Kotlinski, B. 71
Kratz, J.V. 57
Kraus, J.H., Jr. 94
Krebs, G. 108, 130, 131
Kurck, J.M. 117

Kwan, W.P. 54

Lam, R. 195
Lanza, E.G. 154
Larimer, R.M. 66
Lattimer, J. 139
Leander, G.A. 135
Lee, D. 52, 54, 55, 57
Lee, I.Y. 71
Lee, M.K. 205
Leemann, B. 66
Leigh, J. 71
Lemmertz, P.K. 61, 198
Lerch, M. 57
Li Wenxin 52, 54, 95, 112
Lindstrom, P.J. 115, 207, 209
Liu, Z.H. 81, 89, 91
Löhner, H. 96, 100, 110, 204
Loveland, W. 94, 95, 107, 112, 113
Ludewigt, B. 96, 100, 110, 204
Luehring, F. 131
Lund, T. 113
Lyneis, C.M. 195

Macchiavelli, A.O. 73, 75, 77, 78
Madansky, L. 130, 131
Maier, M. 211
Majka, Z. 84
Martoff, C.J. 117
Matis, H. 130, 131
Matsui, T. 180
McDonald, R.J. 73, 82, 89, 91
McDonald, W.J. 117
McGaughey, P.L. 95, 107, 113
McGrath, R.L. 48
McMahan, M.A. 81, 86, 89, 91
McParland, C. 209
Mehrem, R.A. 157
Meyerhof, W.E. 98
Miake, Y. 101, 102
Miller, D. 130, 131
Miller, J. 108, 130, 131
Miller, J.P. 117
Möhring, K. 150
Molitoris, J.M. 98
Möller, P. 135, 137, 142
Moltz, D.M. 48
Moody, K.J. 54, 55, 57
Morenzoni, E. 98
Moretto, L.G. 81, 82, 84, 86, 88, 89, 91, 153, 154, 159

Appendix IV Author Index

Morris, D. 195
Morrissey, D.J. 82, 84, 107
Muehry, H. 75
Mulera, T. 127, 129, 130, 131
Murphy, D.L. 117
Murphy, M.J. 200
Musser, J.A. 58, 125
Mustafa, M.G. 86
Myers, W.D. 137, 138, 142, 143

Nagamiya, S. 59, 101, 102, 103
Nakayama, K. 103
Newton, J.O. 71
Nitschke, J.M. 61, 197, 198
Nix, J.R. 135
Nojiri, Y. 59

Odyniec, G. 105, 120, 121, 124, 161, 210, 211
van Oers, W. t. H. 66
Olson, D.L. 115, 207
Ortiz, M. 121, 210

Pacheco, A.J. 82
Padgett, M.L. 81, 86, 89, 91
Perez-Mendez, V. 127, 129, 130, 131
Peterson, R. 195
Phillips, W.R. 71
Planeta, R. 84, 149
Plümer, M. 191
Porile, N.T. 113
Poskanzer, A.M. 96, 100, 110, 204
Prakash, M. 139
Price, P.B. 49
Pugh, H.G. 105, 108, 120, 121, 124, 130, 131, 210, 211

Radi, H.M.A. 157
Rafelski, J. 186
Randrup, J. 148, 150, 151
Rasmussen, J.O. 93, 98, 103, 117, 157
Rauch, W. 105, 120, 121, 124, 210, 211
Ravn, H.L. 49
Reiff, J.E. 45, 46, 48
Renfordt, R.E. 105, 120, 121, 124, 210, 211
Renner, T. 96, 100, 110, 204
Renteln, P. 108
Riedesel, H. 96, 100, 110, 204
Rioux, C. 67, 68
Ritter, H.G. 96, 100, 110, 204
Roche, G. 108, 130, 131
von Rossen, P. 66
Russo, P. 71

Sandoval, A. 105, 120, 121, 124, 210, 211
Sano, M. 164
Schädel, M. 57
Schall, D. 105, 120, 121, 124, 210, 211
Schloemer, E.C. 45, 46
Schnetzer, S. 102
Schroeder, L.S. 105, 108, 120, 121, 124, 130, 131, 210, 211
Seaborg, G.T. 52, 54, 55, 57, 94, 95, 107, 112, 113
Shapiro, G. 101
Shi, Y.-J. 144, 148
Shida, Y. 59, 101, 102, 103
Shor, A. 127, 129, 131
Sie, S. 71
Siemiarczuk, T. 204
Signarbieux, C. 81, 89, 91
Simon, R.S. 71
Sobotka, L.G. 81, 82, 84, 86, 88, 89, 91, 159
Soni, V. 185
Sprinkle, J.K. 71
Srebrny, J. 71
Stager, C.V. 73
Steiner, H. 102
Stepaniak, J. 204
Stephens, F.S. 71, 73, 75, 76, 77, 78, 205
Stephenson, E.J. 66
Stevenson, J.D. 49, 58, 125
Stock, R. 105, 120, 121, 124, 210, 211
Stokstad, R.G. 84, 200
Stoller, Ch. 98
Ströbele, H. 105, 120, 121, 124, 210, 211
Sümmerer, K. 57
Sugimoto, K. 59
Sullivan, J.P. 117
Sumiyoshi, H. 166
Świątecki, W.J. 138, 142, 143, 144, 149, 150
Symons, T.J.M. 115, 207
Szczodrak, M. 84

Takahashi, N. 59
Tanihata, I. 59, 101, 102, 103
Taras, P. 73
Trautmann, N. 57
Treiner, J. 139, 142, 143
Trentalange, S. 127, 129, 130, 131

Appendix IV Author Index

Treuhaft, R.N. 108
Truöl, P. 117
Tserruya, I. 84, 200

Van Bibber, K. 200
Vater, P. 113

Wakai, M. 164
Wald, S. 84, 200
Wang, C.S. 138
Ward, D. 73
Warwick, A.I. 93, 96, 100, 110, 204
Watson, J.W. 66
Weiner, R.M. 191
Weiss, M.S. 143
Welch, R.B. 52, 54, 55, 57
Wieman, H. 96, 100, 110, 204
Willmarth, P.A. 61
Wirth, G. 57
Wolf, K.L. 108, 120, 124, 211
Wozniak, G.J. 81, 82, 84, 86, 89, 91, 153
Wu, C.Y. 71

Xu, J.-S. 98
Xu, X.J. 48
Xu, Z.-Z. 93, 98

Yamakawa, O. 59, 103
Yao, Z.Q. 81, 89, 91
Yashita, S. 51
Yoo, E. 117
Yoshikawa, N. 59, 103

Zajc, W.A. 117
Zhou, Z.Y. 45, 46
Zielińska-Pfabé, M. 150

This report was done with support from the Department of Energy. Any conclusions or opinions expressed in this report represent solely those of the author(s) and not necessarily those of The Regents of the University of California, the Lawrence Berkeley Laboratory or the Department of Energy.

Reference to a company or product name does not imply approval or recommendation of the product by the University of California or the U.S. Department of Energy to the exclusion of others that may be suitable.

Lawrence Berkeley Laboratory
Technical Information Department
University of California
Berkeley, California 94720